University of Nottingham

School of Chemistry

Sugar-derived Compounds for Gelation of Various Solvents and Forming Supramolecular Dual-Network Materials for 3D Printing Applications

By

Glenieliz Dizon
4343574

ABSTRACT

Low molecular weight gelators (LMWGs) are a class of organic compounds with molecular weights of less than 2000 Da that show gelation behaviour in a solvent. In recent years, LMWGs have been the subject of intensive research from material, synthetic, supramolecular, and biological chemists. They are an essential class of functional materials, finding applications in various industries such as cosmetics, food processing, healthcare and many more. During the development of soft material systems inspired by green chemistry, this research shows that naturally occurring starting materials can prepare benzylidene sorbitol and xylitol derivatives. These compounds gelate a range of organic solvents, aqueous mono- and divalent salt solutions, photocurable monomers, DMSO/water solutions, and ethanol-water solutions, with the equimolar mixture of two of the gelators gelling all compositions from 100% ethanol to 100% water (something neither of the individual components does). We explored the influence of modifications to the acetal substituents on the formation of the compounds and the impact of steric bulk on the self-assembly properties of the gelators. The effect of solvent on the self–assembly, morphology, and rheology of the 1,3:2,4-di(4-isopropylbenzylidene)-D-sorbitol (DBS-iPr), 2,4(4-isopropylbenzylidene)-D-sorbitol (MBS-iPr) and the equimolar multicomponent (DBS-MBS-iPr) gels have been investigated using scanning electron microscopy (SEM). By virtue of lamellar segregation of hydrophilic and hydrophobic regions of the molecules, DBS-iPr gelates polar solvents to form smooth flat fibres. In non-polar solvents such as cyclohexane, aided by strong hydrogen bonding interactions, it results in helical fibres where the chirality is determined by the stereochemistry of the sugar. Oscillatory rheology revealed that MBS-iPr gels have appreciable higher strength and elasticity than DBS-iPr gels, regardless of the solvent medium employed. Powder X-ray diffraction was used to probe the arrangement of the gelators in the xerogels they form, and two single-crystal X-ray structures of related MBS derivatives give the first precise structural information concerning layering and hydrogen bonding in the monobe highernzylidene sorbitol compounds. This kind of layering could explain the apparent self-sorting behaviour of the DBS-MBS-iPr multicomponent gels.

Furthermore, thixotropic and 'self-healing' behaviour were observed on some gels formed in DMSO:H_2O ratios and an alkyl monomer, ethyl acrylate, by recovering their 3D network after strong mechanical shaking. Few of the monomer gels were photo polymerised to form dual-network materials. These composites were characterised using infrared spectroscopy and dynamic mechanical analysis to identify how the gelators affect the polymer material. Depending on the monomer used, some gelators act as good rheological modifiers for the photocurable monomers, improving the material's storage modulus. A xylitol-based di-acid gelator, DBX-CO_2H, showed instant gelation abilities in water-miscible

photocurable monomers *via* pH switch. A formulation of DBX-CO$_2$H in 2-hydroxyethyl acrylate(HEA):H$_2$O improved the surface adhesion and increased the viscosity of HEA. With these results, success was found in identifying a printable photocurable HEA ink for reactive inkjet 3D Printing. After a few optimisations, a pattern was 3D printed layer-by-layer using the di-acid gelator as a significant rheological modifier. The combination of sorbitol/xylitol-derived gelators reported in this work could find potential applications as a single or multicomponent system in different fields such as soft materials for personal care products, polymer nucleation/clarification, and energy technology.

ACKNOWLEDGMENTS

DECLARATION

The work described in this thesis was conducted at the University of Nottingham, School of Chemistry, between October 2018 and November 2021. I, Glenieliz Dizon, declare that the work is my own and has not been submitted for a degree of another university.

Symbols, Nomenclature and Abbreviations

*	=	denotes a chiral centre
δ	=	chemical shift in parts per million
%	=	percent
°C	=	degree Celsius
3D	=	3-dimensional
3DP	=	3-dimensional printing
4-TSA	=	4-toluenesulfonic acid monohydrate
Ar	=	argon
AM	=	additive manufacturing
AMA	=	allyl methacrylate
BA	=	butyl acrylate
BMA	=	benzyl methacrylate
br	=	broad peak
Bn	=	benzyl
CAD	=	computer-aided design
CAM	=	computer-aided manufacturing
CD	=	circular dichroism
$CDCl_3$	=	chloroform-*d*
CHMA	=	cyclohexyl methacrylate
ClHPMA	=	3-chloro-2-hydroxypropyl methacrylate
CTAB	=	cetyl-trimethyl ammonium bromide
DBS	=	dibenzylidene sorbitol
DBX	=	dibenzylidene xylitol
DCM	=	dichloromethane
DED	=	directed energy deposition
d	=	doublet
dd	=	doublet of doublet
ddd	=	doublet of doublet of doublet
d.e	=	diastereoisomeric excess
dEAmEMA	=	2-(diethylamino)ethyl methacrylate
dEGdMA	=	di(ethylene)glycol dimethacrylate
DEGMEMA	=	diethylene glycol methyl ether methacrylate
DETX	=	2,4-diethyl-9H-thioxanthen-9-one
DMF	=	*N,N*-dimethyl formamide
DMSO	=	dimethyl sulfoxide
dt	=	double triplet

e.e.	=	enantiomeric excess
EA	=	ethyl acrylate
EBM	=	electron beam melting
EDB	=	ethyl 4-(dimethylamino)benzoate
EGdCEA	=	ethylene glycol dicyclopentenyl ether acrylate
EGdMA	=	ethylene glycol dimethacrylate
EGMEMA	=	ethylene glycol methyl ether methacrylate
EGPhEMA	=	ethylene glycol phenyl ether methacrylate
EHMA	=	2-ethylhexyl methacrylate
EMA	=	ethyl methacrylate
EWG	=	electron withdrawing group
FDM	=	fused deposition modelling
FN	=	fibronectin
g	=	gram
G′	=	storage modulus
G″	=	loss modulus
G (O)	=	opaque gel
G (T)	=	transparent gel
GdL	=	glucuno-d-lactone
HA	=	hexyl acrylate
HBMA	=	hydroxybutyl methacrylate
HddA	=	1,6-hexanediol diacrylate
HEA	=	hydroxyethyl acrylate
HEAm	=	2-hydroxyethyl acrylamide
HEMA	=	2-hydroxyethyl methacrylate
HMA	=	hexyl methacrylate
HPA	=	hydroxypropyl acrylate
hrs	=	hours
Hz	=	hertz
I	=	insoluble
iBA	=	*iso*-Butyl acrylate
iBnA	=	*iso*-Bornyl acrylate
iBnMA	=	*iso*-Bornyl methacrylate
iDMA	=	*iso*-Decyl methacrylate
iPr	=	*iso*-Propyl
IR	=	infra-red
J	=	coupling in hertz
LAM	=	laser additive manufacturing

LENS	=	laser engineered net shaping
LMA	=	lauryl methacrylate
LMWGs	=	low molecular weight gelators
LOM	=	laminated object manufacturing
LVER	=	linear viscoelastic region
m	=	multiplet
MA	=	methyl acrylate
MBS	=	monobenzylidene sorbitol
MDA	=	D-mannitol diacetonide
MDP	=	D-mannitol diphenyl
Me	=	methyl
ME	=	material extrusion
mg	=	milligram
MHz	=	megaHertz
mins	=	minutes
MJ	=	material jetting
mL	=	millilitre
MMA	=	methyl methacrylate
mmol	=	millimole
Mp.	=	melting point
NMR	=	nuclear magnetic resonance
PBA	=	poly(butyl acrylate)
PCHMA	=	poly(cyclohexyl methacrylate)
PEA	=	poly(ethyl acrylate)
PEGdCEA	=	poly(ethylene glycol dicyclopentenyl ether acrylate)
PG	=	partial gel
Ph	=	phenyl
PhMA	=	phenyl methacrylate
PHA	=	poly(hexyl acrylate)
PHEA	=	poly(2-hydroxyethyl acrylate)
PiBnA	=	poly(isobornyl acrylate)
PMA	=	poly(methyl acrylate)
ppm	=	parts per million
PXRD	=	powder X-ray diffraction
q	=	quartet
RBF	=	round-bottomed flask
rt	=	room temperature
s	=	singlet

S	=	solution
SEM	=	scanning electron microscope
SHS	=	selective heat sintering
SLM	=	selective laser melting
SLS	=	selective laser sintering
spt	=	septet
t	=	triplet
THF	=	tetrahydrofuran
TLC	=	thin layer chromatography
TriCdMdA	=	tricyclo[5.2.1.02,6]decanedimethanol diacrylate
triMOSiPMA	=	3-(trimethyloxysilyl)propyl methacrylate
TriPGdA	=	tripropylene glycol diacrylate
UV	=	ultra violet
w	=	weak

Table of Contents

List of Figures

Chapter 3

Chapter 4

Chapter 5

List of Tables

Chapter 2

Chapter 3

Chapter 4

Chapter 5

List of Schemes

Chapter 1

Chapter 2

Chapter 3

Chapter 4

Chapter 5

CHAPTER ONE

Introduction

1.1 Introduction to Gels

A gel is a colloid in which the majority disperse phase (fluid) in combination with the minority continuous phase (solid), form a three-dimensional (3D) network resulting in a colloidal suspension, shown in Figure 1.1. The composition of the heterogeneous biphasic system distinguishes the gel from ordinary solids and liquids; the heterogeneous biphasic system is also responsible for the unique viscoelastic behaviour of these systems.[1] Gels are encountered on a day to day basis, however, they are not acknowledged as such. These interesting solid-like materials containing mostly liquid have developed not only as an academic interest but also in industry on account of their applications. Such applications can be found in cosmetics[2] (e.g. emollients), food processing,[3] health care[4] (e.g. medicine) and in a lot more fields that are permeated in everyday life.[5] Flory[6] defined a gel with the utmost simplification stating that a substance is classified as a gel when these two conditions are met: (i) the substance must have a continuous structure with macroscopic dimensions and (ii) the rheological and mechanical properties of the material should be solid-like. Gels are materials with solid-like flow properties despite being mostly liquid in composition, which is why these materials are truly interesting. The gel state arises when the solvent is immobilised (at the macroscopic level) *via* surface tension by an elastic cross-linked network.[7] This structure may be a covalent/physical aggregation polymeric network or lamellar structure. At the same time, the liquid phase often prevents the collapse of the network.
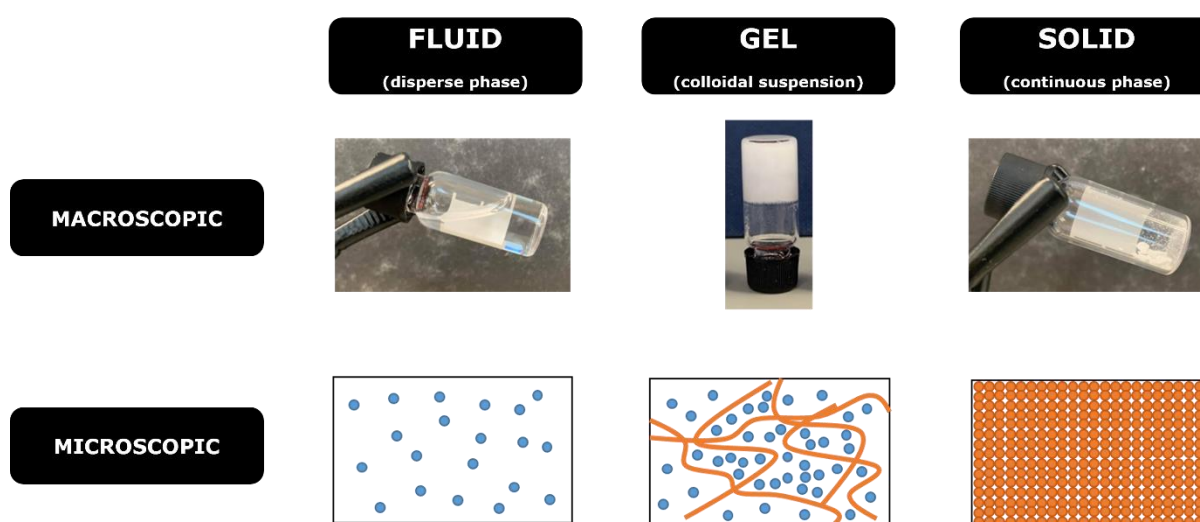
Figure 1.1 | Macroscopic and microscopic level of fluid, gel and solid states

1.1.1 Gel Classification

A fluid and an elastic cross-linked network are encompassed in gels. The elastic cross-linked network traps the solvent *via* surface tension and prevents the fluid from flowing.[7] The solid-like appearance of gel results from the entrapment and adhesion of the liquid in the large surface area solid 3D matrix. The origin, constitution and the type of cross-linking that create the gels 3D network and the medium they hold are the major factors considered for the classification of gels (Figure 1.2). A gel having a solvent medium of organic solvent (e.g. THF, toluene or cyclohexane) is called an organogel. In addition, if the medium is aqueous or water with a minor component of an organic solvent (e.g. ethanolic solutions), the gel is classified as a hydrogel. Hydrogels have shown potential applications in drug delivery[8], wound healing[9] and tissue engineering[10]. Furthermore, a gel with no liquid medium between the solid phase is called an aerogel (gas used as the dispersed phase – obtained by solvent displacement using gas at supercritical conditions) or xerogel (liquid dispersed phase evaporated). The aerogel retains the shape of an expanded network observed in the gel, whereas for xerogels, the 3D network shrinks when the solvent is evaporated.

GELS

Source

Natural   Artificial

Fluid Medium

Organo   Hydro   Aero

Supramolecular   Macromolecular

Cross-Linking
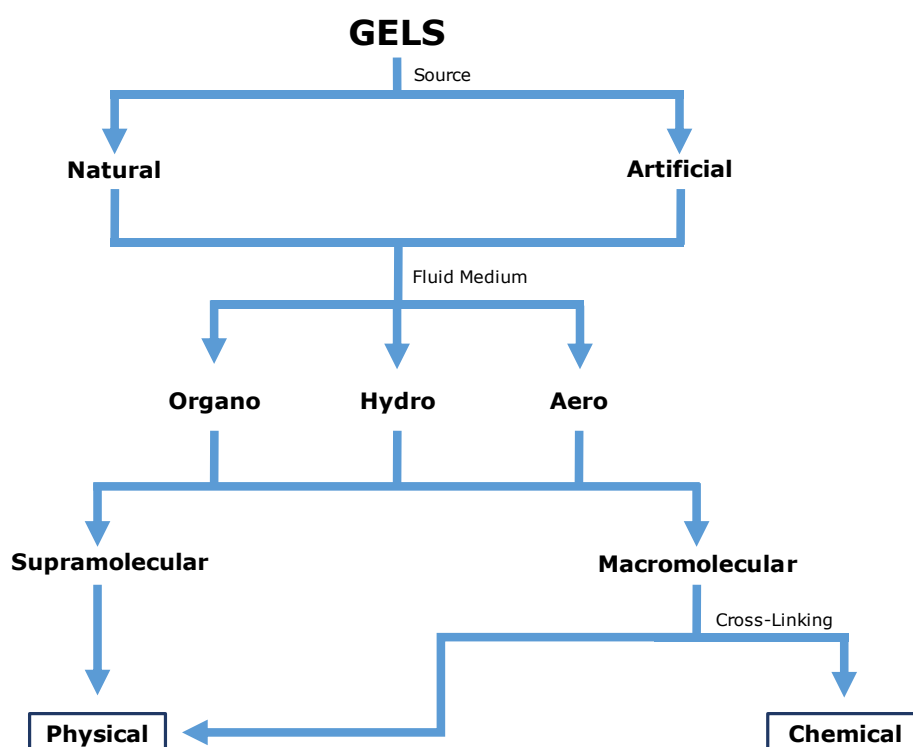
Physical   Chemical

Figure 1.2 | Classification of gels

The gel network can form through covalent chemical cross-linking or non-covalent physical interactions. Chemical gels are cross-linked covalently, and therefore the gelation is irreversible.[9] Meanwhile, physical gels are formed by non-covalent or physical interactions

such as hydrogen bonding, van der Waals interactions, π-π stacking, donor-acceptor interactions, dipole-dipole interactions and metal coordination. Due to the non-covalent interactions, physical gels are thermally reversible and easily liquefied by heating.[11,12]

1.1.2 Methods of Gelation

Changing the solubility of the gelator in a solvent medium is the main factor in gelation tests. As the gelator comes out of the solution, it will self-assemble and form network fibres (forming the gel) that immobilise the solvent. Stimuli such as sonication[13], light[14], pH change[15], temperature change[16] and addition of an enzyme[17] can induce gelation.

The most common and used gelation technique is the temperature change. For this method to be successful, the gelator must have a solvent that it is partially soluble in. When the gelator in the solvent medium is heated, solubility increases and allows the gelator to dissolve fully (giving the sol form). Then, as the solution is allowed to cool, solubility decreases. The gelator precipitates back out of the solution inducing the gelator to self-assemble into a supramolecular network (mostly fibrous). It then traps the solvent medium and forms the gel (giving the gel form).[7] The temperature at which the network starts to form a gel is called the gel transition temperature, T_{gel}. For physical gels, heating the gel for a second time will revert it back to the sol form.

One of the simplest tests for gel properties is the inversion test (Figure 1.3). This approach is when a tube or a vial containing the 'gel' sample is inverted. The sample has 'passed', and gelation is assumed to be successful if the gel sample does not exhibit gravitational flow in the inverted vial.
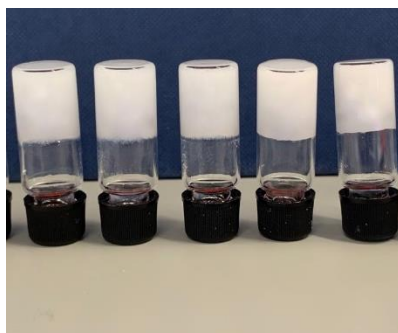
Figure 1.3 | Gel containing vials passing the inversion test

1.2 Green Gels

As we face challenging environmental problems, interest in sustainable solutions in all areas of science is growing, and in the context of this research in particular in the field of sol-gel science.[18] Within this area, a contemporary challenge is to target existing sustainable feedstocks to synthesise supramolecular gelators.[19,20] The incorporation of

environmentally friendly approaches guided by the principles of green chemistry can give alternatives to the more conventional chemical designs, reducing or eliminating the use of hazardous and toxic solvents.[21,22] A wide range of naturally occurring molecular motifs, including polysaccharides (alginates[23] and carrageenans[24]), ureas[25], sugars[15,26,27], steroids[28], peptides[29], acids (for example gallic acid derivatives[30–32]) and other naturally occurring compounds have proven their potential as gelators.[33]

1.2.1. 'Macromolecular' Polymer Gels

Polymer gels are three-dimensional materials composed of macromolecules or aggregates that immobilise a large amount of solvent. They usually represent a polymer-solvent system.[34] All existing polymer gels are split into two types (Figure 1.4), thermally irreversible (chemical gel) or thermoreversible (physical gel).[34]
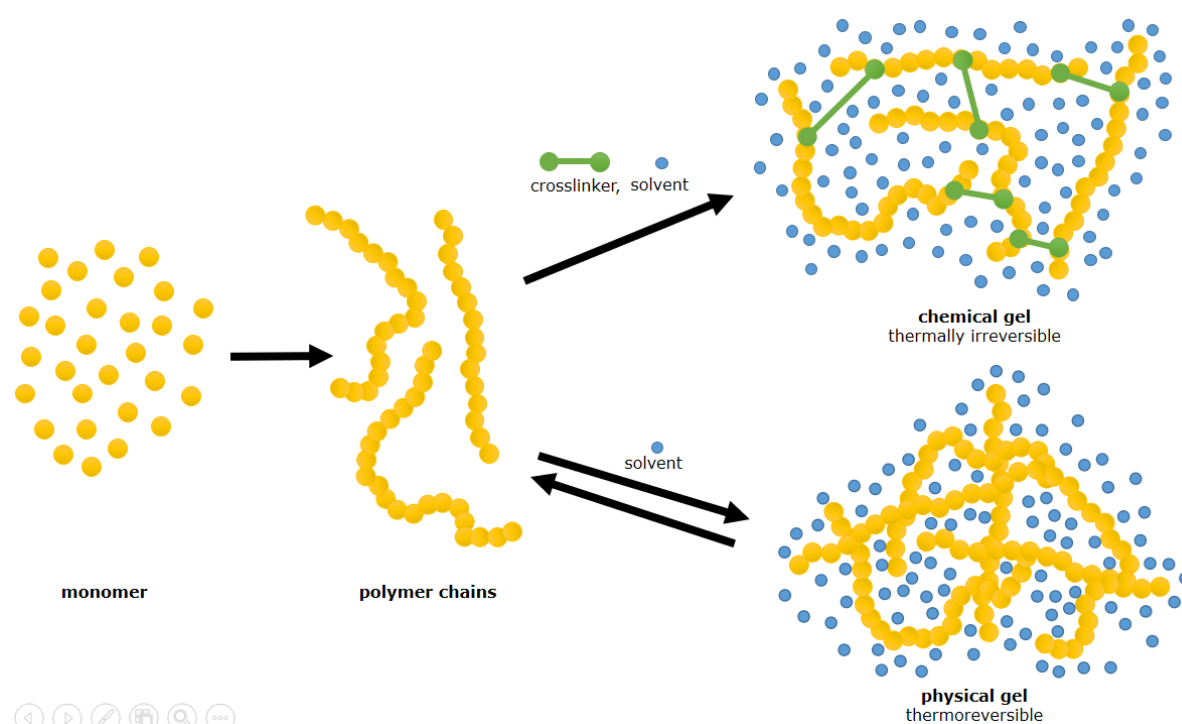
Figure 1.4 | Representation of the two types of polymer gelators

Polystyrene, **1**, and poly(methyl methacrylate), **2**, and the most common gelators such as agarose, **3**, and gelatin, **4**, are examples of thermoreversible PGs. Polystyrene is one of the most versatile polymers that have several stereoisomers. Kobayashi *et al.*[35] worked around syndiotactic polystyrenes and reported that they gelate in chloroform, carbon tetrachloride, and benzene, classifying them as organogelator. Similarly, Saiani and coworkers[36,37] focused their research on poly(methyl methacrylate) (PMMA) and reported that syndiotactic PMMA forms a thermoreversible organogel in bromobenzene, chlorobenzene and toluene. It was proven that the formed chains were rigid due to their helical conformation. In 2010, Song *et al.*[38] incorporated agarose into their self-assembled

gels to provide mechanical robustness and stability. Gelatin is an animal protein produced from collagen; it consists of a long α helix with high glycine content. Its chemical structure has been described in detail since the 1950s.[39] It was proven that gelatin chains can form physical interactions *via* helices in their junction zones which are stabilised by hydrogen bonds at adequately low temperatures.
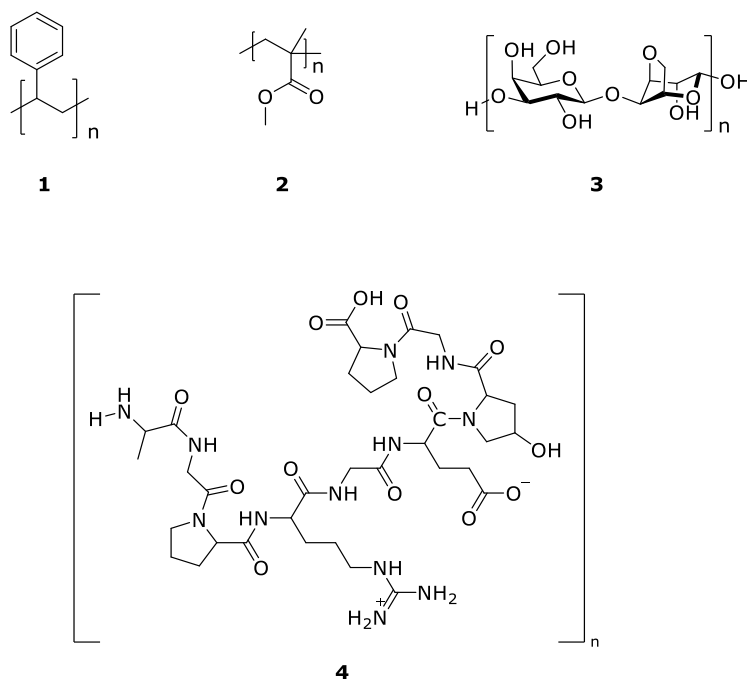
Figure 1.5 | Examples of 'macromolecular' polymer gelators

Furthermore, alginate is an example of a polysaccharide polymer gel with favourable properties, including biocompatibility and ease of gelation; therefore, they are found in numerous biomedical science and engineering applications.[40] Alginates, **5**, are naturally present in brown seaweed cell walls, and they can be produced as an extracellular material by bacteria that are abundant in vegetative grown cells.[41] Lee *et al*.[40] have written a review on the properties and biomedical application of alginate where they mentioned four various approaches to cross-link alginate chains: (i) ionic cross-linking, (ii) covalent cross-linking, (iii) thermal gelation and (iv) cell cross-linking. Furthermore, carrageenan is another example of a polysaccharide polymer gel widely used in the food industry (mainly in dairy and meat products) due to its strong interactions with protein. Carrageenans are extracted from red seaweeds.[42] In 1984, Rochas and Rinaudo[43] reported the mechanism of gel formation in κ-Carrageenan, **6**, which is based on the aggregation of helical dimers.

5   **6**
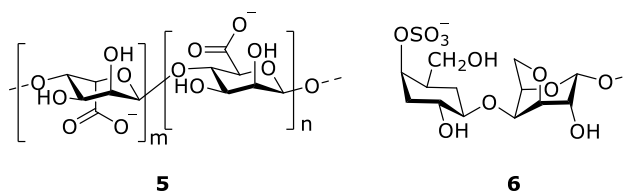
Figure 1.6 | Structure of alginate and κ-Carrageenan

PGs often form relatively robust networks, which is an excellent advantage in the field of gelators. Unfortunately, they are sometimes unresponsive to stimuli, which can be difficult to modify, enhance, or develop the compound and add the desired properties.

1.2.2.   'Supramolecular' Low Molecular Weight Gelators

Low molecular weight gelators (LMWGs) have gained increasing attention as an alternative to polymer derived gels. LMWGs can be more responsive to stimuli, which aid in modifying, enhancing, or developing additional desired properties to the systems. Furthermore, molecular subunits in polymer gels are relatively large in comparison to LMWGs. The syntheses of derivatives of these naturally occurring compounds and identifying LMWGs has been the focal point in the field of sustainable gelators.[44,45] The hierarchical process of self-assembly of LMWGs (Figure 1.7) shows that the gel fibres that immobilises the surrounding solvent medium are developed by fibrils that were established by the combination of non-covalent interactions of the gelator molecules.
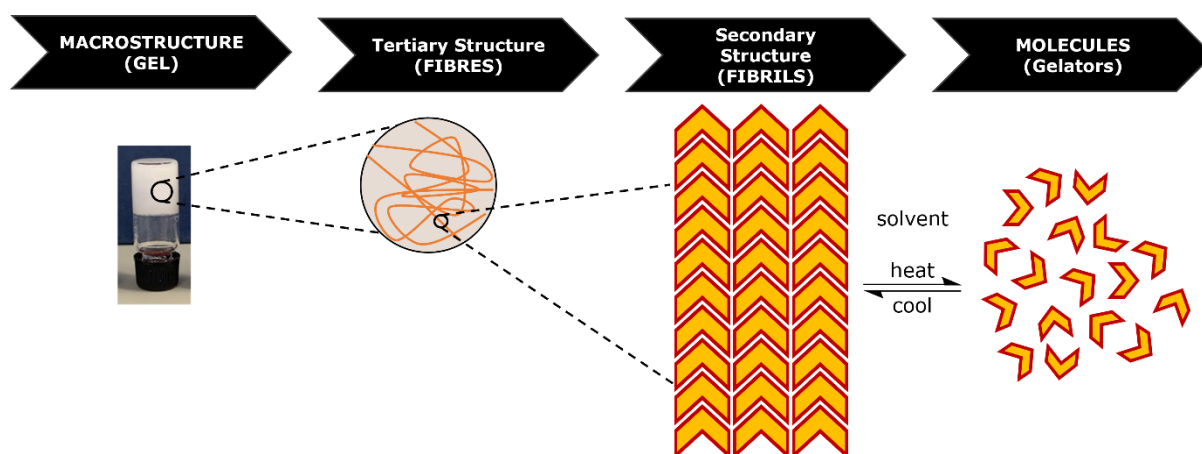
Figure 1.7 | Low molecular weight physical gelators reversible network connections

1.2.2.1 Amino Acid and Amine Derived LMWGs

Many new gelators can be designed by modifying amino acids. Bhattacharya[46] discovered the efficiency of *N*-lauroyl-L-alanine and its derivatives (**7 – 11**) in forming a gel in various

organic fluids (including oils). They reported that gelator **7** is an effective system for the selective gelation of non-polar organic solvents. Furthermore, organogelator **7** was described as the first organogelator capable of achieving solvent-specific gelation from a two-phase mixture at room temperature.
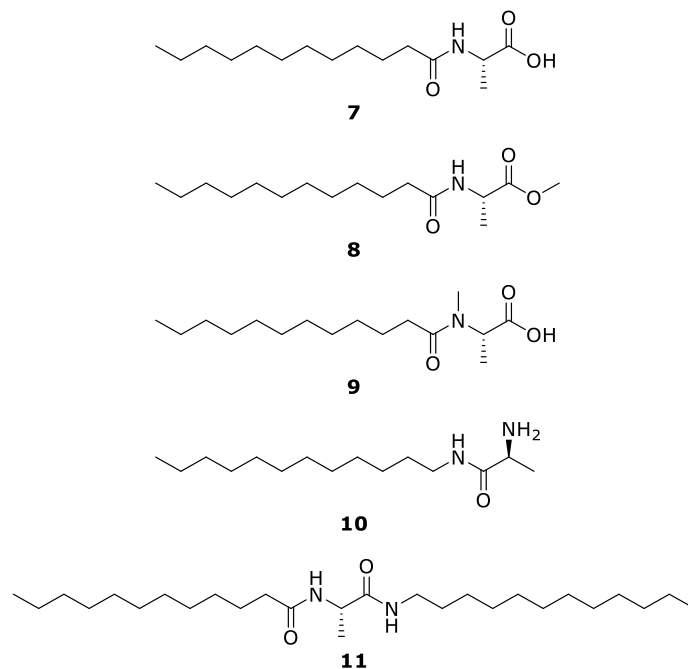
Figure 1.8 | *N*-lauroyl-L-alanine and its derivatives

In 2017, Lu *et al*.[47] synthesised an amino acid-based gelator for injectable and multi-responsive hydrogel (Figure 1.9, compound **12**). They designed the gelator to possess thermo-, photo- and pH-responsive properties and it was investigated as a thixotropic compound. The team believes that this gel could be good for potential use in tissue engineering and drug delivery. Another amino acid-derived urea was presented as a supramolecular gel lubricant by Liu *et al*.[48]. The gelator has also displayed good thixotropic characteristics that became mobile under shearing, restraining base oil creeping, oil permeation or leakage – especially for the gears and rolling bearings.

12
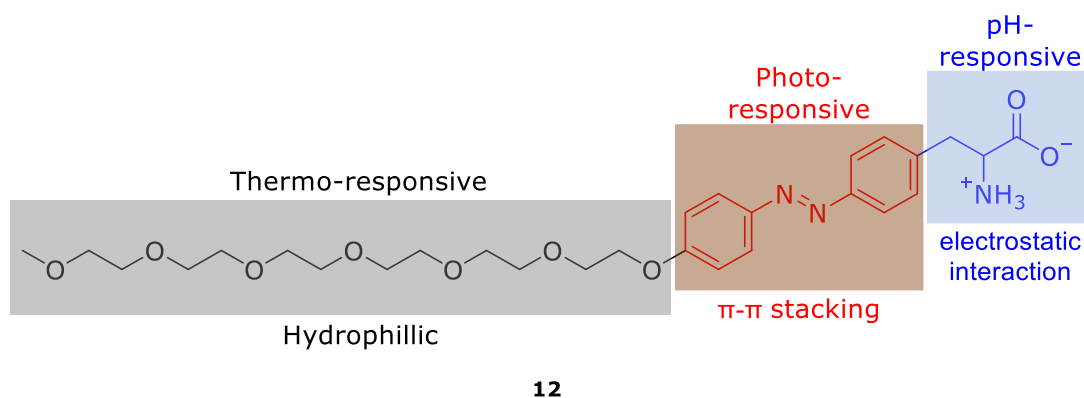
Figure 1.9 | Molecular structure of AA-Azo-EG$_6$ gelator showing the photoreactive groups and the interaction they contribute to self-assembly.[47]

Hum *et al.*[49] added an amino acid-based organogelator to the literature in 2020. They have investigated *N*-fatty amino acid amide, **12b**, where the substitution of an acid group with a primary amide has improved gelation properties of the compound. The studied gelators further displayed gelation abilities in oils and classified the gelator as oleogelators which may be good for oil spill remediation applications. Briefly, in designing a potential gelator, using an amino acid gets the potential diversity of gelators due to how relatively simple introducing a substituent on the functional groups at the end of the molecule. Furthermore, amino acids are all chiral, having D and L isomers.

12a   **12b**

R = ala, val, leu, phe
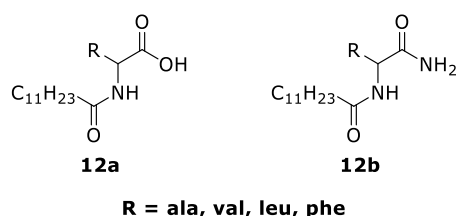
Figure 1.10 | *N*-fatty amino acid organogelators[49]

1.2.2.2 Acid Derived LMWGs

Gallic Acid, **13**, is a member of the hydroxybenzoic acids occurring mostly in red fruits, black radish and onions.[50] It is a well-known natural antioxidant that has been used as a building block for LMWGs. Faggi *et al.*[30] isolated fluorous derivatives of gallic acid as LMWGs (**14a-c**). In their study, alkyl analogues instead of semiperfluoroalkyl chains did not exhibit any gelation properties, hence revealing the crucial role of perfluorinated chains in the self-assembly of these compounds. Another fluorescent gelator was synthesised by Cao *et al.*[32] using a simple Knoevenagel condensation reaction. The fluorescent gelator, **15**, self-assembles into nanofibers or microspheres depending on the solvent used to

gelate the material. They also prepared a multifunctional supramolecular self-assembly system based on azobenzene and gallic acid derivative, **16**. The material can be used to detect Hg^{2+}, Fe^{3+} and Cu^{2+} in a solution.[31] Overall, over the past century, a wide range of molecular motifs and naturally occurring compounds have proven their potential as gelators.
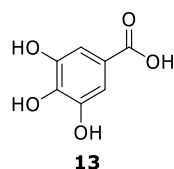
Figure 1.11 | Structure of Gallic Acid
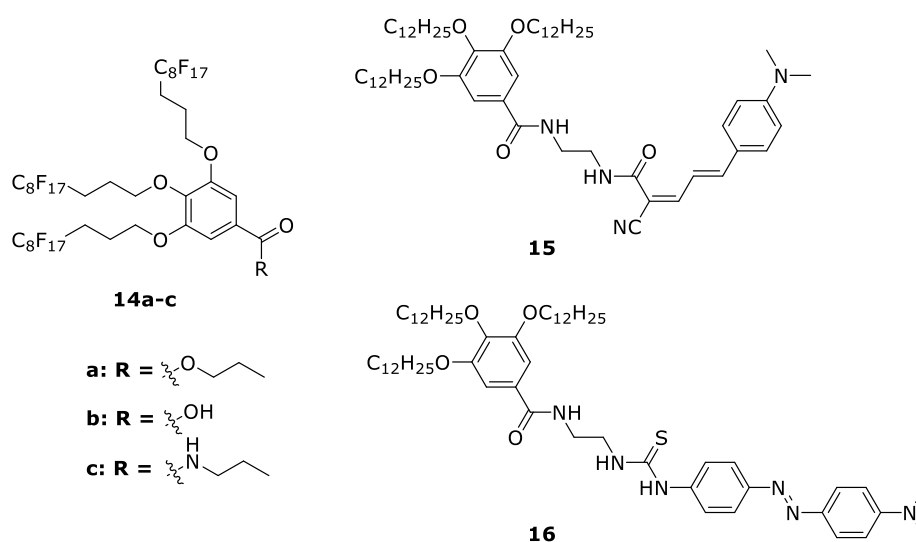
Figure 1.12 | Examples of gallic acid derivatives that act as gelators[30–32]

1.2.2.3 Carbohydrate Derived LMWGs

Carbohydrates (*i.e.* sugars or starches) have become an attractive feedstock for designing and producing LMWGs because they are natural, inexpensive, and renewable with high biocompatibility and low environmental impact.[51] Generally, sugar is a source of energy to organisms, and glucose plays a role in the metabolism of organisms. Sugar derived gels have significant advantages as most of them are biocompatible, biodegradable, non-toxic, eco-friendly, have good structural diversity and also chiral self-assembly.[52] These advantages impact the importance of sugar-based gelators research in the sol-gel field. Furthermore, sugar compounds are commonly used as building blocks for LMWGs because of the hydroxyl groups that can be readily functionalised and can easily form hydrogen

bonds, which will be very useful in gel formation. Different approaches were taken to modify carbohydrate structures.

Shimizu and co-workers[53] synthesised an amphiphilic new sugar-based gelator, **17**, which was found to gelate in both organic solvent and water. They functionalised to glucose with a long alkyl chain to isolate the amphiphilic gelator. Furthermore, Amanokura *et al.*[54] prepared sugar-based gelators (**18-21**) using galactose and glucose. The gelation of these compounds was reinforced by hydrogen bonding interactions and metal coordination. They reported that the addition of $AgNO_3$, $CoCl_2$ or $CdCl_2$ improved the T_{gel} values of the gel in ethanol.
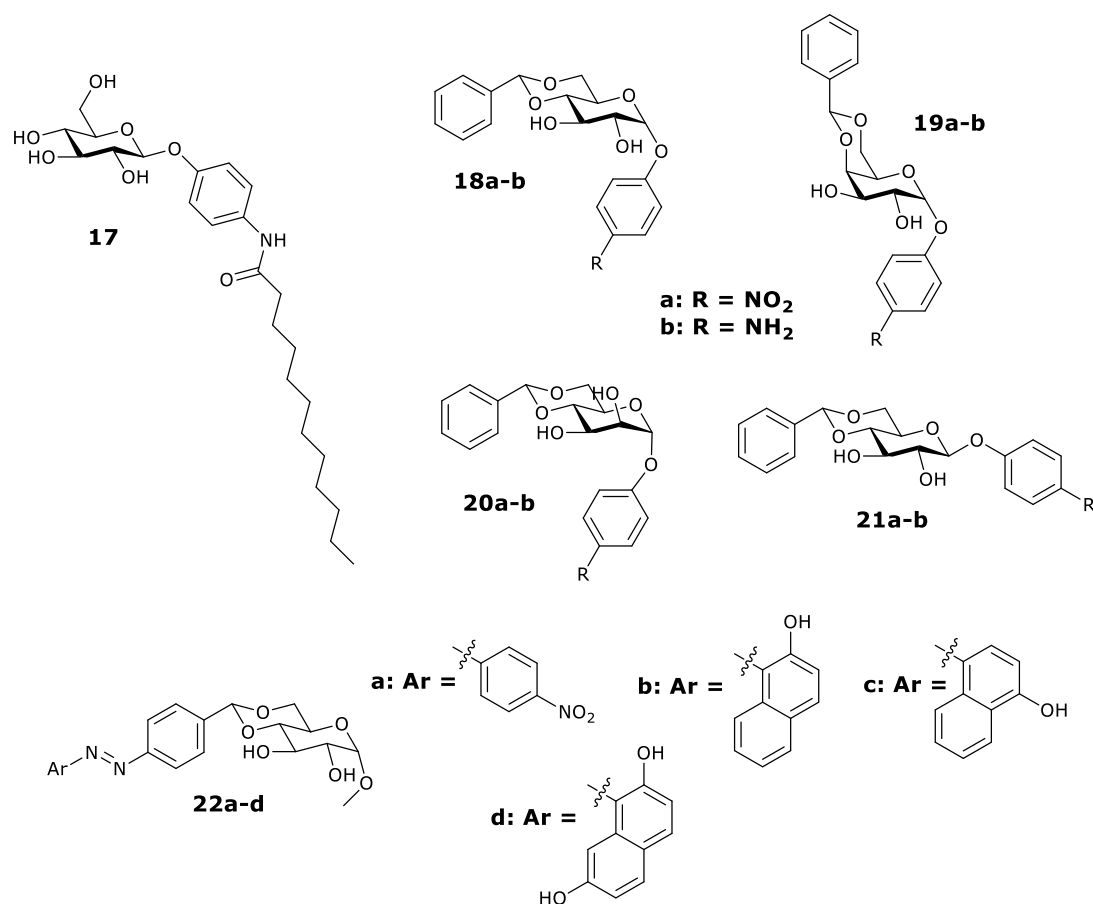
Figure 1.13 | Examples of sugar derived gels[53–55]

Sugar derived gelators can also be used as dyes and pigments, Khayat *et al.*[55] isolated sugar-based azo dyes as multi stimuli-responsive supramolecular gelators and chemosensors (**22a-d**). They have classified compounds **22b** and **22d** as supergelators as they form gels at concentrations equal to or less than 1.0% w/v. Furthermore, it is revealed that the gelators **22b** and **22d** form gels at a pH range of 1.6 – 12.4; any pH outside the range, the gels transform to a sol state.

In 2001, Shinkai *et al.*[56] designed a sugar-appended porphyrin gelator, **23**. Porphyrin has a conjugated structure that provides π-π stacking interactions. However, there is nothing in the literature that shows porphyrin forms a gel in any solvent on its own. Therefore, Seiji Shinkai's group introduced a carbohydrate, *β*-D-galactopyranoside groups, in porphyrin.[56] They stated that the gelator aggregate in a one-dimensional direction, resulting in very robust gels in organic solvents. The carbohydrate provides hydrophilic properties into the porphyrin structure, which induce hydrogen bonding. The gelator's spectroscopic studies support the gelator π-π stacking interaction among porphyrin moieties and the hydrogen bonding interactions among sugar moieties that form a stable one-dimensional aggregate structure (Figure 1.14).
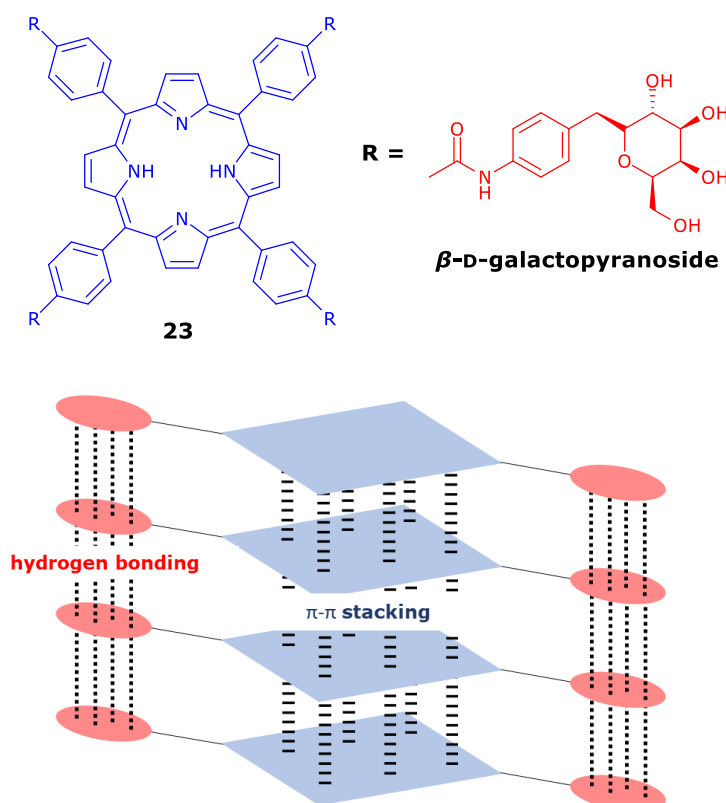
Figure 1.14 | Molecule structure of sugar-appended porphyrin gelator and the interaction for self-assembly into a one-dimensional aggregate.[56]

The hydrophobic interaction is a factor just as crucial as hydrophilic interaction in forming gels. As sugars are usually very polar due to the amount of hydroxyl groups in the molecule, introducing a long chain into the sugar structure has been an interest in balancing the polarity. In 2004, long-chain alkane and alkenes were linked to the *β*-hydroxyl group in glucose to form aryl glycolipids by Shimizu *et al.*[57] They synthesised three aryl glycolipids (**24a-c**) to study the unsaturation effect on gelation behaviours. The gelation test displayed that the increase of unsaturation decreases the gelation ability of the compound where compounds **24a** and **24b** could both form gels in alcohol/water mixture and various organic solvents, whereas **24c** was not able to form a gel in any of

the tested solvents. The gelling compound with a saturated long-chain, **24a**, showed a higher T_{gel} value than the gel formed by **24b**, meaning that the increase of saturation also decreases the thermal stability of the molecule. X-ray diffraction was measured for **24a** and **24b**, where it displayed how the compounds self-assemble *via* non-covalent interactions. Compounds **24a** and **24b** form ordered bilayer during self-assembly forming a three-dimensional network to trap and immobilise solvent molecules.
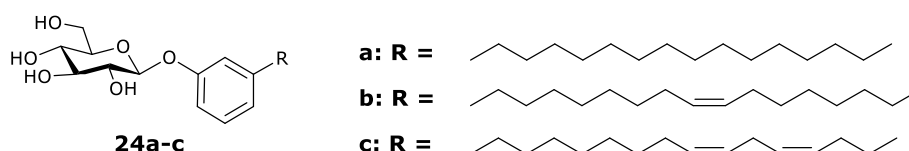
Figure 1.15 | Aryl glycolipids

Overall, these numerous studies have demonstrated that carbohydrates such as sugars or saccharides are promising building blocks for new gelators with various gelation abilities and different three-dimensional network structures.

1.3   Benzylidene Sorbitol/Xylitol and Derivatives

Benzylidene sorbitol and xylitol derivatives, such as dibenzylidine sorbitol (DBS) and dibenzylidene xylitol (DBX), are sugar-based gelators that are of much interest for their facile preparation and many applications[58]. DBS and DBX derivatives are the product of a condensation reaction of a sugar alcohol (in this case, sorbitol or xylitol) and a benzaldehyde, in the presence of an acid catalyst. The molecules are believed to self-assemble by adopting a 'butterfly' conformation (Figure 1.16), with two aromatic 'wings' on either side of an aliphatic body and held together by hydrogen bonds,[59]. However, no direct structural evidence exists to date. The exact nature of the self-assembly of DBS and DBX derivatives upon gelation has been the subject of much research and debate.[58] It has been suggested that these compounds undergo self-assembly in appropriate solvents through relatively weak intermolecular interactions such as hydrogen bonding, electrostatic, van der Waals, π-π stacking or solvophobic interactions; all have been inferred.[58] The acetal carbon atoms in the DBS and DBX molecule is a new chiral centre after the condensation reactions, however, not many papers have mentioned its stereochemistry. Smith *et al*.[60] gave a safe assumption that the bulky phenyl groups occupy the equatorial positions since they are formed under thermodynamic control.
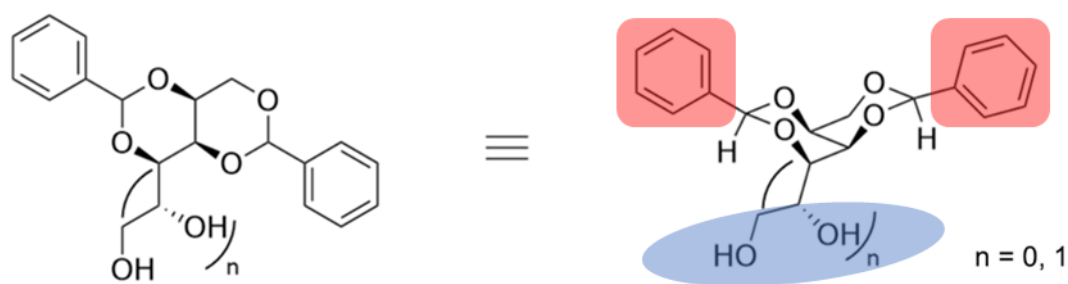
Figure 1.16 | 'Butterfly-shape' conformation of DBS or DBX. blue: hydrophilic group; red: hydrophobic group

It is clear from the morphology of the xerogels that the molecules self-assemble into fibrous networks like other LMWGs.[61–63] DBS and DBX are important LMWGs, given the molecules versatility in gelling a range of organic solvents[64] and polymers[65] (where it creates a dual network of covalent and non-covalent systems) in a range of concentrations and temperatures.[66,67]

1.3.1. Dibenzylidene Sorbitol

Dibenzylidene sorbitol (DBS) was primarily identified by Meunier[68] in 1891 and have become a known chiral LMWG of organic solvents.[58] At that time, due to the chirality of the sugar alcohol, it was reported that the simple condensation reaction gave a mixture of isomeric diacetals, each having a unique solubility in boiling water and different melting points. After working through a series of DBS derivatisation, Wolfe *et al.*[69] initially converted the free alcohols found on DBS molecules into a variety of esters and discovered that the product of the reaction performed by Meunier[68] was not a mixture of isomeric diacetals, but instead, it was the mono- (MBS) and tri- (TBS) acetal by-products. A careful hydrolysis of DBS with acetic acid by Angyal and Lawler[70] confirms the structure of DBS having a 1,3:2,4 connection pattern. The simple condensation reaction of DBS is shown in Scheme 1.1.
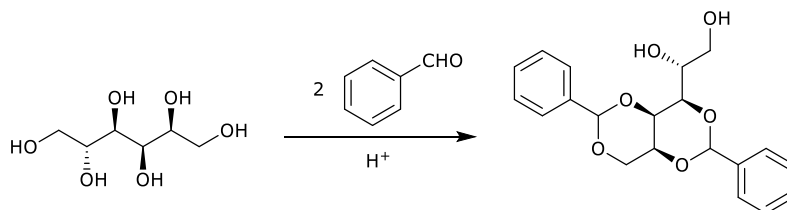
Scheme 1.1 | Condensation reaction of 1,3:2,4-dibenzylidene-D-sorbitol[60]

As mentioned above, the efficiency of DBS as a gelator is due to the 'butterfly-like' conformation that the compound form during self-assembly into a fibrillar network. The types of non-covalent intermolecular interactions likely to occur are hydrogen bonding – due to the hydrophilic hydroxyl group on the sorbitol backbone and π-π interactions – due

to the hydrophobic aromatic rings.[71] It, however, remains unclear which of the two physical interactions is the primary driving force for self-assembly or if it is the interplay of both forces.[71]

Most recently, there has been a growing interest in synthesising DBS derivatives by either modifying the free hydroxyl groups on the sorbitol 'body' or by using a functionally substituted benzaldehyde on the aromatic 'wings'. DBS and its derivatives are applied in different domains such as gel electrolytes[72], adsorption of dyes[15], light stabilisers[73] and controlled drug delivery[74]. All these applications rely upon the formation of dibenzylidene sorbitol's (or DBS derivatives') nanofibres in different solvent media, and therefore, the research on DBS gels witnessed considerable growth.

Patents on benzylidene sorbitol compounds. An abundance of patents have been reported on the synthesis and derivatisation of benzylidene sorbitol compounds with a wide range of applications (not just on pure gelation behaviour). Uchiyama[75] conveyed a process for purifying crude dibenzylidene sorbitol in 1978. His described process affords DBS having a purity of at least 98% from crude DBS with a purity of 95%. He stated that heating the crude DBS in methanol to between 60 °C and 70 °C will form a slurry-like mixture, which can be separated *via* filtration. Washing the filtered precipitate with cold methanol led him to afford purified dibenzylidene sorbitol as a powder. Uchiyama[76] continued his research on DBS derivatives and reported a polyolefin resin composition consisting of a polymer of an aliphatic mono olefin and a DBS derivative compound. The DBS derivatives have different alkyl chains (methyl, ethyl and propyl), as well as a hydrogen atom (DBS) and a chlorine atom (DBS-Cl) on the *para* position of the benzyl ring. He proposed several methods for synthesising asymmetric DBS derivatives in a two-step reaction. He reacted 1:1 equivalents of benzaldehyde (or their derivatives) and sorbitol using different acid catalysts such as *p*-toluenesulfonic acid, 50% sulphuric acid and hexahydrophthalic anhydride. Shortly after stirring the reagents, a large amount of fine white crystals precipitated within the reactor and formed a creamy white reaction mixture. To the creamy white reaction mixture, 1 mole of the different benzaldehyde derivatives was added, followed by 10% of aqueous hydrochloric acid solution to initiate the second-step reaction. The reaction mixture was then neutralised with a 10% sodium hydroxide solution, then filtration *via* a centrifugal separator. The filtrated material was washed with water and dried to give an asymmetric DBS derivative.[76] Cobb III *et al.*[77] further investigated the field on liquid dispersion comprising dibenzylidene sorbitol acetals ethoxylated nonionic surfactants.

Moreover, Mattai *et al.*[78] reported an antiperspirant product that consisted of dibenzylidene sorbitol and elastomer in dimethicone. The research is based on emulsions comprising a gellant/solvent phase with DBS and an oil phase. The oil phase is made with a silicone

elastomer in a selected dimethicone. In addition, Boutique *et al*.[79] described structured fluid detergent compositions comprising DBS acetal derivatives. The team mentioned that carrying the substituents of the DBS molecule allows the formulator to increase or decrease the dissolution temperature of the DBS in low-water premixes. It is advantageous if processing temperatures are lower for the thermally sensitive materials such as enzymes, in making the present fluid detergent composition. Bernreitner *et al*.[80] found an application of DBS derivatives in food applications. According to their research, DBS and derivatives are good examples of suitable α-nucleating agents.

1.3.2. Dibenzylidene Xylitol

Dibenzylidene xylitol (DBX) has a very similar structure to DBS, with one hydroxyl group rather than two. Instead of sorbitol, xylitol was used for the condensation reaction in yielding the gelators. Xylitol, having a five-carbon atom backbone and five-hydroxyl groups instead of six, was reacted with benzaldehyde (Figure 1.17). Xylitol further differs from sorbitol because whilst sorbitol is chiral, xylitol is a meso compound consisting of 3 chiral centres but exhibits a plane of symmetry, making DBX and its derivatives racemic.
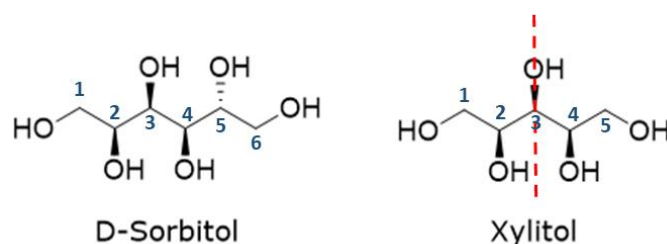
Figure 1.17 | Structure of D-sorbitol and xylitol showing the plane of symmetry (red dashed line)

There is only limited literature precedent on the synthesis and the gelation behaviour of DBX derivatives in comparison to the well-reported DBS gelator. Following the DBS preparation in 1981, the synthesis of DBX was first reported in 1899 by Lobry de Bruyn *et al*.[81], without reporting any preparative and synthetic details in that specific publication. Metcalf and colleagues[82] expanded the research by reacting xylitol with benzaldehyde using an acid catalyst, 50% sulphuric acid. They further modified the DBX structure by reacting tetraacetyl-D-glucosyl bromide with DBX, forming an ether where they managed to separate two isomeric forms of the compound. Furthermore, Raju *et al*.[83] reported the successful preparation of xylitol based phase selective organogelators for potential oil spillage recovery. The di-acetal and di-ketal gelator compounds were produced in a single step reaction *via* acid catalysed reaction between xylitol and aromatic aldehyde/ketone in a biphasic system (Scheme 1.2).
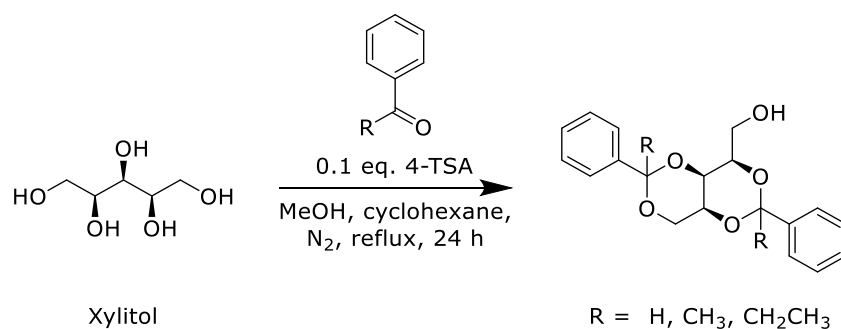
Scheme 1.2 | Synthesis of xylitol based gelators according to Raju *et al.*[83]

Patents on benzylidene xylitol compounds. Although only a few journals are focused on the synthesis of DBX and its derivatives, there are still a handful of patents that revolve around these compounds. Murai *et al.*[84] has reported a process for preparing both dibenzylidene sorbitol and dibenzylidene xylitol. They isolated DBX-Cl affording an excellent yield of 92% with a purity of 97%. In addition, Mathew and colleagues[85] described that dibenzylidine sorbitol, xylitol, and ribitol are great solidifying agents as they can be used to produce cleansing bar compositions.

Overall, DBS, DBX and their derivatives have been widely studied (more on DBS) as they can be synthesised under mild conditions and easily derivatised. The modification of the molecules allows the compound to exhibit different properties and may be widely used in different types of applications.

1.4   LMWGs in Additive Manufacturing and 3D Printing

Additive manufacturing (AM) compromises different technologies that allow the direct generation of objects through computer-aided design (CAD) or computer-aided manufacturing (CAM). AM can also be referred to as rapid prototyping or simple three-dimensional printing (3DP).[86,87]

In 3DP, products are built on a layer-by-layer basis through a series of cross-sectional geometry. Due to its fast-emerging technology, 3D Printing is widely used for mass customisation or production of any open-source design. The reproducible, controlled, and automatic supply of materials within a 3D space without using moulds was made possible by 3D printers.[87]

There are different types of 3DP[88]: (i) Binder jetting, (ii) directed energy deposition, (iii) materials extrusion, (iv) materials jetting, (v) powder bed fusion, (vi) sheet lamination and (vii) Vat Photopolymerisation. These types have been developed with different functions.

Binder jetting. Binder jetting was known as a type of 3DP in the early 1990s[89]. The processes of this type of 3DP include seven steps: printing, curing, de-powdering, sintering, infiltration, annealing and finishing. No power or heat source is involved during the building process, and therefore it is cost-effective. Furthermore, binder jetting is simple, fast and has the ability to print very large products. It can print a range of materials, including polymers, ceramics, metals and sands.

Directed energy deposition. Directed energy deposition (DED) is a laser additive manufacturing (LAM) process in which a high-powered laser is used to join materials to make dense three-dimensional structures, such as laser deposition and laser engineered net shaping (LENS). DED processes are commonly used to repair or add additional material to existing modules. Moreover, it is currently widely used in the field of aerospace and repairing industries.[90]

Material jetting. Material jetting (MJ), also known as inkjet 3D printing, can create parts by depositing droplets of liquid photopolymers using piezo printing heads and curing the photopolymers using ultraviolet lamps.[91] Objects produced with MJ are typically weaker than ME, which unfortunately makes it unsuitable for functional applications. The materials that can be printed *via* inkjet printing are also limited. On the other hand, the accuracy of material jetting is one of the highest levels amongst 3D printing technologies due to the deposition precision of the tiny droplets of material forming a very smooth surface finish.

Material extrusion. Material extrusion (ME) 3DP is used to print multi-materials and multi-colour printing of plastics, food or living cells. It is also used to process thermoplastic materials in filament form *via* pinch roller mechanism. There are two primary components for the extrusion-based 3D printer: the printer (controls movement and position of the nozzle) and the extruder (controls the material flow). The feedstock is melted in a heated liquefier, and when the melt is pushed through the print nozzle, the melted bead solidifies, creating three-dimensional objects.[92] ME is based on fused deposition modelling (FDM) technology, and it is one of the most commonly used additive manufacturing methods due to its advantages.[93] Material extrusion has a low initial and running cost that allow a wide selection of print materials.

Powder bed fusion. Powder bed fusion uses a laser (selective laser sintering (SLS) or selective laser melting (SLM)), heat (selective heat sintering (SHS)), or electron beam (electron beam melting (EBM)) to melt and fuse materials together to form a three-dimensional object.[88] SLS is a 3DP technology that uses a high power laser to sinter polymer powders and has functionally fast speed, high accuracy and various surface finish; polymers are the primary materials that can be printed with SLS, whilst SLM can print

metal. SHS and EBM work the same as the SLS and SLM but using a head thermal and electron beam instead of a laser, respectively.

Sheet lamination. Helisys Inc developed sheet lamination or laminated object manufacturing (LOM) in 1991.[94] LOM process fused sheets of material together and used a digitally guided laser to cut away the desired object. The process was upgraded in 2003, where a standard inkjet printer printed a shape onto a piece of paper that was then glued onto the sheet. When the paper is removed, the object will be revealed. LOM can do full-colour prints and is relatively inexpensive with the ease of material handling and recycling. However, LOM is typically not able to produce the same geometric complexity as other 3DP processes as it may not be possible to access internal portions and remove excess material from inside of the printed object[94]

Vat photopolymerisation. Vat photopolymerisation, also known as stereolithography or SLA, creates three-dimensional objects by selectively curing liquid resin through targeted photoreactive polymerisation using laser, light or ultraviolet. SLA is used for the fabrication of tissue scaffolds on a micron-scale for use in regenerative medicine. It can create large parts with sub-millimetre details where it uses light (often UV) to selectively cross-link, solidifying a photopolymer resin layer by layer.[95] SLA is a relatively quick process and has a high level of accuracy.

1.4.1. LMWGs in Material Extrusion

Recently, there has been a vast increase in studies into extrusion-based 3D printing due to its low initial and running cost that allow a wide selection of print materials. LMWGs and polymer blends have been investigated for extrusion-based 3D printing inks. The LMWG and the polymer composites can result in a continuous 3D network (with optimised material and printing parameters) with various processes such as photopolymerisation pathways[96–99] and temperature change.[100] The advantage of photopolymerisation in 3D printing is the fast cure time, which provides a rapid and stable phase change into the solid. Furthermore, LMWGs form a 3D network *via* physical non-covalent interactions; the photopolymerisation process provides a covalent network (formed *via* chemical interactions) for the hydrogels in 3D printing.[101] However, 3D printing prepared from low molecular weight gelators is far less common and expanding this research would be an excellent idea.

Inks can be categorised depending on the extrusion procedures: cold extrusion, hot-melt extrusion and gel-forming extrusion. Hot-melt and gel-forming extrusion involve a phase change of the ink during extrusion, whilst cold extrusion occurs typically at room temperature with no phase transition.[102] Cold extrusion relies merely on the mechanical

properties of the ink during printing. The ink should allow extrusion without manipulation of temperature and should be capable of forming self-supporting 3D network layers.[102]

The breaking and recovery of a supramolecular gel network formed by the non-covalent interactions are one of the advantages of using LMWGs in material extrusion. The reversibility of the physical interactions can be seen upon heating and cooling, where the mechanical properties are destroyed upon heating and recovered during cooling. Furthermore, the reversibility of the non-covalent interactions can also be seen when the 3D network breaks down during an application of a force, followed by a rapid formation of the 3D network when force is removed. If a gel possesses the latter reversibility property, the material is classified to have a 'thixotropic' property. During manual extrusion, a force is applied to a material to permit the extrusion to take place. It would be ideal for the ink to have thixotropic properties to rapidly form the 3D network and be suitable for extrusion-based 3D printing.

1.4.1.1 Thixotropic Gels

Thixotropy is a mechanical property of a material and can be defined as the continuous decrease of viscosity with time when flow is applied to a rested sample and the subsequent recovery of viscosity in time when the flow is discontinued.[103] Such materials with thixotropic properties can also be called 'shear-thinning' or 'self-healing' materials.

Thixotropic gels (polymer or LMWGs) are materials that have been used for material extrusion type of 3DP, and therefore the study and therefore the study around thixotropic gels have been expanded in recent years. Nolan *et al*.[104] developed two LMWGs (**25** and **26**) based on Fmoc-dipeptides for automated 3D printing using solvent triggered and pH-triggered approaches. The formed gels from **25** and **26** can be extruded into superimposed layers to form 3D constructs. For the solvent triggered approach, the team used DMSO to dissolve the material and triggered self-assembly with the anti-solvent water. In contrast, for the pH-triggered technique, the material was dissolved in NaOH, followed by the addition of glucono-D-lactone (GdL) to hydrolyse in water and acidify the solution. Their findings are that the quality of the solvent-triggered gels prints is better than those made *via* pH trigger.

Moreover, Li *et al*.[105] discovered injectable supramolecular gel, **27**, localise ethanol and loaded chemotherapeutic drug for *in situ* synergistic therapy. They dissolved their material (different concentrations) in ethanol *via* heating and formed a gel as it cooled down. The rheological data shows that the recovery rate of the gel is 64% after immediate removal of the applied strain of 50%.
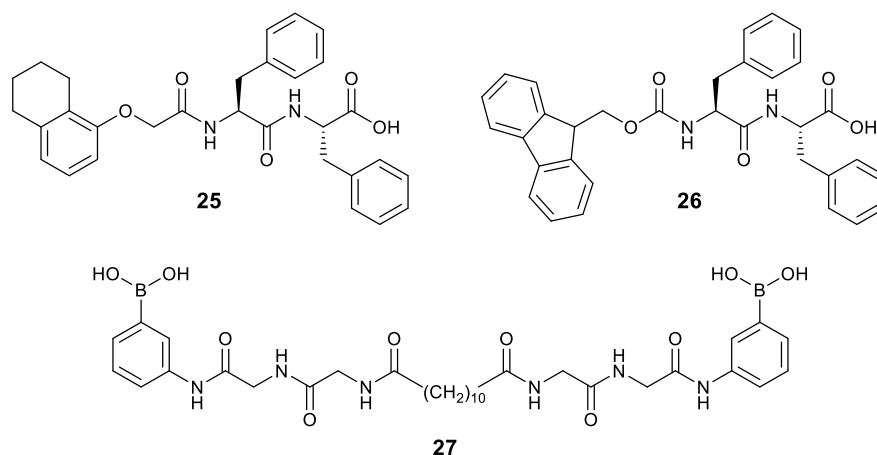
Figure 1.18 | Examples of thixotropic LMWG

Furthermore, Fitremann and co workers[106] described a wet spinning and radial self-assembly of the LMWG **28**. With their research, 2.5%, 4.0% and 5.0% w/v of the gelator was dissolved in DMSO, and the solution was extruded in a bath of ultrapure water (21-23 °C). They stated that a counter diffusion between DMSO and water occurs and results in the progressive gelation of the jet. Additionally, Xiong *et al.*[47] synthesised an amino acid-based gelator (Figure 1.9) that possesses responsiveness to multiple triggers, including light (azobenzene for π-π stacking), temperature (long-chain for hydrophilicity) and pH (zwitterion for electrostatic interaction). Moreover, Wang *et al.*[107] discovered thixotropic hydrogels from the racemate of chiral OFmoc monosubstituted cyclo(glu-glu) derivatives (compounds **29** and **30**). A gelator was dissolved in a mixture of DMSO and phosphate-buffered saline (PBS) and was heated to get a homogeneous solution and cooled down to room temperature to form a gel. The racemate displays a fast thixotropic recoverable and recyclable behaviour.
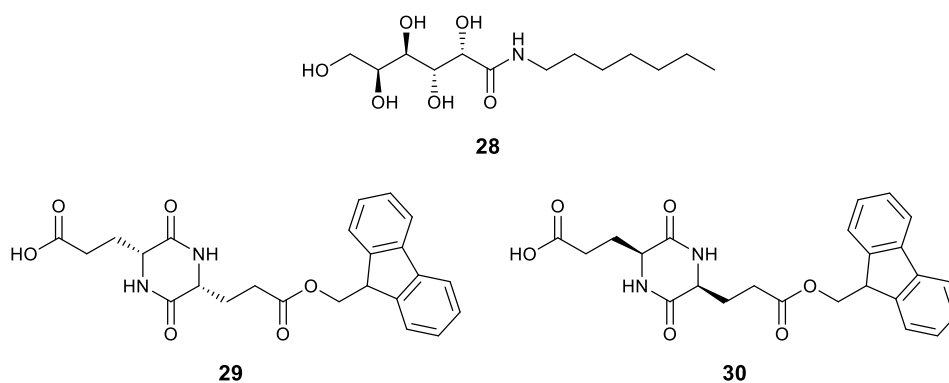
Figure 1.19 | Further thixotropic hydrogels in literature

In 2016, Yang *et al.*[108] reported a calixarene-based LMWG that formed gels upon heating and cooling. The established material was extruded in a syringe from a hot solution and reformed the 3D network with shape control, producing printed organogel shapes.[108]

Moreover, extrudable G-quadruplex hydrogels were prepared by Das and co-workers.[109] The 3D printing process in their research is driven by the injectability and the highly thixotropic and 'self-healing' property of the gel. Highley *et al*.[110] extended the investigation of thixotropic hydrogels when they explored the materials to behave as inks and printing supports. Two compounds were synthesised by the team derived from hyaluronic acid; one is covalently bonded with adamantane, and the other with cyclodextrine. As the investigation continues, a 'self-healing' hydrogel was observed when the two hyaluronic acid-based compounds were combined in the same system. This thixotropic property is driven by the interaction between the adamantane and the cyclodextrin. The hydrogel composite discovered can be extruded and self-heal when an object is inserted into the gel system. This finding allowed the researchers to 3D print one hydrogel into the other.[110]

1.5. Project Aims

Research in LMWGs continue to attract attention due to the extensive possibilities of the compounds to make 3D scaffolds that can be adapted precisely to further applications. The main advantages of molecular gels are that, compared to polymer gels, they can be more responsive to stimuli, which aid in modifying and enhancing additional desired properties to the molecule.

The main focus of this research is to create a library of sustainable or 'green' low molecular weight gelators concentrating on sugar-based building blocks. The derivatisation of the efficient dibenzylidene sorbitol (DBS) organogelator is the primary motivation of the study. We are interested in synthesising efficient organo/hydrogelators to form a gel in various solvents (organics solvents, aqueous solutions and photocurable monomers) and investigating the materials' mechanical and physical characteristics.

Furthermore, LMWGs in 3D printing introduce vast advantages in different applications such as drug delivery, food industry and cosmetics. We hope that after this research, we can deliver organo/hydrogels into the production of printable inks, concentrating on extrusion-based 3D printing.

CHAPTER TWO

Benzylidene Sorbitol Derivatives

2.1 Synthesis of Benzylidene Sorbitol Derivatives

The benzylidene sorbitol derivatives were synthesised from D-sorbitol and sustainable and economically viable aromatic aldehydes (benzaldehyde, methyl 4-formylbenzoate, cuminaldehyde, vanillin, cinammaldehyde, [1,1'-biphenyl]-4-carbaldehyde, 4-formylbenzonirile, vanillin acetate, 4-*tert*-butylbenzaldehyde and 4-diethylaminobenzaldehyde) in the presence of catalytic 4-toluenesulfonic acid to yield white crystalline materials (Scheme 2.1 and Table 2.1). This equilibrium condensation reaction can yield monobenzylidene sorbitol (MBS), dibenzylidene sorbitol (DBS) and tribenzylidene sorbitol (TBS) compounds depending on a range of factors such as the stoichiometry, pH, aldehyde and solubility of the starting materials and the intermediates.[60,111] All reactions were performed using 2.0 equivalents of the aromatic aldehyde with respect to sorbitol, except for the preparation of MBS-*i*Pr, which was carried out using 1.0 equivalent of cuminaldehyde.

Seven of the sorbitol derivatives in this research were isolated in yields of 45–75% (with respect to sorbitol being the limiting reagent) from reactions performed at room temperature, where only one sorbitol derivative gave a poor yield of 17%, MBS-CN. The di-substituted sorbitol product is clearly disfavoured in all cases. Only the compounds derived from cuminaldehyde and methyl 4-formylbenzoate gave isolable yields of the DBS in our hands. Contrarily, all the MBS products could be isolated in yields superior to 58%, excluding MBS-CN. Reactions involving vanillin required an inert atmosphere due to the oxidation of the compound noted by the colouration of the reaction performed in air.

Furthermore, vanillin acetate was investigated for condensation with D-sorbitol. This aldehyde was reacted with sorbitol and 4-toluenesulfonic acid under both the room temperature conditions recommended by Gardlik[112] and the Dean-Stark procedure.[113] In both cases, the acetal group of the vanillin acetate was deprotected under the acidic conditions, and the final product was MBS-Van (58%). Products were isolated *via* filtration and characterised by NMR, HRMS, optical rotation and FTIR spectroscopy. Unfortunately, three reactions could not produce any desired mono- or di-substituted sorbitol derivative.

Furthermore, an attempt was made to synthesise a hetero-acetal gelator by reacting a mono-acetal with an aldehyde. MBS-Van was chosen as the mono-acetal and cuminaldehyde as the other reagent; the latter was chosen because it was the only aldehyde screened that formed the di-acetal. Milder reaction conditions were chosen (Gardlik's[112] method at room temperature) in an attempt to minimise the reverse reaction
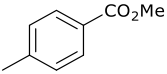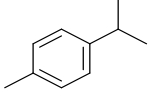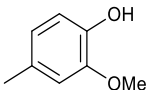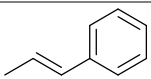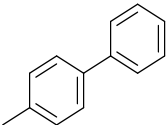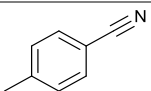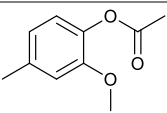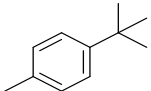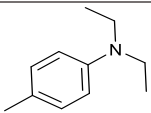
of the mono-acetal back to vanillin and sorbitol. Analysis of the reaction mixture by time-of-flight mass spectrometry showed the substitution of aldehydes was occurring (Figure 2.1). It is believed that even these mildly acidic conditions cause equilibration of the mono-acetal that undergoes the reverse reaction to vanillin and sorbitol, which then reacts with the cuminaldehyde forms MBS-iPr. This hypothesis is supported by the reaction mixture turning purple after being exposed to air for a short time, which is indicative of the presence of unreacted vanillin (MBS-Van does not oxidise readily in air in our experience).

As 1,3:2,4-dibenzylidene-D-sorbitol, DBS, has been a known chiral LMWG of organic solvents, different approaches were carried out for the simple condensation reaction of DBS.[68–70] The preparation of DBS-CO₂Me was reported by Smith *et al.*,[114] where the inventors used the Dean-Stark procedure using the same reagents. Furthermore, the synthesis of DBS-iPr was reported in a patent[84] where the inventors used C₉ alkylbenzene sulfonic acid, dimethylsulfoxide, benzene and *iso*-propanol as the reaction medium, apparently obtaining a high yield of the product. There is no specific procedure for synthesising MBS-iPr or its characterisation in the literature, although, an asymmetric synthesis of diacetal compounds where MBS-iPr could be a reagent is contained in a patent.[115] The reactions that produced MBS-Cinn, MBS-Ph and MBS-Van did not yield isolable amounts of the desired diacetal. The selectivity of these reactions to result in the mono-acetal is quite remarkable in our view. Experiments have been run over weeks, at elevated temperatures (60–100 °C), under an inert atmosphere and with an excess of aldehyde in an attempt to force production of the di-acetals. However, all of these resulted only in mono-acetal formation. Mass spectra of the reaction mixtures inevitably show a strong mono-acetal peak and a minimal di-acetal peak. Clearly, the formation of the di-acetals derived from these two compounds is unfavourable under the reaction conditions employed. As for MBS-iPr, we could not locate a synthetic procedure or characterisation for MBS-Van, although its antioxidant activity against free radicals and anti-inflammatory properties were patented recently.[116]
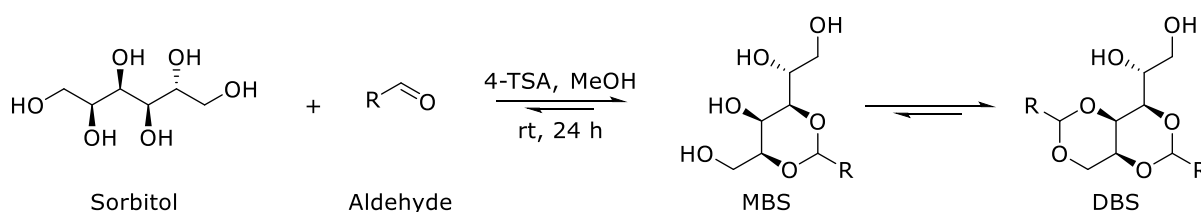
Scheme 2.1 | General approach for the synthesis of benzylidene sorbitol derivatives

Table 2.1 | Reactivity of different aldehydes with sorbitol

Aldehyde	R substituent	DBS	MBS	Yield (%)	Compound
Benzaldehyde		✓	✗	60	DBS
Methyl 4-formylbenzoate		✓	✗	60	DBS-CO$_2$Me
Cuminaldehyde		✓	✓	45 59[a]	DBS-iPr MBS-iPr
Vanillin		✗	✓	73[b]	MBS-Van
Cinnamaldehyde		✗	✓	68	MBS-Cinn
[1,1'-biphenyl]-4-carbaldeyde		✗	✓	63	MBS-Ph
4-formylbenzonitrile		✗	✓	17	MBS-CN
Vanillin Acetate		✗	✗	N/A	MBS-Van
4-*tert*-butylbenzaldehyde		✗	✗	N/A	No isolated compound
4-diethylaminobenzaldehyde		✗	✗	N/A	No isolated compound

All reactions were done using 2.0 e.q. of the aromatic aldehyde for 24 h, unless stated

[a] reaction carried out using 1.0 eq of the aromatic aldehyde for 12 h

[b] reactions performed under inert atmosphere

a)

b)
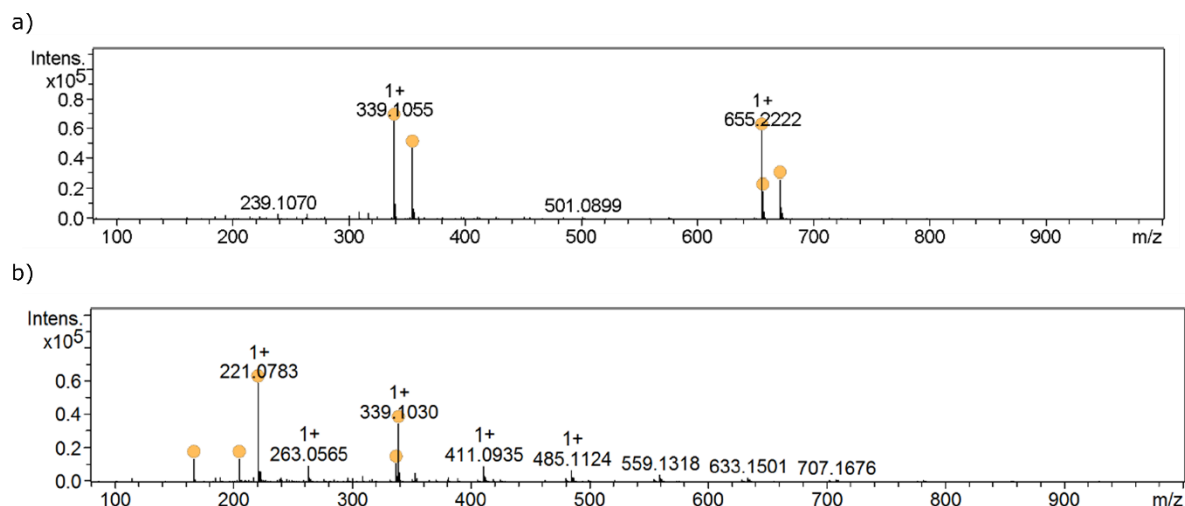
Figure 2.1 | HRMS of MBS-Van from a) vanillin reaction and b) vanillin acetate reaction

In 2013, Smith *et al.*[114] published the preparation of DBS-CO$_2$H in a two-step reaction from DBS-CO$_2$Me. Replicating the reaction, we treated DBS-CO$_2$Me with 1M NaOH for 12 hours under reflux, then acidified the resulting salt solution to pH 3 using NaHSO$_4$. White stable gel was formed during acidification, generating DBS-CO$_2$H in an excellent yield of 84% (Scheme 2.2).
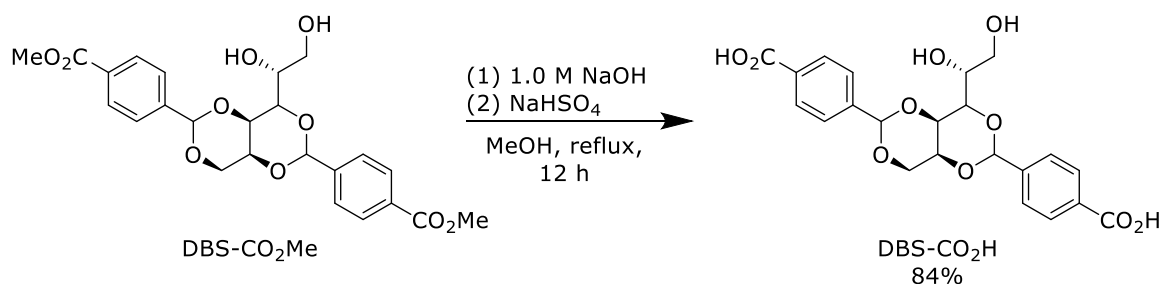
Scheme 2.2 | Preparation of DBS-CO$_2$H reported by Smith et al.[114]

The condensation of the aldehyde with sorbitol is proposed to proceed *via* the solvent acetals.[117] Song *et al.*[113] noted that aromatic aldehydes with electron-donating substituents react more sluggishly with sorbitol than ones with electron-withdrawing substituents, although they do not provide a rationale. Kobayashi's[118] work suggests that the reaction mechanism for the formation of the di-acetal proceeds *via* nucleophilic attack of the alcohol on the oxonium (Figure 2.2).[71] From this proposed mechanism, it appears that electron-donating substituents on the aromatic ring would reduce the electrophilicity of the carbon atom attached to the phenyl ring.
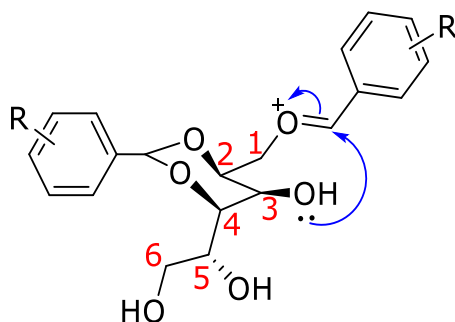
Figure 2.2 | The proposed final step in DBS formation[71]

This inductive effect will decrease the rate of the forward reaction. Possibly, the aldehyde will detach from the sorbitol before the nucleophilic attack of a second aldehyde can occur because the system is under equilibrium conditions. However, this hypothesis does not account for the observation of the relatively rapid precipitation of a white solid in the reaction vessels, indicating that the formation of the mono-acetal is not particularly inhibited – which it surely would be if the above hypothesis were correct, as it forms through the same mechanism. Furthermore, this hypothesis also contradicts the fact that only the MBS-CN was formed rather than the diacetal derivative, DBS-CN. It is also possible that the insoluble nature of the intermediate halts the reaction and freezes the equilibrium as the reaction is no longer homogenous. The exact origin of the effect will require further investigation beyond the scope of the present work. However, an essential conclusion of this research is that MBS and DBS derivatives of electron-deficient aldehydes can be isolated independently.

One of the most common factors of an efficient gelator is having a long chain on the compound molecular structure. Since it is possible to modify a DBS derivative molecule through its free hydroxyl group, DBS-*i*Pr was reacted with lauroyl chloride under primary conditions at 40 °C for 10 hours to yield Lauryl-DBS-*i*Pr (Scheme 2.3). The completion of this reaction means that the isolated product has one less hydroxyl group than its starting material; however, a long chain was incorporated into its molecular structure. The importance of the hydroxyl group and the long-chain will be identified through a series of gelation tests.
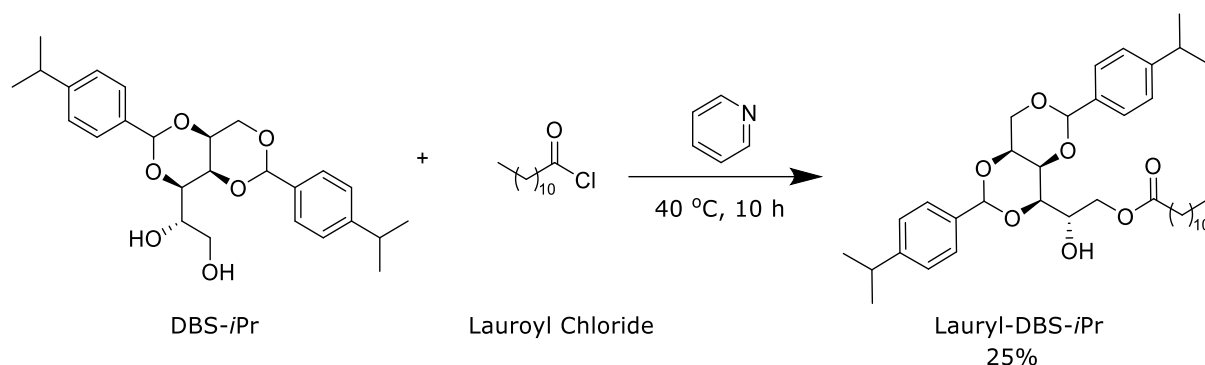
Scheme 2.3 | Preparation of Lauryl-DBS-*i*Pr

2.2 Crystallography of Monobenzylidene Sorbitol Derivatives

Single crystals of both MBS-Van and MBS-Cinn were obtained *via* crystallisation from aqueous KCl and CaCl$_2$ (2% w/v), heating and cooling over 48 hours to afford needle-like crystals. To this date, there have been no single-crystal structures reported in the literature for either MBS or DBS and their derivatives (to the best of our knowledge) which makes the following observations useful for the field. However, we should emphasise that these derivatives that crystallise do not form gels. The packing of MBS-Van (Figure 2.3 and Figure 2.5) and MBS-Cinn (Figure 2.4 and Figure 2.5) are similar overall, where sugar and aromatic layers alternate. The asymmetric unit of MBS-Van contains one molecule, whereas the asymmetric unit of MBS-Cinn contains two distinct molecules possessing the same type of conformation. Location and refinement of the hydroxyl hydrogen atoms were handled differently in the two structures (full details are in the experimental procedures and relevant sections of the CIFs).

MBS-Van crystallises in the space group $P2_1$ (monoclinic crystal system) with neighbouring molecules in the γ-packing motif (Figure 2.4).[119] Crystals of MBS-Van diffracted strongly; three of the four hydroxyl hydrogen atoms were located in the electron density map, and their positions were refined. Intermolecular hydrogen bonds (Figure 2.3, summarised in Appendix A.Table 1) are observed between adjacent sugar hydroxyl groups with H⋯A separations of 1.84, 1.87, and 1.93 Å for pairs O4-H4⋯O8, O8-H8⋯O4 and O12-H12⋯O2, respectively. The [O⋯H⋯O] angles between the molecules are 165.1°, 155.9° and 174.9°, respectively. The final hydroxyl hydrogen atom (O2-H2) was geometrically placed to donate a hydrogen bond to the closest suitable acceptor; detailed discussion of the hydrogen bond geometry is not warranted. Furthermore, there are two additional less evident interactions present on the vanillin aromatic group (Figure 2.3b), which are O22-

H22···O20 (2.21 Å, 141.9°) and C21-H21B···O22 (2.65 Å, 141.6°). The distances are relatively long, and the torsion angles are relatively low compared to those of hydrogen bonds in the sugar backbone. It is also observed that there is a C-H···π interaction between H13 to the centroid of C14-C19 with a short contact of 2.71 Å (Figure 2.3c).

MBS-Cinn crystallises in the space group $P2_1$ (monoclinic crystal system) with neighbouring molecules in a herringbone packing motif (Figure 2.5).[119] Crystals of MBS-Cinn diffracted weakly; the hydrogen positions of the OH groups were not observed in the electron density map. The hydroxyl hydrogen atoms in the model were geometrically placed to donate hydrogen bonds to the closest suitable acceptors. There are several plausible combinations of hydrogen atom positions in network of OH groups; the hydrogen bond positions are ambiguous, and disorder cannot be discounted. The calculated positions are in A.Table 1.

Furthermore, a hydrogen bonding interaction is observed between the H20A of the aromatic group (phenyl) from the cinnamaldehyde and the O10A in the sorbitol acetal backbone (H···A distance 2.65 Å), which propagate in one direction (Figure 2.4b). The rest of the interactions are between the hydroxyl groups of the sugar backbones, as seen in Figure 2.4. The H···A distances range from 2.312–2.660 Å.
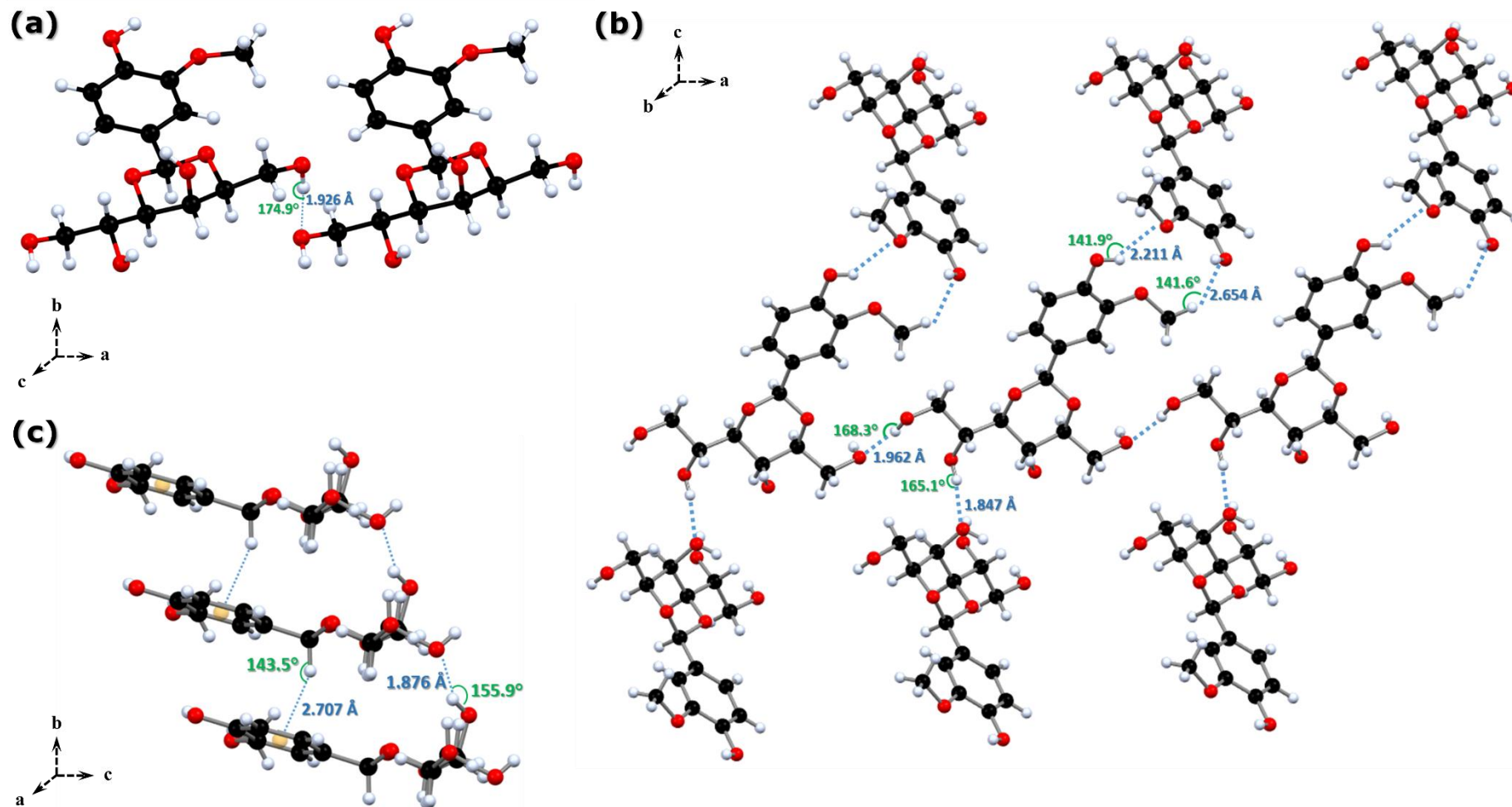
Figure 2.3 | Molecular packing of MBS-Van showing different interactions between the molecules (O2-H2⋯O12 distance obtained from calculated positions).
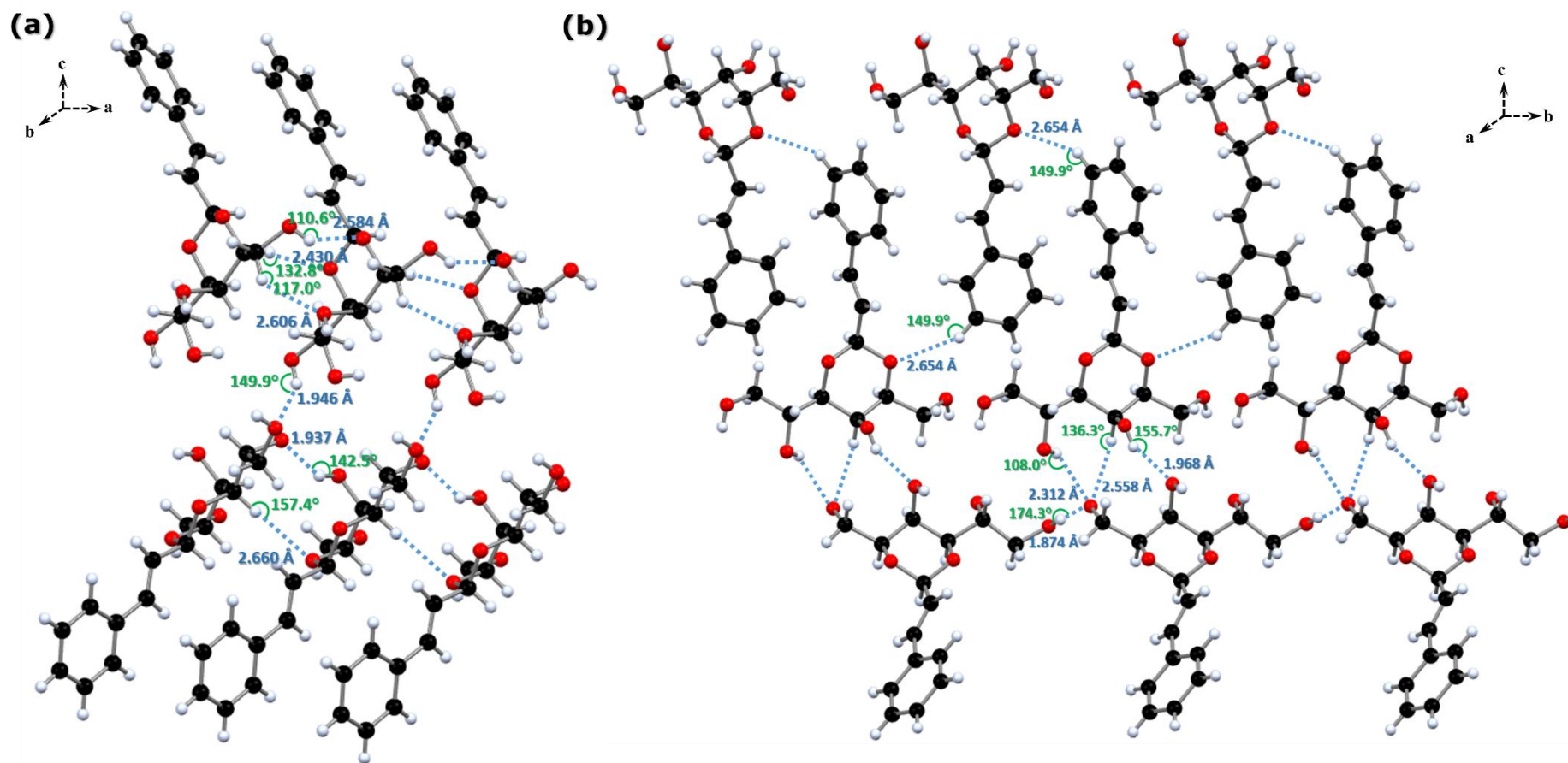
Figure 2.4 | Molecular packing of MBS-Cinn showing hydrogen interactions between the molecules. (All hydrogen bonds obtained from calculated positions).
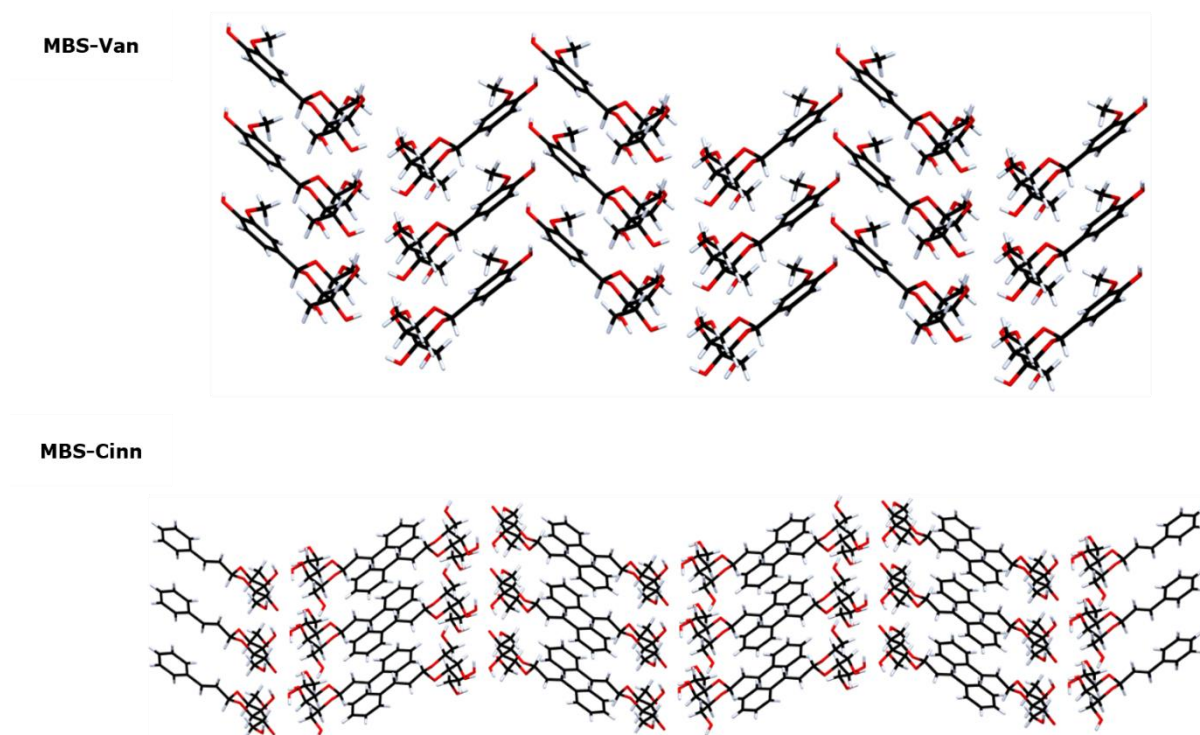
MBS-Van

MBS-Cinn

Figure 2.5 | Packing motifs of MBS-Van and MBS-Cinn

In summary, the single-crystal structures of the MBS derivatives show the same general packing (Figure 2.6), where hydrophilic and hydrophobic groups alternate. This organisational pattern of the mono-acetal compounds from the single X-ray crystallography is similar to molecular packing models of related compounds reported by Song *et al.*[113] and Fan *et al.*[120] in terms of hydrogen bonding interactions. However, in our case, the crystal structures show no significant π-π interactions. The interactions of the molecules are mainly hydrogen bonding between the sorbitol moieties. This bonding is also revealed in the FTIR spectrum of MBS-*i*Pr in Figure 2.9b. It is possible that DBS derivatives could have an analogous lamellar structure with hydrogen bonds between the sugar residues.
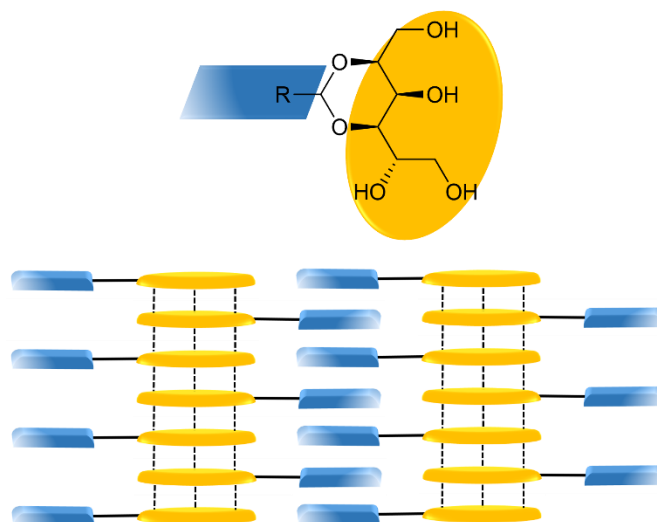
Figure 2.6 | Molecular packing model of mono-acetal compounds

2.3 Gelation Tests

2.3.1 Gelation behaviour of individual benzylidene derivatives

A series of gel tests were carried out on most of the successfully isolated benzylidene sorbitol compounds, investigating their gelation behaviour at 10 mg mL^{-1} (1% w/v). Solvents were selected to represent a broad range of different types, such as linear, cyclic, aromatic, chlorinated, alcohols, ethers, esters, and aqueous ethanolic and salt solutions (Table 2.2 and Table 2.3). Gelation tests were performed upon heating and cooling where the solvent was heated (until all solid is dissolved by eye) then left to cool down to room temperature. DBS and DBS-CO$_2$Me are already known as organogelators, whereas DBS-CO$_2$H is known as a hydrogelator. The mentioned compounds were included with the tests to directly compare the gelation properties with the rest of the isolated compounds.

As reported, dibenzylidene sorbitol, DBS, has proven to be a good organogelator as it formed gels in 80% of the tested organic solvents in this research. Furthermore, two dibenzylidene sorbitol derivatives, DBS-CO$_2$Me and DBS-iPr, gel a broad range of solvents, although they did not gel water because they are essentially insoluble at this concentration. Contrarily, DBS-CO$_2$H shows insolubility in all the selected solvents, which was reported before by Smith et al.[15]; however, DBS-CO$_2$H shows gelation properties with pH switch.[121] Lauryl-DBS-iPr, only formed a gel in cyclohexane, partial gels in hexane and toluene and was a solution in the rest of

the tested organic solvents. On the other hand, MBS-iPr gels water and aqueous salt solutions upon heating and cooling (Table 2.2 and Table 2.3).

Meanwhile, the remaining mono-acetals (MBS-Cinn, MBS-Van, MBS-Ph and MBS-CN) show no gelation ability in any of the listed organic solvents or aqueous salts tested. Instead, when soluble upon heating, they form homogeneous solutions or crystals. The MBS compounds are essentially insoluble in the apolar solvents tested. However, solvents with good hydrogen bonding character (e.g. methanol) tend to solubilise the compound or show slow precipitation, presumably because of the large amount of hydroxyl groups on the mono-acetals.

The compounds were also tested in aqueous ethanolic solutions (ethanol-water mixtures) at 10 mg mL^{-1}. DBS gels all the aqueous ethanol mixtures even at 100% water content despite not having all the solute dissolve due to solubility. Although DBS-CO$_2$Me and DBS-iPr are essentially insoluble in water itself, these DBS derivative gelators gel all the aqueous ethanol mixtures while MBS-iPr gels water and mixtures containing 10-30% water by volume. The long-chain DBS derivative, Lauryl-DBS-iPr, forms gels in 50% water by volume and below but was only a solution in 100% ethanol. Furthermore, MBS-Ph shows insolubility in water, precipitates in ethanol and shows gelation ability on ethanolic mixtures containing 60-20% ethanol by volume. In contrast, the remaining mono-acetals displayed no gelation behaviour. MBS-Cinn is soluble in ethanol and precipitates in water, while the inverse is true for MBS-Van. MBS-CN only precipitates in all ethanolic mixtures. In addition, DBS and DBS-iPr further show gelation of glycerol and castor oil, which is also the same as MBS-iPr. On the other hand, DBS-CO$_2$Me forms a transparent gel in glycerol but remains as a solution in castor oil after heating and cooling. The rest of the tested gelator either formed a precipitate or remained insoluble or in solution.

It has already been shown that certain MBS derivatives of DBS can act as hydrogelators in some salt solutions.[113] A study of the effect of salt on the gelation mechanism of an MBS derivative hydrogelator showed that aqueous NaCl affects the morphology of the resulting xerogel and aids gelation.[122] Inspired by this result, we attempted the addition of salts to MBS-iPr. Gelation tests for the salt solutions were performed using a Crystallisation Systems Crystal 16. Samples were heated from 20 °C to 80 °C at a rate of 5 °C min^{-1}, held at 80 °C for five minutes, and then cooled back to 20 °C at a rate of -5 °C min^{-1}.

Table 2.2 | Gelation test in organic solvents (1% w/v) upon heating and cooling. I = insoluble, G = gel, PG = partial gel, S = solution, P = precipitate, (T) = transparent, (O) = opaque.

Solvent	Compounds									
	DBS	DBS-CO$_2$Me	DBS-CO$_2$H	DBS-iPr	Lauryl-DBS-iPr	MBS-iPr	MBS-Cinn	MBS-Van	MBS-Ph	MBS-CN
Hexane	G (O)	I	I	I	PG	I	I	I	I	I
Cyclohexane	G (O)	I	I	G (O)	G (T)	P	P	I	I	I
Toluene	G (T)	P	I	G (T)	PG	P	I	P	P	I
Chloroform	G (T)	PG	I	G (T)	S	I	I	I	P	I
Dichloromethane	G (T)	PG	I	G (T)	S	I	I	I	P	I
Tetrahydrofuran	S	PG	I	S	S	I	P	I	P	I
2-Butanone	G (T)[a]	G (O)	I	S	S	P	P	P	P	PG
Ethyl acetate	G (T)	G (O)	I	G (T)	S	P	I	P	P	PG
Acetonitrile	G (T)[a]	G (O)	I	S	S	P	P	P	P	I
Isopropanol	G (T)	G (O)	I	G (T)	S	S	P	I	P	P
Methanol	S	G (O)	I	G (O)	S	S	P	S	P	P
Ethanol	G (T)	G (T)	I	G (O)	S	S	S	P	P	P
90:10	G (T)	G (T)	I	G (O)	G (O)	S	S	P	P	P
80:20	G (T)	G (T)[b]	I	G (O)	G (O)	S	S	S	P	P
70:30	G (T)	G (T)[b]	I	G (O)	G (O)	S	S	S	P	P
60:40	G (T)	G (T)[b]	I	G (O)	G (O)	S	S	S	G (O)	P
50:50	G (T)	G (T)[b]	I	G (O)	G (O)	S	S	S	G (O)	P
40:60	G (T)	G (T)[b]	I	G (O)	PG	S	S	S	G (O)	P
30:70	G (T)	G (T)[b]	I	G (O)	PG	G (O)	P	S	G (O)	P
20:80	G (T)	G (T)[c]	I	G (O)	P	G (O)	P	S	G (O)	P
10:90	G (T)	G (T)[c]	I	G (O)	P	G (O)	P	S	PG	P
Water	G (T)[c]	I	I	I	I	G (O)	P	S	I	P
Glycerol	G (O)	G (T)	I	G (O)	S	G (T)	S	S	P	P
Castor Oil	G (T)	S	I	G (O)	S	G (O)	S	S	P	P

[a]gelation occurred overnight
[b]opaque fibrous clump was formed during the heating process – unable to dissolve fully
[c]not all solid dissolved

Table 2.3 | Synthesised mono-acetals in salt solutions (1% w/v) upon heating and cooling. I = insoluble, G = gel, PG = partial gel, S = solution, P = precipitate, (T) = transparent, (O) = opaque.

Salt Solution (2% w/v)	Compounds				
	MBS-Cinn	MBS-Van	MBS-iPr	MBS-Ph	MBS-CN
NaCl	P	S	G (O)	I	P
KCl	P	S	G (O)	I	P
LiCl	P	S	G (O)	I	P
ZnCl$_2$	P	S	G (O)	I	P
CaCl$_2$	P	S	G (O)	I	P
MgCl$_2$	P	S	G (O)	I	P
CuCl$_2$	P	S	S	I	P
NaOH	P	S	P	I	P
Na$_2$SO$_4$	P	S	G (O)	I	P

Table 2.3 shows that MBS-iPr gels most aqueous solutions of all the salts listed, except sodium hydroxide and copper (II) chloride. The reported MBS-derived gelator, DCBS[122] (DBS with 3,4 dichloro substituent on the benzyl ring), showed gelation in 2% NaOH (aq) whilst our MBS-iPr formed a precipitate with no indication of gelation. This information indicates that the benzyl substituent influences the gelation of MBS derivatives in aqueous NaOH, although the precise reasons for this effect are unclear. On the other hand, specific coordination of Cu (II) by the gelator

through the hydroxyl groups may have impacted why MBS-iPr forms a solution with $CuCl_2$.

Further gelation tests on the remaining mono-acetals were performed. However, they do not show any gelation in the presence of salts (Table 2.3). MBS-Van forms solutions at 10 mg mL^{-1} concentration but precipitates as fibrous, needle-like crystals at 20 mg mL^{-1} concentrations. On the other hand, MBS-Cinn produces similar needle-like crystals at 10 mg mL^{-1}. These results are in line with the previous series of tests, which showed that MBS-Cinn and MBS-CN precipitate from water at the stated concentrations while MBS-Van is soluble, and MBS-Ph is insoluble.

MBS-Cinn, MBS-Van and MBS-CN show no signs of gelation in any organic solvents, ethanolic mixtures and aqueous salt tested. This observation shows that a possible factor of gelation ability is the functionality offered by these acetal substituents and the lack of solubilising bulky substituents. The acetal substituent of MBS-Ph and MBS-iPr both have a greater steric bulk with respect to MBS-CN, MBS-Van and MBS-Cinn. It is possible that the bulkier the substituent is on the acetal group, the higher the chance it will self-assemble and exhibit gelation properties; hence, MBS-iPr and MBS-Ph both formed gelation in some of the ethanolic mixtures.

Raeburn et al.[123] studied the effect of solvent choice on gelation. The team focused on dissolving their gelator, Fmoc-diphenylalanine, in an organic solvent followed by the addition of water to test the gelation behaviour. The organic solvent can be removed post-gelation without significant changes in the rheological properties. One of the organic solvents that they have used was DMSO. Gelation tests were extended and were carried out for the isolated benzylidene sorbitol derivatives in DMSO:H_2O mixture. The tests were performed by dissolving 10 mg of the gelator in DMSO (i.e. 90:10 = 0.9 µL = 90%). Application of heat and sonication was used to dissolve the gelator in a lower content of DMSO fully. When fully dissolved, the correct water ratio was added to the mixture at room temperature. The gel formed instantaneously, unless stated (Table 2.4).

Table 2.4 | Gelation test of benzylidene derivatives in DMSO:H_2O solutions at 10 mg mL^{-1}. I = insoluble, G = gel, PG = partial gel, S = solution, P = precipitate, (T) = transparent, (O) = opaque. [a]gelation occurred overnight

DMSO: H₂O Mixture	Compounds									
	DBS	DBS-CO₂Me	DBS-CO₂H	DBS-iPr	Lauryl-DBS-iPr	MBS-iPr	MBS-Cinn	MBS-Van	MBS-Ph	MBS-CN
DMSO	S	S	S	S	S	S	S	S	S	S
90:10	S	G (T)	S	S	S	S	S	S	S	S
80:20	S	G (O)	S	G (O)	S	S	S	S	S	S
70:30	S	G (O)	G (O)	G (O)	P	S	S	S	S	S
60:40	G (T)	G (O)	G (O)	G (O)	P	PG	S	S	P	S
50:50	G (O)	G (O)	G (O)	G (O)	P	G (T)	S	S	P	S
40:60	G (O)	G (O)	G (O)	G (O)	P	G (T)	S	S	PG	S
30:70	G (O)	G (O)	G (O)	G (O)	P	G (T)	P	S	G (O)	S
20:80	G (O)	G (O)	G (O)	G (O)	P	G (O)	P	S	G (O)	P
10:90	G (O)	G (O)[a]	P	G (O)	P	G (O)	P	S	P	P
H₂O	I	I	I	I	I	I	I	S	I	I

At room temperature, all the isolated gelators are insoluble in water, except for MBS-Van. Therefore, the water acts as an anti-solvent that triggers the rapid formation of the fibre network, causing an instant gelling of the solvent. Most of the di-acetal derivatives, including DBS-CO₂H, which is insoluble in all the tested solvents, have gelation properties in some DMSO:H_2O mixtures. DBS-CO₂Me revealed the best gelation abilities as it formed gels at a higher volume of DMSO, followed by DBS-*i*Pr, DBS-CO₂H and DBS. The gelation observations show that the steric hindrance of the substituent on the benzyl ring of the molecule plays a significant role in the gelation ability. The -CO₂Me substituent has the most steric hindrance, followed by -*i*Pr then -CO₂H substituents. The more steric hindered substituent gelled a more comprehensive range of DMSO:H_2O mixture.

On the other hand, Lauryl-DBS-*i*Pr refuse to form gelation in the mixtures; the formed precipitate from this compound makes the solution opaque white. For the mono-acetal derivatives, only MBS-*i*Pr and MBS-Ph performed gelation abilities in DMSO:H_2O mixtures. The rest remained as a solution or formed precipitate that remained at the bottom of the vial. Again, the steric bulk of the substituent plays an account on the gelation abilities of the gelator.

Apart from the steric bulk of the substituent, another critical observation from all the gelation tests performed in this chapter is the significance of the hydroxyl group and the long-chain on a DBS derivative. It is proven that DBS-*i*Pr is a better organogelator than Lauryl-DBS-*i*Pr. Therefore, it appears that the hydroxyl group (responsible for hydrogen bonding) improves the gelation properties of the compound in comparison to a long chain (responsible for van der Waals forces). As only one DBS derivative was synthesised with a long chain, unfortunately, only one direct comparison can be observed.

2.3.2 Gelation Behaviour of DBS-*i*Pr and MBS-*i*Pr mixture

Although DBS-*i*Pr and MBS-*i*Pr are both reported in patents[84,115], their gelation abilities were not studied. The apparent differences in the gelation properties of DBS-*i*Pr and MBS-*i*Pr shown in Table 2.2, where the former is insoluble and the latter forms a gel in water, drove the research to focus on both compounds. Phase diagrams for DBS-*i*Pr and MBS-*i*Pr were carried out in aqueous ethanolic mixtures (Figure 2.7). The phase diagrams show that DBS-*i*Pr displays significant gelation properties since it forms gels in aqueous ethanolic mixtures at different concentrations as low as 1 mg mL^{-1}. The diagrams further show that DBS-*i*Pr gelates in ethanol at 7 mg mL^{-1} and precipitates at 5 mg mL^{-1}. Because of its insolubility, no gelation was observed for DBS-*i*Pr in water regardless of the concentration. Conversely, MBS-*i*Pr gelates in water at concentrations as low as 7 mg mL^{-1} and forming a partial gel at 5 mg mL^{-1}.

Given the array of dissolution profiles between the mono and the diacetal compounds reported here, in ethanol:H_2O mixtures, it seemed fitting to mix the gelators and analyse their combined gelation phase diagram in ethanol:H_2O mixtures. The inspiration for this work came from research performed by Fan and colleagues[120]. They demonstrated the tunability of self-assembly of two-component gels from donor and acceptor MBS derivatives, where dual component material behaviour was observed.[124] Their experiments were focused on different organic solvents and inferred a π donor-acceptor interaction as the driving force for gelation. Here we focus on the full range of ethanol:H_2O compositions because the extremes of composition are only gelled by one of the components.

Ethanol:Water Volume Ratio	1mg	3mg	5mg	7mg	10mg	15mg
EtOH	S	P	P	G (O)	G (O)	G (O)
90:10	S	P	P	G (O)	G (O)	G (O)
80:20	S	P	G (O)	G (O)	G (O)	G (O)
70:30	PG (T)	G (O)	G (O)	G (O)	G (O)	G (O)
60:40	G (T)	G (O)	G (O)	G (O)	G (O)	G (O)
50:50	G (T)	G (O)	G (O)	G (O)	G (O)	G (O)
40:60	G (T)	G (O)	G (O)	G (O)	G (O)	G (O)
30:70	G (T)[b]	G (O)	G (O)	G (O)	G (O)[a]	G (O)[a]
20:80	G (T)[b]	G (O)	G (O)	G (O)[a]	G (O)[a]	G (O)[a]
10:90	PG (T)[a]	G (T)[a]	G (O)	G (O)[a]	G (O)[a]	G (O)[a]
H_2O	I	I	I	I	I	I

Concentration of DBS-iPr (mg/mL)

Ethanol:Water Volume Ratio	3mg	5mg	7mg	10mg	15mg	20mg	25mg
50:50	S	S	S	S	S	S	P
40:60	S	S	S	S	P	P	G (O)[b]
30:70	S	S	P	G (O)	G (O)	G (O)	G (O)
20:80	S	S	P	G (O)	G (O)	G (O)	G (O)
10:90	S	S	P	G (O)	G (O)	G (O)	G (O)
H_2O	S	PG (O)	G (O)	G (O)	G (O)	G (O)	G (O)

Concentration of MBS-iPr (mg/mL)

Figure 2.7 | DBS-iPr and MBS-iPr phase diagram. Gelation upon heating and cooling. I = insoluble, G = gel, PG = partial gel, S = solution, P = precipitate, (T) = transparent, (O) = opaque. [a]not all solid dissolved, [b]gelation occurred overnight.

Ethanol:Water Volume Ratio					
EtOH	S	P	G (O)	G (O)	G (O)
90:10	S	P	G (O)	G (O)	G (O)
80:20	S	G (O)[b]	G (O)	G (O)	G (O)
70:30	G (O)[b]	G (O)	G (O)	G (O)	G (O)
60:40	G (O)[c]	G (O)	G (O)	G (O)	G (O)
50:50	G (O)[c]	G (T)	G (O)	G (O)	G (O)
40:60	G (O)	G (O)	G (O)	G (O)	G (O)
30:70	G (O)	G (O)	G (O)	G (O)	G (O)
20:80	G (O)	G (O)	G (O)	G (O)	G (O)
10:90	G (T)[a]	G (O)[a]	G (O)[a]	G (O)[a]	G (O)[a]
H$_2$O	I	I	G (T)[a]	G (O)[a]	G (O)[a]
	3mg	5mg	7mg	10mg	15mg
	(1.8:1.2) mg	(2.9:2.1) mg	(4.1:2.9) mg	(5.9:4.1) mg	(8.8:6.2) mg
	Concentration of equimolar DBS-iPr and MBS-iPr (mg/mL)				

Figure 2.8 | Phase diagram of equimolar ratio of DBS-*i*Pr and MBS-*i*Pr upon heating and cooling. G = gel, S = solution, I = insoluble, P = precipitate, (T) =transparent, (O) = opaque. [a]not all solid dissolved, [b]gelation occurred overnight and [c]transparent to opaque gel occurred overnight at 25 °C.

Equimolar amounts of DBS-*i*Pr and MBS-*i*Pr were placed in a vial, aqueous ethanolic solutions with the appropriate ratios were added afterwards. Gelation properties were tested upon heating (until the mixture was entirely transparent by eye) and cooling. Figure 2.8 shows that gelation was observed between 7-15 mg mL^{-1} of equimolar amounts of DBS-*i*Pr and MBS-*i*Pr in 100% ethanol, 100% water and all aqueous ethanolic solution ratios in between (lowest concentration consisting of 4.1 mg and 2.9 mg of DBS-*i*Pr and MBS-*i*Pr, respectively). The phase diagram of DBS-*i*Pr (Figure 2.7) has a similar trend with the equimolar DBS-MBS-*i*Pr phase diagram (Figure 2.8). The noticeable difference to the phase diagram of DBS-*i*Pr is that the gelation extended into water. Also, considering only the concentration of the DBS-*i*Pr component, the phase diagram is shifted to a lower concentration. Overall, this phase diagram shows that MBS-*i*Pr has a positive influence on the gelation of DBS-*i*Pr.

2.4. Infrared Spectroscopy

Given that both DBS-*i*Pr and MBS-*i*Pr efficiently immobilise polar solvents such as water and ethanol, we considered that hydrogen bonding might be playing an essential role in the formation of the gels. FTIR was used to investigate the effect of these solvents on the gel structure focusing on both intermolecular and

intramolecular interactions between −OH groups that might contribute to the stabilisation of the self-assembled aggregates.[59]

IR spectra of MBS-*i*Pr and DBS-*i*Pr as crystalline powders, gel and xerogels were measured, and the results are shown in Figure 2.9. Lai *et al*.,[125] reported that according to the IR handbook[126], the intermolecular hydrogen bonds for the OH groups appear in the range of 3200-3550 cm^{-1}, and the intramolecular hydrogen bonds appear in the range of 3400-3590 cm^{-1}. For all samples, peaks at approximately 3250 – 3350 cm^{-1} were observed, assigned to the intermolecular hydrogen bonding. This observation indicates that intermolecular hydrogen bonding between the −OH groups in the molecule is one of the driving forces for the self-assembly of DBS-*i*Pr and MBS-*i*Pr. It is noteworthy that for the crystals of the MBS compounds derived from vanillin and cinnamaldehyde (that do not form gels), the IR spectra between 3200 and 3400 cm^{-1} are very similar to the xerogel of MBS-*i*Pr (Figure 2.10), indicating that the hydrogen bonding is similar in all the MBS compounds, whether in crystal or gel form.

Furthermore, the IR spectra for MBS-*i*Pr show no change in wavenumber between the xerogel, wet gel and the crystalline powder (Figure 2.9b). In contrast, the DBS-*i*Pr crystalline spectrum shows peaks at 2956 and 3267 cm^{-1} (Figure 2.9a); these peaks were seen to have shifted to higher wavenumbers in the xerogel and wet gel spectra. These observations indicate that the hydrogen bonding between the −OH groups are being modified by the introduction of ethanol. The spectra show that DBS-*i*Pr in the crystalline state has stronger hydrogen bonds than that in DBS-*i*Pr gel in ethanol and its xerogel. Furthermore, the polymeric hydrogen bond peak was reported by Liddel and Becker[127] to be near 3350 cm^{-1}, whereas the dimer band is found near 3500 cm^{-1}. As DBS-*i*Pr xerogel and wet gel in ethanol showed peaks at 3347 cm^{-1} and 3349 cm^{-1}, respectively, we suggest that DBS-*i*Pr self-assembles into a polymeric structure *via* hydrogen bond chains.
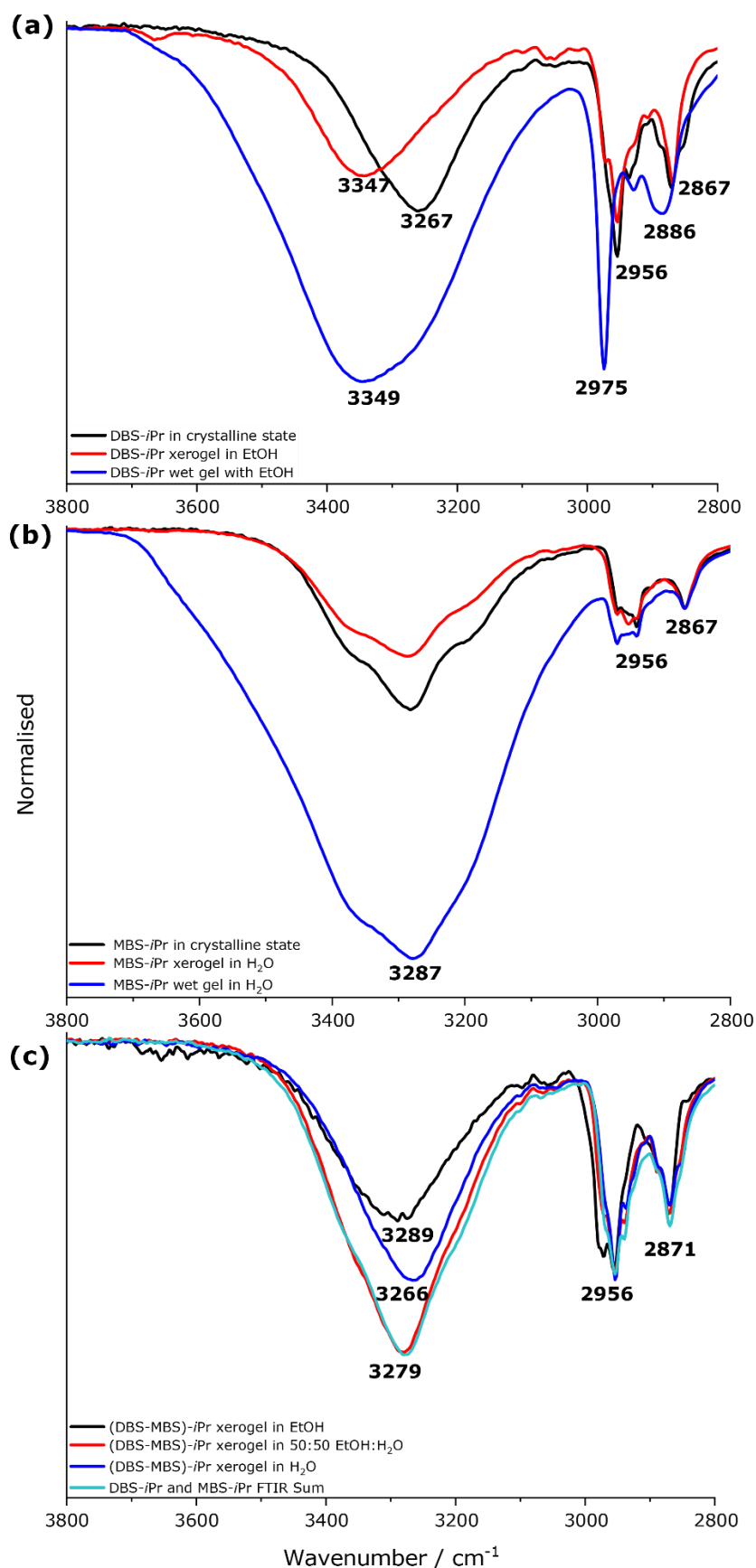
Figure 2.9 | IR spectra of crystalline powder, xerogels and gels: (a) DBS-*iPr* and (b) MBS-*iPr*. (c) Xerogels of equimolar DBS-*iPr* and MBS-*iPr*. Gels were formed with respective solvents: EtOH for DBS and water for MBS, and the xerogels are air-dried gels. Data were normalised.

It is apparent that the wet gels have the strongest intensities at around 3250 – 3350 cm^{-1} because of the strong hydrogen bonding interactions between (i) the solvent molecules, (ii) the gelator molecules and (iii) both the solvent and gelator molecules. As xerogels have the weakest intensities, we believe that the intermolecular interactions between the solvent molecules contribute significantly to the intensity of the damp gel. Nevertheless, the xerogels' intensities imply that the stretch's dipole moment in the xerogel state is weaker than the dipole moment in the crystalline state.[128]
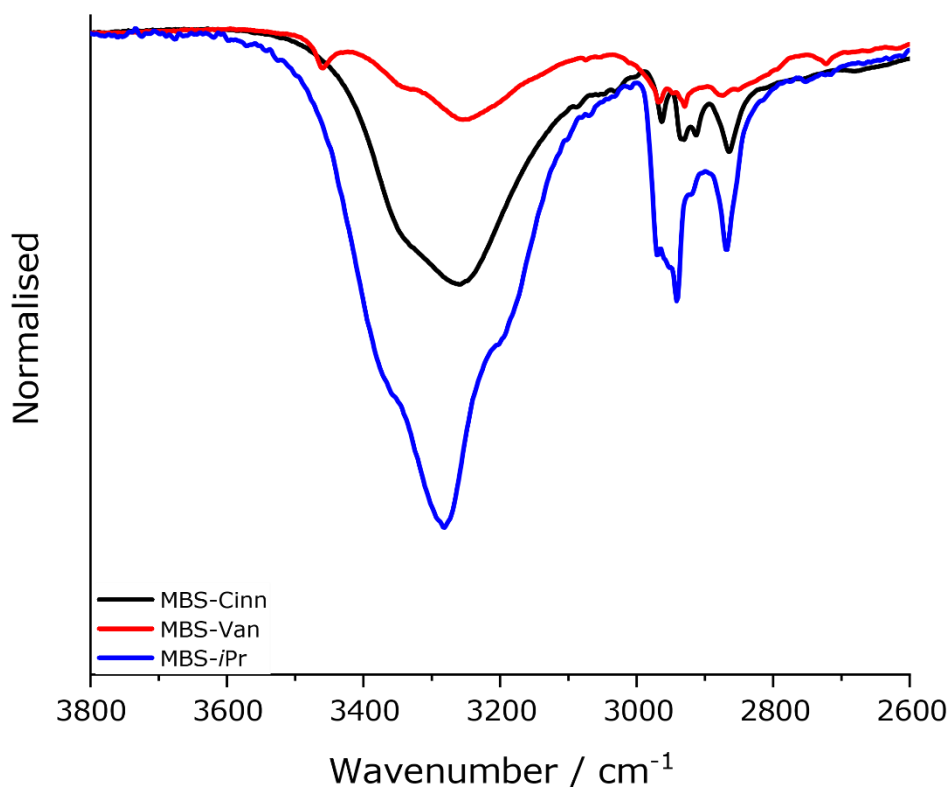
Figure 2.10 | FTIR spectra of MBS-Cinn and MBS-Van crystals, and MBS-*i*Pr xerogel.

The sum of the IR data of DBS-*i*Pr and MBS-*i*Pr was calculated and plotted with the FTIR spectra of equimolar DBS-*i*Pr and MBS-*i*Pr in (i) ethanol, (ii) 50:50 ethanol:H_2O and (iii) H_2O (Figure 2.9c). It shows that the IR spectra of the xerogels resemble the sum of the spectra of their individual components, meaning that the interactions present in the pure compounds are also found in the equimolar xerogels and indicate self-sorting. Should a co-assembly occur, in which the MBS and DBS compounds are hypothetically incorporated in the same lamellae in the fibres, one would expect a significantly different IR signature. Furthermore, only the equimolar xerogel from 50:50 ethanol:H_2O has the same intensity as the FTIR sum at the −OH stretch at 3279 cm^{-1}. It was also observed that the higher the ethanol content of the solvent, the higher the frequency of the −OH stretch. This observation suggests that xerogels

from ethanol have weaker hydrogen bonds than xerogels from water,[129] possibly because water is a better hydrogen bond donor than ethanol.

2.5. Xerogel Morphologies

The difference in morphology between the mono- and di-benzylidene sorbitol xerogels was investigated by scanning electron microscopy (SEM). Samples were prepared by drying MBS-*i*Pr and DBS-*i*Pr gels obtained from the various solvents and mixtures on an SEM stub *in vacuo* followed by iridium coating under vacuum. While the drying process causes collapse of the gel and could result in some dissolved material precipitating during drying, the results indicate significant differences between the samples that are indeed a result of the initial gel structure in the solvent. However, caution is recommended in interpretation because the drying of samples with different liquid compositions could result in contrasting drying times and fibre coalescence, and it is likely that the observed dimensions in the SEM images are larger than those of the solvated fibres in the gels.[50]

The fibres widths were quantified by plotting a histogram. The histogram is displayed as a frequency distribution graph where 300 width measurements were taken per sample using the image analysis software, ImageJ, which has been used for micrograph quantification in recent years.[155,156] A line was drawn along the scale bar of a SEM micrograph using the straight-line tool. The 'set scale' analysis option was then applied to calibrate the software for that specific micrograph. The widths of single fibre and fibre bundles were measured manually by the use of the 'measure' tool in ImageJ (pressing key 'M' for a shortcut).[157] It is ensured that the measurement is perpendicular to the edge of the fibres to measure the minimum width on a specific fibre. The histograms are plotted using the Origin software. LogNormal distribution curve was applied in the software for the peak function of the histograms, where the maximum of the peak is stated as the width of the fibres.

SEM micrographs of DBS-*i*Pr, shown in Figure 2.11, comprise different xerogel morphologies depending on the solvent medium. The DBS-*i*Pr fibres remaining from the ethanol gel (Figure 2.11) are relatively wider than the fibres grown from the evaporation of 70:30 ethanol:H_2O from the gel (Figure 2.11b). They do, however, show similar morphology of a ribbon-like structure. On the other hand, the fibres formed from the evaporation of the toluene gel are much thinner than those formed in ethanol (31 ± 0.7 nm vs 700 ± 30 nm width as seen in Figure 2.11a and c). This difference is probably a result of the different solubility of DBS-*i*Pr in the two solvents, with the gelator being more soluble in toluene (and therefore better

solvated) than in ethanol. Furthermore, the difference is easily observable on the macroscale. Gels in toluene and most of the organic solvents are transparent, while the gels in ethanol, ethanol:H_2O solutions, methanol and cyclohexane are opaque. The effect of gel fibre size on gel transparency is, therefore, quite apparent. SEM micrographs were also taken for the DBS-*i*Pr xerogel formed from 1 mg mL^{-1} in 50:50 ethanol:H_2O (A 66a). The morphology is dissimilar to the fibres in the xerogel formed from ethanol.

Only the xerogel from cyclohexane shows helical fibres in different sizes consistently (Figure 2.11d). This finding is in accordance with that of Song and colleagues[61], who described how polar solvents (such as *i*PA, H_2O and ethanol) discourage helical fibre formation and lead to a smooth, straight structure. On the other hand, non-polar solvents can induce twisting in the chiral assemblies as the gelator self-assembled with strong hydrogen bonding interactions.[61]

The helical fibres in xerogel formed from cyclohexane have an average width of 42 ± 1.2 nm. All the DBS-*i*Pr fibres in this material show anti-clockwise twisting. A plot of the full twist period (2P or pitch) against the smallest fibre size in cross-section (*h* or minimum width) is given in Figure 2.12.
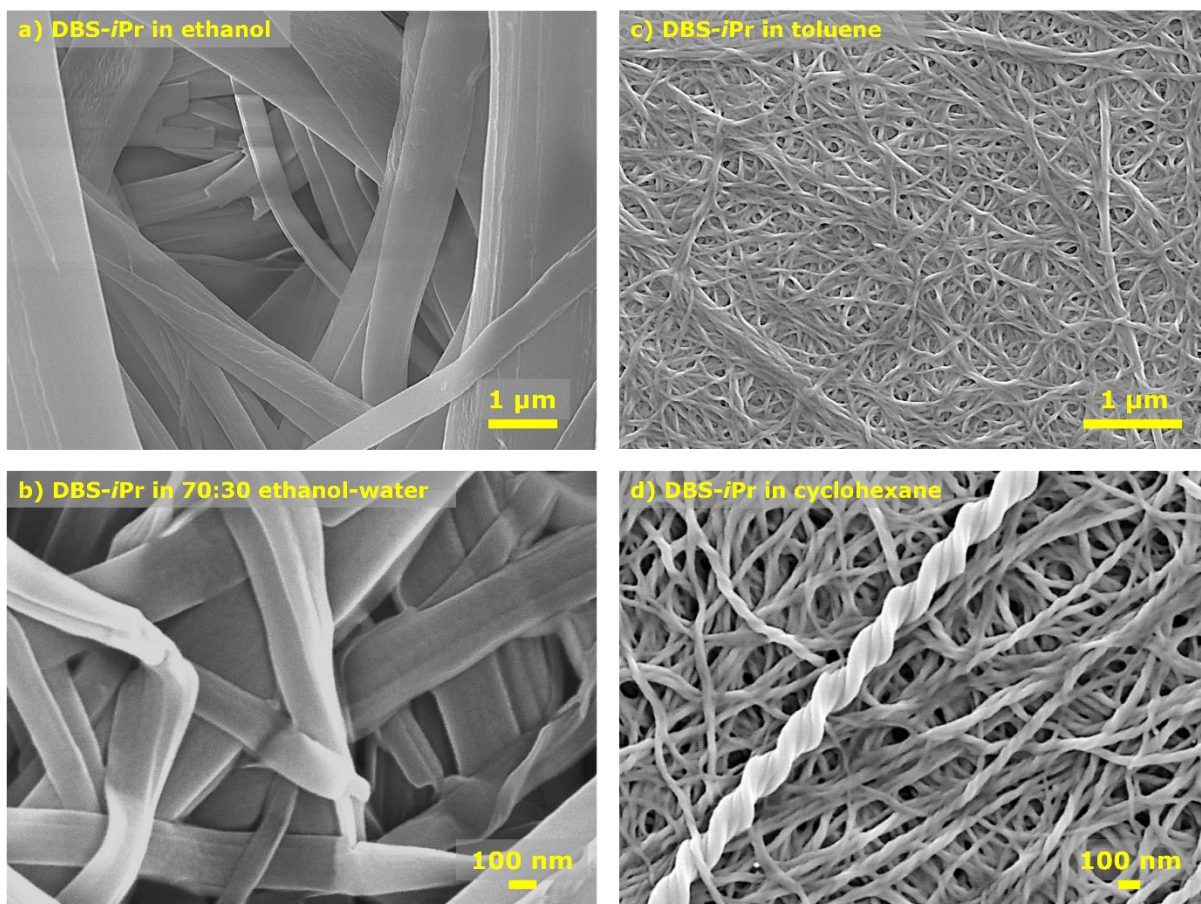
Figure 2.11 | SEM micrographs of DBS-*i*Pr xerogels formed by 1% w/v. Conditions: xerogel was prepared by drying the gel in air and then coating it with 5 nm Ir before imaging under vacuum at 5 kV. Scale bar represents: 1 µm in a and c; 100 nm in b and d.
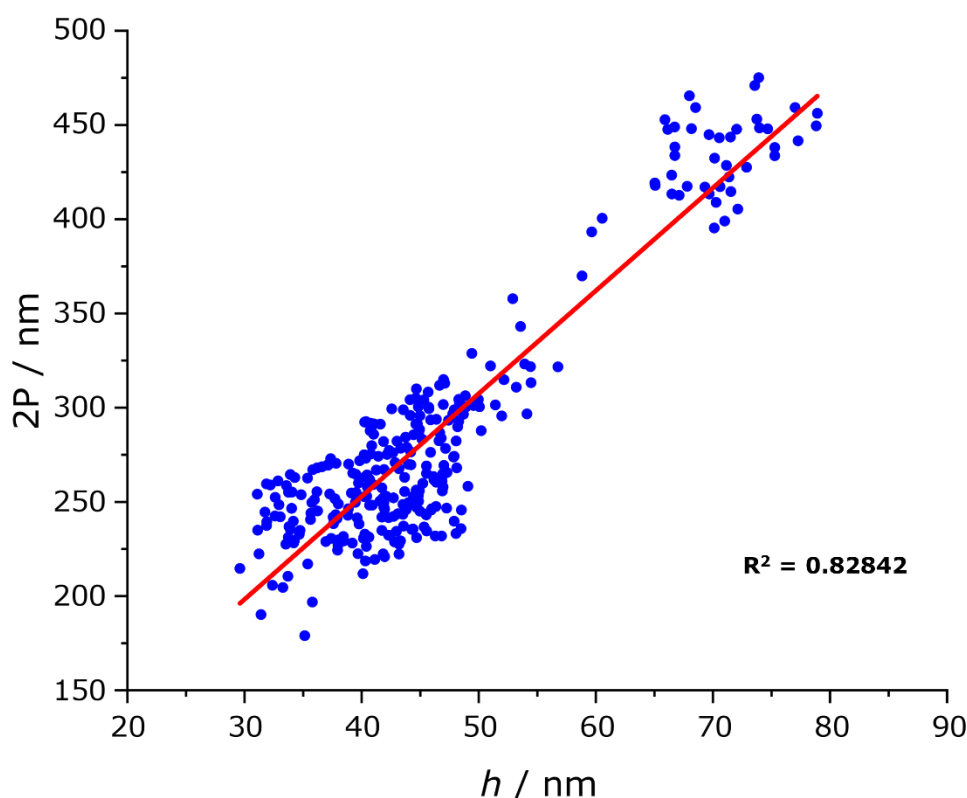
Figure 2.12 | Correlation between full twist period (2P, 2π rotation, nm) and the smallest fibre size in cross-section (h, nm) of DBS-*i*Pr twisted fibres in cyclohexane upon heating and cooling

It has been reported that as twisted fibres narrow, the pitch changes sharply.[130] Furthermore, Shtukenberg *et al.*[52] reported that for all twisted crystals in the size range from nm to cm, the twist period is proportional to the cross-section size. This effect is observed as a positive correlation is obtained between the pitch and the minimum width. It has been shown that strain induces the twisting of fibres, and for an elastically twisted fibre, the maximum strain (γ_{max}) forms on the outer surface and approaches $\gamma_{max} = \pi h/(2P)$.[53] In addition, the curvature radius, R, could also be obtained from $\gamma_{max} = h/(2R)$. With an average of 287 nm for the pitch and 46 nm for the minimum width, a strain of 0.500 and a curvature radius of 45.7 nm were calculated. The strain value indicates that the fibres formed in cyclohexane have elastic properties.

There is a common thread for the morphology of the fibres between the xerogels formed from ethanol:H_2O, water and aqueous salt solutions present in the MBS-*i*Pr. The majority of the fibres present from ethanol:H_2O mixtures (A 66g-i) and aqueous salt solutions (Figure 2.13b and A 66d and f) are similar to the morphology of MBS-*i*Pr xerogel in water (Figure 2.13a). They are all quite thick tape-like fibres.

Furthermore, the xerogels of MBS-*i*Pr from a salt solution of Na_2SO_4 (Figure 2.13b) with an average width of 160 ± 4.3 nm, and 10:90 ethanol:H_2O solution (A 66i) with an average width of 77 ± 4.1 nm, are very similar where distorted rod-like fibres intertwine with smaller fibres. As for the xerogel formed from $CaCl_2$ solution, the morphology appears to be different from the majority of the gels (Figure 2.13c). The fibres are a mixture of clustered and individual fibres with an average width of 340 ± 11 nm. The gel formed in the $ZnCl_2$ solution exhibited 'webbed' fibres connected with an average width of 650 ± 22 nm (A 66e) . All MBS-*i*Pr gels are opaque; it is useful to see the difference in the microstructure of the MBS-*i*Pr xerogels to see the effect of aqueous salt solutions on the change of morphology, which is correlated with the mechanical properties of the materials (see below).
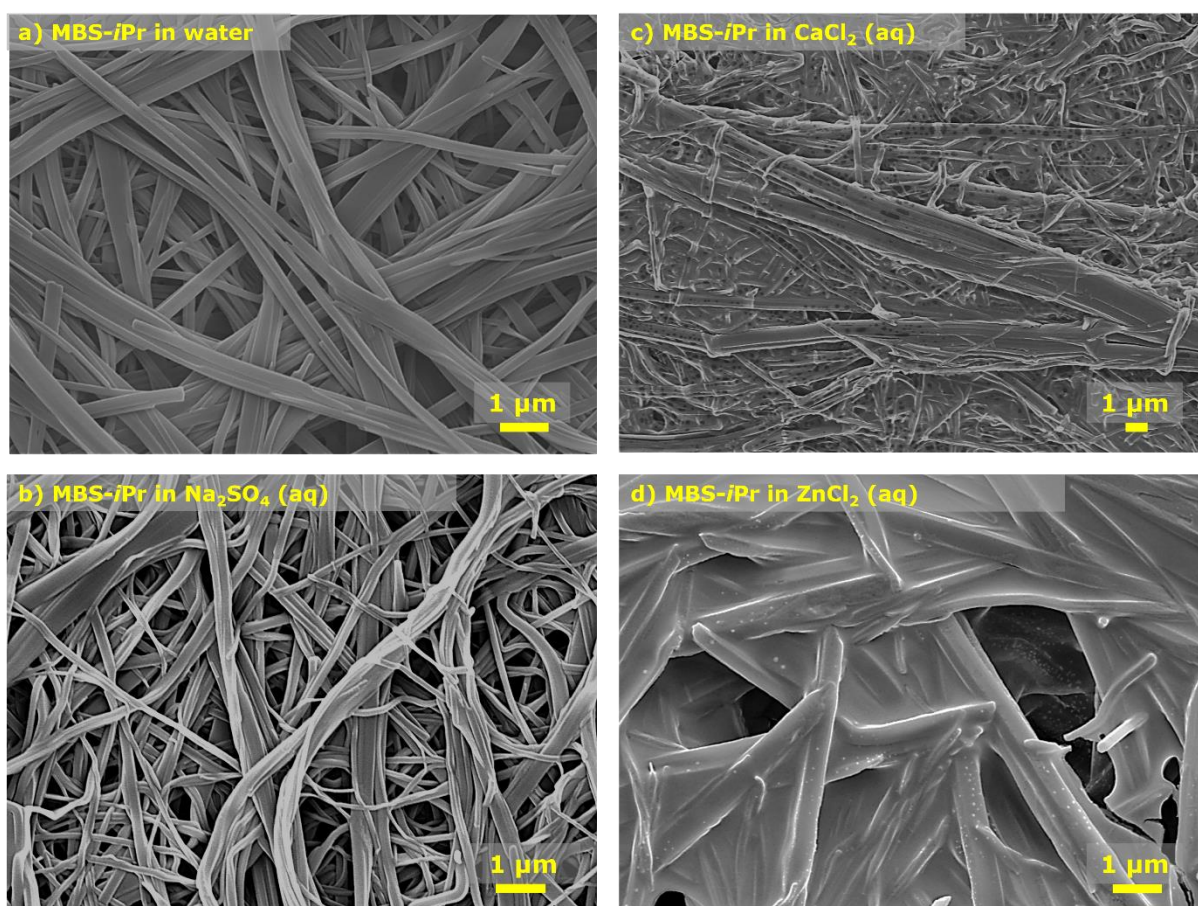
Figure 2.13 | SEM micrographs of MBS-*i*Pr xerogels formed by 1% w/v in 2% w/v aqueous salt solutions. Conditions: xerogel was prepared by drying the gel in air and then coating it with 5 nm Ir before imaging under vacuum at 5 kV. Scale bars represent 1 μm.

SEM imaging was also done for the equimolar xerogels of DBS-*i*Pr and MBS-*i*Pr to investigate their morphology (Figure 2.14 and A 69). In pure solvents (water and ethanol), a mixture of thick and thin fibres was seen. Precise bimodal distribution of widths is observed. The thin fibres in both solvents exhibit similar average widths, as seen in Figure 2.15 and Table 2.5, whereas the thick fibres are quite different.

Thick fibres of the equimolar xerogel in water (Figure 2.15a) resemble the MBS-iPr xerogel in water (Figure 2.13a), with an average fibre width of 260 ± 4 nm and 190 ± 8.5 nm, respectively. On the other hand, the equimolar xerogel in ethanol (Figure 2.15c), which also displays a bimodal distribution of fibre width (Figure 2.14c), appears to have root-like fibres tangling around the thick fibres with an average fibre width of 590 ± 20 nm for the thick fibres and 21 ± 1 nm for the thin ones. Although the morphology and the fibre width are not similar to DBS-iPr in ethanol (700 ± 30 nm, Figure 2.11a), both possess the highest fibre width. As a result of this inspection, we anticipate that the thick fibres in water and ethanol correspond to MBS-iPr and DBS-iPr, respectively, whilst the thinner fibres are other components that could partially precipitate during the solvent evaporation process. Nevertheless, they clearly have an influence on gel properties. Remarkably, the equimolar mixture, (DBS-MBS)-iPr, xerogel formed in 50:50 ethanol:H_2O solution (where individual MBS-iPr did not form a gel at this concentration) only contain uniform-sized fibres (Figure 2.14b) with an average width of 120 ± 6.5 nm. On the other hand, the DBS-iPr xerogel formed in the same solution has fibres with an average width of 89 ± 2.7 nm (A 66b).
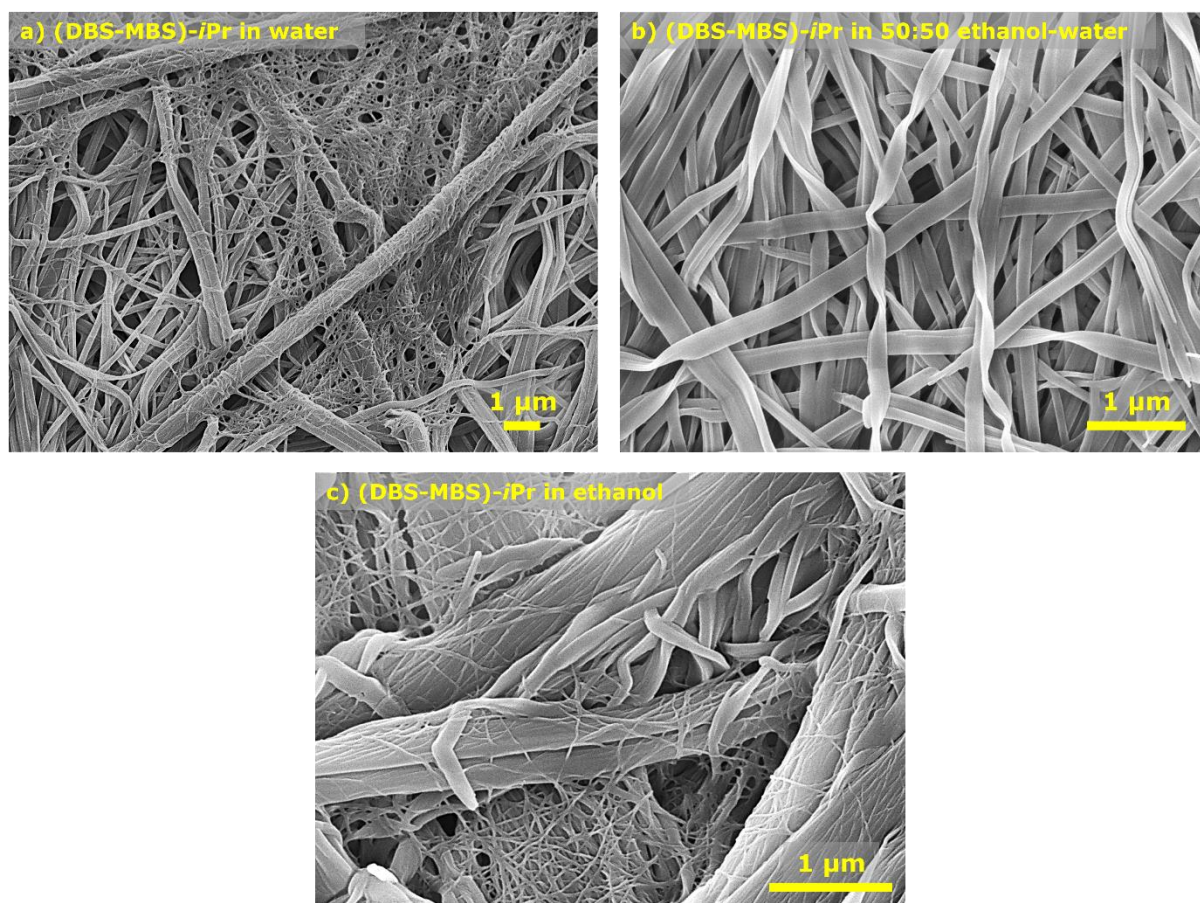
Figure 2.14 | SEM micrographs of dried xerogel formed by equimolar 1% w/v DBS-*iPr* and MBS-*iPr* upon heating and cooling. Conditions: xerogel prepared by drying the gel in air and then coating with 5 nm Ir before imaging under vacuum at 5 kV. Scale bar in all images represents 1 μm.

All SEM micrographs of the xerogels revealed that DBS-*iPr* and MBS-*iPr* form fibrous networks, in common with other sorbitol xerogels.[10,15,62,133] We show that the nature of the networks in the solids remaining after solvent evaporation depends on the liquid and the presence of salts in the case of hydrogels. While caution is advised in the interpretation of SEM textures from dried gels, exemplified by the work of Mears *et al*.[134] where drying can significantly affect the fibre network, we believe that the dramatic differences seen between morphologies of xerogels from the same solvents in the present case at least provide a strong indication of significant differences in gel structure.

Table 2.5 | Fibre average width for xerogels made from DBS-*i*Pr and MBS-*i*Pr gels at 10 mg mL^{-1}. [a]xerogel made from 1 mg mL^{-1} (A 67 and A 68)

Solvent	Average Width / nm
DBS-*i*Pr	
Ethanol	700 ± 30
*i*PA	25 ± 0.9
Toluene	31 ± 0.7
Cyclohexane	42 ± 1.2
50:50 e-w	89 ± 2.7
[a] 50:50 e-w	78 ± 2.4
MBS-*i*Pr	
CaCl$_2$ (aq)	340 ± 11
ZnCl$_2$ (aq)	650 ± 22
MgCl$_2$ (aq)	390 ± 14
LiCl (aq)	310 ± 11
NaCl (aq)	300 ± 13
KCl (aq)	170 ± 5.6
Na$_2$SO$_4$ (aq)	160 ± 4.3
30:70 e-w	310 ± 12
20:80 e-w	340 ± 11
10:90 e-w	77 ± 4.1
H$_2$O	190 ± 8.5
(DBS-MBS)-*i*Pr	
Ethanol	20 / 590 ± 0.5 / 17
50:50 e-w	120 ± 6.5
Water	20 / 260 ± 0.3 / 9.3

In the present case, the chiral nature of the compounds might have aided the characterisation of the gels in the presence of the immobilised solvent. Li *et al.*[61] studied the chiral structure of the aggregate in a gel using circular dichroism (CD) spectroscopy. Comparison of the morphologies of the xerogels with the CD spectra of the wet gels could have provided helpful information. In our hands, this has not been possible because of the high concentrations required and the light scattering by the samples. For example, 10 mg mL^{-1} DBS-*i*Pr in cyclohexane would be an excellent example to see how the twisted helical fibres behave in circularly polarised light. The DBS-*i*Pr powder is difficult to dissolve in cyclohexane and must be heated up to boiling until no solid is seen by eye. The rapid formation of the gels during cooling makes it challenging to transfer the solution into a cuvette. Therefore, the attempt to obtain CD spectra for DBS-*i*Pr in cyclohexane was a struggle. Furthermore, the opaqueness of the gels and their effective light scattering because of the fibre dimensions observed by SEM for both MBS-*i*Pr and DBS-*i*Pr, make CD spectra very difficult to obtain in any case irreproducible and unreliable in our hands. The obtained CD spectra are shown in the appendix (A 73).
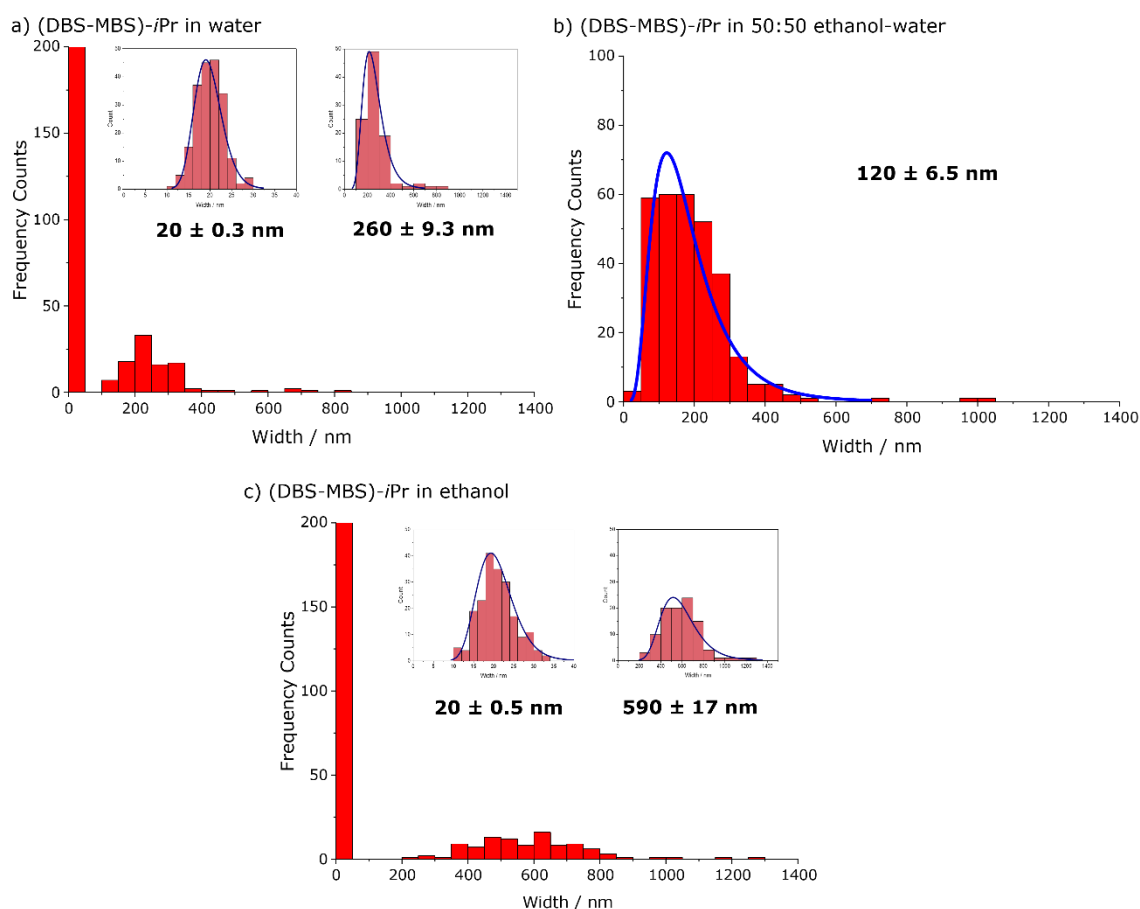
Figure 2.15 | Distribution histograms of fibres widths for xerogels formed from equimolar (DBS-MBS)-*i*Pr in (a) water, (b) 50:50 ethanol:H_2O and (c) ethanol.

2.6. Gel Rheology

Rheological data were collected for DBS-*i*Pr gels in dichloromethane (DCM) and *iso*propyl alcohol (*i*PA) and MBS-*i*Pr samples formed in water and salt solutions. Oscillatory measurements were conducted on samples of the gels by applying strain deformation to the sample and measuring the stress response while keeping the frequency at a constant value of 1 Hz. This method allows determination of their storage and loss moduli (G' and G" respectively) across a range of applied strain (Figure 2.16, Figure 2.17, Figure 2.18). Materials exhibit elastic properties when G' > G", viscoelastic properties when the two values are equal, and viscous properties when G' < G" .[8] Elastic and viscous in this context mean elastic solid and viscous liquid. Therefore, the crossing point on a graph where storage and loss moduli are plotted against strain shows the point where strain causes the gel to flow like a Newtonian liquid.[135] We can see that the two DBS-*i*Pr gels exhibit different strain percentages (the DCM gel at 3% strain, the *i*PA gel at 6%) and that the G'

and G" values for the *i*PA gel are approximately an order of magnitude greater than those for the DCM gel.
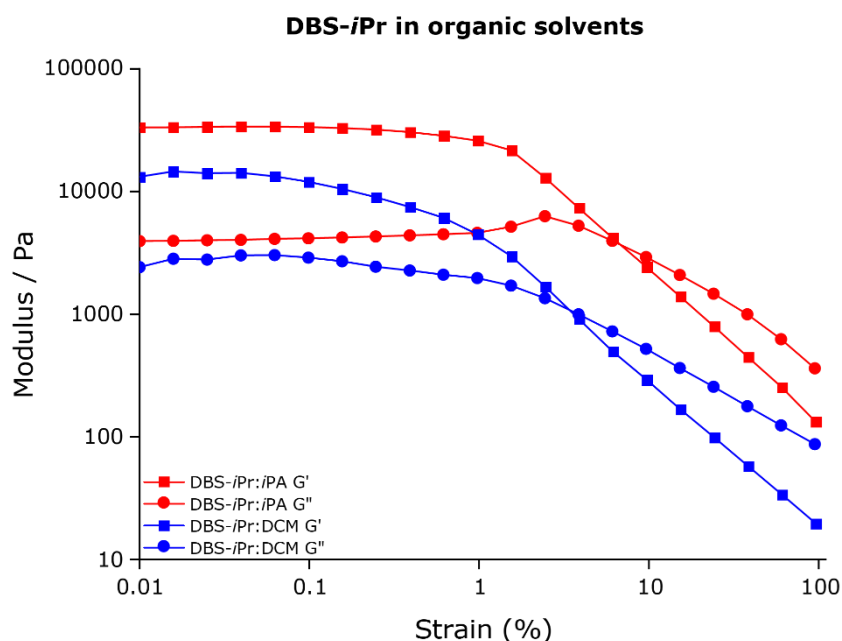
Figure 2.16 | Amplitude sweep rheological data of DBS-*i*Pr gels formed from IPA and DCM formed at 1.5% w/v upon heating and cooling. G' as Storage Modulus and G" as Loss Modulus.

Rheological data of MBS-*i*Pr gels formed in water and 2% w/v monovalent and divalent salts solutions are summarised in Figure 2.17. MBS-*i*Pr gels formed from water and monovalent salts solutions (Figure 2.17a) show a good G', G" and strain percentage. However, they do not exhibit elastic and robust gel features as high as the value obtained for the gels formed from divalent salt solutions. MBS-*i*Pr gels formed from divalent aqueous salt solutions (2% w/v) exhibit the highest values of G' and G", having a strain value of ~10%. This parameter demonstrates the appreciable elasticity of the gels and the positive effect these divalent salts have on this property.

On the other hand, Figure 2.18 shows the rheological data of MBS-*i*Pr and equimolar (DBS-MBS)-*i*Pr gels formed from ethanol:H_2O solutions. The MBS-*i*Pr gels display two trends where the higher the volume of water in the solution ratio, (i) the higher the value of G' and G", and (ii) the less elastic the gel is. Remarkably, the multicomponent gels formed from ethanol:H_2O mixtures display a very similar trend to MBS-*i*Pr. The higher the volume of water in the solution ratio, the higher the value of G' and G". Conversely, it is apparent that the equimolar gel in 50:50 ethanol:H_2O ratio exhibits the highest strain value, and therefore, it is the most

elastic gel. This property can be ascribed to the morphology of the equimolar gel having uniform-sized fibres in a weaved-like network (Figure 2.14b).
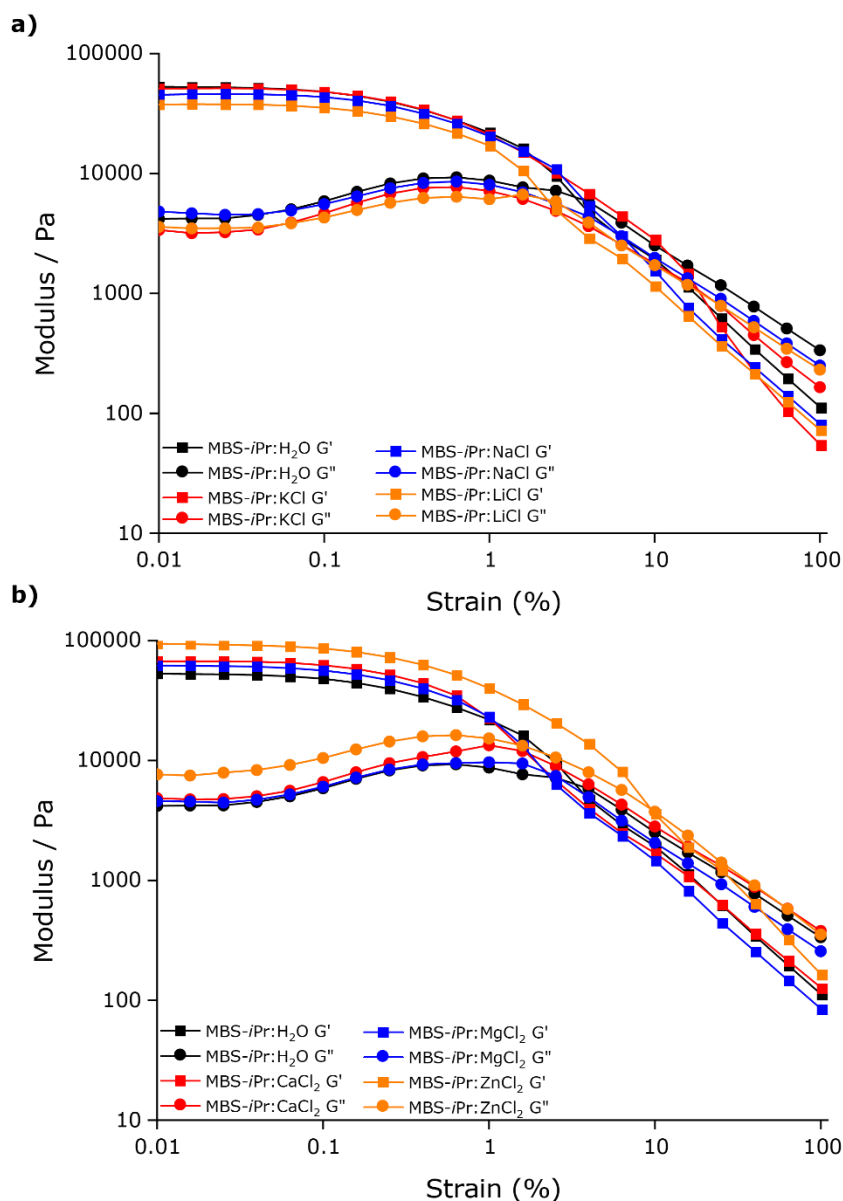
Figure 2.17 | Amplitude sweep rheological data for 10 mg mL^{-1} MBS-*i*Pr gels formed from 2% w/v a) aqueous monovalent salts and b) aqueous divalent salts upon heating and cooling. G' as Storage Modulus and G" as Loss Modulus.

The rapid formation of the gels during cooling makes measurement of the gel formation time difficult at ambient temperature in the thermal equilibrium state of the DBS-*i*Pr gels. Also, transferring the sample is impractical as we could not obtain a reliable oscillatory measurement. This phenomenon means we cannot directly compare the gel strength of the monobenzylidene and dibenzylidene sorbitol gelators.
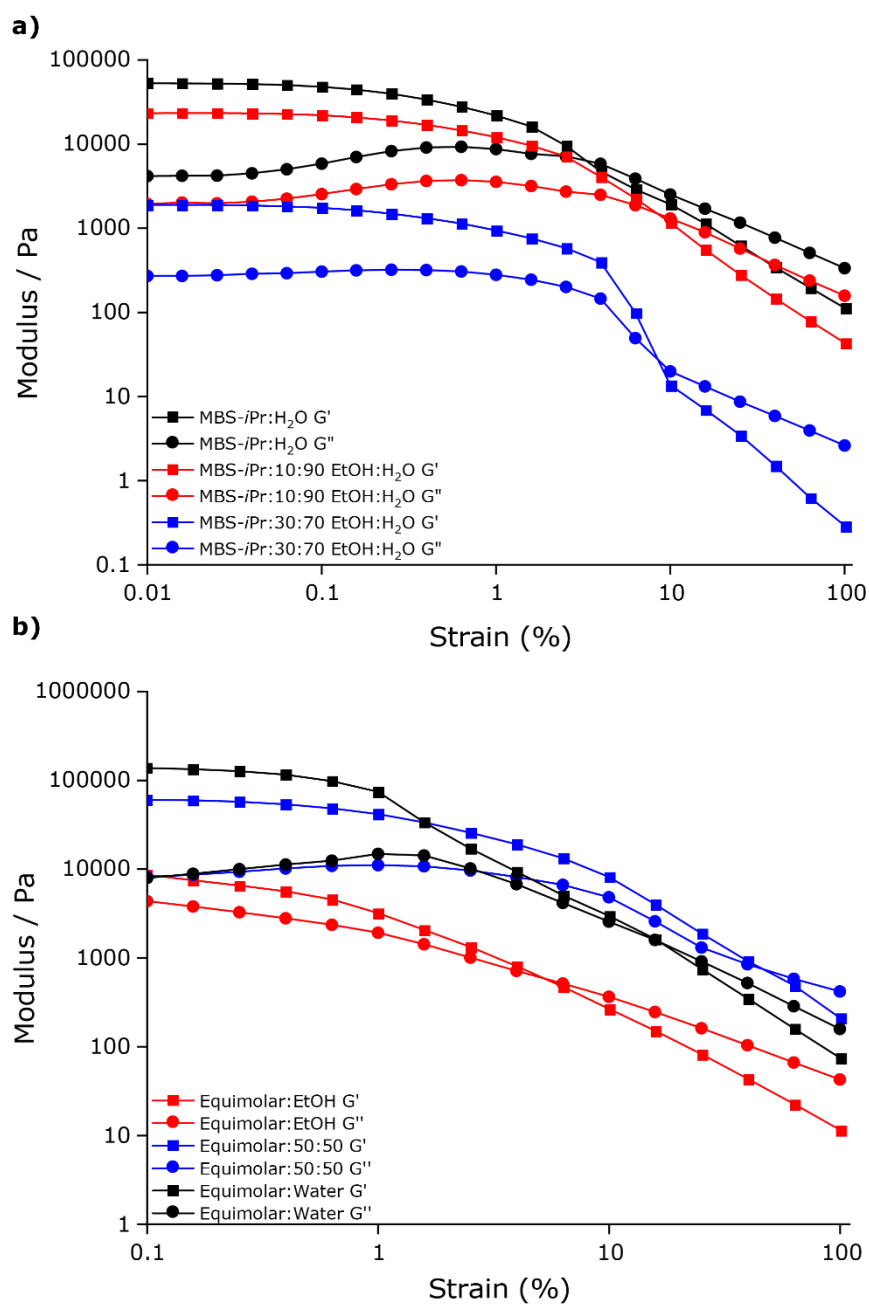
Figure 2.18 | Amplitude sweep rheological data for: (a) MBS-*i*Pr and (b) equimolar (DBS-MBS)-*i*Pr gels formed from ethanol:H_2O solutions at 1.0% w/v upon heating and cooling. G' as Storage Modulus and G" as Loss Modulus.

2.7. Xerogel Powder X-Ray Diffraction

Powder X-ray diffraction (PXRD) measurements were employed for the (i) MBS-*i*Pr, (ii) equimolar MBS-*i*Pr and DBS-*i*Pr, and (iii) DBS-*i*Pr xerogels, all from 20:80 ethanol:H_2O solvent mixture (Figure 2.19) to explore and provide a direct comparison of the possible packing mode of the equimolar gelator samples. The xerogels exhibited well-resolved X-ray diffraction patterns that were characteristic of a relatively long-range ordering of the molecules. The xerogels from the pure MBS-*i*Pr and DBS-*i*Pr gelators exhibit unique diffraction peaks where some of these peaks have relatively similar distances (Figure 2.19).

The diffraction pattern of the MBS-*i*Pr xerogel displayed a series of sharp diffraction peaks with the main ones centred at $2\theta = 4.50°$ ($d = 19.6$ Å), $9.06°$ ($d = 9.75$ Å) and $15.7°$ ($d = 5.63$ Å). The *d*-spacing ratio is 1: 1/2 : 1/3, indicating that MBS-*i*Pr assembles into a lamellar organisation[136] with an interlayer distance of 19.6 Å (evidenced by peak a in Figure 2.19).[122] As DBS-*i*Pr has a sharp diffraction peak at $2\theta = 4.36°$ which is similar to the MBS-*i*Pr 19.6 Å interlayer distance, we hypothesise that the interlayer distance of DBS-*i*Pr is 20.2 Å. The larger spacing is expected because of the presence of an additional benzyl group when compared with MBS-*i*Pr. No significant diffraction peaks might indicate a strong contribution from π-π stacking (in the region of 25°), but rather a general layered structure of the type shown in Figure 2.6 is present.

The MBS-*i*Pr diffractogram was plotted with the simulated PXRD data of MBS-Cinn and MBS-Van from their single-crystal diffraction (A 72). There are significant differences between the patterns of MBS-*i*Pr and the crystalline materials, indicating a somewhat different organisation in the gel and perhaps explaining why MBS-Van and MBS-Cinn do not gel.
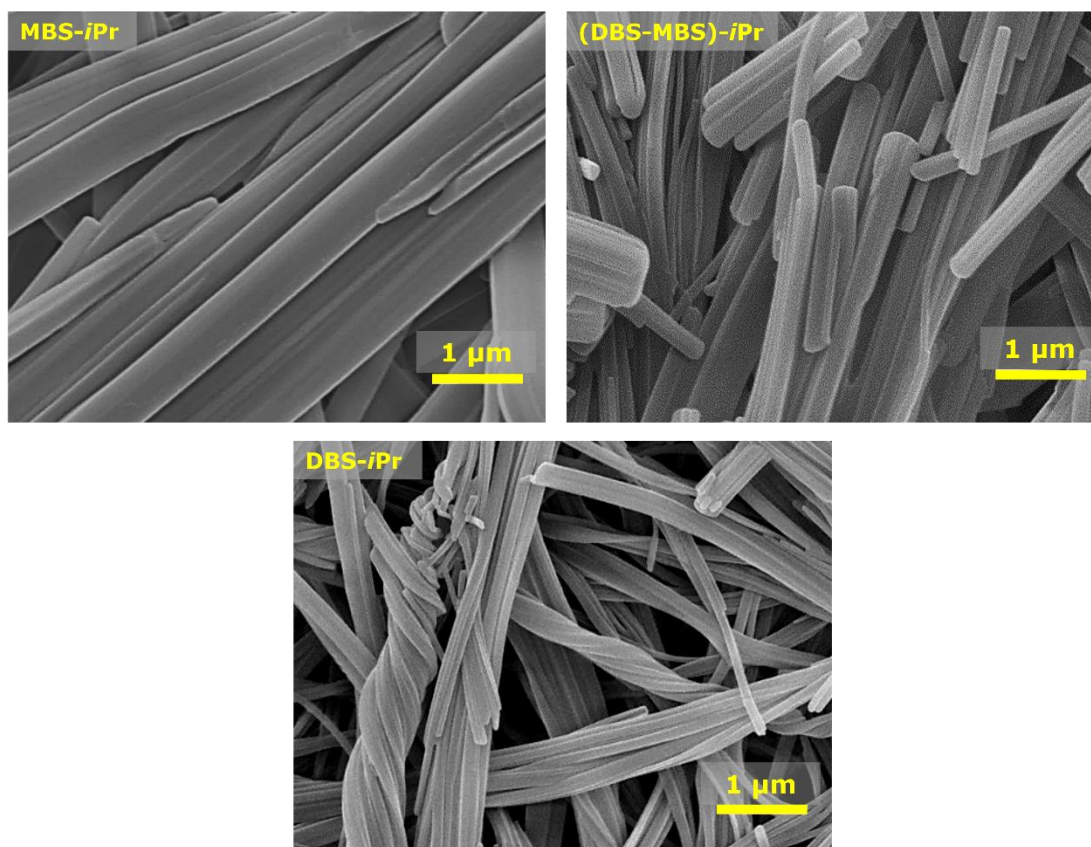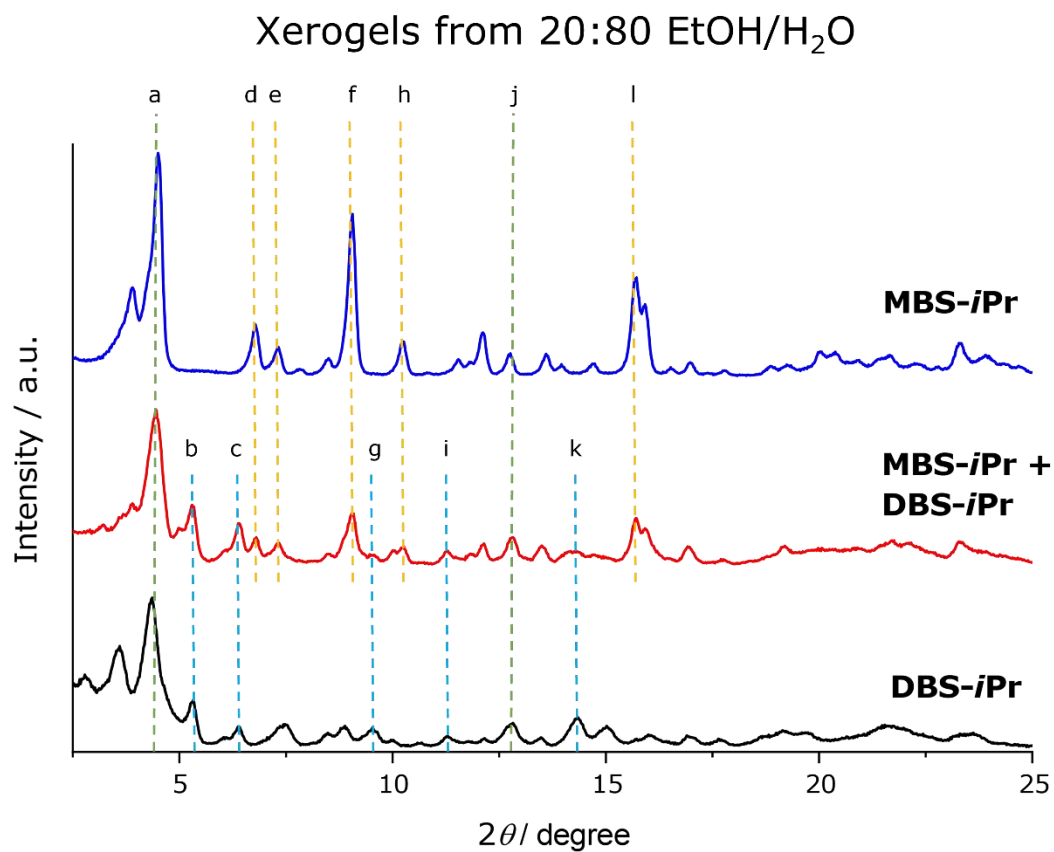
Figure 2.19 | Powder X-ray diffraction patterns on xerogels of MBS-*i*Pr, (DBS-MBS)-*i*Pr, and DBS-*i*Pr formed in 20:80 ethanol:H_2O solution (top) and SEM images of these samples (bottom). Scale bars in images are all in 1 µm.

The equimolar mixture of gelators show distinctive DBS-*i*Pr peaks at 2θ = 5.32° (d = 16.6 Å, line b), 6.32° (d = 13.8 Å, line c), 9.52° (d = 9.28 Å, line g), 11.3° (d = 7.84 Å, line i), 14.3° (d = 6.17 Å, line k) and MBS-*i*Pr peaks at 2θ = 6.78° (d = 13.0 Å, line d), 7.32° (d = 12.1 Å, line e), 9.06° (d = 9.75 Å, line f), 10.3° (d = 8.61 Å, line h), 15.7° (d = 5.63 Å, line l) are seen present in the diffractogram. The observed peaks suggest that DBS-*i*Pr and MBS-*i*Pr self-assemble into layered structures independently in the equimolar gel. Some of the diffraction peaks occur at the same position for the pure xerogels and essentially coincide in the equimolar mixture (lines a and j). In contrast, interlayer diffraction peaks that are detected in MBS-*i*Pr and DBS-*i*Pr spectra between 3° – 4° (d = 22.6 Å and 24.5 Å, respectively) are not present in the equimolar gel. This effect could indicate possible layering of unlike lamellae (for example, a DBS-*i*Pr lamellar stacking on top of MBS-*i*Pr fibre) in the 3D network leading to a lesser degree of long-range crystalline order compared with the pure gelators. Therefore, self-sorting of the gelators would occur over a few lamellae, and, for the xerogels at least, lamellae of the other component form over the first-formed fibres. Co-assembly at the lamellar level does not occur because the diffraction data corresponding to short distances coincide over all samples for a given component.
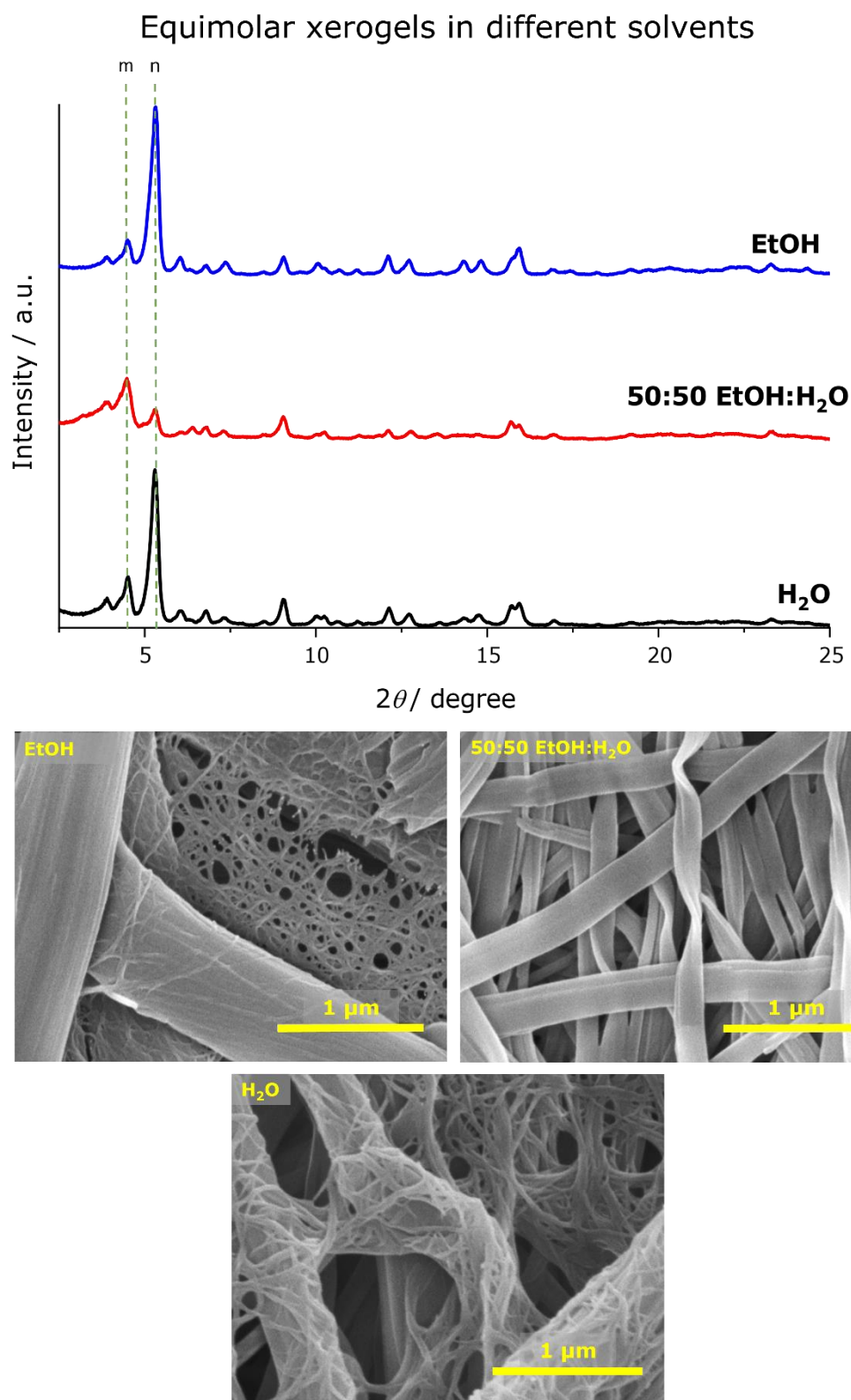
Figure 2.20 | Powder X-ray diffraction patterns of equimolar xerogels in ethanol, 50:50 ethanol:H_2O and water (top) and SEM images of these samples (bottom). Scale bars in images are all in 1 μm.

Further PXRD experiments were performed for all the equimolar xerogels and are summarised in Figure 2.20, showing (i) ethanol, (ii) 50:50 ethanol:H_2O and (iii) water (all are plotted in A 70). The diffraction peaks arise at similar positions, however, a difference of intensity for the peaks associated to DBS-*i*Pr at $2\theta = 5.32°$ ($d = 16.6$ Å) and interlayer at $2\theta = 4.50°$ ($d = 19.6$ Å) is apparent. From the solution of ethanol to 60:40 ethanol:H_2O solution, the DBS-*i*Pr peak is more intense than the interlayer peak. Interestingly, the opposite can be seen from 50:50 to 20:80 ethanol:H_2O solution, whereas the xerogel at 10:90 ethanol:H_2O solution displays similar intensities. As it reached pure water, the DBS-*i*Pr diffraction peak, once again, had a stronger intensity. These observations could be related to the solubility of both DBS-*i*Pr and MBS-*i*Pr. Changing the solubility of the gelator in a solvent medium is the main factor in determining the outcome of gelation tests; as the gelator comes out of solution, it will self-assemble and form network fibres that immobilise the solvent.

In conclusion, DBS-iPr has more crystalline domains with a higher ethanol content because self-assembly takes place readily in ethanol, whilst MBS-*i*Pr stays as a solution in ethanol (Table 2.2). On the other hand, for lower ethanol content, DBS-*i*Pr becomes less soluble, whilst MBS-*i*Pr self-assembles readily because of the higher water content. Therefore, DBS-*i*Pr has fewer crystalline domains in this xerogel. As seen in the phase diagram in Figure 2.8, from 10:90 ethanol:H_2O solution to pure water, not all solid dissolved. The undissolved solid is believed to be DBS-*i*Pr because of the very poor solubility in water. It may cause the intensity of the DBS-*i*Pr diffraction peak to increase in the diffractogram.

2.8. Motivation: Mannitol Based Gelators

In 2011, Vidyasagar *et al.*[137] demonstrated the synthesis of D-mannitol diacetonide (MDA) and its gelation properties. It was stated to be both organogelator and oleogelator (gels with oil as the dispersed phase). Another D-mannitol-based compound, MDP, was synthesised by Lin *et al.*[138] in 2013 but not for gelation purposes. For this research, MDA and MDP were synthesised using the approach proposed by Srikanth *et al.*[139] and McNiece and co workers[140], respectively (Scheme 2.4). MDA was isolated with a relatively good yield of 69% compared to MDP having a 10% yield. The purification of MDA is a recrystallisation approach in 1:9 chloroform/hexane – the recrystallisation was also attempted to purify MDP. Unfortunately, after recrystallisation and several washes, the crude product was still impure. Flash column chromatography was carried out for further purification, where the isolation of MDP as a pure white solid became successful with a low yield due to the difficulty in purification at the start.
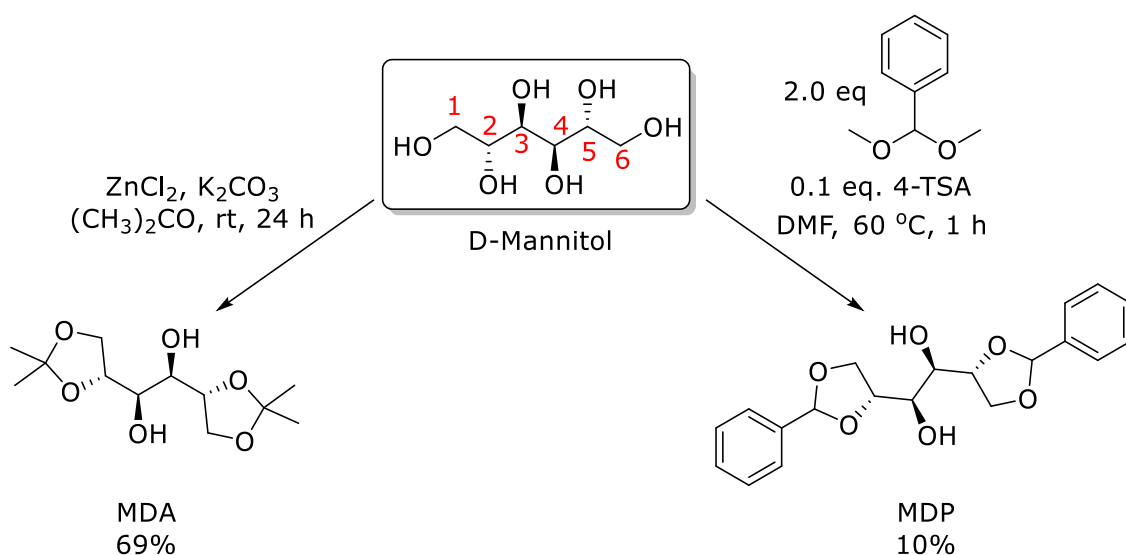
Scheme 2.4 | Synthesis of D-mannitol based acetal compounds

Sorbitol and mannitol are isomers and have the same molecular formula, but their spatial arrangement is different; it is similar in the case of dibenzylidene sorbitol (DBS), and D-mannitol diphenyl (MDP) - DBS and MDP are stereoisomers. DBS has two –OH groups at one "end" of the molecule, whilst MDP has two –OH groups in the middle of the molecule. Due to its stereochemistry, the acetal or ketal forms at the end of the mannitol compound (C1, C2 and C5, C6). The –OH groups in C2 and C5 positions face down, and the –OH groups in C3 and C4 positions face forward.

Furthermore, one of the most significant differences between the two compounds is that DBS has a six-membered acetal ring, whereas MDP has a five-membered acetal ring. If MDP is to be a successful gelator, a comparison against DBS will be a good idea. It may add evidence on the importance of the 'butterfly'-like conformation of the DBS molecule.

2.8.1. Gelation behaviour of mannitol-based compounds

A series of gel tests on MDA and MDP were carried out to investigate their gelation behaviour at 10 mg mL^{-1} (1% w/v). The selected solvents are the same as the solvents for benzylidene sorbitol derivatives, where they represent a broad range of different types, such as linear, cyclic, aromatic, chlorinated, alcohols, ethers, esters, and aqueous ethanolic solutions (Table 2.6). Gelation tests were performed upon heating and cooling where the solvent was heated (until all solid is dissolved by eye) then left to cool down to room temperature.

Table 2.6 | Gelation test in organic solvents (1% w/v) upon heating and cooling. I = insoluble, G = gel, PG = partial gel, S = solution, P = precipitate, (T) = transparent, (O) = opaque.

Solvent	Compounds	
	MDA	MDP
Hexane	G (O)	I
Cyclohexane	G (O)	G (O)
Toluene	G (T)	G (O)
Chloroform	S	P
Dichloromethane	S	S
Tetrahydrofuran	S	S
2-Butanone	S	S
Ethyl acetate	S	S
Acetonitrile	S	S
Isopropranol	S	S
Methanol	S	S
Ethanol	S	S
90:10	S	S
80:20	S	S
70:30	S	S
60:40	S	S
50:50	S	P
40:60	S	P
30:70	S	P
20:80	S	P
10:90	S	P
Water	S	I

All the mannitol-based sugar gelators are not as efficient as the benzylidene sorbitol compounds. No mannitol-based compounds were able to immobilise any of the ethanolic solutions (Table 2.6). MDA was soluble in ethanol and water at room temperature, whereas MDP was essentially insoluble in water even with the heating of the solvent. MDA and MDP were soluble at room temperature or have remained as a solution after heating and cooling in dichloromethane (DCM) and solvents more polar than DCM. On the other hand, MDA shows gelation abilities in three non-polar solvents. For the MDP compound, adding a benzyl ring on each end of the mannitol sugar backbone (forming acetal groups) shows insolubility in the most non-polar solvent tested, hexane. MDP formed opaque gels with cyclohexane and toluene and precipitated in chloroform.

As mentioned earlier, DBS and MDP are stereoisomers. The gelation tests are shown in Table 2.6 prove that the DBS molecule's 'butterfly'-like conformation is vital; it makes the gelator more efficient in gelling more solvents. The 'butterfly'-like conformation of the DBS molecule allows the alignment of the hydrophobic group together and the hydrophilic group together. This orientation is not possible for MDP because the hydrophilic hydroxyl groups are in the middle of the mannitol sugar backbone and the benzyl hydrophobic group is on each side of the compound. Although the isolated mannitol-based compounds formed a gel on a few of the non-polar solvents, the gelators were not as efficient as the DBS derivative gelators (i.e. DBS-*i*Pr and MBS-*i*Pr). Therefore, detailed characterisation for the compounds was not as focused as it was compared to the other gelators.

In summary, benzylidene sorbitol derivatives (di-acetals and mono-acetals) were successfully isolated from green starting materials. The dibenzylidene compounds proved to be an efficient organogelator whereas only two of the monobenzylidene derivatives demonstrated gelation properties. Furthermore, mannitol-based compounds were also tested for gelation abilities and were not successful in forming any gels. In addition, a hydroxyl group in DBS-*i*Pr was replaced with a long chain to synthesise Lauryl-DBS-*i*Pr to form a long chain gelator. Lauryl-DBS-*i*Pr tested for gelation and was established to be less efficient than DBS-*i*Pr. These observations show the importance of the 'butterfly'-like conformation of the dibenzylidene sorbitol derivatives on the self-assembly of the gelators. Also, the hydroxyl group is more essential than a long chain group in the dibenzylidene derivatives and is evidenced by the infrared spectra showing that hydrogen bonds are the main driving force of the gelators' self assembly. Moreover, the chapter focused on the difference in solubility of DBS-*i*Pr and MBS-*i*Pr, hence the gelation of the two together as an equimolar multicomponent gel (DBS-MBS)-*i*Pr was investigated. The multicomponent gelator displayed gelation in all ethanol–water mixtures and at a lower concentration than the single component system, which indicates that MBS-iPr has an influence on the gelation of DBS-iPr and *vice versa*. However, co-assembly at the lamellar level does not take place, as indicated by both IR and PXRD results. Rather, the gelators self-sort and possibly layer through interactions of the hydroxyl groups, as indicated in the structural model in Figure 2.6.

CHAPTER THREE

Benzylidene Xylitol Derivatives

3.1 Synthesis of Dibenzylidene Xylitol Derivatives

The preparation of DBX-*i*Pr and DBX-CO$_2$Me, shown in Scheme 3.1 is a single step acid-catalysed reaction between xylitol and an aromatic aldehyde. DBX-*i*Pr was isolated in a yield of 38% after reacting xylitol with cuminaldehyde using the same conditions as in Scheme 2.1/Table 2.1 in chapter 2, except using 0.6 equivalents of 4-TSA. With the same approach, reacting xylitol and methyl 4-formylbenzoate produced isolated DBX-CO$_2$Me in a low yield of 10%. Due to the low yield attained, the Dean-Stark procedure proposed by Raju *et al*.[83] was used to synthesise DBX-CO$_2$Me in a biphasic system comprising methanol and cyclohexane and had an isolated yield of 70%. The introduction of cyclohexane and the removal of methanol/water azeotrope in the reaction *via* Dean-Stark apparatus effectively drove the reaction forward, resulting in the precipitation of white solid.
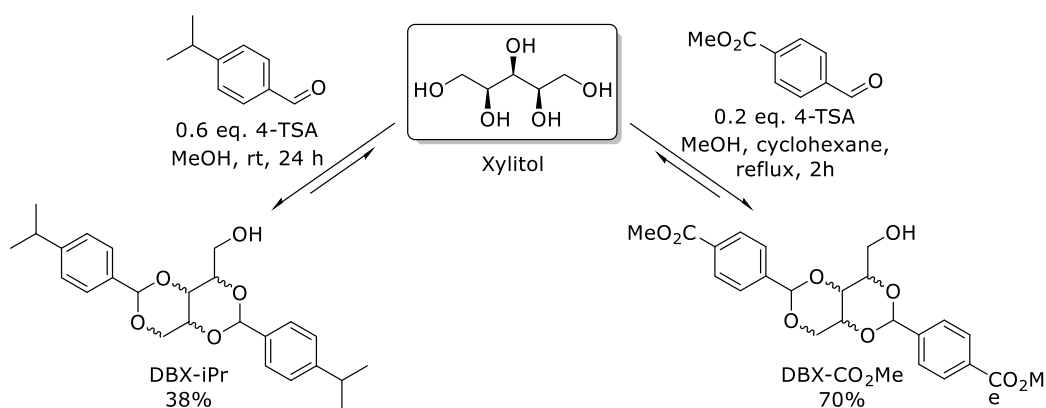
Scheme 3.1 | Synthesis of DBX-*i*Pr and DBX-CO$_2$Me (yields were calculated with respect to xylitol as the limiting reagent)

Figure 3.1 shows the difference of DBX-*i*Pr and DBS-*i*Pr in ^{1}H NMR spectra (Figure 3.1a), where DBS-*i*Pr presents two -OH proton peaks and DBX-*i*Pr only shows one. It is also apparent that in the FTIR spectra in Figure 3.1b, the O-H stretch absorption peak from DBS-*i*Pr is broader than DBX-*i*Pr due to having two hydroxyl groups. Furthermore, the absorption band of the O-H stretch for DBS-*i*Pr appears to have a lower wavelength (~3260 cm^{-1}) than the O-H stretch for DBX-*i*Pr (~3330 cm^{-1}), this observation shows that the O-H bond length is shorter in DBX-*i*Pr than DBS-*i*Pr.
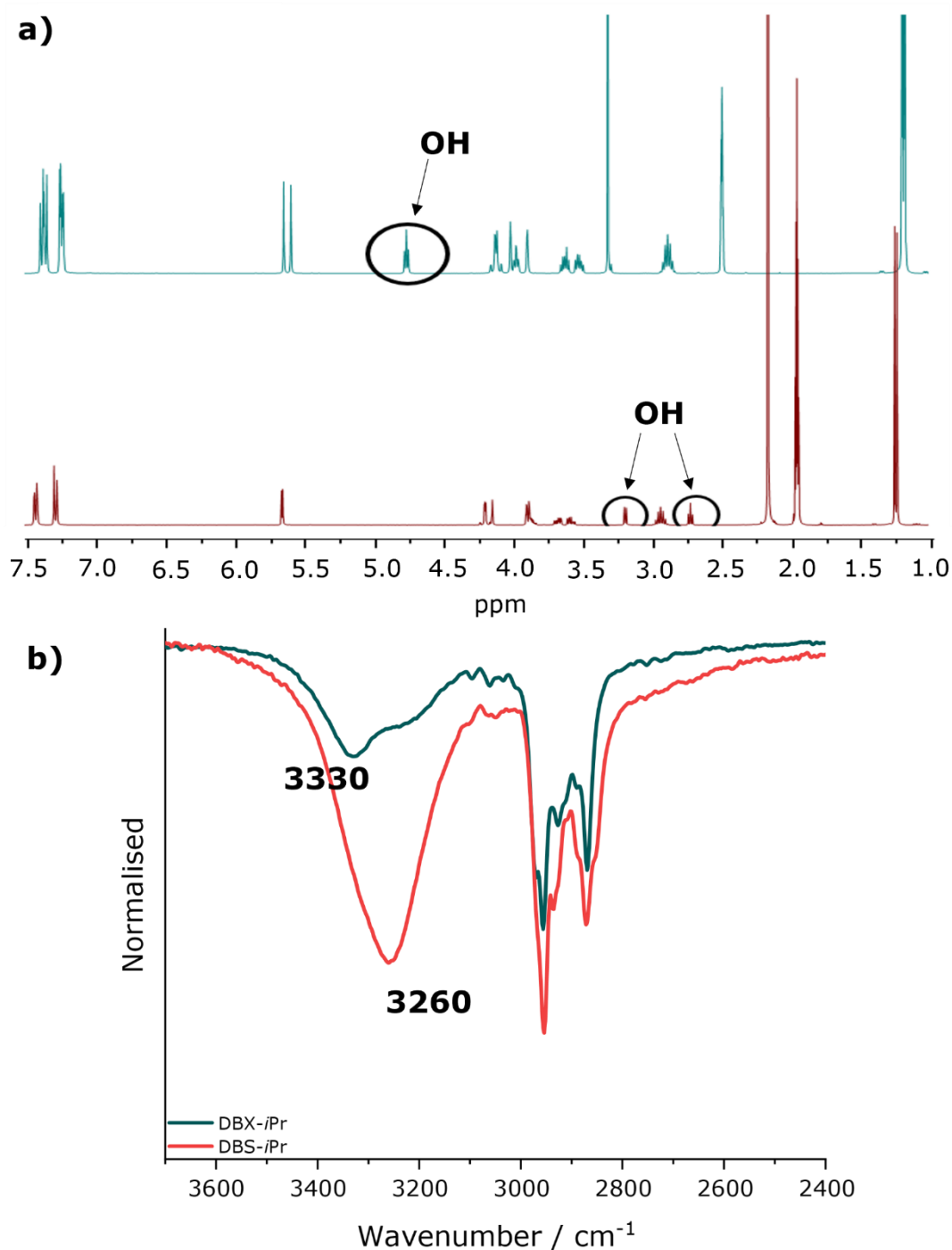
Figure 3.1 | a) ^{1}H NMR of DBX-iPr and DBS-iPr in DMSO-d_6 and CD$_3$CN, respectively; b) IR spectra of DBX-iPr and DBS-iPr xerogels between 3700 – 2400 cm^{-1}

In addition, DBX-CO$_2$Me was used as a starting material to synthesise two further DBX derivatives, DBX-CO$_2$H and DBX-CONHNH$_2$ (Scheme 3.2). The hydrolysis of DBX-CO$_2$Me to DBX-CO$_2$H was achieved when the methyl ester was treated with 1 M NaOH in methanol for 12 hours under reflux. The resulting colourless reaction mixture shows the formation of the sodium carboxylate salt of the product (Na$^+$$^-$OOC-DBX-COO$^-Na^+$). Using sodium bisulfate, NaHSO$_4$, the clear solution was acidified to pH 3, causing the precipitation of a

white gel filtered under reduced pressure to obtain DBX-CO$_2$H with an excellent yield of 94%. The hydrazine dizbenzylidene xylitol derivative, DBX-CONHNH$_2$, was synthesised when the methyl ester was treated with hydrazine monohydrate in THF. The reaction proceeded at reflux for 12 hours, resulting in the formation of a white precipitate. After filtering, washing with water, and drying the white precipitate, DBX-CONHNH$_2$ was isolated at a yield of 76%.
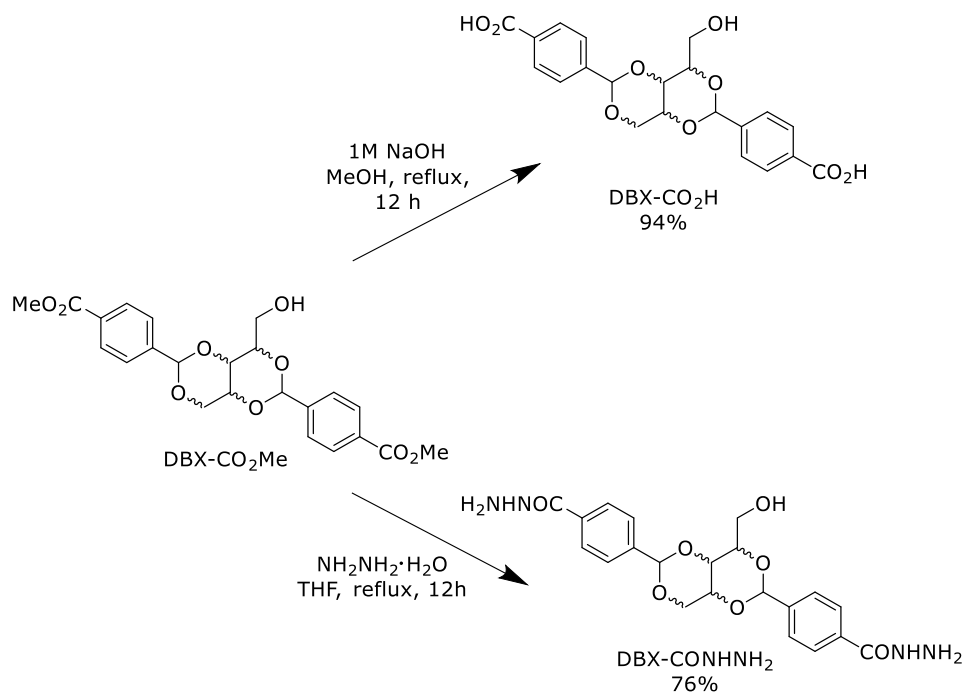
Scheme 3.2 | Synthesis of DBX-CO$_2$H and DBX-CONHNH$_2$

Xylitol is a meso compound, and therefore the obtained products are in principle racemic, a fact confirmed by measuring the optical rotations – they are close to 0. DBX-*i*Pr, DBX-CO$_2$Me, DBX-CO$_2$H and DBX-CONHNH$_2$ had very low optical rotation values of +0.005°, +0.003°, +0.002° and +0.004°, respectively (c 10 mg mL^{-1}, DMSO). Moreover, there was an attempt to synthesise a mono benzylidene xylitol derivative, MBX-*i*Pr, following the reaction of MBS-*i*Pr (Chapter 2, Scheme 2.1/Table 2.1) by reacting xylitol with 1.0 equivalent of cuminaldehyde. Surprisingly, no MBX-*i*Pr was isolated from the reaction, but instead, DBX-*i*Pr was collected. This phenomenon may suggest two things: (1) the diacetal is more thermodynamically stable than the monoacetal for the xylitol derivatives; (2) the monoacetal xylitol reacts faster with aldehyde than the xylitol.

3.1.1. Attempted Resolution of Dibenzylidene Xylitol Derivatives

Chirality is a significant factor in directing and intervening in the self-assembly of LMWGs.[141] Tomasson *et al*.[141] studied the gelation behaviour of a LMWG in its racemic form and its separate enantiomers (1*R* and 1*S*). They widened the research by mixing

equimolar mixtures of enantiomers (1R + 1S) which showed enhanced mechanical and thermal stability than the racemate and separate enantiomers gel. Furthermore, Zentel and co workers[142] presented the first report on the synthesis of chiral ureas, (R)- and (S)-2-heptylurea, and their gelation behaviours. The enantiomeric ureas have higher gelling abilities than the corresponding racemate. They reported that the enhanced gelation properties of the enantiomeric ureas are because of the formation of a one-dimensional supramolecular structure during self-assembly, whereas the racemate crystallises into two-dimensional lamellae.

On the other hand, Žinić et al.[143] designed a new class of optically active and racemic efficient LMWG with hydrogen bonding sites. Their studies observed that the racemates are generally more efficient gelators gelling up to 16 times larger volumes of certain solvents (i.e. p-xylene) than the pure enantiomers. Another example of this type of study is the research of Shen et al.[144], where they explored the gelation ability of a racemic mixture by melamine. They observed that the racemic hydrogels show a lower critical gelation concentration (CGC) value, enhanced mechanical rigidity and dual pH-responsive ability than the pure enantiomer hydrogels.

In many cases of chiral gelators, pure enantiomers were found to be more efficient gelators, individually, than the racemates; enantiomers can form aggregates that lead to fibril growth and network formation for solvent immobilisation, hence, forming a gel.[145] The use of racemates frequently results in precipitation.[146] However, several outcomes showed that the racemic form could be a more effective gelator of certain solvents than the corresponding pure enantiomer.[147] Therefore, it would be interesting to separate and test the enantiomers if there will be a difference in gelation behaviours compared to the racemic compound. The resolution of compounds is challenging for the reason that enantiomers have identical physical properties. The two most common techniques to separate enantiomers are crystal growth (in the case that the compound forms a conglomerate) and the conversion of the racemic mixture into their separate diastereoisomeric salts using a chiral resolving agent.

Direct crystallisation. In 1848, Louis Pasteur had discovered the occurrence of the spontaneous resolution of enantiomers during crystallisation.[148] Pasteur's innovation, therefore, began the study and interest in spontaneous resolution for racemic chiral compounds. In a spontaneous resolution method, the homogeneous melt or solution from the racemate forms a heterogeneous solid system during crystallisation. This solid system comprises single crystals formed by pure enantiomers. In 2006, Janiak and colleagues[149] performed an example of a spontaneous resolution of a racemic mixture into homochiral helix-enantiomers upon crystallisation. To date, there have been no single-crystal structures reported in the literature for dibenzylidene sorbitol and xylitol compounds. Here,

a variety of crystallisation tests were done for the racemate DBX-CO$_2$Me, to attempt resolution into the compound enantiomers in the case of a conglomerate appearing (Table 3.1). These tests were performed using a Crystallization Systems Crystal 16 apparatus. Samples were heated to 2 °C below the solvent boiling point at a rate of 5 °C min^{-1}, held at that temperature for 10 mins and then cooled back to 10 °C at a rate mentioned. Slow evaporation for crystal growth was also performed.

Table 3.1 | Crystallisation tests on DBX-CO$_2$Me

Solvent	Concentration / mg mL^{-1}							
	6		8		10		12	
iso-Propanol	S		P	P	P	P	P	I
Ethanol:H$_2$O (50:50)	S		S		S		S	
Acetonitrile	S		S		S		P	
Cyclohexane	I		I		I		I	
Chloroform	P		P		P		P	
THF	P		P		I		I	
Methanol	I		I	P	I	P	I	P
Acetone	I		I		I		I	
Ethyl Acetate	I		S		S		S	
MeTHF	I		I		I		I	
MEK	I		I		I		I	

▮	-2 °C min^{-1}
▮	-0.5 °C min^{-1}
▮	Slow Evaporation
P	Precipitate
S	Solution
I	Insoluble

Regrettably, no crystals were formed after several crystallisation tests in different conditions, and the results were non-conclusive. The precipitate obtained from the tests were inspected under a polarising optical microscope where microcrystals were observed, an example is shown in Figure 3.2. The analysis shows that chloroform could be the best solvent to achieve crystals of DBX-CO$_2$Me; therefore, further crystallisation analyses were carried out for DBX-CO$_2$Me – crystallisation *via* slow evaporation at different concentrations 6 – 12 mg mL^{-1}. Despite the modification of conditions, no success was found in the attempt of crystalising the compound.

Figure 3.2 | Precipitate of DBX-CO$_2$Me formed in 10 mg mL^{-1} chloroform

Chiral Resolving Agents. Resolution of racemic compounds is possible with optically pure resolving agents. They can convert the racemic compound into diastereoisomers which can be separated directly by conventional techniques in physical chemistry, such as column chromatography or crystallisation. Basic chiral resolving agents, such as quinine and methyl phenylamine, should react with DBX-CO$_2$H to give salts.

Quinine is an inexpensive chiral resolving agent that achieves resolution by forming diastereoisomeric salts; hence, it has been extensively used to resolve racemic mixtures. Kaboudin *et al*.[150] successfully prepared C$_2$ symmetric *N,*-bis(phosphinomethyl)amines in high enantiomeric purity through the diastereoisomeric salt formation with (-)-quinine. Therefore, in the research described here, (-)-quinine was used to attempt the resolution of racemic DBX-CO$_2$H into pairs of diastereoisomers (*S,R,R* and *R,S,S*) which are shown in Scheme 3.3.
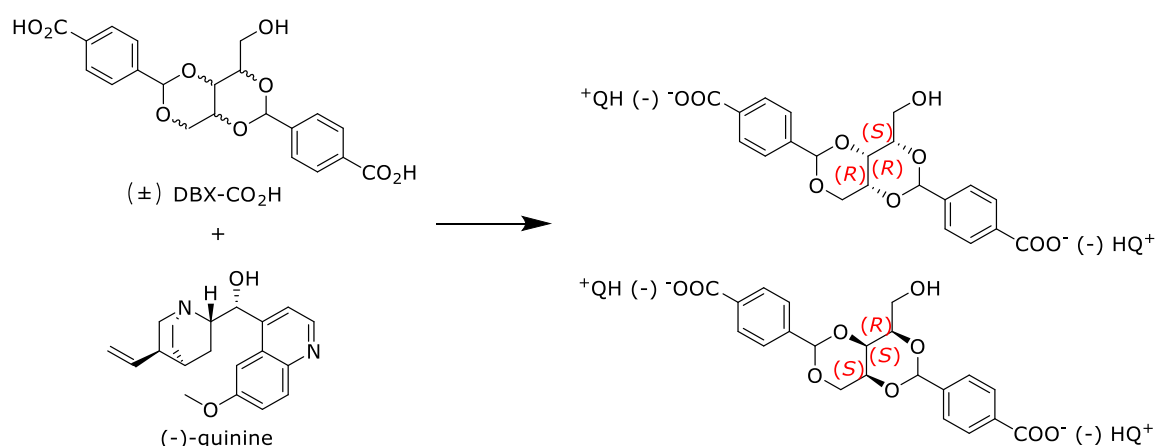
Scheme 3.3 | Theoretical diastereoisomeric salt formation of *S,R,R* DBX-CO$_2$H and *R,S,S* DBX-CO$_2$H with (-)-quinine

A variety of conditions for Scheme 3.3 were performed, attempting to isolate the desired products. The reaction was first studied with 1.0 equivalent of (-)-quinine in ethanol/water with the expectation that the quinine to only solubilise one of the enantiomers in the racemate and form its diastereoisomeric salt (which will be in the solution) whilst the other

enantiomer of the DBX derivative remains insoluble and can be filtered easily. The solution with the diastereoisomeric salt was concentrated under *vacuo* and was treated with 1 M NaOH in methanol and water. The removal of methanol effectively caused the quinine to crash out due to its insolubility in water and was easier to remove *via* filtration. The solution containing the proposed DBX enantiomer was then acidified to pH 3 using NaHSO$_4$, forming a stable white gel, which was then filtered and dried (mimicking the synthesis of DBX-CO$_2$H in Scheme 3.2). Unfortunately, the 'resolved' compound and the filtered material were still essentially racemic (ascertained with their optical rotation of +0.002° - the same positive values for both) under polarised light, *c* 20 mg mL^{-1}, DMSO. A 50:50 mixture of enantiomers (racemates) has no observable optical activity; therefore, the optical rotation value is expected to be 0°. Although the value is not exactly 0°, it is still very low to evident an enantiomeric compound.

As the usage of one equivalent of (-)-quinine failed to produce the desired results, the experimentation was adjusted accordingly by mixing DBX-CO$_2$H with 2.0 equivalents of (-)-quinine, varying the solvent as well as the length of reflux Table 3.2. It was anticipated that the 2.0 equivalents of quinine would dissolve all the molecules of racemic DBX-CO$_2$H; driving the reaction to provide complete dissolution and form the *R,S,S* and *S,R,R* as a diastereoisomeric salt, where one would precipitate out or crystallise first before the other. Unfortunately, only partial dissolutions were observed with all the different reactions shown in Table 3.2. The final collected compounds remained racemic.

Table 3.2 | Reaction conditions performed to form DBX-CO$_2$H diastereoisomeric salts

Reaction	Equivalents of Quinine	Solvent	Conditions	Observation
1	1	Water	4 h reflux	Partial dissolution – opaque
2	1	Ethanol	4 h reflux	Partial dissolution – opaque
3	2	Water	6 h reflux	Partial dissolution – opaque
4	2	Ethanol	No reflux	Partial dissolution – opaque
5	2	Ethanol	6 h reflux	Partial dissolution – less opaque than the rest
6	2	Methanol	5 h reflux	Partial dissolution – less opaque than the rest

For reaction 5 in Table 3.2, 2.0 equivalents of quinine in ethanol under reflux for 6 hours, the collected diastereoisomeric salts were further recrystallised using acetone. ^{1}H NMR of the proposed DBX-CO$_2$H enantiomer and the racemic DBX-CO$_2$H in DMSO-*d$_6$* in Figure 3.3, focusing on the chemical shifts of the two acetal peaks in the molecules. There are studies where NMR chemical shifts are compared to see if the compound is enantiopure or not.[151,152] The ^{1}H NMR showed promising results as it displayed a slight chemical shift difference. Unfortunately, from a starting mass of 150 mg, the yield produced due to the recrystallisation was very low (< 20 mg, 10%). Therefore, further characterisation in the

polarimeter was not possible. Due to the promising results illustrated on the chemical shifts, it would be good to modify the method to improve the yield and examine possible resolutions for future research.
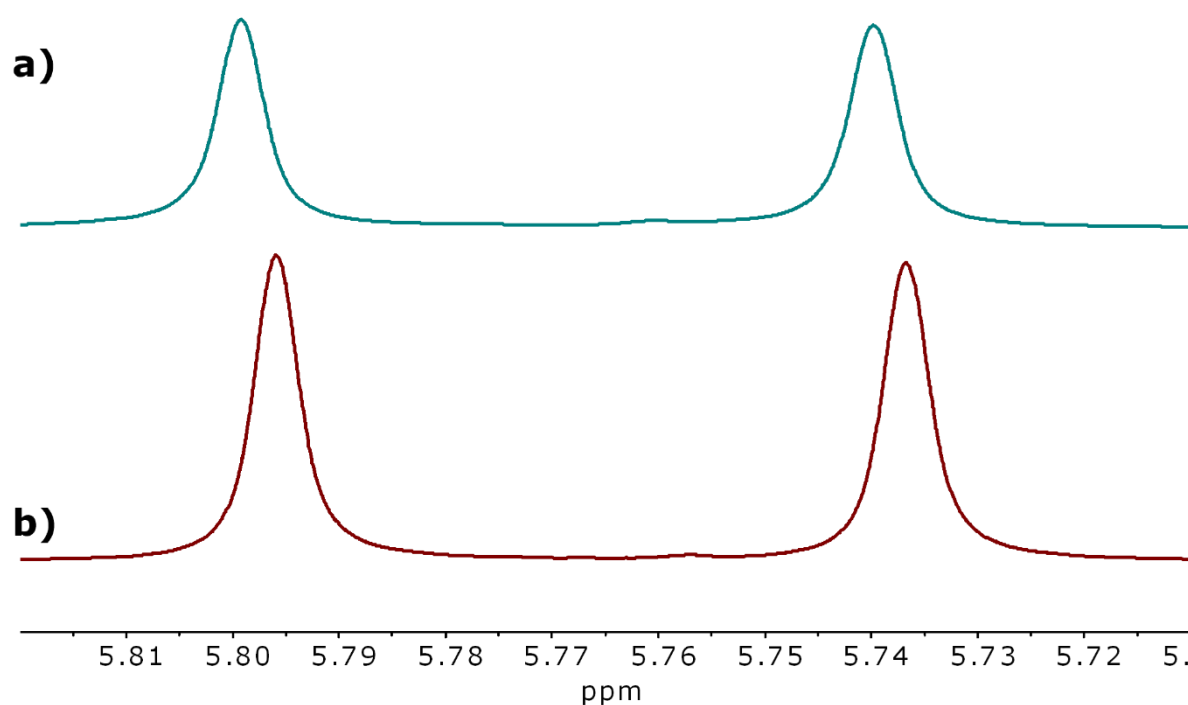
Figure 3.3 | ^{1}H NMR peaks for the two acetal groups in the (a) proposed diastereoisomer of DBX-CO$_2$H and (b) racemic DBX-CO$_2$H in DMSO-d_6

Apart from (-)-quinine, the use of α-methyl phenylamine was also examined to resolve racemic DBX-CO$_2$H. The racemate was treated with 1.1 equivalents of α-methyl phenylamine and was stirred in water for 30 minutes. The solution turned opaque when the racemic material started to dissolve. After complete dissolution, ethyl acetate was used to extract the organic compounds, and the aqueous solution was evaporated under reduced pressure. It was expected that one of the diastereoisomers would be in the organic layer and the other diastereoisomer in the aqueous solution, in the form of a salt. Crystalline solid was collected from the evaporated aqueous solution. The crystalline solid was dissolved in 10 mL of water, and 5 mL of 0.5 M HCl was added to release the salt. After 30 minutes of stirring, white precipitate started to form, which according to the ^{1}H NMR, was the DBX-CO$_2$H compound. ^{1}H NMR spectra (Figure 3.4) indicate that DBX-CO$_2$H formed a diastereoisomeric salt with α-methyl phenylamine and was released after the addition of HCl. The −OH peak of the carboxylic acid (yellow box in Figure 3.4b) disappeared when it formed a salt with the chiral base. Aromatic peaks also increased after the introduction of the base due to the phenyl group. Unfortunately, the obtained optical rotation value of DBX-CO$_2$H after the release is the same as the value of the final products in the quinine resolution, +0.002°, which again is really low. At this stage, it might be possible that the compound is, in fact, scalemic and not racemic because of the

consistent optical rotation value of +0.002° and not 0°. Scalemic is a mixture of enantiomers at a ratio other than 1:1.
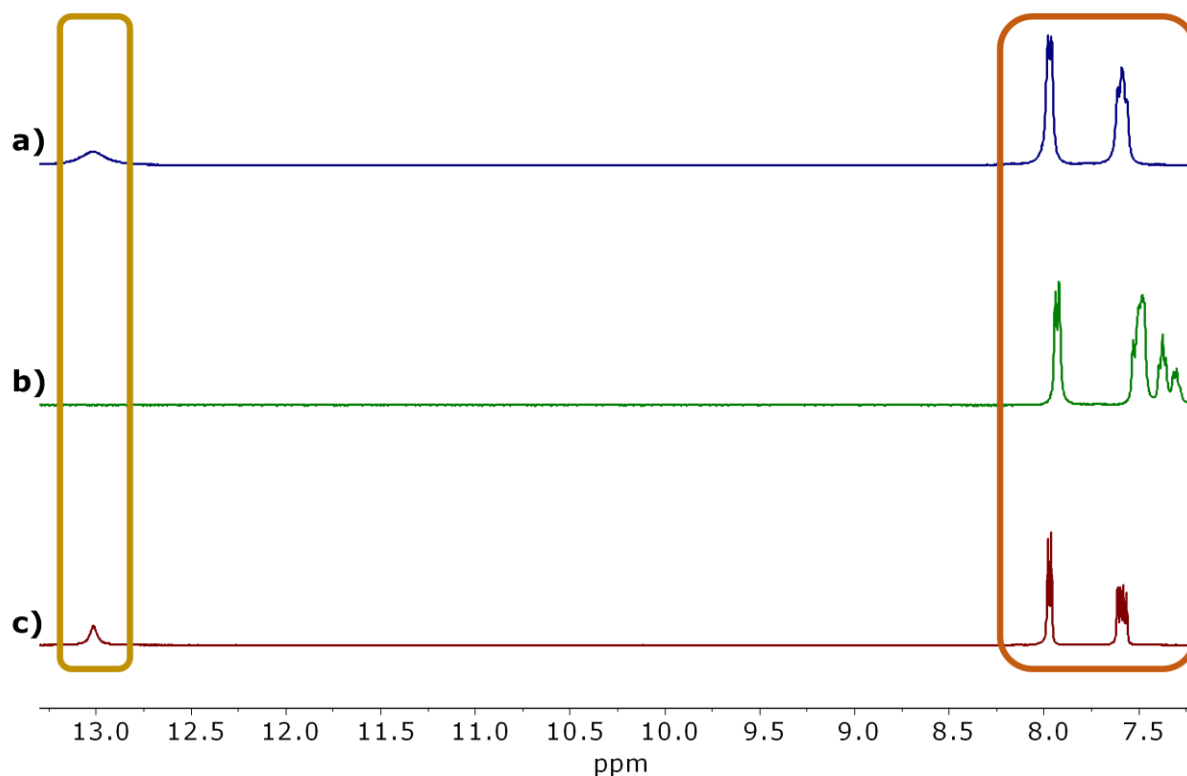
Figure 3.4 | ^{1}H NMR of (a) DBX-CO$_2$H as synthesised, (b) DBX-CO$_2$H with α-methyl phenylamine (before salt release) and (c) DBX-CO$_2$H after salt release in DMSO-d_6

Overall, the resolution of racemic DBX-CO$_2$H was unsuccessful even after using various reaction media and conditions and a different resolving agent. On the other hand, both the resolution attempts provided insight into the successful release of the compound and removal of the chiral resolving agent without disrupting the acetal groups on the structure of DBX-CO$_2$H. The ineffectual resolution meant that all experiments carried out on the DBX materials were on the racemate.

3.2. Gelation Tests

A series of gel tests were carried out on all four isolated dibenzylidene xylitol compounds, investigating their gelation behaviour at different concentrations using a range of stimuli. The methods for the tests are the same as the methods used for the dibenzylidene sorbitol derivatives. Unless stated, gel samples were prepared by transferring 10 mg of the solid material into a vial and adding 1 mL of the selected solvent. The vial was closed, and the sample was heated to near the solvent boiling point to maximise the solubility. The

homogeneous solution was then allowed to cool to room temperature, and gelation was observed visually by the vial inversion test.

3.2.1. Gelation behaviour in Organic Solvents

Table 3.3 shows that DBX-iPr and DBX-CO$_2$Me gel a broad range of organic solvents. It is noticeable that DBX-iPr is gelated in the least polar solvents, whereas DBX-CO$_2$Me forms gels in the more polar solvents. The substituent on the benzyl ring is attributed to this result, where the dimethyl ester is more polar than the *iso*propyl group; hence, it is expected that DBX-CO$_2$Me is insoluble or forms a precipitate in non-polar solvents even at elevated temperatures. On the other hand, DBX-CO$_2$H and DBX-CONHNH$_2$ exhibit low solubility in the selected solvents (the former being lower) and cannot form gels.

Table 3.3 | Gelation test of compounds in organic solvents at 10 mg mL^{-1} upon heating and cooling. I = insoluble, G = gel, PG = partial gel, S = solution, P = precipitate, (T) = transparent, (O) = opaque

Solvent	Compounds			
	DBX-iPr	**DBX-CO$_2$Me**	**DBX-CO$_2$H**	**DBX-CONHNH$_2$**
*i*PA	PG	G (O)	I	P
ACN	S	P	I	P
MEK	S	G (O)	I	P
DCM	S	G (O)	I	I
CHCl$_3$	S	P	I	P
EtOAc	S	G (O)	I	P
THF	S	P	I	P
Toluene	G (O)	G (O)	I	I
Heptane	G (O)	I	I	I
Hexane	G (O)	I	I	I
Cyclohexane	G (O)	P	I	I

The results show that DBX-CO$_2$Me has the most efficient gelation ability in organic solvents compared to the other compounds. Therefore, further experiments were carried out to determine the minimum gelation concentration (MGC) of DBX-CO$_2$Me in the organic solvents gelled by the compound (Table 3.4). The MGC of DBX-CO$_2$Me in the organic solvent varies with the nature of the liquid. Gelation of DBX-CO$_2$Me in toluene shows the best gelation behaviour having the lowest MGC of 3 mg mL^{-1} (0.3% w/v), with a partial gel forming at 1 mg mL^{-1} (0.1% w/v). Moreover, DBX-CO$_2$Me showed gelation behaviour from 5 mg mL^{-1} (0.5% w/v) in DCM and from 7 mg mL^{-1} (0.7% w/v) in both *i*PA and MEK. On the other hand, DBX-CO$_2$Me in EtOAc only exhibited gelation properties at 10 mg mL^{-1} (1.0% w/v). These results suggest that DBX-CO$_2$Me is a 'super' organogelator as it formed gels in a concentration of less than 1.0% w/v.[153]

Table 3.4 | Minimum gelation concentration determination of DBX-CO$_2$Me *via* gelation test, upon heating and cooling. I = insoluble, G = gel, PG = partial gel, S = solution, P = precipitate, (T) = transparent, (O) = opaque

DBX-CO$_2$Me concentration / mg mL^{-1}	Solvents				
	*i*PA	MEK	DCM	EtOAC	Toluene
10	G (O)	G (O)	G (O)	G (O)	G (O)
7	G (O)	G (O)	G (O)	P	G (O)
5	P	PG	G (O)	P	G (O)
3	P	P	PG	S	G (O)
1	S	P	S	S	PG

3.2.2. Gelation behaviour in Aqueous Ethanolic Solutions

The DBX derivatives were also tested for gelation behaviour in aqueous ethanolic solutions (ethanol-water mixtures) (Table 3.5). Compared with non-polar organic solvents, ethanolic solutions have very low toxicity and environmental impact and are more appropriate for applications. These mixtures are suitable for various uses, such as drug delivery and tissue engineering, considering ethanol content (lower ethanol content is better).

Table 3.5 | Gelation test of DBX derivatives in ethanolic solutions at 10 mg mL^{-1} upon heating and cooling. I = insoluble, G = gel, PG = partial gel, S = solution, P = precipitate, (T) = transparent, (O) = opaque

Ethanolic Mixture	Compounds			
	DBX-*i*Pr	DBX-CO$_2$Me	DBX-CO$_2$H	DBX-CONHNH$_2$
Ethanol	P	G (O)	I	G (O)
90:10	P	G (O)	I	G (O)
80:20	G (O)	G (O)	I	P
70:30	G (O)	G (O)	I	P
60:40	G (O)	G (O)	I	P
50:50	G (O)	G (O)	I	P
40:60	G (O)	G (O)	I	P
30:70	G (O)	G (O)	I	I
20:80	I	I	I	I
10:90	I	I	I	I
Water	I	I	I	I

No tested DBX derivative formed a gel in 100% water content as they are all insoluble. In addition, DBX-CO$_2$H still displays insolubility in all aqueous ethanolic solutions as it did in organic solvents (similar to DBS-CO$_2$H in chapter two), whereas DBX-CONHNH$_2$ forms gels in 100% and 90% ethanol by volume and forms precipitate at 80% ethanol content and below. From 30% ethanol content and below, DBX-CONHNH$_2$ is essentially insoluble. Although DBX-*i*Pr and DBX-CO$_2$Me are insoluble in 20% ethanol content and below, they exhibit good gelation behaviour with higher ethanol content. They demonstrate gelation in 80% - 30% and 100% - 30% ethanol by volume, respectively. These results show that DBX-iPr, DBX-CO$_2$Me and DBX-CONHNH$_2$ are all classified as hydrogelators. They formed gel in a solution containing water.

Seeing that DBX-CO$_2$Me showed a wide range of gelation behaviour in ethanolic solutions, the hydrogelator was further investigated, where a phase diagram was determined to see the MGC in the ethanol:H$_2$O mixtures (Figure 3.5).

Regardless of the concentration, DBX-CO$_2$Me is insoluble in 90% and 100% water by volume. On the other hand, it exhibits excellent gelation properties in 100% ethanol content forming a gel as low as 3 mg mL^{-1} (0.3% w/v). Noticeably, the higher the water content is in the mixture, the lower the chance of gel formation. It only forms a partial gel, precipitate or is insoluble. Although water enhances the hydrophobic effect (which should induce gelation), an excess of water results in a decrease in solubility; therefore, it inhibits self-assembly during cooling.

Ethanol:Water Volume Ratio					
EtOH	P	G (O)	G (O)	G (O)	G (O)
90:10	P	PG	G (O)	G (O)	G (O)
80:20	P	PG	G (O)	G (O)	G (O)
70:30	P	PG	G (O)	G (O)	G (O)
60:40	P	PG	PG	G (O)	G (O)
50:50	P	P	PG	G (O)	G (O)
40:60	P	P	P	G (O)	G (O)
30:70	P	P	P	G (O)	G (O)
20:80	P	P	P	PG	I
10:90	I	I	I	I	I
H$_2$O	I	I	I	I	I
	1mg	3mg	5mg	7mg	10mg
Concentration of DBX-CO$_2$Me (mg/mL)					

Figure 3.5 | Phase diagram of DBX-CO$_2$Me upon heating and cooling to room temperature. I = insoluble, G = gel, PG = partial gel, S = solution, P = precipitate, (T) = transparent, (O) = opaque. [a]not all solid dissolved,

3.2.3. Gelation behaviour in DMSO:H$_2$O solutions

As mentioned in chapter two, Raeburn *et al*.[123] studied the effect of solvent choice on gelation. The gelation technique of dissolving the gelator and adding an anti-solvent was carried out for three of the isolated DBX derivatives, DBX-CO$_2$Me, DBX-CO$_2$H and DBX-CONHNH$_2$ (Table 3.6). Gelation tests were performed in the same procedure with the benzylidene sorbitol derivatives by dissolving 10 mg mL^{-1} of the gelator in DMSO. DBX-CO$_2$Me required the application of heat to dissolve the compound, whereas DBX-CO$_2$H and DBX-CONHNH$_2$ were dissolved in DMSO at room temperature. The addition of water at room temperature formed the gel instantaneously unless stated.

Table 3.6 | Gelation test of three DBX derivatives in DMSO water solutions at 10 mg mL^{-1}. I = insoluble, G = gel, PG = partial gel, S = solution, P = precipitate, (T) = transparent, (O) = opaque. [a]not all solid dissolved

DMSO:H_2O Mixture	Compounds		
	DBX-CO_2Me	DBX-CO_2H	DBX-CONHNH$_2$
DMSO	S	S	S
90:10	PG[a]	S	S
80:20	G (O)	S	S
70:30	G (O)	PG	P
60:40	G (O)	G (O)	PG
50:50	G (O)	G (O)	PG
40:60	G (O)	G (O)	G (O)
30:70	G (O)	G (O)	G (O)
20:80	G (O)	G (O)	G (O)
10:90	G (O)	G (O)	G (O)
Water	I	I	I

The gelation behaviour of DBX derivatives in DMSO:H_2O mixtures is somewhat different from that of ethanolic solutions. All compounds are soluble in 100% DMSO and insoluble in 100% water. Water is an anti-solvent that induces gelation by forcing the gelator from DMSO to precipitate out as fibres that gel instantly.[154] The results show that DBX-CO_2Me again shows the broadest range of gelation behaviour across the DMSO:H_2O mixture, 10% - 80% DMSO by volume. On the other hand, DBX-CONHNH$_2$ only exhibit gelation properties at 10% - 40% DMSO content.

Out of the three tested DBX derivatives, DBX-CONHNH$_2$ is the only gelator that did not gel in 50:50 DMSO:H_2O ratio. Therefore, it was interesting to see at what concentration DBX-CONHNH$_2$ gelate in 50:50 DMSO:H_2O mixture. The increase of gelator concentration in the mentioned mixture was carried out for DBX-CO_2Me, DBX-CO_2H and DBX-CONHNH$_2$ (Table 3.7). As expected, DBX-CO_2Me and DBX-CO_2H still displayed gelation at higher concentrations. DBX-CONHNH$_2$ finally exhibited gelation at 15 mg mL^{-1} in 50:50 DMSO:H_2O solution.

Table 3.7 | Gelation tests of DBX-CO_2Me, DBX-CO_2H, DBX-CONHNH$_2$ in 50:50 DMSO:H_2O mixture. I = insoluble, G = gel, PG = partial gel, S = solution, P = precipitate, (T) = transparent, (O) = opaque. [a]gelation occurred overnight

Gelator Concentration / mg mL^{-1}	Compounds		
	DBX-CO_2Me	DBX-CO_2H	DBX-CONHNH$_2$
20	G (O)	G (O)	G (O)
17	G (O)	G (O)	G (O)
15	G (O)	G (O)	G (O)
10	G (O)	G (O)	PG
7	G (O)	G (O)	PG
5	G (O)	G (O)	S
3	G (O)	G (O)[a]	S
1	P	PG[a]	S

Furthermore, it was pleasing to see that DBX-CO_2H showed gelation behaviour in DMSO:H_2O mixture from 10% - 60% DMSO content after displaying insolubility in all organic solvents and ethanolic solutions. Seeing that DBX-CO_2H formed a gel in DMSO:H_2O

mixture, a phase diagram was established (Figure 3.6a). By decreasing the concentration of DBX-CO_2H, it was observed that gelation forms at lower DMSO content. It is fascinating to see that even at a low concentration of 1 mg mL^{-1}, DBX-CO_2H exhibit gelation properties from 10% - 30% DMSO content. Moreover, tests that had higher concentration and higher water percentage showed gelation that took place almost instantly. Taking this into context and considering that the addition of water to DMSO is exothermic, the formation of bubbles within the gel occurred as illustrated in Figure 3.6b.

a)

DMSO:Water Volume Ratio	DMSO	S	S	S	S	S
	90:10	S	S	S	S	S
	80:20	S	S	S	S	S
	70:30	S	S	S	S	PG
	60:40	S	S	P	PG	G (O)
	50:50	PG^a	G (O)^a	G (O)	G (O)	G (O)
	40:60	PG	G (O)	G (O)	G (O)	G (O)
	30:70	G (O)	G (O)	G (O)	G (O)	G (O)
	20:80	G (O)	G (O)	G (O)	G (O)	G (O)
	10:90	G (O)	G (O)	G (O)	G (O)	G (O)
	H_2O	I	I	I	I	I
		1mg	3mg	5mg	7mg	10mg
		Concentration of DBX–CO_2H (mg/mL)				

b)
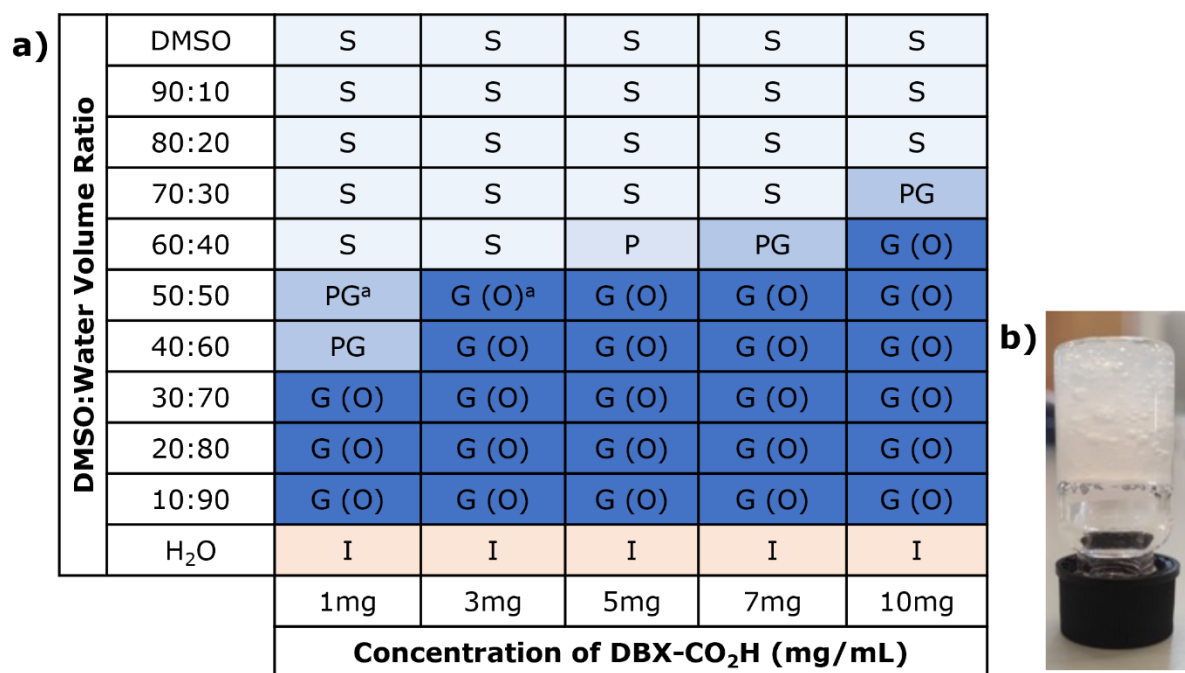
Figure 3.6 | (a) Phase diagram of DBX-CO_2H in DMSO:H_2O mixtures; (b) 10 mg mL^{-1} DBX-CO_2H gel formed in 50:50 DMSO:H_2O. I = insoluble, G = gel, PG = partial gel, S = solution, P = precipitate, (T) = transparent, (O) = opaque. ^{a}gelation occurred overnight

It is interesting to see if the gel's mechanical properties remain unaffected after manipulation with heat or shear. The changes caused by manipulation were observed after the formed DBX-CO_2H gel, in 50:50 DMSO:H_2O, was shaken to replicate shear or was heated to dissolve the gel and see if it would self-assemble homogeneously (Figure 3.7). It was visually apparent that the heated gel formed a clear solution compared to the shaken gel that formed an opaque solution. The shaken and heated vials were left at rest for 15 minutes before the inversion test was carried out. It was observed that the heated gel only transformed into a partial gel which is in contrast with the shaken gel, which has the ability to regenerate and self-heal back into a gel.

Furthermore, the exact method was also used to investigate gels formed with DBX-CO_2Me and DBX-CONHNH$_2$ at DMSO:H_2O ratios of 50:50 and 60:40, respectively. The DBX-CO_2Me gel gave results similar to DBX-CO_2H, regenerating and self-healing back into a gel after shaking and remaining a partial gel after heating. Therefore, DBX-CO_2H and DBX-CO_2Me in 50:50 DMSO:H_2O exhibit shear-thinning or thixotropic behaviour, proven by the

obtained rheological data (section 3.5 on rheology., Figure 3.27 and Figure 3.28). On the other hand, DBX-CONHNH$_2$ remained as an opaque solution after the network was destroyed *via* shaking. The destroyed fibres are apparent and can be seen in the opaque suspension.
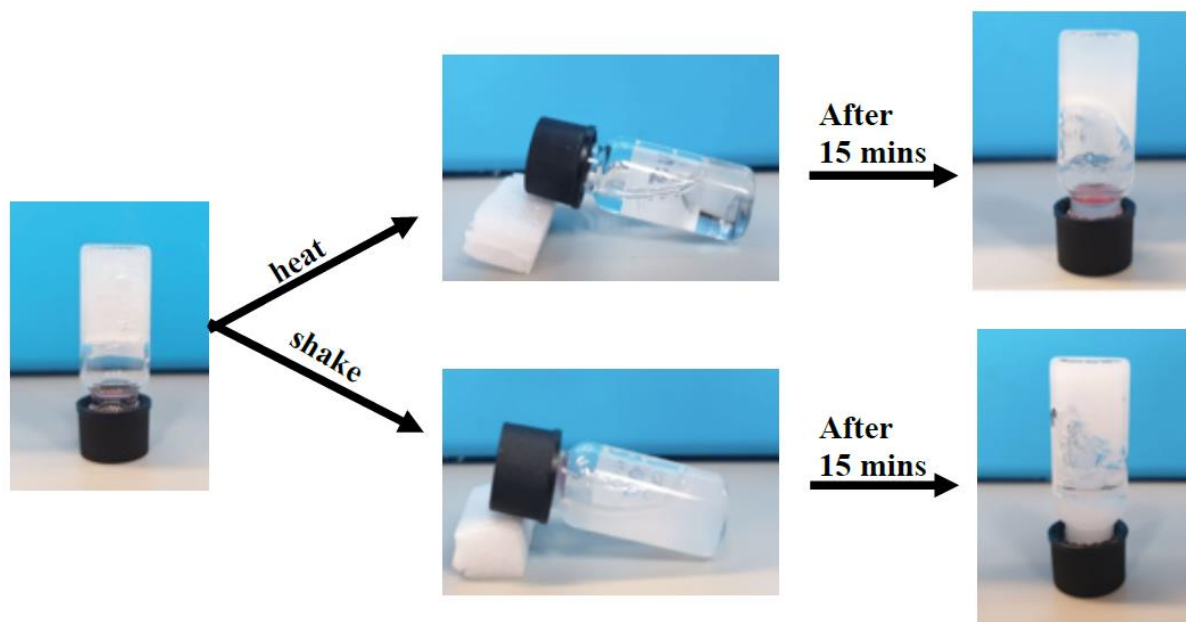
Figure 3.7 | Physical appearance of 10 mg mL^{-1} of DBX-CO$_2$H in 50:50 DMSO:H$_2$O before, during and after manipulation of heating or shaking.

An insight for 3D extrusion printing application is promising with these self-healing hydrogels. To mimic the process, the gelator was dissolved in DMSO and was transferred inside a syringe. Water was added straight into the syringe to pre-form the gel. The gel was slowly extruded out of the syringe onto a transparent plate and raised vertically to observe if the gels would remain formed at different angles (Figure 3.8). The results in Figure 3.8 and Table 3.8 show that DBX-CO$_2$H formed a continuous gel structure after extrusion in 10% - 60% DMSO content. During extrusion, DBX-CO$_2$H in 50% - 60% DMSO by volume was noticed to extrude out easier than the others. Furthermore, DBX-CO$_2$Me showed a wider range of extrusion ability than DBX-CO$_2$H, as it extends to 70% DMSO by volume. In contrast, DBX-CONHNH$_2$ did not form continuous gel regardless of the DMSO:H$_2$O ratio.
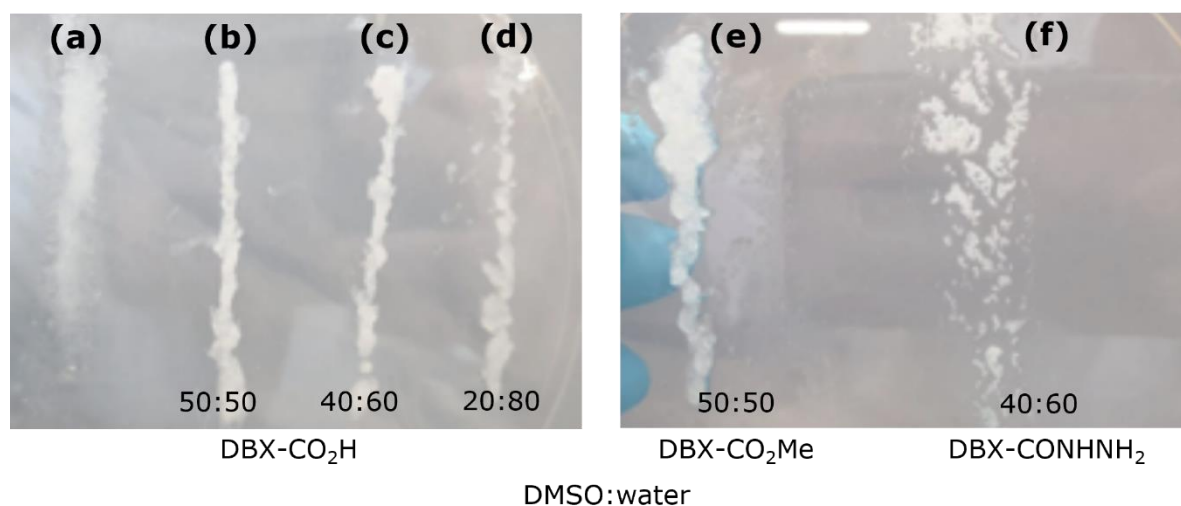
Figure 3.8 | Extruded gels formed with DBX-CO$_2$H at DMSO:H$_2$O ratios of (a) 60:40, (b) 50:50, (c) 40:60 and (d) 20:80; (e) DBX-CO$_2$Me in 50:50 DMSO:H$_2$O ratio and (f) DBX-CONHNH$_2$ in 40:60 DMSO:H$_2$O at 90°

Table 3.8 | Extrusion ability of DBX derivatives at 10 mg mL^{-1} in different DMSO:H$_2$O ratios. Determination of extrusion ability was deemed by eye after applying contact angle into the extruded gel.

DMSO:H$_2$O Mixture	Compounds		
	DBX-CO$_2$Me	DBX-CO$_2$H	DBX-CONHNH$_2$
DMSO	X	X	X
90:10	X	X	X
80:20	X	X	X
70:30	✓	X	X
60:40	✓	✓	X
50:50	✓	✓	X
40:60	✓	✓	X
30:70	✓	✓	X
20:80	✓	✓	X
10:90	✓	✓	X
Water	X	X	X

3.2.4. pH-induced gelation of DBX-CO$_2$H

Smith *et al.*[121] reported a multicomponent self-assembling system based on DBS-CO$_2$H, which forms gels when the pH is lowered in a controlled way. They dissolved DBS-CO$_2$H in sodium hydroxide to form a carboxylate salt. The addition of glucuno-*d*-lactone (GdL) was followed (hydrolyses to gluconic acid when in contact with water) and made the solution acidic. A stable gel is formed as the Na$^+$ is released from the carboxylate salt. Their hydrogelator DBS-CO$_2$H is very similar to the DBX-CO$_2$H, where the DBX derivative only has one –OH group in the sugar backbone. It would be interesting to see if DBX-CO$_2$H will be just as effective as DBS-CO$_2$H in forming gel *via* pH switch.

During the workup for the synthesis of DBX-CO$_2$H, NaHSO$_4$ was added, and a white stable gel formation was seen. This observation is already an indication that DBX-CO$_2$H does form a gel with pH change and behaves as a hydrogelator. To expand the investigation, DBX-

CO_2H was dissolved in 0.92 mL of water and 0.08 mL of 0.5 M NaOH. The solution was sonicated to ensure the complete dissolution of the compound by forming sodium carboxylate (DBX-COO$^-$Na$^+$), with the solution having a pH value of 11. The sodium carboxylate solution was transferred into a separate vial that contained the acidification agent (GdL) and was shaken (unless stated) to allow the hydrolysis of GdL to form gluconic acid. When the solution reduces to pH 4, it indicates that the sodium carboxylate has reacted with the acid, forming a sodium salt. As the DBX-CO_2H ionises, solubility reduces in water, forcing self-assembly.

Glucuno-*d*-lactone (GdL) and hydrochloric acid (HCl) were used to study the gelation abilities of DBX-CO_2H. The experiment was first carried out with 1.0 equivalents of GdL and HCl, which only formed partial gels. This observation may be attributed to the pH value being above the pH threshold of gelation (pH 4). Using 2.0 equivalents of GdL and HCl, gelation behaviour was observed for DBX-CO_2H in concentrations as low as 3 mg mL^{-1} for GdL and 5 mg mL^{-1} for HCl (Table 3.9).

Table 3.9 | Gelation properties of DBX-CO_2H in different concentrations with 2 equivalents of GdL and HCl. G = gel, PG = partial gel. [a]no shaking involved

DBX-CO_2H concentration / mg mL^{-1}	Acidification Agent	
	GdL	HCl[a]
20	G (O)	G (O)
17	G (O)	G (O)
15	G (O)	G (O)
10	G (O)	G (O)
7	G (O)	G (O)
5	G (O)	G (O)
3	G (O)	PG
1	PG	PG
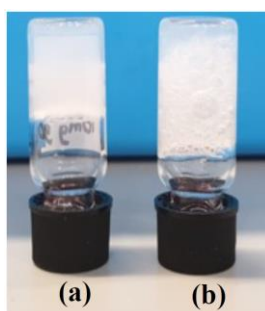
Figure 3.9 | DBX-CO_2H gelation *via* pH switch with (a) GdL and (b) HCl

Figure 3.9 shows the difference in the appearance of the DBX-CO_2H gel formation by switching pH with (a) GdL and (b) HCl. The difference in appearance is attributed to the gelation times with GdL taking place for a few hours, whilst the gelation with HCl induced self-assembly instantaneously. The addition of HCl in water is exothermic; hence, the immediate gelation creates a turbid, inhomogeneous gel. On the other hand, glucono-*d*-lactone (GdL) undergoes slow hydrolysis with water into gluconic acid, which will lower the pH of the solution at a uniform rate and, therefore, forms a homogeneous gel, as shown

in Figure 3.9a. Furthermore, citric acid (2.0 equivalents) was added with DBX-COO$^-$Na$^+$ to determine whether it would form a gel. It was observed that citric acid reacts similarly to HCl, which forms an inhomogeneous gel with DBX-CO$_2$H instantaneously.

3.3. Infrared Spectroscopy

Infrared (IR) spectra of DBX-CO$_2$Me as a crystalline powder, xerogel and wet gel in ethanol were measured, and the results are shown in Figure 3.10. As mentioned in chapter two, the intermolecular hydrogen bonds for the OH groups appear in the range of 3250-3550 cm^{-1}, and the intramolecular hydrogen bonds appear in the range of 3400-3590 cm^{-1}. Whilst the IR spectra of DBS-*i*Pr, MBS-*i*Pr, and the two together displayed peaks at approximately 3250-3350 cm^{-1}, IR spectra of crystalline powder and xerogel DBX-CO$_2$Me exhibit peaks in the range of 3450-3500 cm^{-1} which are assigned to the intramolecular hydrogen bonding. Moreover, the –OH band of the crystalline powder shifts from a wavenumber of 3486 cm^{-1} to 3473 cm^{-1} in the xerogel, which shows that the hydrogen bonding strength of the –OH groups are altered with the introduction of ethanol. The addition of ethanol allowed the formation of stronger hydrogen bonds as the O-H peak shifted to a lower wavenumber. This result shows the opposite from the results obtained for the benzylidene sorbitol derivatives, where DBS-*i*Pr displayed apparently stronger hydrogen bonds in the crystalline state than its xerogel state. Therefore, having one less hydroxyl group in the molecule (DBX-derivatives) seems to decrease the strength of the hydrogen bonds in the crystalline state, and increases in the xerogel state.
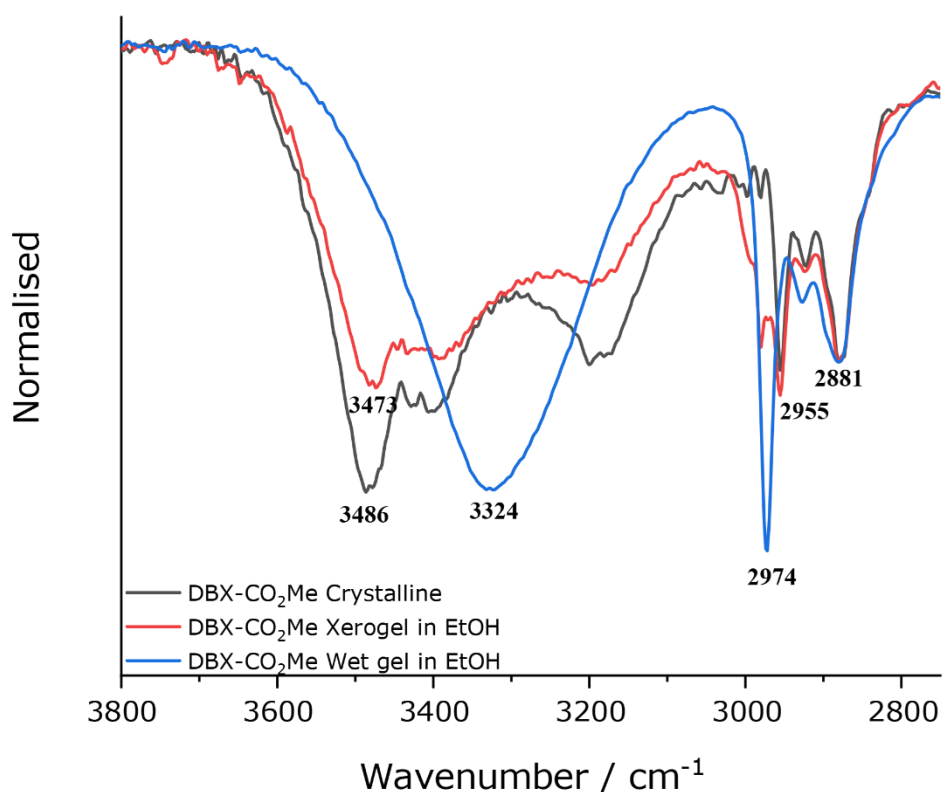
Figure 3.10 | FTIR spectra of DBX-CO$_2$Me in crystalline, xerogel (ethanol) and wet gel (ethanol) state

Furthermore, IR spectra of DBX-CO$_2$Me as a crystalline powder, xerogels and wet gels in different ethanol:H$_2$O ratios were measured and summarised in Figure 3.11. The xerogels of DBX-CO$_2$Me formed in 100:0 and 60:40 ethanol:H$_2$O ratios exhibit similar peaks and shifts in the -OH band. Contrarily, the wet gels displayed significant differences in both intensity and wavenumber. This observation can again be correlated to the wet gels spectra measured for the benzylidene sorbitol derivatives in chapter two. The strong intensities are attributed to the strong hydrogen bonding interactions between (i) the solvent molecules, (ii) the gelator molecules and (iii) both the solvent and gelator molecules. The broadness and the intensity of the –OH band for the wet gel in 60:40 ethanol:H$_2$O is greater than the –OH band for the wet gel in 100% ethanol content. These observations clearly indicate more hydrogen bonding interactions between the solvent molecules, likely due to water being a better hydrogen bond donor than ethanol.
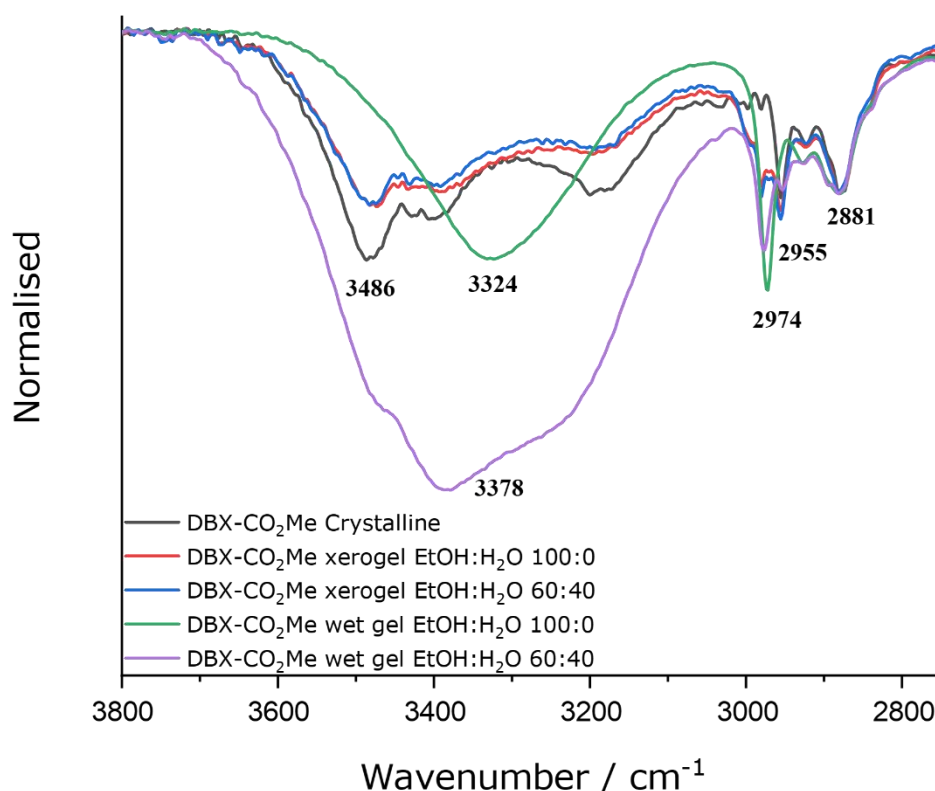
Figure 3.11 | FTIR spectra of DBX-CO$_2$Me in crystalline, xerogels and wet gel state in varying ratios of ethanol:H$_2$O

Figure 3.12 shows the FTIR spectra of DBX-CO$_2$H in crystalline, xerogel and wet gel states in 50:50 DMSO:H$_2$O. The peak at ~3375 cm^{-1} in the wet gel is attributed to the O-H stretch from the water molecules. DBX-CO$_2$H in the xerogel state (from 50:50 DMSO:H$_2$O) display a relatively higher intensity at the absorption peak around ~3393 cm^{-1} than the crystalline state. This peak is attributed to the O-H stretch of the hydroxyl group in the gelator molecule. The observed result implies that the dipole moment of the stretch in the xerogel state is stronger than the dipole moment in the crystalline state, which is the opposite observation from DBX-CO$_2$Me, meaning that DMSO and ethanol have different effects on the dipole moment of the stretches in the gelator which may mean that the structures of the DBX derivatives are polymorphic. This phenomenon might be the effect of the compounds being scalemic or racemic.
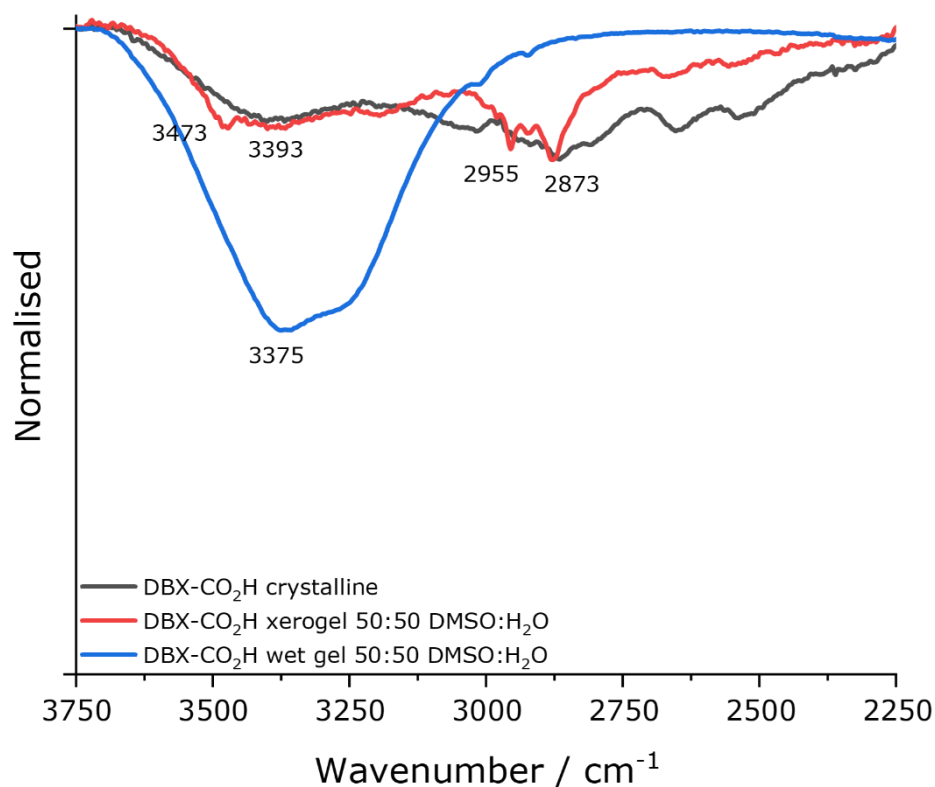
Figure 3.12 | FTIR spectra of DBX-CO$_2$H in crystalline, xerogel and wet gel state in 50:50 DMSO:H$_2$O

The FTIR spectra were also collected for DBX-iPr and DBX-CONHNH$_2$ (displayed in Figure 3.13 and Figure 3.14, respectively) in their crystalline state, and the xerogels formed in various solvents to compare the differences of the O-H stretch in each spectrum. The formation of xerogel fibres in any solvents affect the O-H stretch of the molecule, where it displayed a noticeable shift of wavenumber to a lower value.

DBX-iPr in the crystalline state and xerogels in any of the solvents have O-H stretches values of 3315 and 3306 cm^{-1}, respectively. As the −OH band in the crystalline state has a higher wavenumber, the O-H stretch in the molecule is shorter than in the xerogel states. Therefore, the formed hydrogen bond in the crystalline state is longer and weaker than the present hydrogen bonds in the xerogel states.

On the other hand, DBX-CONHNH$_2$ in the crystalline state presented a maximum absorption IR band peak at a lower wavenumber than the xerogels. This observation means that the hydrogen bonds in the crystalline state are stronger than the xerogels, which may be due to the secondary amide and the primary amine that offers further hydrogen bonds than the rest of the DBX derivatives did not have. In addition, the xerogels formed from incorporating DBX-CONHNH$_2$ into ethanol and 90:10 ethanol:H$_2$O ratio made the absorption band less broad than the crystalline state. This phenomenon indicates that the hydrogen bonding between the -OH groups differs between the solid-state and the gels.

a)

b)
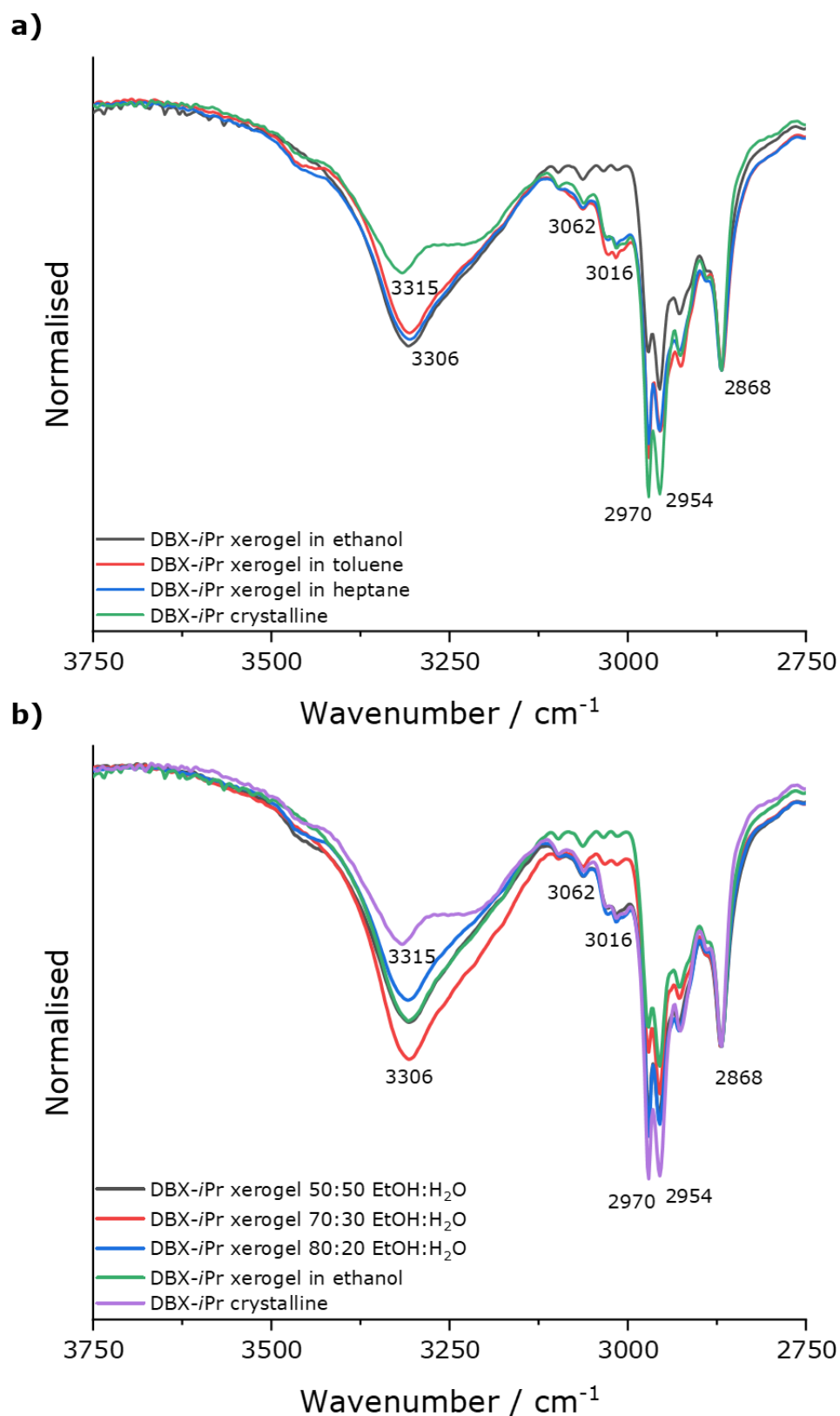
Figure 3.13 | FTIR spectra of DBX-*i*Pr in crystalline state with (a) xerogels in organic solvent and (b) xerogels in ethanol:H_2O solutions.
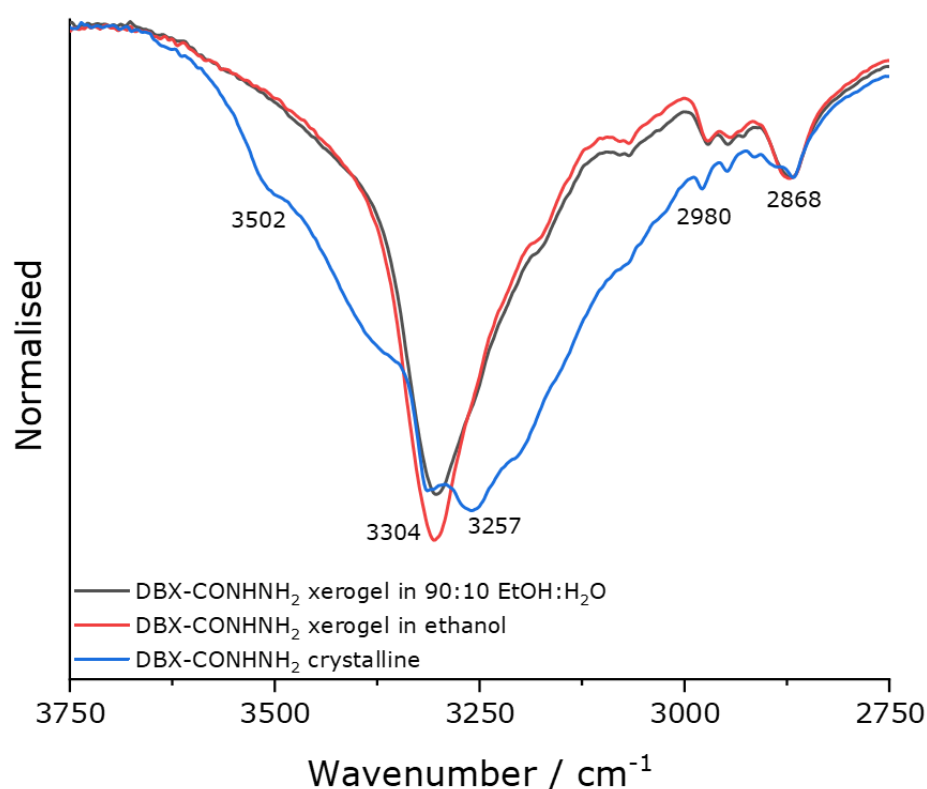
Figure 3.14 | FTIR spectra of DBX-CONHNH$_2$ in the crystalline state, and xerogels in 90:10 ethanol:H$_2$O ratio and ethanol.

3.4. Xerogel Morphologies

The difference in morphology between the DBX derivatives was investigated by scanning electron microscopy (SEM). Samples were prepared by drying the obtained gels from the various solvents and mixtures on a SEM stub in *vacuo* followed by iridium coating under vacuum. Figure 3.15 and Figure 3.16 display the different morphologies and size histograms of DBX-*i*Pr of xerogels from various solvents, respectively. DBX-*i*Pr forms smooth non-helical fibres regardless of the solvent and the solvent's polarity, which is the opposite of the outcome of the fibre structures of DBS-*i*Pr. This phenomenon is perhaps unsurprising given that DBX-*i*Pr is racemic (although some gels do resolve spontaneously[158]) and does not have the chiral assemblies of DBS-*i*Pr that self-order *via* strong hydrogen bonding in non-polar solvents. DBX-*i*Pr in toluene (Figure 3.15a) generated fibres with the broadest width at 1980 ± 80 nm, whereas DBX-*i*Pr in cyclohexane (Figure 3.15b) formed much thinner fibres, 230 ± 9.5 nm.
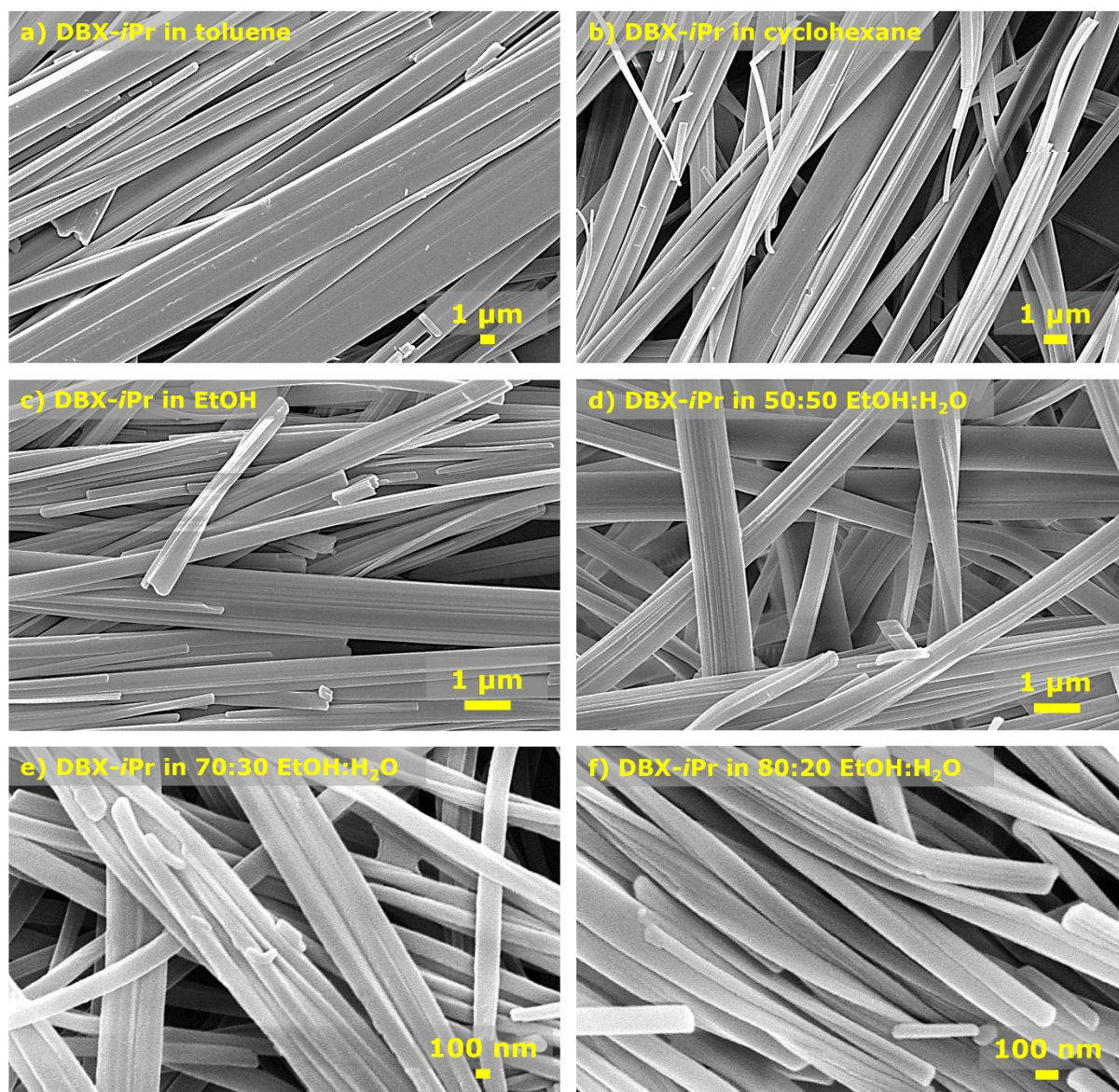
Figure 3.15 | SEM micrographs of xerogels formed by 10 mg mL^{-1} of DBX-iPr in (a) toluene, (b) cyclohexane, (c) EtOH, (d) DBX-iPr in 50:50 EtOH:H$_2$O, (e) DBX-iPr in 70:30 EtOH:H$_2$O and (f) DBX-iPr in 80:20 EtOH:H$_2$O. Conditions: xerogel was prepared by drying the gel in air and then coating it with 5 nm Ir before imaging under vacuum at 5 kV. Scale bars represent 1 µm for a, b, c, and d; 100 nm for e and f.

For the DBX-iPr formed from ethanol (Figure 3.15c), the width of the fibres is much narrower than DBS-iPr fibres formed from ethanol with values of 270 ± 9.0 nm and 700 ± 4.0 nm, respectively. Introducing water into the DBX-iPr gel system to have a ratio of 50:50 EtOH:H$_2$O, the smooth non-helical fibres reduce in size by approximately 20 nm in comparison to DBX-iPr in 100% ethanol by volume. In reference with the DBX-iPr fibres in 50:50 EtOH:H$_2$O, the increase of ethanol volume into the ratio decreases the width of the fibres where 70:30 and 80:20 EtOH:H$_2$O formed widths of DBX-iPr fibres with 170 ± 5.0 and 120 ± 3.0 nm, respectively.
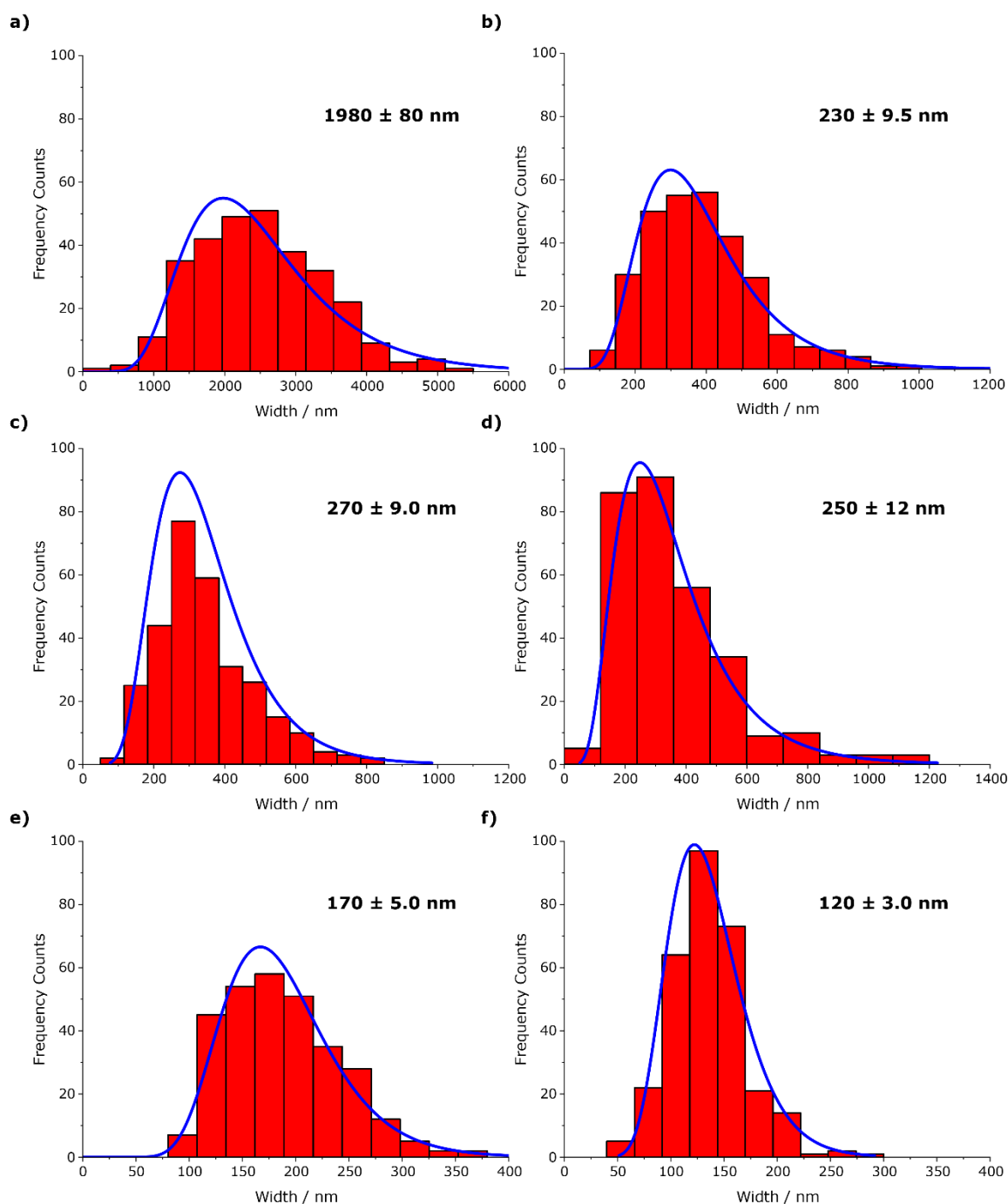
Figure 3.16 | Distribution histograms of xerogels' fibre sizes formed by 10 mg mL^{-1} of DBX-iPr in (a) toluene, (b) cyclohexane, (c) EtOH, (d) DBX-iPr in 50:50 EtOH:H$_2$O, (e) DBX-iPr in 70:30 EtOH:H$_2$O and (f) DBX-iPr in 80:20 EtOH:H$_2$O.

The micrographs of DBX-CONHNH$_2$ xerogels show interesting fibre structures (Figure 3.17). Unlike the rest of the xerogels, DBX-CONHNH$_2$ forms cuboid fibres with thin strands netting the cuboid structure. The dimensions of one of the fibres formed from ethanol were measured with a 268 x 262 nm cross-sectional area. The measurements show that the cross-sectional area is nearly a perfect square. In addition to that, the xerogel of DBX-

$CONHNH_2$ from ethanol and 90:10 $EtOH:H_2O$ have relatively thin cuboid fibres with 116 ± 5.0 and 145 ± 6.2 nm, respectively (Figure 3.18).
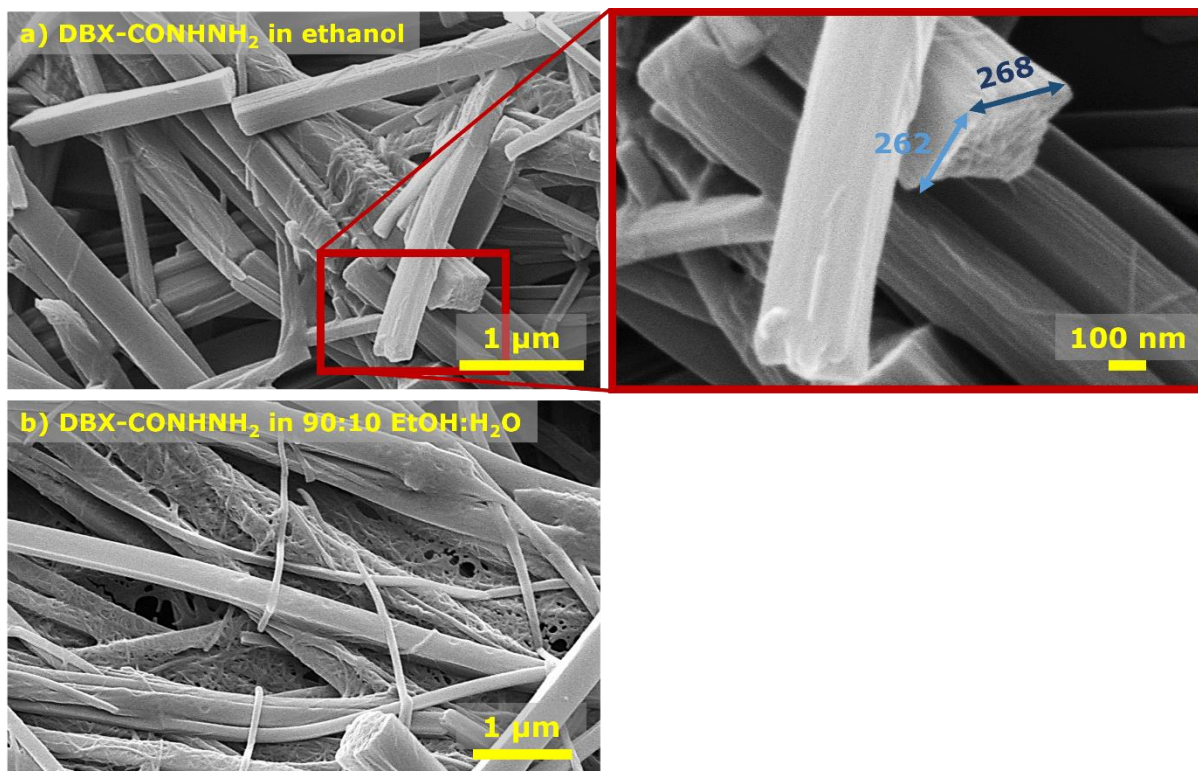
Figure 3.17 | SEM micrographs of xerogels formed by 10 mg mL^{-1} of DBX-$CONHNH_2$ in (a) ethanol and (b) 90:10 $EtOH:H_2O$. Conditions: xerogel was prepared by drying the gel in air and then coating with 5 nm Ir before imaging under vacuum at 5 kV. Scale bars represent 1 μm for a and b; 100 nm for zoomed in micrograph.
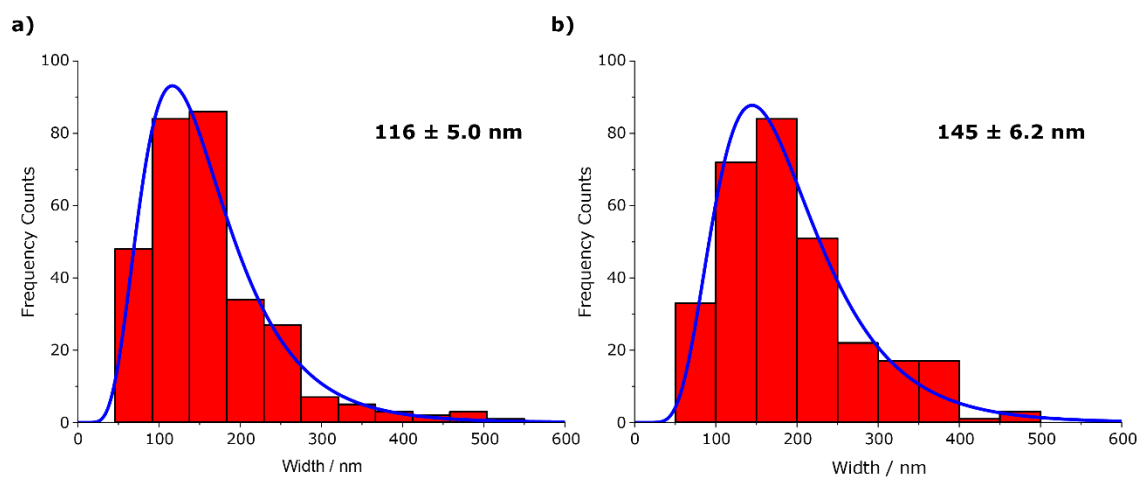
Figure 3.18 | Distribution histograms of xerogels' fibre sizes formed by 10 mg mL^{-1} of DBX-CONHNH$_2$ in (a) ethanol and (b) 90:10 EtOH:H$_2$O.

Figure 3.19 displays the different morphologies seen in DBX-CO$_2$Me from gels in different solvent media. The quantification of the xerogel fibres is shown in Figure 3.20. The xerogel fibres formed in ethyl acetate (Figure 3.19b), dichloromethane (Figure 3.19c) and *iso*propyl alcohol (Figure 3.19d) exhibit similar ribbon-like structures with average widths of 140 ± 3.0 nm, 110 ± 3.0 nm and 190 ± 4.0 nm, respectively. On the other hand, the fibres formed in MEK (Figure 3.19a) are thicker than the ribbon-like fibres. However, looking closer to the micrograph, thinner fibres are seen bundled and densely packed together. MEK fibre widths have a smaller distribution of 70 ± 1.0 nm.

The morphology of the xerogel DBX-CO$_2$Me from toluene (Figure 3.19e) differs significantly from the morphologies in other organic solvents. A mixture of thick and thin fibres was observed where the thin fibres wrap around the thicker fibres. A clear bimodal distribution of widths is observed. The thin fibres have an average width of 50 ± 1.0 nm whilst the thicker fibres have an average width of 1300 ± 90 nm. The root-like thin fibres shows a better distribution varying width length between 20 – 100 nm in comparison to the thicker fibres with width values spanning from 450 – 2800 nm. The findings on the morphology of toluene may be a contributing factor for the successful gelation behaviour of DBX-CO$_2$Me at concentrations as low as 3 mg mL^{-1}. Overall, the self-assembly of DBX-CO$_2$Me changes depending on the organic solvent that was used.
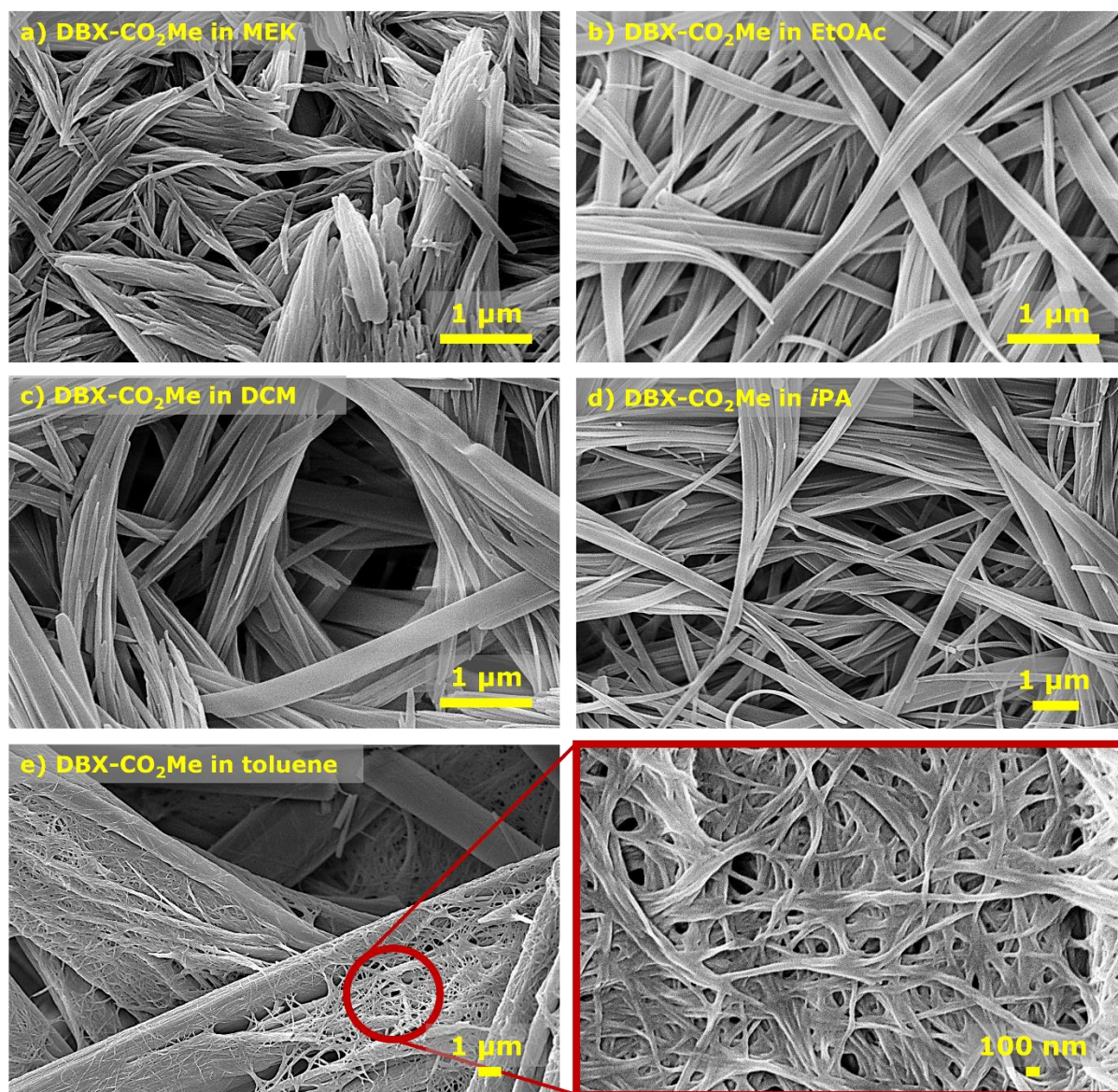
Figure 3.19 | SEM micrographs of xerogels formed by 10 mg mL^{-1} of DBX-CO$_2$Me in (a) MEK, (b) EtOAc, (c) DCM, (d) iPA and (e) toluene. Conditions: xerogel was prepared by drying the gel in air and then coating with 5 nm Ir before imaging under vacuum at 5 kV. All scale bars represent 1 µm, zoomed in micrograph represent 100 nm scale bar.
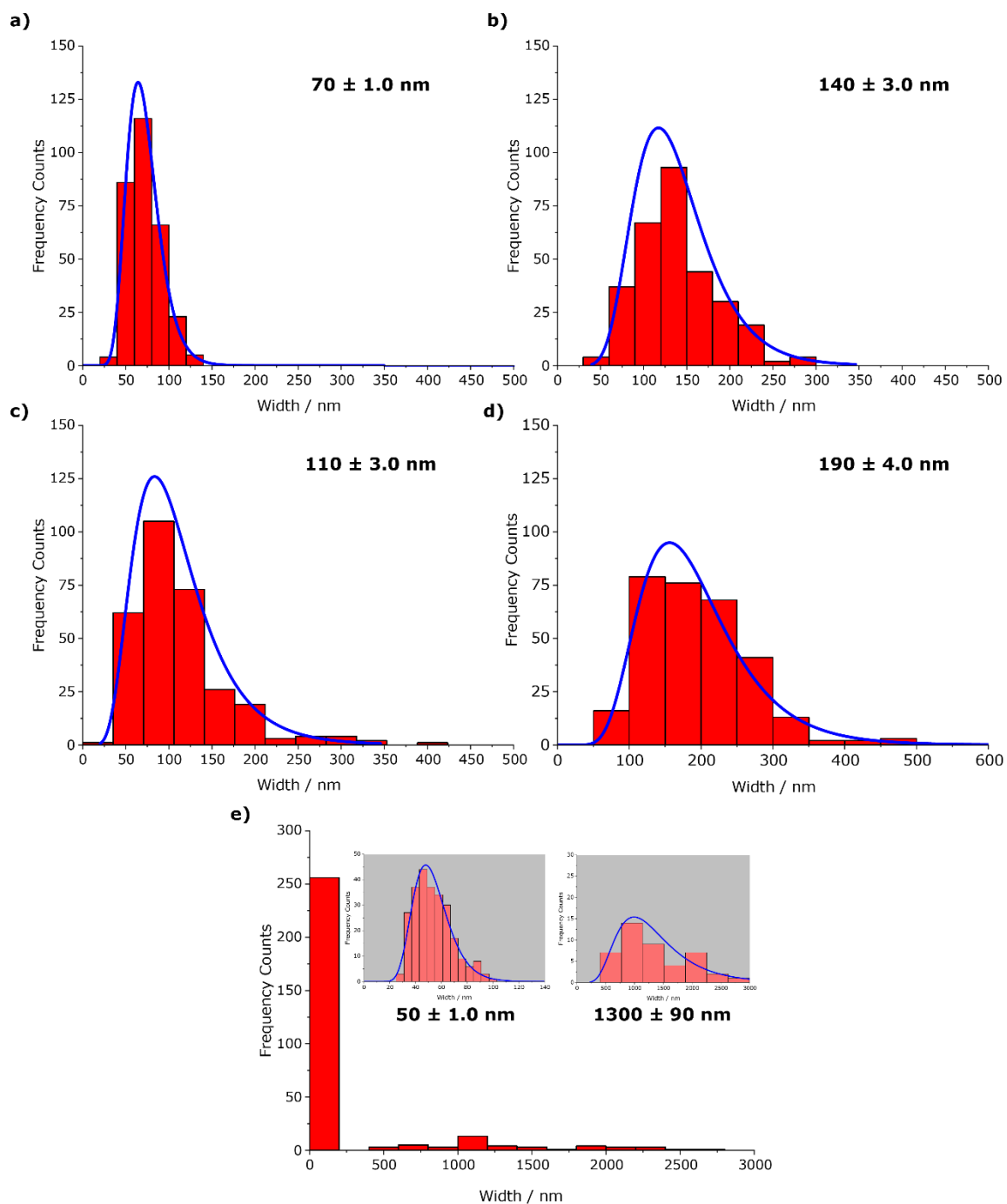
Figure 3.20 | Distribution histograms of xerogels' fibre sizes formed by 10 mg mL^{-1} of DBX-CO$_2$Me in (a) MEK, (b) EtOAC, (c) DCM, (d) iPA and (e) toluene.

The morphologies of xerogels from 10 mg mL^{-1} DBX-CO$_2$Me in 50:50 DMSO:H$_2$O and DBX-CONHNH$_2$ in 60:40 DMSO:H$_2$O were investigated using SEM. The two xerogels show significant differences. DBX-CO$_2$Me exhibit long and thin fibres; some of the thin fibres line up parallel to form bundles that intertwine (Figure 3.21a). The fibres show an excellent width distribution with an average of 40 ± 0.5 nm (Figure 3.22). Contrarily, the fibres formed in the xerogel of DBX-CONHNH$_2$ display stacked and short fibres with an average width of 100 ± 2.0 nm. The distribution of the fibres in DBX-CONHNH$_2$ xerogel is not as narrow as it is for DBX-CO$_2$Me. Overall, bundled up long and thin fibres intertwining may have had an effect on why DBX-CO$_2$Me showed thixotropic behaviour and DBX-CONHNH$_2$ did not.
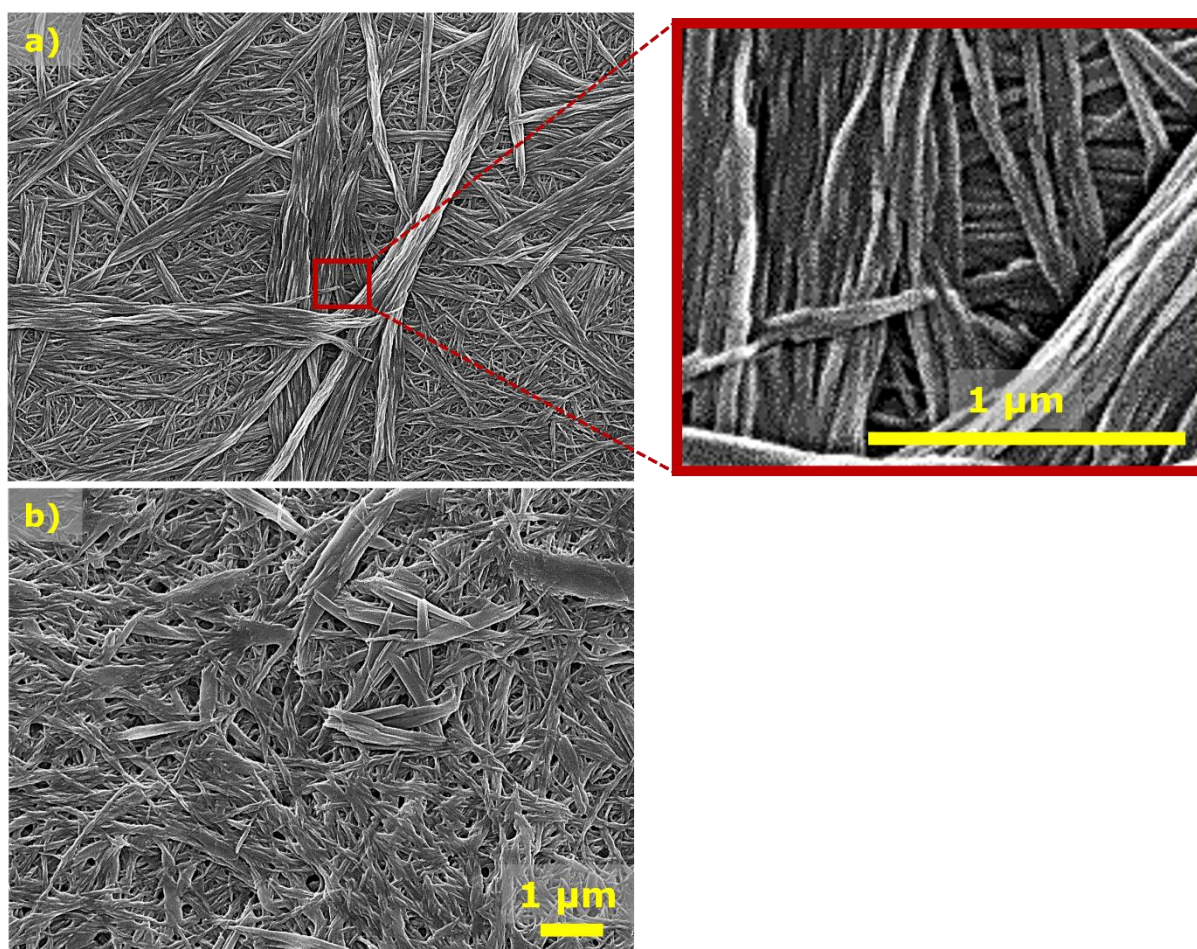
Figure 3.21 | SEM micrographs for xerogels at 10 mg mL^{-1} of (a) DBX-CO$_2$Me from 50:50 DMSO:H$_2$O and (b) DBX-CONHNH$_2$ from 60:40 DMSO:H$_2$O. Conditions: xerogel was prepared by drying the gel in air and then coating with 5 nm Ir before imaging under vacuum at 5 kV. All scale bars represent 1 μm
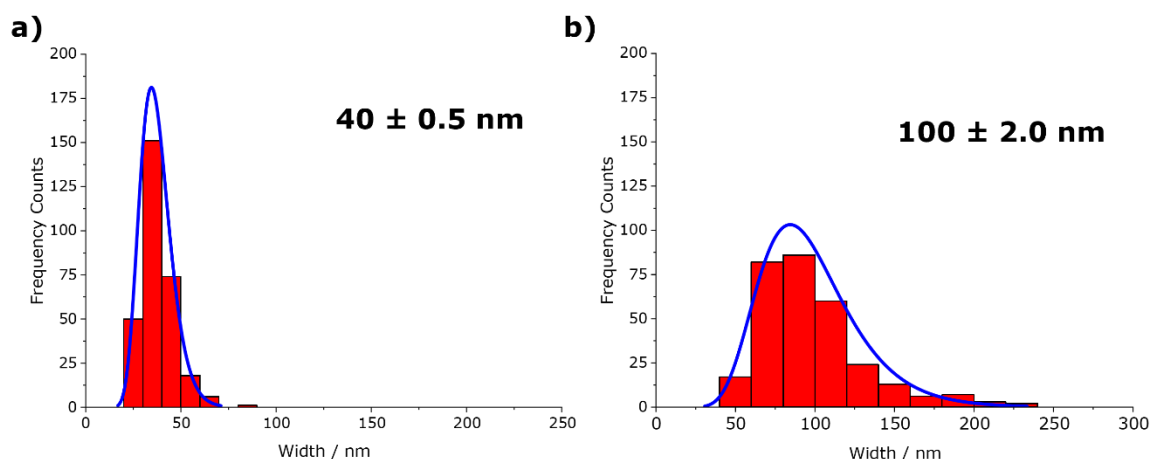
Figure 3.22 | Corresponding distribution histograms for xerogels at 10 mg mL^{-1} of (a) DBX-CO$_2$Me from 50:50 DMSO:H$_2$O and (b) DBX-CONHNH$_2$ from 60:40 DMSO:H$_2$O.

SEM imaging was also done for the formed and manipulated DBX-CO$_2$H gel in 50:50 DMSO:H$_2$O to give an insight into how the system changed after the gel was physically manipulated by heat or shear. Figure 3.23a displays the morphology of DBX-CO$_2$H gel in 50:50 DMSO:H$_2$O as a well-connected 3D network with an average width of 250 ± 3.0 nm. The morphology is very similar to the shaken gel in the same solvent (Figure 3.23b), but with thicker and wider fibres having an average width of 370 ± 5.0 nm. The similarity of the morphologies suggests that the application of shear *via* shaking, breaks the network; however, when the broken network is put at rest, it reforms back into a gel with similar fibrous network. On the other hand, the morphology of the same gel after being heated and cooled differs from the first two (Figure 3.23c). It formed a uniform network of long narrow fibres that are bundled together with an average width of 70 ± 1.0 nm. The dissimilarity of the morphologies explain why the gel only transforms into a partial gel after the manipulation with heat. However, the accuracy of the xerogel structure of DBX-CO$_2$H from 50:50 DMSO:H$_2$O is uncertain. A spatula of a wet gel is placed on a SEM stub which was allowed to dry in the desiccator letting the solvent evaporate and form the xerogel. As DMSO has a lower vapour pressure than water, water will evaporate first. Some gel fibres may dissolve partially in the leftover DMSO, which precipitate when DMSO fully evaporates. This hypothesis must be considered, but regardless of the mentioned problem, we cannot ignore the fact that the DBX-CO$_2$H gel from 50:50 DMSO:H$_2$O and the shaken gel in the same solvent have a similar 3D network structure. Therefore, we can confirm its thixotropic properties.
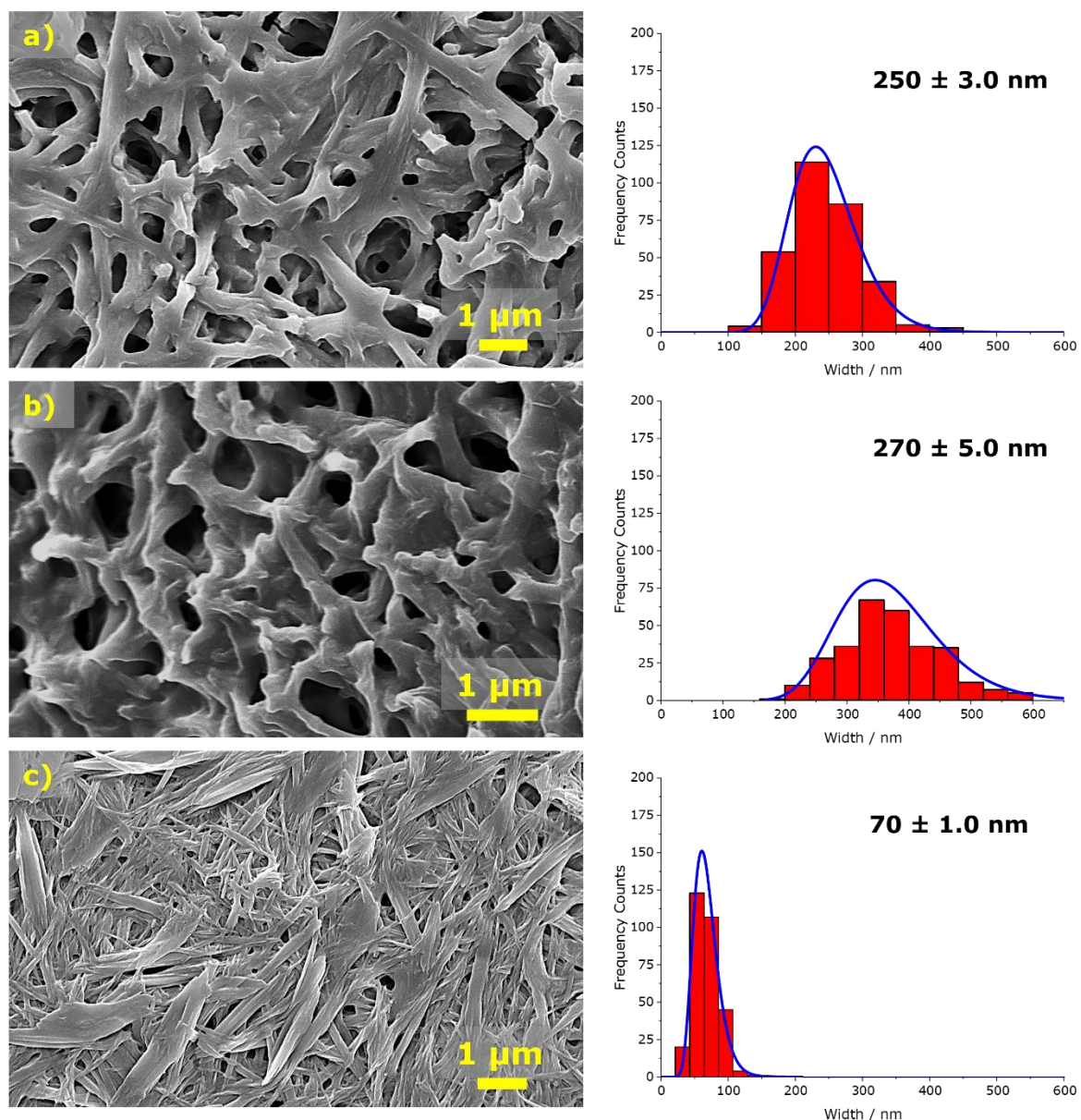
Figure 3.23 | SEM micrographs and their corresponding distribution histograms of 10 mg mL^{-1} DBX-CO$_2$H xerogels in 50:50 DMSO:H$_2$O (a) as formed, (b) after shaking, and (c) after heating and cooling. Conditions: xerogel was prepared by drying the gel in air and then coating it with 5 nm Ir before imaging under vacuum at 5 kV. All scale bars represent 1 μm

The xerogels of DBX-CO$_2$H formed using the pH switch approach with GdL and HCl are very similar to one another, consisting of extremely narrow and short fibres that are weaved together. They also possess relatively close average width values of 47.7 ± 0.5 nm and 49.5 ± 0.5 nm, respectively (Figure 3.24). Furthermore, the cube precipitates are seen in the micrograph of DBX-CO$_2$H with HCl is expected to be sodium chloride salt which would have formed when DBX-COO$^-$Na$^+$ is reacted with HCl. The uniqueness of the structure connects to the thixotropy properties of DBX-CO$_2$H gels that were not observed on the rest of the dibenzylidene sorbitol and xylitol compounds.
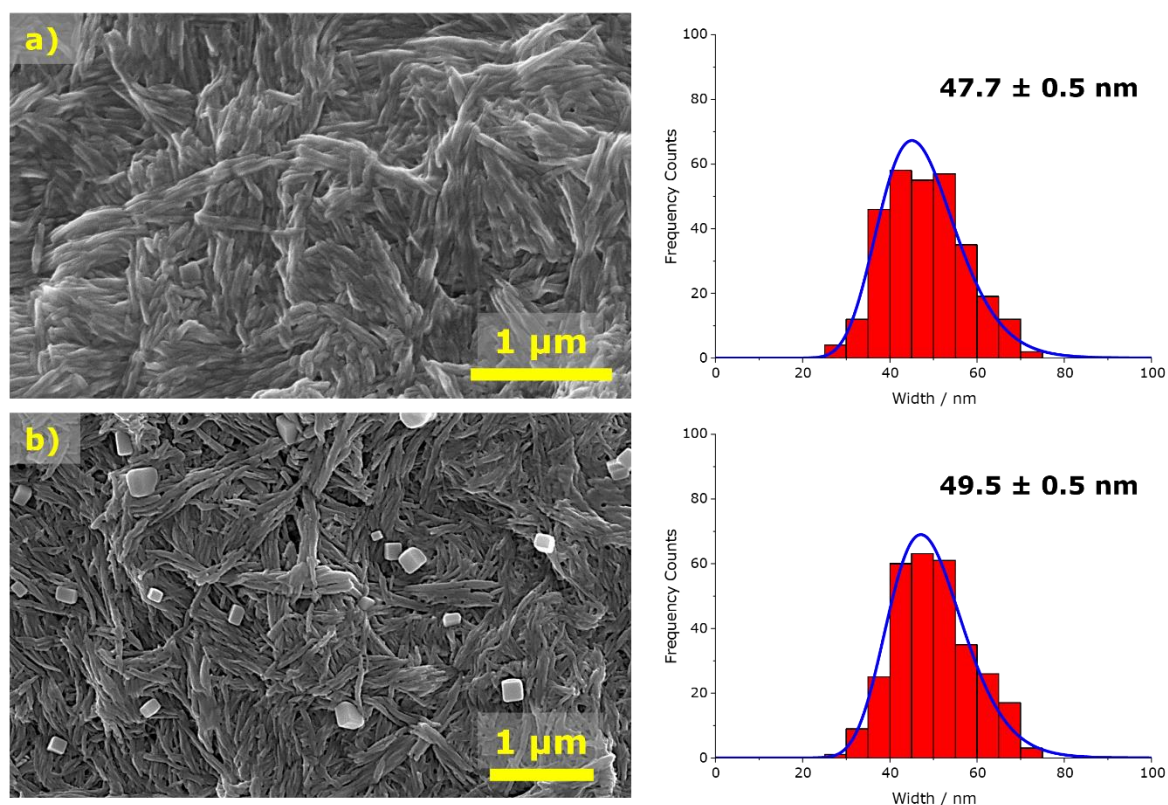
Figure 3.24 | SEM micrographs and corresponding distribution histograms for xerogels of 10 mg mL^{-1} DBX-CO$_2$H with 2.0 equivalents of (a) GdL and (b) HCl. Conditions: xerogel was prepared by drying the gel in air and then coating it with 5 nm Ir before imaging under vacuum at 5 kV. All scale bars represent 1 µm

3.5. Gel Rheology

Rheological data were collected for DBX-CO$_2$Me and DBX-CO$_2$H gels in different solvents. Oscillatory measurements were conducted on each gel sample by applying strain deformation and measuring the stress response while keeping the frequency at a constant value of 1 Hz.

Rheological data for 10 mg mL^{-1} DBX-CO$_2$Me in different organic solvents are plotted in Figure 3.25 and summarised in Table 3.10. The data illustrate that the values of G' and G" at low strains are unaffected by strain and indicate linear viscoelastic region (LVER), hence, classifying the formed gels as a viscoelastic solid. Furthermore, it is apparent that gels in *i*PA and DCM exhibit the sturdiest network with G' values of 9.42 and 9.04 x 10^4 Pa, respectively. In contrast, gels in EtOAc and MEK are less sturdy with lower G' values of 6.25 and 3.50 x 10^4 Pa, respectively. It appears that the three gels that have the highest value also have the highest value of fibre width (disregarding the thick fibres in toluene).
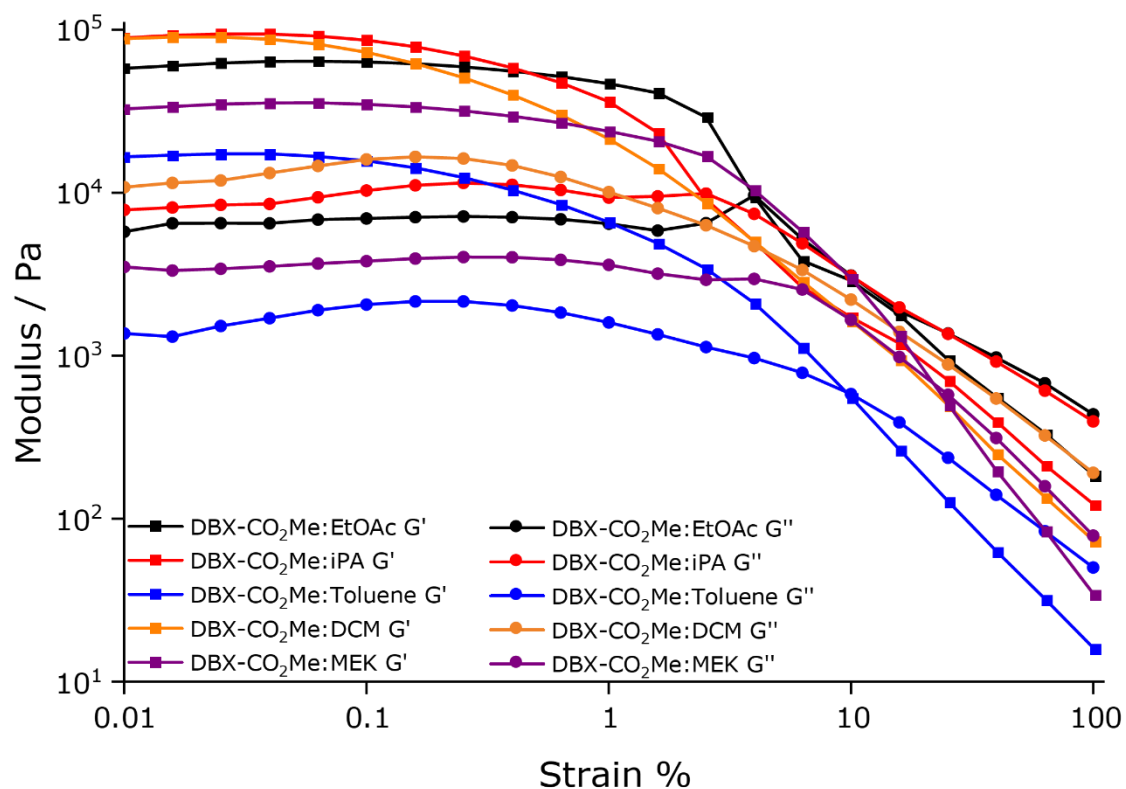
Figure 3.25 | Amplitude sweep rheological data for DBX-CO$_2$Me in different organic solvents at 10 mg mL^{-1}

As the applied strain increases, the gels' microstructure undergoes mechanical deformation as the G' values decrease. The crossover point (G' = G") corresponds to a strain-induced transition from a viscoelastic solid to a viscoelastic liquid. The MEK gel was observed to be the most elastic gel with a strain crossover point of 25.1%, whilst the rest of the gels have a strain crossover point of less than 10%. This observation may correlate to the fibre widths where the MEK gel consists of very thin and narrow fibres. In contrast, toluene displayed the poorest viscoelastic properties with a G' value of 1.73×10^4 Pa but showed better elasticity than *i*PA, DCM and EtOAc gel, which can again be attributed to the morphology of the xerogel as toluene have really thin fibres wrapped around thick fibres.

Table 3.10 | Tabulated rheological data for DBX-CO$_2$Me in different organic solvents at 10 mg mL^{-1} with their corresponding fibre widths

Solvent	Storage Modulus / x 10^4 Pa	Strain at G' = G'' / %	Average fibre widths / nm
*i*PA	9.42	2.51	190 ± 4.0
DCM	9.04	6.12	110 ± 3.0
EtOAc	6.25	2.57	140 ± 3.0
MEK	3.50	25.1	70 ± 1.0
Toluene	1.73	9.67	50 ± 1.0 / 1300 ± 90

Figure 3.26 and Table 3.11 show the amplitude sweep rheological data for the 10 mg mL^{-1} DBX-CO$_2$Me and DBX-CO$_2$H gels in 50:50 DMSO:H$_2$O. The results show that the formed gels in 50:50 DMSO:H$_2$O are weaker than the DBX-CO$_2$Me gel formed in *i*PA

and DCM. In addition, the starting storage modulus at 0.01% strain for DBX-CO$_2$Me in 50:50 DMSO:H$_2$O is a bit higher than the storage modulus of DBX-CO$_2$H gel in the same solvent. At 0.25% strain, the storage modulus of the gelators are the same; above 0.25% strain, DBX-CO$_2$H gel in 50:50 DMSO:H$_2$O is relatively stronger than DBX-CO$_2$Me gel in the same solvent. However, the crossover point (G' = G") differs significantly, with values of 39.7% and 18.6% for DBX-CO$_2$Me and DBX-CO$_2$H, respectively (Table 3.11). These results illustrate that DBX-CO$_2$Me gel in 50:50 DMSO:H$_2$O show better elasticity than DBX-CO$_2$H gel in the same solvent. This feature is attributed to the morphologies of the gels, where DBX-CO$_2$Me have bundles of thin fibres (the same as MEK – having the highest crossover strain value) whilst DBX-CO$_2$H gels showed well connected fibres. It appears that having a 3D network of thin fibres bundled together makes the gel more elastic.
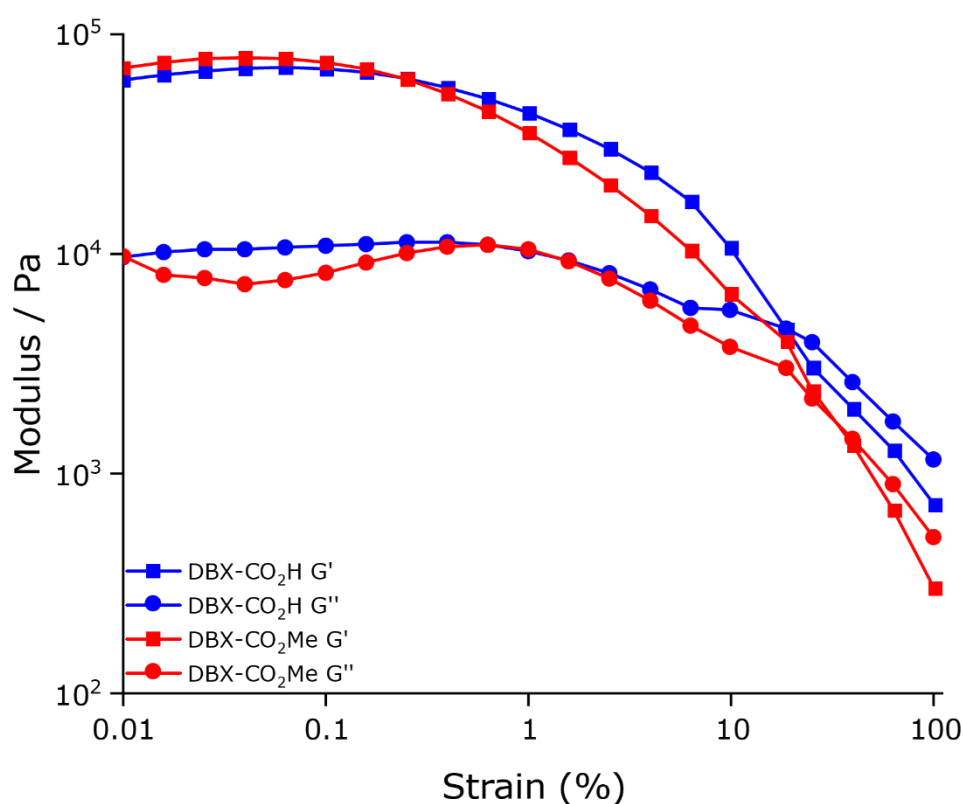
Figure 3.26 | Amplitude sweep rheological data for 10 mg mL^{-1} of DBX-CO$_2$Me and DBX-CO$_2$H in 50:50 DMSO:H$_2$O

Table 3.11| Tabulated rheological data for 10 mg mL^{-1} of DBX-CO$_2$Me and DBX-CO$_2$H in 50:50 DMSO:H$_2$O with their corresponding fibre widths

Gelator	Storage Modulus @ 0.01 % Strain / x 10^4 Pa	Storage Modulus @ 0.40% Strain / x 10^4 Pa	Strain at G' = G'' / %	Average fibre widths / nm
DBX-CO$_2$Me	7.75	5.37	39.7	40 ± 0.5
DBX-CO$_2$H	6.81	5.72	18.7	250 ± 3.0

Seeing that the manipulation *via* shaking of the 10 mg mL^{-1} DBX-CO$_2$Me and DBX-CO$_2$H gel show self-healing properties, which was also seen in the morphology of the gel, it is a good idea to have rheological data to evidence the earlier findings. Dynamic rheological experiments were conducted to test the mechanical recoverability of the hydrogels in 50:50 DMSO:H$_2$O. The parameters were set up according to the amplitude sweep results in Figure 3.26. For the first 200 s, 0.01% of strain was applied because it is within the linear viscoelastic region where the gel remains stable. At 75% strain, according to the amplitude sweep rheological data, DBX derivative gels has broken down; therefore, 75% strain was applied for the following 200 – 400 s. Without any rest, the strain was adjusted back to 0.01% for the last 200 s. As expected, the results (Figure 3.27 and Figure 3.28) show shear-thinning and thixotropic properties in both gels as they both recovered back into viscoelastic liquid after mechanical deformation. It was fascinating to see that without letting the gels rest, they quickly re-establish their mechanical strength with almost 80% and 45% recovery for DBX-CO$_2$H and DBX-CO$_2$Me.
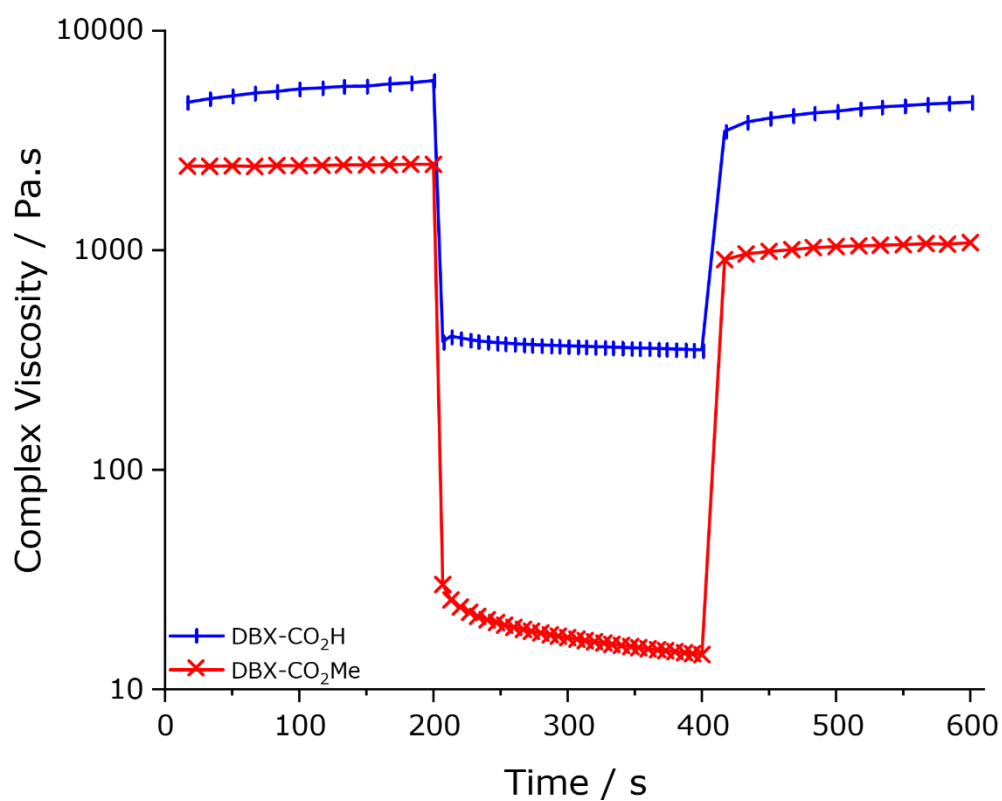
Figure 3.27 | Shear-thinning rheological data for 10 mg mL^{-1} of DBX-CO$_2$Me and DBX-CO$_2$H in 50:50 DMSO:H$_2$O. Complex viscosity were measured as a function of time. (No strain applied for 0 to 200 s and 400 to 600 s; 75% strain applied for 200 to 400 s)
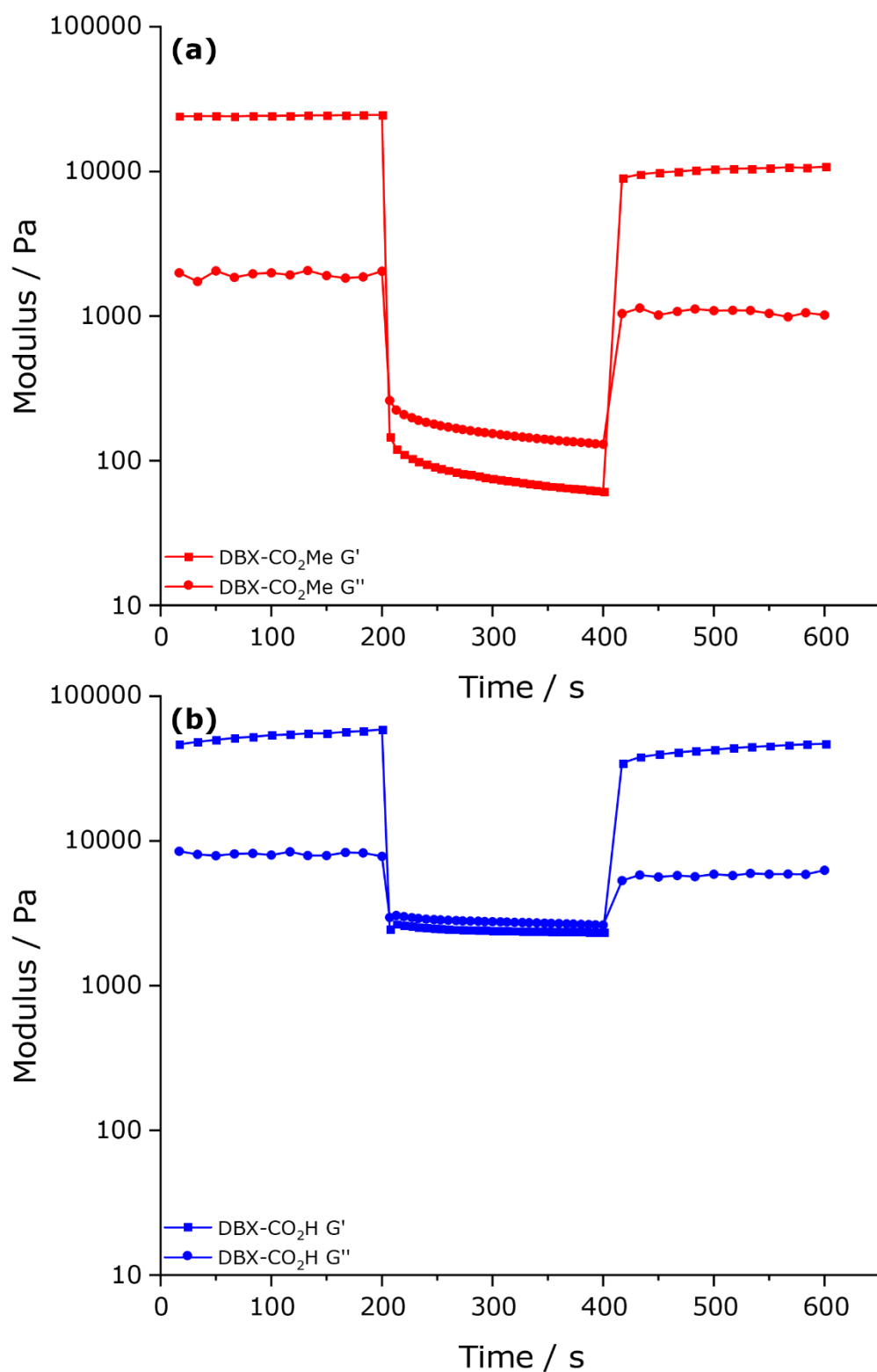
Figure 3.28 | Shear-thinning rheological data for 10 mg mL^{-1} of DBX-CO$_2$Me and DBX-CO$_2$H in 50:50 DMSO:H$_2$O. The G' and G'' values were measured as a function of time. (No strain applied for 0 to 200 s and 400 to 600 s; 75% strain applied for 200 to 400 s)

In summary, the attempts to resolve xylitol-based compounds to yield pure enantiomers were unsuccessful. However, they led to a hypothesis that the DBX derivatives might be scalemic compounds. Furthermore, according to a few investigations, it was observed that benzylidene sorbitol derivatives are more efficient gelators compared to xylitol derivatives. The importance of the extra hydroxyl group in the sorbitol-based gelators that the xylitol-based compounds do not have is acknowledged in the gelation abilities of the materials – DBS and MBS derivatives can form gelation in a broader range of solvents compared to DBX derivatives. The fibre structure of the xerogels also differs in DBS and MBS derivatives with DBX derivatives. Helical fibres are noticed from DBS-iPr xerogels in non-polar solvents due to the chirality aiding hydrogen bonding. These helical fibres are not seen in DBX-iPr xerogel. DBX-CONHNH$_2$ fibres show unique characteristics having cuboid structures to form the 3D network of the gel. Furthermore, thixotropic abilities are observed in some DBX-CO$_2$Me and DBX-CO$_2$H; these rheological properties are excellent in various applications, especially in additive manufacturing.

CHAPTER FOUR
Light Responsive Gels

4.1   Introduction to Light Responsive Gels

Low molecular weight gelators can respond to different types of external stimuli such as mechanical stress[159], light[14], pH[160] and enzymes[17]. These responses involve colour change, gel-sol transitions, isomerisation, dimer formation and morphology change. Amongst the various stimuli-responsive gels, the light-responsive gels have been of particular interest recently.[12,14,161–164] The light-induced alteration of gels is clean and controllable, and the change can also be easily located, allowing patterning, unlike for other stimuli (*i.e.* chemical or temperature). A photoresponsive gelator typically holds a chromophore in the gelator molecule structure attached to other functional groups, which aids the self-assembly of the compound.[165] Chromophores are conjugated systems that absorb light of a specific wavelength that induce photoreaction (*i.e.* bond formation, bond cleavage, isomerisation and dimerisation depending on the chromophore present.

One type of photoreaction that may occur in gelators is photoisomerisation. This type of photoreaction is generally the changing of a *cis* isomer to a *trans* isomer or *vice versa* (also known as the E-Z isomerisation) (Figure 4.1). It has been known that the *trans* isomers often self-assemble, and the *cis* isomer of the molecule could not self-sort due to the lack of preferential stacking of the molecules in solution – this photoreaction, therefore, leads to a gel-sol transition.[162]
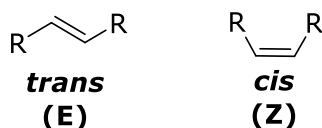
trans
(E)   **cis**
            (Z)

Figure 4.1 | *trans* (E) and *cis* (Z) isomers of the same molecule

4.2   BHC-n Light Responsive Gels in Literature

In 2016, Zhang *et al*.[166] synthesised three cinnamoyl derivatives (Figure 4.2) that displayed gelation properties in various organic solvents. From the team's investigation, BHC-6 has performed the most gelation in the organic solvents tested, followed by BHC-11. BHC-cho only gelled two out of twenty-six organic solvents.
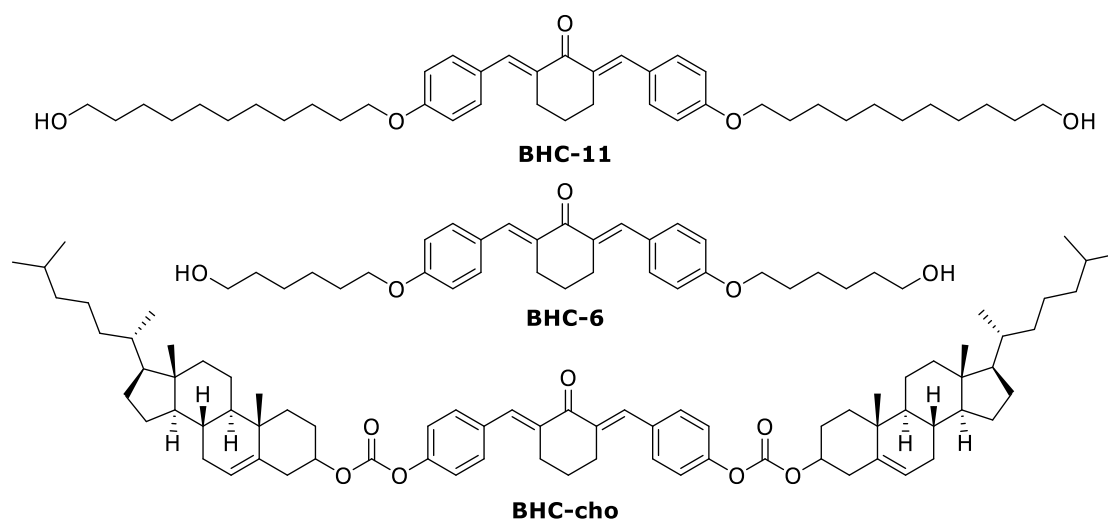
Figure 4.2 | Chemical structures of the cinnamoyl derivatives gelators in literature, BHC-11, BHC-6 and BHC-cho[166]

The *E-Z* isomerisation and photo cross-linking of the cinnamoyl derivatives were studied by UV irradiating the gelators at 365 nm and 254 nm.[166] Their idea was inspired from the work of Balamurugan *et al.*[163] in 2008, where they isolated polyesters containing oxadiazole and bis(benzylidene cycloalkanone units (BHC-n; n = number of carbon) which is shown in Scheme 4.1. Balamurugan *et al.*[163] presented two possible photochemical reactions: a) photoisomerisation and b) photodimerisation, that may occur on the generated polyesters when irradiated under the UV lamp (Figure 4.3). The UV-spectra of a polyester in chloroform that their team reported is shown in Figure 4.4.[163] They stated that the regular decrease in intensity at ~ 360 nm with irradiation time and its disappearance after 30 minutes indicate the completion of photo cross-linking. The photo cross-linking involves the formation of dimerisation of olefinic double bond of the cycloalkanone chromophores – entailing the 2π-2π cycloaddition reactions leading to the formation of a cyclobutane ring as shown in Figure 4.3. Furthermore, they further asserted that the observed appearance of a new absorption peak at ~ 510 nm, is the evidence of *trans-* to *cis*-photoisomerisation of the bis-benzylidene-cyclohexanone chromophores on irradiation.[163]
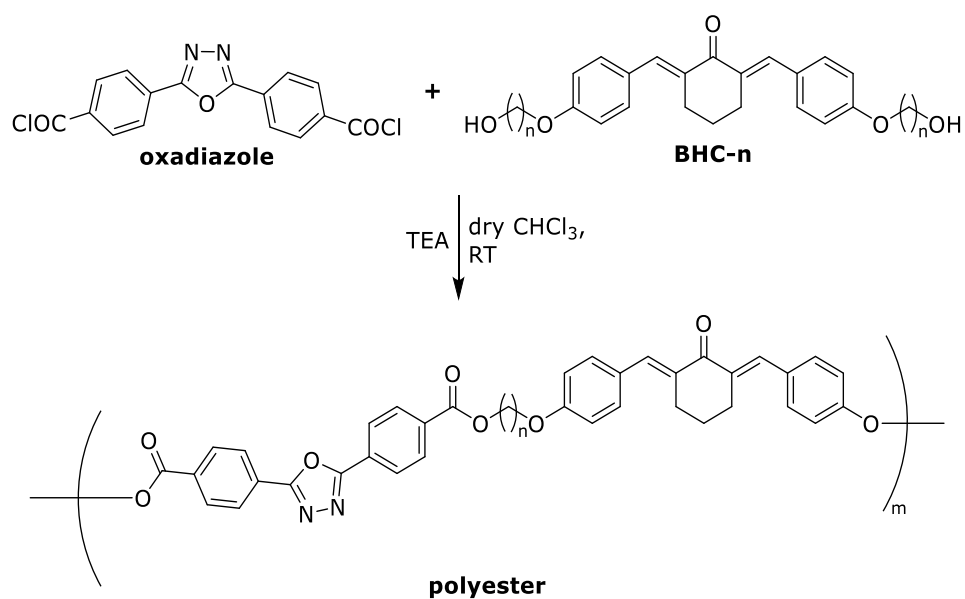
Scheme 4.1 | synthesis of polyester reported by Balamurugan *et al.*[163]
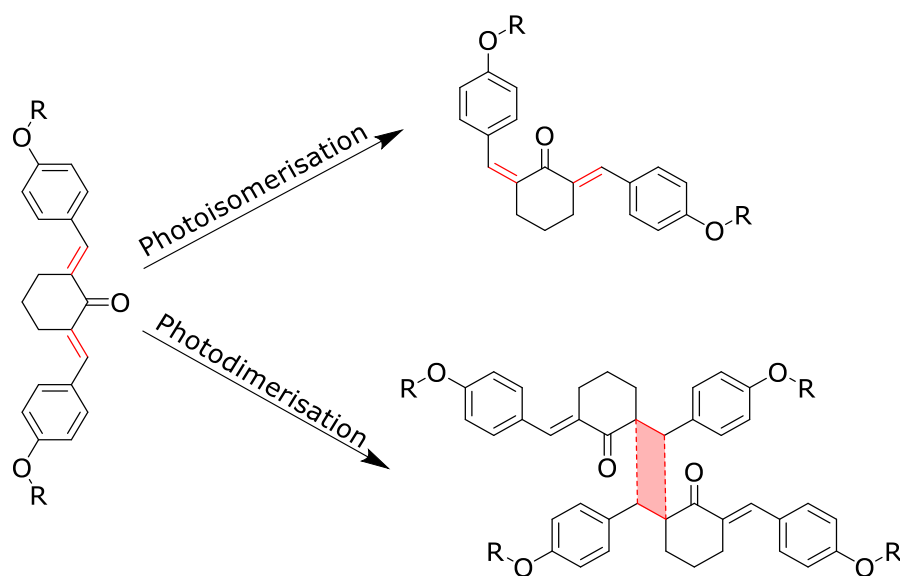
Figure 4.3 | Photochemical reactions of bis (benzylidene)cycloalkanones[163]
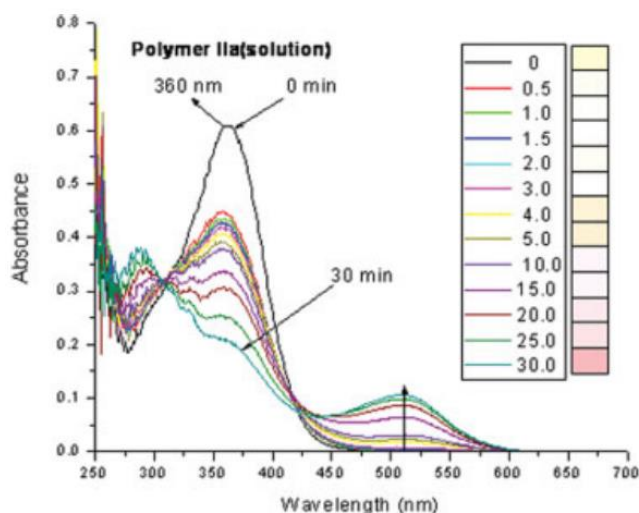
Figure 4.4 | Changes in UV spectral characteristics during photolysis of polyester in chloroform solution at various time intervals obtained and reported by Balamurugan *et al*.[163]

In collaboration with a team working at the University of Reading (UoR), we synthesised BHC-11 and BHC-6 and used them to synthesise a polymer to be employed as an ink for extrusion 3D printing.

BHC was prepared from cyclohexanone and 4-hydroxybenzaldehyde using boron trifluoride diethyl etherate (BF_3OEt_2) as the catalyst, which is the same approach as it was in literature.[166] To yield the BHC-n gelators, BHC is reacted with bromo-1-alkanols, with the presence of caesium carbonate in dry acetonitrile for 48 hours under reflux (Scheme 4.2). This approach in synthesising the BHC-n gelators is a more environmentally friendly method in comparison to the syntheses that were seen in some literature, as they use dry DMF instead of dry acetonitrile.[161,163]
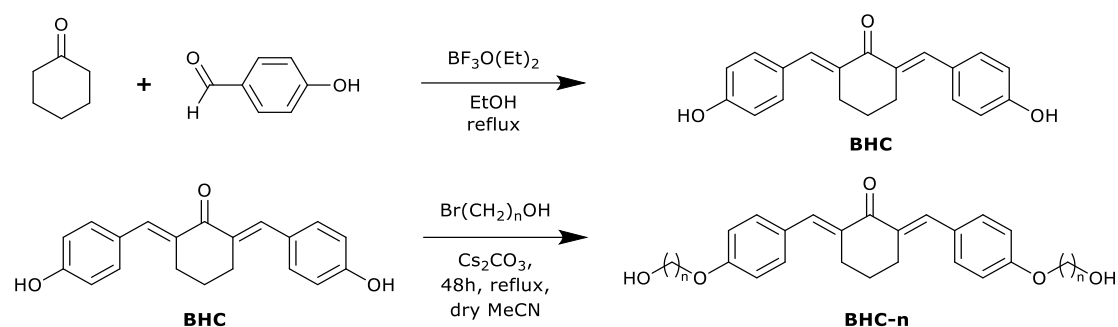
Scheme 4.2 | Synthesis of BHC and BHC-n gelators

The team in UoR used a polyol, 4,4'-MDI, morpholinoethanamine and the BHC-n gelator in a simple one-pot, two-step synthesis to generate the polymer for extrusion 3D printing (Scheme 4.3). This approach forms a polymer-gelator dual-network *via* intramolecular networks (Figure 4.5). Another attempted approach was to create a polymer-gelator dual-network *via* intermolecular networks (Figure 4.5). This method is achieved by excluding the BHC-n gelators from the synthesis in Scheme 4.3; instead, the BHC-n gelators were melted with the isolated polymer and were printed together for extrusion 3D printing (Figure 4.6).
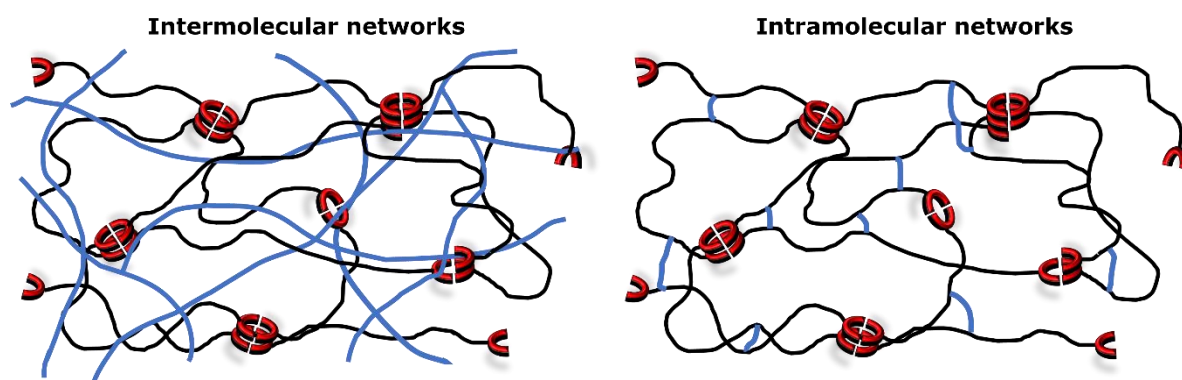
Figure 4.5 | The two approaches for the formation of polymer-gelator dual-network materials.

Their team investigated the difference in mechanical properties while varying the molar ratio of the components in the material. The material with 7.50 mmol of polyol, 21.0 mmol of 4,4'-MDI, 23.0 mmol of morpholinoethanamine, and 2.50 mmol of BHC-n gelator displayed the best rheological properties and therefore was used for extrusion 3D printing in the Faculty of Engineering in UoN.
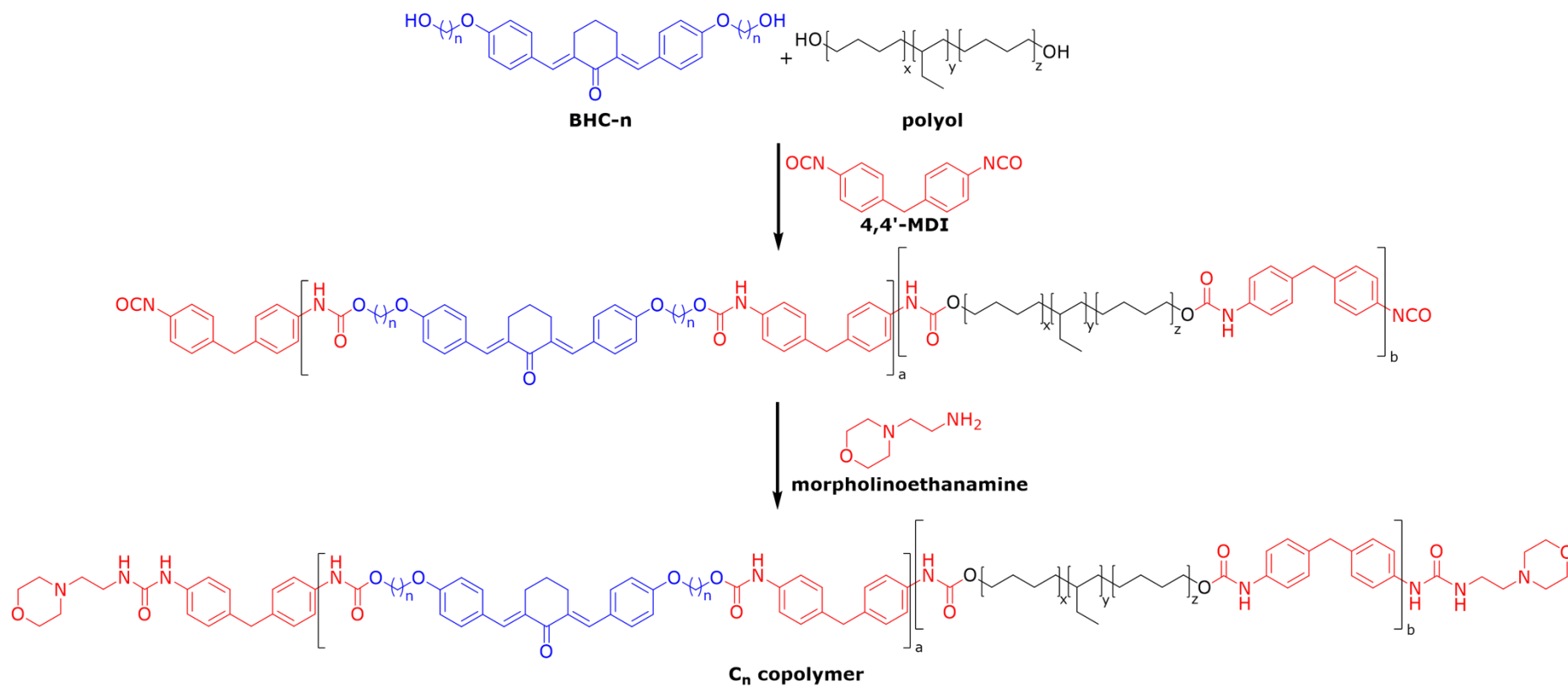
Scheme 4.3 | synthesis of the polymer with the BHC-n gelators isolated by the team in UoR
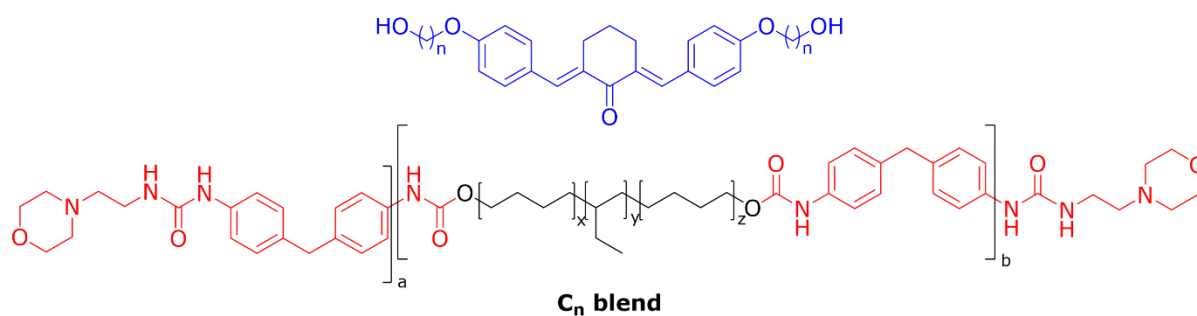
Figure 4.6 | Structure of C$_n$ blend

4.2.1.   Photoreactivity measurements of BHC-n materials

The printed samples were studied under UV irradiation as part of my work. Firstly, the focus was to see how the gelators will behave on their own under the UV light before investigating the printed materials. As mentioned above, BHC-6 and BHC-11 gelators are believed to undergo photoisomerisation and photo cross-linking when irradiated under UV light.[166] It is reported that the "UV-vis spectra of BHC-11 in solvent CHCl$_3$ under 365 and 254 nm irradiation" show a change, with λ_{max} at ~250 and ~375 nm. BHC-11 and BHC-6 samples were prepared in chloroform ready for UV irradiation. UV irradiations of the BHC-n material in solution and thin films were carried out using the Photoluminescence Spectrometer FLS9800 with a µF920H 60W Xenon Flash lamp. The absorbances of the irradiated samples were measured using the UV-Vis NIR Agilent CARY 5000 Spectrometer.

BHC-11 in chloroform was placed under 365 nm UV irradiation first, then the absorbance spectra at different time intervals were obtained. The absorbances were measured between 700 – 200 nm. The UV cut-off point of chloroform is 245 nm. Therefore, only the peak at λ_{max}, 363 nm, was seen for the BHC-11 in chloroform (Figure 4.7). Furthermore, BHC-6 was not irradiated in chloroform solution due to the solvent's UV cut-off point.

For the attained result of UV irradiating BHC-11 in chloroform at 365 nm, the λ_{max} at 363 nm is kept for all the UV-Vis spectra and π-π* transition, as well as two isosbestic points (326 and 426 nm) were observed. Furthermore, the longer the material is irradiated under the UV lamp, the intensity of the peak at λ_{max}, 363 nm, decreases. After the exposure time of an hour, the λ_{max} peak does not disappear. These observations suggest that the photoreactive groups (C=C) begin to react as photodimersation occurs during the excitation of BHC-11 in solution at 365 nm UV irradiation.[163,167] The primary results drove the investigation of the BHC-n gelators to continuation.
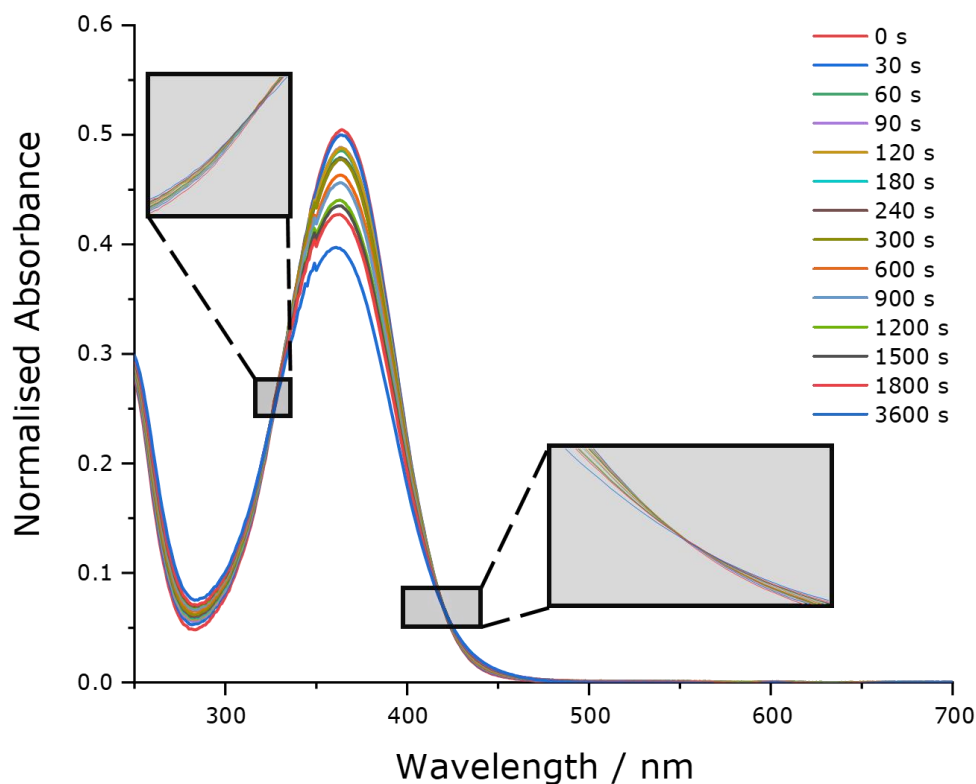
Figure 4.7 | Changes in UV spectral characteristics of BHC-11 in chloroform solution at various time intervals

It is still unclear how Zhang *et al*.[166] irradiated the BHC-n gelators to attain good absorbance peaks featuring two λ_{max} at ~250 and ~365 nm, although it clearly is not in chloroform. Going back to the approach of Balamurugan *et al.*[163], they irradiated the polyesters as thin films; it was then decided to use a spin coater to create thin films of the BHC-n gelators on quartz discs. The thin films must be translucent to ensure reliable absorbances reading less than 1.0. It was not difficult for the BHC-6 to form a translucent thin film; however, BHC-11 could not be formed with the translucency needed for the UV Vis spectrometer measurement. The film was opaque, and very significant light scattering occurred.

BHC-n thin films were irradiated under 254 and 365 nm light at different time intervals. For the BHC-6 gelator irradiated under 254 nm (Figure 4.8a), two λ_{max} were observed at 249 and 350 nm. There is a very gradual decrease of intensity for the two λ_{max} with increasing irradiation time, meaning the decay rate of the BHC-6 photoreactive group is relatively slow under 254 nm irradiation. Although we see decay in the photoreactive groups, the rate is too slow. Therefore, it will require a tremendous amount of energy for supposed photo cross-linking to occur at 254 nm.

On the other hand, the result for the BHC-6 gelator irradiated under 365 nm (Figure 4.8b) shows significant changes in the absorption spectrum. Two absorption bands at 249 and 350 nm are present due to the benzyl rings and the unsaturated enone moiety,

respectively. A noticeable decrease in the intensity of the absorption band at 350 nm was observed during the successive irradiation. The irradiation was carried out for about 1 hour and 20 mins (5060 seconds), where at the mentioned exposure time, the band at 350 nm essentially disappeared, meaning the photoreactive moiety has fully reacted during irradiation. This observation is similar to the reported data of Balamurugan *et al.*,[161,163] which implies that the dimerisation of the olefinic double bond on the BHC-6 occurs *via* [2π-2π] cycloaddition reaction, causing the formation of the cyclobutane ring. This phenomenon is also described in other sources.[154,161,164,168,169] Furthermore, the BHC-6 photoreactive unsaturated enone moiety shows an exponential decrease in intensity during 365 nm irradiation for 5060 seconds until the completion of the photo cross-linking reaction.

On the other hand, no absorption bands appeared at ~ 510 nm, which according to literature,[163] the appearance of absorption bands at that wavelength indicates the occurrence of *trans-* to *cis-* photoisomerisation during the UV irradiation time. As no absorption band emerged at ~ 510 nm during the irradiation of BHC-6 thin-film under 365 nm, no photoisomerisation had occurred.
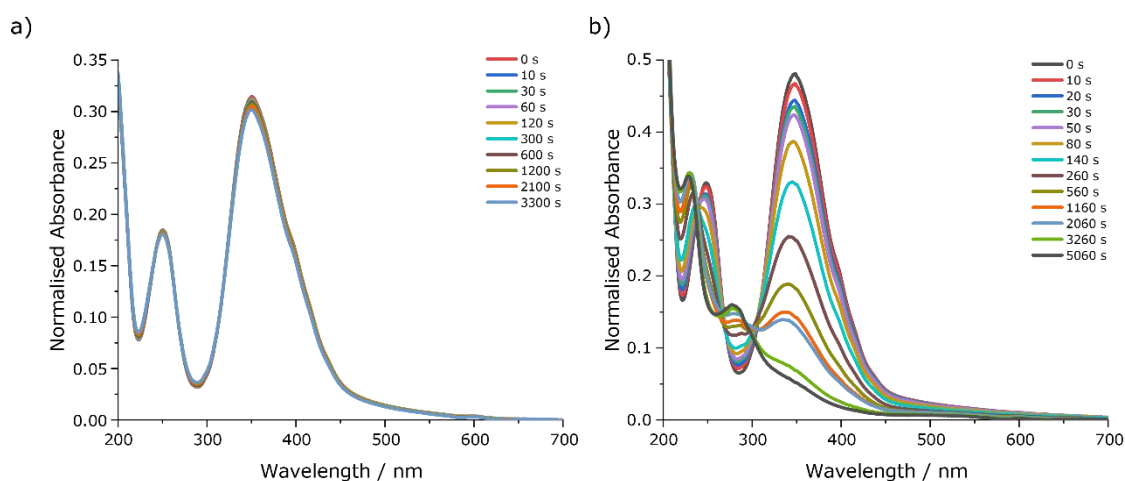
Figure 4.8 | UV-Vis extinction spectra of BHC-6 thin film under a) 254 nm and b) 365 nm irradiation at various time intervals.

a)

b)
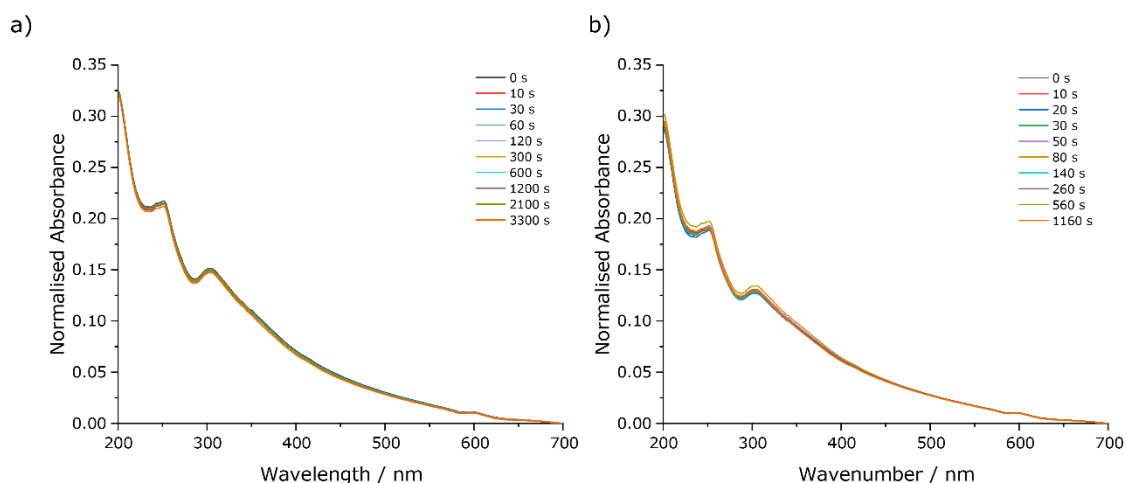
Figure 4.9 | UV-Vis extinction spectra of BHC-11 thin film under a) 254 nm and b) 365 nm irradiation at various time intervals.
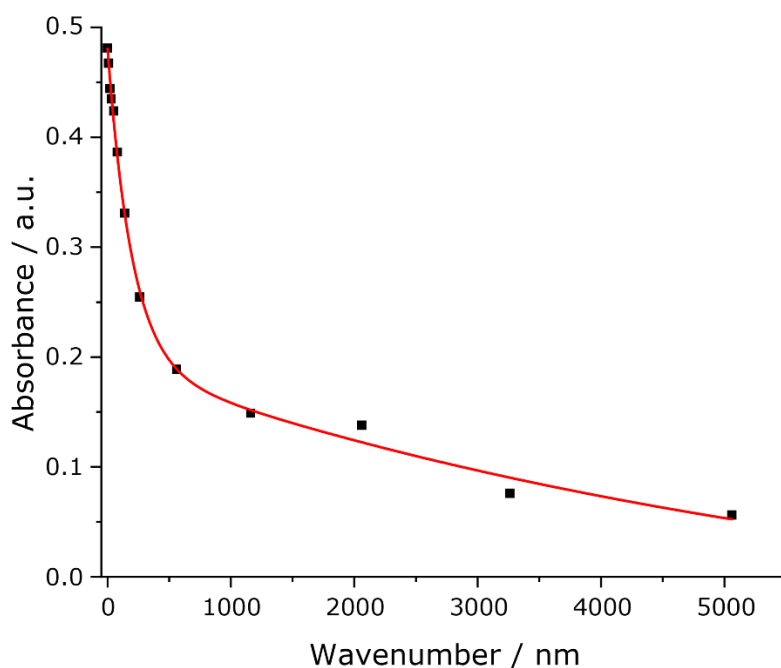
Figure 4.10 | Absorbance of the λ_{max} vs time graph of the UV-vis extinction spectra of BHC-6 thin film under 365 nm irradiation

The spun-cast film of BHC-11 is not translucent; much scattering was seen in the UV-Vis extinction spectra (Figure 4.9). There is a slight decrease in the absorbance peaks with irradiation at 254 and 365 nm over time. Therefore, the rate of photoreaction is slow and requires prolonged 254 and 365 nm irradiation. However, it is crucial to consider that due to scattering, the spectra are not reliable.

To explore the nature of the decrease of the intensity of the peak at λ_{max}, 365 nm, whether it is the effect of photo cross-linking (or similar reaction) or maybe photoisomerisation, the reversibility of the photoreaction that had occurred was tested. Photoisomerisation is usually a reversible reaction as the compound would be expected to return to the most

thermodynamically stable conformation. The first attempt was to see the thermoreversibility of the photoreaction. For this test, BHC-6 thin film was irradiated at 365 nm UV-light to induce and achieve photoreaction. After the photoreaction, the material was heated at 40 °C at different time intervals, where the UV absorption of the material was collected between the time intervals. The collected absorption spectra from irradiating the material at 365 nm and heating the material at 40 °C are displayed in Figure 4.11. The expectation is that the peak at 363 nm would reappear if the reaction were thermoreversible. However, after heating at 40 °C for 180 minutes, there was no indication of the reappearance of the absorption peak. Although there are very slight changes in intensities around that area, no trend outside the error associated with the measurement. Therefore, the photoreaction that the BHC-6 thin-film material undergoes and is reflected in the λ_{max} is not thermoreversible.
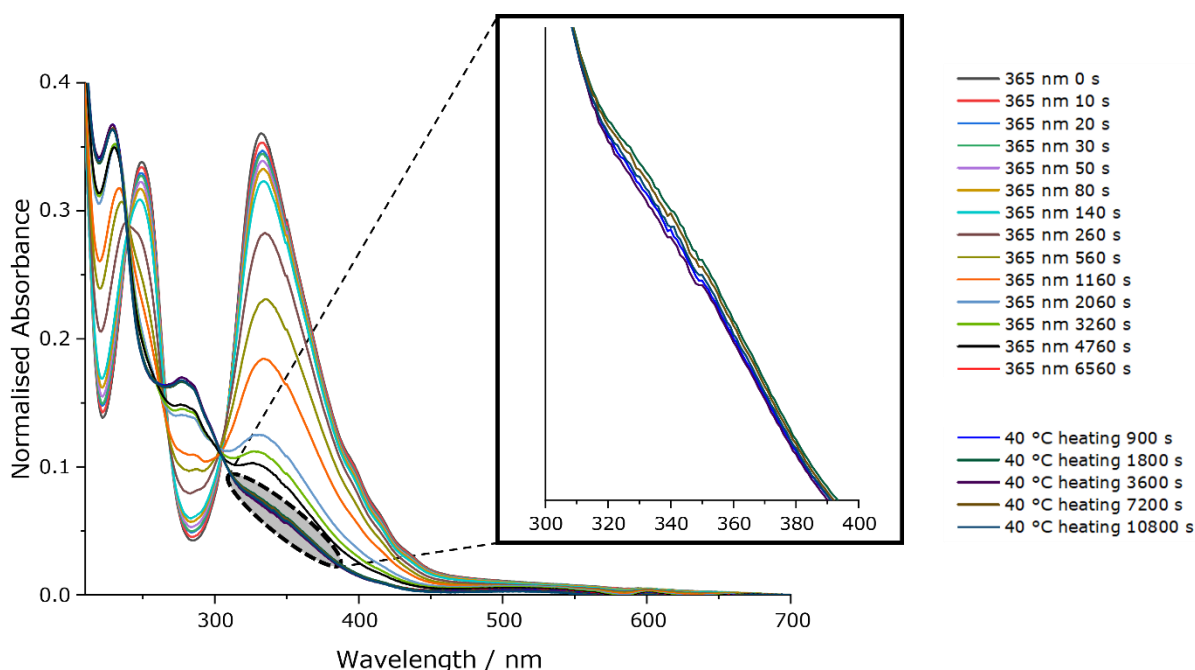
Figure 4.11 | Thermoreversibile test for the BHC-6 thin film after 365 nm irradiation

The second attempt for testing reversibility is by exposing the 365 nm irradiated materials under 277 nm UV light. The wavelength exposure was chosen as it is the λ_{min} between the two λ_{max} absorption peaks at 249 and 350 nm. For this approach, BHC was irradiated at 365 nm UV-light to induce and achieve the photoreaction, followed by irradiating at 277 nm in different time intervals. The UV absorption of the material was collected between the time intervals. The collected absorption spectra from exposing the material at 365 and 277 nm are displayed in Figure 4.12. Like the thermoreversibility test, the expectation is that the peak at 363 nm would reappear if the reaction were reversible after 277 nm irradiation. However, there was again no reappearance of the absorption peak. Slight intensity changes were seen, but again, no obvious trend is seen and therefore, it

can be concluded that the photoreaction that occurred in BHC-6 is not reversible *via* inverse irradiation. The reversibility tests that were carried out strongly suggest that the photoreaction characterised by the disappearance of λ_{max} in the BHC-6 gelator is a result of a change in the bonding in the covalent backbone of the gelator, hence, photo cross-linking.
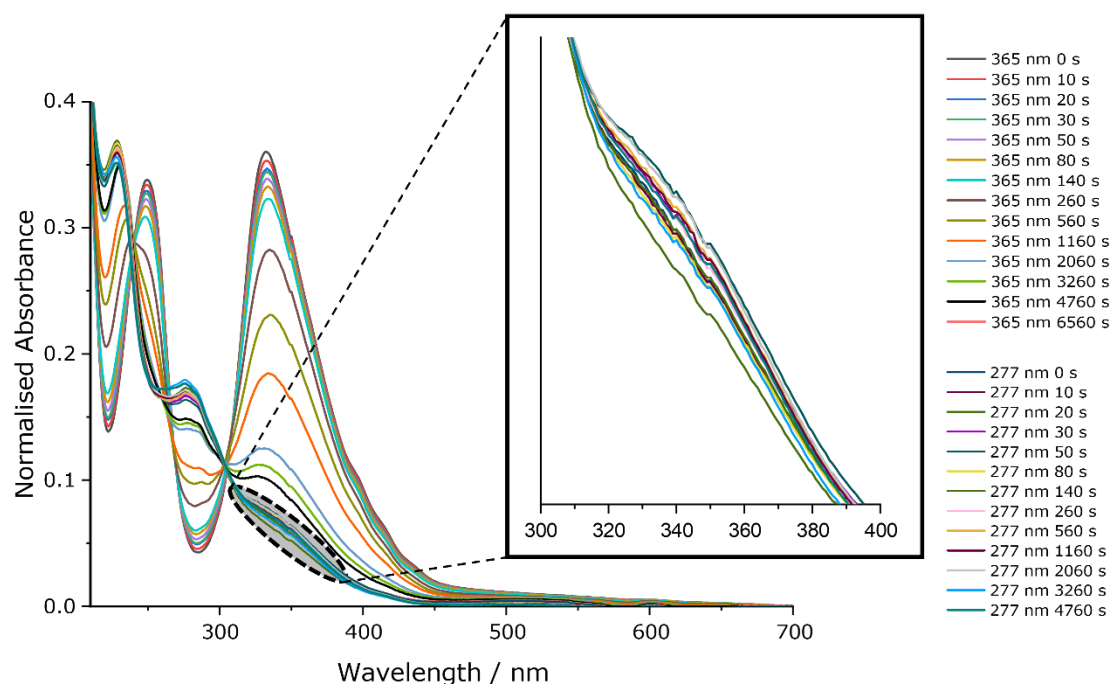
Figure 4.12 | Reversibility test of BHC-6 thin-film *via* inverse irradiation after 365 nm irradiation

To investigate how BHC-n gelators will behave in the printed materials, we tried to make a thin film of the actual C_n blend and copolymer materials printed using extrusion melt 3D printing. The printed sample was placed on a petri dish where it was heated until semi-melted for the Cn blend and copolymer thin film preparation. The quartz disc was dipped into the semi-melted sample, and when it had cooled down, the material was stretched to form a translucent thin film. Regrettably, the thin film closest to translucent, shown in Figure 4.13, is still too concentrated - reading absorbance values up to 2.0. The spectra are not given here as they are not accurate and reliable. This problem was not resolved – even after several attempts of creating a really thin film of the materials, it was still too thick.

Figure 4.13 | C_6 blend thinfilm

As seen from the absorbance spectra of the BHC-6 gelator, photodimerisation goes to completion when irradiated at 365 nm. The next plan was to irradiate the printed C_6, and C_{11} printed samples under 254 and 365 nm UV light and investigate the difference in appearance and mechanical properties.

The photoluminescence spectrometer only irradiated a specific area on the thin film; we tried to obtain separate UV lamps to irradiate a broader area on the samples. The highest power UV lamps that we could access were: 9 W 254 nm UV lamp and 36 W (9 W x 4) 365 nm UV lamp.

A 1 cm x 1 cm square was sliced from the printed sample (thickness of 0.7 mm). It was ensured that all samples for irradiation were the same size and thickness to avoid any anomaly. The pigment of the printed samples seems to be the same before and after 3 hours of irradiation under 254 nm (Table 4.1). This result was expected because, according to the UV-Vis spectra of BHC-6 under 254 nm irradiation, the photoreaction is relatively slow.

Table 4.1 | Differences of the samples' pigment before and after 3h of 254 nm irradiation

SPU/Gelator	Before irradiation	After 3h irradiation
Copolymer C_{11}		
Copolymer C_6		
Blend C_{11}		
Blend C_6		

On the other hand, irradiating the materials under 365 nm for 3 hours, colour change was observed on the appearance of the materials (Table 4.2). The yellow pigment of the materials became darker with an orange tint. This observation means that the photoreactive group underwent a reaction during irradiation, which again was anticipated from the absorption spectra of the gelator on its own.

Table 4.2 | Differences of the samples' pigment before and after 3h of 365 nm irradiation. The samples were sliced and were investigated for IR.

Printed Material	Before irradiation	After 3h Irradiation
Copolymer C_{11}		
Copolymer C_6		
Blend C_{11}		
Blend C_6		

4.2.2. Infrared Spectroscopy

BHC-n gelators in their solid-state (powder) were irradiated under 254 and 365 nm UV light at different time intervals. The FTIR spectra of the BHC-n gelators before and after 254 and 365 nm UV irradiation in their solid-state (powder irradiated) were obtained to see the differences in the infrared absorption bands during irradiation (Figure 4.14). For both BHC-6 and BHC-11 irradiated powders, the most significant difference in the spectra is the change of intensity of the absorbance bands at around 1739 and 1361 cm^{-1}, which correlates to the C=O stretch of the carbonyl, and the O-H bend of the hydroxyl group, respectively. Regardless of the wavelength, the intensity of the absorption bands relating to C=O stretch and O-H bend decrease with the increasing irradiation time of BHC-n powders. The peak at around 1090 cm^{-1}, relating to the C-O bend of the primary alcohol, also decreases. The IR spectra show that the mentioned absorption bands disappear when BHC-6 is irradiated for 5 hours under 365 nm UV. Moreover, there is no apparent increase in the intensity of any vibration bands. In contrast, the same absorption bands did not disappear but had only decreased in intensity when BHC-11 is irradiated with the same conditions due to kinetic effects. The only explanation of the decrease of C=O stretch that comes to mind is that a photo process occurs during the irradiation of the BHC-n materials. There are photo processes of ketones that Albini[170] reported in 2020, however, the actual process that might have occurred in the BHC-n materials is still not identified due to lack of evidence. The phenomenon that happens during irradiation of the powdered gelators would be suitable for future research.

Moreover, if photo cross-linking had occurred, the peaks at around 970 and 730 cm^{-1} (correlated to the alkene peaks) should have disappeared or decreased (Figure 4.15). This was not the case for the BHC-n gelators. In addition to that, the disappearance or the

decrease of the O-H bend and the C-O bend peaks could only mean that the hydroxyl group had reacted, which contradicts with the O-H stretch still being present at around 3296 cm^{-1} (Figure 4.16). This phenomenon indicates that the peak at 1361 cm^{-1} may not be the O-H bend. The other possible functional group at around 1361 cm^{-1} is a C-H methyl rock absorption band, only seen in long chains. If there is a decrease in methyl rock absorption bands, there should also be a decrease in the C-H stretches between 3000 – 2940 cm^{-1}, which, again, is not the case. Apart from the O-H bend and the C-H methyl rock, nothing in mind can correlate to the 1361 cm^{-1} absorption band. There are no coherent explanations of what had occurred during the irradiation of the BHC-n powders.

Unfortunately, it was not feasible to obtain FTIR data for the BHC-n thin films irradiated under UV light. The thin films were prepared on a quartz disc where only a specific area on the thin film was irradiated. With all the attained results and observations, it is challenging to explain what is happening in the BHC-n gelator with FTIR data alone.
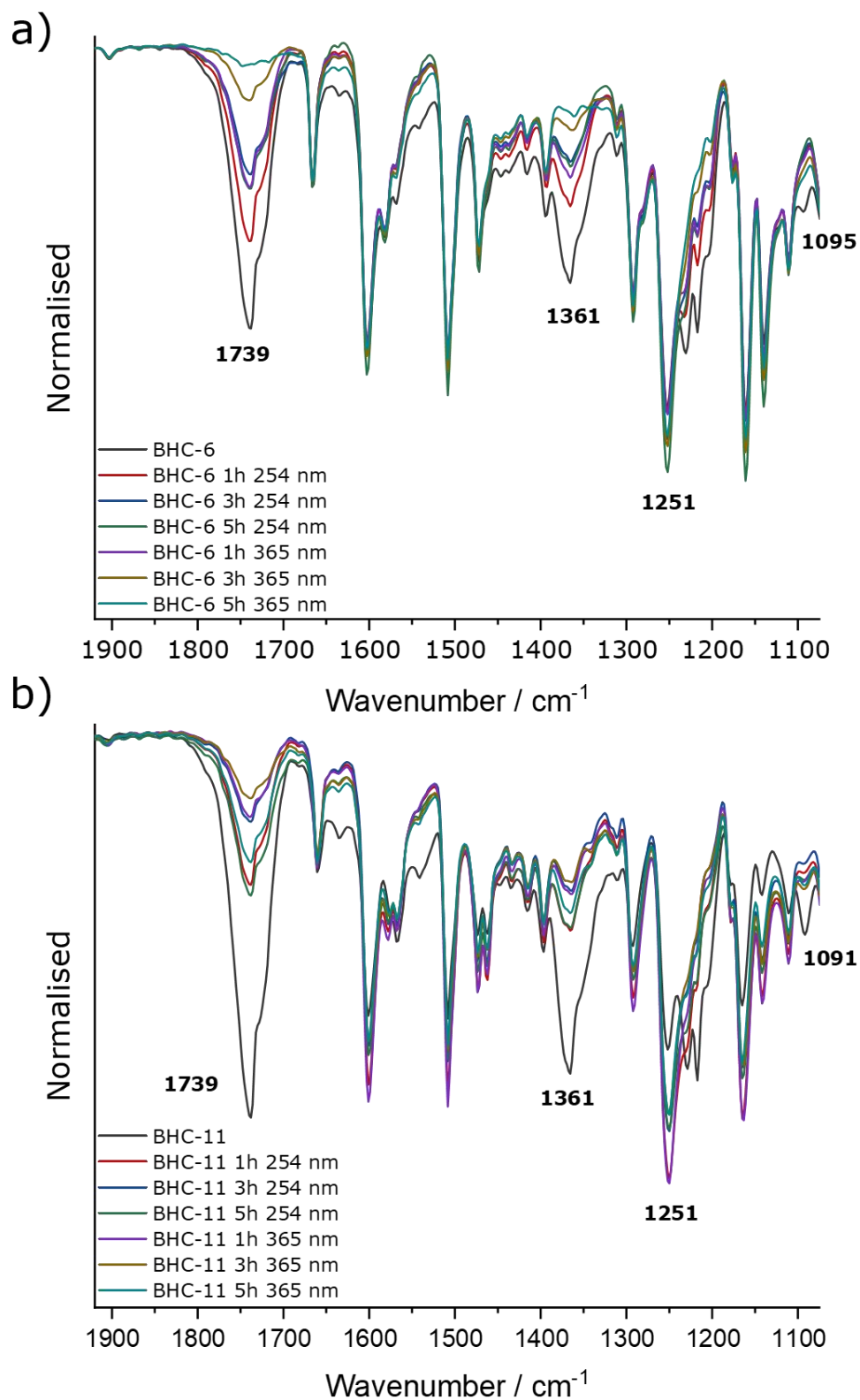
Figure 4.14 | Fingerprint region (1920 – 1075 cm^{-1}) of the FTIR spectra of a) BHC-6 and b) BHC-11 powders, before and after UV irradiation
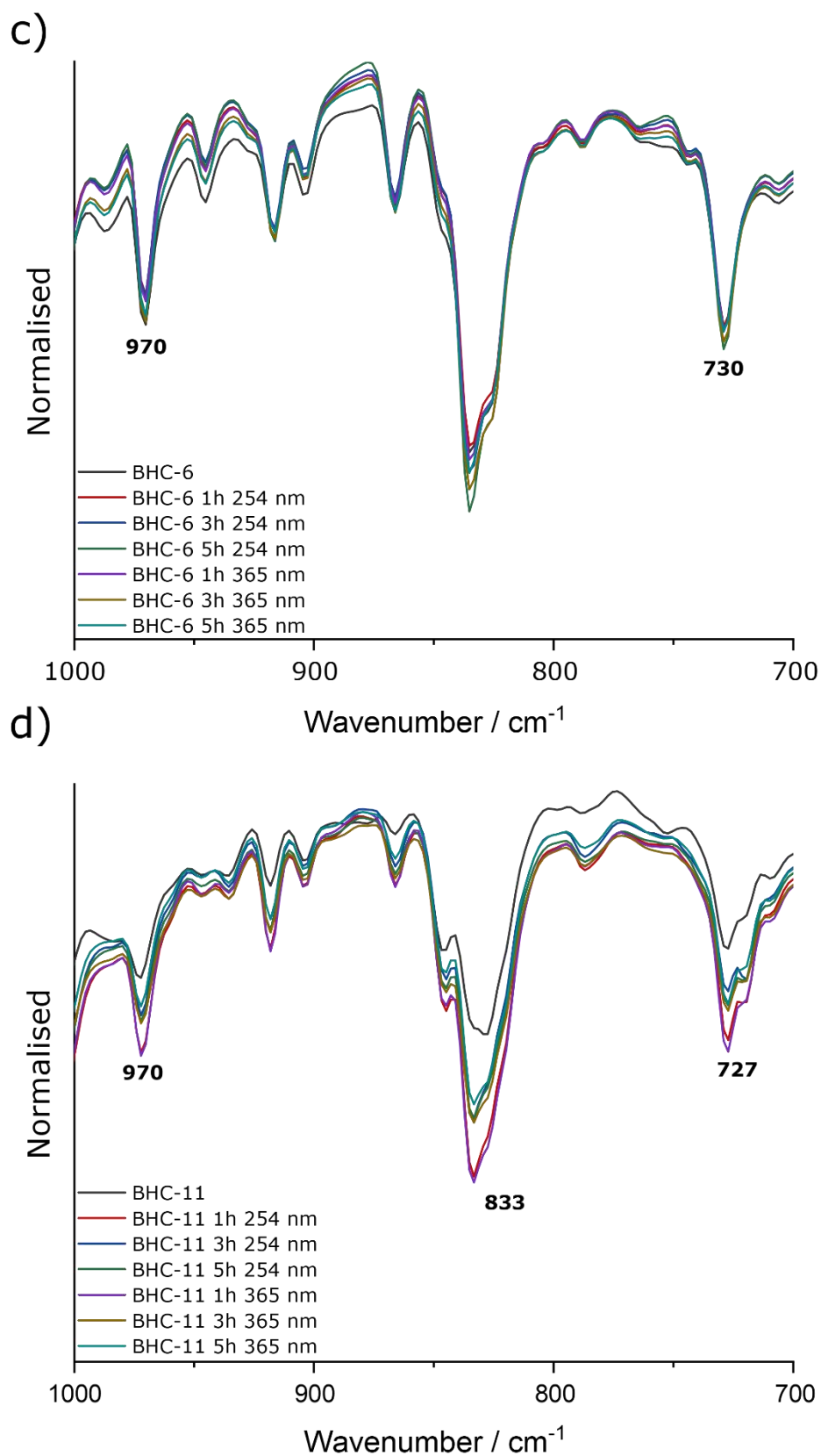
Figure 4.15 | Fingerprint region (1000 – 700 cm^{-1}) of the FTIR spectra of a) BHC-6 and b) BHC-11 powders, before and after UV irradiation
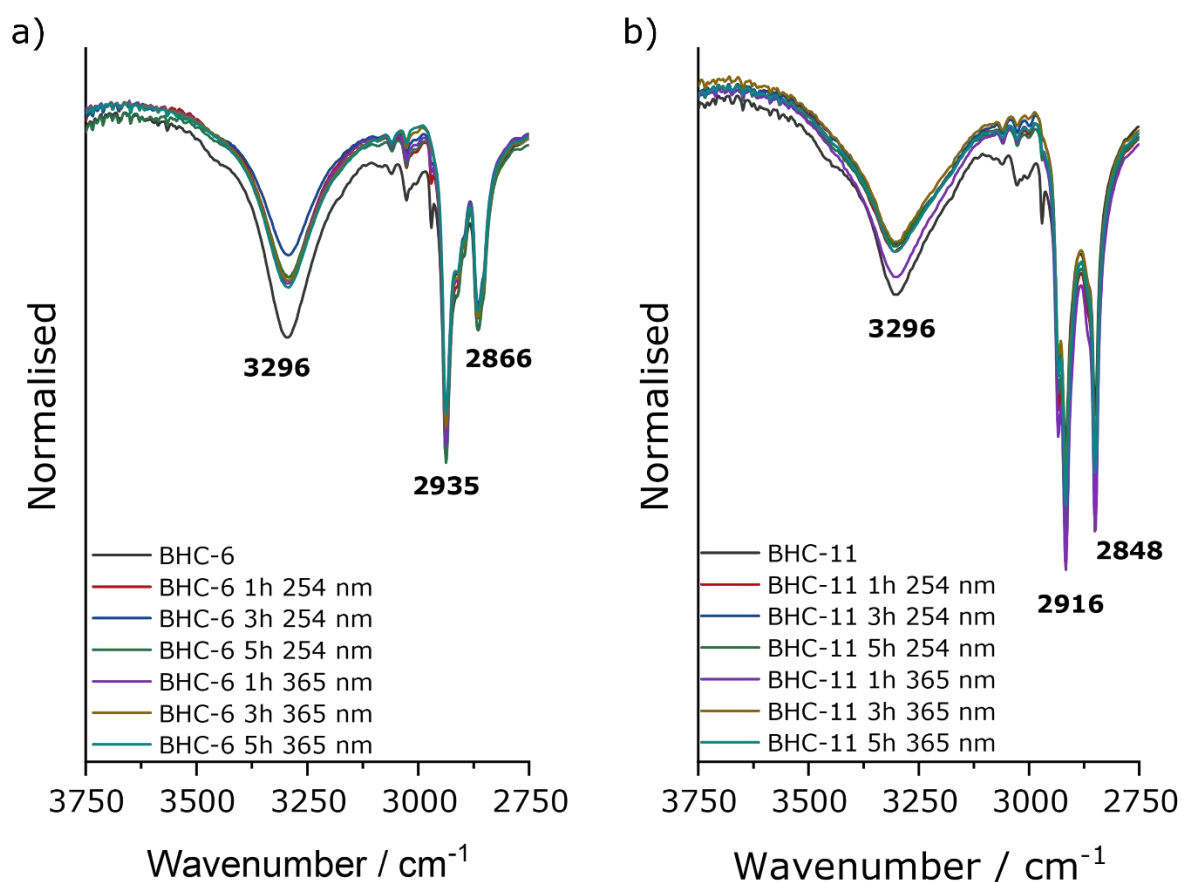
Figure 4.16 | FTIR spectra (3750 – 2750 cm^{-1} region) for a) BHC-6 and b) BHC-11 powders, before and after UV irradiation

The FTIR of the BHC-n materials and the 3D printed materials were overlaid in Figure 4.17 to observe the differences in their absorption bands. Apart from the O-H and the C-H alkane stretches around the 3750 -2750 cm^{-1} wavenumber region, the only distinct peak present in all the individual spectrum is the absorption peak around 1600 cm^{-1}. This absorption band correlates to the C=C stretch on the exocyclic olefin double bond of the gelator. Although there is only 25% of the gelator in the C$_n$ materials, it is strange to see only a few absorption peaks of the BHC-n gelators in the IR spectra of the C$_n$ materials. The peaks that decrease in intensity for the BHC-n powders do not appear in the 3D printed materials.
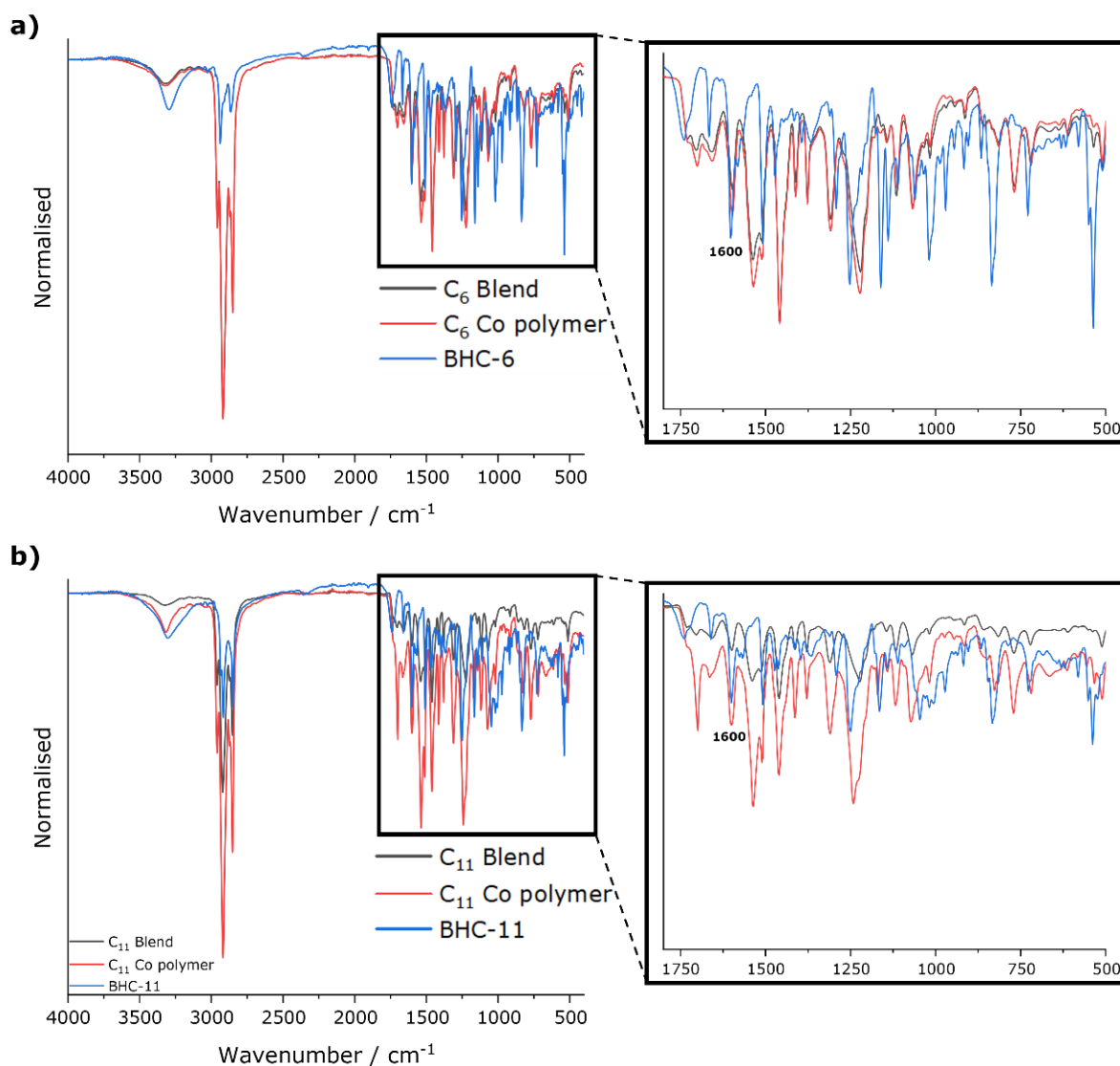
Figure 4.17 | FTIR spectra of a) BHC-6 and C_6 materials and b) BHC-11 and C_{11} materials.

The FTIR data were also obtained for the 3D printed materials before and after 365 nm irradiation to see if infrared absorption bands changed during irradiation (Figure 4.18 and Figure 4.19). The IR absorption peaks at around 1705 cm^{-1} and about 1600 cm^{-1} correspond to the C=O stretch on the cyclohexanone and the C=C stretch on the exocyclic olefin double bond of the gelator, respectively. Only the latter absorption band was seen on the FTIR spectra of the BHC-n gelators. Another relevant IR peak displayed in the spectra is around 817 cm^{-1}, which relates to the C=C bend of a trisubstituted alkene – which again is the exocyclic olefin bond of the gelator. The remaining peaks are mostly correlated to the vibration bend and stretch for the other functional groups on the polymer, *i.e.* ~1540 cm^{-1} for the N-H bend and ~1222 cm^{-1} for the N-C stretch of the amine. It is expected that if photo cross-linking occurs on the gelator molecule in the printed sample,

the IR absorption band peaks at around 1705 and 817 cm^{-1} should disappear. From the obtained data, the IR spectra of the materials before irradiation and after irradiation do not show any significant changes to demonstrate that the photoreaction occurred in the material. The fact that the peak for the C=C stretch on the exocyclic olefin bond ($\sim$1705 and 817 cm^{-1}) did not decrease in intensity (except for the C$_{11}$ copolymer) nor disappear in the IR spectrum after irradiation may mean that the cross-linking may not have occurred when the BHC-n gelator is incorporated into the polymer *via* blend or covalently bonded. In addition to that, the C=C bending of a *trans*- disubstituted alkene has an absorption peak generally between 980 – 960 cm^{-1} which is not present in any of the IR spectra. Furthermore, the C=O stretch absorption bands on all the spectra did not show the same outcome as the IR spectra for the BHC-n gelators. The absorption peaks correlating to the C=O stretch (1705 cm^{-1}) did not disappear. This phenomenon could mean that even photoisomerisation also did not happen in the printed composite materials. However, three factors must be considered:

i)   the gelators on their own react differently from the composite 3D printed materials

ii)   the accessible UV lamps used to irradiate the printed samples were low in power (9 W and 36 W) in comparison to the UV lamp used to irradiate the BHC-n thin films (60 W). This factor could mean that the rate of photo cross-linking in the printed sample would be slower than photo cross-linking in the BHC-n thin films. Therefore, the IR absorption peaks will not have significant changes as no or slow reaction has occurred.

iii)   the percentage of the gelator in the system is relatively low compared to the rest of the functional group. This factor could mean that the C=C stretch and bend peaks might also relate to the benzene rings on the polymer. Therefore, it is not evident if there is a change of IR absorption peaks (due to photochemical reaction) for the gelator structure.

The FTIR spectra of the C$_6$ blend and C$_6$ copolymer before and after irradiation were also collected and displayed in Figure 4.20a and Figure 4.20b, respectively, to compare the influence of irradiation at the different wavelengths (254 and 365 nm). The relevant absorption peaks are similar to the previous, correlating to the C=O stretch on the cyclohexanone ($\sim$1705 cm^{-1}) and the C=C stret ch and bend on the exocyclic olefin double bond of the gelator ($\sim$1600 and $\sim$814 cm^{-1}, respectively). Unfortunately, just like the previous results, the absorption peaks related to the C=C stretch and C=C bend did not vanish nor show any significant changes in intensity to prove that photo cross-linking has occurred. The relatively low mass percentage of the gelator in the system may be why we do not see significant differences in the absorption peaks. Again, these factors are only assumptions and must be studied in future work.
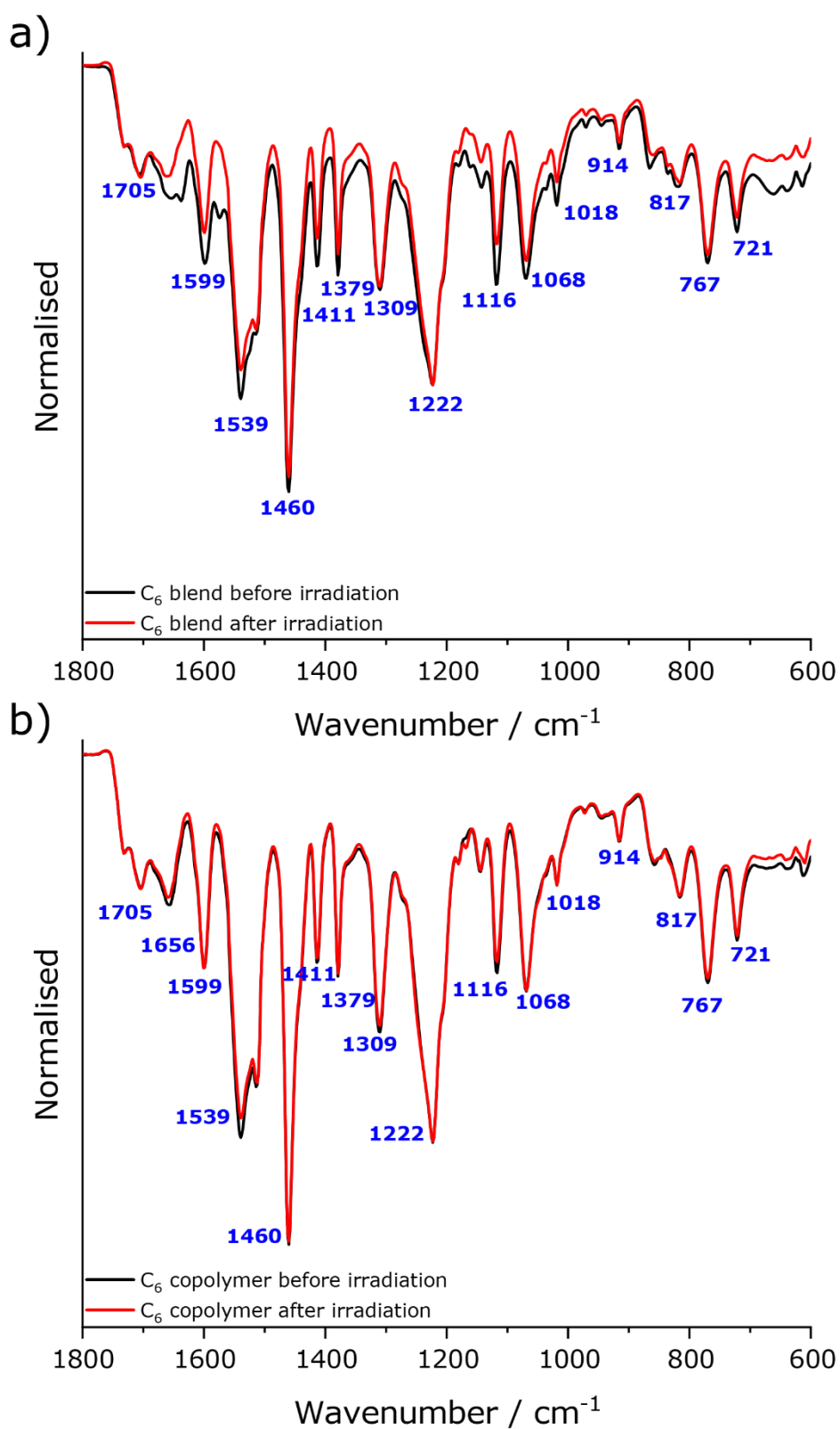
Figure 4.18 | Fingerprint region (1800 – 600 cm^{-1}) of the FTIR spectra of a) C$_6$ blend and b) C$_6$ copolymer, before and after 3 h of 365 nm irradiation
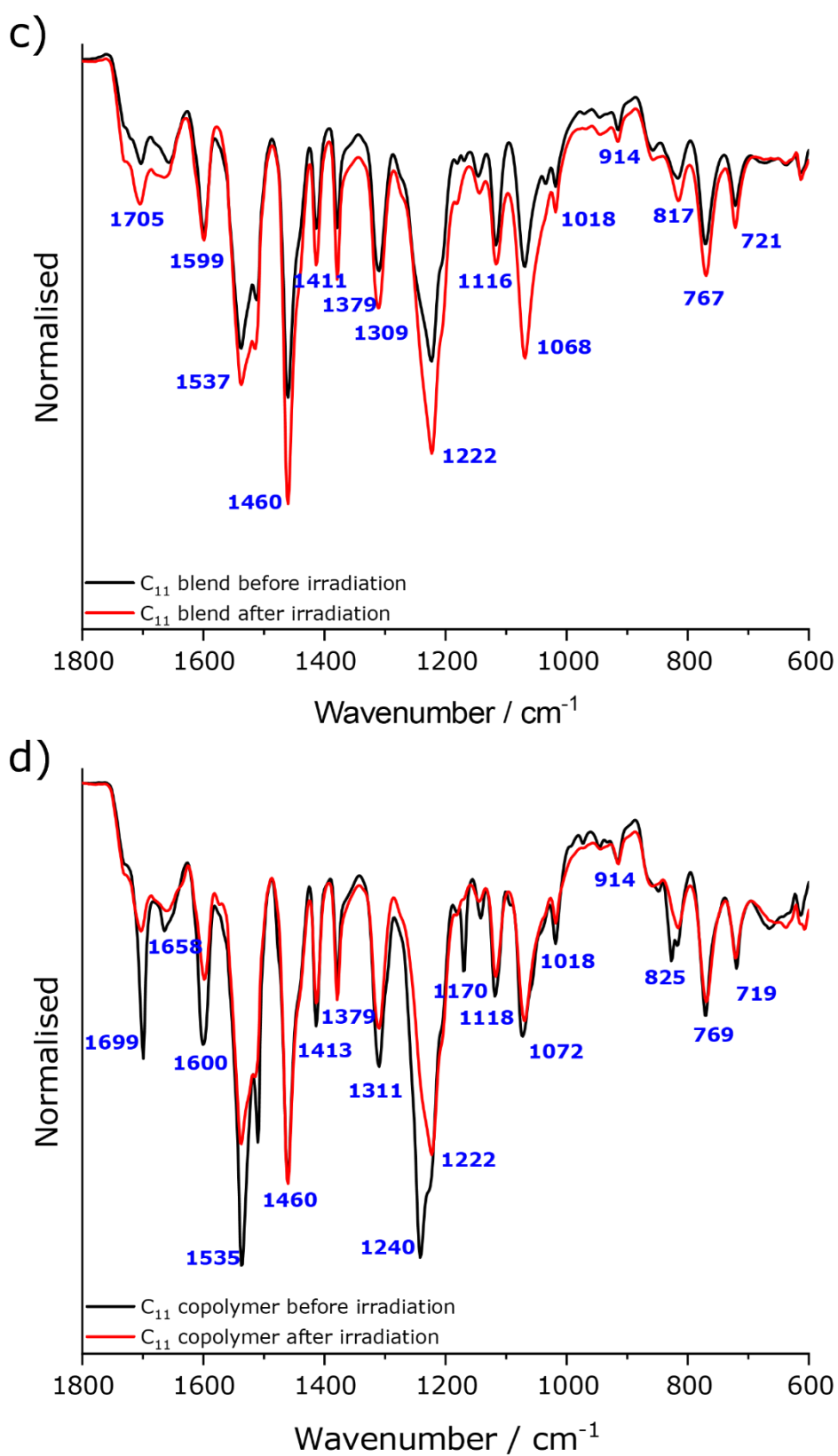
Figure 4.19 | Fingerprint region (1800 – 600 cm^{-1}) of the FTIR spectra of a) C$_{11}$ blend and b) C$_{11}$ copolymer, before and after 3 h 365 nm irradiation

The crystallinity of the printed materials was investigated using X-Ray Diffraction (XRD) to see how well the molecules are packed in the composite material. If the materials have a more ordered packing, it will be easier for photo cross-linking to occur. The XRD data are displayed in Figure 4.21 and Figure 4.22. Broad peaks are observed in all the spectra, one at around 20° 2θ, and around 42° 2θ, which means that the polymer/gelator C_n materials are highly amorphous. From this outcome, it is safe to suggest that photo cross-linking may not have occurred in the materials due to their disordered packing.

Furthermore, three sharp peaks are seen on the C_6 blend with distances of 13.4025, 6.7746 and 3.7313 Å (sharp with high intensity), whereas only one sharp with low-intensity peak is observed for the XRD of C_{11} blend with the distance of 3.8013 Å. The 'blend' composite is prepared by mixing the gelator and the polymer during 3D printing, where no covalent bonds were formed. With this preparation, the sharp peaks on the XRD of the blend composites relate to the molecular packing of the gelator. As the gelator is covalently bonded with the polymer on the C_n copolymer materials, the distinct peaks were not present on the XRD.
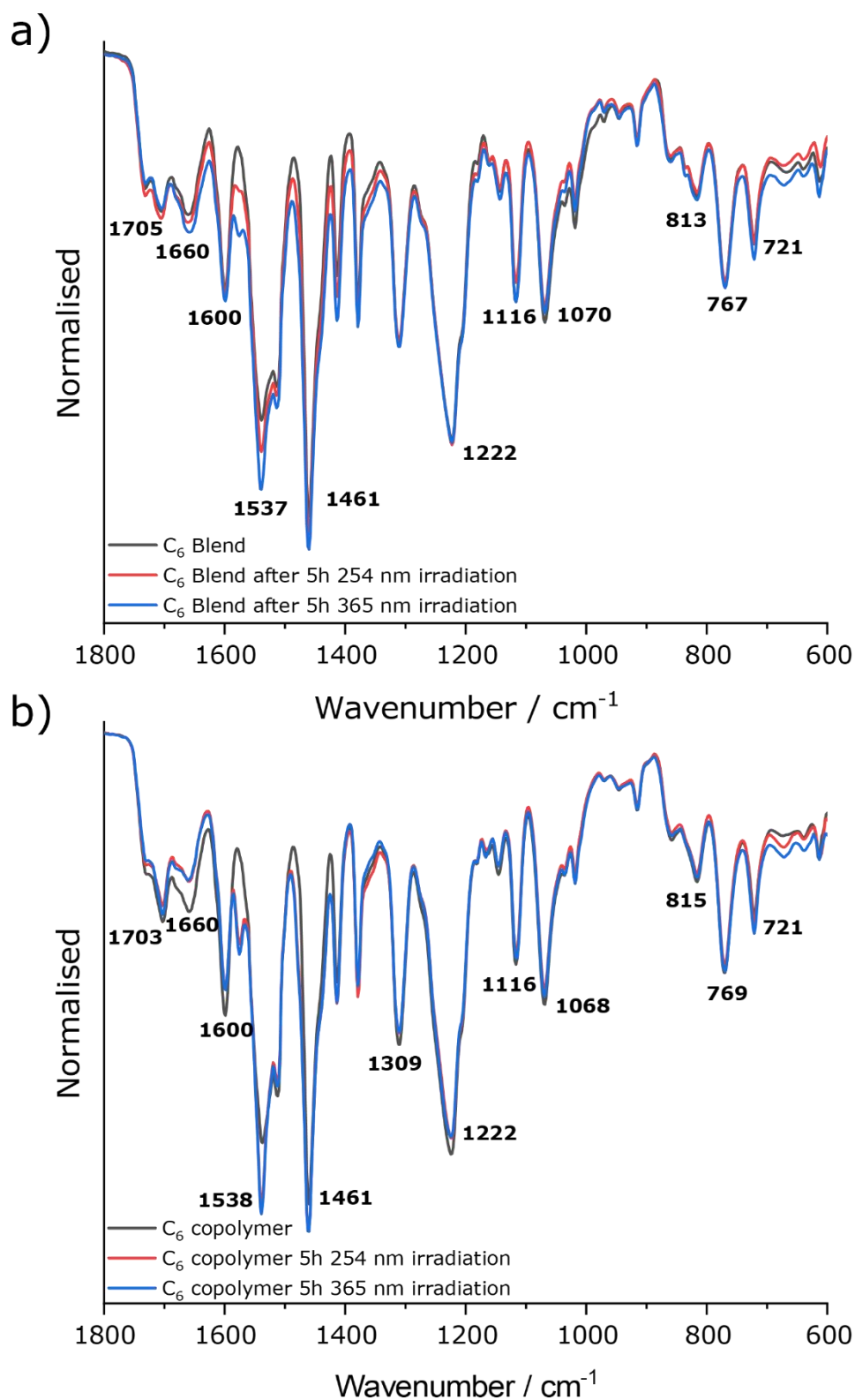
Figure 4.20 | Fingerprint region of the FTIR spectra of a) C_6 blend and b) C_6 copolymer, before and after irradiation
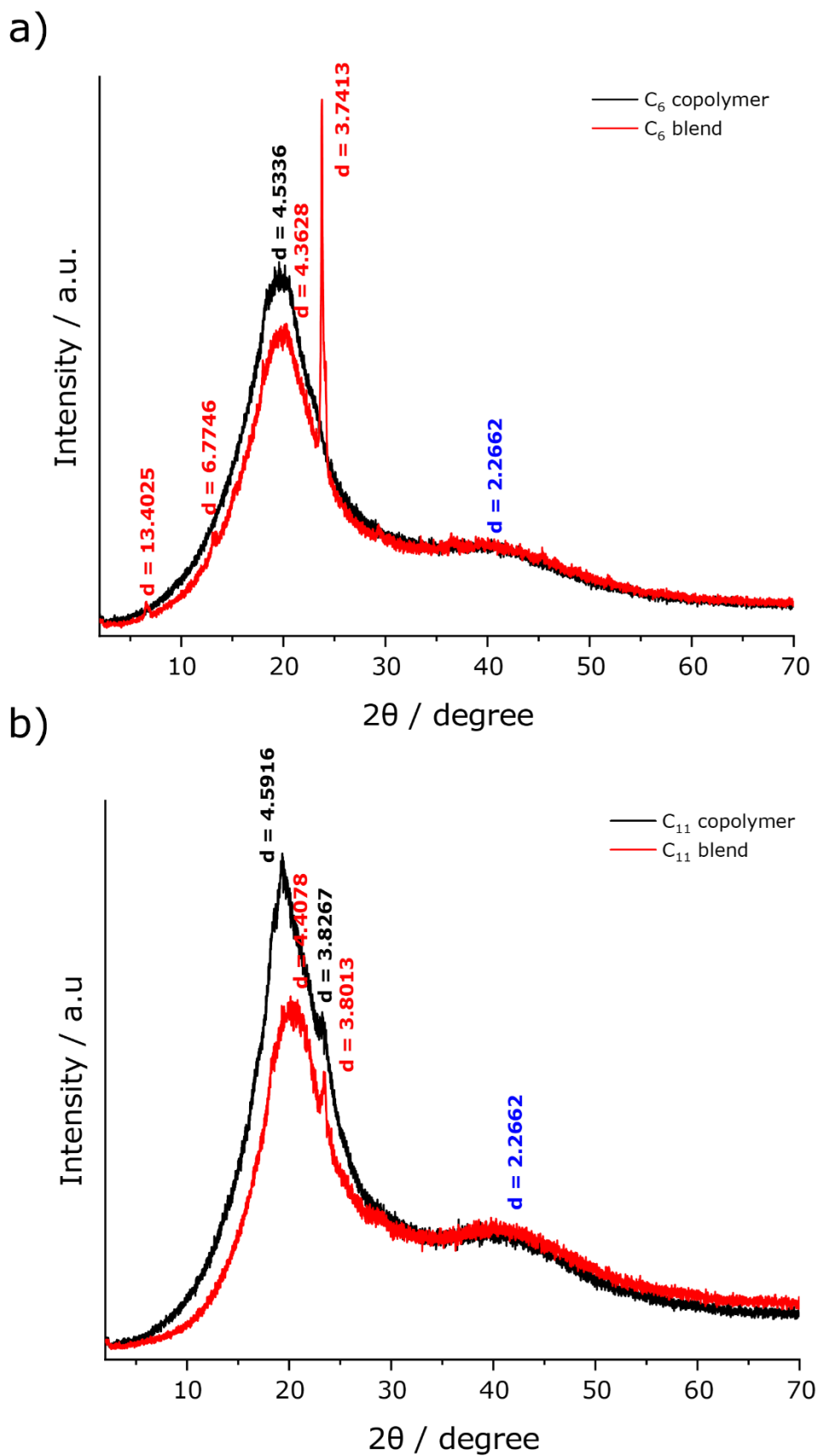
Figure 4.21 | Overlap XRD data of a) C_6 copolymer and blend and b) C_{11} copolymer and blend; distance, d, is calculated in Å
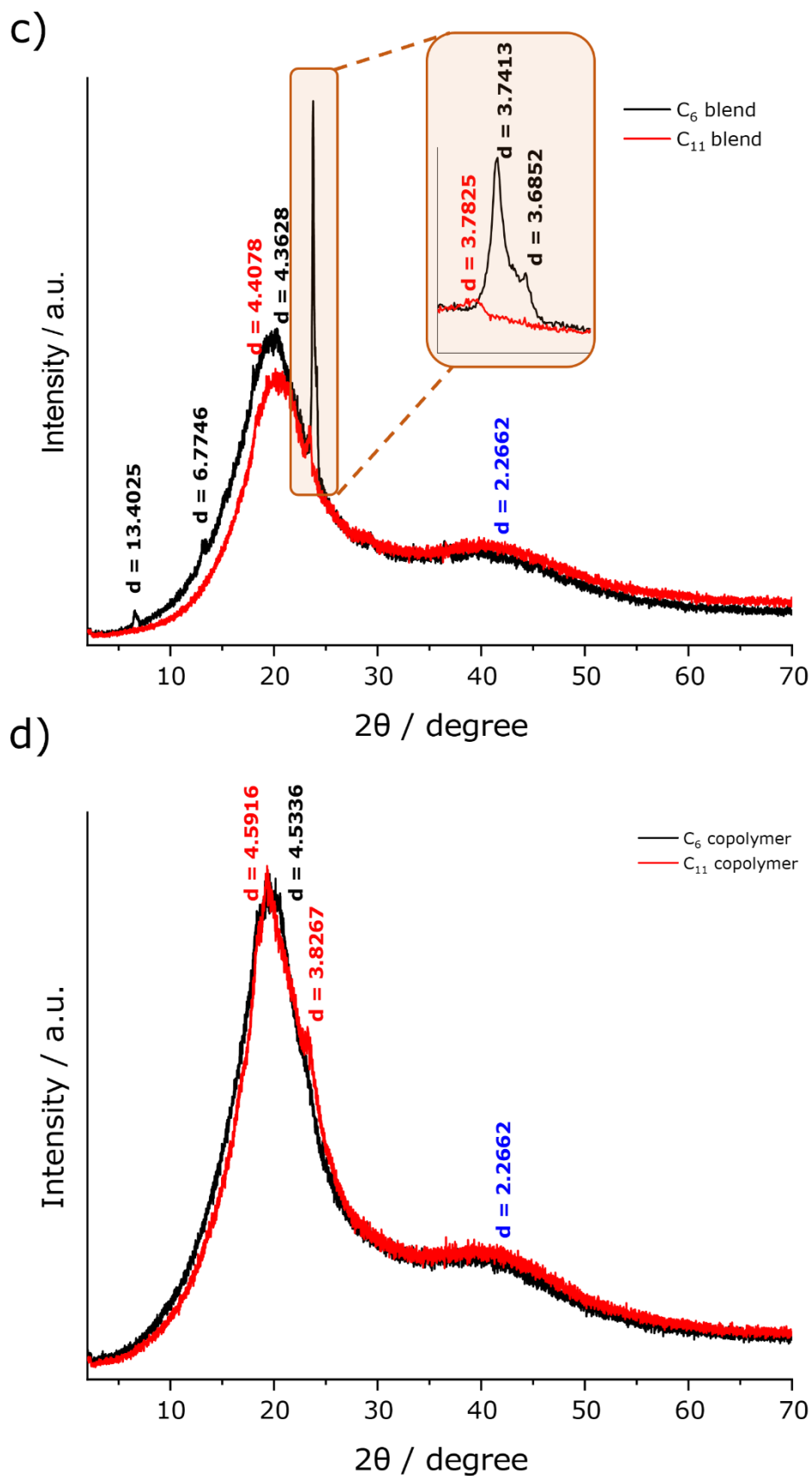
Figure 4.22 | Overlap XRD data of c) C_6 and C_{11} blend and d) C_6 and C_{11} copolymer; distance, d, is calculated in Å

4.2.3. Dynamic mechanical analysis of the C_n materials

Dynamic mechanical analysis (DMA) was conducted to see how the Cn materials' rheological viscoelastic properties change after UV irradiation. The material is subjected to sinusoidal stress or strain *via* oscillation, and the response of the stress or strain is measured. A Perkin Elmer Dynamic Mechanical Analyser DMA 8000 was used for the measurements, using the Isotherm 'tension' programme to analyse the printed materials. The applied strain for the tension test is 0.10 mm with a frequency of 1.0 Hz at 25 °C and was held for 2 minutes. The analysis was done in triplicate (Figure 4.23).
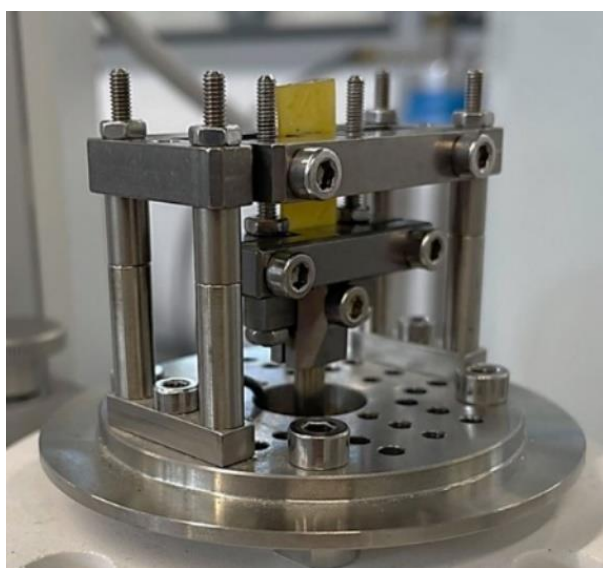
Figure 4.23 | Tension programme for DMA analysis. Material in image: C_6 copolymer

The DMA results show that all the materials have viscoelastic mechanical properties (Figure 4.24, Figure 4.25 and Figure 4.26). The C_{11} blend and C_{11} copolymer appear to have a higher storage and loss modulus than the C_6 blend and C_6 copolymer, meaning that the long chain on the gelator influences the modulus of the material. For the C_6 materials, the copolymer displayed a higher modulus in comparison to the blend. However, the opposite is seen for the C_{11} materials. The possible explanation for this phenomenon is how the self-assembled gelator manipulates the dual-network in the blended material. The hypothesis is that the mechanical property of BHC-11 self-assembled gel is better than the BHC-6. Therefore, incorporating the gelator into the polymer as a blend retained the gelator's mechanical property and formed a robust dual-network material. In addition to that, the C_6 and C_{11} copolymer also have a similar value of storage modulus, meaning that they both have the same amount of stored energy in the structure of the materials. With this result, the addition of a long chain into the actual molecule structure did not improve the mechanical property of the material. This justification is still a hypothesis at present and must be investigated further by perhaps performing additional mechanical analysis on the gels and the printed materials.
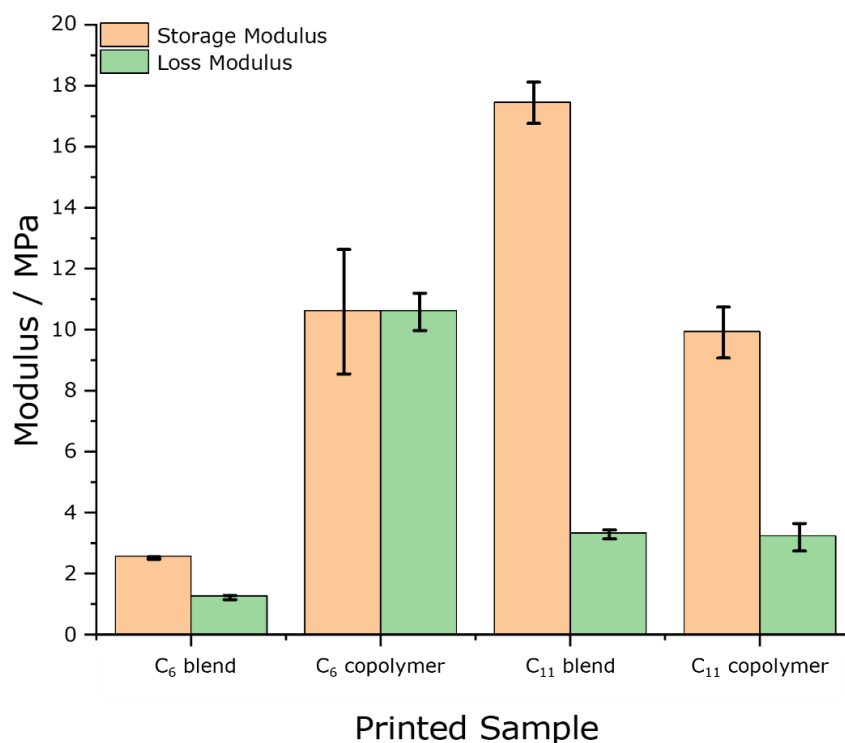
Figure 4.24 | Storage and loss modulus of the printed samples

Further tension tests were carried out for the C_n blend and copolymer materials (Figure 4.25 and Figure 4.26). The expectation is that should photoisomerisation occur in the gelator structures, the modulus of the material will decrease due to the disruption of the layers during conformation transition. On the other hand, if photo cross-linking occurs between the gelator structures in the material, the modulus of the material is anticipated to increase during the [2+2] cycloaddition due to the formation of a cyclobutane ring. Unfortunately, the results were not as expected as there is no trend seen for the obtained DMA data of the C_n materials before and after UV irradiation. The UV-Vis data above shows that irradiating the BHC-6 gelator under 365 nm forms dimerisation in the gelator alone due to photo cross-linking. However, this result is difficult to prove when the gelator is incorporated into the polymer as a blend and covalently bonded since there are no significant changes seen in IR.

The DMA data of the C_6 blend and C_6 copolymer show that the irradiation of the material at 254 nm has increased the storage modulus more significantly than irradiating the material under 365 nm. For the C_{11} blend and C_{11} copolymer, the change in modulus is relatively similar when irradiated in 254 and 365 nm. A reasonable explanation for this observation could be that the materials undergo thermal annealing during irradiation. When the material is being exposed under the UV lamp, the heat from the lamp may have influenced the material's storage modulus, which shows non-trend storage modulus results. Again, this is only a hypothesis that should be investigated in future research with further mechanical analysis.
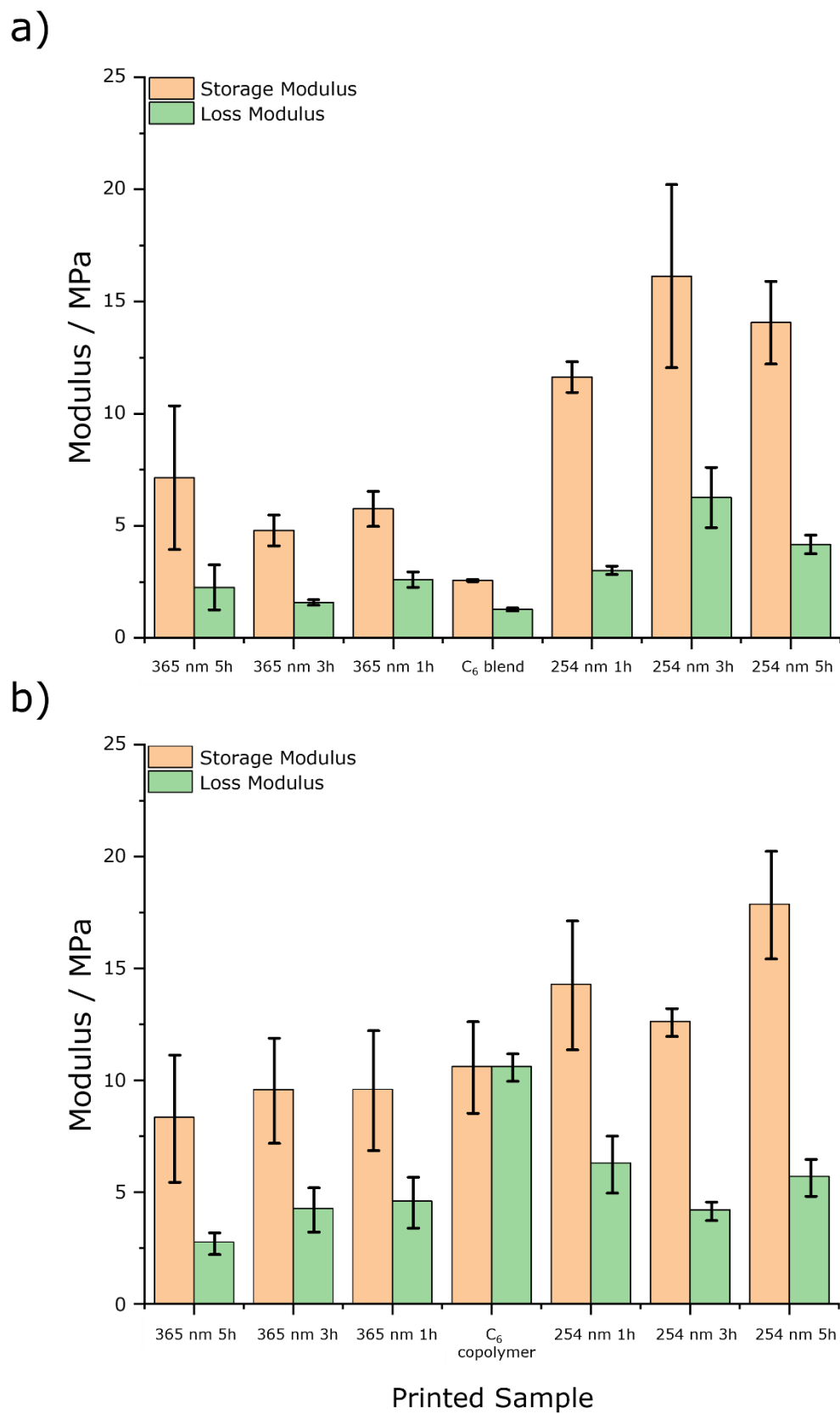
Figure 4.25 | Storage and loss modulus of a) C$_6$ blend materials and b) C$_6$ copolymer materials before irradiation at 365 and 254 nm

a)

b)

Printed Sample
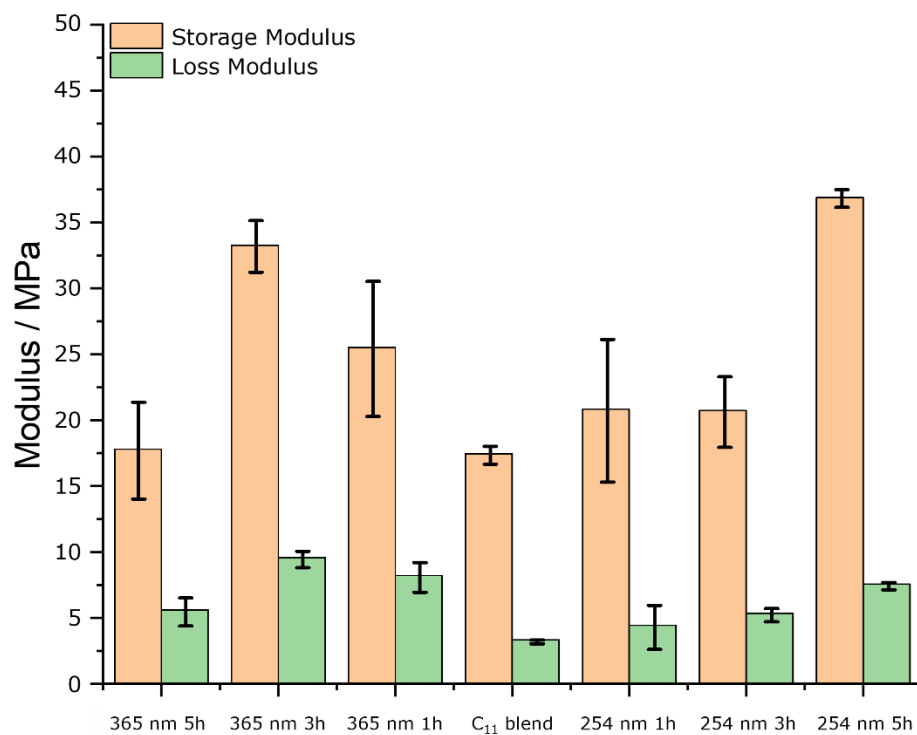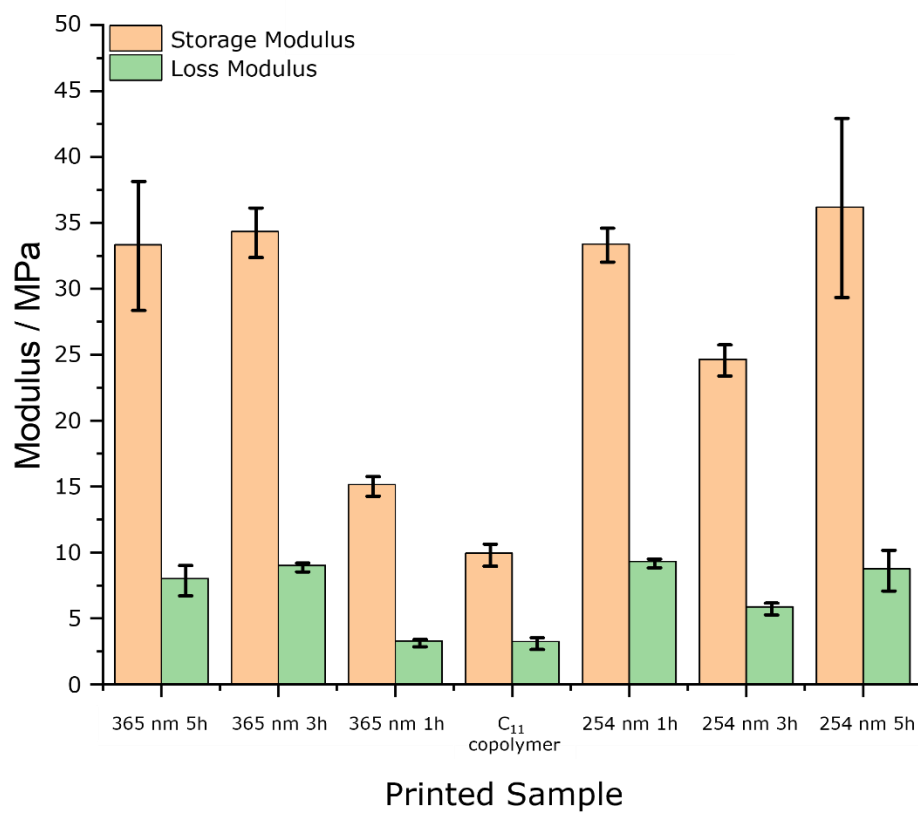
Figure 4.26 | Storage and loss modulus of c) C_{11} blend materials and d) C_{11} copolymer materials before irradiation at 365 and 254 nm

In conclusion, BHC-6 gelator (on its own) as a thin film is found to undergo photo cross-linking when irradiated at 365 nm UV light for 1 hour and 20 minutes. So far, the only evidence that can support this phenomenon is the UV-vis extinction spectral data of the BHC-6 thin film under 365 nm irradiation at various time intervals. The absorption band of the conjugated moiety of the molecule decreases with increasing UV exposure time until it reaches the photostationary state, indicating the completion of the photo cross-linking. Unfortunately, the FTIR data could not be collected on the thin film because only a specific area was irradiated on the quartz disc. These observations are not seen on the 3D printed materials. Furthermore, the FTIR data of the BHC-n powders illustrate a photoreaction happening in the solid-state when irradiated under UV light. However, the photoreaction is not identified due to incoherent and insufficient results to prove the hypothesis.

The XRD data of the printed materials show broad peaks in all the spectra, which means that the polymer/gelator C_n materials are highly amorphous. The lack of crystallinity suggests that photo cross-linking may not have occurred in the 3D printed materials due to their disordered packing. Furthermore, the DMA analysis shows that all the 3D printed materials have viscoelastic properties. The irradiation of the C_6 blend and C_6 copolymer at 254 nm demonstrate an increase in storage modulus more significantly than irradiating at 365 nm. A concluded hypothesis is that the materials undergo thermal annealing during irradiation that may have influenced the materials' storage modulus. With the difficulty of explaining the results from the IR, and the hypothesis about thermal annealing, it would be a good subject of interest in future research to investigate what photoreaction is taking place in gelators and the materials during irradiation and possibly find potential applications.

CHAPTER FIVE

Dual-Network Materials

5.1 Introduction of Dual-Network Materials

There is an increase of interest in the study of incorporating low molecular weight gelators (LMWGs) with polymers to form dual-network materials. LMWG-polymer combinations enhance the resulting composite material performance (e.g. mechanical properties), which would be useful for traditional mechanical applications and advanced areas, including drug delivery and tissue engineering.[171] There are five categories that the LMWG-polymer systems are divided into:

(a) **the polymerisation of LMWG fibres** – *via* polymerisable groups in gelator molecules;

(b) **the capture of LMWG fibres in a polymer matrix** – fluid monomer phase polymerised around the self-assembled network;

(c) **addition of non-gelling polymer to LMWG gel** – can directly or indirectly influence LMWG network (no polymerisation occurs);

(d) **directed interactions between LMWG and polymer** – *via* a recognition motif of controlled supramolecular interactions; and

(e) **hybrid gel combining LMWG and PG networks** – multi-component system utilising properties of both networks.[171]

The research presented here focuses on the second category of the LMWG-polymer system, where the 3D LMWG network is incorporated into a polymerisable solvent followed by polymerisation. In 1996, Gankema *et al*.[172] reported the first gelation of two low molecular weight compounds where one is crystallisable (LMWG), and the other is curable (monomer solvent). The self-assembled LMWG network remains inside a polymer matrix when the monomer solvent is cured into a semi-interpenetrating polymer network (semi-IPN). The LMWG was removed from the resin by leaching or sublimation to give nano/microporous membranes (Figure 5.1). Their team then functionalised the porous membrane by charging the pore walls with anionic sites. The advantages of incorporating the LMWG fibres in the polymer matrix becomes vital because of the easy functionalisation of the material. One of the objectives of this thesis is to form gelator-polymer composites and characterise them for different possible applications.
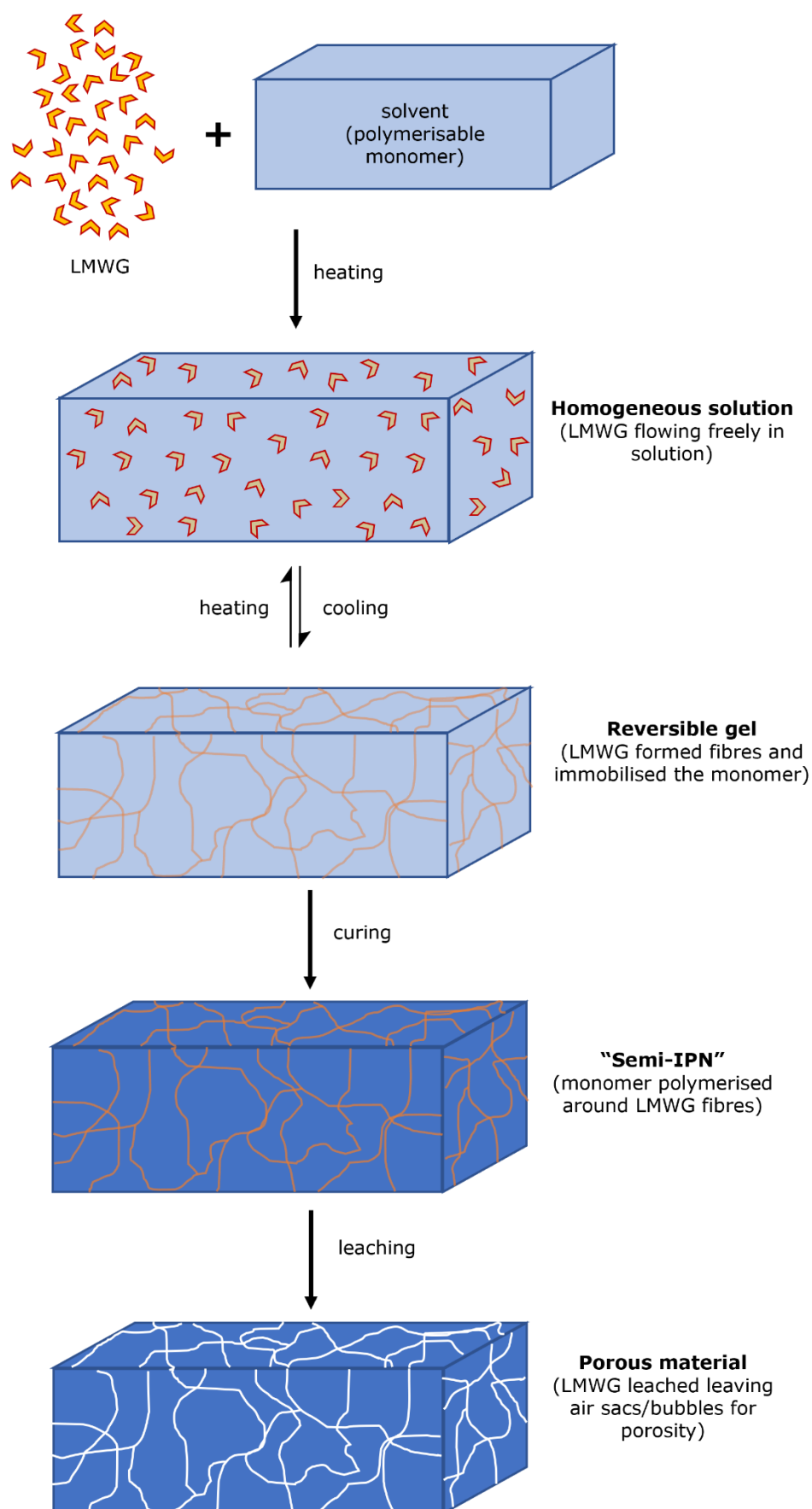
Figure 5.1 | Formation of porous material from gelation of a LMWG and a polymerisable monomer solvent[172]

5.2 Motivation: Poly(alkyl acrylates) as protein adsorbents

In 2016, Bathawab *et al.*[173] studied the translation of polymer mobility into interfacial mobility of extracellular matrix proteins that are absorbed on the material surface, which affects cell response. They reported that the ability of the cells to reorganise the protein layer is improved on the more mobile surfaces. The work utilised a family of poly(alkyl acrylates) with similar chemistry (Figure 5.2) but different degrees of mobility combined with fluorescent fibronectin. Phase imaging using atomic force microscopy (AFM) supported that poly(ethyl acrylate) (PEA), poly(butyl acrylate) (PBA), and poly(hexyl acrylate) (PHA) has formed surfaces with fibrillar protein networks. In contrast, poly(methyl acrylate) (PMA) formed globular aggregates.
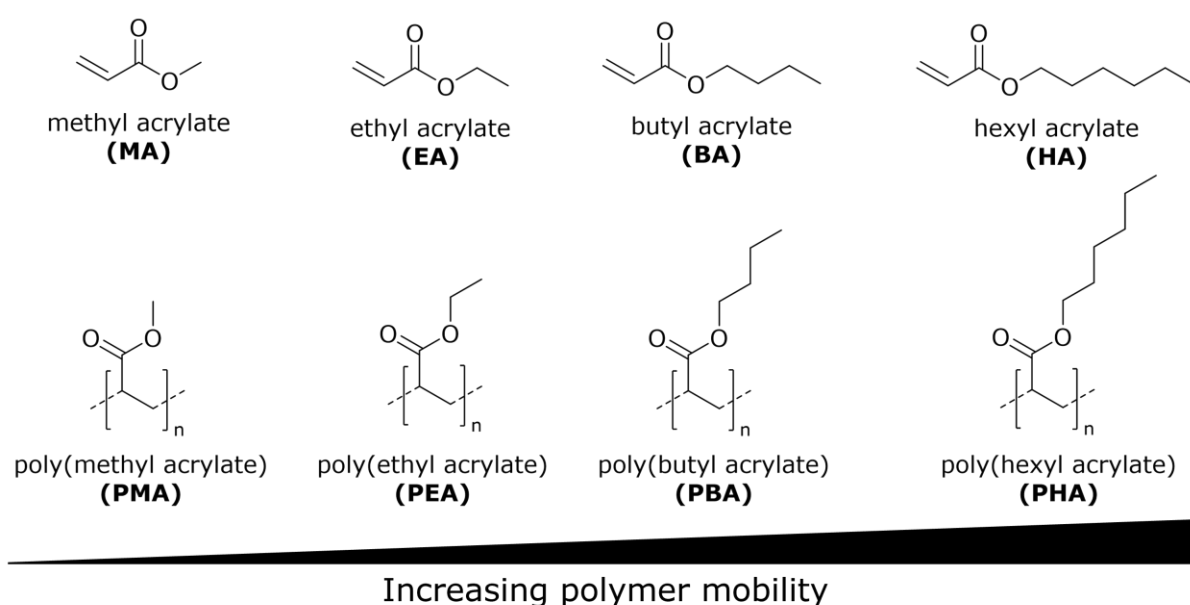
Figure 5.2 | Poly(alkyl acrylates) used for the study of Bathawab et al.[173]

PEA, PBA and PHA all demonstrated the formation of fibrillar protein networks; the micrographs of the polymer surfaces with coated fibronectin (FN) using atomic force microscopy show the difference in the fractal dimension of their network connectivity. PEA demonstrates the highest fractal dimension offering the best network connectivity compared to PBA and PHA.[173] In this research, the curiosity of gelation properties in ethyl acrylate has grown due to having the best fractal dimension. It is also used to produce different types of materials such as resin, dentures, and artificial nail products.

The work presented here aims to investigate the gelation abilities of some of the sugar gelators prepared in this work for the various alkyl monomers and eventually to study the effects of the dual network on the material's interaction with proteins.

5.3 Gelators in Poly(alkyl acrylates)

Five of the compounds from chapters two and three that have displayed gelation are selected for their gelation properties in ethyl acrylate (Figure 5.3). For gelation tests, 10 mg of the gelator and 1 mL of the monomer were transferred into a vial. The mixture was heated until all the solid had dissolved. The solution was allowed to stand and cool to room temperature, ready for gelation observations.
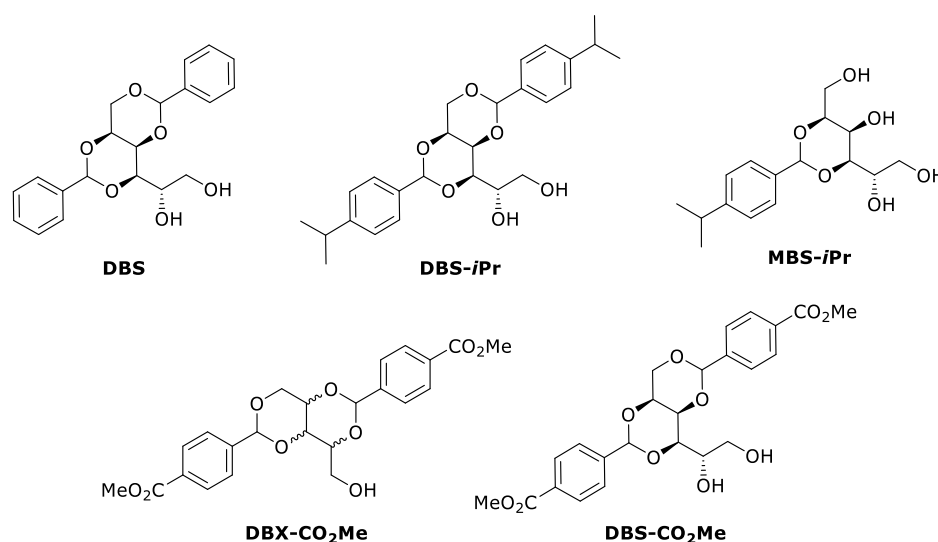
Figure 5.3 | Previously identified gelators (chapters 2 and 3) that were tested for gelation in ethyl acrylate

DBS and DBS-*i*Pr, demonstrate good gelation properties of gelling all the three alkyl monomers tested (Table 5.1). Both DBS and DBS-*i*Pr formed transparent gel at 10 mg mL^{-1} in concentration. On the other hand, the results show that MBS-*i*Pr only formed precipitate in all the tested alkyl monomers. The gelators with the most rigid benzylidene substituent, DBX-CO$_2$Me and DBS-CO$_2$Me, only formed partial gels as the developed fibres could not hold and immobilise the monomers. Both gelators' solubility was poor with the alkyl monomers as not all solid was dissolved even at the monomers boiling point.

Table 5.1 | Gelation test of 1 % w/v compounds in various alkyl monomers upon heating and cooling. I = insoluble, G = gel, PG = partial gel, S = solution, P = precipitate, (T) = transparent, (O) = opaque.

	DBX-CO₂Me*	DBS-CO₂Me*	DBS	DBS-*i*Pr	MBS-*i*Pr
MA	PG	PG	G (T)	G (T)	P
EA	PG	PG	G (T)	G (T)	P
BA	P	PG	G (T)	G (T)	P
*not all solid dissolved					

The gelation properties of DBS and DBS-*i*Pr in ethyl acrylate at different concentrations were investigated. The organogelator, DBS, displayed good gelation ability gelling ethyl acrylate with concentrations from 7 mg mL^{-1} to 25 mg mL^{-1}. Adding an *iso*propyl substituent at the benzyl ring increases the minimum gelation concentration (MGC). It

only forms a partial gel at 7 mg mL^{-1} and self-supporting gels from 10 mg mL^{-1} (Table 5.2) due to its better solubility in the ethyl acrylate.

Table 5.2 | Phase diagram of DBS-CO$_2$Me, DBS and DBS-iPr in ethyl acrylate upon heating and cooling. I = insoluble, G = gel, PG = partial gel, S = solution, P = precipitate, (T) = transparent, (O) = opaque.

	Concentration / mg mL^{-1}					
	25	**20**	**15**	**10**	**7**	**5**
DBS	G (T)	G (T)	G (T)	G (T)	G (T)	PG
DBS-iPr	G (O)[a]	G (O)[a]	G (O)[b]	G (T)	PG[c]	S

[a]transparent gel to opaque gel overnight
[b]transparent gel to opaque gel after three hours
[c]fibres collapsed overnight – forming a partial gel

All the gels generated by DBS and DBS-iPr in ethyl acrylate were transparent. However, the gel formed from DBS-iPr at 15 mg mL^{-1} of concentration, the opacity increases gradually for the first three hours whilst gels at concentrations 20 and 25 mg mL^{-1}, the opacity increased overnight. Contrarily, all DBS gels remained transparent (Figure 5.4).

Curiously, it was observed that DBS in ethyl acrylate forms a gel by simply shaking the vial that consists of the solid gelator compound and the liquid monomer – no heating and cooling was needed to be applied to the sample (Figure 5.5). This phenomenon is interesting, as not many gelators immobilise a solvent medium just by shaking. Possible applications of this effect include remediation of oil spillage by gelling crude oils to reduce marine pollution.[174,175] The workup during the synthesis of the gelator may have influenced the macrostructure of the solid, which possibly affected the interaction with the monomer when triggered and shaken. The morphology of the DBS powder and the xerogels were examined to explore the possible reasons for this behaviour.
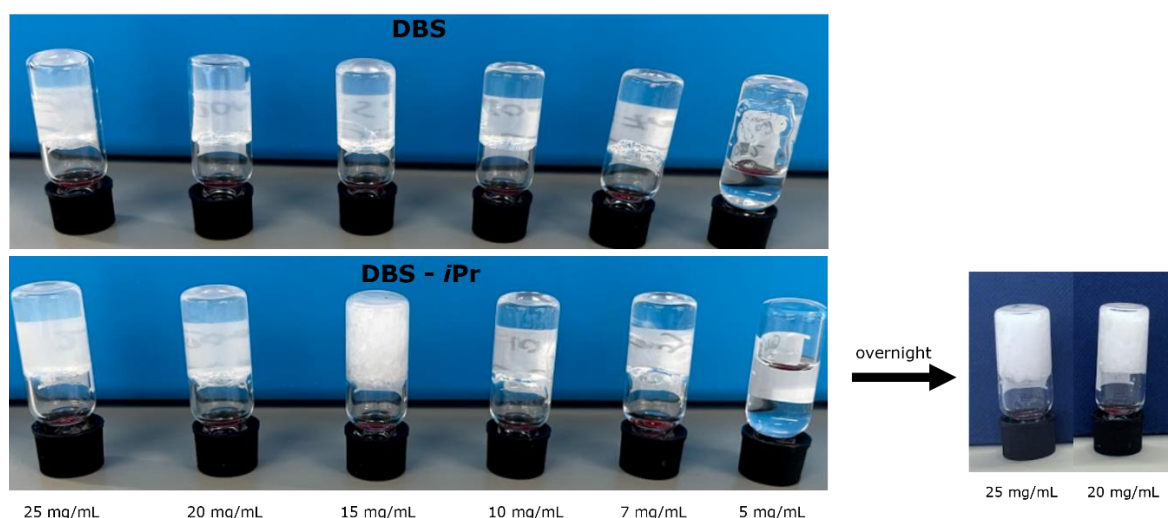
Figure 5.4 | DBS and DBS-iPr gels in ethyl acrylate

| 25 mg/mL | 20 mg/mL | 15 mg/mL | 10 mg/mL | 7 mg/mL |
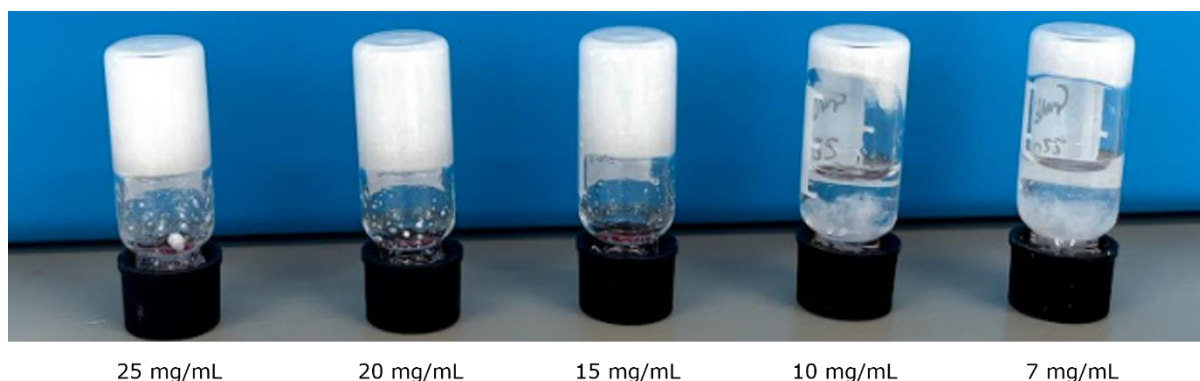
Figure 5.5 | Opaque gels formed from DBS in ethyl acrylate by shaking the vial containing the solid gelator and the liquid monomer

5.3.1 Thixotropic properties of ethyl acrylate gels

As mentioned in the first chapter, thixotropic gels (polymer or LMWGs) have a mechanical property that can be defined as the continuous decrease of viscosity with time when flow or stress is applied to a rested sample and the subsequent recovery of the material's viscosity with time when the flow is discontinued.[103] Thixotropic gels have been used for material extrusion type of 3DP,[110,176–178], and therefore, it would be fascinating to discover if some of these ethyl acrylate gels are thixotropic.

Unfortunately, due to the high vapour pressure of ethyl acrylate, it was not possible to characterise the gel for thixotropic properties using the rheometer. Once the gel is transferred to the rheometer, the evaporation of ethyl acrylate occurs quickly, which means that the results will not be accurate and consistent as the concentration will change due to fluid loss. Therefore, the thixotropic test was done qualitatively where stress was applied to the gel *via* vial shaking, stimulating gel disruption. After gel disruption, the vial was left standing for 30 seconds – allowing the gel to "heal" – before doing the inversion test.

Table 5.3 | DBS and DBS-*i*Pr thixotropy table

	Concentration / mg mL^{-1}					
	25	**20**	**15**	**10**	**7**	**5**
DBS	✔	✔	✔	✔	✔	X
DBS-*i*Pr	✔	✔	X	X	X	X

All the DBS gels in ethyl acrylate with different concentrations show "self-healing" properties (Table 5.3). It is noticeable that during gel disruption of the DBS gel in 25 mg mL^{-1}, the solvent is still immobilised by the gelator's 3D network as no fluid was seen flowing inside the vial (Figure 5.6). Instead, the gel was broken into smaller gel pieces. When the vial was left standing for 30 seconds, the small broken gel pieces were set at the bottom of the vial. After the 30 seconds rest, it again forms interaction between

the molecules, developing a gel similar to the material before the disruption. The ethyl acrylate flowing inside the vial during gel disruption increases as the concentration of the gel decreases; however, even with more ethyl acrylate flowing, the material still manages to form a fibrous 3D network and can therefore be concluded as thixotropic.

The thixotropic observation is similar to the DBS-iPr gels formed at 25 and 20 mg mL^{-1} (Figure 5.7). For the DBS-iPr gel in 15 mg mL^{-1}, ethyl acrylate was seen to be opaque and free-flowing inside the vial. No gels were formed after the 30-second rest of the vial. The resting time was increased to 1 minute then 5 minutes to see if it was just slower at healing, but no gels were formed.
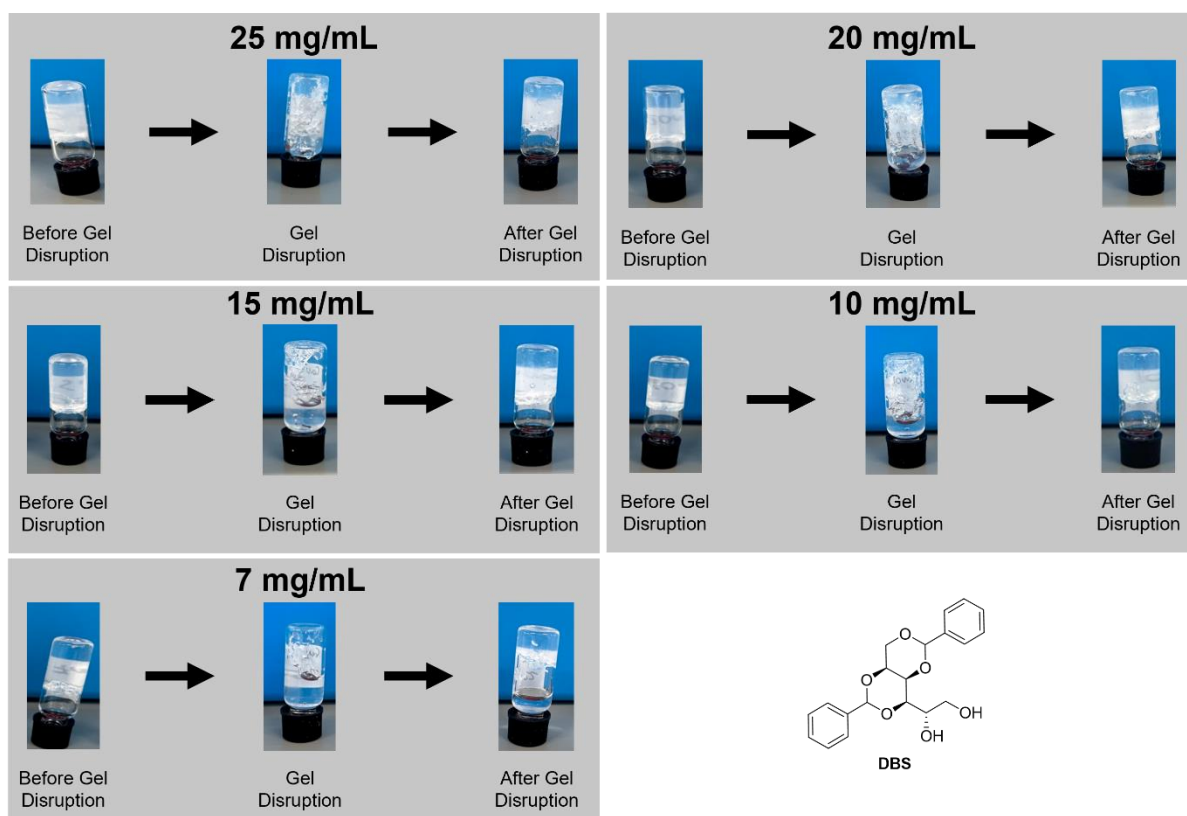
Figure 5.6 | Images of DBS gels in ethyl acrylate before, during and after gel disruption for thixotropic property test
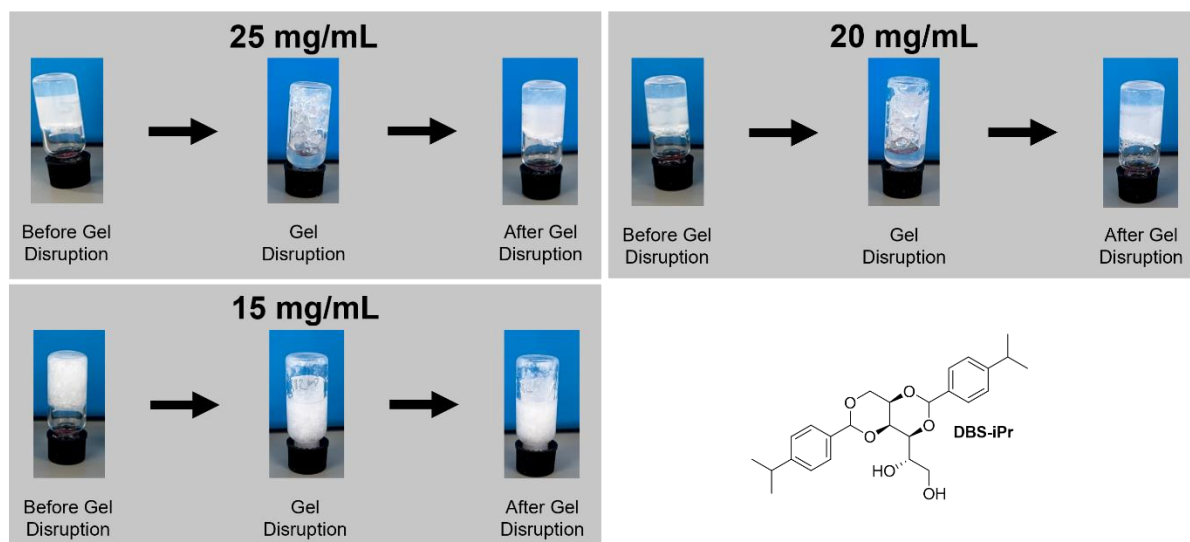
Figure 5.7 | Images of DBS-*i*Pr gels in ethyl acrylate before, during and after gel disruption for thixotropic property test

As mentioned earlier, thixotropic gels have been used for extrusion-based 3DP. It would be noteworthy to see how the thixotropic ethyl acrylate gels would behave during extrusion. If the gels hold their structure during extraction, photopolymerising them would be a great idea to find out if we can use the gels for potential 3D printer extrusion inks.

For a manual extrusion, 10 mg of gelator was dissolved in 1 mL of ethyl acrylate *via* heating. The solution was transferred into a syringe, and the gel was allowed to form overnight before extrusion. It is crucial that only the minimum amount of ethyl acrylate evaporates overnight. Therefore, parafilm was wrapped around the opening of the syringe, and the syringe was placed in a beaker covered with more parafilm to decrease the evaporation of ethyl acrylate. After forming the gel in the syringe, the gel was extruded onto the back of a glass petri-dish in the attempt to release the sample creating a straight line. The glass was then tilted to 90° to see if the material held its structure (Figure 5.8).
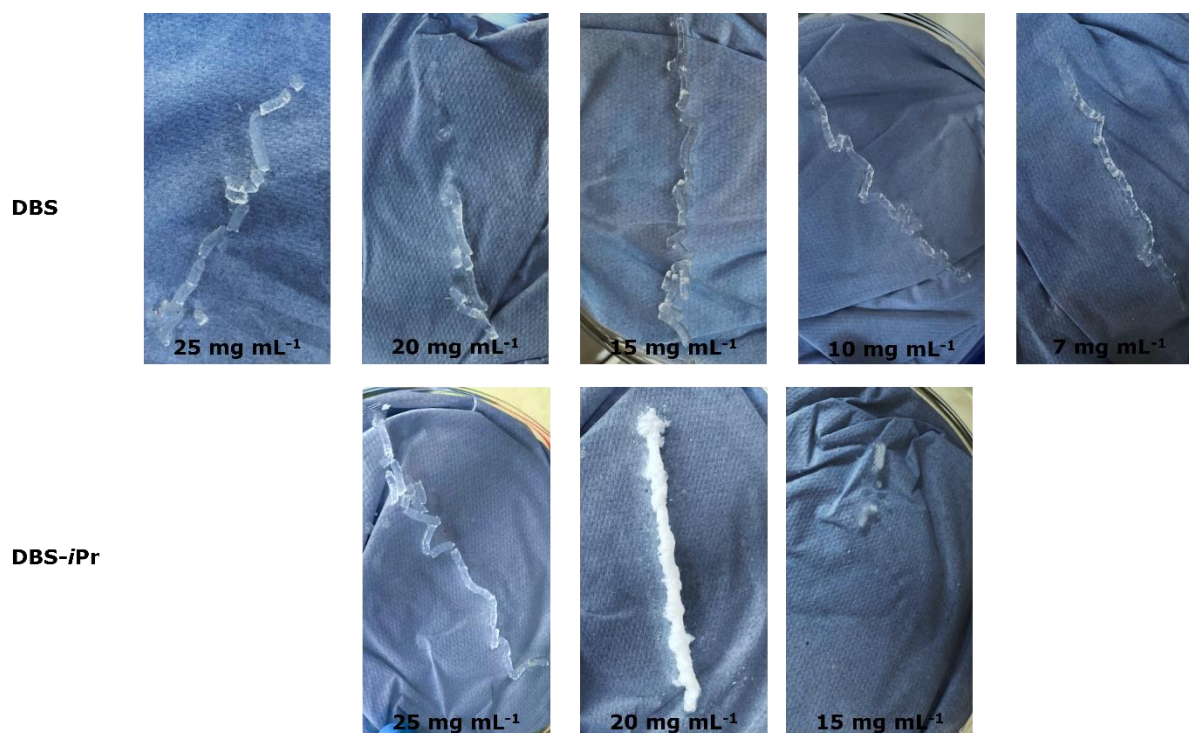
Figure 5.8 | Manually extruded ethyl acrylate gels

Unfortunately, all the ethyl acrylate gels formed from DBS and DBS-*i*Pr did not hold their structure during manual extrusion except the 20 mg mL^{-1} DBS-*i*Pr gel. The gels were broken into smaller gel network pieces like during the thixotropy test and did not let the gel' heal'. However, extrusion using a 3D printer differs from manual extrusion as it can be optimised in different ways.

5.3.2.   Photopolymerisation of ethyl acrylate gels

Photopolymerisation of the ethyl acrylate gels was carried out using an ELEGOO Mercury Curing Machine with a 25 W, 405 nm UV light with two photoinitiators: ethyl 4-(dimethylamino)benzoate (EDB) and 2,4-diethyl-9H-thioxanthen-9-one (DETX). SpeedCure DETX (or any other Norrish Type II photoinitiators) forms its excited state when irradiated under UV light. The excited molecule will then need an electron or a hydrogen atom from a donor molecule. The hydrogen donors are most commonly amine synergists which SpeedCure EDB is. After donating the hydrogen, the synergist then reacts with the monomer to initiate radical polymerisation. The DETX and EDB duo were used to free radical polymerise the acrylate gels (Scheme 5.1).
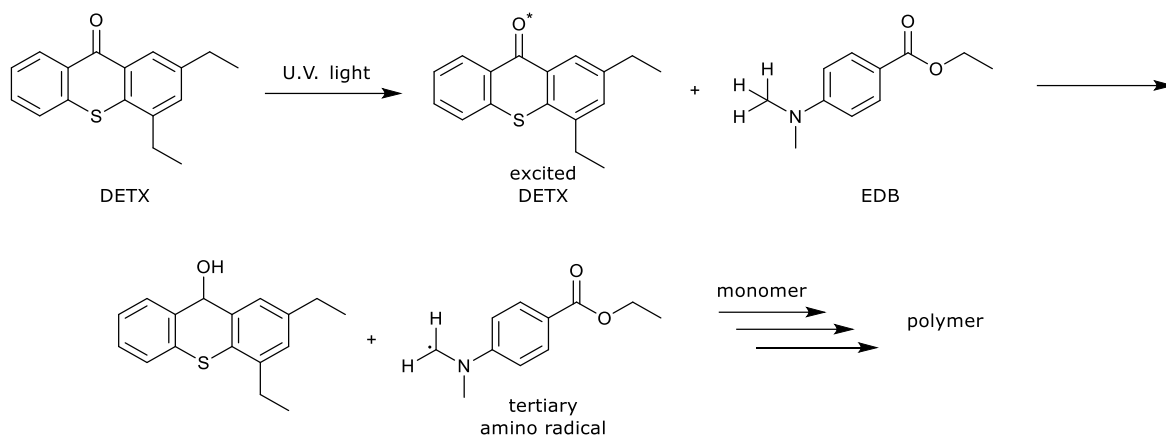
Scheme 5.1 | Norrish Type II initiator and tertiary amine synergist reaction scheme

For each sample, 3 mg of each photoinitiator were placed into a vial with 10 mg of the gelator, 1 mL of monomer was added into the vial, and the mixture was heated up until all solid dissolved. The solution was transferred into a material mould using a syringe, where it was left for 10 minutes for the gel network to form. The mould with the gel was then placed into the curing machine to photopolymerise (Figure 5.9). The material used to create the mould *via* 3D printing is acrylonitrile butadiene styrene (ABS), an oil-based plastic material resistant to high temperatures.
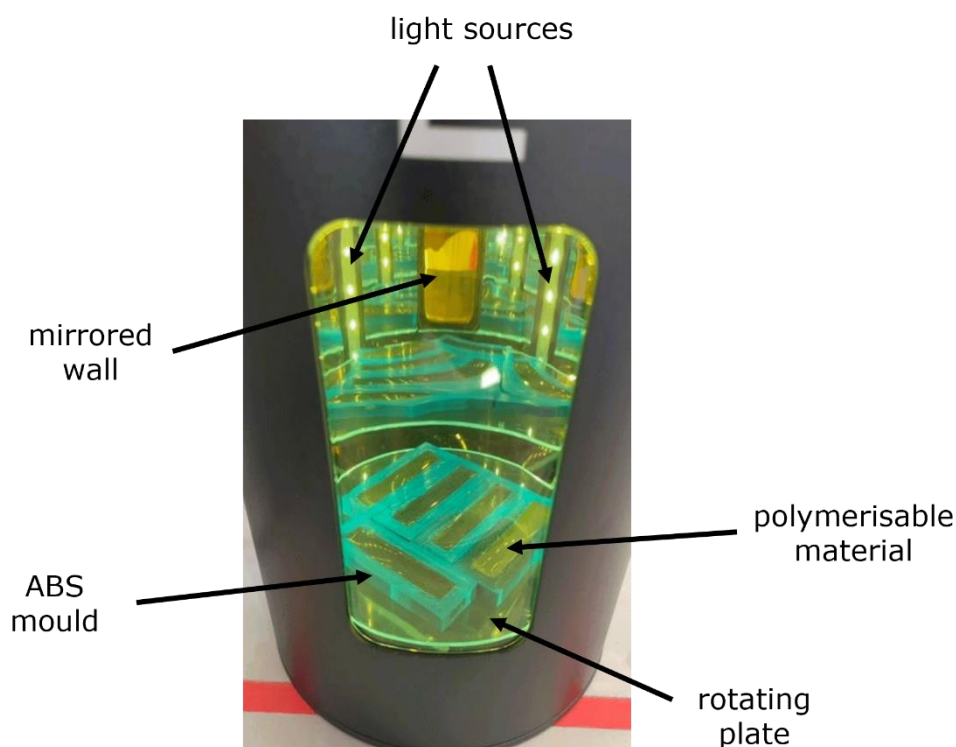
Figure 5.9 | ELEGOO Mercury Curing Machine, 25 W 405 nm UV lamp with gel samples in ABS material moulds.

Unfortunately, the first few attempts of photopolymerising the ethyl acrylate gels in the mould were a struggle, the gel shrinks due to evaporation. Furthermore, as polymerisation is an exothermic process (due to the conversion of pi bonds to sigma bonds), the exposure of the thermoreversible gel under the UV lamp breaks the physical non-covalent bonds that form the 3D fibre network because of sample warming. Therefore, it converts the gel into a solution. More prolonged exposure to the solution boils the liquid, creating an additional problem: evaporation before polymerisation. The issue was resolved by making the ethyl acrylate gel in a sample vial and polymerising the gel while the vial was in an ice bath. Also, a glass petri dish was placed on top of the vial (Figure 5.10). The purpose of the ice bath and the petri dish on top is to avoid evaporation and ensure that the gel remains as a 3D fibre network and does not transform into a solution. The gel polymerised after 15 minutes, where the poly (ethyl acrylate) (PEA) gels were removed from the vial. For the removal of the polymer, water is added to the vial to ease the release. Water is used because it is immiscible with ethyl acrylate.
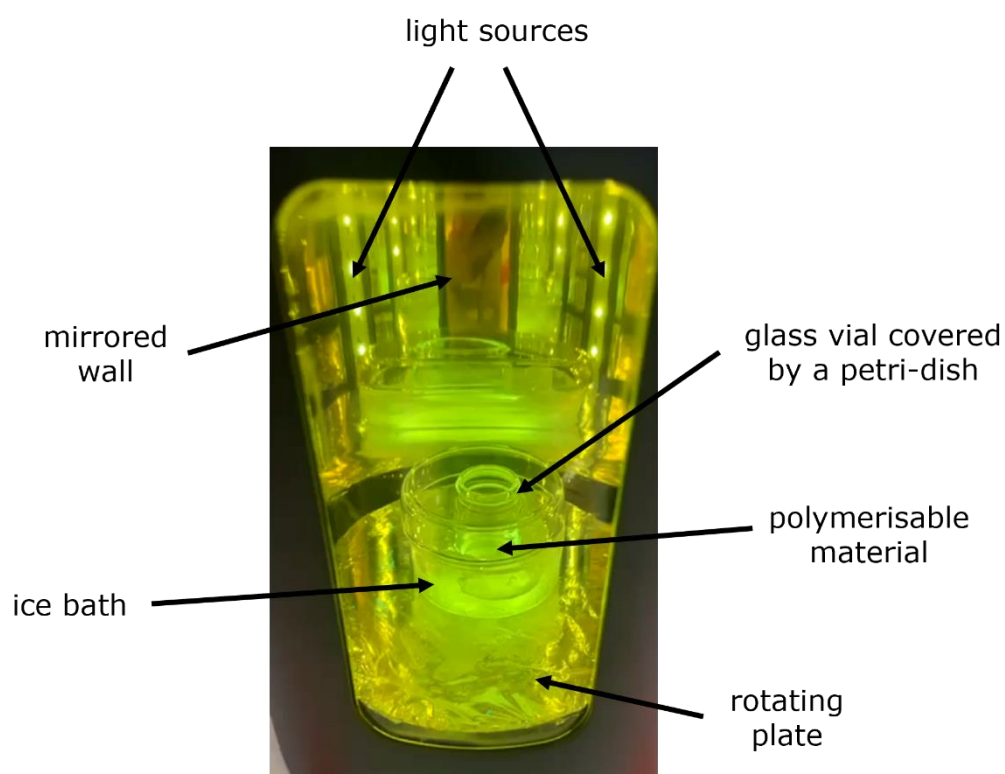
Figure 5.10 | Polymerising ethyl acrylate gels
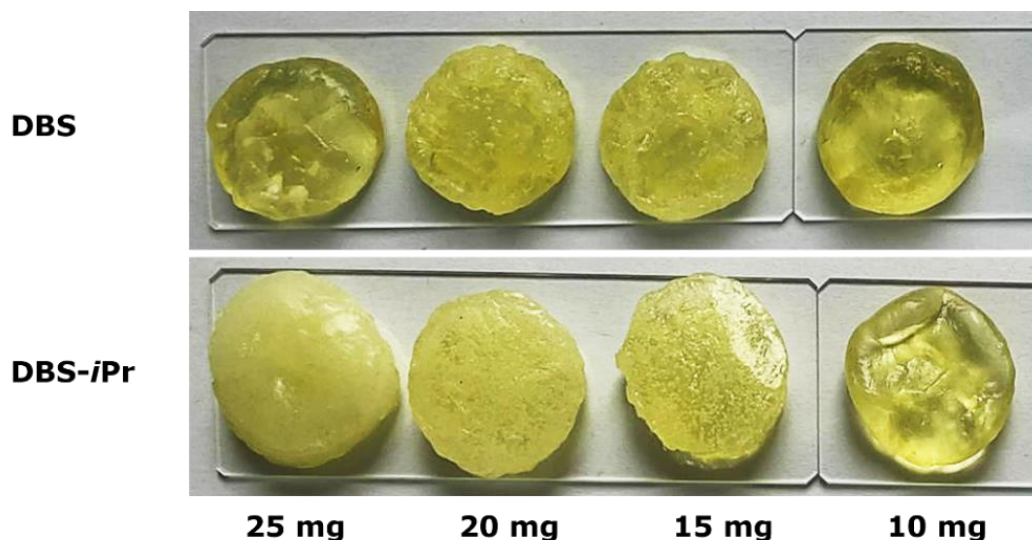
Figure 5.11 | Photopolymerised ethyl acrylate gels

Polymerising ethyl acrylate gels formed materials that are soft and flexible. When force is applied, the materials bend freely, and as soon as pressure is removed, the material goes back to its original shape. This observation indicates that the capture of LMWG fibres in PEA matrices forms elastic materials. DBS in PEA formed more relatively translucent materials than DBS-*i*Pr in PEA that formed opaque materials as the concentration increases (Figure 5.11).

Furthermore, the shaken DBS gels were also polymerised. For these samples, the two photoinitiators were dissolved in ethyl acrylate *via* heating. The solution was left to cool before the DBS gelator was added and shaken. The sample vial was left for 5 minutes to allow gel formation. The gel was then polymerised in a vial placed in an ice bath with a petri-dish on top during the UV curing. The materials obtained after polymerisation show consistent opaqueness (Figure 5.12) in comparison to the DBS in PEA with heating and cooling (Figure 5.11). For all the polymerised materials, the appearance (opaqueness, transparency or translucency) matches the appearance of the gel before polymerisation. However, the polymerised materials are yellow because of the SpeedCure DETX photoinitiator.

25 mg   20 mg   15 mg
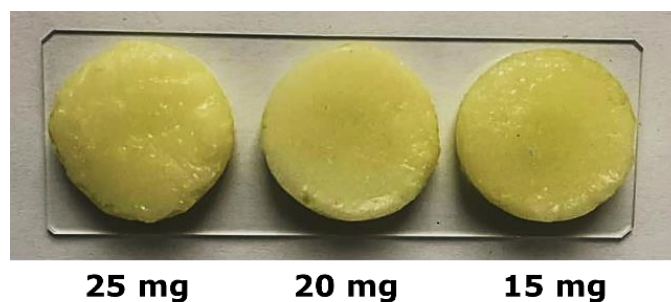
Figure 5.12 | Photopolymerised shaken DBS in ethyl acrylate

The easiest way to quantitatively distinguish that ethyl acrylate has polymerised is to collect infrared data of the materials. According to Sherman Hsu[179], infrared spectrometry can detect molecular impurities or additives present in amounts of 1% and, in some cases, even as low as 0.01%.

The obtained IR spectra of EA and PEA were plotted together (Figure 5.13), and the PEA IR spectrum shows similarity with the PEA IR spectrum in the literature.[180] Both spectra showed characteristic IR bands corresponding to alkyl saturated chains ($\sim$2919 cm^{-1}), C=O non-conjugated carboxylic ester ($\sim$1726 cm^{-1}) and the C-O ester stretch ($\sim$1188 cm^{-1} for EA and $\sim$1154 cm^{-1} for PEA). The significant differences of EA and PEA spectra are shown beyond 1700 cm^{-1}. There are two relevant peaks in the EA spectrum, peaks at $\sim$1637 and at $\sim$985 cm^{-1} which relate to the C=C stretching and the C=C bending of the monosubstituted alkene in the monomer, respectively. As these peaks are not present in the PEA spectrum, it is a substantial indicator that the radical polymerisation did occur, losing the alkene and forming PEA.

On the other hand, there are also two relevant peaks in both EA and PEA spectra, peaks at $\sim$1446 and at $\sim$1379 cm^{-1} which correlate to the sp^3 C-H bend on the molecule. The peaks are more intense and distinct on the PEA spectra, which is another evidence that the material has photopolymerised. PEA polymer has seven sp^3 carbons, whereas the EA monomer has two. These proofs have displayed that radical polymerisation had essentially happened.

The IR spectra of PEA, 25 mg DBS-*i*Pr in PEA and 25 mg DBS in PEA were plotted together (Figure 5.14). As the materials consist of only 2.5% w/v gelator, there is not much difference seen in the spectra of the materials.
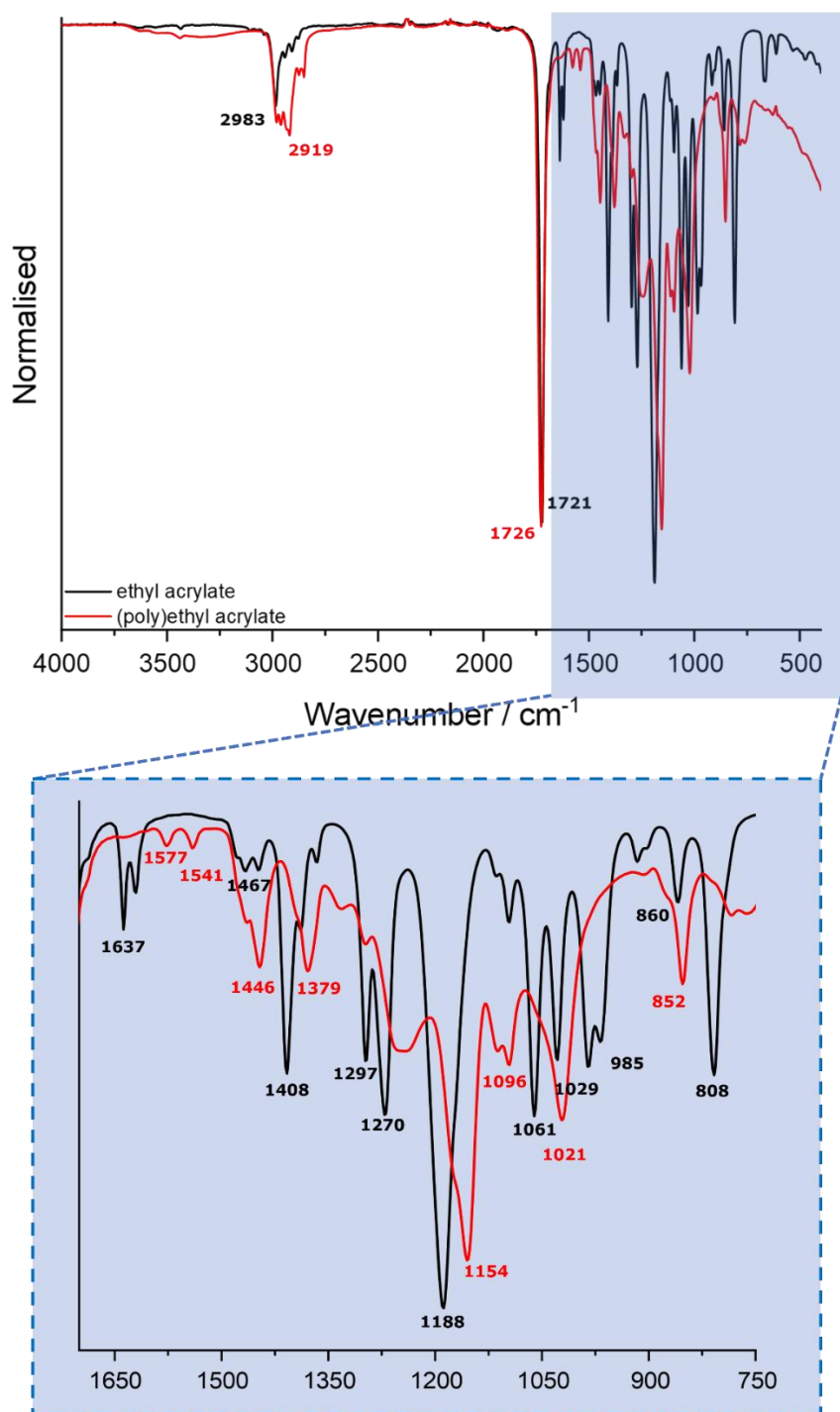
Figure 5.13 | IR spectra of ethyl acrylate and poly (ethyl acrylate)
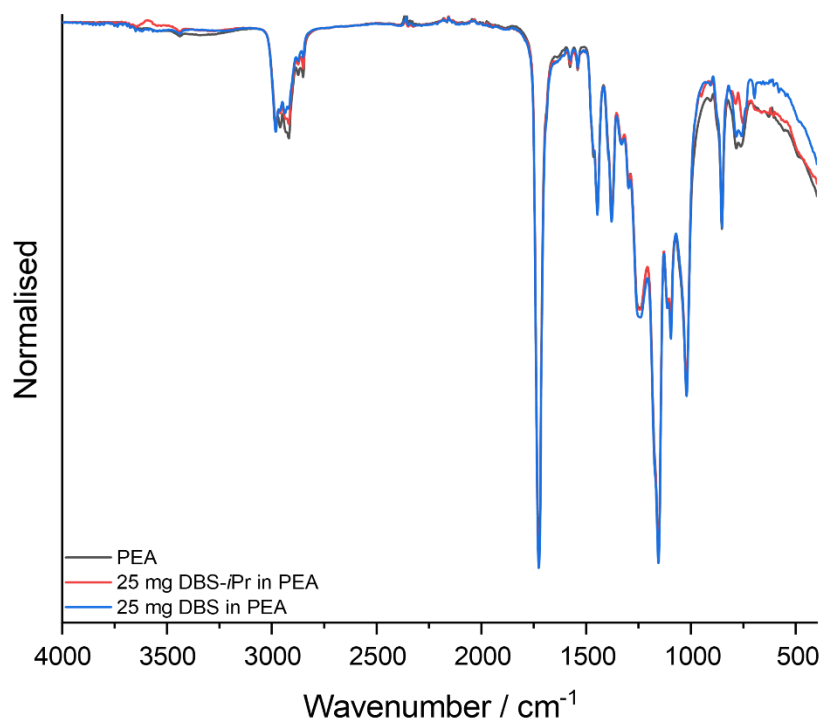
Figure 5.14 | IR spectra of PEA and gelators in PEA

5.3.3. Morphologies of ethyl acrylate materials

Scanning electron microscopy (SEM) was used to investigate the difference in morphology between the ethyl acrylate gel and poly(ethyl acrylate) dual network materials. Xerogels were prepared by drying the gels on an SEM stub *in vacuo*. PEA materials were prepared by slicing the polymer, placed on the SEM stub using adhesive conductive carbon tabs (cross-sectional area facing upwards). The stubs were then coated with 5 nm iridium under vacuum before imaging at 5 kV.

First of all, the isolated white DBS powder shows fibrous morphology under the scanning electron microscope (Figure 5.15a). The fibres are smooth, short and inconsistent in length. Incorporating DBS into EA with just shaking the system, the xerogels forms thick, smooth and long fibres (Figure 5.15b-d). In addition to that, the shaken gels also form really thin and small fibres that self-assemble along with the thick fibres. The area occupied by the thick fibres becomes broader when the concentration of the DBS compound increases. The SEM micrographs suggest that non-covalent interactions occur between the DBS molecules when the system is shaken, forming a more prolonged fibrillar 3D network and can trap and immobilise the solvent medium.
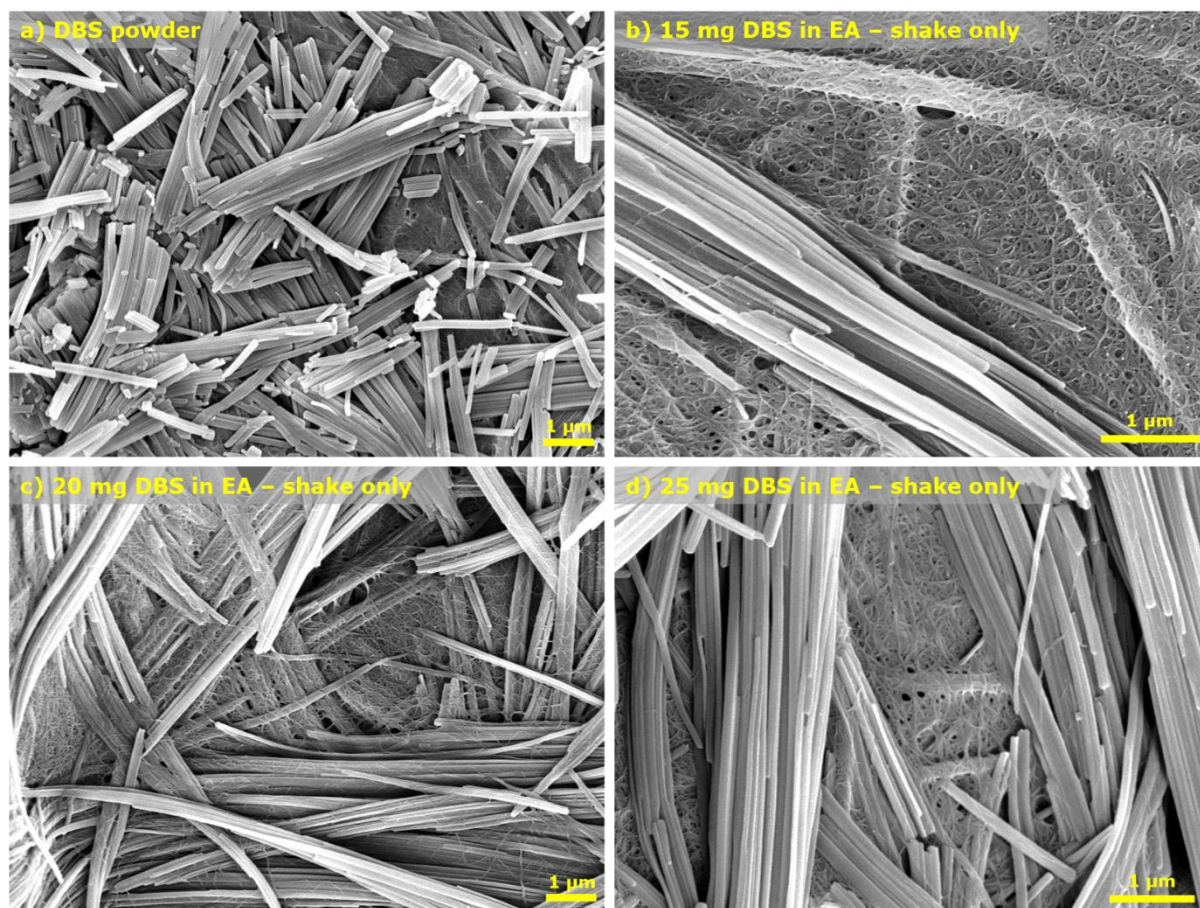
Figure 5.15 | SEM micrographs of DBS powder and DBS xerogels formed *via* shaking in different concentrations. Conditions: xerogel was prepared by drying the gel in air and then with 5 nm Ir coating before imaging under vacuum at 5 kV. Scale bar represents: 1 μm in all micrographs

SEM micrographs of the xerogels before and after gel disruption were also obtained to examine if the morphologies of the gels change after disrupting the material. All the micrographs for before and after mechanical gel disruption for both DBS and DBS-*i*Pr in ethyl acrylate are very similar (A 74). The micrographs of 15 mg DBS and 20 mg DBS-*i*Pr in ethyl acrylate were selected to represent the general structure of the fibres (Figure 5.16).
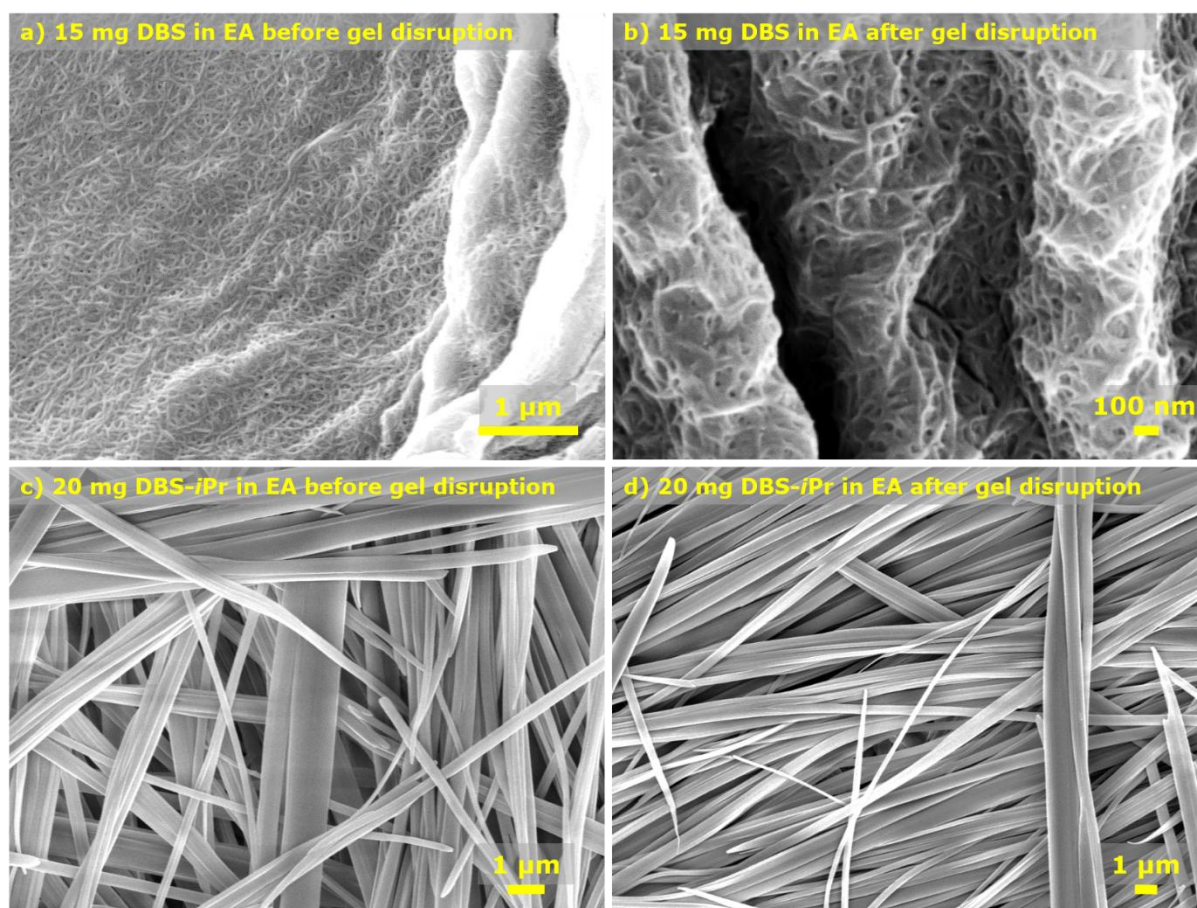
Figure 5.16 | SEM micrographs of xerogels formed from 15 mg DBS and 20 mg DBS-*i*Pr in EA before and after gel disruption. Conditions: xerogel was prepared by drying the gel in air and then coating it with 5 nm Ir before imaging under vacuum at 5 kV. Scale bar represents: 1 μm in a), c) and d); 100 nm in b) micrographs

In both DBS and DBS-*i*Pr xerogels, the xerogel fibres have very similar structures before (Figure 5.16a and Figure 5.16c) and after (Figure 5.16b and Figure 5.16d) gel disruption. This observation implies that after disturbing and breaking the gel, the gel fibres regenerate *via* non-covalent interactions between the gelator molecules, which occurs within the 30 seconds rest-time. Moreover, the microstructure of the material also correlates with its macrostructure. The fibres of the DBS xerogel formed from ethyl acrylate are extremely thin, demonstrated as translucent gels. The opposite is true for the fibres of the DBS-*i*Pr xerogel formed from ethyl acrylate. It exhibited long and thick fibres established as opaque gels.

Furthermore, the fibres formed from DBS in EA show wider fibre widths before disruption than after disruption, with values of 22 ± 0.5 and 14 ± 0.3 nm, respectively. On the other hand, the fibres formed from DBS-*i*Pr in EA displayed narrower fibre widths before disruption than after disruption, with values of 230 ± 11 and 370 ± 20 nm, respectively (Figure 5.17).

a) DBS in EA before disruption

~ 22 ± 0.5 nm

b) DBS in EA after disruption

~ 14 ± 0.3 nm

c) DBS-*i*Pr in EA before disruption

~ 230 ± 11 nm

d) DBS-*i*Pr in EA after disruption

~ 370 ± 20 nm
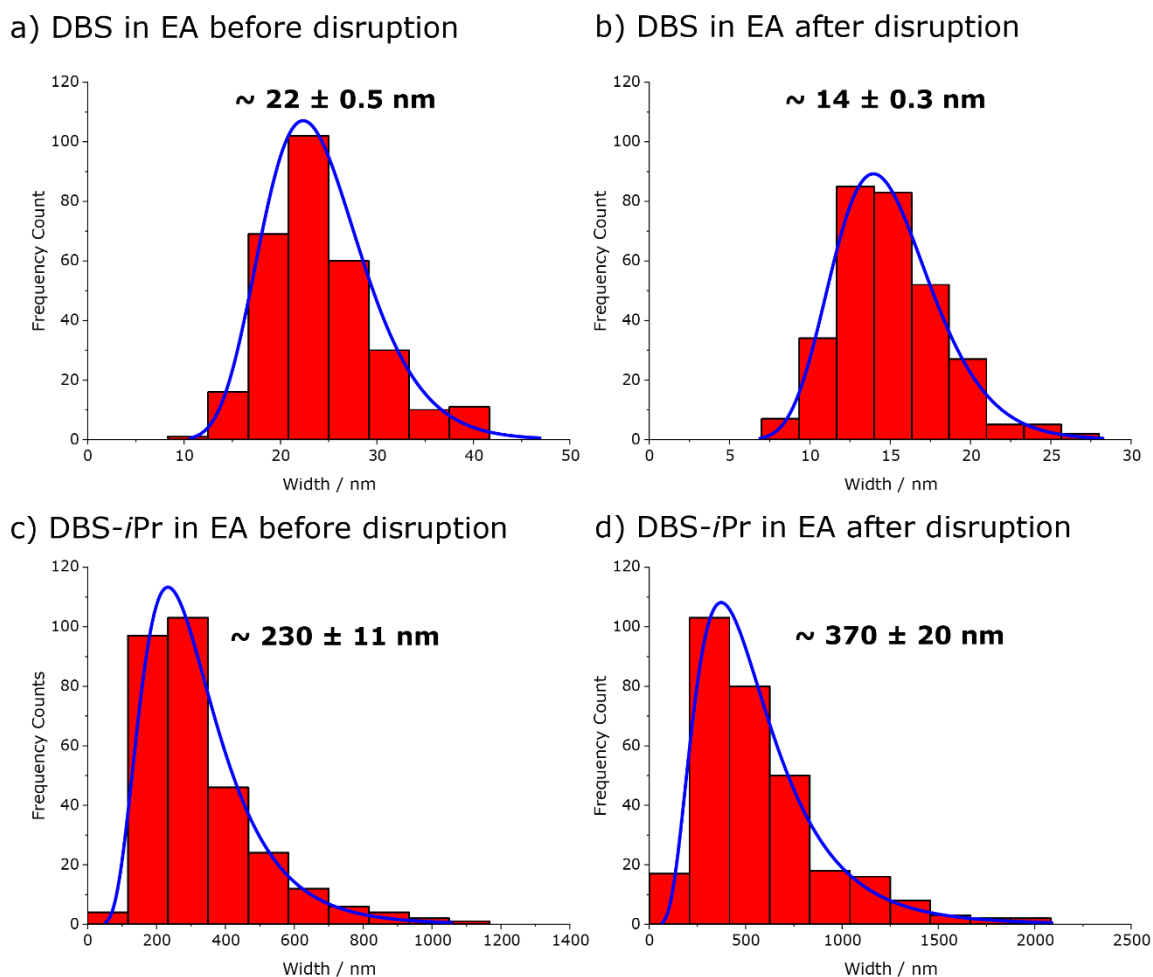
Figure 5.17 | Histogtam of xerogels formed from 15 mg DBS and 20 mg DBS-*i*Pr in EA before and after gel disruption.

SEM imaging for the PEA and gelators in PEA materials were carried out. First of all, it is evident that the network structure of PEA (Figure 5.18a) is not fibrous; instead, the morphology displays a consistent wrinkled and creased network that covalently forms during radical polymerisation. For the materials that consist of DBS gelator, it is evident that fibres are present on the surface structure of the materials. The micrograph in Figure 5.18b shows that there are long fibres parallel to each other just under the material's surface, where some of the fibres are penetrating the surface. For DBS-*i*Pr in PEA, there seems to be an outline of globular aggregates under the fibrous surface (Figure 5.18c). The SEM micrographs show that pure PEA material appears to have a relatively rougher texture than the PEA material with gelators incorporated in it. This observation may perhaps be the effect of the strong interactions between the monomer molecules during radical polymerisation. When gelation is allowed to occur by incorporating gelators into the system, the formation of physical interaction between the gelator and the monomer molecules enable the material to form fibres during polymerisation that generates a relatively smoother surface. Furthermore, the micrographs in Figure 5.18b and Figure

5.18c verify that establishing a dual-network material with a gelator and a polymer matrix was successful. It displays two different structures on the materials' morphologies.
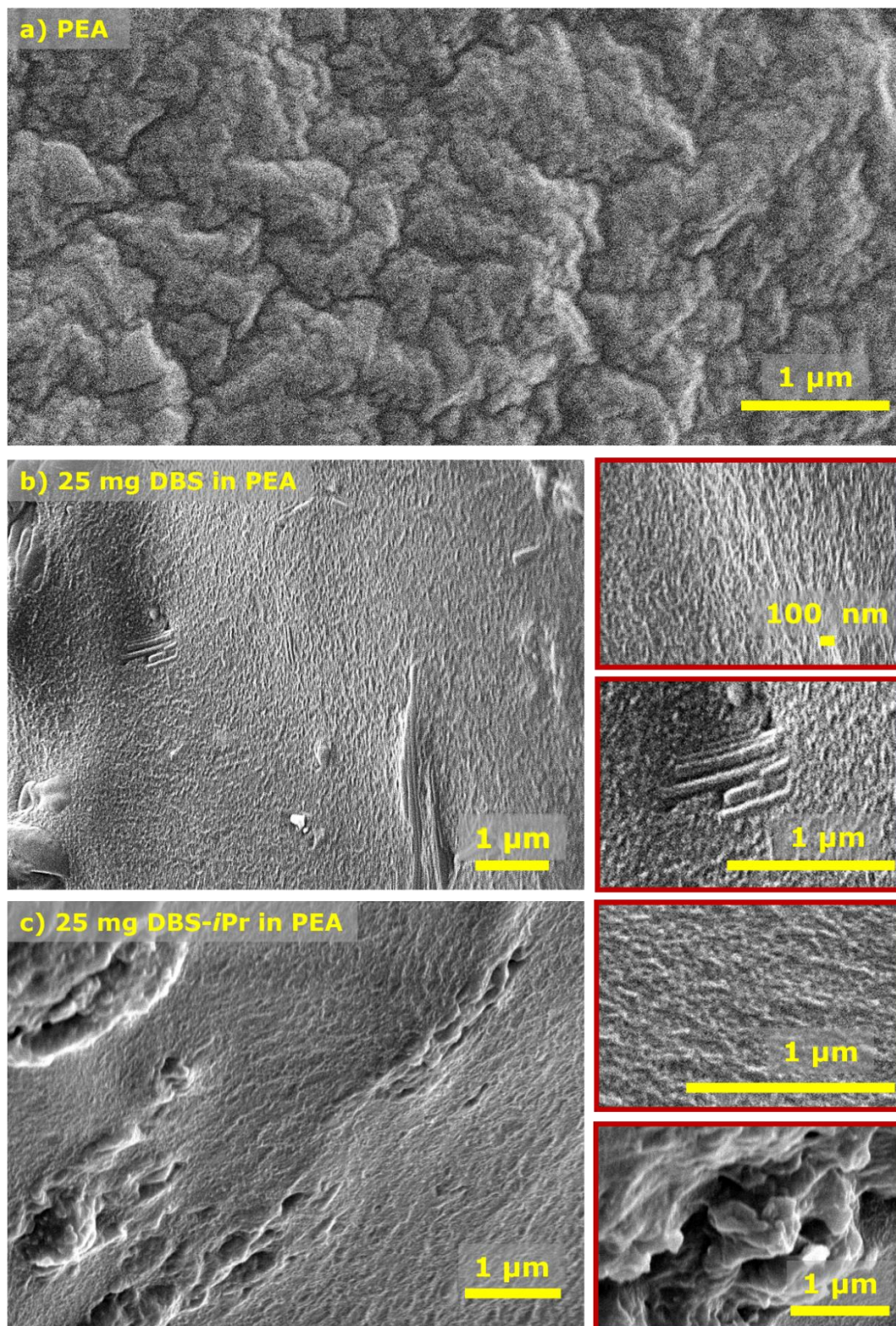
Figure 5.18 | SEM micrographs of a) PEA, b) 25 mg DBS in PEA and c) 25 mg DBS-*i*Pr in PEA. SEM images with red outlines are zoomed-in sections of the micrograph on the left. Conditions: polymers were sliced and was placed on an SEM stub, then with 5 nm Ir coating before imaging under vacuum at 5 kV. Scale bar represents: 1 µm in all micrographs excluding the first zoomed-in micrograph of b), which is 100 nm

Finally, the morphologies of PEA materials with DBS incorporated into the polymer *via* shaking before polymerisation are very similar. The structure of 20 mg DBS in PEA *via* shaking is displayed in Figure 5.19 to represent the polymer structure of the shaken materials. The fibres are thicker in the shaken composite than the fibres formed from the same components but generated upon heating and cooling (Figure 5.15a and b). The results also reflect the macrostructures of the materials where the heated and cooled materials are translucent (relatively thin fibres), and the shaken polymers are opaque (relatively thick fibres).
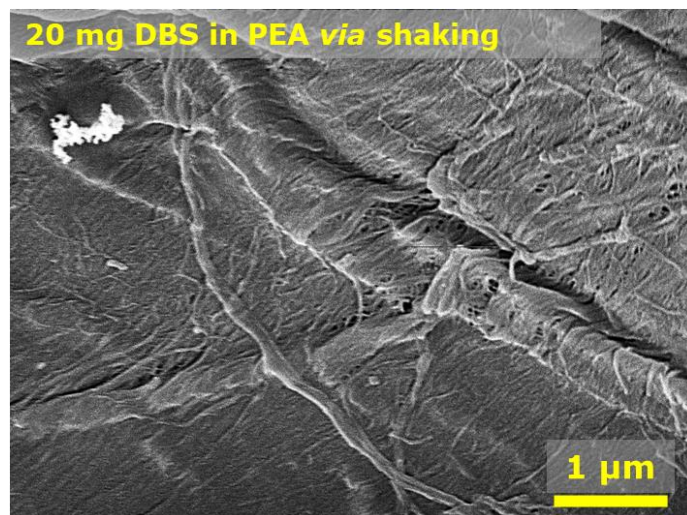
Figure 5.19 | SEM micrograph of 20 mg DBS in PEA *via* shaking. Conditions: polymer was sliced and was placed on an SEM stub, then coating with 5 nm Ir before imaging under vacuum at 5 kV. Scale bar represents: 1 μm for a) and b); 100 nm for c).

5.3.4. Dynamic mechanical analysis of poly(ethyl acrylate) materials

Dynamic mechanical analysis (DMA) was carried out on the PEA samples to understand the viscoelastic properties of the materials. The material is subjected to sinusoidal stress or strain in an oscillatory measurement, and the stress or strain response is measured. DMA analyses the elastic (storage modulus) and the viscous (loss modulus) material response simultaneously. Perkin Elmer Dynamic Mechanical Analyser DMA 8000 was used for the samples, using the Isotherm 'tension' programme to analyse the ethyl acrylate polymer. The applied strain for the tensile test is 0.50 mm with a frequency of 1.0 Hz at 25 °C left to hold for 1 minute.

All the materials tested under the DMA 8000 displayed viscoelastic properties as they attained storage and loss modulus values. PEA without any gelator shows a storage modulus, G', of 1.02 MPa (Table 5.4). Adding 10 mg DBS-*i*Pr into PEA increases the value of G' very slightly (1.56 kPa). For 10 mg DBS in PEA, there is a noticeable decrease in the polymer's storage modulus. However, considering the error bars for the storage and loss modulus of 10 mg DBS in EA, they are within the range of the moduli results for poly (ethyl

acrylate) and 10 mg DBS-iPr in poly (ethyl acrylate). Therefore, the result means that the addition of 10 mg of each gelator into the polymer to form a dual-network material did not significantly affect the mechanical property of PEA. A one-way or single factor anova was carried out to validate the data statistically. The null hypothesis assumes that there is no relationship between two variables – one variable does not affect the other. In this case, the null hypothesis is that the addition of gelators (DBS and DBS-iPr) does not affect the mechanical properties of PEA. If the p-value from the data turns out to be less than 0.05, then the null hypothesis is considered to be false or nullified; the obtained p-value from the single factor anova is 3.29413×10^{-18}. The acquired statistics mean that the null hypothesis is false; therefore, although the capture of DBS and DBS-iPr fibres in the PEA matrix did not show massive changes in mechanical properties, it still affected the properties of PEA.

Despite that, a trend is evident in the DMA results (Figure 5.20), where it shows that incorporating a higher concentration of gelator into the material increases the storage modulus of the composite. The higher gelator concentration means that there would be more gelator-gelator and gelator-monomer interaction occurring in the system, forming a stronger 3D dual-network. Therefore, this dual network gives a positive influence on the mechanical property of the material after photopolymerising as the storage moduli of the composite material is higher than the pure polymer.

On the other hand, when the highest tested concentration was added (25 mg DBS or DBS-iPr) into the polymer material, the storage and loss modulus of the polymer decrease considerably, but the modulus was still higher than the polymer without any gelator. This phenomenon could be the effect of phase-separation, where the gelator material would clump together, interrupting and intercepting the 3D dual network.

Table 5.4 | Storage and loss modulus of PEA samples. G' = storage modulus; G" = loss modulus.

	Concentration of Gelator / mg mL^{-1}	Modulus / MPa	
		G'	G"
PEA	-	1.02	0.49
DBS in PEA	10	0.92	0.47
	15	1.22	0.57
	20	1.40	0.66
	25	1.03	0.53
DBS-iPr in PEA	10	1.03	0.47
	15	1.18	0.53
	20	1.48	0.70
	25	1.44	0.67
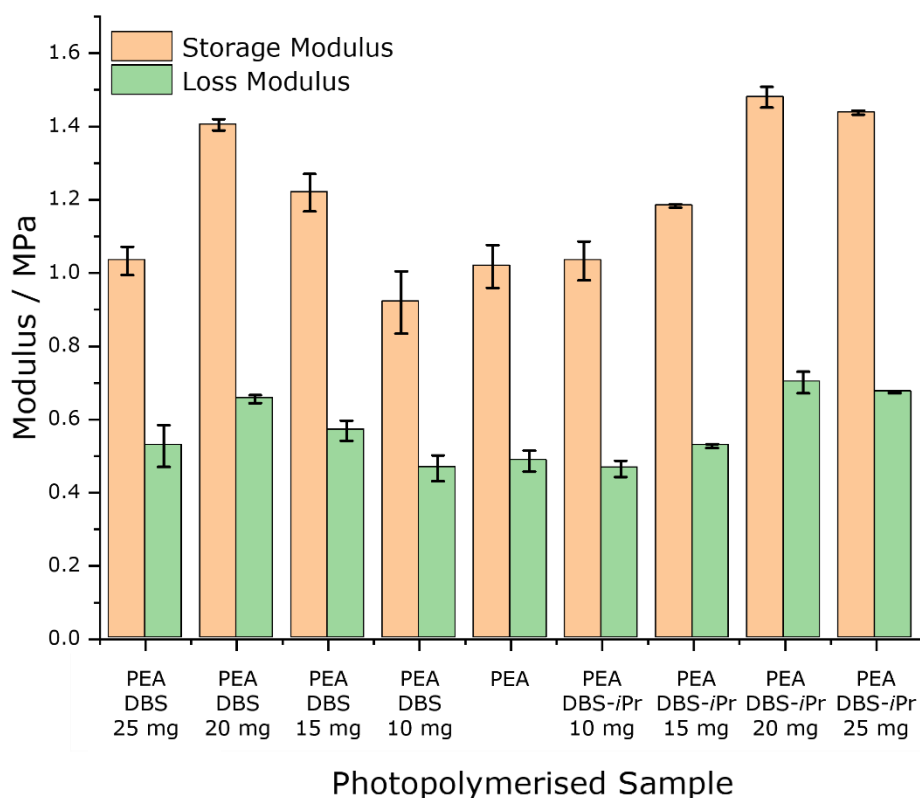
Figure 5.20 | Storage and loss moduli of poly(ethyl acrylate) materials

DMA was also carried out for the composites generated from the DBS in PEA *via* shaking (Figure 5.21a). When ethyl acrylate is polymerised around the DBS gel fibres by simply shaking the vial improves the material's storage modulus. Similar to the results witnessed for the PEA materials with the gels formed upon heating and cooling (Figure 5.20), the trend is the same as the other composites. An increase in moduli is seen when ethyl acrylate is polymerised around 15 mg and 20 mg of the incorporated DBS, followed by a slight decrease when the highest tested concentration, 25 mg, was introduced. This phenomenon could be again the effect of phase-separation of the material.

In addition to that, it is evident that the material prepared from shaking the DBS into the EA showed the highest storage modulus of 3.3 MPa in comparison to the storage modulus of PEA and gelators in PEA formed upon heating and cooling with values about 1.0 – 1.2 MPa (Figure 5.21b). This observation may be due to the strong interactions formed from the contact between the gelator fibres upon shaking. The results correlate with the morphologies of the materials where the polymers and xerogels formed from shaking DBS into the system displayed two fibre types.

a) DBS in PEA *via* shaking
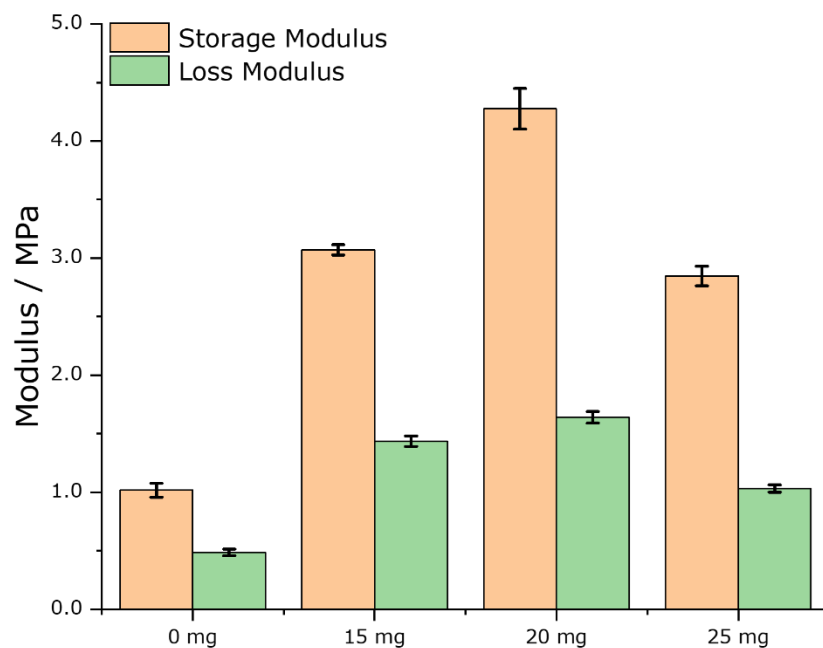
b) Gelators in PEA
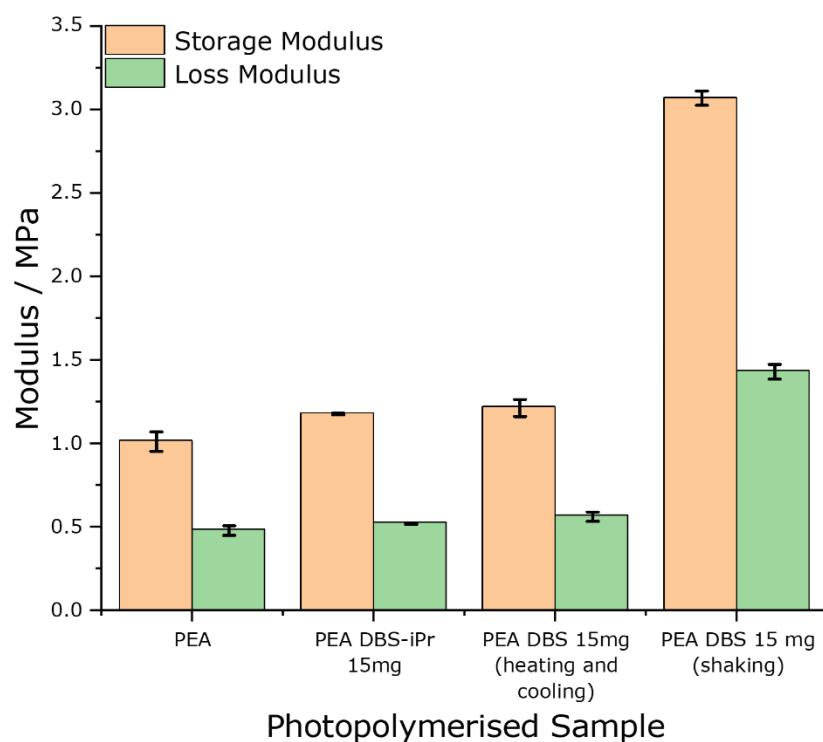
Figure 5.21 | Storage and loss modulus of a) DBS in PEA *via* shaking and b) 15 mg mL^{-1} gelators in PEA

5.4 Gelators for a library of UV-curable monomers

In recent years, there has been an advance in the studies of photocurable monomers for additive manufacturing (3D printing) applications.[181–186] Inkjet 3D printing is a type of 3D printing identified as an appropriate technology for multi-colour or multi-material processing. 3D inkjet printing has numerous advantages making it popular in manufacturing. Inkjet printing is a digital non-contact process offering great versatility in terms of patterning through drop deposition. Furthermore, inkjet printing is scalable and is less susceptible to contamination with good compatibility with multiple printheads. Inkjet printing is also compatible with different fluids, including polymer solutions and particle suspensions, provided that the 'ink' satisfies specific fluid requirements.[187] The limitation of ink composition brings the disadvantage of this 3D printing method, where it is essential to control the particle content and compound's molecular weight. The most important property of the ink for inkjet printing is the viscosity, which is typically under 50 mPa.[188]

The idea of this part of the research reported here is to find a way to formulate inks that fit the requirement needed for inkjet 3D printing. As the gelators tested in poly(alkyl acrylates) show that they modify the monomer's rheology and show improvement in the polymer's mechanical properties when forming the dual-network material, the plan is to screen the most efficient tested gelators (from previous chapters) in various UV-curable monomers. Seven sugar-based gelators from chapters two and three (DBX-*i*Pr, Lauryl-DBS-*i*Pr, DBS-*i*Pr, MBS-*i*Pr, MBS-Ph, DBX-CO$_2$Me and DBS-CO$_2$Me – Figure 5.22) were examined for gelation properties in various UV-curable monomers (Figure 5.23 and Table 5.5). These gelators were selected as they show good gelation abilities in organic solvents and aqueous solutions tested. The objective is to discover what molecule forms the most gels in the monomer library and characterise the most promising materials.
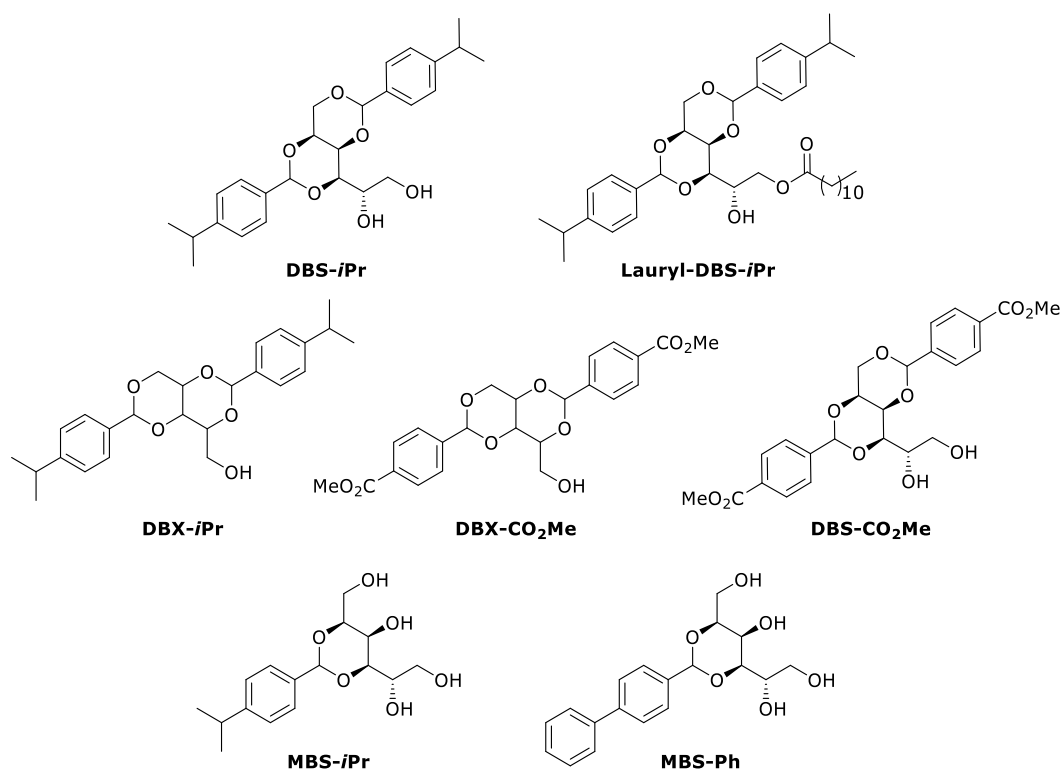
Figure 5.22 | Chemical structure of the selected sugar-based gelators investigated for gelation properties in different UV-curable monomers.

Twenty-nine UV-curable monomers (Figure 5.23 and Table 5.5) were studied as solvents for the gelation tests of the compounds mentioned above. The library of UV-curable monomers consists of both methacrylates and acrylates, including a vast diversity of solvent characteristics that would be good for investigating gelation properties in this research.

1. TriPGdA

2. PhMA

3. TriCdMdA

4. HBMA

5. AMA

6. MMA

7. TriMOSiPMA

8. HEA

9. EGdCEA

10. EGdMA

11. dEGdMA

12. HddA

13. iBnA

14. iBA

15. HPA

16. DEGMEMA

17. EHA

18. CHMA

19. BMA

20. dEAmEMA

21. ClHPMA

22. EHMA

23. EMA

24. EGPhEMA

25. EGMEMA

26. HMA

27. iBnMA

28. iDMA

29. LMA

Figure 5.23 | The chemical structures of UV-curable acrylate and methacrylate monomers that were studied here

Table 5.5 | Full IUPAC names for the investigated UV-curable acrylate and methacrylate monomers

Monomer	Abbreviation	IUPAC nomenclature
1	TriPGdA	tripropylene glycol diacrylate
2	PhMA	phenyl methacrylate
3	TriCdMdA	tricyclo[5.2.1.02,6]decanedimethanol diacrylate
4	HBMA	hydroxybutyl methacrylate
5	AMA	allyl methacrylate
6	MMA	methyl methacrylate
7	triMOSiPMA	3-(trimethyloxysilyl)propyl methacrylate
8	HEA	2-hydroxyethyl acrylate
9	EGdCEA	ethylene glycol dicyclopentenyl ether acrylate
10	EGdMA	ethylene glycol dimethacrylate
11	dEGdMA	di(ethylene)glycol dimethacrylate
12	HddA	1,6-hexanediol diacrylate
13	iBnA	isobornyl acrylate
14	iBA	isobutyl acrylate
15	HPA	hydroxypropyl acrylate
16	DEGMEMA	diethyleneglycol methyl ether methacrylate
17	EHA	2-ethylhexyl acrylate
18	CHMA	cyclohexyl methacrylate
19	BMA	benzyl methacrylate
20	dEAmEMA	2-(diethylamino)ethyl methacrylate
21	ClHPMA	3-chloro-2-hydroxypropyl methcrylate
22	EHMA	2-ethylhexyl methacrylate
23	EMA	ethyl methacrylate
24	EGPhEMA	ethylene glycol phenyl ether methacrylate
25	EGMEMA	ethylene glycol methyl ether methacrylate
26	HMA	hexyl methacrylate
27	iBnMA	isobornyl methacrylate
28	iDMA	isodecyl methacrylate
29	LMA	lauryl methacrylate

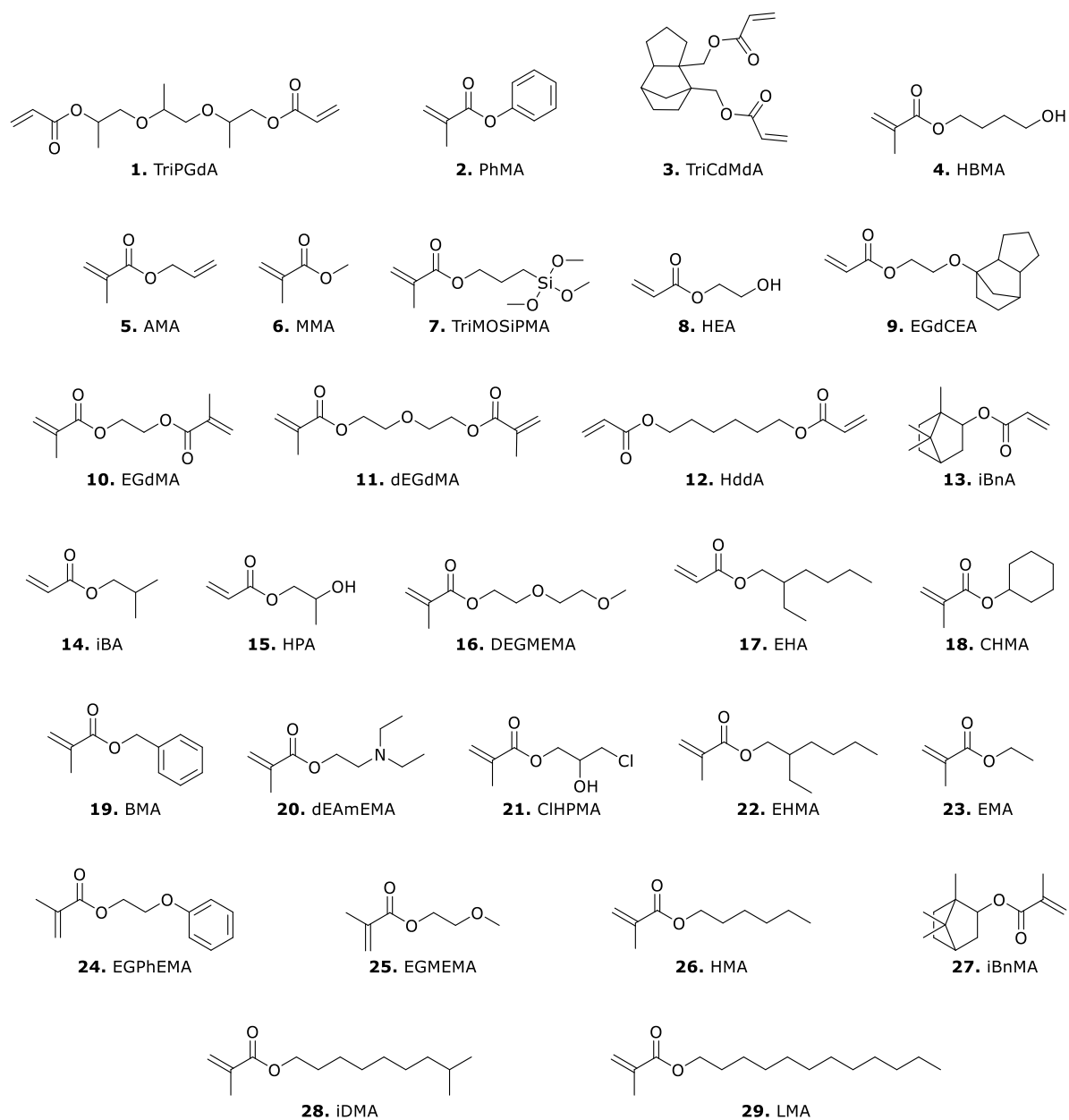Gelation abilities were assessed by adding a known volume of the UV-curable monomer into a vial with the weighed gelator – the concentration is at 10 mg mL^{-1} unless stated. A stirrer bar was used to ensure the complete dissolution of the gelator into the monomer during heating. The screening for the gelator-monomer interaction was carried out using the Crystal16 parallel crystalliser as it provides precise control of the heating and cooling of the samples. The designed parameters used for the screening are as follows: (1) 20 °C to 120 °C at 8 °C/minute; (2) Isotherm at 120 °C for 10 minutes; (3) 120 °C to 25 °C at -8 °C/minute; (4) Isotherm at 25 °C for 30 minutes. After the cycle (1)-(4) was completed, the samples were left on the bench for another 10 hours to ensure gelation could complete.

Referring to the previous chapters, the gelators used in this screening can gel a range of organic solvents and aqueous ethanolic mixtures. Overall, the monomer library consists of

two di-methacrylates, three di-acrylates, six acrylates and eighteen methacrylates. At a concentration of 10 mg mL^{-1}, all gelators were able to show gelation abilities in a few or numerous monomers except for DBX-*i*Pr and MBS-Ph (Figure 5.24). DBX-*i*Pr did not exhibit gelation properties at 10 mg mL^{-1} as it remained in solution after heating and cooling. The increase of concentration to 20 mg mL^{-1} of DBX-*i*Pr, showed an improvement in immobilising the monomer solvents, gelling thirteen of them.

Furthermore, both MBS-Ph and MBS-*i*Pr did not form a gel in any of the organic solvents tested in the second chapter; they only showed gelation abilities in ethanolic mixtures and DMSO:H$_2$O solutions. Despite that result, MBS-*i*Pr gelled an astounding number of monomers in comparison to MBS-Ph. Whether the monomers were acrylates, methacrylates, di-acrylates or di-methacrylates, MBS-Ph did not form any gel in any of the tested monomers even at higher concentrations; instead, precipitate has formed. Presumably, the benzyl substituent on the benzyl ring in the structure has poor solubility. On the other hand, the other monobenzylidene compound, MBS-*i*Pr, successfully formed a mix of transparent and opaque gels in sixteen monomers. The *i*Pr substituent in the benzyl ring makes the molecule more soluble and, in this case, more prone to act as a gelator.

The dibenzylidene derivative of MBS-*i*Pr, DBS-*i*Pr, also successfully formed gels in seventeen of the tested monomers with mixed macrostructure showing opaque and transparent gels. Adding a long chain and removing an -OH group to DBS-*i*Pr, Lauryl-DBS-*i*Pr shows inferior gelation properties. Most of the gelator-monomer samples remain as a solution, and only eight formed a gel after heating and cooling. The monomer with the shortest chain, methyl methacrylate (MMA – monomer 6), and the only monomer that has a chlorine atom in its molecular structure, 3-chloro-2-hydroxypropyl methacrylate (ClHPMA – monomer 21), were not immobilised and gelled by any of the gelators tested.

The two most versatile gelators for the tested monomers in this research are compounds DBX-CO$_2$Me and DBS-CO$_2$Me, having the most rigid and polar substituent on the benzyl rings. Both exhibited good gelation abilities where the former formed eighteen gels (seventeen are opaque) and the latter generated twenty-one gels (twenty are transparent). The opaqueness and the transparentness of the gels formed by the di-ester gelators are supported by the fibre sizes seen on the SEM micrographs of the xerogels (Figure 5.33 and Figure 5.34) where opaque DBX-CO$_2$Me gels have thicker fibres than the transparent DBS-CO$_2$Me gels. For all the monomers that have a hydroxyl group in the structure, hydroxybutyl methacrylate (HBMA - monomer 4), 2-hydroxyethyl acrylate (HEA - monomer 8), and hydroxypropyl acrylate (HPA – monomer 15), only the di-esters, DBX-CO$_2$Me and DBS-CO$_2$Me acted as gelators.
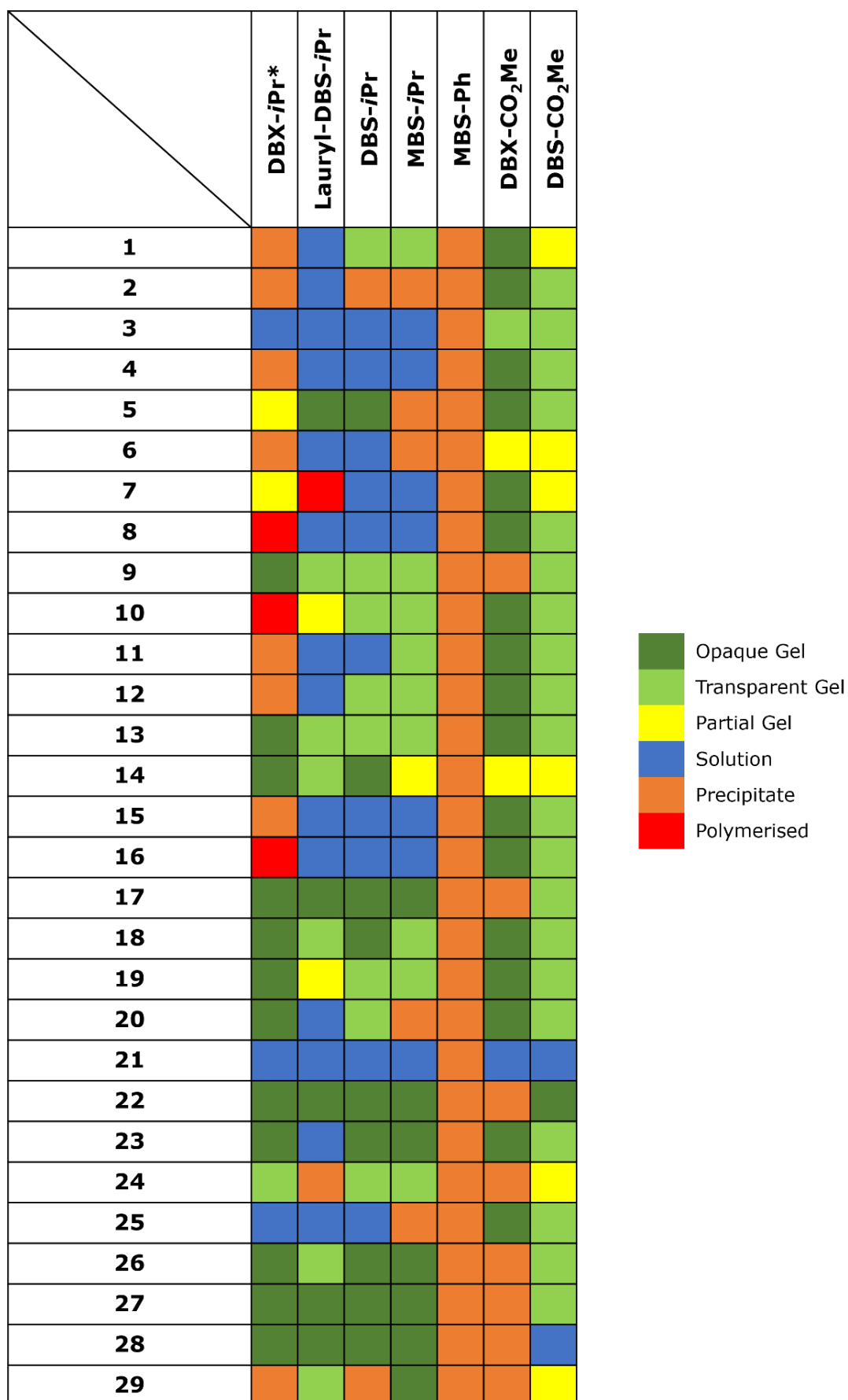
Figure 5.24 | Gelation screening of UV curable monomers at 10 mg mL^{-1} upon heating and cooling. *DBX-iPr was carried out at 20 mg mL^{-1}.

Free-radical polymerisation was initiated during the heating cycle for some gelator-monomer samples, leading to polymerised samples. Only the poorest gelators for the monomers, DBX-*i*Pr and Lauryl-DBS-*i*Pr, initiated free-radical polymerisation, where four formed solid samples. The reasons for this behaviour (initiation) are unclear at present.

5.4.1 Thermal stability and FTIR of UV-curable monomer gels

The thermal stability of a gel is defined as the ability of the gel network material to resist breaking down under heat stress and maintain its mechanical properties.[189] The thermal stability is illustrated by the gel-to-solution phase transition at temperature, T_{gel}. It is the maximum temperature the material can be termed a 'gel'. The most common characterisation method for measuring the T_{gel} of a material is the "dropping ball method".[190] This approach uses a small ball placed on top of the gel's upper surface at the air-gel interface. The gel temperature will then be increased slowly until the gel transforms into a solution, and the ball sinks until it touches the bottom of the vial (Figure 5.25).
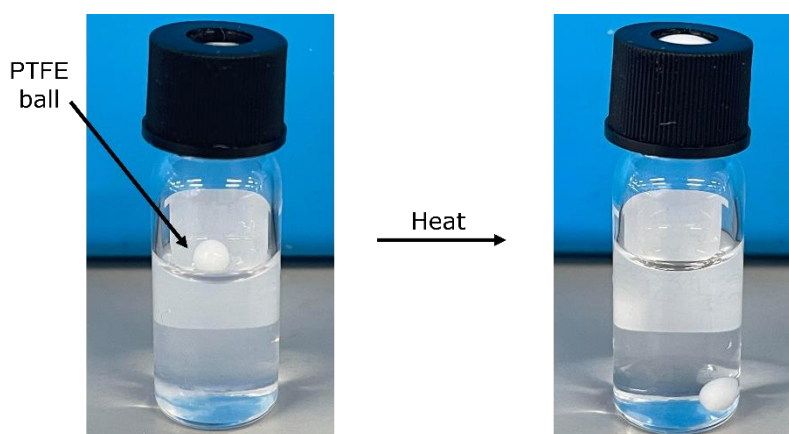
Figure 5.25 | "dropping ball method" for T_{gel} measurement

The thermal stabilities of the UV-curable monomer gels were determined using the "dropping ball method". We used a small polytetrafluoroethylene (PTFE) ball for this technique, placing it in the middle of the gel surface. The vial was placed in a paraffin oil bath, and the temperature was increased by 5 °C/min. The temperature at which the ball touches the bottom of the vial was recorded as T_{gel} (Table 5.6).

Even at a higher concentration of 20 mg mL^{-1}, DBX-*i*Pr shows the worst thermal stability out of all the UV-curable gels. Despite the big molecular structure difference of Lauryl-DBS-*i*Pr and DBS-*i*Pr, the T_{gel} values of the formed gels are not far from each other. The MBS-*i*Pr gels are more thermally stable than the first three gelators mentioned – presumably, this result is because the amount of hydroxyl groups in MBS-*i*Pr is twice that in DBS-*i*Pr and four times that in DBX-*i*Pr and Lauryl-DBS-*i*Pr. This reality means more

possibilities of forming hydrogen bonds with the monomers (see FTIR in Figure 5.26). In addition, DBX-CO$_2$Me, which has only one hydroxyl group in its molecular structure, shows similar or even slightly better thermal stability than MBS-*i*Pr. The possible reason behind this is that DBX-CO$_2$Me has the most rigid benzylidene substituent, which creates a better packing of the gelator molecules. The importance of a hydroxyl group and a rigid substituent is established by the T$_{gel}$ values obtained from DBS-CO$_2$Me gels. DBS-CO$_2$Me has an extra carbon that attaches a hydroxyl group that DBX-CO$_2$Me does not have. All the DBS-CO$_2$Me gels needed temperatures higher than 102 °C before all/most of the fibre network collapses and turns the gel into a solution. DBS-CO$_2$Me gels, therefore, have the best thermal stability property.

Measuring the T$_{gel}$ value of DBS-CO$_2$Me in monomer 3 led to free-radical polymerisation due to the high temperature. The T$_{gel}$ measurement for this specific gel was repeated three times, and all the replicates ended up with a solid polymer sample. At about 140 °C, the material was noticed to had turned solid.

Table 5.6 | T$_{gel}$ of UV-curable gels

| | T$_{gel}$ / °C | | | | | |
	DBX-*i*Pr*	Lauryl-DBS-*i*Pr	DBS-*i*Pr	MBS-*i*Pr	DBX-CO$_2$Me	DBS-CO$_2$Me
1			78	101	110	
2					102	126
3					90	Polymerised
4					118	129
5		64	73		70	141
6						
7					105	
8					89	102
9	67	67	74	98		144
10			55	85	116	135
11				80	128	144
12			63	75	108	119
13	75	75	90	98	111	172
14	47	57	69			
15					85	105
16					89	141
17	99	99	95	127		149
18	84	84	83	108	89	167
19	57		82	105	123	149
20	35		32		110	152
21						
22	76	105	104	124		176
23	55		33	97	134	130
24	56		64	105		
25					119	131
26	71	78	91	119		125
27	42	121	101	118		177
28	85	99	107	131		
29		100		132		

■ < 40 °C   ■ 41 – 60 °C   ■ 61 – 80 °C   ■ 81 – 100 °C   ■ 100 – 130 °C   ■ > 130 °C

FTIR was used to investigate the effect of the intermolecular and intramolecular interactions between the -OH groups in the molecules as well as the solvent that might contribute to the stabilisation of the self-assembled 3D network. As mentioned in chapter

two, the intermolecular and the intramolecular hydrogen bonds for the -OH groups appear in the range 3200-3550 cm^{-1} and 3400-3590 cm^{-1}, respectively.[125] The FTIR data of all samples (except DBX-CO$_2$Me) had peaks between 3250 – 3350 cm^{-1} (Figure 5.26) which are given to be the intermolecular hydrogen bonding of the -OH groups in the molecules; therefore, similar to the results displayed by DBS-*i*Pr and MBS-*i*Pr in chapter two, the intermolecular hydrogen bonding is one of the driving forces for self-assembly of the gelators in PiBnA and CHMA. DBX-CO$_2$Me has distinctive FTIR peaks between 3400 – 3590 cm^{-1}, hinting that the intramolecular hydrogen bonding in the O-H covalent bond of the DBX-CO$_2$Me molecule is stronger than the intramolecular hydrogen bonding in the rest of the gelators in iBnA and CHMA.

Furthermore, the intensities of the -OH peaks are higher in CHMA for the xerogels formed from the dibenzylidene sorbitol gelators, DBS-*i*Pr and DBS-CO$_2$Me. The rest of the gelators, MBS-*i*Pr, DBX-*i*Pr, DBX-CO$_2$Me and Lauryl-DBS-*i*Pr, have O-H stretches with higher intensities in xerogels formed in iBnA than gels formed in CHMA. The higher the intensity of the peak is, the stronger the dipole moment of the O-H stretch is in the xerogel.[128] The stronger the dipole moment of the O-H stretch, the weaker the hydrogen bonding is between the molecules. This phenomenon indicates that the hydrogen bonds formed by DBS-*i*Pr and DBS-CO$_2$Me in CHMA are weaker than those formed by the same gelators in iBnA. This behaviour is the opposite for the rest of the gelators, MBS-*i*Pr, DBX-*i*Pr, DBX-CO$_2$Me and Lauryl-DBS-*i*Pr.

The FTIR spectra of crystalline DBS-*i*Pr and MBS-*i*Pr are plotted together and those of the xerogels of the same gelators in CHMA in Figure 5.27. It is apparent that in the crystalline state, MBS-*i*Pr has a higher O-H stretch intensity than the DBS-*i*Pr in the crystalline form, which was expected because MBS-*i*Pr has more hydroxyl groups (four) than DBS-*i*Pr (two). However, incorporating the same gelators into CHMA, the xerogels displayed very similar intensities, meaning, during self-assembly in CHMA, the O-H dipole moment and the hydrogen bonds formed have similar strength in both gelators. With the IR data obtained, it is safe to conclude that MBS-*i*Pr gels are more thermally stable than DBX-*i*Pr, Lauryl-DBS-*i*Pr and DBS-*i*Pr not because it has stronger hydrogen bonds but because it has formed more hydrogen bonds during self-assembly due to having more hydroxyl groups in the gelator molecule. Furthermore, the solubility of the gelator into the solvent also plays a role in the gels' thermal stability, which must then be considered.
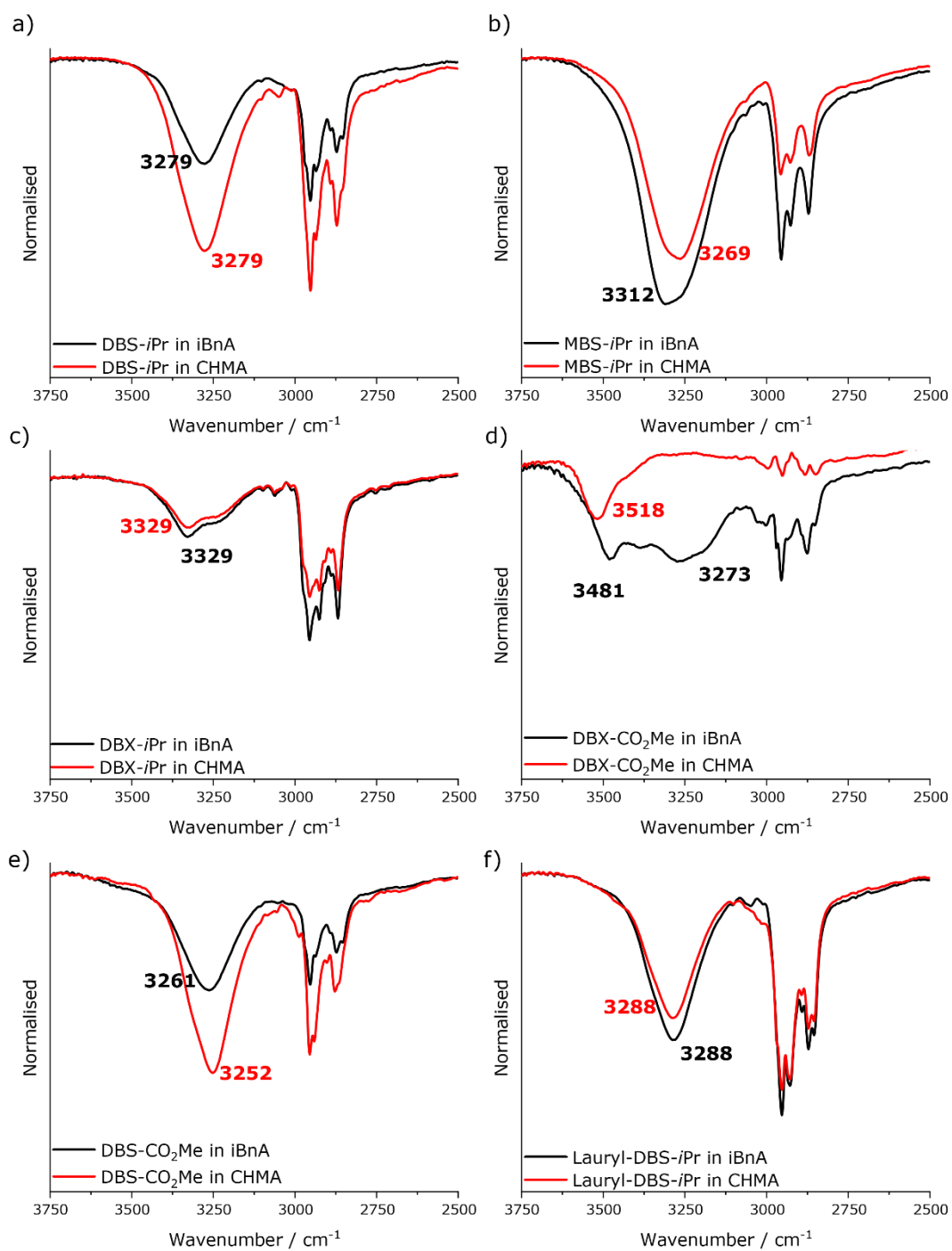
Figure 5.26 | IR spectra for a) DBS-*i*Pr, b) MBS-*i*Pr, c) DBX-*i*Pr, d) DBX-CO$_2$Me, e) DBS-CO$_2$Me and f) Lauryl-DBS-*i*Pr in iBnA (black) and CHMA (red)
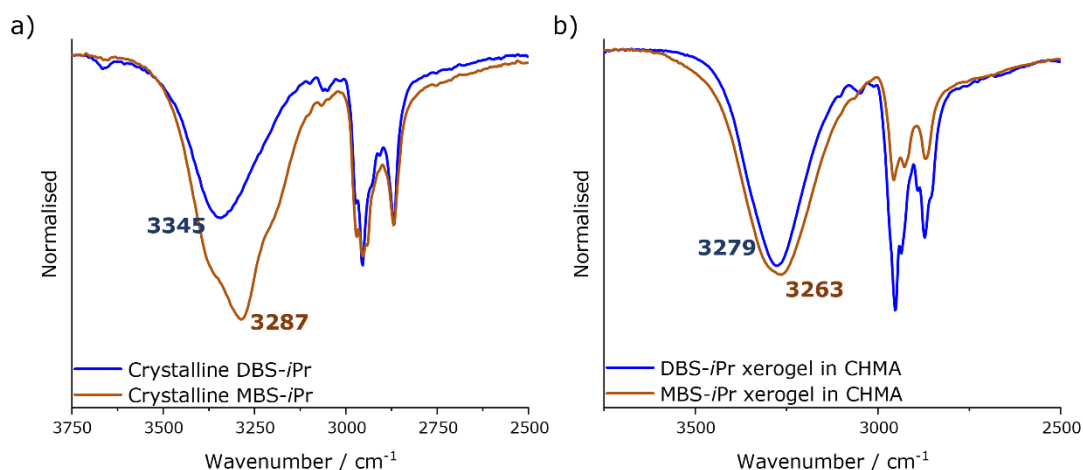
Figure 5.27 | IR spectra of a) crystalline and b) xerogels in CHMA of DBS-*i*Pr (blue) and MBS-*i*Pr (orange)

5.4.2 Photopolymerisation and dynamic mechanical analysis of UV-cured gels

The monomers and the monomer gels were cured the same way as the first attempt in polymerising the ethyl acrylate gels. ELEGOO Mercury Curing Machine with a 25 W, 405 nm UV light was used with two photoinitiators: ethyl 4-(dimethylamino)benzoate (EDB) and 2,4-diethyl-9H-thioxanehen-9-one (DETX). The monomers on their own were examined to see which of them initiated radical polymerisation and cured the quickest. For each sample, 3 mg of each photoinitiator were placed into a vial with 10 mg of gelator, 1 mL of monomer was added into the vial and was heated up until all solid dissolves. The solution was transferred into the mould, where it was left for 10 minutes for the gel network to form. The ABS mould with the gel was then placed onto the curing machine to photopolymerise (Figure 5.28).
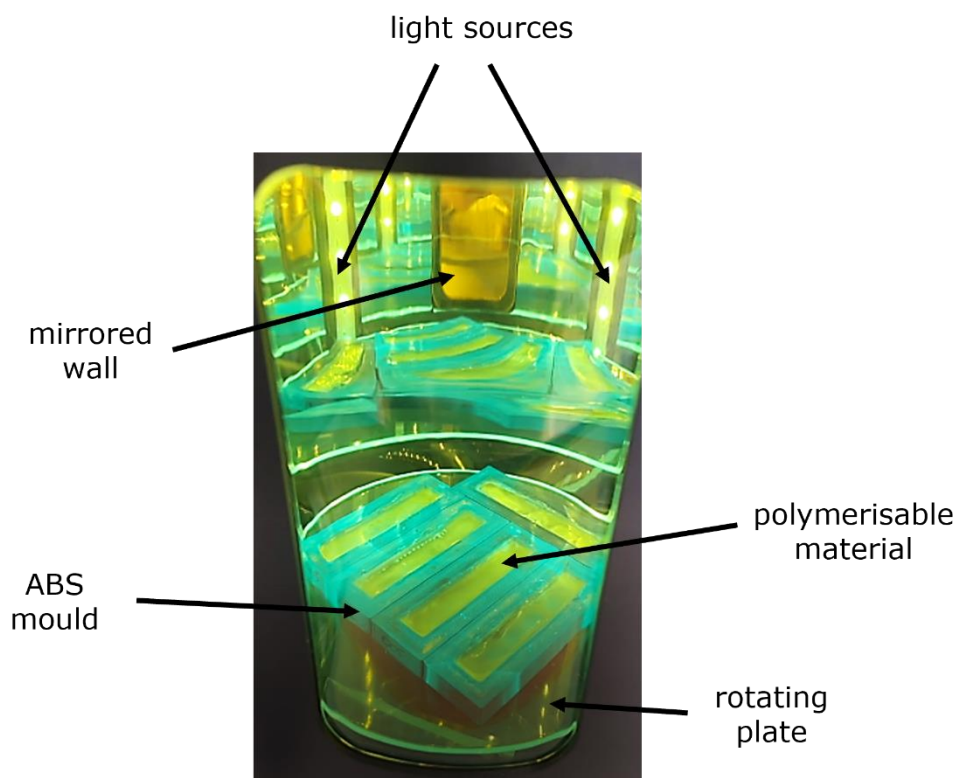
Figure 5.28 | Polymerisation of UV-curable gels

Isobornyl acrylate (monomer 13) and cyclohexyl methacrylate (monomer 18) were the two monomers that formed gels in most of the incorporated gelators (six out of seven); therefore, these monomer gels were the focus for photopolymerising. Using the method of radical polymerisation mentioned above, the formed polymer materials, poly (isobornyl acrylate) (PiBnA) and poly (cyclohexyl methacrylate) (PCHMA), established hard and rigid dual-network materials. Furthermore, 2-hydroxyethyl acrylate (HEA - monomer 8) gels and ethylene glycol dicyclopentenyl ether acrylate (EGdCEA - monomer 9) gels were also polymerised using the same polymerisation reaction. In 2017, Pilkington *et al.*[191] designed and demonstrated the use of star-shaped poly (2-hydroxyethyl acrylate) (PHEA) nanostructures for promoting aggregation while improving the toxicity of human islet amyloid polypeptide (IAPP), where the peptide was involved in glycemic control and the pathology of type 2 diabetes. In addition, poly (ethylene glycol dicyclopentenyl ether acrylate) (PEGdCEA) has been useful in anti-bacterial films and coatings.[192–195] The materials formed by PHEA and PEGdCEA (Figure 5.29 – images of DBS-CO$_2$Me in PEGdCEA to represent all PEGdCEA materials) are soft and relatively flexible in comparison to the PiBnA and PCHMA materials. The infrared spectra of the materials were taken to quantitatively ensure that polymerisation was successful (A 75 – FTIR spectra of iBA and PiBA to represent how the materials are quantitatively observed for polymerisation).

| before bending | backward bending | forward bending | after bending |
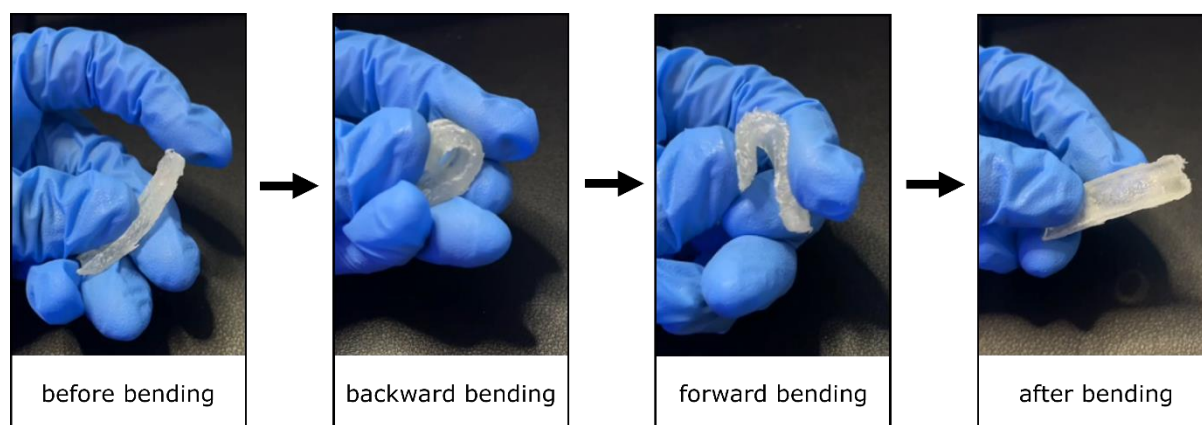
Figure 5.29 | DBS-CO$_2$Me in PEGdCEA

The Perkin Elmer DMA 8000 was used for the dynamic mechanical analysis of the materials. The PiBnA and PCHMA are more rigid than the PEA materials, so the "Dual-Cantilever" programme was used. The applied strain is 0.20 mm, with a frequency of 1.0 Hz at 24 °C for 1 min (Figure 5.30).

Figure 5.30 | Dual-cantilever programme for DMA analysis. Material on image: DBS-*i*Pr in PiBnA

Both PiBnA and PCHMA show viscoelastic mechanical properties and have storage modulus with about four magnitudes more than PEA. However, the DMA results for the materials did not deliver the outcomes that were expected. The addition of gelators onto the material decreases the storage modulus of the polymer (Figure 5.31). The storage modulus of PiBnA decreased an order of magnitude when DBX-CO$_2$Me was incorporated, which was not the same with PCHMA. In contrast, the storage modulus of PCHMA also decreased an order of magnitude when DBX-*i*Pr was combined, which again was not the same with PiBnA. This phenomenon shows that the incorporated gelators affect the polymer materials differently. The fact that no trend is seen from the DMA results means that the fibre

structures' nature and interconnection vary, which is the effect of the interactions between the gelator and monomer molecules forming the dual-network material.

With a direct comparison of the polymer materials, the storage modulus of PCHMA is at least 6000 MPa more than PiBnA, and therefore PCHMA is a stronger material. Interestingly, while the addition of gelators into the polymer material decreases the modulus of the material, the addition of DBS-CO$_2$Me to PiBnA increases the material's storage modulus to the same value of PCHMA with ~17000 MPa. This observation might have resulted from two factors: i) the nature of the dual-network fibres formed in the polymer matrix, and ii) the strong interactions between the *iso*-Bornyl group on the monomer and the gelator molecule, DBS-CO$_2$Me.
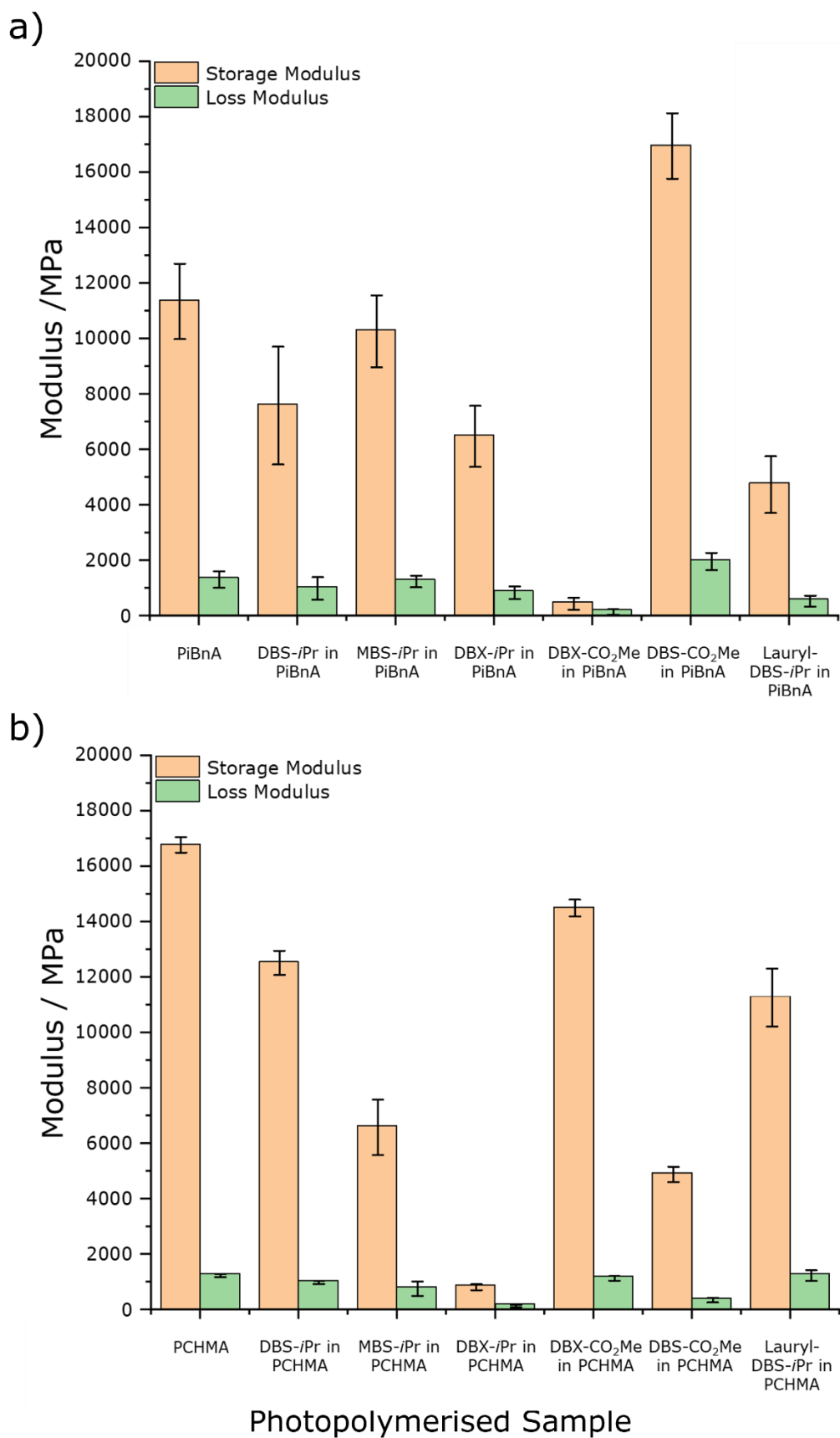
Figure 5.31 | Dynamic mechanical analysis data for a) PiBnA materials and b) PCHMA materials

DMA was also carried out for the PHEA and PEGdCEA materials (Figure 5.32). For PHEA materials, it is evident that polymerising ethyl acrylate around the di-ester gelator molecules formed stronger dual-network materials as they displayed higher storage modulus values. The xylitol derivative, DBX-CO$_2$Me, increased the storage modulus of PHEA by about 3-fold and the sorbitol derivative, DBS-CO$_2$Me, increased the storage modulus of PHEA by approximately 7-fold. With these results, it is secure to conclude that the di-esters are suitable mechanical modifiers when they are involved in forming PHEA polymer matrices comprising dual-network materials.

The results for PEGdCEA materials presented that having the PEDGdCEA polymer matrix around specific gelators (MBS-*i*Pr, DBX-*i*Pr and Lauryl-DBS-*i*Pr) give the composite a higher modulus than the neat polymeric material. However, with the two of the DBS derivatives, DBS-*i*Pr and DBS-CO$_2$Me, the mechanical properties of the materials deteriorate, as seen by the decrease in the value of storage modulus. In addition, obtained results from the DMA of the PEGdCEA materials are unusual and different from the rest of the findings. The loss modulus values of the PEGdCEA materials are higher than the values attained for the storage modulus, except for MBS-*i*Pr in PEGdCEA. The results mean that the viscous property of the material and the energy loss as heat or dissipated during one cyclic load is higher than the energy stored in the elastic structure of the sample. Therefore, whilst all the materials tested show elastic properties (material comes back to its original shape relatively quick), PEGdCEA polymers is less elastic and show anelastic properties (materials takes time to get back to original form) instead. On the other hand, the polymerisation around MBS-*i*Pr increased the material's storage modulus, making it more elastic even though the difference between the storage and loss modulus values is not prominent.
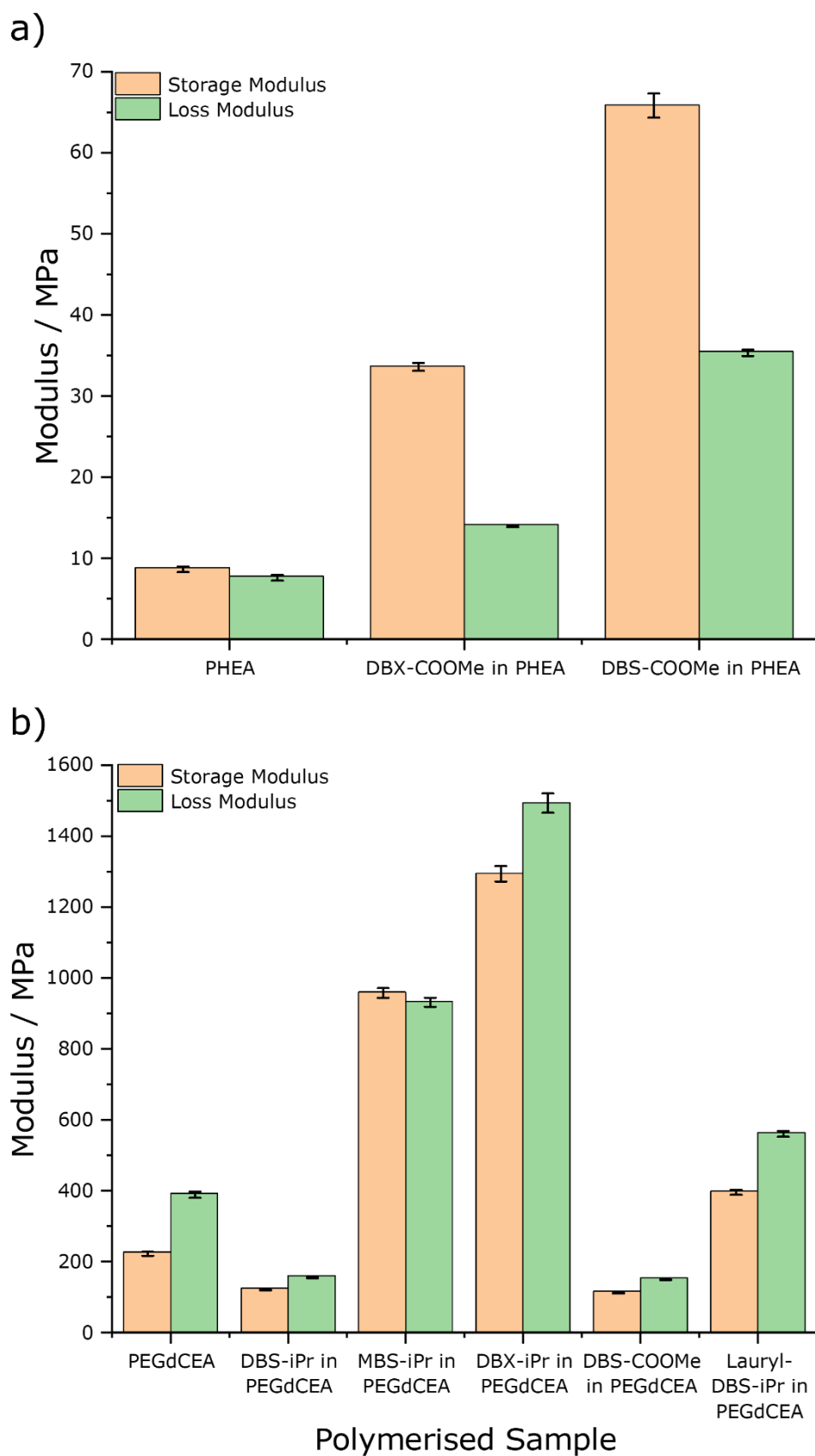
Figure 5.32 | Dynamic mechanical analysis data for a) PHEA materials and b) PEGdCEA materials

5.4.3 Morphologies of monomer gels and dual-network materials

Scanning electron microscopy (SEM) was used to investigate the difference in morphology between the monomer gels and the dual-network materials. Monomer xerogels were prepared by drying the gels on an SEM stub *in vacuo*. Dual-network materials were prepared depending on the property of the material: soft and flexible materials were sliced, whereas the hard and brittle materials were ground using pestle and mortar. These samples were then placed on the SEM stub using adhesive conductive carbon tabs (the sliced materials' cross-sectional area was facing upwards). The stubs were then coated by 5 nm iridium under vacuum before imaging.

The fibre structure of a gelator in iBnA is similar to the fibre structure formed in CHMA from the same gelator (Figure 5.33 and Figure 5.34). The fibre sizes formed in CHMA are relatively thinner than fibres formed in iBnA for the benzylidene sorbitol derivatives compounds (Figure 5.35), and the opposite is true for the benzylidene xylitol derivatives compounds (Figure 5.36).

Like the observed morphologies in chapter two, MBS-*i*Pr xerogels formed very thin fibres (Figure 5.33c and d) compared to DBS-*i*Pr xerogels (Figure 5.33a and b). MBS-*i*Pr have fibre width sizes in iBnA and CHMA of approximately 17 ± 0.40 and 14 ± 0.37 nm, respectively; whereas, DBS-*i*Pr have fibre width sizes of 26 ± 0.58 and 26 ± 0.63 nm in iBnA and CHMA, respectively. Furthermore, DBS-CO$_2$Me also formed thin xerogel fibres of 22 ± 0.38 and 20 ± 0.49 nm (Figure 5.34i and j). The gelator with a long chain, Lauryl-DBS-*i*Pr, show a minuscule increase in the fibre sizes in both iBnA with 30 ± 0.66 nm but still have similar width sizes in CHMA with sized of approximately 18 ± 0.37 nm (Figure 5.35).

On the other hand, it is evident that the fibres formed by the dibenzylidene xylitol derivatives, DBX-*i*Pr and DBX-CO$_2$Me, are wider and broader than the rest of the xerogels. Comparing the two, DBX-CO$_2$Me has fibre widths of approximately 540 ± 21 and 1130 ± 47 nm in monomers iBnA and CHMA, respectively, which is wider than DBX-*i*Pr in the same solvents with around 140 ± 4.2 and 920 ± 52 nm, respectively (Figure 5.36). It is also evident that the gels formed in CHMA formed thicker fibres than gels formed in iBnA.
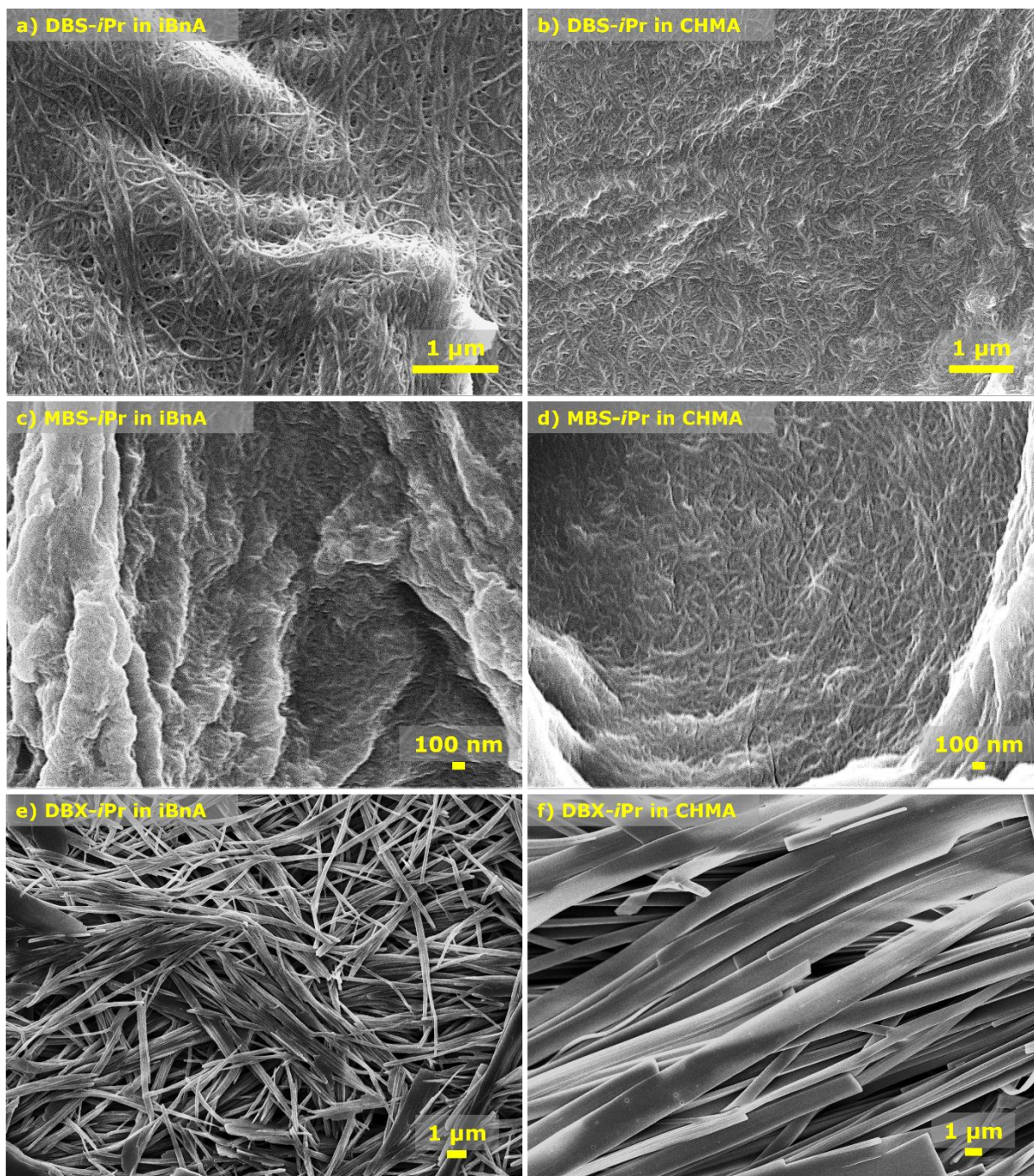
Figure 5.33 | SEM micrographs of xerogels formed from a) DBS-*i*Pr in iBnA, b) DBS-*i*Pr in CHMA, c) MBS-*i*Pr in iBnA, d) MBS-*i*Pr in CHMA, e) DBX-*i*Pr in iBnA and f) DBX-*i*Pr in CHMA. Conditions: xerogels were prepared from evaporating the gel on an SEM stub, then coating with 5 nm Ir before imaging under vacuum at 5 kV. Scale bar represents: 1 µm for a), b), e) and f); 100 nm for c) and d)
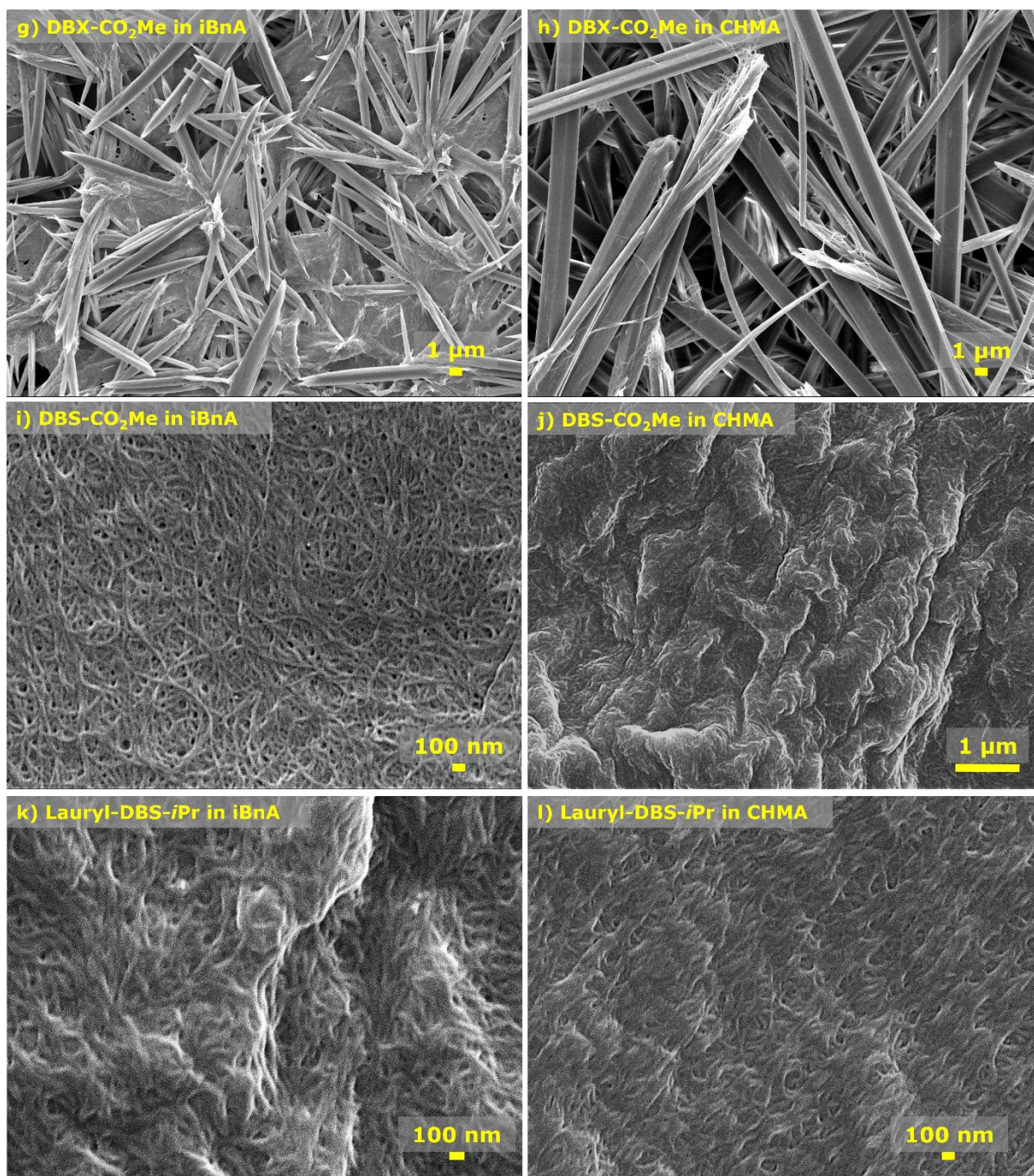
Figure 5.34 | SEM micrographs of xerogels formed from g) DBX-*i*Pr in iBnA, h) DBX-*i*Pr in CHMA, i) DBS-CO$_2$Me in iBnA, j) DBS-CO$_2$Me in CHMA, k) Lauryl-DBS-*i*Pr in iBnA and l) Lauryl-DBS-*i*Pr in CHMA. Conditions: xerogels were prepared from evaporating the gel on an SEM stub, then coating with 5 nm Ir before imaging under vacuum at 5 kV. Scale bar represents: 1 µm for g), h) and j); 100 nm for i), k) and l)
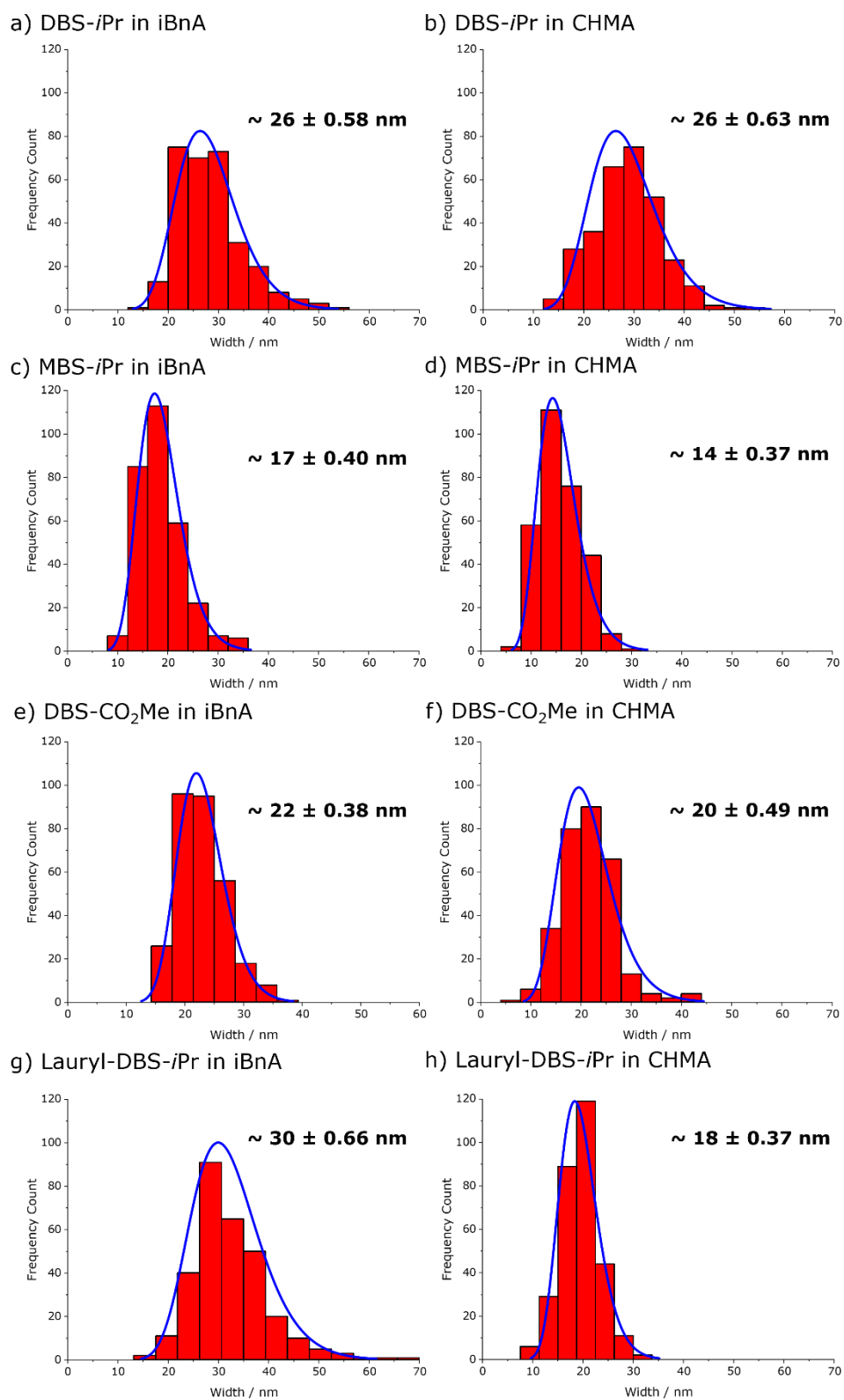
Figure 5.35 | Histograms for the xerogel fibres of benzylidene sorbitol derivatives: a) DBS-*i*Pr in iBnA, b) DBS-*i*Pr in CHMA, c) MBS-*i*Pr in iBnA, d) MBS-*i*Pr in CHMA, e) DBS-CO$_2$Me in iBnA, f) DBS-CO$_2$Me in CHMA, g) Lauryl-DBS-*i*Pr in iBnA and h) Lauryl-DBS-*i*Pr in CHMA

a) DBX-*i*Pr in iBnA

b) DBX-*i*Pr in CHMA
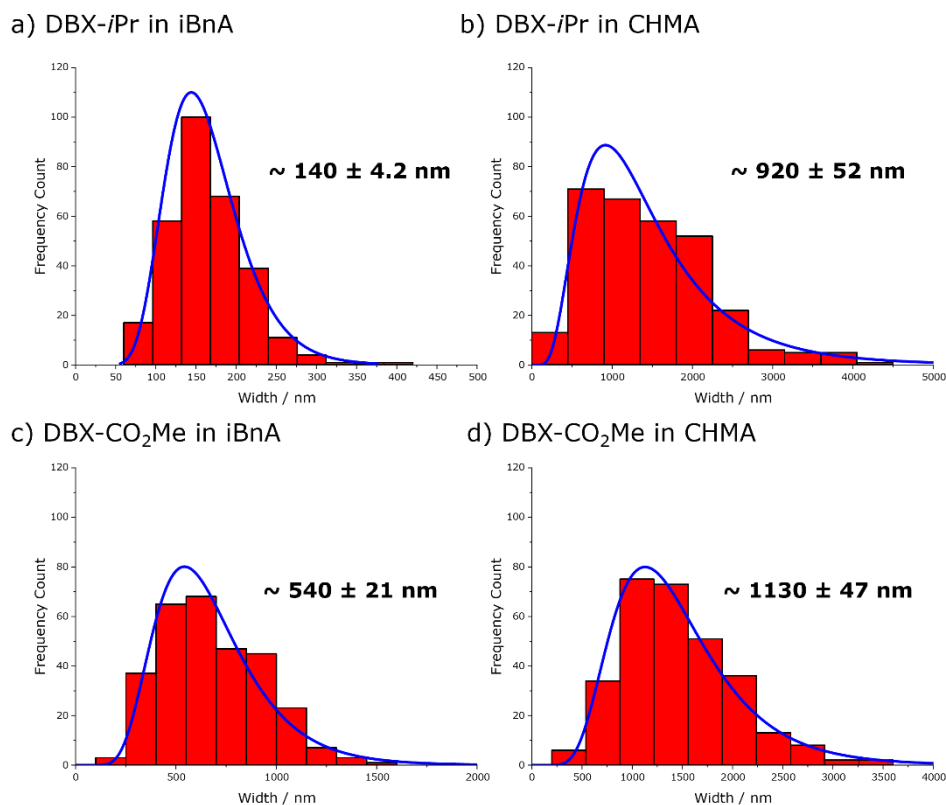
c) DBX-CO$_2$Me in iBnA

d) DBX-CO$_2$Me in CHMA

Figure 5.36 | Histograms for the xerogel fibres of benzylidene xylitol derivatives: a) DBX-*i*Pr in iBnA, b) DBX-*i*Pr in CHMA, c) DBX-CO$_2$Me in iBnA, and d) DBX-CO$_2$Me in CHMA.

SEM micrographs for the PiBnA and PCHMA materials were also obtained (Figure 5.37 and Figure 5.38). The structure of PiBnA and PCHMA is similar to the PEA material's morphology from the previous section – the polymer matrix shows a crumpled and wrinkled surface on the material. The polymerised materials around 1% w/v gelators (2% w/v for DBX-*i*Pr) maintain the crumpled-like surfaces but display various fibre structures on the surface, proving that there are two systems in the material. The fibre morphology in the material depends on the gelator and the polymer. There are long thin fibres sitting on top of the crumpled surface seen from DBS-*i*Pr, DBX-*i*Pr, DBX-CO$_2$Me, DBS-CO$_2$Me and Lauryl-DBS-*i*Pr in PCHMA and MBS-*i*Pr and DBX-CO$_2$Me in PiBnA. The rest of the materials seem to have an additional structure beneath the crumpled surface that generated bulges and lumps on the polymer matrix.
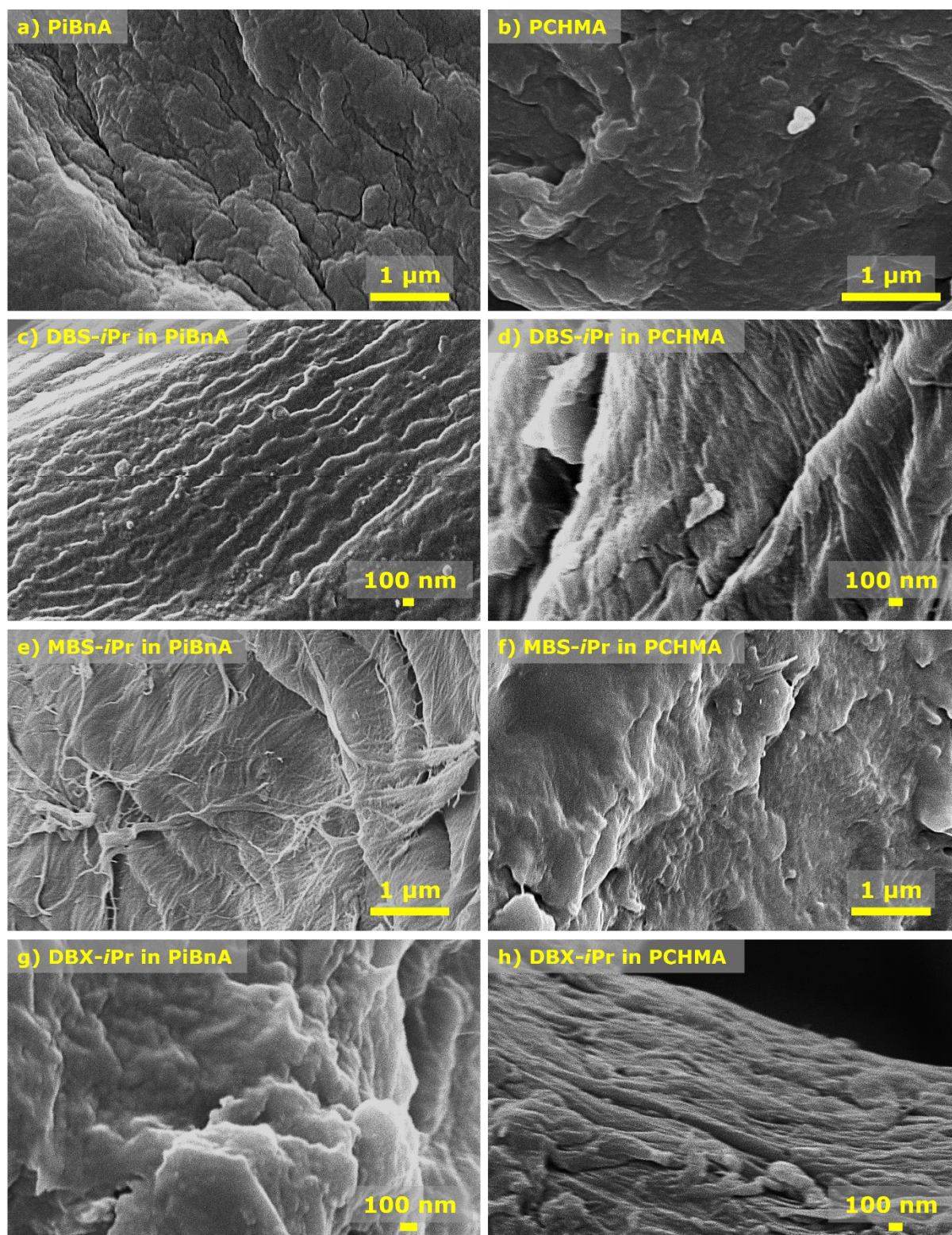
Figure 5.37 | SEM micrographs of a) PiBnA, b) PCHMA, c) DBS-*i*Pr in PiBnA, d) DBS-*i*Pr in PCHMA, e) MBS-*i*Pr in PiBnA, f) MBS-*i*Pr in PCHMA, g) DBX-*i*Pr in PiBnA and h) DBX-*i*Pr in PCHMA. Conditions: polymers were prepared by slicing the material and placing it on an SEM stub, then coating it with 5 nm Ir before imaging under vacuum at 5 kV. Scale bar represents: 1 μm for a), b), e) and f); 100 nm for c), d), g) and h).
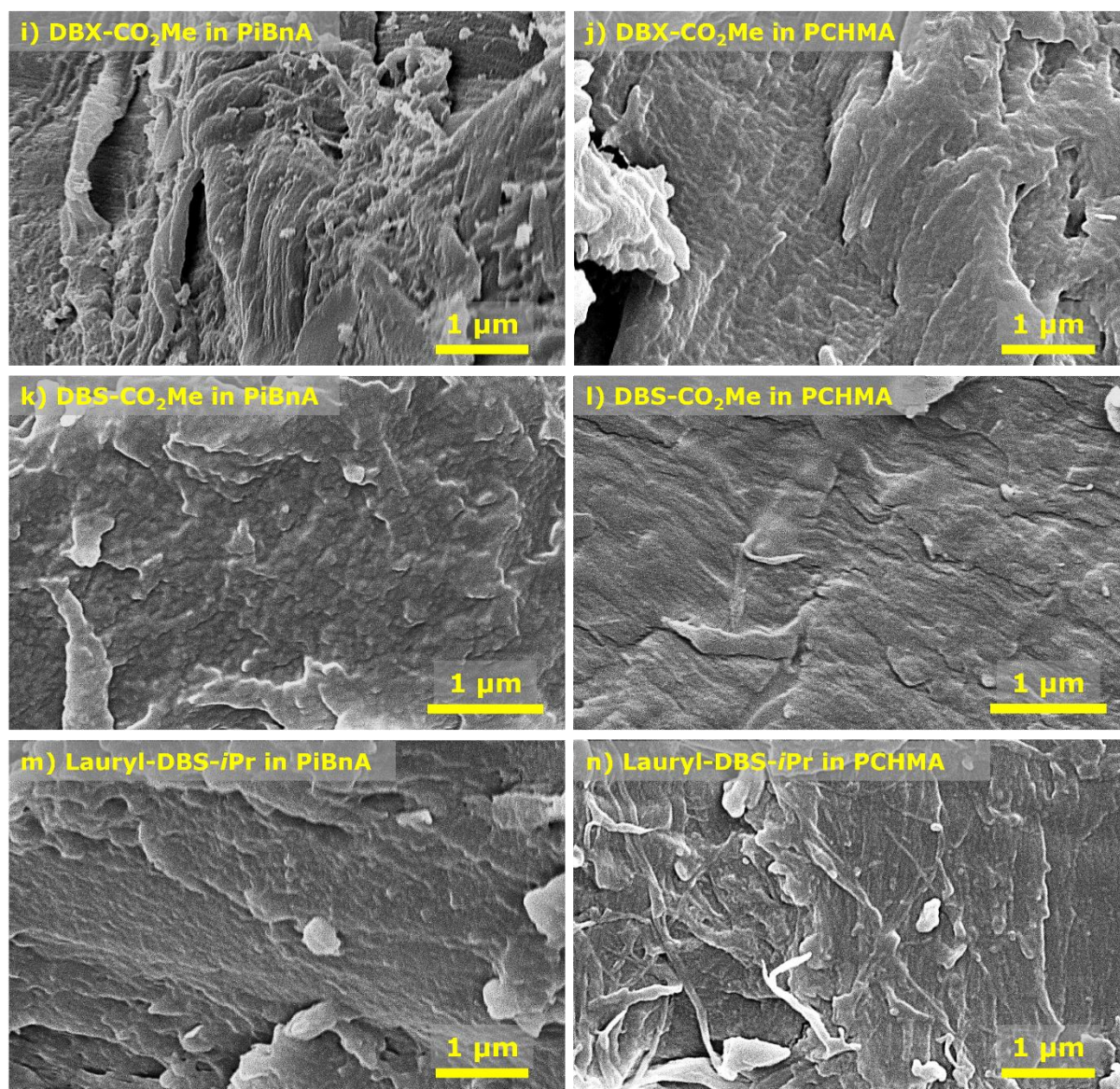
Figure 5.38 | SEM micrographs of i) DBX-CO₂Me in PiBnA, j) DBX-CO₂Me in PCHMA, k) DBS-CO₂Me in PiBnA, l) DBS-CO₂Me in PCHMA, m) Lauryl-DBS-*i*Pr in PiBnA, and n) Lauryl-DBS-*i*Pr in PCHMA. Conditions: polymers were prepared by slicing the material and placing it on an SEM stub, then coating it with 5 nm Ir before imaging under vacuum at 5 kV. Scale bar represents: 1 µm for all micrographs

5.5   Dual-Network Gel for reactive inkjet 3D printing

Referring to chapter 3, DBX-CO$_2$H behaved as a hydrogelator by switching the pH of the solution from 11 to 4. To recap, the gelator was dissolved by adding aqueous NaOH solution forming the sodium carboxylate form of the compound (DBX-COO$^-$Na$^+$) with a pH value in the solution of 11. The salt solution formed a gel after the addition of 2.0 equivalents of the acidification agent. The acidification agents tested from chapter 3 were glucono-*d*-lactone (GdL) and hydrochloric acid (HCl). GdL slowly lowers the pH of the solution to 4; therefore, the solution gels gradually, whereas HCl is the opposite. DBX-CO$_2$H instantly forms a gel when HCl is added to the solution. Instantaneous gelation is

more ideal than slow gelation for 3D printing applications because patterns are normally printed layer-by-layer for good resolution. However, HCl is a corrosive and toxic acid even at low concentrations. A naturally occurring acid, citric acid, was tested with DBX-CO$_2$H for gelation test:

- 10 mg of DBX-CO$_2$H was dissolved in 100 μL of 0.5 M NaOH
- 900 μL of water added
- 15% (150 μL) of citric acid added

The final concentrations of the constituents in the gels are 10 mg mL^{-1} for DBX-CO$_2$H, 0.05 M NaOH and 0.13 M citric acid. Following the steps mentioned above, the solution gels instantly.

The effect of DBX-CO$_2$H gelation with monomers in water to form a dual-network material was explored. Few alkene monomers are miscible with water, but 2-hydroxyethyl acrylate (HEA), 2-hydroxyethyl acrylamide (HEAm) and 2-hydroxymethyl acrylate (HEMA) (Figure 5.39) are excellent candidates.
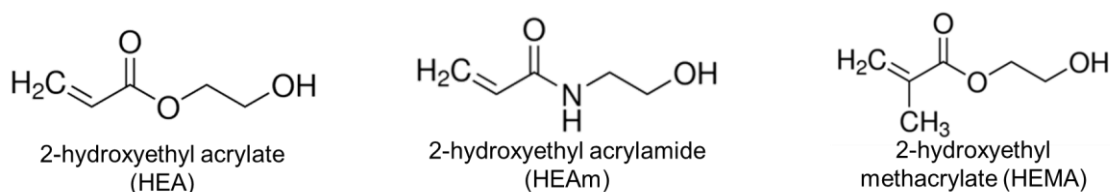

Figure 5.39 | Few monomers that are miscible with water

The first monomer:H$_2$O solvent gelation test was with 1:1 HEA:H$_2$O (50% HEA), which have the following steps:

- 10 mg of DBX-CO$_2$H was dissolved in 100 μL of 0.5 M NaOH
- 400 μL of water added
- 500 μL of HEA added
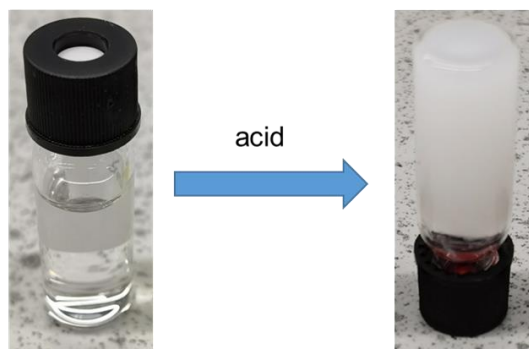- 15% (150 μL) of citric acid added

Figure 5.40 | Instant gelation of 50:50 HEA:H_2O when 15% citric acid is added

Successful instantaneous gelation was seen after adding citric acid to the 50% HEA gelator solution Figure 5.40. The range of HEA percentage for the test was increased from 30% HEA to 70%, and all the tested HEA:H_2O ratios have formed opaque gels. Therefore, the gelator was tested with the rest of the water-miscible monomers mentioned in Figure 5.39. DBX-CO_2H formed opaque gels in all the tested monomer:H_2O ratios using the pH switch approach (Table 5.7).

Table 5.7 | Gelation test for DBX-CO_2H in water miscible monomer and water ratios. G = gel, P = precipitate, S = solution, (O) – opaque, (T) = transparent

	monomer percentage / %				
	30	**40**	**50**	**60**	**70**
HEA	G (O)	G (O)	G (O)	G (O)	G (O)
HEAm	G (O)	G (O)	G (O)	G (O)	G (O)
HEMA	G (O)	G (O)	G (O)	G (O)	G (O)

The pH reading of the solutions was taken to see the differences in the acidity of the solvents. HEA is the most acidic with a pH of 4.50, followed by HEAm with a pH value of 4.98, and then the least acidic is HEMA with a pH of 5.59. The monomer:H_2O solutions' pH was also collected to see the change in pH when the system is in sol state or gel state (Table 5.8).

As mentioned earlier, the pH switch of the gelation without the monomer (100% H_2O) is from pH 11 to pH 4. Having a monomer in the system decreases the reference pH of 11 to about pH 7-8. The addition of 15% citric acid lowers the pH of the solvent medium to about 4-5, which is similar to the usual value for the pH switch type of gelation in literature.[15,160]

Table 5.8 | pH reading of the aqueous monomer solutions and samples solutions

	monomer percentage / %				
	30	**40**	**50**	**60**	**70**
HEA	3.70	3.72	3.89	4.06	4.34
HEAm	3.96	4.19	4.29	4.40	4.57
HEMA	5.10	5.15	5.40	5.75	6.07
1.0 M citric acid	1.39				
1.0 M NaOH	14.0				
HEA:H$_2$O 3:7 + 15% 1.0 M NaOH	7.16				
HEA:H$_2$O 3:7 + 15% 1.0 M NaOH + 15% 1.0 M citric acid	4.02				
HEAm:H$_2$O 3:7 + 15% 1.0 M NaOH	7.39				
HEAm:H$_2$O 3:7 + 15% 1.0 M NaOH + 15% 1.0 M citric acid	4.24				
HEMA:H$_2$O 3:7 + 15% 1.0 M NaOH	8.01				
HEMA:H$_2$O 3:7 + 15% 1.0 M NaOH + 15% 1.0 M citric acid	4.97				

HEA, HEAm and HEMA are monomers that have been used as active diluents for few 3D printing techniques.[196,197] The goal was to use the pH switch gelation technique as a rheological modifier for the monomers in reactive inkjet 3D Printing. The viscosity of HEA is low, and therefore when HEA is printed, the ink flows and does not hold the printed pattern before curing. As the concept is to photopolymerise the HEA, Irgacure 2959 photoinitiator was added, followed by water and gelator to the HEA ink. This formulation improved surface adhesion due to the water molecules properties; therefore, the fluid was more resistant to flow (Figure 5.41a).

For a printed sample to have a better resolution, printing the material layer by layer is essential. Without forming a gel on the printed pattern, printing the material layer by layer will not be possible because the viscosity of HEA is low and, therefore, will not hold the first layer on the printed pattern. It is therefore essential to add the acid ink for the printed pattern to form a gel. Citric acid ink was jetted on top of the 30% HEA gelator ink with the same printed pattern and formed a gel instantaneously (Figure 5.41b).
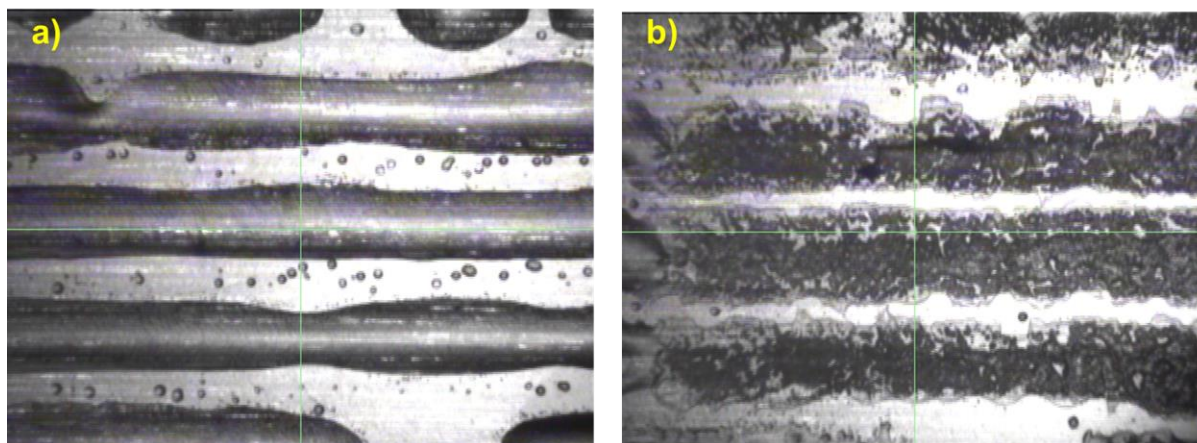
Figure 5.41 | (a) printed pattern of 30% HEA gelator ink; (b) printed pattern after acid ink was jetted on top of the gelator ink

Without optimisation, the shape is not smooth, and there is no specific outline for the printed pattern (Figure 5.42). After optimisation (focused mainly on the substrate, drop spacing, inkjet waveform, droplet formation and printing sequence), the outline of the printed pattern started to show sharp edges, and the gel began to show smoothness relative to the gel before optimisation Figure 5.42.

There is approximately 70% of water in the solvent medium from the gelator ink and the acid ink. The water must evaporate on the first layer before the second later is printed on top. The resolution will decrease if a layer is printed on top of a wet layer because, over time, the water will evaporate and leave air bubbles within the material. If the goal is to have a porous material, air bubbles may be a positive thing. However, in this specific research, we would prefer to have well-packed layers for good resolution. Therefore, the importance of drying each layer before printing the next must always be taken into consideration.
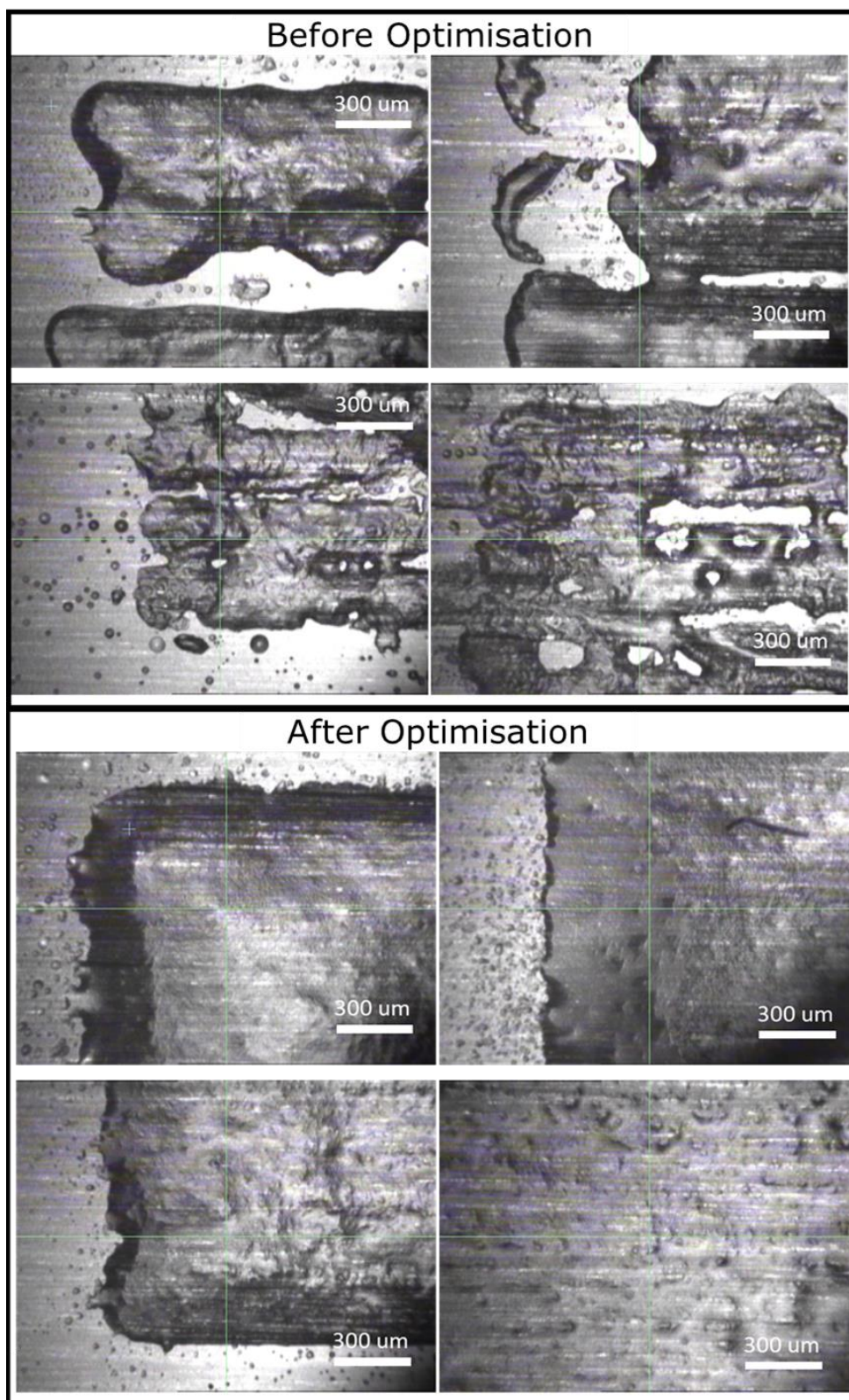
Figure 5.42 | Micrographs of printed pattern 30% HEA DBX-CO$_2$H gelator ink before and after optimisation. Optimisation: substrate, drop spacing, inkjet waveform, droplet formation and printing sequence.

For reactive jetting, 30% HEA gelator ink was printed in a pattern followed by the jetting of acid ink on top of the gelator ink. Printing time is approximately 10 – 15 minutes per layer, depending on the pattern. The printed pattern was a 30-layered and a 15-layered 100 mm^2 samples with two 2 mm x 6 mm rectangle gaps (Figure 5.43 and Figure 5.44).
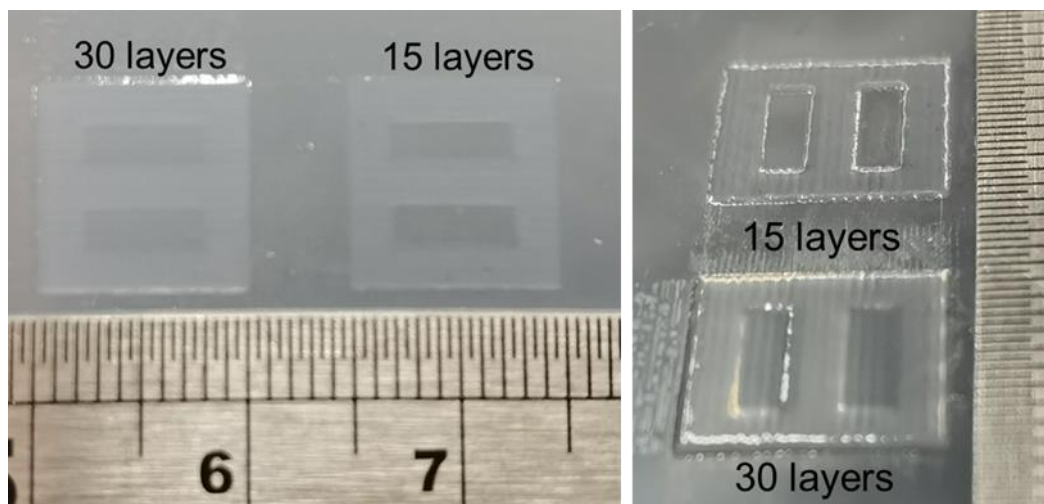
Figure 5.43 | Reactive jetting layer by layer printed pattern with 30% HEA
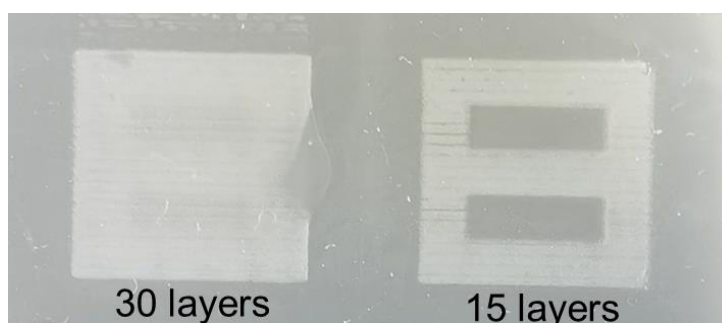
Figure 5.44 | Dried out printed pattern from reactive jetting

The results clearly show that DBX-CO$_2$H is successful in being an excellent rheological modifier for HEA. It allows HEA to be printed using a reactive inkjet 3D printer. It is interesting to cure the dried out printed pattern under the UV lamp to form that dual-network material. Those investigations will be the subject of future work.

Conclusion

Benzylidene sorbitol and xylitol derivatives were successfully isolated in excellent and acceptable yields from green staring materials. Dibenzylidine sorbitol and xylitol derivatives showed gelation properties in organic solvents and ethanol:water mixtures except for the di-acid derivatives. MBS-*i*Pr, on the other hand, can be classified as a hydrogelator that formed gels in water, including salt solutions with various dissolved ions such as Na^+, K^+, Li^+, Ca^{2+}, Zn^{2+}, Mg^{2+}, Cl^-, and SO_4^-. The di-acid derivatives, DBS-CO_2H and DBX-CO_2H, were essentially insoluble in most solvents. However, they exhibited gelation behaviour in DMSO:water mixtures the same with DBX-CO_2Me and DBX-$CONHNH_2$. Making a sodium carboxylate salt with the di-acid derivatives *via* acidifying the solution also forces self-assembly of DBS-CO_2H and DBX-CO_2H, forming a homogeneous or inhomogeneous gel depending on the acidification agent. Unfortunately, the resolution of DBX derivatives to separate the stereoisomers was not successful for the two techniques used.

SEM micrographs showed that DBS-*i*Pr in a non-polar solvent, cyclohexane, resulted in helical fibres. IR results indicated that ethanol and water modified the intramolecular hydrogen bonding between the –OH groups. The difference in solubility of the two gelators, MBS-*i*Pr and DBS-*i*Pr, were apparent; hence we investigated the gelation of the two together as an equimolar multicomponent gel, (DBS-MBS)-*i*Pr. This mixture displayed gelation in all ethanol:water mixtures and at a lower concentration than the single-component system, which indicates that MBS-*i*Pr has a positive influence on the gelation of DBS-*i*Pr and vice-versa. However, co-assembly at the lamellar level does not occur, as indicated by both IR and PXRD results. Instead, the gelators self-sort and possibly layer through interactions of the hydroxyl groups, as indicated in the structural model.

Oscillatory rheology measurements showed that MBS-*i*Pr and the equimolar DBS-MBS-*i*Pr gel self-assembled to a much stronger gel than the DBS-*i*Pr. A possible explanation for this effect is seen in the SEM images, where connections between the lamellae through hydrogen bonding of the sugar hydroxyl groups, already indicated in the IR spectroscopy and supported by the layering of the different gelators shown by the PXRD measurements. The less bulky substituent on the mono-acetal compounds MBS-Van and MBS-Cinn, which did not exhibit any gelation properties from the solvents tested, may allow close packing that provides the crystals. On the other hand, these mono-acetal compounds were characterised by X-ray crystallography. The single-crystal X-ray structures show that both molecules' packing is similar and focuses on the hydrogen bonding between the sugar backbones. These structures provide the first precise supramolecular bonding motifs to this family of compounds. Indeed, IR spectroscopy indicates that hydrogen bonding is

similar in the xerogels and crystals, and PXRD shows a lamellar structure comprising sugar-aromatic reside alternating layers.

The gelation of photocurable monomers was successful. Manipulation *via* shaking of the formed DBX-CO$_2$H and DBX-CO$_2$Me gel in 50:50 DMSO:water showed self-healing properties, evidenced by the thixotropic rheological data. This property is also seen from the gels formed from DBS and DBS-*i*Pr in ethyl acrylate. They showed the ability to recover their 3D network quickly; even without resting the disrupted and destroyed gel, the rheological data shows that it re-generates back immediately to a viscoelastic solid. This phenomenon can also be seen in the SEM micrographs of the xerogels, where the morphology is the same before and after gel disruption.

The formed photocurable gels were photo polymerised to develop dual-network composite materials. The materials possess different mechanical properties; dynamic mechanical analysis (DMA) illustrated that the gelators act as excellent rheological modifiers depending on the photocurable monomer used. The xylitol-based di-acid gelator, DBX-CO$_2$H, showed instant gelation abilities in water-miscible photocurable monomers *via* pH switch. A formulation of DBX-CO$_2$H in 2-hydroxyethyl acrylate(HEA):water improved the surface adhesion and increased the viscosity of HEA. With these results, success was found in identifying a printable photocurable HEA ink for reactive inkjet 3D Printing. After a few optimisations, a pattern was 3D printed layer-by-layer using the di-acid gelator as a significant rheological modifier.

The gelation tests of the compounds have shown that solubility is a significant factor in gelation properties, as in other systems. It is likely that in the multicomponent systems, solubility and effects of the two gelators upon one another's behaviour in solution have a determining effect on the outcome of the assembly, whereby these gels are stronger than the single component gels. Using multicomponent gelling systems in a controlled way could lead to exciting applications in soft materials for personal care products, polymer nucleation/clarification, and energy technology. Finally, the good properties shown by the benzylidene sorbitol and xylitol derivatives make them potential candidates for 3D printing and should be studied for future work.

References

1   P. Dastidar, *Chem. Soc. Rev.*, 2008, **37**, 2699–2715.

2   A. Wynne, M. Whitefield, A. Dixon and S. Anderson, *J. Dermatolog. Treat.*, 2002, **13**, 61–66.

3   M. De Loos, B. L. Feringa and J. H. Van Esch, *European J. Org. Chem.*, 2005, 3615–3631.

4   O. Wichterle and D. Lim, *Nature*, 1960, **185**, 117.

5   A. R. Hirst, B. Escuder, J. F. Miravet and D. K. Smith, *Angew. Chemie - Int. Ed.*, 2008, **47**, 8002–8018.

6   P. J. Flory, *Faraday Discuss. Chem. Soc.*, 1974, **57**, 7–18.

7   P. Terech and R. G. Weiss, *Chem. Rev.*, 1997, **97**, 3133–3160.

8   K. J. Skilling, F. Citossi, T. D. Bradshaw, M. Ashford, B. Kellam and M. Marlow, *Soft Matter*, 2014, **10**, 237–256.

9   N. M. Sangeetha and U. Maitra, *Chem. Soc. Rev.*, 2005, **34**, 821–836.

10   A. M. Ariciu, T. Staicu, M. Micutz, M. V. Neacsu, P. Ionita, V. Tecuceanu, C. Munteanu and G. Ionita, *Appl. Magn. Reson.*, 2015, **46**, 1395–1407.

11   D. J. Abdallah and R. G. Weiss, *Langmuir*, 2000, **16**, 352–355.

12   A. Ajayaghosh, V. K. Praveen and C. Vijayakumar, *Chem. Soc. Rev.*, 2008, **37**, 109–122.

13   W. Zhang, X. Wang, S. Wang, J. Zhao, L. Xu, C. Zhu, D. Zeng, J. Chen, Z. Zhang, D. L. Kaplan and X. Jiang, *Biomaterials*, 2011, **32**, 9415–9424.

14   S. Peng, Q. Guo, P. G. Hartley and T. C. Hughes, *J. Mater. Chem. C*, 2014, **2**, 8303–8312.

15   B. O. Okesola and D. K. Smith, *Chem. Commun.*, 2013, **49**, 11164–11166.

16   G. C. Dizon, G. Atkinson, S. P. Argent, L. T. Santu and D. B. Amabilino, *Soft Matter*, 2020, **16**, 4640–4654.

17   R. V. Ulijn, N. Bibi, V. Jayawarna, P. D. Thornton, S. J. Todd, R. J. Mart, A. M. Smith and J. E. Gough, *Mater. Today*, 2007, **10**, 40–48.

18   B. Gioia, N. Ben Ghalia and P. Kirilov, *J. Pharm. Pharm. Sci.*, 2018, **7**, 1–11.

19   P. K. Vemula and G. John, *Acc. Chem. Res.*, 2008, **41**, 769–782.

20   J. R. Silverman, M. Samateh and G. John, *Eur. J. Lipid Sci. Technol.*, 2016, **118**, 47–55.

21   S. Mukherjee, C. Shang, X. Chen, X. Chang, K. Liu, C. Yu and Y. Fang, *Chem. Commun.*, 2014, **50**, 13940–13943.

22   J. H. Clark, V. Budarin, F. E. I. Deswarte, J. J. E. Hardy, F. M. Kerton, A. J. Hunt, R. Luque, D. J. Macquarrie, K. Milkowski, A. Rodriguez, O. Samuel, S. J. Tavener, R. J. White and A. J. Wilson, *Green Chem.*, 2006, **8**, 853–860.

23   S. Thakur, B. Sharma, A. Verma, J. Chaudhary, S. Tamulevicius and V. K. Thakur, *J. Clean. Prod.*, 2018, **198**, 143–159.

24   K. Prasad, Y. Kaneko and J. I. Kadokawa, *Macromol. Biosci.*, 2009, **9**, 376–382.

25   K. Yabuuchi, E. Marfo-Owusu and T. Kato, *Org. Biomol. Chem.*, 2003, **1**, 3464–3469.

26   N. Basu, A. Chakraborty and R. Ghosh, *Gels*, 2018, **4**, 52.

27   B. O. Okesola and D. K. Smith, *Chem. Soc. Rev.*, 2016, **45**, 4226–4251.

28   H. Svobodová, Nonappa, M. Lahtinen, Z. Wimmer and E. Kolehmainen, *Soft Matter*, 2012, **8**, 7840–7847.

29   K. Basu, N. Nandi, B. Mondal, A. Dehsorkhi, I. W. Hamley and A. Banerjee, *Interface Focus*, 2017, **7**, 1–9.

30   E. Faggi, R. M. Sebastian and A. Valiribera, *Tetrahedron*, 2010, **66**, 5190–5195.

31   X. Cao, Y. Li, Y. Yu, S. Fu, A. Gao and X. Chang, *Nanoscale*, 2019, **11**, 10911–10920.

32   X. Cao, Y. Li, A. Gao, Y. Yu, Q. Zhou, X. Chang and X. Hei, *J. Mater. Chem. C*, 2019, **7**, 10589–10597.

33   D. B. Amabilino, D. K. Smith and J. W. Steed, *Chem. Soc. Rev.*, 2017, **46**, 2404–2420.

34   L. Z. Rogovina, V. G. Vasil'ev and E. E. Braudo, *Polym. Sci. Ser. C*, 2008, **50**, 85–92.

35   M. Kobayashi, T. Nakaoki and N. Ishihara, *Macromolecules*, 1990, **23**, 78–83.

36   A. Saiani and J. M. Guenet, *Macromolecules*, 1997, **30**, 966–972.

37   A. Saiani, *Macromol. Symp.*, 2005, **222**, 37–47.

38   Z. Song, D. Kong, J. Wang, H. Wang, Z. Yang and X. Chen, *Colloids Surfaces B Biointerfaces*, 2010, **80**, 155–160.

39   C. Michon, G. Cuvelier, P. Relkin and B. Launay, *Int. J. Biol. Macromol.*, 1997, **20**, 259–264.

40   K. Y. Lee and D. J. Mooney, *Prog. Polym. Sci.*, 2012, **37**, 106–126.

41   A. R. Nesic and S. I. Seslija, in *Food Packaging*, ed. A. M. Grumezescu, Academic Press, 2017, pp. 637–697.

42   M. Y. Kariduraganavar, A. A. Kittur and R. R. Kamble, in *Natural and Synthetic Biomedical Polymers*, eds. S. G. Kumbar, C. T. Laurencin and M. Deng, Elsevier, Oxford, 2014, pp. 1–31.

43   C. Rochas and M. Rinaudo, *Biopolymers*, 1984, **23**, 735–745.

44   H. L. Hwang, S. R. Jadhav, J. R. Silverman and G. John, *J. Chem. Educ.*, 2014, **91**, 1563–1568.

45   G. John, B. Vijai Shankar, S. R. Jadhav and P. K. Vemula, *Langmuir*, 2010, **26**, 17843–17851.

46   S. Bhattacharya and Y. Krishnan-Ghosh, *Chem. Commun.*, 2001, 185–186.

47   W. Xiong, H. Zhou, C. Zhang and H. Lu, *Chinese Chem. Lett.*, 2017, **28**, 2125–2128.

48   Q. Yu, D. Li, M. Cai, F. Zhou and W. Liu, *Tribol. Lett.*, 2016, **61**, 1–13.

49   J. Chen, C. E. Boott, L. Lewis, A. Siu, R. Al-Debasi, V. Carta, A. A. Fogh, D. Z. Kurek, L. Wang, M. J. Maclachlan and G. Hum, *ACS Omega*, 2020, **5**, 18758–18765.

50   R. Nowak, M. Olech and N. Nowacka, eds. R. R. Watson, V. R. Preedy and S. B. T.-P. in H. H. and D. Zibadi, Academic Press, San Diego, 2014, pp. 1289–1307.

51   J. Bietsch, M. Olson and G. Wang, *Gels*, 2021, **7**, 1–23.

52   S. Datta and S. Bhattacharya, *Chem. Soc. Rev.*, 2015, **44**, 5596–5637.

53   J. H. Jung, G. John, M. Masuda, K. Yoshida, S. Shinkai and T. Shimizu, *Langmuir*, 2001, **17**, 7229–7232.

54   N. Amanokura, Y. Kanekiyo, S. Shinkai and D. N. Reinhoudt, *J. Chem. Soc. Perkin Trans. 2*, 1999, 1995–2000.

55   Z. Khayat and H. Zali-Boeini, *Dye. Pigment.*, 2018, **159**, 337–344.

56   S. I. Tamaru, M. Nakamura, M. Takeuchi and S. Shinkai, *Org. Lett.*, 2001, **3**, 3631–3634.

57   G. John, J. H. Jung, M. Masuda and T. Shimizu, *Langmuir*, 2004, **20**, 2060–2065.

58   B. O. Okesola, V. M. P. Vieira, D. J. Cornwell, N. K. Whitelaw and D. K. Smith, *Soft Matter*, 2015, **11**, 4768–4787.

59   S. Yamasaki, Y. Ohashi, H. Tsutsumi and K. Tsujii, *Bull. Chem. Soc. Jpn.*, 1995, 68, 146–151.

60   B. O. Okesola, V. M. P. Vieira, D. J. Cornwell, N. K. Whitelaw and D. K. Smith, *Soft Matter*, 2015, **11**, 4768–4787.

61   J. Li, K. Fan, X. Guan, Y. Yu and J. Song, *Langmuir*, 2014, **30**, 13422–13429.

62   J. Li, K. Fan, L. Niu, Y. Li and J. Song, *J. Phys. Chem. B*, 2013, **117**, 5989–5995.

63   W. C. Lai and P. H. Huang, *Soft Matter*, 2017, **13**, 3107–3115.

64   E. A. Wilder and J. M. Antonucci, *Macromol. Symp.*, 2005, **227**, 255–263.

65   D. Wang, X. Zhang, Y. Liu, L. Li, Z. Bo, J. Zhou and H. Huo, *Org. Electron. physics, Mater. Appl.*, 2017, **46**, 158–165.

66   D. Knani and D. Alperstein, *J. Phys. Chem. A*, 2017, **121**, 1113–1120.

67   Y. Ohsedo, *Gels*, 2016, **2**, 13.

68   M. J. Meunier, *Ann. Chim. Phys.*, 1891, **22**, 412.

69   J. K. Wolfe, R. M. Hann and C. S. Hudson, *J. Am. Chem. Soc.*, 1942, **64**, 1493–1497.

70   S. J. Angyal and J. V Lawler, *J. Am. Chem. Soc.*, 1944, **66**, 837–838.

71   E. A. Wilder, R. J. Spontak and C. K. Hall, *Mol. Phys.*, 2003, **101**, 3017–3027.

72   W. C. Lai and C. C. Chen, *Soft Matter*, 2014, **10**, 312–319.

73   H. Wang, F. Fang, X. Li, C. Fu and Y. J. Yang, *Chinese Sci. Bull.*, 2012, **57**, 4257–4263.

74   S. S. Sagiri, B. Behera, R. R. Rafanan, C. Bhattacharya, K. Pal, I. Banerjee and D. Rousseau, *Soft Mater.*, 2014, **12**, 47–72.

75   H. Uchiyama, US Pat., 4131612, *US Pat. 4131612*, 1978, 58–60.

76   H. Uchiyama, US Pat., 4483952, *US Pat. 4483952*, 1984.

77   J. D. Cobb III, J. L. Rolen and N. A. Mehl, US Pat., 6127470, *US Pat. 6127470*, 2000.

78   J. D. Cobb III, J. L. Rolen and N. A. Mehl, US Pat., 6338841 B1, *US Pat. 6338841 B1*, 2002.

79   J.-P. Boutique, J. C. T. R. B. S. Laurent, M. Bouilliche, D. A. Beckholt, S. R. Murthy and M. E. Tremblay, US Pat., 8293697 B2, *US Pat. 8293697 B2*, 2012.

80   K. Bernreitner and C. Grein, US Pat., 8207272 B2, *US Pat. 8207272 B2*, 2012.

81   C. A. Lobry de Bruyn and W. Alverda van Ekenstein, *Rec. Trav. Chim.*, 1899, **18**, 150–152.

82   M. L. Wolfrom, W. J. Burke and E. A. Metcalf, *J. Am. Chem. Soc.*, 1947, **69**, 1667–1668.

83   C. S. Kesava Raju, B. Pramanik, R. Ravishankar, P. V. Chalapathi Rao and G. Sriganesh, *RSC Adv.*, 2017, **7**, 37175–37180.

84   K. Bernreitner and C. Grein, US Pat., 4429140 A, *US Pat. 4429140 A*, 1984.

85   K. Bernreitner and C. Grein, US Pat., 2002/0128163 A1, *US Pat. 2002/0128163 A1*, 2002.

86   K. V. Wong and A. Hernandez, *ISRN Mech. Eng.*, 2012, **2012**, 1–10.

87   T. Jungst, W. Smolan, K. Schacht, T. Scheibel and J. Groll, *Chem. Rev.*, 2016, **116**, 1496–1539.

88   N. Shahrubudin, T. C. Lee and R. Ramlan, *Procedia Manuf.*, 2019, **35**, 1286–1296.

89   S. Mirzababaei and S. Pasebani, *J. Manuf. Mater. Process.*, 2019, **3**, 8–12.

90   Z. Liu, Q. Jiang, W. Cong, T. Li and H. C. Zhang, *Int. J. Environ. Sci. Technol.*, 2018, **15**, 2273–2282.

91   Y. L. Yap, C. Wang, S. L. Sing, V. Dikshit, W. Y. Yeong and J. Wei, *Precis. Eng.*, 2017, **50**, 275–285.

92   B. N. Turner, R. Strong and S. A. Gold, *Rapid Prototyp. J.*, 2014, **20**, 192–204.

93   C. R. Rocha, A. R. Torrado Perez, D. A. Roberson, C. M. Shemelya, E. MacDonald and R. B. Wicker, *J. Mater. Res.*, 2014, **29**, 1859–1866.

94   M. Molitch-Hou, in *Additive Manufacturing*, eds. J. Zhang and Y.-G. Jung, Butterworth-Heinemann: Cambridge, 2018, pp. 1–38.

95   N. A. Chartrain, C. B. Williams and A. R. Whittington, *Acta Biomater.*, 2018, **74**, 90–111.

96   L. Ouyang, C. B. Highley, C. B. Rodell, W. Sun and J. A. Burdick, *ACS Biomater. Sci. Eng.*, 2016, **2**, 1743–1751.

97   L. Ouyang, C. B. Highley, W. Sun and J. A. Burdick, *Adv. Mater.*, 2017, **29**, 1–7.

98   L. Shi, H. Carstensen, K. Hölzl, M. Lunzer, H. Li, J. Hilborn, A. Ovsianikov and D. A. Ossipov, *Chem. Mater.*, 2017, **29**, 5816–5823.

99   L. C. Hsiao, A. Z. M. Badruddoza, L. C. Cheng and P. S. Doyle, *Soft Matter*, 2017, **13**, 921–929.

100   R. Suntornnond, J. An and C. K. Chua, *Macromol. Mater. Eng.*, 2017, **302**, 1–15.

101   Z. Zhou, M. Samperi, L. Santu, G. Dizon, S. Aboarkaba, D. Limón, C. Tuck, L. Pérez-García, D. J. Irvine, D. B. Amabilino and R. Wildman, *Mater. Des.*, 2021, **206**, 109792.

102   F. C. Godoi, S. Prakash and B. R. Bhandari, *J. Food Eng.*, 2016, **179**, 44–54.

103   J. Mewis and N. J. Wagner, *Adv. Colloid Interface Sci.*, 2009, **147**–**148**, 214–227.

104   M. C. Nolan, A. M. Fuentes Caparrós, B. Dietrich, M. Barrow, E. R. Cross, M. Bleuel, S. M. King and D. J. Adams, *Soft Matter*, 2017, **13**, 8426–8432.

105   G. Li, Y. Liang, C. Sun, X. Peng, N. Hao, M. Liu, W. Gao, H. Wu and B. He, *Artif. Cells, Nanomedicine Biotechnol.*, 2018, **46**, 683–693.

106   A. Chalard, P. Joseph, S. Souleille, B. Lonetti, N. Saffon-Merceron, I. Loubinoux, L. Vaysse, L. Malaquin and J. Fitremann, *Nanoscale*, 2019, **11**, 15043–15056.

107   L. Wang, X. Jin, L. Ye, A. Y. Zhang, D. Bezuidenhout and Z. G. Feng, *Langmuir*, 2017, **33**, 13821–13827.

108   H. Yang, S. Zhang, K. Liu and Y. Fang, *RSC Adv.*, 2016, **6**, 109969–109977.

109   A. Biswas, S. Malferrari, D. M. Kalaskar and A. K. Das, *Chem. Commun.*, 2018, **54**, 1778–1781.

110   C. B. Highley, C. B. Rodell and J. A. Burdick, *Adv. Mater.*, 2015, **27**, 5075–5079.

111   M. Watase, Y. Nakatani and H. Itagaki, *J. Phys. Chem. B*, 1999, **103**, 2366–2373.

112   J .M. Gardlik, R. V. Burkes, US Pat., 5106999, *US Pat. 5106999*, 1992.

113   J. Song, H. Sun, S. Sun and R. Feng, *Trans. Tianjin Univ.*, 2013, **19**, 319–325.

114 D. J. Cornwell, B. O. Okesola and D. K. Smith, *Soft Matter*, 2013, **9**, 8730–8736.

115 K. Bernreitner and C. Grein, US Pat., 6500964 B2, *US Pat. 6500964 B2*, 2002.

116 G. Giuliani, A. Benedusi, B. Marzani and S. Baroni, US Pat., 20180072698 A1, *US Pat. 20180072698 A1*, 2018.

117 R. Feng, L. Chen, Z. Hou and J. Song, *Trans. Tianjin Univ.*, 2007, 13, 35–41.

118 T. Kobayashi, S. Kitagawa, H. Yagi, K. Fujitani, S. Sakai and T. Hasimoto, *Nippon Kagaku Kaishi*, 1994, 713–718.

119 J. E. Campbell, J. Yang and G. M. Day, *J. Mater. Chem. C*, 2017, **5**, 7574–7584.

120 K. Fan, H. Kong, X. Wang, X. Yang and J. Song, *RSC Adv.*, 2016, **6**, 80934–80938.

121 D. J. Cornwell, O. J. Daubney and D. K. Smith, *J. Am. Chem. Soc.*, 2015, **137**, 15486–15492.

122 J. Li, K. Fan, L. Niu, Y. Li and J. Song, *J. Phys. Chem. B*, 2013, **117**, 5989–5995.

123 J. Raeburn, C. Mendoza-Cuenca, B. N. Cattoz, M. A. Little, A. E. Terry, A. Zamith Cardoso, P. C. Griffiths and D. J. Adams, *Soft Matter*, 2015, **11**, 927–935.

124 E. R. Draper and D. J. Adams, *Chem*, 2017, **3**, 390–410.

125 W. C. Lai and Y. C. Lee, *RSC Adv.*, 2016, **6**, 98042–98051.

126 G. Socrates, *Infrared and Raman characteristic group frequencies: tables and charts*, Wiley, Chichester, U.K., 2001.

127 U. Liddel and E. D. Becker, *Spectrochim. Acta*, 1957, **10**, 70–84.

128 W. B. Person and J. H. Newton, *J. Chem. Phys.*, 1974, **61**, 1040–1049.

129 C. P. Lawrence and J. L. Skinner, *J. Chem. Phys.*, 2003, **118**, 264–272.

130 A. G. Shtukenberg, X. Cui, J. Freudenthal, E. Gunn, E. Camp and B. Kahr, *J. Am. Chem. Soc.*, 2012, **134**, 6354–6364.

131 A. G. Shtukenberg, A. Gujral, E. Rosseeva, X. Cui and B. Kahr, *CrystEngComm*, 2015, **17**, 8817–8824.

132 A. G. Shtukenberg, Y. O. Punin, A. Gujral and B. Kahr, *Angew. Chemie - Int. Ed.*, 2014, **53**, 672–699.

133 B. O. Okesola, V. M. P. Vieira, D. J. Cornwell, N. K. Whitelaw and D. K. Smith, *Soft Matter*, 2015, **11**, 4768–4787.

134   L. L. E. Mears, E. R. Draper, A. M. Castilla, H. Su, Zhuola, B. Dietrich, M. C. Nolan, G. N. Smith, J. Doutch, S. Rogers, R. Akhtar, H. Cui and D. J. Adams, *Biomacromolecules*, 2017, **18**, 3531–3540.

135   G. M. Kavanagh and S. B. Ross-Murphy, *Prog. Polym. Sci.*, 1998, **23**, 533–562.

136   C. Tong, K. Fan, L. Niu, J. Li, X. Guan, N. Tao, H. Shen and J. Song, *Soft Matter*, 2014, **10**, 767–772.

137   A. Vidyasagar, K. Handore and K. M. Sureshan, *Angew. Chemie - Int. Ed.*, 2011, **50**, 8021–8024.

138   F. Lin, X. Zhu, J. Chen and Q. Xu, *CN Pat. 103420811A*, 2013.

139   V. Srikanth, R. B. N. Prasad, Y. Poornachandra, V. S. Phani Babu, C. Ganesh Kumar, B. Jagadeesh and R. C. R. Jala, *Eur. J. Med. Chem.*, 2016, **109**, 134–145.

140   P. McNeice, Y. Zhao, J. Wang, G. F. Donnelly and P. C. Marr, *Green Chem.*, 2017, **19**, 4690–4697.

141   D. A. Tómasson, D. Ghosh, Z. Kržišnik, L. H. Fasolin, A. A. Vicente, A. D. Martin, P. Thordarson and K. K. Damodaran, *Langmuir*, 2018, **34**, 12957–12967.

142   J. U. Kim, D. Schollmeyer, M. Brehmer and R. Zentel, *J. Colloid Interface Sci.*, 2011, **357**, 428–433.

143   V. Čaplar, M. Žinić, J. L. Pozzo, F. Fages, G. Mieden-Gundert and F. Vögtle, *European J. Org. Chem.*, 2004, 4048–4059.

144   Z. Shen, T. Wang and M. Liu, *Langmuir*, 2014, **30**, 10772–10778.

145   J. Raeburn and D. J. Adams, *Chem. Commun.*, 2015, **51**, 5170–5180.

146   J. H. Fuhrhop and C. Boettcher, *J. Am. Chem. Soc.*, 1990, **112**, 1768–1776.

147   J. Makarević, M. Jokić, L. Frkanec, V. Čaplar, N. Š. Vujičić and M. Žinić, *Beilstein J. Org. Chem.*, 2010, **6**, 945–959.

148   L. Pasteur, *Ann. Chim. Phys.*, 1848, **24**, 442–459.

149   M. Enamullah, A. Sharmin, M. Hasegawa, T. Hoshi, A. C. Chamayou and C. Janiak, *Eur. J. Inorg. Chem.*, 2006, 2146–2154.

150   B. Kaboudin, M. R. Faghihi, F. Kazemi and T. Yokomatsu, *Chirality*, 2015, **27**, 71–74.

151   M. Pérez-Trujillo, T. Parella and L. T. Kuhn, *Anal. Chim. Acta*, 2015, **876**, 63–70.

152   R. J. Lewis, M. A. Bernstein, H. F. Chang, D. Chapman and N. Pemberton, *Tetrahedron Asymmetry*, 2013, **24**, 866–870.

153   D. Podder, S. R. Chowdhury, S. K. Nandi and D. Haldar, *New J. Chem.*, 2019, **43**, 3743–3749.

154   P. Sahoo, D. K. Kumar, S. R. Raghavan and P. Dastidar, *Chem. - An Asian J.*, 2011, **6**, 1038–1047.

155   G. Chinga-Carrasco, O. Solheim, M. Lenes and Å. Larsen, *J. Microsc.*, 2013, **250**, 15–20.

156   R. M. Sencu, Z. Yang, Y. C. Wang, P. J. Withers, C. Rau, A. Parson and C. Soutis, *Compos. Part A Appl. Sci. Manuf.*, 2016, **91**, 85–95.

157   J. Müssig and S. Amaducci, *Ind. Crops Prod.*, 2018, **113**, 28–37.

158   D. K. Smith, *Chem. Soc. Rev.*, 2009, **38**, 684–694.

159   Z. Xie, A. Zhang, L. Ye, X. Wang and Z. G. Feng, *J. Mater. Chem.*, 2009, **19**, 6100–6102.

160   X. Q. Dou, X. M. Yang, P. Li, Z. G. Zhang, H. Schönherr, D. Zhang and C. L. Feng, *Soft Matter*, 2012, **8**, 9539–9544.

161   P. Sudhakara, G. V. Prasanna, S. Balamurugan, P. Kannan and J. I. Song, *J. Polym. Res.*, 2013, **20**, 1–11.

162   S. Tamesue, Y. Takashima, H. Yamaguchi, S. Shinkai and A. Harada, *Angew. Chemie - Int. Ed.*, 2010, **49**, 7461–7464.

163   R. Balamurugan and P. Kannan, *J. Polym. Sci. Part A Polym. Chem.*, 2008, **46**, 5760–5775.

164   M. Murali and A. B. Samui, *J. Polym. Sci. Part A Polym. Chem.*, 2006, **44**, 53–61.

165   G. S. Vadehra, B. D. Wall, S. R. Diegelmann and J. D. Tovar, *Chem. Commun.*, 2010, **46**, 3947–3949.

166   Y.-S. Zhang, A. V. Emelyanenko and J. H. Liu, *J. Taiwan Inst. Chem. Eng.*, 2016, **65**, 444–451.

167   K. Ichimura, Y. Akita, H. Akiyama, K. Kudo and Y. Hayashi, *Macromolecules*, 1997, **30**, 903–911.

168   Gangadhara and K. Kishore, *Macromolecules*, 1993, **26**, 2995–3003.

169   Gangadhara and K. Kishore, *Polymer (Guildf).*, 1995, **36**, 1903–1910.

170   A. Albini, *Photochem. Photobiol. Sci.*, 2021, **20**, 161–181.

171   D. J. Cornwell and D. K. Smith, *Mater. Horizons*, 2015, **2**, 279–293.

172   H. Gankema, M. A. Hempenius, M. Möller, G. Johansson and V. Percec, *Macromol. Symp.*, 1996, **102**, 381–390.

173   F. Bathawab, M. Bennett, M. Cantini, J. Reboud, M. J. Dalby and M. Salmero, *Langmuir*, 2016, **32**, 800–809.

174   C. Ren, G. H. B. Ng, H. Wu, K. H. Chan, J. Shen, C. Teh, J. Y. Ying and H. Zeng, *Chem. Mater.*, 2016, **28**, 4001–4008.

175   A. M. Vibhute, V. Muvvala and K. M. Sureshan, *Angew. Chemie - Int. Ed.*, 2016, **55**, 7782–7785.

176   Y. Chen, Y. Wang, Q. Yang, Y. Liao, B. Zhu, G. Zhao, R. Shen, X. Lu and S. Qu, *J. Mater. Chem. B*, 2018, **6**, 4502–4513.

177   Y. Liu, Y. Yu, C. Liu, J. M. Regenstein, X. Liu and P. Zhou, *Lwt - Food Sci. Technol.*, 2019, **102**, 338–346.

178   Y. Chen, X. Xiong, X. Liu, R. Cui, C. Wang, G. Zhao, W. Zhi, M. Lu, K. Duan, J. Weng, S. Qu and J. Ge, *J. Mater. Chem. B*, 2020, **8**, 5500–5514.

179   C.-P. Sherman Hsu, in *Handbook of Instrumental Techniques for Analytical Chemistry*, 1997, pp. 247–283.

180   E. Yara-Varón, J. Eras Joli, M. Balcells, M. Torres and R. Canela-Garayoa, *RSC Adv.*, 2012, **2**, 9230–9236.

181   V. S. D. Voet, T. Strating, G. H. M. Schnelting, P. Dijkstra, M. Tietema, J. Xu, A. J. J. Woortman, K. Loos, J. Jager and R. Folkersma, *ACS Omega*, 2018, **3**, 1403–1408.

182   J. Zhang and P. Xiao, *Polym. Chem.*, 2018, **9**, 1530–1540.

183   D. A. Komissarenko, P. S. Sokolov, A. D. Evstigneeva, I. A. Shmeleva and A. E. Dosovitsky, *Materials (Basel).*, 2018, **11**, 2350.

184   A. Bagheri and J. Jin, *ACS Appl. Polym. Mater.*, 2019, **1**, 593–611.

185   V. Schimpf, A. Asmacher, A. Fuchs, K. Stoll, B. Bruchmann and R. Mülhaupt, *Macromol. Mater. Eng.*, 2020, **305**, 2000210.

186   V. S. D. Voet, J. Guit and K. Loos, *Macromol. Rapid Commun.*, 2021, **42**, 1–11.

187   Y. Guo, H. S. Patanwala, B. Bognet and A. W. K. Ma, *Rapid Prototyp. J.*, 2017, **23**, 562–576.

188   W. Xu, S. Jambhulkar, Y. Zhu, D. Ravichandran, M. Kakarla, B. Vernon, D. G. Lott, J. L. Cornella, O. Shefi, G. Miquelard-Garnier, Y. Yang and K. Song, *Compos. Part B Eng.*, 2021, **223**, 109102.

189   I. Dranca and S. Vyazovkin, *Polymer (Guildf).*, 2009, **50**, 4859–4867.

190   T. Akira, S. Masato and K. Tadaya, *Polym. J.*, 1980, **12**, 335–341.

191   E. H. Pilkington, M. Lai, X. Ge, W. J. Stanley, B. Wang, M. Wang, A. Kakinen, M. A. Sani, M. R. Whittaker, E. N. Gurzov, F. Ding, J. F. Quinn, T. P. Davis and P. C. Ke, *Biomacromolecules*, 2017, **18**, 4249–4260.

192   A. L. Hook, C. Y. Chang, J. Yang, J. Luckett, A. Cockayne, S. Atkinson, Y. Mei, R. Bayston, D. J. Irvine, R. Langer, D. G. Anderson, P. Williams, M. C. Davies and M. R. Alexander, *Nat. Biotechnol.*, 2012, **30**, 868–875.

193   K. Adlington, N. T. Nguyen, E. Eaves, J. Yang, C. Y. Chang, J. Li, A. L. Gower, A. Stimpson, D. G. Anderson, R. Langer, M. C. Davies, A. L. Hook, P. Williams, M. R. Alexander and D. J. Irvine, *Biomacromolecules*, 2016, **17**, 2830–2838.

194   B. J. Tyler, A. Hook, A. Pelster, P. Williams, M. Alexander and H. F. Arlinghaus, *Biointerphases*, 2017, **12**, 02C412.

195   P. Mikulskis, A. Hook, A. A. Dundas, D. Irvine, O. Sanni, D. Anderson, R. Langer, M. R. Alexander, P. Williams and D. A. Winkler, *ACS Appl. Mater. Interfaces*, 2018, **10**, 139–149.

196   S. Baudis, T. Pulka, B. Steyrer, H. Wilhelm, G. Weigel, H. Bergmeister, J. Stampfl and R. Liska, *MRS Proc.*, 2010, **1242**, 1239-VV08-04.

197   Q. Cheng, Y. Zheng, T. Wang, D. Sun and R. Lin, *J. Appl. Polym. Sci.*, 2020, **137**, 48369.

Experimental Procedures

Materials and methods

All starting materials and solvents were purchased from standard chemical suppliers: **Acros** (D-sorbitol, 97%; 4-toluene sulfonic acid, 97.5%; cyclohexanone, 99%); **Merck** (benzaldehyde, 99%; vanillin, 98%; cinnamaldehyde, 98%; pyridine, 99%; lauroyl chloride, 98%; [1,1'-biphenyl]-4-carbaldehyde, 99%; 4-formylbenzonitrile, 95%; xylitol, 99%; hydrazine monohydrate, 98%; 4-hydroxybenzaldehyde, 98%; 6-bromo-1-hexanol, 97%; 11-bromo-1-undecanol, 98%); **Alfa Aesar** (methyl 4-formylbenzoate, 98%); **VWR** (NaOH, 99.4%).

1H NMR and **13C NMR** spectra were recorded on a Bruker Ascend 400, 400 MHz for ^{1}H and 100 MHz for ^{13}C. Chemical shifts were reported in parts per million, referenced to the solvent peaks. Integration is provided and multiplicities are as indicated: s (singlet), d (doublet), t (triplet), q (quartet), m (multiplet), dd (doublet of a doublet) and dt (doublet of a triplet). Coupling constants, *J*, are reported in Hertz along with assignments as indicated. **FTIR** spectra were recorded on a Bruker Alpha Platinum ATR, 100 scans between 4000 – 400 cm^{-1}. **Melting points** were recorded on a Stuart SMP20. **Optical rotations** were recorded using an Anton Paar MCP100 Polarimeter, at 25.0 °C, at a concentration of 10 mg mL^{-1}, equipped with a 2.50 mm cell length and $[a]^{25}_D$ values are given in deg cm^2 g^{-1}. **Mass Spectra** were obtained using Bruker Compass MicroTOF, using electron spray ionisation (ESI). **CHN Analysis** were obtained using the CE-400 Elemental Analyzer, Exeter Analytical, INC. 1.6 mg of each sample was combusted at temperature 975 °C. **Rheological measurements** were taken using an Anton Paar Physica MCR 301 rheometer. Samples were heated to solution and were transferred into a mould on a rheometer plate. Samples were ensured to gel before rheological measurements were taken using a 50 mm cone plate. **Photopolymerisation** were done using the ELEGOO Mercury Curing Machine, 25W, 405 nm wavelength. **Absorption and Circular Dichroism** spectra for DBS-*i*Pr and MBS-*i*Pr were collected using the Chirascan-plus CD spectrometer (Applied Photophysics Limited, U.K) with 0.02 mm path length.

Powder X-Ray diffraction (PXRD) patterns were obtained by the Bruker D8 Advance with Da Vinci. 5 mL of each sample was prepared and were dried under reduced pressure to obtain xerogels. The xerogels were placed on a silicon wafer zero background sample holders for data acquisition in 2-Theta scale between 1 – 65°, with step size of 0.02°, a step time of 6 seconds per step, using parallel beam mode at 40 kV and 40 mA. **X-ray diffraction (XRD)** data were collected in a Rigaku Oxford Diffraction (Rigaku, Tokyo, Japan) at 120(2) K with an Agilent Diffraction microfocus tube with Cu K\α radiation type at 1.54184, equipped with an Atlas CCD area detector (S2).

Scanning Electron Microscopy Measurements (SEM) samples were prepared by dropping a small amount of gel onto a SEM stub with a Pasteur pipette. The samples were left to dry in *vacuo* overnight to give a xerogel, and then coated with iridium for imaging. For high resolution imaging on an FEG-SEM work, Iridium is the finest grading of coating and is recommended because it produce significantly better results than the other metal coatings. An argon plasma is used in a vacuum chamber to sputter particles of metal from the targets, which form a thin (5 nm) layer on the sample. Images of the xerogels were captured using a JEOL 7100F FEG-SEM microscope. **Fibre quantification** were calculated by displaying a frequency distribution graph, where 300 width measurements were taken per sample using the image analysis software, ImageJ. A line was drawn along the scale bar of a SEM micrograpg using the straight-line tool. The 'set scale' analysis option was then applied to calibrate the software for that specific micrograph. The widths of single fibre and fibre bundles were measured manually by the use of the 'measure' tool in ImageJ. It is ensured that the measurement is perpendicular to the edge of the fibres to measure the minimum width on a specific fibre. The histograms are plotted using the Origin software. LogNormal distribution curve was applied in the software for the peak function of the histograms, where the maximum of the peak is stated as the width of the fibres.

Gelation tests were completed by transferring the gelator into a vial followed by the addition of the solvent; most gelation tests were done at 10 mg mL^{-1}, unless stated. **Gelation tests in organic and aqueous solvents** were performed upon heating and cooling where the solvent was heated (until all solid is dissolved by eye) then left to cool down to room temperature. **Gelation tests in monomers** were performed using a Crystallisation Systems Crystal 16. Samples were heated from 20 °C to 80 °C at a rate of 5 °C min^{-1}, held at 80 °C for five minutes, and then cooled back to 20 °C at a rate of -5 °C min^{-1}. Stirring was carried out on the ramp up at 800 rpm using stirrer bars. No stirring was done during the hold or the ramp down to avoid disturbing any nascent fibres.

UV irradiations of the BHC-n material in solution and thin films were carried out using the Photoluminescence Spectrometer FLS9800 with a µF920H 60W Xenon Flash lamp. The absorbances of the irradiated samples were measured using the UV-Vis NIR Agilent CARY 5000 Spectrometer.

Single crystal X-ray diffraction

Single crystals were selected and mounted using Fomblin® (YR-1800 perfluoropolyether oil) on a polymer-tipped MiTeGen MicroMountTM and cooled rapidly to 120 K in a stream of cold N$_2$ using an Oxford Cryosystems open flow cryostat.[EP1] Single crystal X-ray diffraction data were collected on an Oxford Diffraction GV1000 (AtlasS2 CCD area

detector, mirror-monochromated Cu-Kα radiation source; $\lambda = 1.54184$ Å, ω scans). Cell parameters were refined from the observed positions of all strong reflections and absorption corrections were applied using a Gaussian numerical method with beam profile correction (CrysAlisPro).[EP2] Structures were solved within Olex2 [EP3] by dual space iterative methods (SHELXT) [EP4] and all non-hydrogen atoms refined by full-matrix least-squares on all unique F2 values with anisotropic displacement parameters (SHELXL). [EP5] Hydrogen atoms were refined with constrained geometries and riding thermal parameters. Structures were checked with checkCIF. [EP6] CCDC- 1945762-1945763 contains the supplementary data for these compounds. These data can be obtained free of charge from The Cambridge Crystallographic Data Centre *via* www.ccdc.cam.ac.uk/data_request/cif.

Crystal structure refinement details

MBS-Van The absolute configuration of the structure is determined by reference to the D-sorbitol starting material. Refinement of each configuration gives the same R1 value. Refinement of the opposite configuration gives a lower Flack parameter however this is not significant given the large uncertainty of the refined value.

The crystal was weakly diffracting with a resolution limit of 0.9 Å. The data was truncated to a resolution of 0.9 Å resulting in a low data to parameter ratio, necessitating application of a large number of restraints to the cinnamyl moieties of the two residues (DFIX, DANG and FLAT). Rigid bond restraints were applied to the anisotropic displacement parameters of all atoms in the structure (RIGU).

The cinnamyl moiety of residue B is disordered over two conformations the occupancies of which have been refined and constrained to sum to unity, having values of 0.65(4) and 0.35(4). The anisotropic displacement parameters of the disordered moieties have been restrained to be similar (SIMU). Geometric restraints applied to the 1,2 and 1,3 distances in the disordered moieties were calculated using Grade Web Server v1.104. The anisotropic displacement parameters of disordered atoms C17C/B and C18C/B have been restrained to have more isotropic character (ISOR).

Hydrogen atoms bound to carbon atoms in the structure were geometrically placed and refined using a riding model. Hydroxyl hydrogen atoms were not observed in the electron density map and are geometrically placed to donate hydrogen bonds to appropriate acceptors. Geometric placement of hydroxyl atoms on O4B and O12B clashed with hydrogen atoms of adjacent hydroxyl groups and were omitted from the model. Their correct positions could not be determined from the electron density map and it is likely that many of the hydrogen bonds are in fact disordered with roles of donors and acceptors interchangeable. The omitted hydrogen atoms are included in the unit cell contents.

MBS-Cinn Hydrogen atoms attached to carbon atoms were observed in the electron density map before being geometrically placed and refined using a riding model. The positions of hydroxyl-hydrogen atoms H8, H8, H12 and H22 are refined with their O-H bond distances restrained to a target value of 0.84 Å (DFIX). Hydroxy-hydrogen atom H2 was geometrically placed and refined with a riding model (AFIX 147). The isotropic displacement parameters of the hydroxyl-hydrogen atoms are fixed at a value of 1.5 time Ueq of their parent oxygen atoms.

Synthetic procedures

(1S)-1-((4R,4aR,8aS)-2,6-Diphenyltetrahydro-[1,3]dioxino[5,4-d][1,3]dioxin-4-yl)ethane-1,2-diol

DBS
$C_{20}H_{22}O_6$
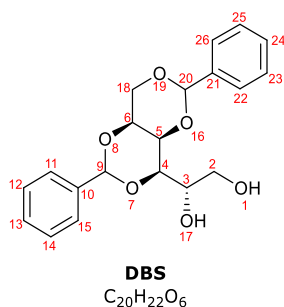
Synthesis of DBS:

D-sorbitol (3.00 g, 16.5 mmol, 1.0 eq.) and 4-toluene sulfonic acid (4-TSA) (0.630 g, 3.29 mmol, 0.2 eq.) were transferred into a round-bottomed flask and were stirred in MeOH (50 mL) at room temperature for 15 mins. Benzaldehyde (3.36 mL, 32.9 mmol, 2.0 eq.) was then added gradually and the reaction was left stirring overnight. Reaction mixture was evaporated under reduced pressure. White solid was obtained and this was digested in H_2O (100 mL), filtered then washed with cold MeOH (100 mL) and was allowed to dry. The collected solid was washed with Et_2O (50 mL) and dried in *vacuo* to yield the titled product as a white powder (3.30 g). Yield: (56%). ^{1}H NMR (400 MHz, DMSO-d_6) δ 7.48 (4H, td, *J* = 7.9, 1.9, 22-*H*, 26-*H*, 11-*H*, 15-*H*), 7.43 – 7.34 (6H, m, 23-*H*, 24-*H*, 25-*H*, 12-*H*, 13-*H*, 14-*H*), 5.67 (2H, s, 20-*H*, 9-*H*), 4.85 (1H, d, *J* = 5.8, 17-*H*), 4.41 (1H, t, *J* = 5.8, 1-*H*), 4.29 – 4.07 (3H, m, 18-*H*₂, 6-*H*), 3.95 (1H, d, *J* = 1.6, 5-*H*), 3.86 (1H, dd, *J* = 9.3, 1.7, 4-*H*), 3.81 – 3.72 (1H, m, 3-*H*), 3.61 (1H, ddd, *J* = 11.4, 5.6, 2.3, 2-*H*ₐ), 3.45 (1H, apparent dt, *J* = 11.4, 5.8, 2-*H*ᵦ). Corresponds to the spectral data reported in literature.[EP7]

Dimethyl 4,4'-((4R,4aR,8aS)-4-((S)-1,2-dihydroxyethyl)tetrahydro-[1,3]dioxino[5,4-d][1,3]dioxine-2,6-diyl)dibenzoate

DBS-CO$_2$Me
C$_{24}$H$_{26}$O$_{10}$
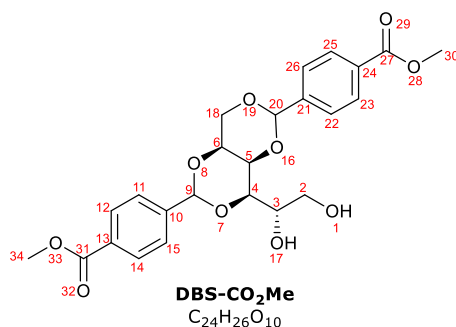
Synthesis of DBS-CO$_2$Me:

Synthesised as in literature[EP7]. Yield (58%). ^{1}H NMR (400 MHz, DMSO-d_6) δ 7.99 (4H, dd, J = 8.4, 3.1, 22-_H_, 26-_H_, 11-_H_, 15-_H_), 7.61 (4H, t, J = 8.4, 23-_H_, 25-_H_, 12-_H_, 14-_H_), 5.77 (2H, s, 20-_H_, 9-_H_), 4.92 (1H, d, J = 5.9, 17-_H_), 4.46 (1H, t, J = 5.9, 1-_H_), 4.35 – 4.13 (3H, m, 18-_H_$_2$, 6-_H_), 4.02 (1H, d, J = 1.6, 5-_H_), 3.90 (1H, dd, J = 9.4, 1.7, 4-_H_), 3.86 (6H, s, 30-_H_$_3$, 34-_H_$_3$), 3.79 (1H, dtd, J = 8.4, 5.5, 2.2, 3-_H_), 3.62 (1H, ddd, J = 11.3, 5.7, 2.3, 2-_H_$_a$), 3.47 (1H, dt, J = 11.4, 5.8, 2-_H_$_b$). Corresponds to the spectral data reported in literature.[EP7]

4,4'-((4R,4aR,8aS)-4-((S)-1,2-dihydroxyethyl)tetrahydro-[1,3]dioxino[5,4-d][1,3]dioxine-2,6-diyl)dibenzoic acid
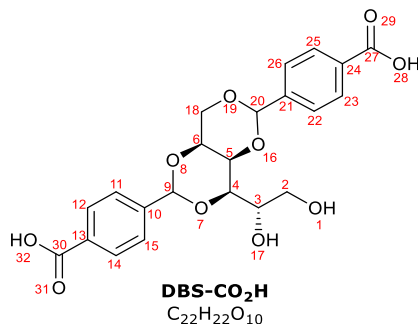
DBS-CO$_2$H
C$_{22}$H$_{22}$O$_{10}$

Synthesis of DBS-CO$_2$H:

Synthesised as in literature[EP7]. Yield (81%). ^{1}H NMR (400 MHz, DMSO-d_6) δ 12.98 (2H, s, 28-H, 32-H), 7.97 (4H, dd, J = 8.3, 2.8, 22-H, 26-H, 11-H, 15-H), 7.59 (4H, t, J = 8.4, 23-H, 25-H, 12-H, 14-H), 5.76 (2H, s, 20-H, 9-H), 4.91 (1H, s, 17-H), 4.45 (1H, s, 1-H), 4.37 – 4.15 (3H, m, 18-H_2, 6-H), 4.01 (1H, s, 5-H), 3.94 – 3.85 (1H, m, 4-H), 3.80 (1H, d, J = 6.6, 3-H), 3.62 (1H, d, J = 10.8, 2-H_a), 3.47 (1H, dd, J = 11.6, 5.3, 2-H_b). Corresponds to the spectral data reported in literature.[EP7]

(1*S*)-1-((4*R*,4a*R*,8a*S*)-2,6-bis(4-isopropylphenyl)tetrahydro-[1,3]dioxino[5,4-d][1,3]dioxin-4-yl)ethane-1,2-diol
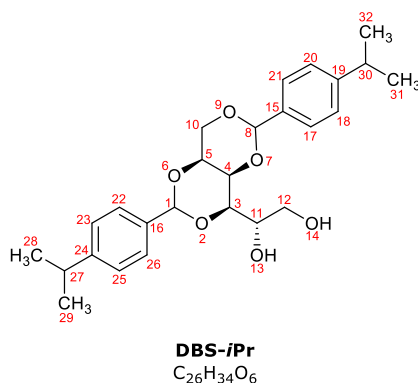
DBS-*i*Pr
$C_{26}H_{34}O_6$

Synthesis of DBS-*i*Pr:

D-sorbitol (5.00 g, 27.4 mmol, 1.0 eq.) and 4-toluene sulfonic acid (4-TSA) (1.00 g, 5.49 mmol, 0.2 eq.) were transferred into a round-bottomed flask and were stirred in MeOH (100 mL) at room temperature for 15 mins. Cuminaldehyde (8.29 mL, 54.9 mmol, 2.0 eq.) was then added gradually and the reaction was left stirring overnight. White paste was formed and was filterted under reduced pressure. White solid was obtained and this was digested in H_2O (100 mL), filtered then washed with cold MeOH (100 mL) and was allowed to dry. The collected solid was washed with Et_2O (50 mL) and dried in *vacuo* to yield the titled product as a white powder. Yield: (45%). Mp. 193–195 °C. ^{1}H NMR (500 MHz, CD_3CN) δ 7.44 (4H, dd, *J* = 8.4, 2.4, 17-*H*, 21-*H*, 26-*H*, 22-*H*), 7.30 (4H, d, *J* = 8.0, 18-*H*, 20-*H*, 25-*H*, 23-*H*), 5.67 (1H, s, 8-*H*), 5.66 (1H, s, 1-*H*), 4.21 (2H, dd, *J* = 4.4, 1.8, 10-*H*$_2$), 4.16 (1H, t, *J* = 1.4, 5-*H*), 3.96 – 3.81 (3H, m, 4-*H*, 3-*H*, 11-*H*), 3.69 (1H, ddd, *J* = 11.4, 5.8, 2.7, 12-*H*$_a$), 3.59 (1H, dt, *J* = 11.2, 5.3, 12-*H*$_b$), 3.19 (1H, d, *J* = 5.4, 13-*H*), 2.95 (2H, hept, *J* = 6.9, 27-*H*, 30-*H*), 2.72 (1H, t, *J* = 6.1, 14-*H*), 1.26 (12H, d, *J* = 6.9, 28-*H*$_3$, 29-*H*$_3$, 30-*H*$_3$, 31-*H*$_3$). ^{13}C NMR (101 MHz, CD_3CN) δ 149.7 (C15), 149.6 (C16), 136.5 (C19), 136.3 (C24), 126.2(2) (C21, C17), 126.2(0) (C26, C22), 126.1(3) (C20, C18), 126.1(1) (C25, C23), 100.1 (C8), 100.0 (C1), 77.9 (C3), 70.4 (C4), 69.7 (C10), 68.9 (C5), 68.2 (C11), 62.8 (C12), 33.7 (C27, C30), 23.3 (C31, C32, C29, C28). v_{max}/cm[-1] 3260br (O-H stretch), 2954m (C-H stretch), 2871m (C-H stretch), 1617w (C=C stretch). (ESI) *m/z* (M+H_4N)[+] calcd. for $C_{26}H_{38}NO_6^+$ 460.2694, found 460.2693. $[α]^{25}_D$ = + 60.0 (c. 10.0 mg mL^{-1}, DMSO). CHN Analysis: calcd. (%) C 70.55; H 7.75; O 21.70; Found (100%) C 68.43, H 7.75, O 23.95.

(2*S*)-2-((4*R*,4a*R*,8a*S*)-2,6-bis(4-isopropylphenyl)tetrahydro-[1,3]dioxino[5,4-d][1,3]dioxin-4-yl)-2-hydroxyethyl dodecanoate

Lauryl-DBS-*i*Pr
$C_{38}H_{56}O_7$
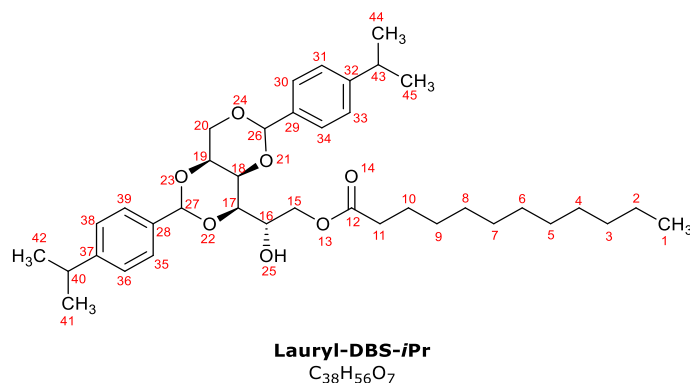
Synthesis of Lauryl-DBS-*i*Pr:

DBS-*i*Pr (2.00 g, 4.52 mmol, 1.0 eq.) was stirred in pyridine (10 mL) for 20 mins at 40 °C. Lauroyl chloride (1.57 mL, 6.78 mmol, 1.5 eq.) was added to the reaction gradually and the reaction was left stirring at 40 °C for 10 h. H_2O was added to the reaction mixture and white precipitate formed. The precipitate was filtered under reduced pressure then washed with hexane to yield Lauryl-DBS-*i*Pr as a white solid (0.73 g). Yield (25%). Mp. 178 – 181 °C. ^1H NMR (400 MHz, CD_3CN) δ 7.43 (4H, t, *J* = 8.2, 30-*H*, 34-*H*, 35-*H*, 39-*H*), 7.30 (4H, dd, *J* = 8.3, 1.4, 31-*H*, 33-*H*, 36-*H*, 38-*H*), 5.67 (1H, s, 26-*H*), 5.64 (1H, s, 27-*H*), 4.28 (1H, dd, *J* = 11.2, 2.1, 20-*H*$_b$), 4.22 (2H, dd, *J* = 4.8, 1.8, 15-*H*$_2$), 4.19 – 4.01 (3H, m, 20-*H*$_a$, 17-*H*, 18-*H*), 3.91 (2H, ddd, *J* = 5.1, 3.7, 2.0, 16-*H*, 19-*H*), 3.43 (1H, d, *J* = 5.6, 25-*H*), 2.98 – 2.91 (2H, m, 40-*H*, 43-*H*), 2.33 (2H, dt, *J* = 7.4, 1.8, 11-*H*$_2$), 1.60 (2H, dd, *J* = 9.1 5.2, 10-*H*$_2$), 1.29 (16H, br s, 9-*H*$_2$, 8-*H*$_2$, 7-*H*$_2$, 6-*H*$_2$, 5-*H*$_2$, 4-*H*$_2$, 3-*H*$_2$, 2-*H*$_2$), 1.26 (12H, d, *J* = 6.9, 41-*H*$_3$, 42-*H*$_3$, 44-*H*$_3$, 45-*H*$_3$), 0.91 (3H, t, *J* = 6.7, 1-*H*$_3$). ^{13}C NMR (100 MHz, CD_3CN) δ 173.5 (C12), 149.8 (C32), 149.7 (C37), 136.5 (C29), 136.1 (C28), 126.2(0) (C30, C34), 126.1(8) (C35, C39), 126.1(3) (C31, C33), 126.1(2) (C36, C38), 100.1(1) (C26), 100.0(5) (C27), 77.9 (C16), 70.4 (C19), 69.7 (C15), 68.5 (C17) , 66.0 (C18), 65.3 (C20), 33.8 (C11), 33.7 (C40, C43), 31.7 (C3), 29.4 (C5, C6), 29.3 (C4), 29.1 (C7), 29.0 (C8) , 28.8 (C9), 24.8 (C10), 23.3 (C41, C42, C44, C45), 22.4 (C2), 13.4 (C1). v_{max}/cm^{-1} 3477br (O-H stretch), 2955m (C-H stretch), 2922m (C-H stretch), 2853m (C-H stretch), 1718m (C=O stretch). (ESI) *m/z* $(M+H_4N)^+$ calcd. for $C_{38}H_{60}NO_7^+$ 642.4364, found 642.4360. $[α]^{25}_D$ = + 40.0 (c. 10.0 mg mL^{-1}, DMSO). CHN Analysis: calcd. (%) C 73.04; H 9.03; O 17.92; Found (100%) C 72.25, H 9.18, O 18.57.

(1*S*)-1-((4*R*,5*R*,6*S*)-5-Hydroxy-2-(4-hydroxy-3-methoxyphenyl)-6-(hydroxymethyl)-1,3-dioxan-4-yl)ethane-1,2-diol
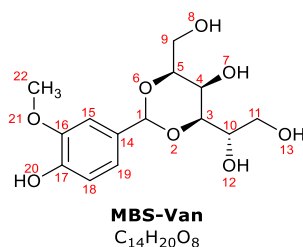
MBS-Van
$C_{14}H_{20}O_8$

Synthesis of MBS-Van:

D-sorbitol (2.00 g, 11.0 mmol, 1.0 eq.), 4-toluene sulfonic acid (4-TSA) (0.400 g, 2.20 mmol, 0.2 eq.) and vannilin (3.34 g, 22.0 mmol, 0.2 eq.) were transferred into a round-bottomed flask and purged with Ar. MeOH (80 mL) was added to the flask and the reaction was left stirring at room temperature under inert Ar atmosphere overnight. A white paste formed and was filtered under reduced pressure. The collected solid was then digested in Et_2O (50 mL) for 3 h. The resulting white powder was then suspended in boiling EtOAc for 1 h, filtered and dried *in vacuo* to isolate MBS-Van as a white solid (2.54 g). Yield (73%). Mp. 173 – 175 °C. ^1H NMR (400 MHz, DMSO-d_6) δ 8.99 (1H, s, 20-*H*), 7.06 (1H, s, 15-*H*), 6.88 (1H, d, *J* = 8.1, 19-*H*), 6.73 (1H, d, *J* = 8.1, 18-*H*), 5.43 (1H, s, 1-*H*), 4.68 (1H, d, *J* = 5.9, 12-*H*), 4.64 (1H, t, *J* = 5.8, 8-*H*), 4.39 (1H, t, *J* = 5.8, 13-*H*), 4.33 (1H, d, *J* = 8.2, 7-*H*), 3.77 – 3.73 (4H, m, 22-H_3, 5-*H*), 3.73 – 3.65 (2H, m, 10-*H*, 4-*H*), 3.64 – 3.49 (4H, m, 3-*H*, 9-H_2, 11-*H*b), 3.42 – 3.37 (1H, m, 11-*H*a). ^{13}C NMR (100 MHz, DMSO-d_6) δ 147.5 (C17), 147.2 (C14), 130.5 (C16), 119.8 (C19), 115.1 (C18), 111.3 (C15), 101.0 (C1), 81.4 (C5), 79.9 (C3), 69.6 (C10), 63.2 (C11), 62.1 (C4), 61.4 (C9), 56.2 (C22). v_{max}/cm^{-1} 3461w (O-H stretch, Ph-OH), 3262br (O-H stretch), 2967w (C-H stretch), 2930w (C-H stretch), 2875w (C-H stretch), 1618w (C=C stretch). (ESI) *m/z* (M+Na)$^+$ calcd. for $C_{14}H_{20}NaO_8^+$ 339.1050, found 339.1043. $[α]^{25}_D$ = + 8.00 (c. 10.0 mg mL^{-1}, H_2O). CHN Analysis: calcd. (%) C 54.86; H 6.14; O 39.00; Found (100%) C 53.12, H 6.44, O 40.44.

(1*S*)-1-((4*R*,5*R*,6*S*)-5-Hydroxy-6-(hydroxymethyl)-2-((E)-styryl)-1,3-dioxan-4-yl)ethane-1,2-diol
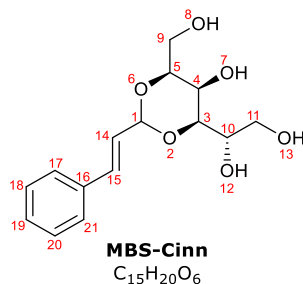
MBS-Cinn
$C_{15}H_{20}O_6$

Synthesis of MBS-Cinn:

D-sorbitol (2.00 g, 11.0 mmol, 1.0 eq.) and 4-toluene sulfonic acid (4-TSA) (0.400 g, 2.20 mmol, 0.2 eq.) were transferred into a round-bottomed flask and were stirred in MeOH (80 mL) at room temperature for 15 mins. Cinnamaldehyde (2.76 mL, 22.0 mmol, 2.0 eq.) was then added gradually and the reaction was left stirring at room temperature overnight. The reaction mixture was evaporated under reduced pressure to obtain white solid. The collected solid was digested in H_2O (100 mL) for 3 h, filtered and dried under reduced pressure. The resulting solid was further washed with Et_2O (100 mL) to yield pure MBS-Cinn as a white powder (2.21 g). Yield (68%). Mp. 124 – 126 °C. ^{1}H NMR (400 MHz, DMSO-*d6*) δ 7.51 – 7.46 (2H, m, 17-*H*, 21-*H*), 7.40 – 7.33 (2H, m, 18-*H*, 20-*H*), 7.32 – 7.26 (1H, m, 19-*H*), 6.74 (1H, d, *J* = 16.2, 15-*H*), 6.23 (1H, dd, *J* = 16.2, 5.1, 14-*H*), 5.19 (1H, d, *J* = 5.1, 1.1, 1-*H*), 4.69 (1H, d, *J* = 6.0, 12-*H*), 4.65 (1H, t, *J* = 5.7, 8-*H*), 4.42 (1H, t, *J* = 5.8, 13-*H*), 4.36 (1H, d, *J* = 7.3, 7-*H*), 3.74 – 3.64 (3H, m, 5-*H*, 10-*H*, 4-*H*), 3.62 – 3.48 (4H, m, 3-*H*, 9-*H*2, 11-*H*b), 3.42 (1H, dt, *J* = 11.3, 5.7, 11-*H*a) ppm. ^{13}C NMR (100 MHz, DMSO-*d6*) δ 136.2 (C16), 133.0 (C14), 129.2 (C17, C21), 128.7 (C19), 127.1 (C18, C20), 126.8 (C15), 100.2 (C1), 81.0 (C5), 79.4 (C3), 69.7 (C10), 63.1 (C11), 62.0 (C4), 61.4 (C9) ppm. v_{max}/cm^{-1} 3271br (O-H stretch), 2962 (C-H stretch), 2633 (C-H stretch), 2864 (C-H stretch), 1663 (C=C stretch), 1578 (C=C stretch). (ESI) *m/z* (M+Na)[+] calcd. for $C_{15}H_{20}NaO_6^+$ 319.1152, found 319.1144. $[α]^{25}_D$ = + 8.00 (c. 10.0 mg mL^{-1}, MeOH). CHN Analysis: calcd. (%) C 60.78; H 6.81; O 32.41; Found (100%) C 58.00, H 6.69, O 35.31.

(1*S*)-1-((4*R*,5*R*,6*S*)-5-Hydroxy-6-(hydroxymethyl)-2-(4-isopropylphenyl)-1,3-dioxan-4-yl)ethane-1,2-diol
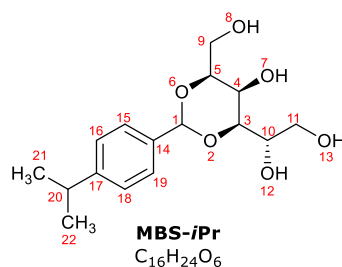
MBS-*i*Pr
$C_{16}H_{24}O_6$

Synthesis of MBS-iPr:

D-sorbitol (5.00 g, 27.4 mmol, 1.0 eq.) and 4-toluene sulfonic acid (4-TSA) (1.00 g, 5.49 mmol, 0.2 eq.) were transferred into a round-bottomed flask and were stirred in MeOH (100 mL) at room temperature for 15 mins. Cuminaldehye (4.15 mL, 27.4 mmol, 1.0 eq.) was then added gradually and the reaction was left stirring at room temperature overnight. The reaction mixture was evaporated under reduced pressure to obtain a white solid. The collected solid was digested in H_2O (100 mL) for 3 h, filtered and dried under reduced pressure. The resulting solid was further washed with Et_2O (100 mL) to yield pure MBS-*i*Pr as a white powder (5.07 g). Yield (59%). Mp. 131 – 133 °C. ^{1}H NMR (400 MHz, CD_3OD) δ 7.48 (2H, d, *J* = 8.1, 15-*H*, 19-*H*), 7.23 (2H, d, *J* = 8.1, 16-*H*, 18-*H*), 5.62 (1H, s, 1-*H*), 3.97 (1H, ddd, *J* = 6.4, 5.7, 1.4, 5-*H*), 3.91 (1H, ddd, 8.8, 5.1, 2.9, 10-*H*), 3.87 (1H, t, *J* = 1.4, 4-*H*), 3.85 – 3.83 (1H, m, 3-*H*), 3.83 – 3.76 (3H, m, 9-*H*$_2$, 11-*H*$_b$), 3.68 (1H, dd, *J* = 11.5, 5.2, 11-*H*$_a$), 2.92 (1H, hept, *J* = 6.9, 20-*H*), 1.25 (6H, d, *J*= 6.9, 21-*H*$_3$, 22-*H*$_3$). ^{13}C NMR (100 MHz, CD_3OD) δ 149.3 (C14), 136.0 (C17), 126.2 (C19, C15), 125.5 (C18, C16), 101.2 (C1), 81.0 (C5), 79.4 (C3), 69.3 (C10), 62.8 (C11), 62.5 (C4), 61.7 (C9), 33.8 (C20), 23.0 (C21, C22). v_{max}/cm[-1] 3282br (O-H stretch), 2941 (C-H stretch), 2868 (C-H stretch), 1619 (C=C stretch). (ESI) *m/z* (M+Na)[+] calcd. for $C_{16}H_{24}NaO_6^+$ 355.1465, found 335.1454. $[\alpha]^{25}_D$ = + 41.0 (c. 10.0 mg mL^{-1}, MeOH). CHN Analysis: calcd. (%) C 61.51; H 7.75; O 30.74; Found (100%) C 61.51, H 7.79, O 30.70.

(1*S*)-1-((4*R*,5*R*,6*S*)-2-([1,1'-biphenyl]-4-yl)-5-Hydroxy-6-(hydroxymethyl)-1,3-dioxan-4-yl)ethane-1,2-diol
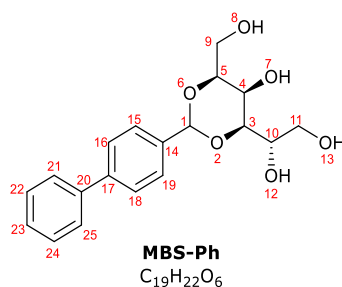
MBS-Ph
$C_{19}H_{22}O_6$

Synthesis of MBS-Ph:

D-sorbitol (2.00 g, 11.0 mmol, 1.0 eq.) and 4-toluene sulfonic acid (4-TSA) (0.400 g, 2.20 mmol, 0.2 eq.) were transferred into a round-bottomed flask and were stirred in MeOH (80 mL) at room temperature for 15 mins. [1,1'-biphenyl]-4-carbaldehyde (2.00 g, 11.0 mmol, 1.0 eq.) was then added gradually and the reaction was left stirring at room temperature overnight. The reaction mixture was evaporated under reduced pressure to obtain white solid. The collected solid was digested in H_2O (100 mL) for 3 h, filtered and dried under reduced pressure. The resulting solid was further washed with Et_2O (100 mL) to yield pure MBS-Ph as a white powder (3.80 g). Yield (63%). Mp. 208 – 210 °C. ^{1}H NMR (400 MHz, DMSO-*d*₆) δ 7.75 – 7.62 (4H, m, 21-*H*, 22-*H*, 24-*H*, 25-*H*), 7.58 (2H, d, *J* = 8.3, 15-*H*, 19-*H*), 7.48 (2H, t, *J* = 7.7, 16-*H*, 18-*H*), 7.42 – 7.30 (1H, m, 23-*H*), 5.62 (1H, s, 1-*H*), 4.71 (1H, d, *J* = 5.5, 12-*H*), 4.68 (1H, t, *J* = 5.7, 8-*H*), 4.52 – 4.27 (2H, m, 7-*H*, 13-*H*), 3.98 – 3.80 (1H, m, 5-*H*), 3.77 – 3.66 (3H, m, 10-*H*, 4-*H*, 3-*H*), 3.66 – 3.51 (3H, m, 9-*H*₂, 11-*H*ᵦ), 3.43 (1H, dt, *J* = 11.2, 5.5, 11-*H*ₐ). ^{13}C NMR (100 MHz, DMSO-*d*₆) δ 140.9 (C14), 140.4 (C17), 138.4 (C20), 129.4 (C16, C18), 128.0 (C23), 127.6 (C15, C19), 127.2 (C21, C25), 126.7 (C22, C24), 100.3 (C1), 81.4 (C5), 79.9 (C3), 69.6 (C10), 63.2 (C11), 62.1 (C4), 61.4 (C9). v_{max}/cm^{-1} 3495m (O-H stretch), 3310br (O-H stretch), 2967 (C-H stretch), 2937 (C-H stretch), 2871 (C-H stretch), 1489 (C-H bend). (ESI) *m/z* (M+Na)$^+$ calcd. for $C_{19}H_{22}NaO_6^+$ 369.1309, found 369.1310. $[α]^{25}_D$ = + 20.0 (c. 10.0 mg mL^{-1}, DMSO). CHN Analysis: calcd. (%) C 65.88; H 6.40; O 27.71; Found (100%) C 65.75, H 6.44, O 27.81.

4-((4*R*,5*R*,6*S*)-4-((S)-1,2-dihydroxyethyl)-5-Hydroxy-6-(hydroxymethyl)-1,3-dioxan-2-yl)benzonitrile
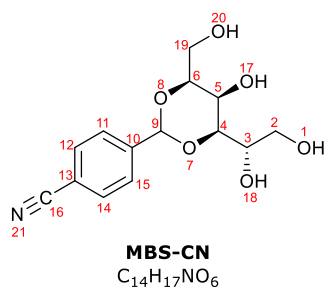
MBS-CN
$C_{14}H_{17}NO_6$

Synthesis of MBS-CN:

D-sorbitol (1.00 g, 5.49 mmol, 1.0 eq.), 4-toluene sulfonic acid (4-TSA) (0.210 g, 1.10 mmol, 0.2 eq.) and 4-formylbenzonitrile (1.44 g, 11.0 mmol, 2.eq.) were transferred into a round-bottomed flask and were stirred in MeOH (50 mL) at room temperature overnight. The reaction mixture was evaporated under reduced pressure to obtain white solid. The collected solid was digested in H_2O (100 mL) for 3 h, filtered and dried under reduced pressure. The resulting solid was further washed with Et_2O (100 mL) to yield pure MBS-CN as a white powder (0.281 g). Yield: 17%. Mp. 202 – 204 °C. ^{1}H NMR (400 MHz, DMSO-*d₆*) δ 7.86 (2H, d, *J* = 8.1, 12-*H*, 14-*H*), 7.69 (2H, d, *J* = 8.1, 11-*H*, 15-*H*), 5.66 (1H, s, 9-*H*), 4.72 – 4.70 (1H, m, 18-*H*), 4.68 (1H, d, *J* = 5.8, 20-*H*), 4.47 (1H, d, *J* = 7.9, 17-*H*), 4.42 (1H, t, *J* = 5.8, 1-*H*), 3.85 (1H, t, *J* = 6.2, 6-*H*), 3.72 – 3.70 (3H, m, 3-*H*, 4-*H*, 5-*H*), 3.63 – 3.53 (3H, m, 19-*H₂*, 2-*H*ᵦ), 3.47 – 3.37 (1H, m, 2-*H*ₐ). ^{13}C NMR (100 MHz, DMSO-*d₆*) δ 144.0 (C13), 132.5 (C12, C14), 128.0 (C11, C15), 119.2 (C16), 111.8 (C10), 99.2 (C9), 81.5 (C6), 79.9 (C4), 69.5 (C3), 63.1 (C2), 62.0 (C5), 61.4 (C19). v_{max}/cm^{-1} 3245br (O-H stretch), 2928 (C-H stretch), 2876 (C-H stretch), 2225 (C≡N stretch), 1613 (C=C stretch). (ESI) *m/z* (M+Na)[+] calcd. for $C_{14}H_{17}NNaO_6^+$ 318.0948, found 318.0947. $[\alpha]^{25}_D$ = + 20.0 (c. 10.0 mg mL^{-1}, DMSO). CHN Analysis: calcd. (%) C 56.95; H 5.80; N 4.74 O 32.51; Found (100%) C 56.96, H 5.75, N 6.09, O 31.20.

(2,6-bis(4-isopropylphenyl)tetrahydro-[1,3]dioxino[5,4-d][1,3]dioxin-4-yl)methanol
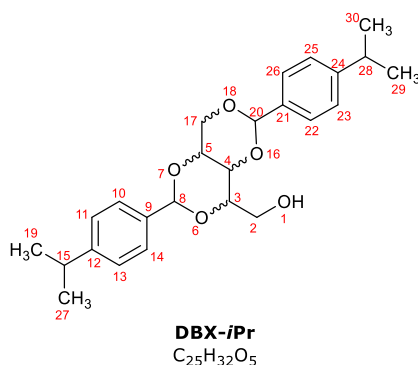
DBX-*i*Pr
$C_{25}H_{32}O_5$

Synthesis of DBX-*i*Pr:

Xylitol (2.00 g, 13.1 mmol, 1.0 eq.) and 4-toluene sulfonic acid (4-TSA) (1.44 g, 7.89 mmol, 0.6 eq.) were transferred into a round-bottomed flask and were stirred in MeOH (60 mL) at rt. Cuminaldehyde (3.97 mL, 26.3 mmol, 2.0 eq.) was then added gradually. A septum was placed and the reaction was left stirring overnight. White paste formed and was collected *via* filtration and the filtrate was concentrated under pressure. The collected solid from filtration and evaporation were digested in Et_2O (150 mL) for 3 hrs and filtered. The residue was then washed with additional Et_2O (50 mL x 2), filtered and dried to yield white powder as a racemic mixture (2.05 g). Yield: 38%. Mp. 162 – 164 °C. ^1H NMR (400 MHz, DMSO-*d₆*) δ 7.40 (2H, d, *J* = 12.0, 10-*H*, 14-*H*), 7.38 (2H, d, *J* = 12.0, 22-*H*, 26-*H*), 7.27 (2H, d, *J* = 4.0, 11-*H*, 13-*H*), 7.25 (2H, d, *J* = 4.0, 23-*H*, 25-*H*), 5.66 (1H, s, 20-*H*), 5.61 (1H, s, 8-*H*), 4.78 (1H, t, *J* = 5.7, 1-*H*), 4.17 – 4.09 (2H, m, 17-*H₂*), 4.03 (1H, t, *J* = 1.6 Hz, 5-*H*), 3.99 (1H, td, *J* = 6.4, 1.8, 4-*H*), 3.91 (1H, d, *J* = 1.6, 3-*H*), 3.64 (1H, dt, *J* = 11.1, 6.1, 2-*H*ₐ), 3.53 (1H, ddd, *J* = 11.0, 6.5, 5.4, 2-*H*ᵦ), 2.90 (2H, spt, *J* = 6.9, 15-*H*, 28-*H*), 1.20 (12H, dd, *J* = 6.9, 2.4, 19-*H*, 27-*H*, 29-*H*, 30-*H*). ^{13}C NMR (100 MHz, DMSO-*d₆*) δ149.4 (C24), 149.3 (C12), 136.8 (C21), 136.6 (C9), 126.9 (C22, C26), 126.6 (C10, C14), 126.3 (C23, C25), 126.2 (C11,C13), 100.0 (C20), 99.8 (C8), 79.3 (C4), 70.1 (C3), 69.7 (C17), 69.4 (C5), 60.0 (C2), 33.8 (C28, C15), 24.3 (C30, C29, C27, C19). v_{max}/cm^{-1} 3329w (O-H stretch), 2956w (C-H stretch), 2869w (C-H stretch), 1617w (C=C stretch), 1465 (C-H bend). (ESI) *m/z* (M+H₄N)⁺ calcd. for $C_{25}H_{36}NO_5^+$ 430.2588, found 430.2582. $[α]^{25}_D$ = +20.0 (c. 10.0 mg mL⁻¹, DMSO). CHN Analysis: calcd. (%) C 72.79; H 7.82; O 19.39; Found (100%) C 72.02, H 7.67, O 20.31.

dimethyl 4,4'-(4-(hydroxymethyl)tetrahydro-[1,3]dioxino[5,4-d][1,3]dioxine-2,6-diyl)dibenzoate
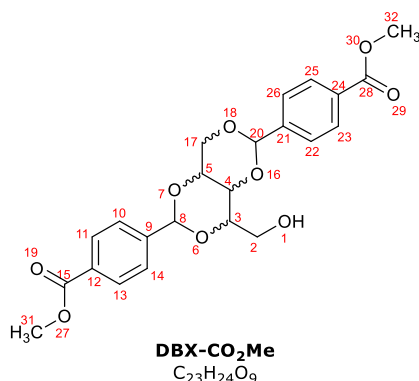
DBX-CO₂Me
$C_{23}H_{24}O_9$

Synthesis of DBX-CO₂Me:

Xylitol (5.00 g, 38.9 mmol, 1 eq.) was transferred into a 2-necked RBF fitted with a Dean-Stark apparatus. Cyclohexane (35 mL) and MeOH (10 mL) were added and the mixture was stirred under Ar at 50 °C for 20 mins. Methyl 4-formylbenzoate (8.63 g, 52.6 mmol, 1.6 eq.) and p-TSA (1.20 g, 6.57 mmol, 0.2 eq.) were dissolved in MeOH (20 mL), stirred for 20 mins at rt and was added dropwise for 1 h to the xylitol solution. After the addition, reaction temperature was increased to 70 °C and was stirred for 2 h until most of the solvent was removed. White paste formed, washed with MeOH (3 x 100 mL) and filtered. Crude product dried overnight, mono- and trisubstituted derivatives were removed by washing with boiling water (4 x 100 mL) and boiling toluene (3 x 100 mL), respectively. Product was dried obtaining pure white powder as a racemic mixture (6.25 g). Yield: 53%. Mp. 267 – 269 °C. ^{1}H NMR (400 MHz, DMSO-d_6) δ 8.00 (4H, d, J = 8.2, 10-_H_, 14-_H_, 22-_H_, 26-_H_), 7.63 (2H, d, J = 12.0, 11-_H_, 13-_H_), 7.61 (2H, d, J = 12.0, 23-_H_, 25-_H_), 5.81 (1H, s, 20-_H_), 5.75 (1H, s, 8-_H_), 4.87 (1H, t, J = 5.7, 1-_H_), 4.26 – 4.15 (2H, m, 17-_H_₂), 4.12 (1H, s, 4-_H_), 4.07 (1H, br t, J = 6.4, 5-_H_), 4.01 (1H, s, 3-_H_), 3.86 (6H, s, 31-_H_₃, 32-_H_₃), 3.69 (1H, dt, J = 12.0, 6.1, 2-_H_ₐ), 3.60 (1H, dt, J = 11.3, 6.1, 2-_H_ᵦ). ^{13}C NMR (100 MHz, DMSO-d_6) δ 166.5 (C15, C28), 143.7 (C24), 143.5 (C12), 130.3 (C21), 130.2 (C9), 129.5 (C11, C13, C23, C25), 127.2 (C22, C26), 126.9 (C10, C14), 99.1 (C20), 98.9 (C8), 79.3 (C5), 70.3 (C3), 69.7 (C17), 69.6 (C4), 59.9 (C2), 52.7 (C31, C32). v_{max}/cm^{-1} 3484w (O-H stretch), 3187w (O-H stretch), 2954w (C-H stretch), 2881w (C-H stretch), 1722s (C=O stretch), 1614m (C=C stretch). (ESI) m/z (M+H₄N)$^+$ calcd. for $C_{23}H_{28}NO_9^+$ 462.1759, found 462.1756. $[α]^{25}_D$ = + 12.0 (c. 10 mg mL^{-1}, DMSO). CHN Analysis: calcd. (%) C 62.16; H 5.44; O 32.40; Found (100%) C 59.28, H 5.23, O 35.49.

4,4'-(4-(hydroxymethyl)tetrahydro-[1,3]dioxino[5,4-d][1,3]dioxine-2,6-diyl)dibenzoic acid
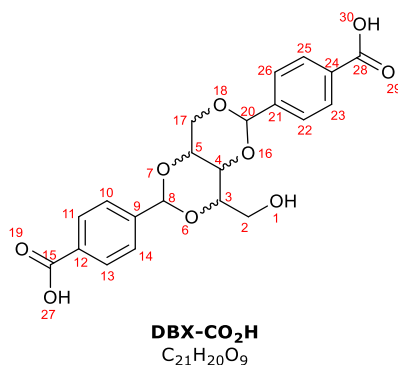
DBX-CO₂H
$C_{21}H_{20}O_9$

Synthesis of DBX-CO₂H:

DBX-CO₂Me (2.00 g, 4.50 mmol, 1 eq.) was dissolved in MeOH (60 mL) and 1M NaOH$_{(aq)}$ (60 mL) was added to the solution. The mixture was heated at 90 °C under reflux overnight. MeOH was removed *via* rotary evaporation and deionised water (50 mL) was added. The mixture was acidified to pH 3 with NaHSO₄. White stable gel started to form, filtered under reduced pressure using a sintered funnel. The residue was washed thoroughly with deionised water (4 x 100 mL), filtered and dried to yield a pure off-white powder as a racemic mixture (1.67 g). Yield: 89%. Mp. 294 – 296 °C. ^{1}H NMR (500 MHz, DMSO-*d₆*) δ 13.02 (2H, s, 27-*H*, 30-*H*), 7.97 (4H, d, *J* = 7.8, 10-*H*, 14-*H*, 22-*H*, 26-*H*), 7.61 – 7.56 (4H, m, 11-*H*, 13-*H*, 23-*H*, 25-*H*), 5.80 (1H, s, 20-*H*), 5.74 (1H, s, 8-*H*), 4.86 (1H, t, *J* = 5.8, 1-*H*), 4.25 – 4.15 (2H, m, 17-*H₂*), 4.12, (1H, s, 4-*H*), 4.09 – 4.04 (1H, m, 5-*H*), 4.01 (1H, s, 3-*H*), 3.69 (1H, dt, *J* = 11.2, 5.7, 2-*H*a), 3.59 (1H, dt, *J* = 11.1, 5.6, 2-*H*b). ^{13}C NMR (100 MHz, DMSO-*d₆*) δ 167.5 (C28, C15), 143.3 (C24), 143.1 (C12), 131.5 (C21), 131.4 (C9), 129.6 (C11, C13, C23, C25), 127.0 (C22, C26), 126.7 (C10, C14), 99.3 (C20), 99.1 (C8), 79.3 (C5), 70.3 (C3), 69.8 (C17), 69.6 (C4), 59.9 (C2). v_{max}/cm^{-1} 3991b (O-H stretch), 2869b (O-H stretch), 2638w (C-H stretch), 2520w (C-H stretch), 1693s (C=O stretch), 1614 (C=C stretch). (ESI) *m/z* (M+H)$^+$ calcd. for $C_{21}H_{21}O_9^+$ 417.1180, found 417.1179. $[α]^{25}_D$ = + 16.0 (c. 10 mg mL^{-1}, DMSO). CHN Analysis: calcd. (%) C 60.58; H 4.84; O 34.58; Found (100%) C 5.81, H 4.52, O 35.31.

4,4'-(4-(hydroxymethyl)tetrahydro-[1,3]dioxino[5,4-d][1,3]dioxine-2,6-diyl)di(benzohydrazide)

DBX-CONHNH$_2$
C$_{21}$H$_{24}$N$_4$O$_7$
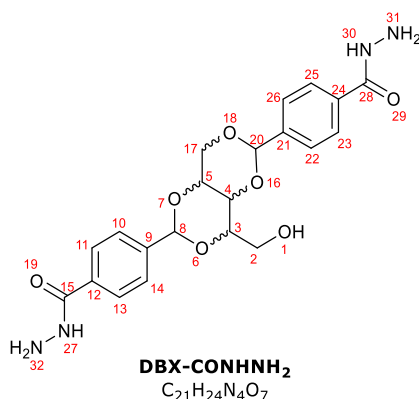
Synthesis of DBX-CONHNH$_2$:

DBX-CO$_2$Me (5.00 g, 11.3 mmol, 1 eq.) was dissolved in THF. Hydrazine monohydrate (28.6 mL) was added to the solution gradually. The reaction was allowed to preceed under reflux at 65 °C overnight. White precipitate formed, filtered and was washed with Et$_2$O (2 x 50 mL) and was dried. The collected solid was further washed with deionised water (3 x 100 mL) and was left to dry overnight obtaining pure DBX-CONHNH$_2$ as a racemic mixcture (2.38 g). Yield (48%). Mp. 266 – 268 °C. ^{1}H NMR (400 MHz, DMSO-d_6) δ 9.80 (2H, s, 27-*H*, 30-*H*), 7.84 (4H, d, J = 7.9, 10-*H*, 14-*H*, 22-*H*, 26-*H*), 7.54 (2H, d, J = 16.0, 11-*H*, 13-*H*), 7.51 (2H, d, J = 16.0, 23-*H*, 25-*H*), 5.76 (1H, s, 20-*H*), 5.70 (1H, s, 8-*H*), 4.85 (1H, t, J = 5.7, 1-*H*), 4.50 (4H, s, 31-*H*$_2$, 32-*H*$_2$), 4.26 – 4.13 (2H, m, 17-*H*$_2$), 4.10 (1H, s, 4-*H*), 4.07 – 4.02 (1H, m, 5-*H*), 3.98 (1H, s, 3-*H*), 3.68 (1H, dt, J = 11.8, 6.1, 2-*H*$_a$), 3.58 (1H, dt, J = 11.4, 6.0, 2-*H*$_b$). ^{13}C NMR (100 MHz, DMSO-d_6) δ 166.1 (C15), 166.0 (C28), 141.6 (C24), 141.4 (C12), 134.1 (C21), 134.0 (C9), 127.2(3) (C23, C25), 127.2(2) (C11, C13), 126.7 (C22, C26), 126.5 (C10, C14), 99.4 (C20), 99.2 (C8), 79.3 (C5), 70.2 (C3), 69.8 (C17), 69.5 (C4), 59.9 (C2). v_{max}/cm^{-1} 3256b (O-H stretch and N-H stretch), 2867w (C-H stretch), 1723s (C=O stretch), 1647 (N-H bend), 1568 (C=C stretch). (ESI) *m/z* (M+H)[+] calcd. for C$_{21}$H$_{25}$N$_4$O$_7$[+] 445.1718, found 445.1718. [α]$^{25}_D$ = + 8.00 (c. 10 mg mL^{-1}, DMSO). CHN Analysis: calcd. (%) C 56.57 H 5.44 N 12.61, O 25.20; Found (100%) C 48.68, H 5.91, N 11.58, O 33.83.

(1*R*,2*R*)-1,2-bis((*R*)-2,2-dimethyl-1,3-dioxolan-4-yl)ethane-1,2-diol

MDA
$C_{12}H_{22}O_6$
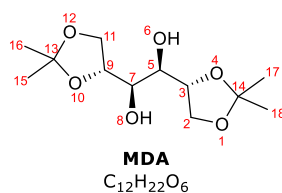
Synthesis of MDA:

$ZnCl_2$ (20.1 g, 147.5 mmol, 2.5 eq.) was stirred in $(CH_3)_2CO$ (100 mL) until all solid dissolved. The solution was cooled to 0 °C then D-mannitol (10.4 g, 57.1 mmol, 1.0 eq.) was added. A septum was placed and reaction was left stirring for 24 h at rt. The solution was cooled to 0 °C. K_2CO_3 (25.1 g, 181.6 mmol, 3.0 eq.) was dissolved in H_2O (25 mL) and added to the cooled reaction mixture. Reaction was left stirring for 1 hr at rt. Any solid were filtered *via* gravity and the filtrate was adjusted to pH 8 by adding NH_4OH (5 mL). The organic compound was extracted from the filtered solid by washed with EtOAc (3 x 50 mL). Combined organic layers was added to the pH 8 filtrate and were concentrated in vacuo. Precipitate formed when concentrated. H_2O (100 mL) was added forming a cloudy solution. Organic compounds were again extracted with EtOAc (3 x 50 mL) and the combined organic layers were dried over anhydrous $MgSO_4$, filtered and evaporated under reduced pressure to obtain white crude solid. The crude was recrystallised in $CHCl_3$/Heptane (1:9) to obtain pure white solid (14.97 g). Yield: 69%. Mp. 121 – 123 °C, lit. 120 – 122 °C. ^{1}H NMR (400 MHz, $CDCl_3$) δ 4.28 – 4.18 (2H, m, 9-H, 3-*H*), 4.14 (2H, dd, *J* = 8.6, 6.3, 11-*H₂*), 4.00 (2H, dd, *J* = 8.5, 5.6, 2-*H₂*), 3.80 – 3.74 (2H, m, 7-*H*, 5-*H*), 2.60 (2H, d, *J* = 6.7, 6-*H*, 8-*H*), 1.44 (6H, s, 16-*H₃*, 15-*H₃*), 1.38 (6H, s, 17-*H₃*, 18-*H₃*). Corresponds to the spectral data reported in literature.[EP8]

(1*R*,2*R*)-1,2-bis((4*R*)-2-phenyl-1,3-dioxolan-4-yl)ethane-1,2-diol

MDP
$C_{20}H_{22}O_6$
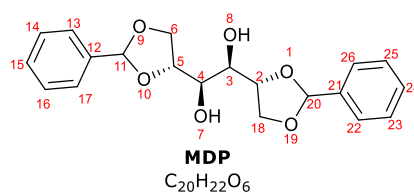
Synthesis of MDP:

D-mannitol (2.00 g, 10.9mmol, 1.0 eq.) and *p*-TSA (0.20 g, 1.10 mmol, 0.1 eq.) were transferred in a 2-necked RBF. DMF (40 mL) was added and suspension was stirred at rt for 10 mins. (dimethoxymethyl)benzene (3.30 mL, 22.0 mmol, 2.0 eq.) was added and the resulting mixture was stirred at 60 °C for 2 h. Triethylamine (1.00 mL) was added to neutralise the reaction mixture. The solution was diluted with 100 mL H_2O and the organic sompound was extracted using EtOAc (4 x 50 mL). The combined organic extract were washed with 5% LiCl (aq) (5 x 100 mL) and H_2O (5 x 100 mL) to remove all the DMF, dried over $MgSO_4$, filtered and evaporated under reduced pressure giving a yellow sticky solid as crude. The material was purified by flash column chromatography (7:3 EtOAc/Petroleum Ether (40-60)) to afford a white solid (0.38 g). Yield: 10%. Mp. 184 – 186 °C. ^1H NMR (400 MHz, CDCl$_3$) δ 7.51 – 7.47 (4H, m, 13-*H*, 17-*H*, 26-*H*, 22-*H*), 7.42 – 7.37 (6H, m, 14-*H*, 15-*H*, 16-*H*, 23-*H*, 24-*H*, 25-*H*), 5.54 (2H, s, 11-*H*, 20-*H*), 4.42 (2H, dd, *J* = 10.9, 5.2, 7-*H*, 8-*H*), 4.32 – 4.17 (4H, m, 6-*H$_2$*, 18-*H$_2$*), 3.68 (2H, dd, *J* = 11.0, 9.6, 2-*H*, 5-*H*), 2.95 (2H, d, *J* = 2.3, 4-*H*, 3-*H*). ^{13}C NMR (100 MHz, CDCl$_3$) δ 137.0 (C24, C15), 129.3 (C14, C16, C23, C25), 128.5 (C13, C17, C22, C26), 126.0 (C12, C21) , 101.6 (C11, C20), 80.5 (C3), 70.6 (C6, C18), 61.7 (C18). v_{max}/cm^{-1} 3480w (O-H stretch), 2978w (C-H stretch), 2858w (C-H stretch), 1495 (C-H bend), 1364s (O-H bend), 1224 (C-O stretch – ether), 1100 (C-O stretch – secondary alcohol), 779 (C-H bend). (ESI) *m/z* (M+H)$^+$ calcd. for $C_{20}H_{23}O_6^+$ 359.1450, found 359.1483. [α]$^{25}_D$ = − 4.00 (c. 10 mg mL^{-1}, EtOH). CHN Analysis: calcd. (%) C 67.03, H 6.19, O 26.78; Found (100%) C 66.65, H 6.20, O 27.15.

2,6-bis((*E*)-4-hydroxybenzylidene)cyclohexan-1-one

BHC
$C_{20}H_{18}O_3$
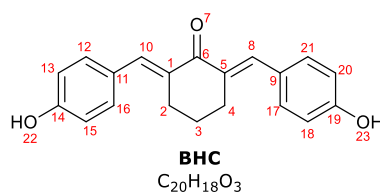
Synthesis of BHC:

A mixture of 4-hydroxybenzaldehyde (4.03 g, 33 mmol, 2.0 eq) and cyclohexanone (1.50 mL, 15 mmol, 1 eq) was exposed to microwave irradiation at 80 °C for 25 mins in the presence of Al_2O_3 (0.10 g, 1 mmol, 0.07 eq). Acetic acid (10 mL) and a catalytic amount of H_2SO_4 were added to the mixture and was sonicated at rt for 2 h. Reaction mixture turns green after the subsequent reaction. The solution was cooled to rt and poured over crushed ice; green precipitate formed. The precipitate was filtered, washed with water (3 x 30 mL) and dried under vacuum to yield a dark green powder (2.93 g). Yield: (64%). ^{1}H NMR (400 MHz, DMSO-d6) δ 9.92 (2H, s, 10-*H*, 8-*H*), 7.55 (2H, s, 2-*H*, 4-*H*), 7.41 (4H, d, *J* = 8.8, 12-*H*, 16-*H*, 17-*H*, 21-*H*), 6.85 (4H, d, *J* = 8.6, 13-*H*, 15-*H*, 18-*H*, 20-*H*), 3.33 (2H, s, 22-*H*, 23-*H*), 2.92 – 2.78 (4H, m, 2-*H*₂, 4-*H*₂), 1.72 (2H, t, *J* = 6.0, 3-*H*₂) Corresponds to spectral data reported in literature.[EP9]

2,6-bis((*E*)-4-((6-hydroxyhexyl)oxy)benzylidene)cyclohexan-1-one
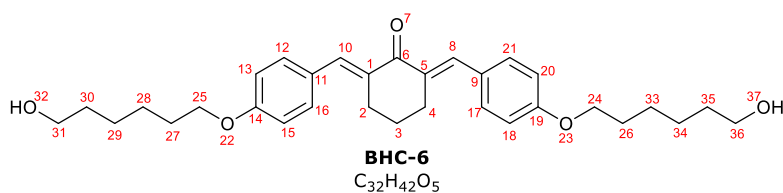
BHC-6
$C_{32}H_{42}O_5$

Synthesis of BHC-6:

Cs_2CO_3 (7.98 g, 24.5 mmol, 1.5 eq) was added to a solution of BHC (5.0 g, 16.3 mmol, 1.0 eq) in dry MeCN (100 mL). After stirring the reaction at reflux for 1 h, a solution of 6-bromo-1-hexanol (6.41 mL, 49.0 mmol, 3.0 eq) in dry MeCN (50 mL) was added dropwise to the reaction mixture and heated at reflux for 48 h. Reaction mixture turns yellow after the subsequent reaction. The solution was cooled to rt and poured over crushed ice, off-yellow precipitate formed. The precipitate was filtered and dried under reduced pressure. The crude product was purified *via* recrystallisation from ethanol to obtain yellow powder (5.67 g) Yield: (69%). ^{1}H NMR (400 MHz, DMSO-d$_6$) δ 7.58 (2H, s, 2-*H*, 4-*H*), 7.50 (4H, d, *J* = 9.0 Hz, 12-*H*, 16-*H*, 17-*H*, 21-*H*), 7.01 (4H, d, *J* = 8.9 Hz, 13-*H*, 15-*H*, 18-*H*, 20-*H*), 4.35 (2H, t, *J* = 5.1 Hz, 32-*H*, 37-*H*), 4.02 (4H, t, *J* = 6.5 Hz, 25-*H*$_2$, 24-*H*$_2$), 3.40 (4H, t, *J* = 6.3 Hz, 31-*H*$_2$, 36-*H*$_2$), 2.99 – 2.66 (4H, m, 2-*H*$_2$, 4-*H*$_2$), 1.72 (2H, dt, *J* = 12.6, 6.6, 3-*H*$_2$), 1.47 – 1.33 (16H, m, 27-*H*$_2$, 28-*H*$_2$, 29-*H*$_2$, 30-*H*$_2$, 26-*H*$_2$, 33-*H*$_2$, 34-*H*$_2$, 35-*H*$_2$). Corresponds to spectral data reported in literature.[EP9]

2,6-bis((*E*)-4-((11-hydroxyundecyl)oxy)benzylidene)cyclohexan-1-one
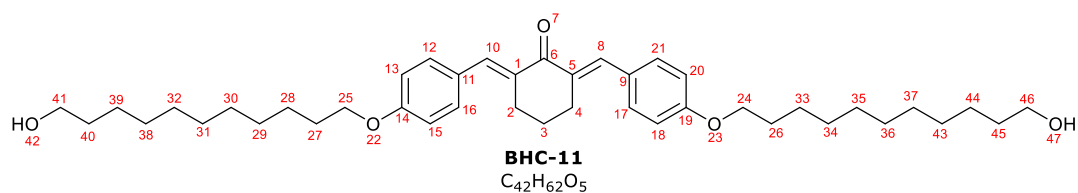
BHC-11
$C_{42}H_{62}O_5$

Synthesis of BHC-11:

Cs_2CO_3 (7.98 g, 24.5 mmol, 1.5 eq) was added to a solution of BHC (5.0 g, 16.3 mmol, 1.0 eq) in dry MeCN (100 mL). After stirring the reaction at reflux for 1 h, a solution of 11-bromo-1-undecanol (12.3 g, 49.0 mmol, 3.0 eq) in dry MeCN (50 mL) was added dropwise to the reaction mixture and heated at reflux for 48 h. Reaction mixture turns yellow after the subsequent reaction. The solution was cooled to rt and poured over crushed ice, off-yellow precipitate formed. The precipitate was filtered and dried under reduced pressure. The crude product was purified *via* recrystallisation from ethanol to obtain yellow powder (7.02 g) Yield: (66%). ^{1}H NMR (400 MHz, CDCl$_3$) δ 7.78 (2H, s, 10-*H*, 8-*H*), 7.46 (4H, d, *J* = 8.8 Hz, 12-*H*, 16-*H*, 17-*H*, 21-*H*), 6.94 (4H, d, *J* = 8.8, Hz, 13-*H*, 15-*H*, 18-*H*, 20-*H*), 4.01 (4H, t, *J* = 6.6 Hz, 25-*H*$_2$, 24-*H*$_2$), 3.67 (4H, t, *J* = 6.6 Hz, 41-*H*$_2$, 46-*H*$_2$), 2.94 (4H, t, *J* = 6.7 Hz, 2-*H*$_2$, 4-*H*$_2$), 1.86 – 1.78 (6H, m, 26-*H*$_2$, 27-*H*$_2$, 3-*H*$_2$), 1.54 – 1.25 (32H, m, 28-*H*$_2$, 29-*H*$_2$, 30-*H*$_2$, 31-*H*$_2$, 32-*H*$_2$, 38-*H*$_2$, 39-*H*$_2$, 40-*H*$_2$, 33-*H*$_2$, 34-*H*$_2$, 35-*H*$_2$, 36-*H*$_2$, 37-*H*$_2$, 43-*H*$_2$, 44-*H*$_2$, 45-*H*$_2$). Corresponds to spectral data reported in literature.[EP9]

EP References

EP1. J. Cosier and A. M. Glazer, J. Appl. Crystallogr., 1986, 19, 105-107.

EP2. CrysAlisPro 1.171.40.45a (Rigaku OD, 2019).

EP3. O. V Dolomanov, L. J. Bourhis, R. J. Gildea, J. A. K. Howard, H. Puschmann, J. Appl. Cryst. 2009, 42, 339–341.

EP4. G. M. Sheldrick, Acta Crystallogr. A 2015, 71, 3–8.

EP5. G. M. Sheldrick, Acta Crystallogr. C 2015, 71, 3–8.

EP6. "CheckCIF," can be found under http://checkcif.iucr.org

EP7. D. J. Cornwell, B. O. Okesola and D. K. Smith, *Soft Matter*, 2013, **9**, 8730–8736

EP8. V. Srikanth, R. B. N. Prasad, Y. Poornachandra, V. S. Phani Babu, C. Ganesh Kumar, B. Jagadeesh and R. C. R. Jala, *Eur. J. Med. Chem.*, 2016, **109**, 134–145

EP9. Y.-S. Zhang, A. V Emelyanenko and J.-H. Liu, *J. Taiwan Inst. Chem. Eng.*, 2016, **65**, 444–451.

APPENDIX

A 1 | ^{1}H NMR of DBS

A 2 | ^{1}H NMR of DBS-CO$_2$Me
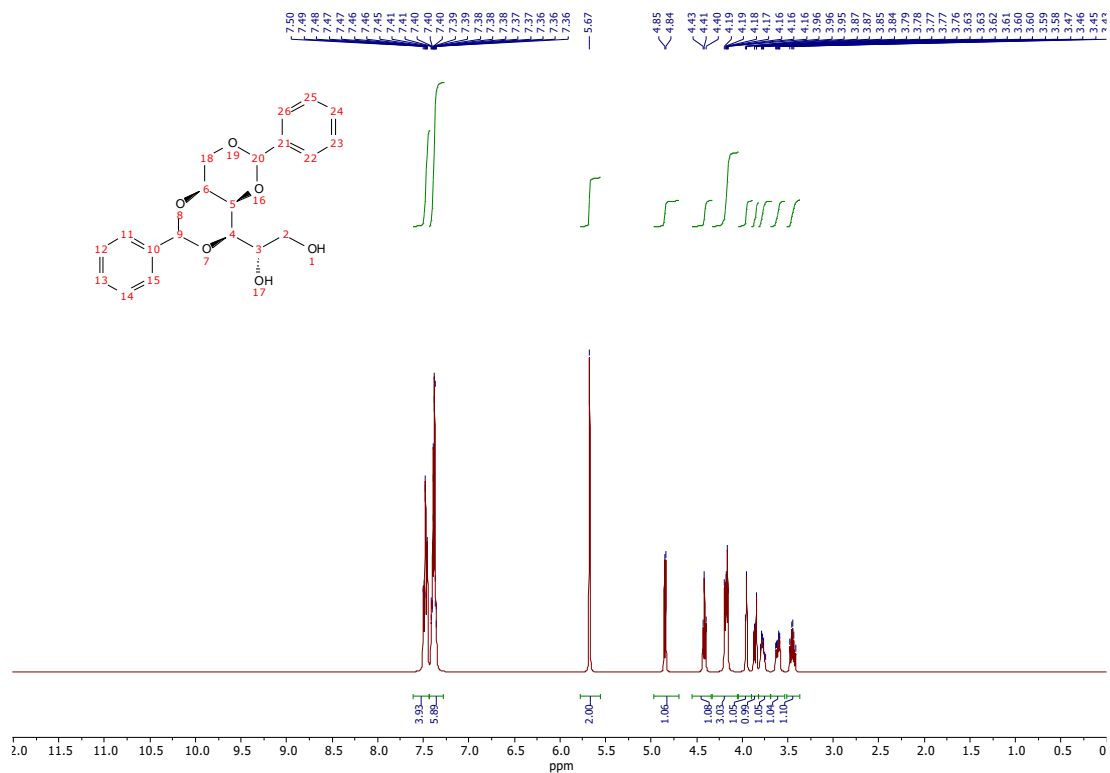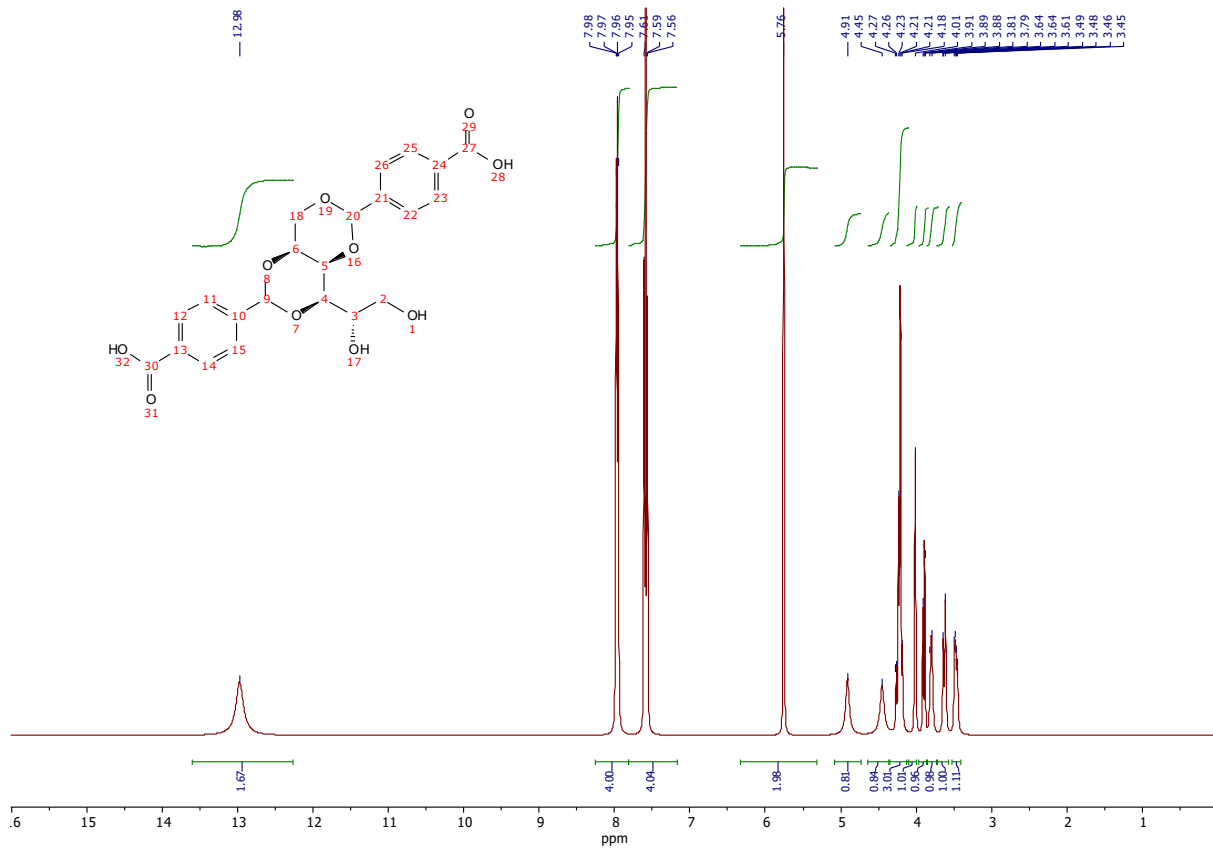
A 3 | ^{1}H NMR of DBS-CO$_2$H
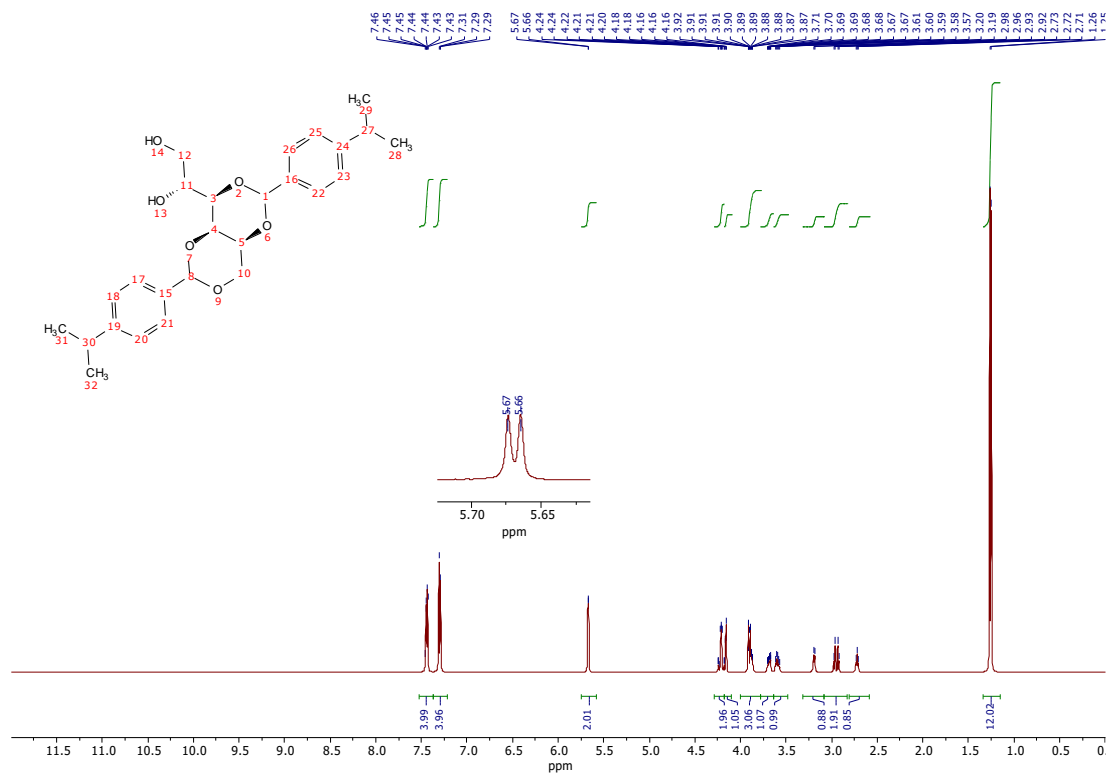
A 4 | ^{1}H NMR of DBS-*i*Pr
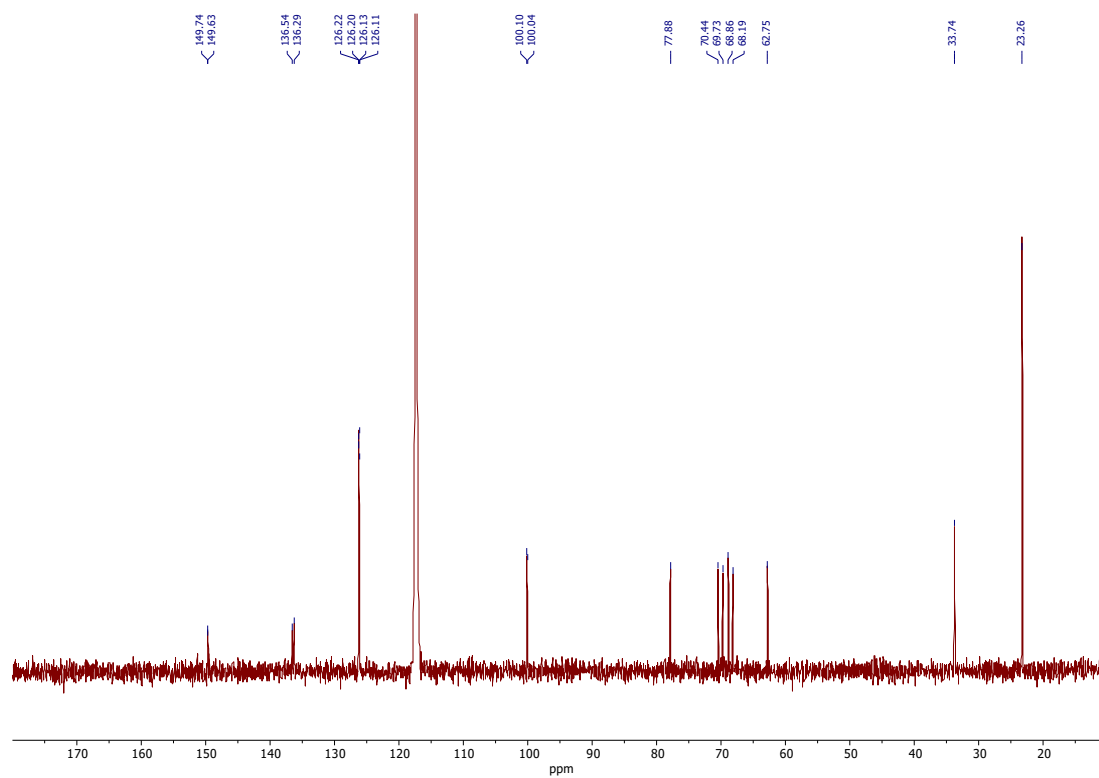
A 5 | ^{13}C NMR of DBS-*i*Pr
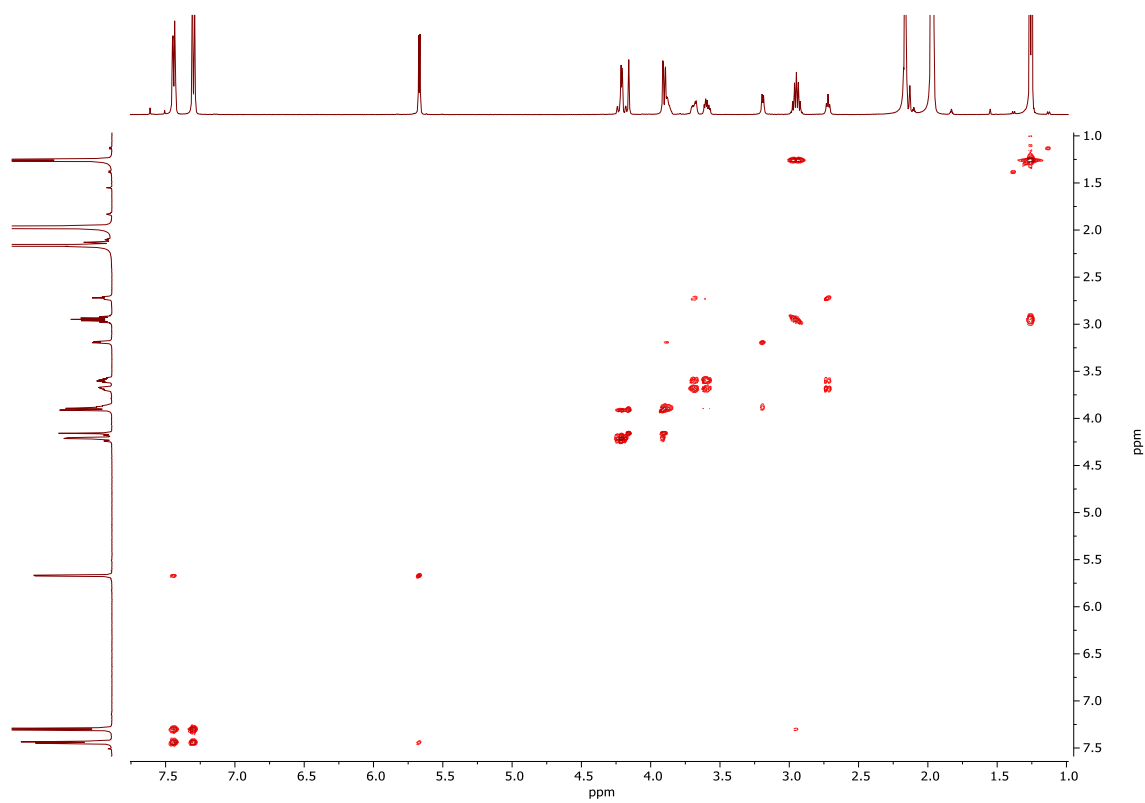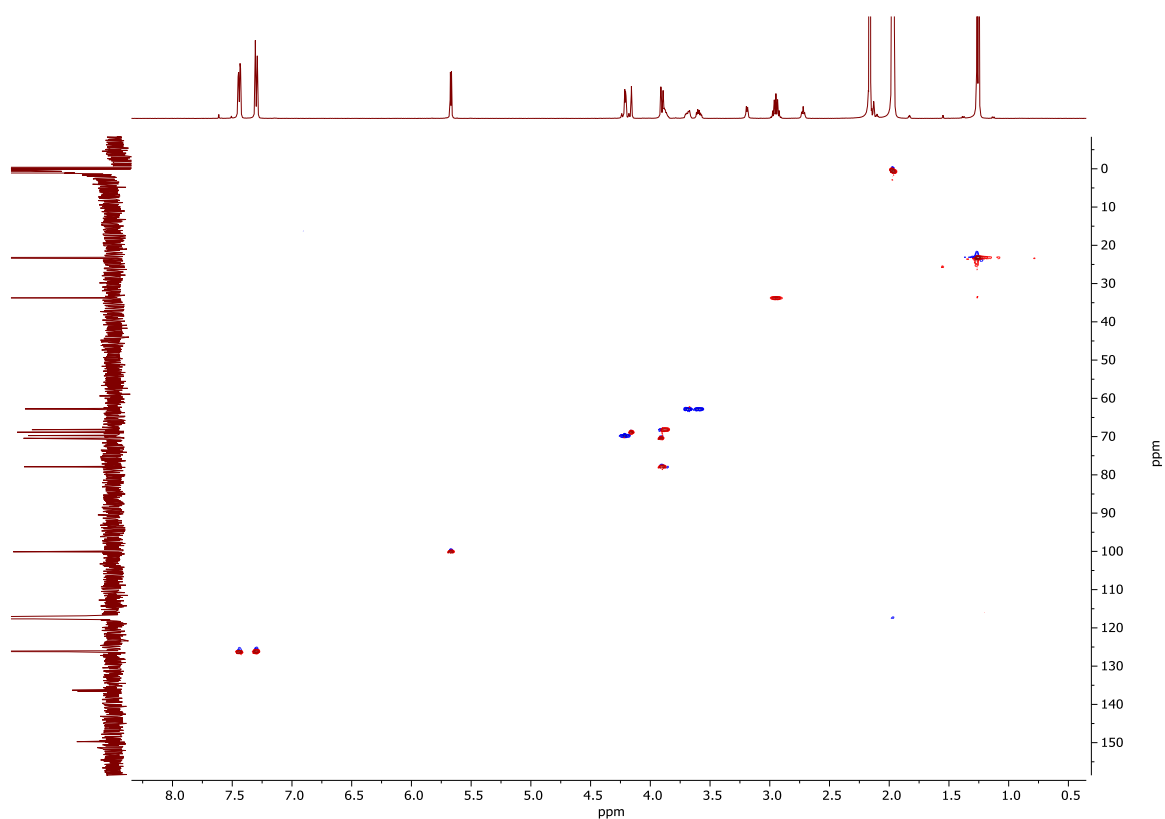
A 6 | COSY of DBS-*i*Pr

A 7 | HSQC of DBS-*i*Pr
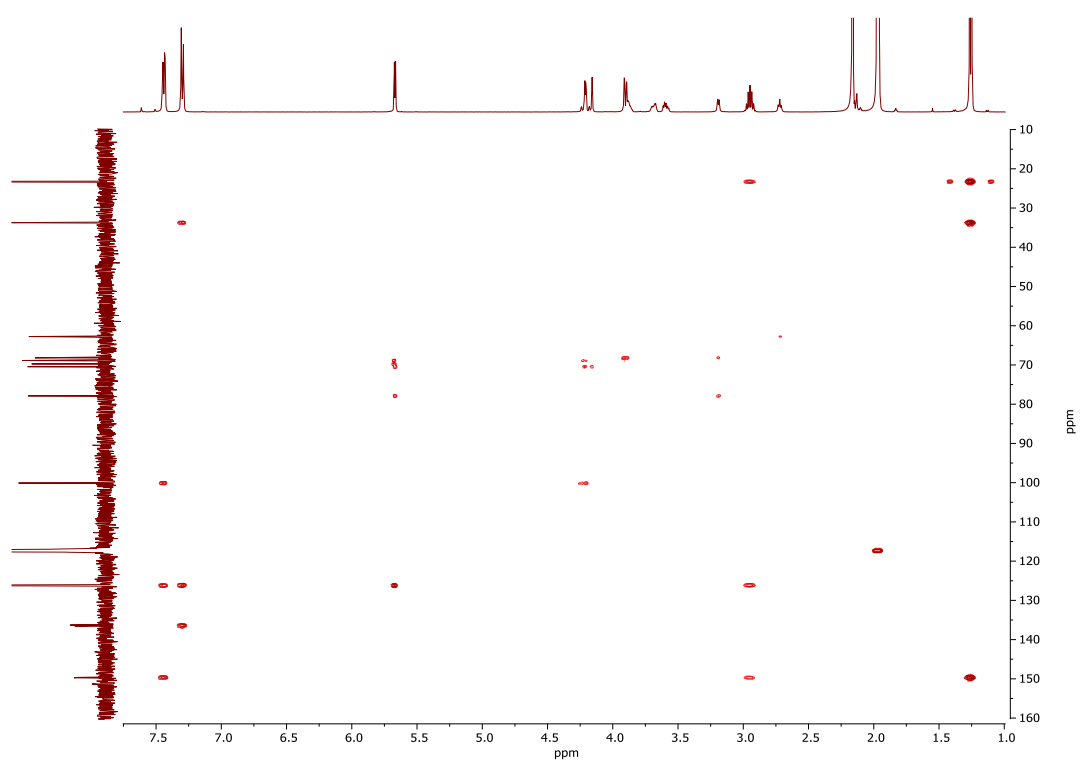
A 8 | HMBC of DBS-*i*Pr
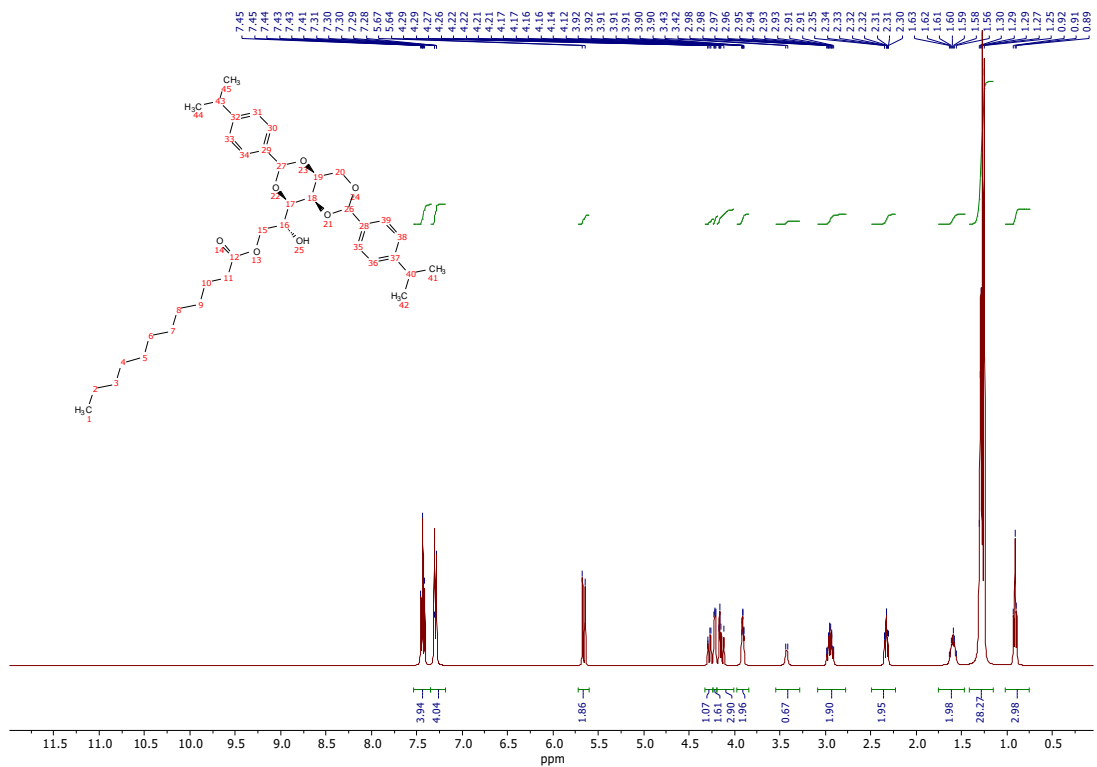
A 9 | ^{1}H NMR of Lauryl-DBS-*i*Pr
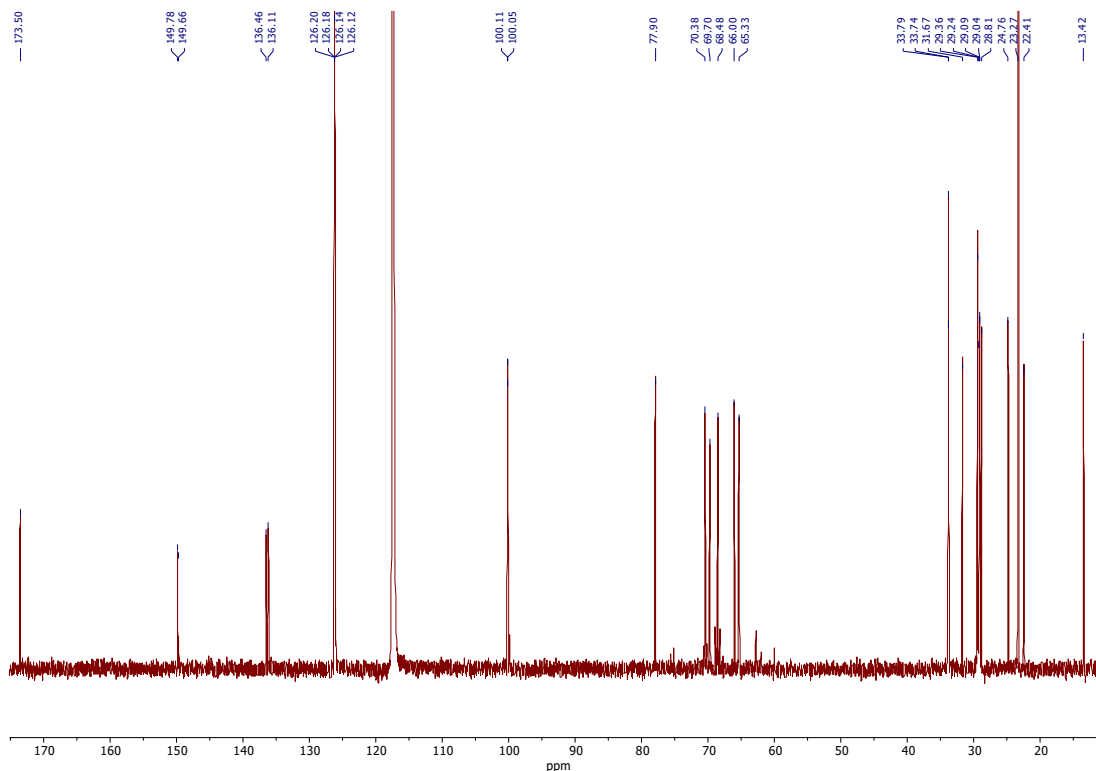
A 10 | ^{13}C NMR of Lauryl-DBS-*i*Pr
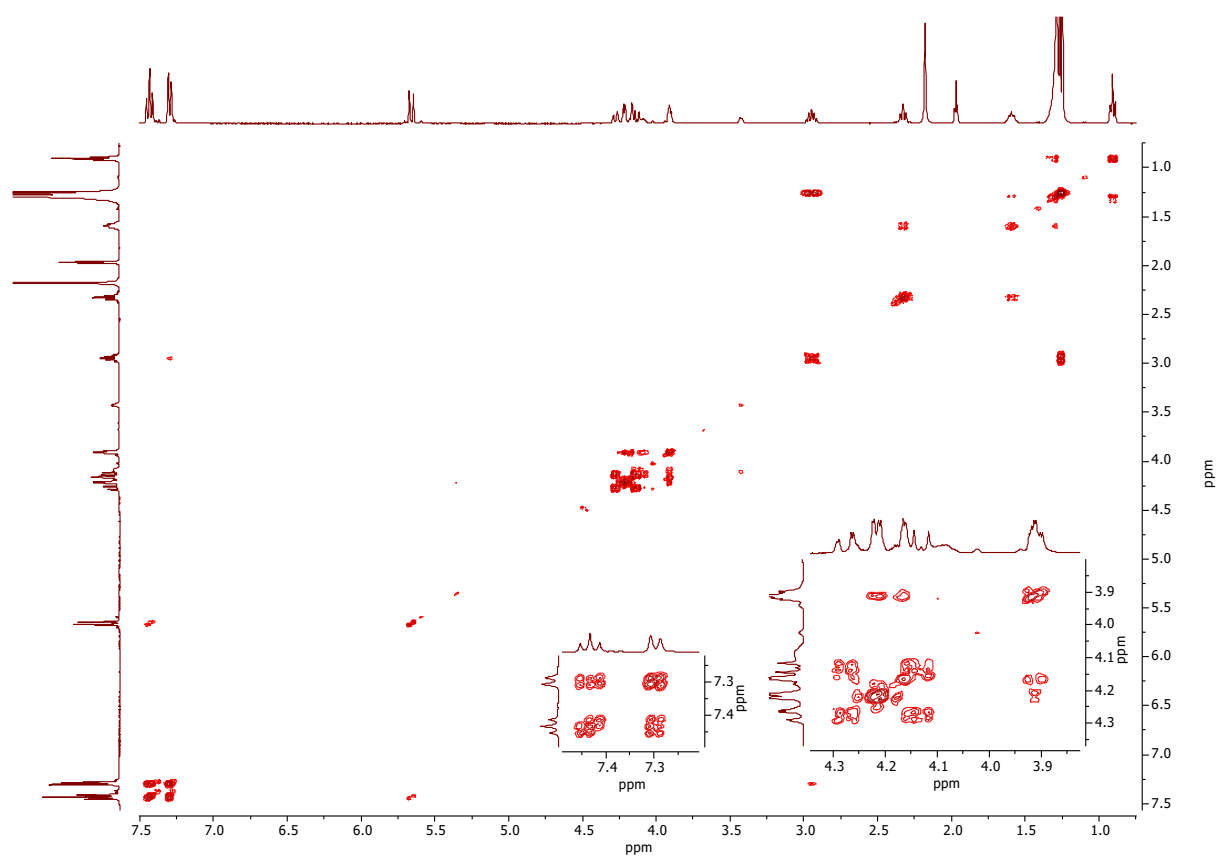
A 11 | COSY of Lauryl-DBS-*i*Pr
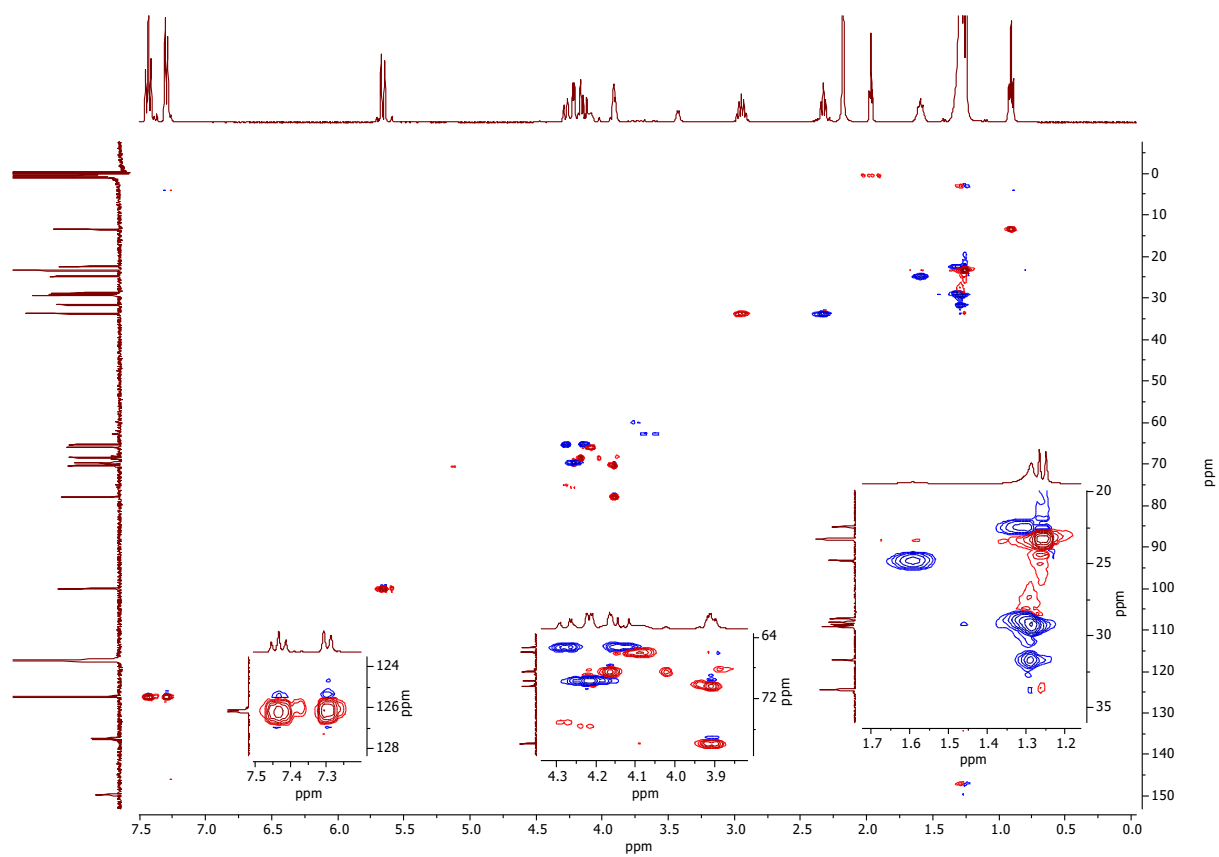
A 12 | HSQC of Lauryl-DBS-*i*Pr
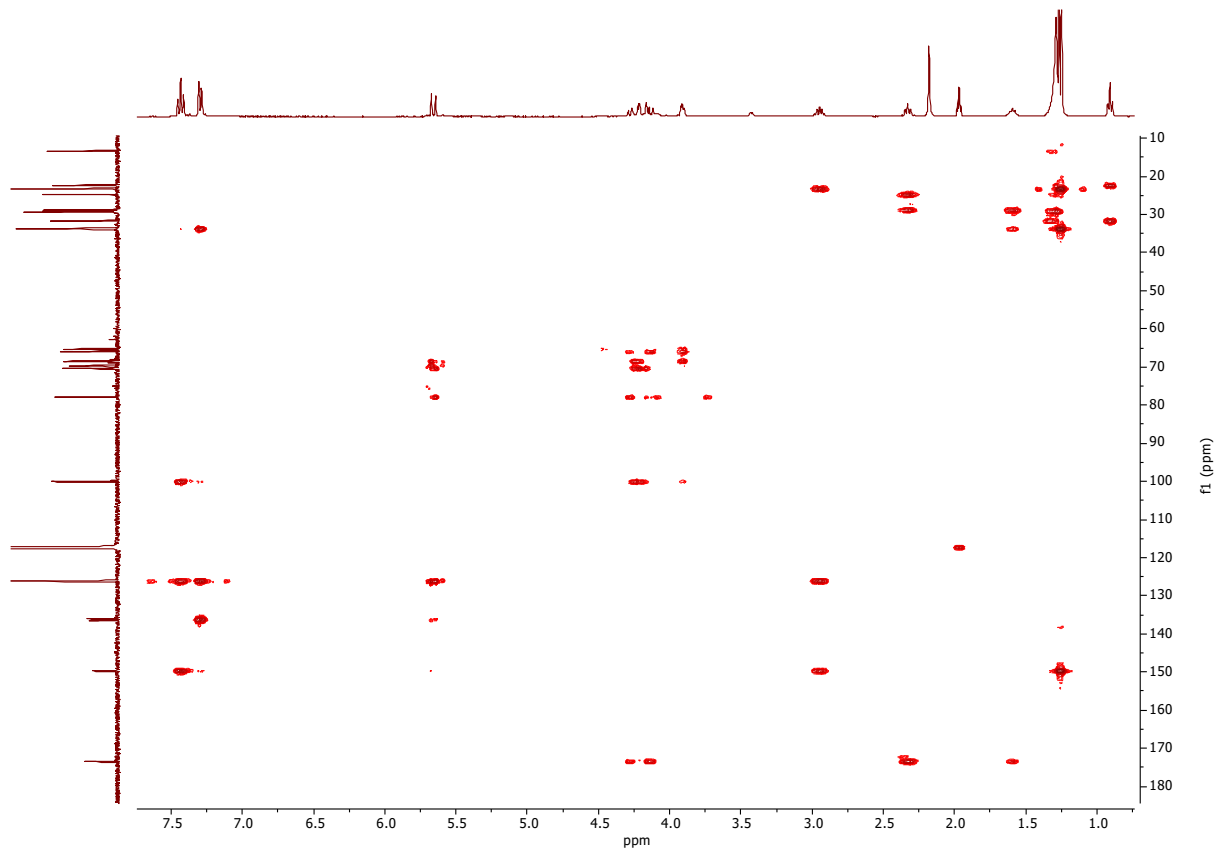
A 13 | HMBC of Lauryl-DBS-*i*Pr
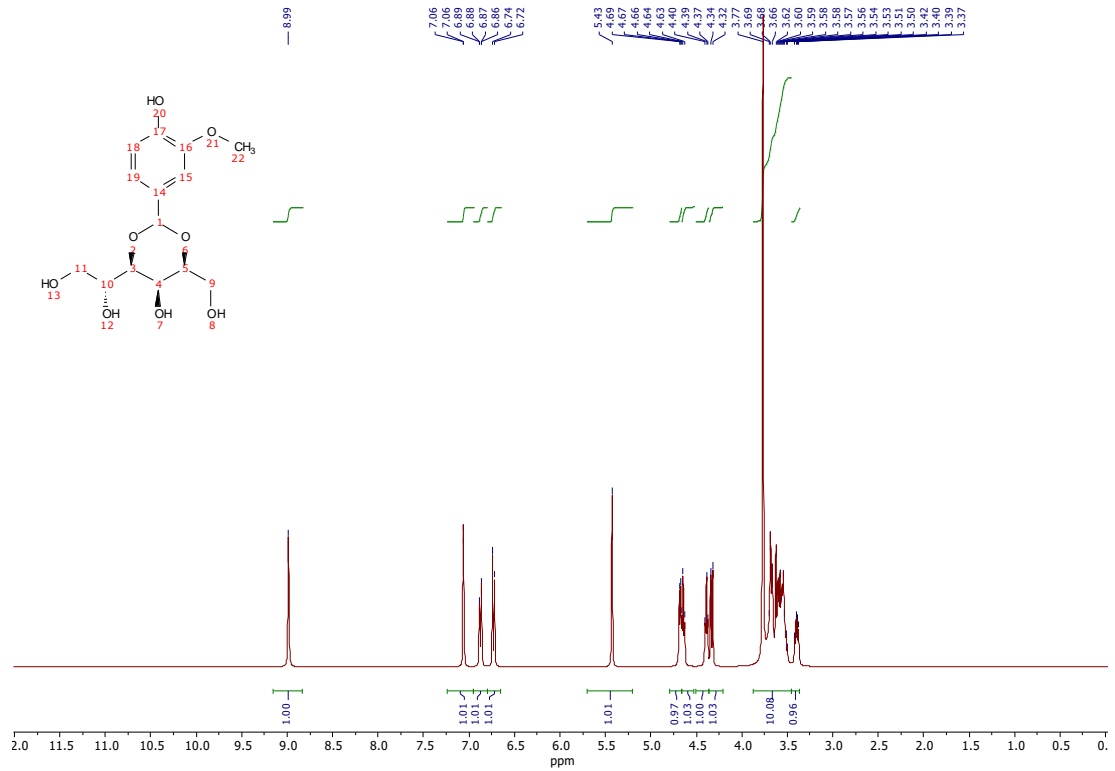
A 14 | ^{1}H NMR of MBS-Van
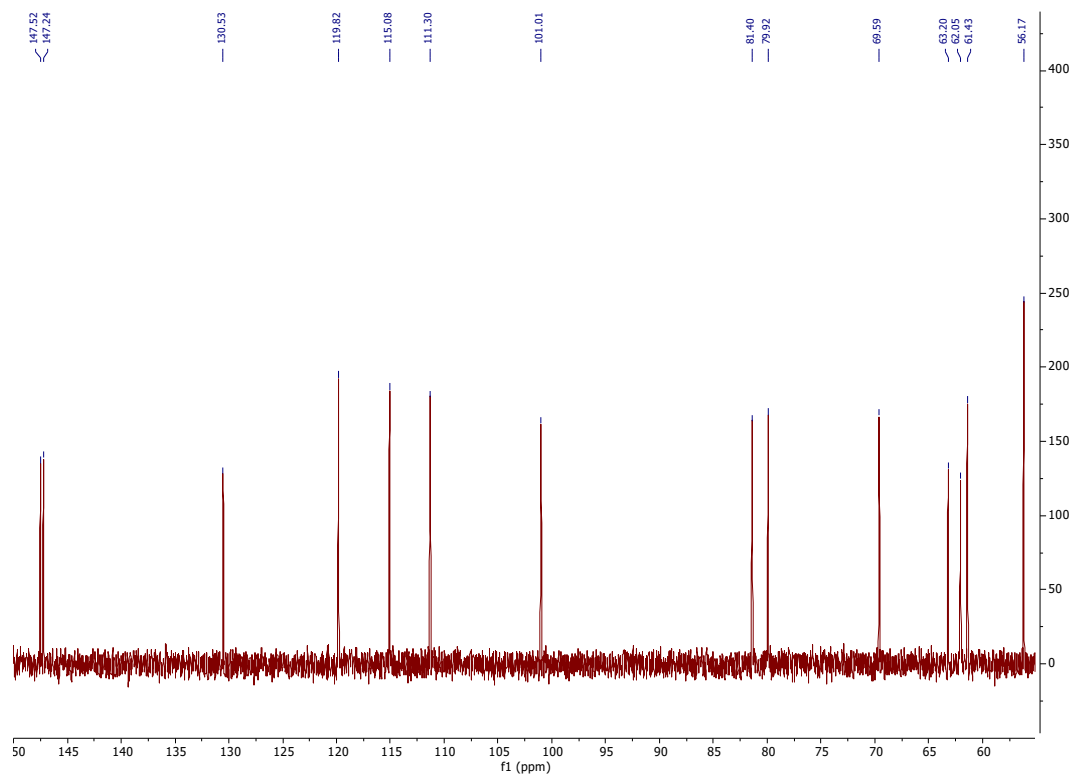
A 15 | ^{13}C NMR of MBS-Van
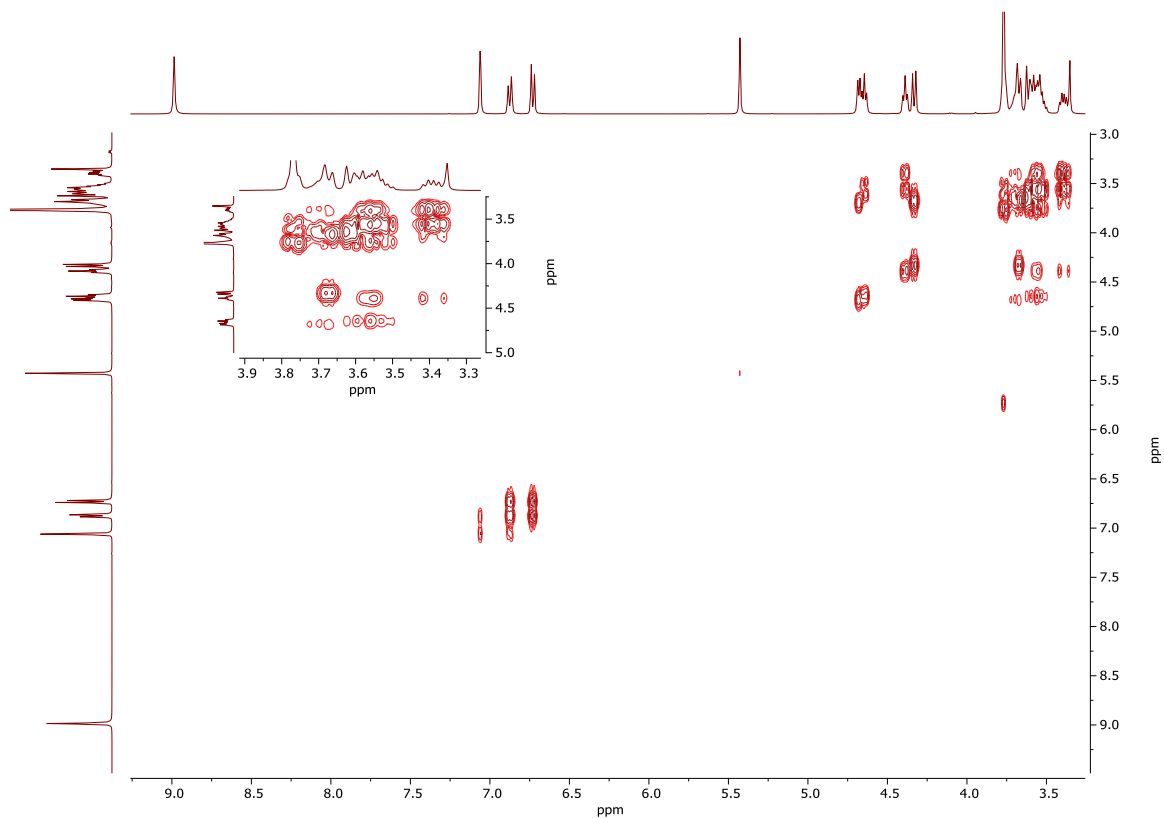
A 16 | COSY of MBS-Van
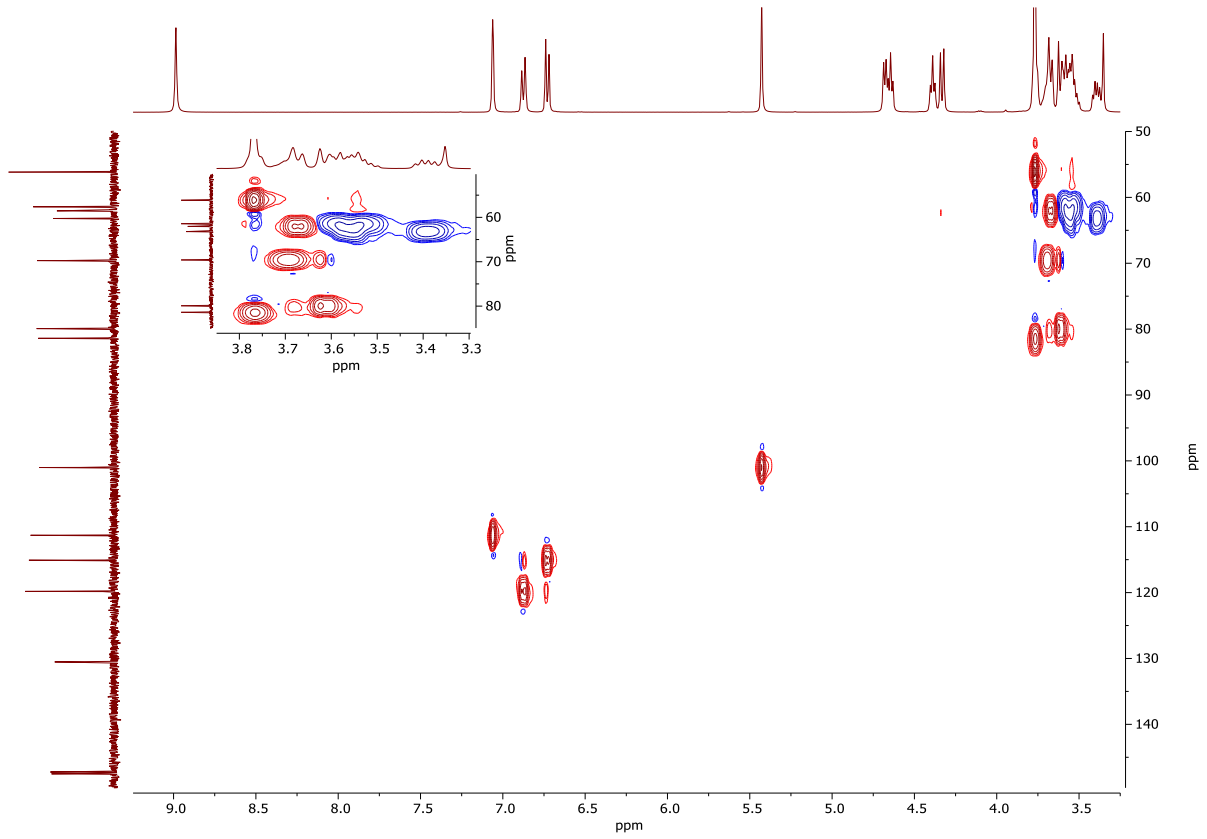
A 17 | HSQC of MBS-Van
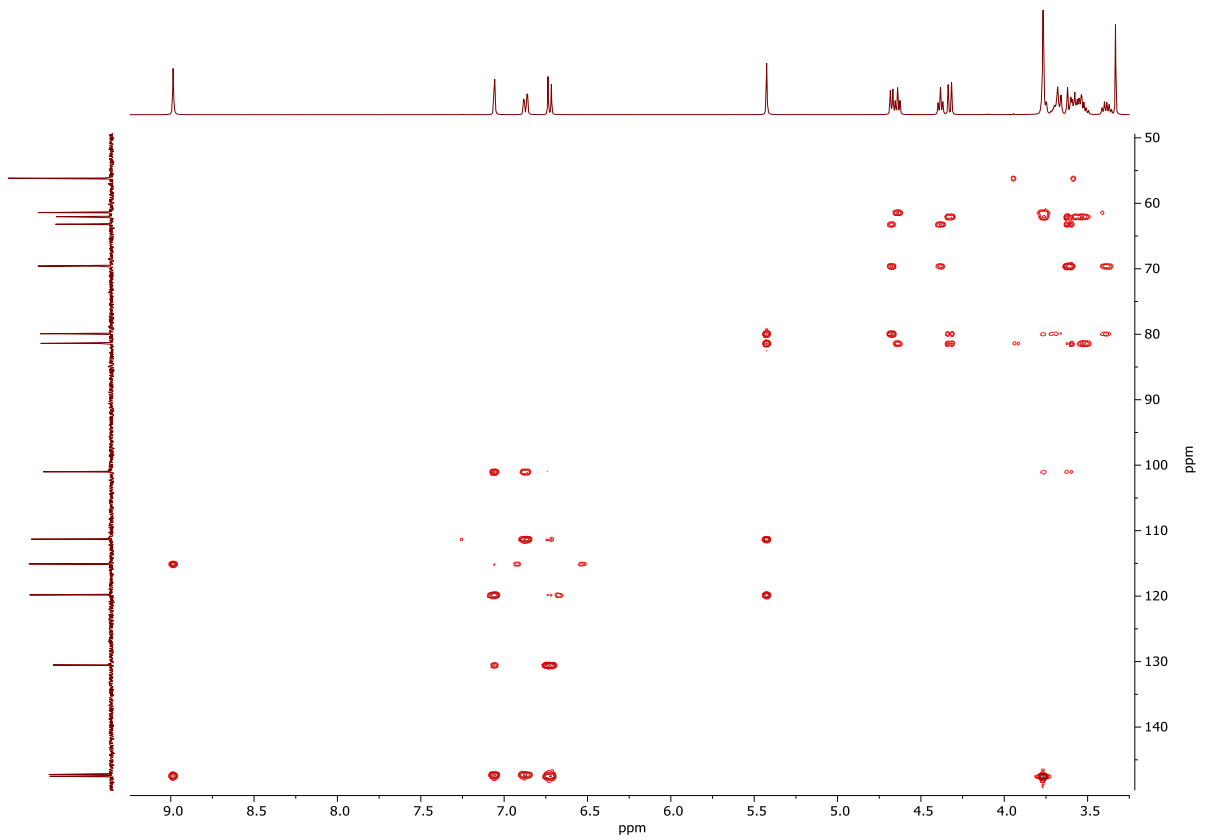
A 18 | HMBC of MBS-Van
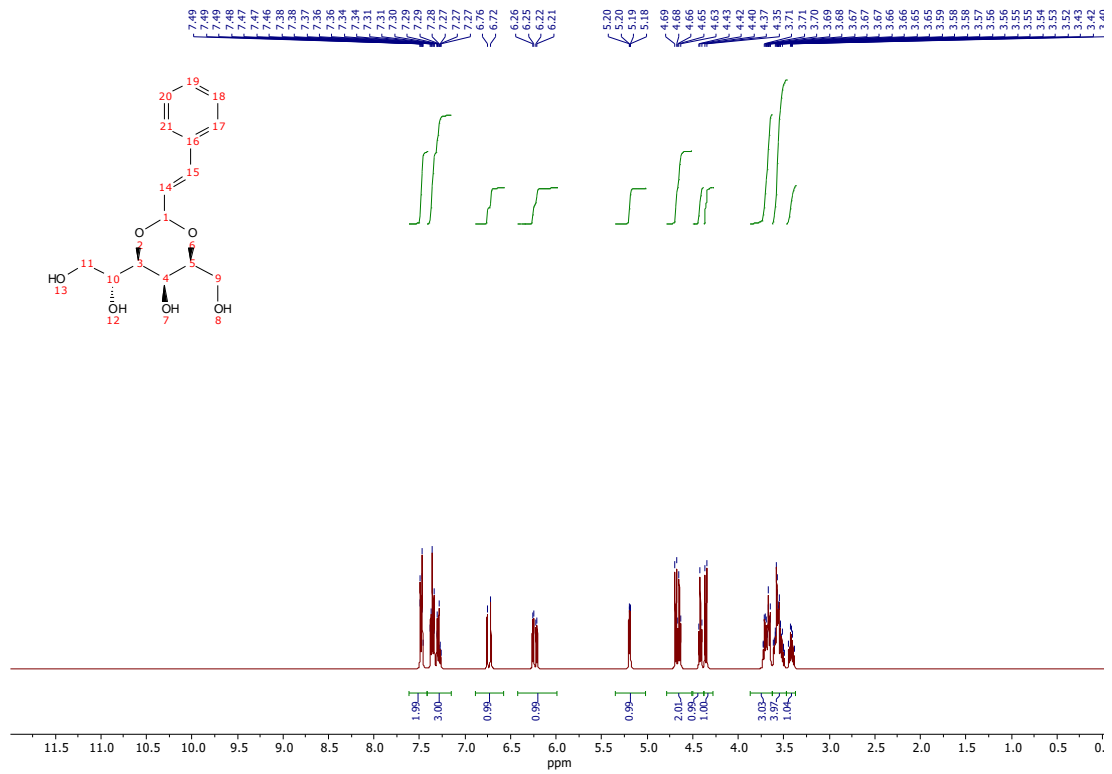
A 19 |^{1}H NMR of MBS-Cinn
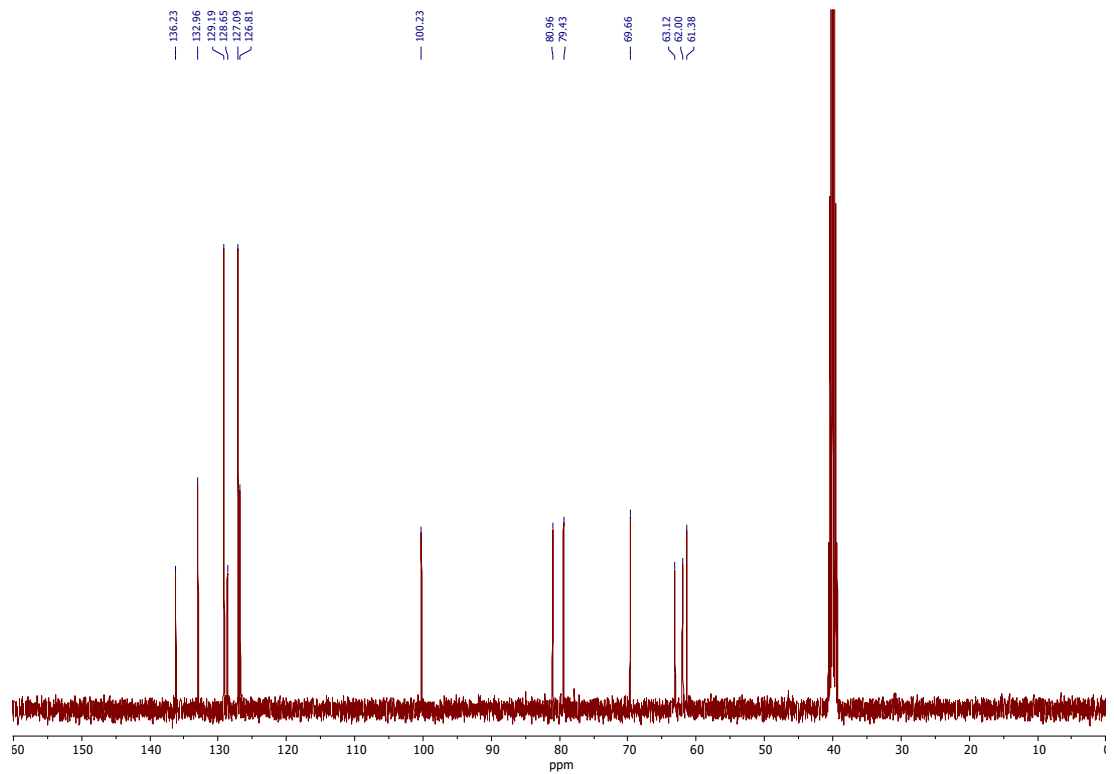
A 20 |^{13}C NMR of MBS-Cinn
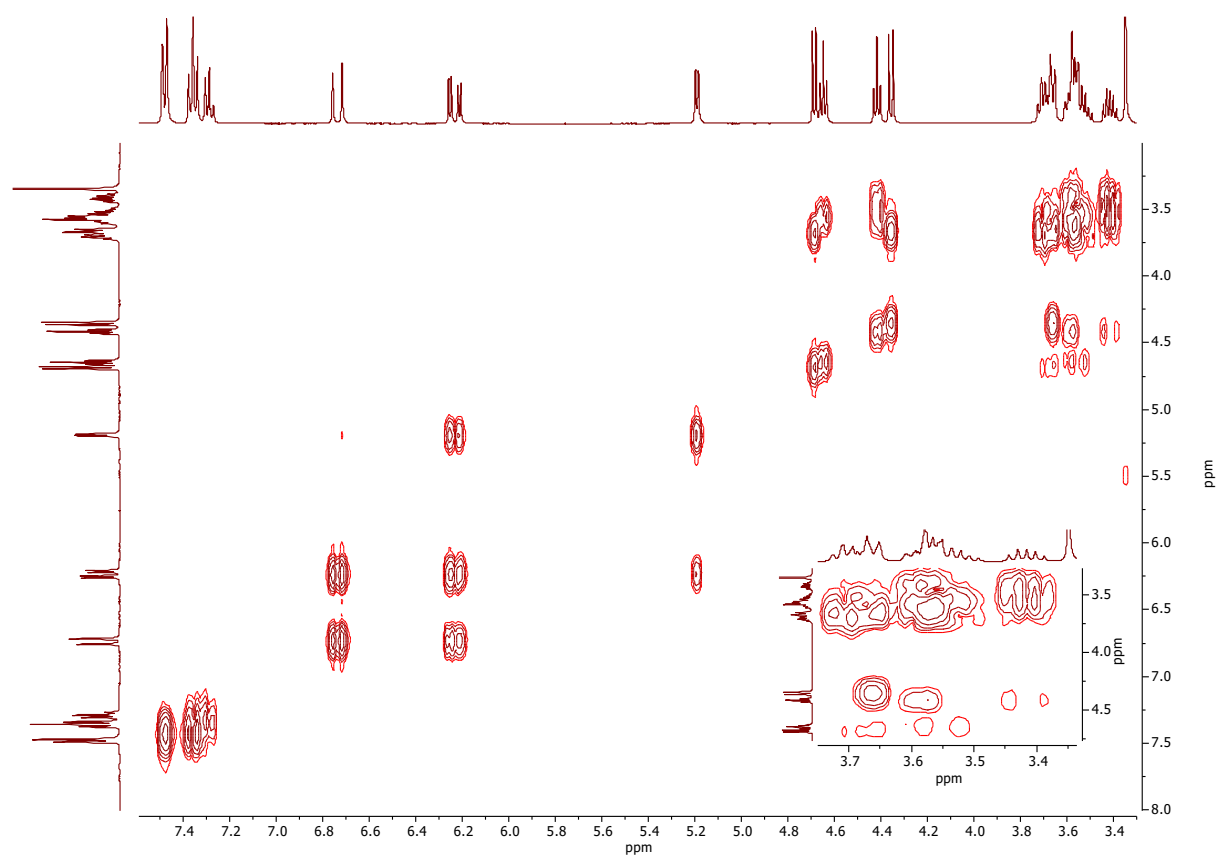
A 21 | COSY of MBS-Cinn
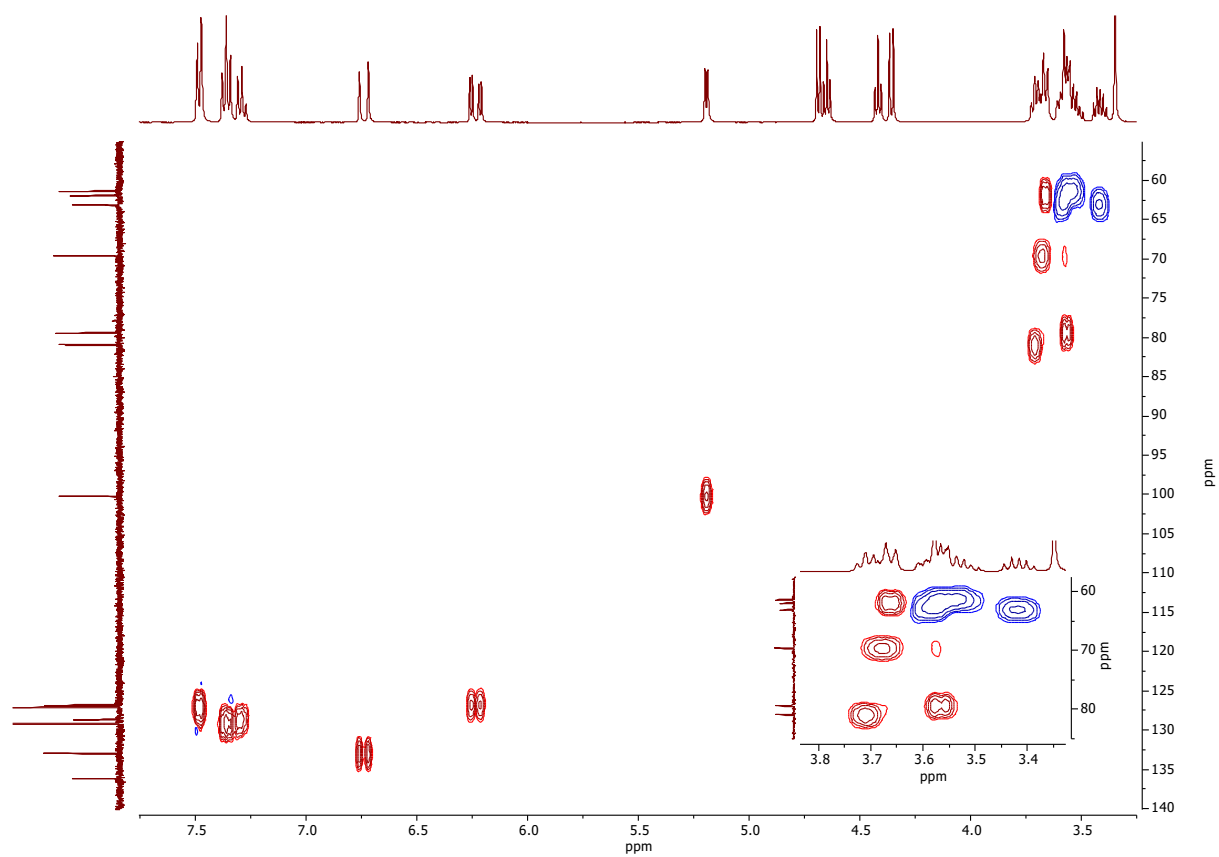
A 22 | HSQC of MBS-Cinn
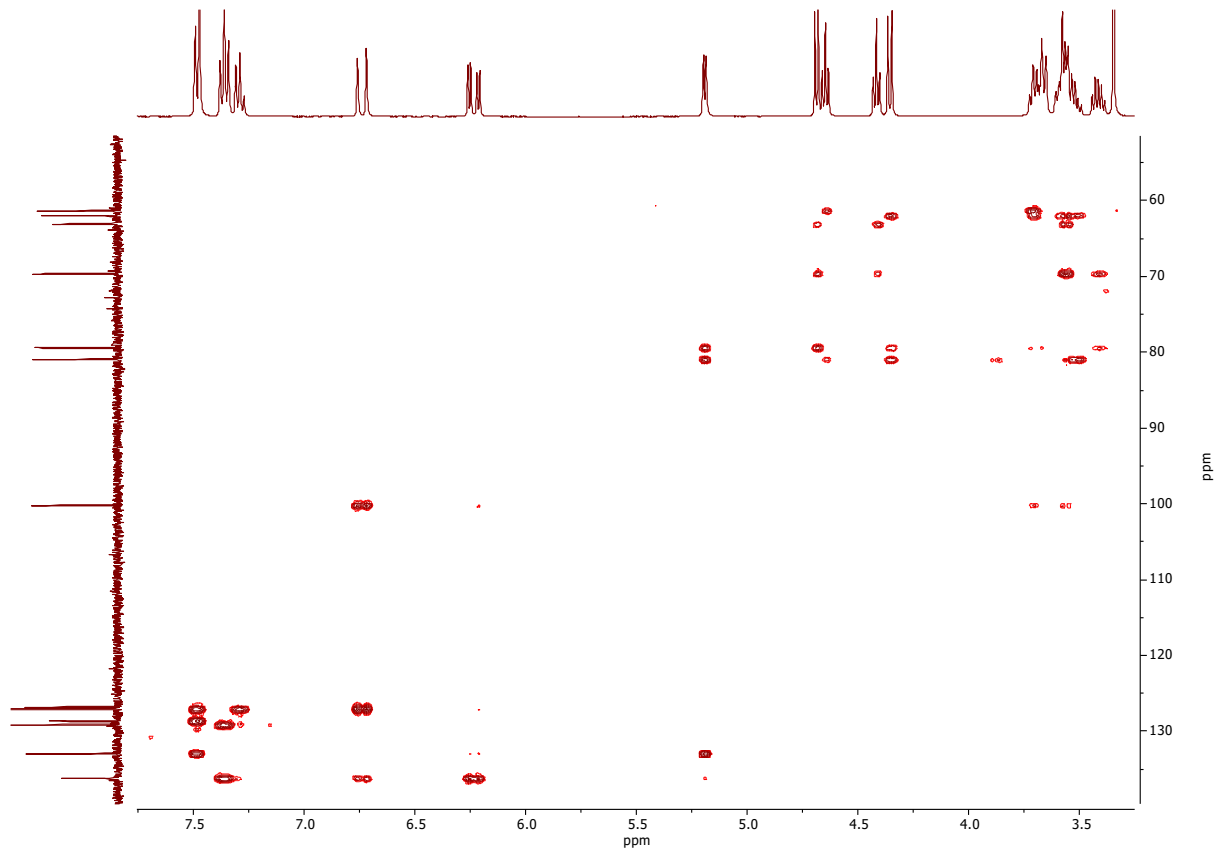
A 23 | HMBC of MBS-Cinn
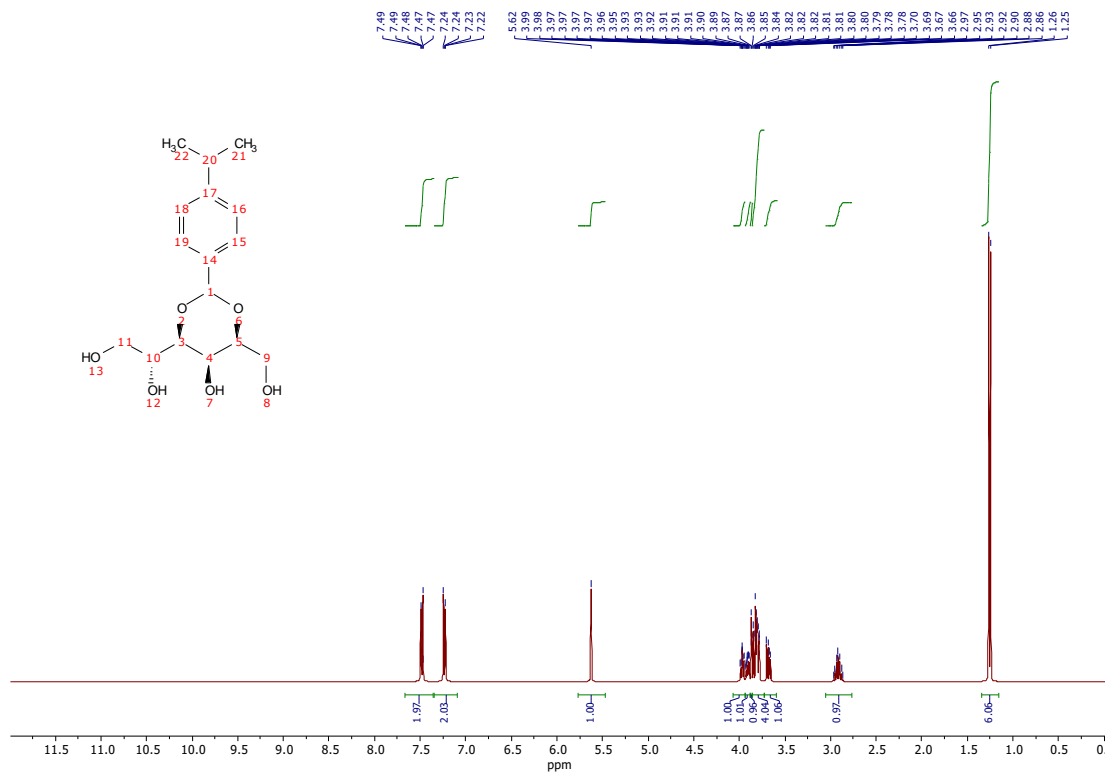
A 24 |^{1}H NMR of MBS-iPr
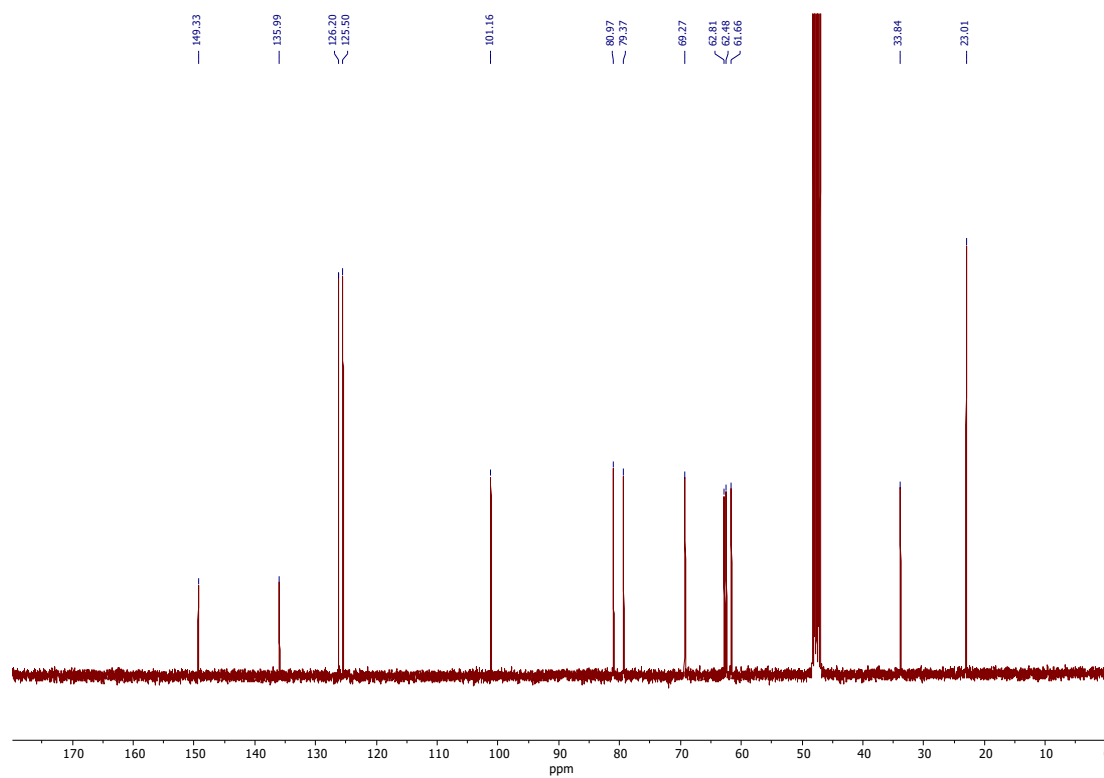
A 25 |^{13}C NMR of MBS-iPr
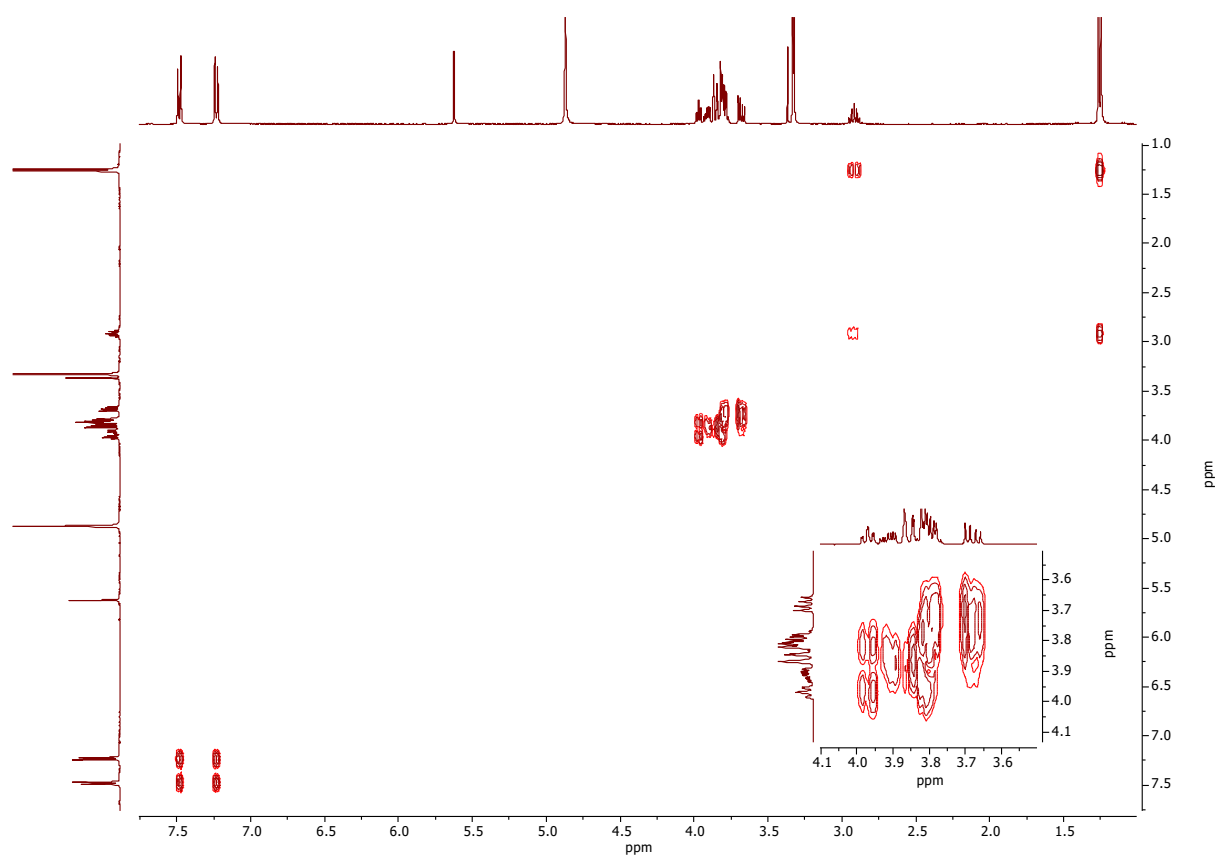
A 26 | COSY of MBS-*i*Pr
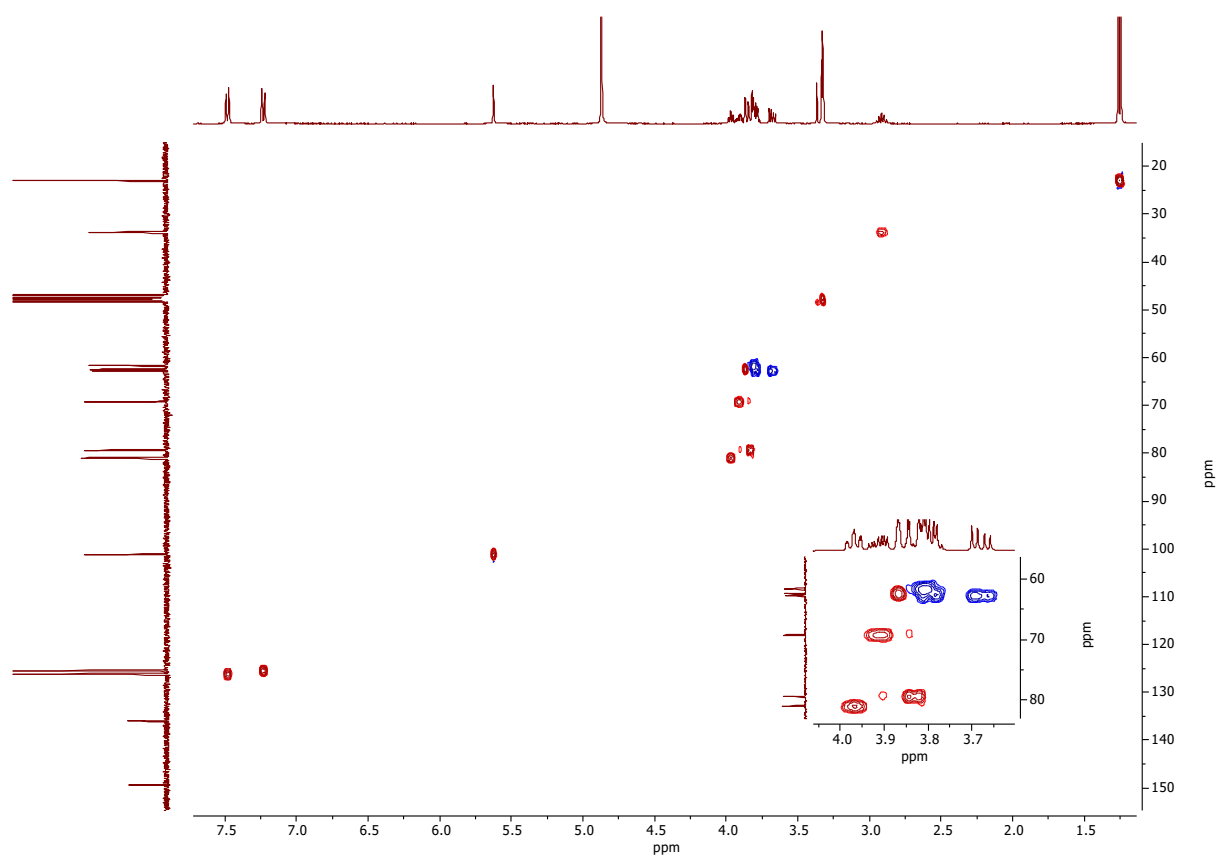
A 27 | HSQC of MBS-*i*Pr
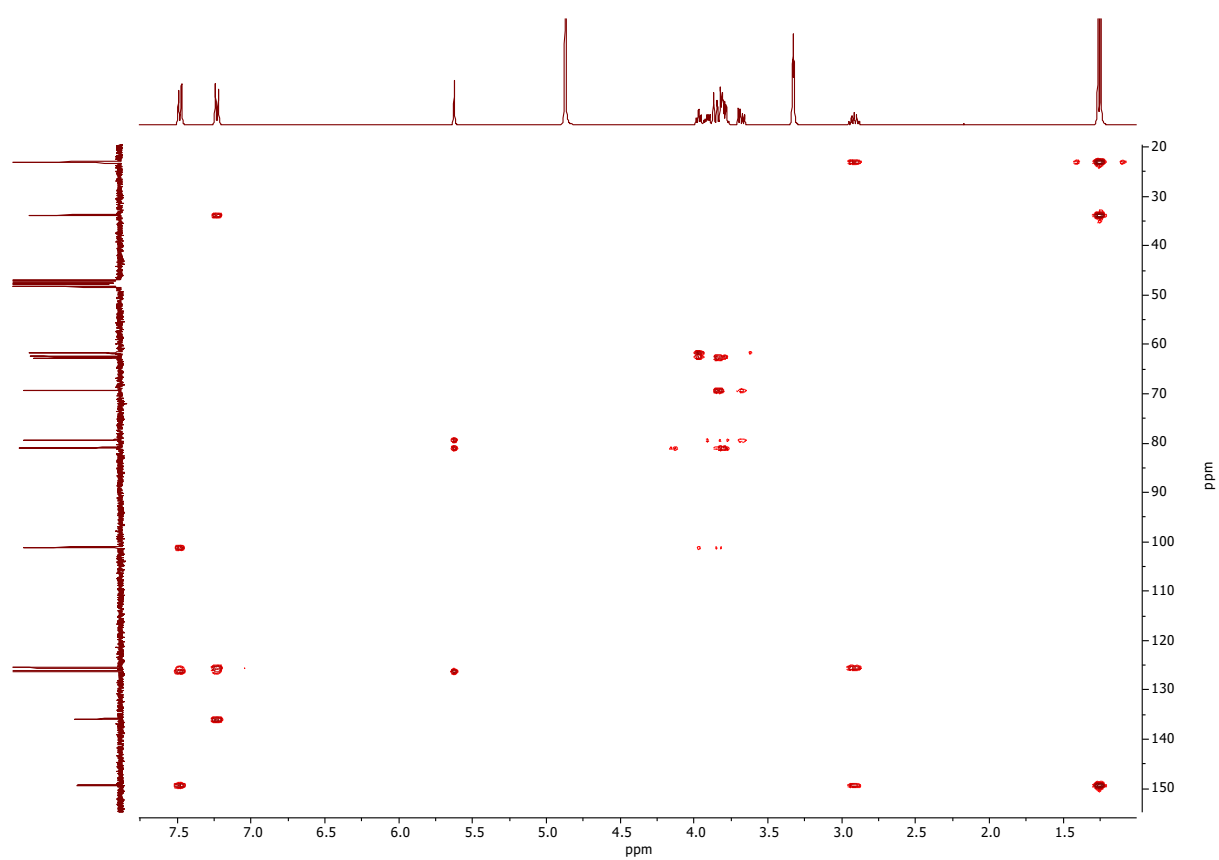
A 28 | HMBC of MBS-*i*Pr
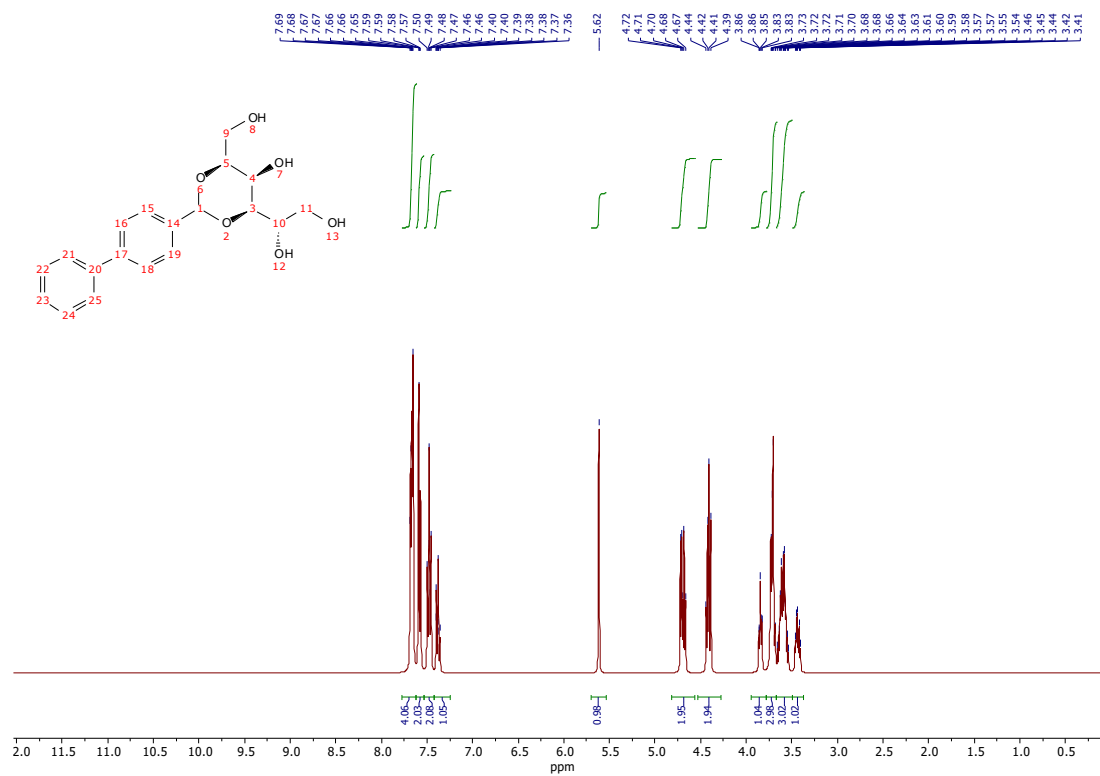
A 29 | ¹H NMR of MBS-Ph
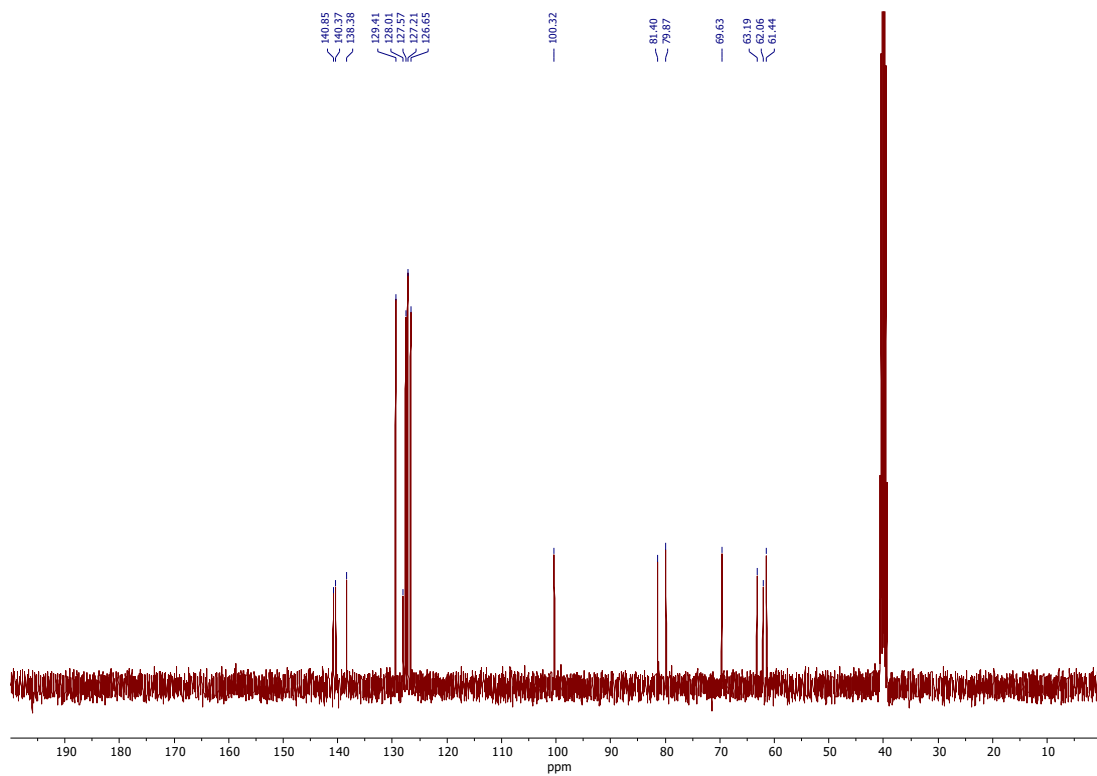
A 30 | ¹³C NMR of MBS-Ph
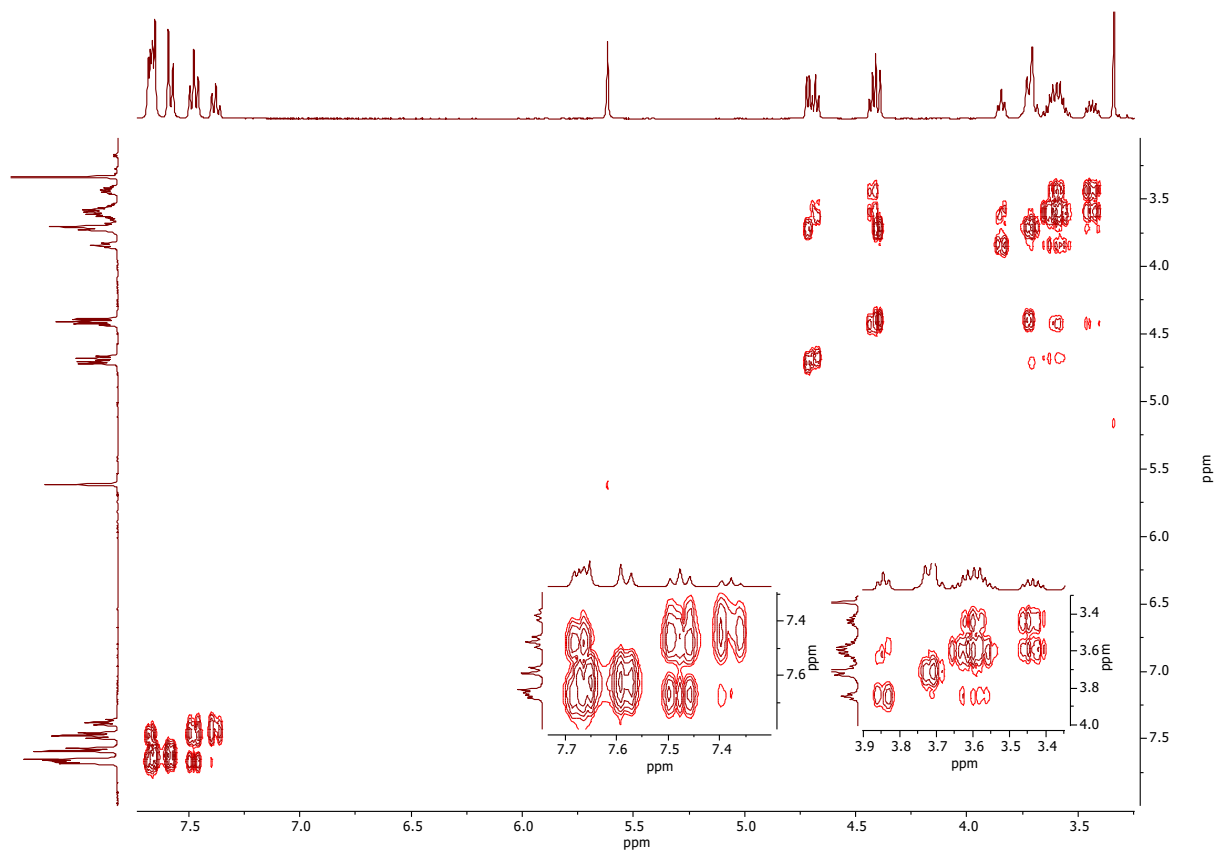
A 31 | COSY of MBS-Ph
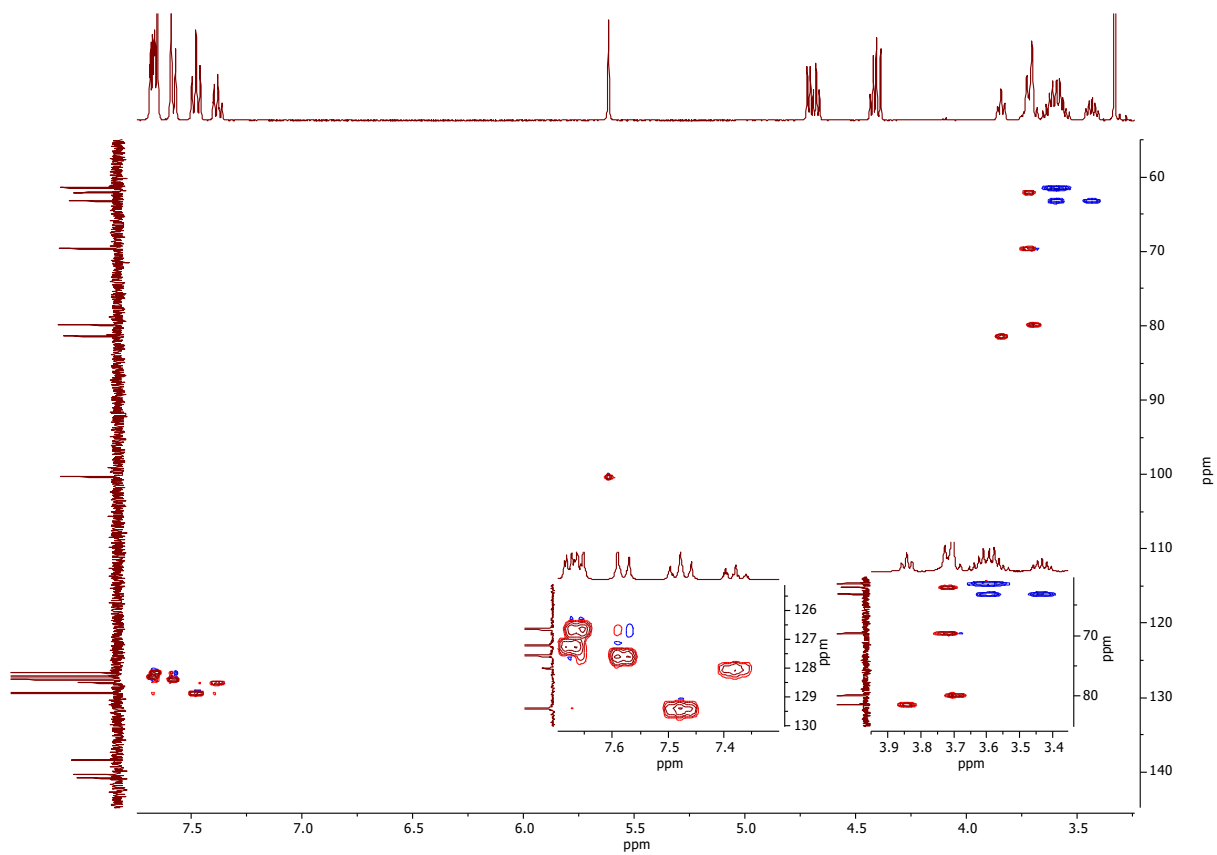
A 32 | HSQC of MBS-Ph
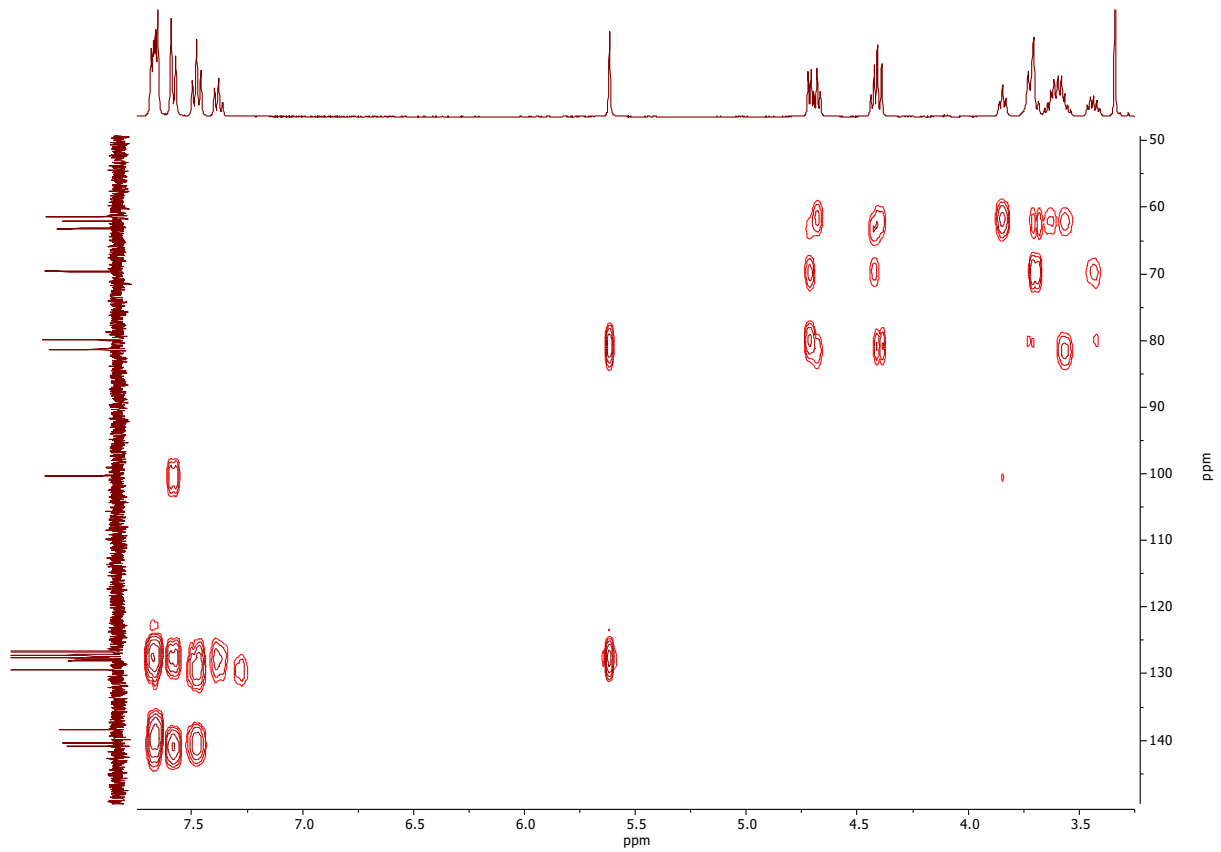
A 33 | HMBC of MBS-Ph
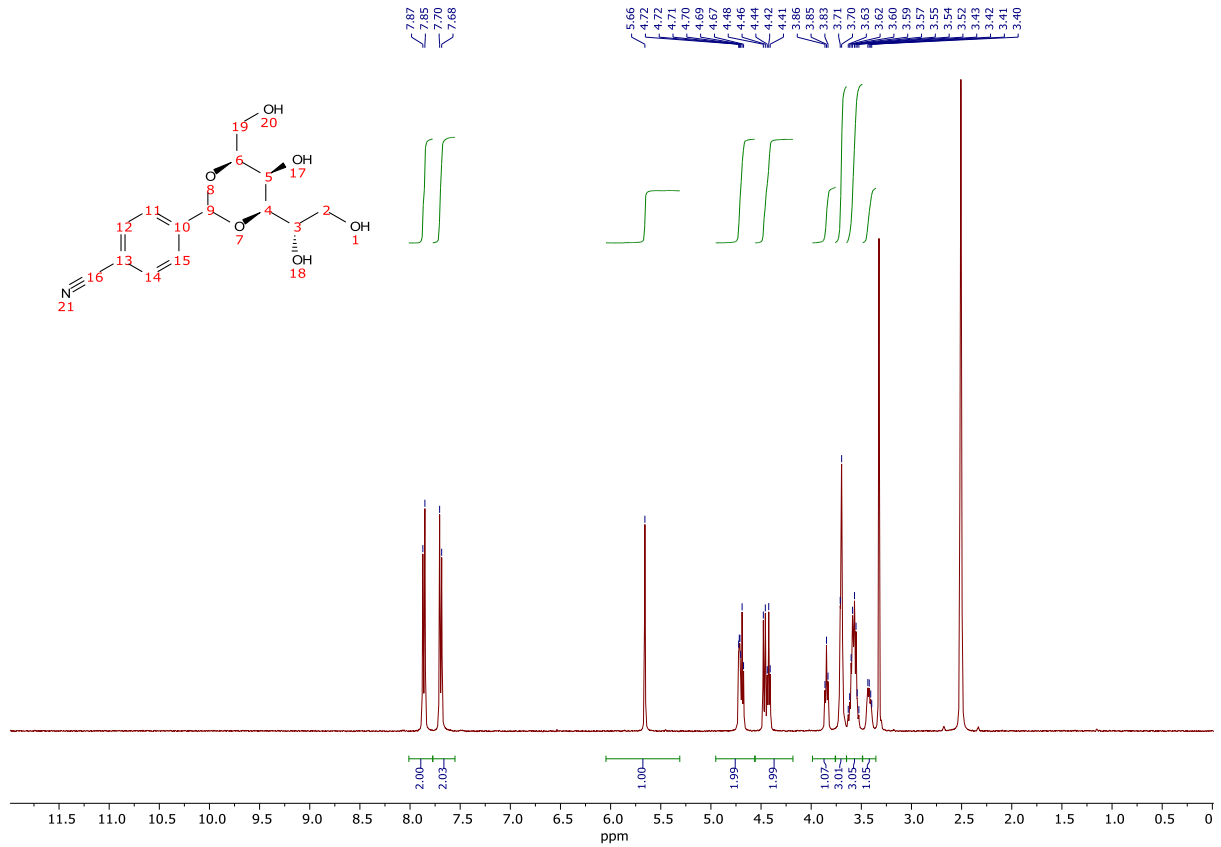
A 34 | ^{1}H NMR of MBS-CN
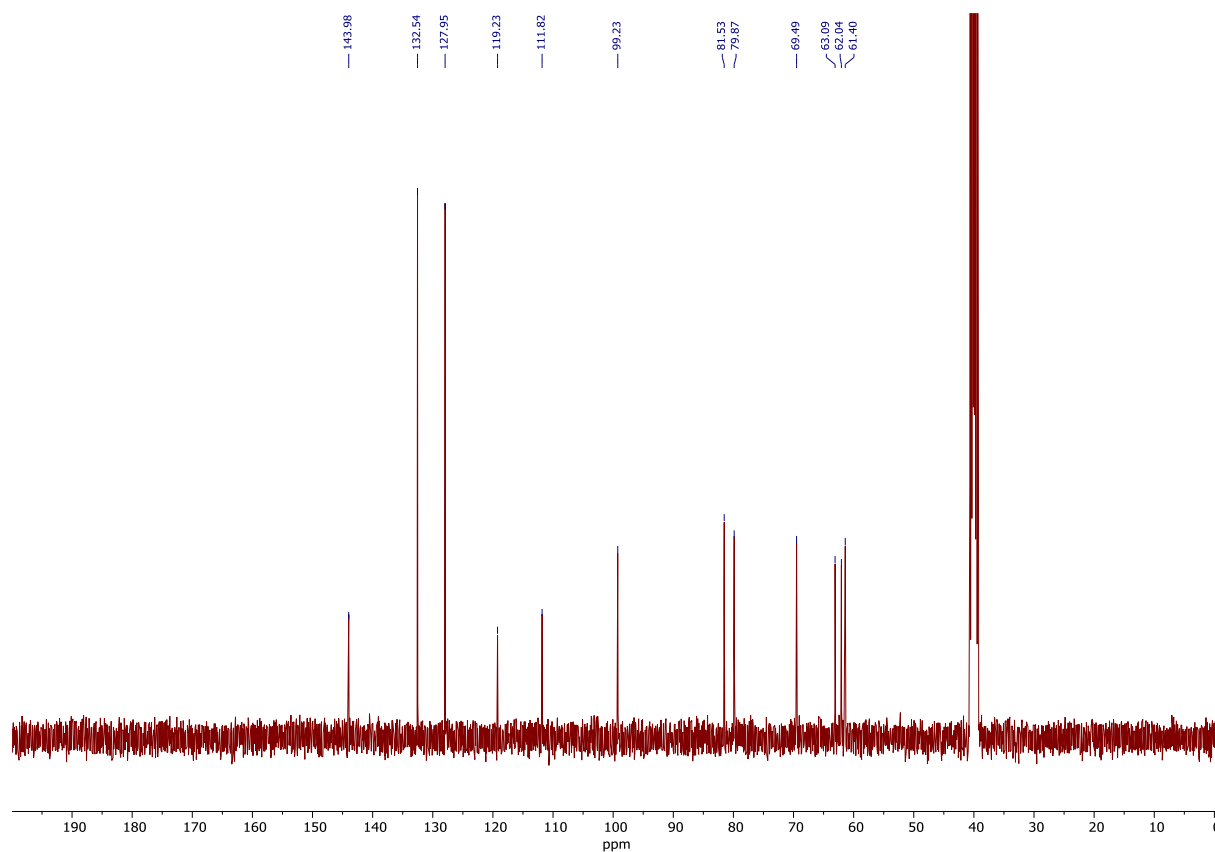
A 35 | ^{13}C NMR of MBS-CN

A 36 | COSY of MBS-CN
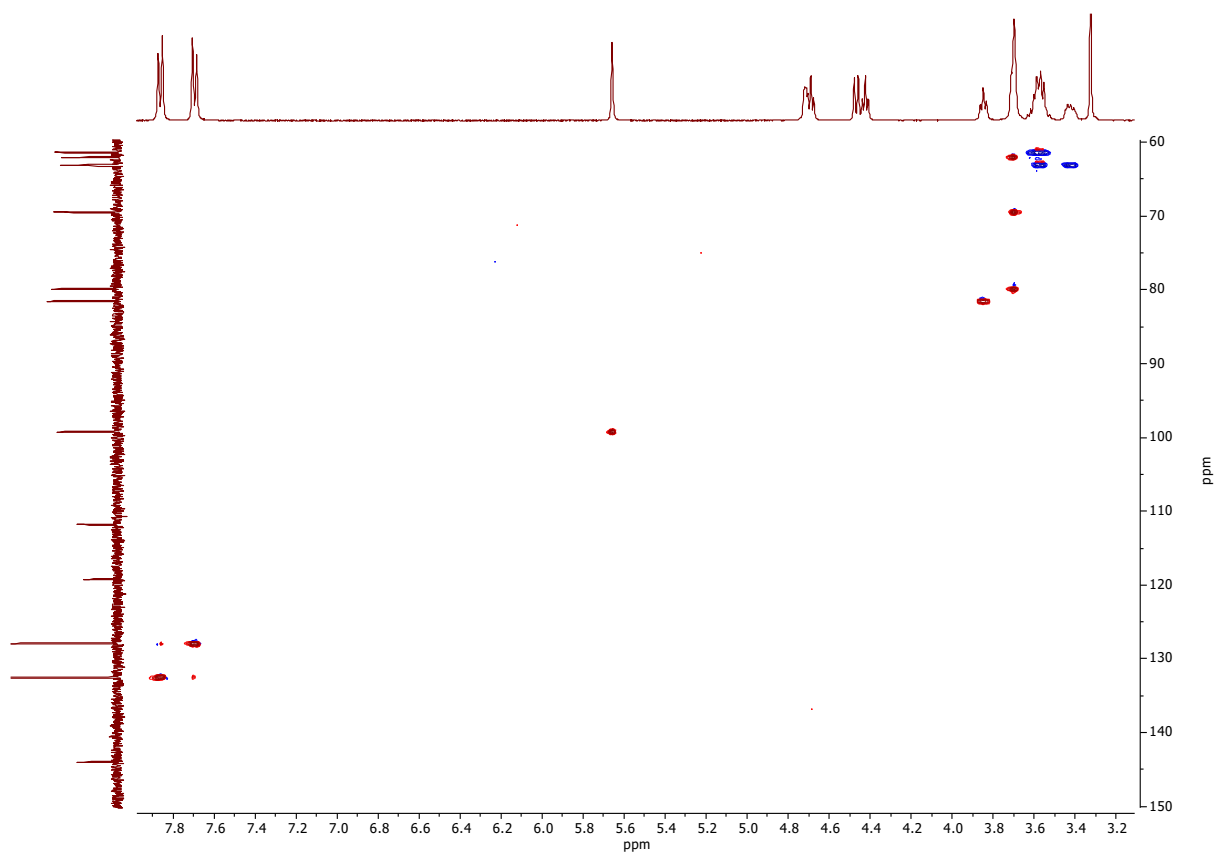
A 37 | HSQC of MBS-CN
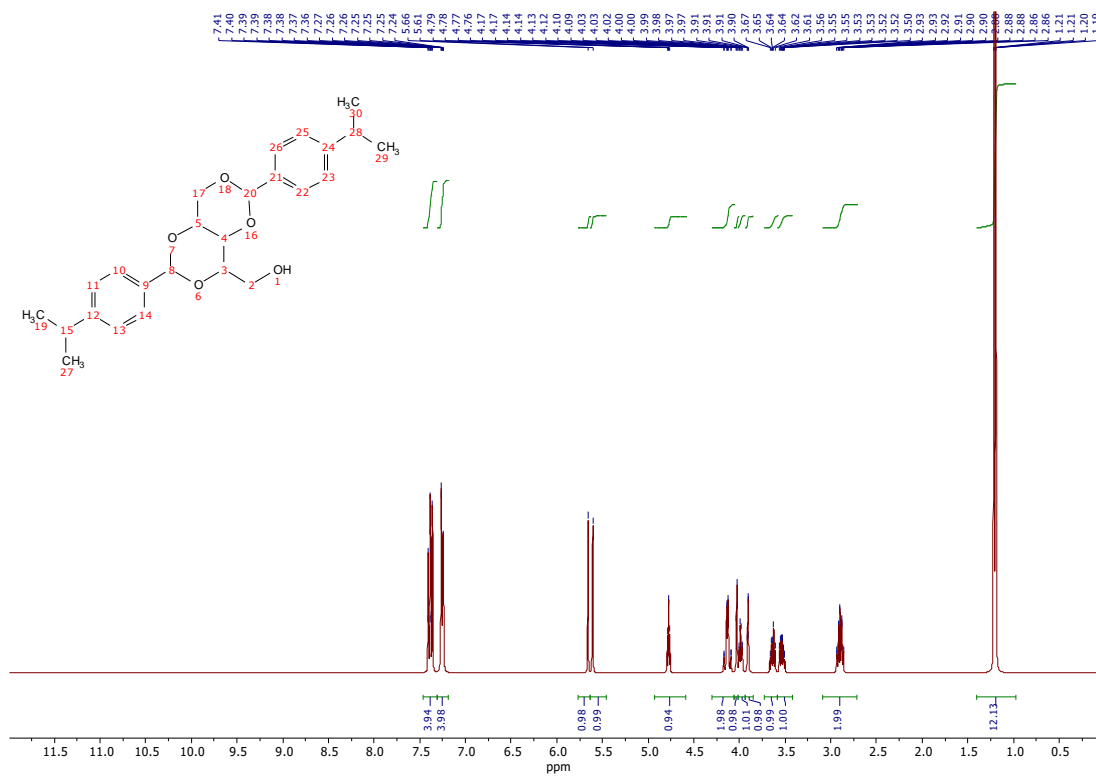
A 38 | ¹H NMR of DBX-*i*Pr
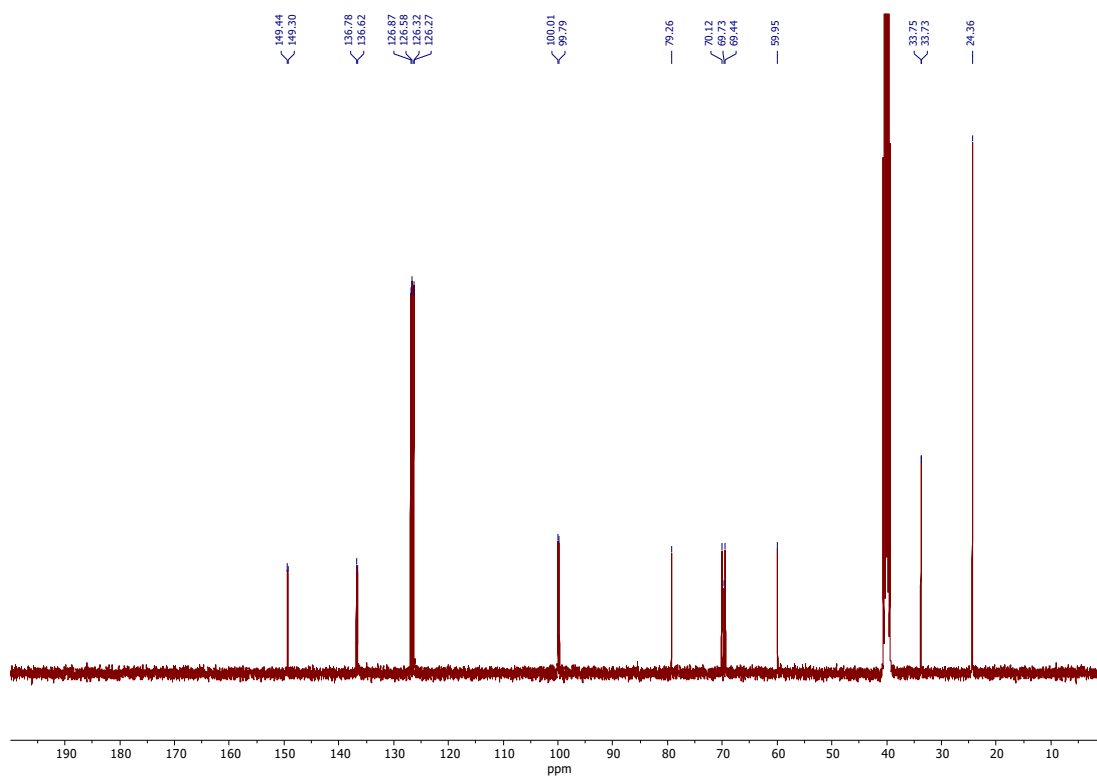
A 39 | ^{13}C NMR of DBX-*i*Pr
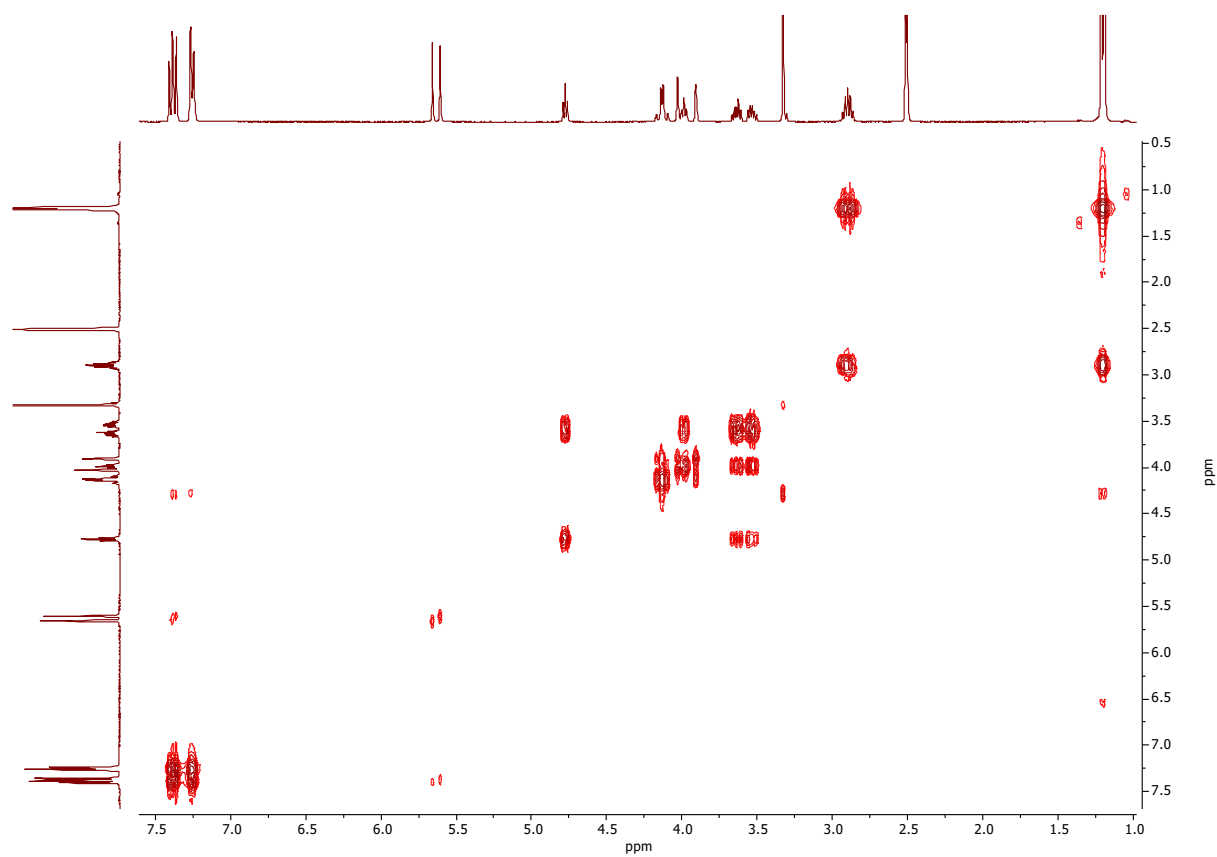
A 40 | COSY of DBX-*i*Pr
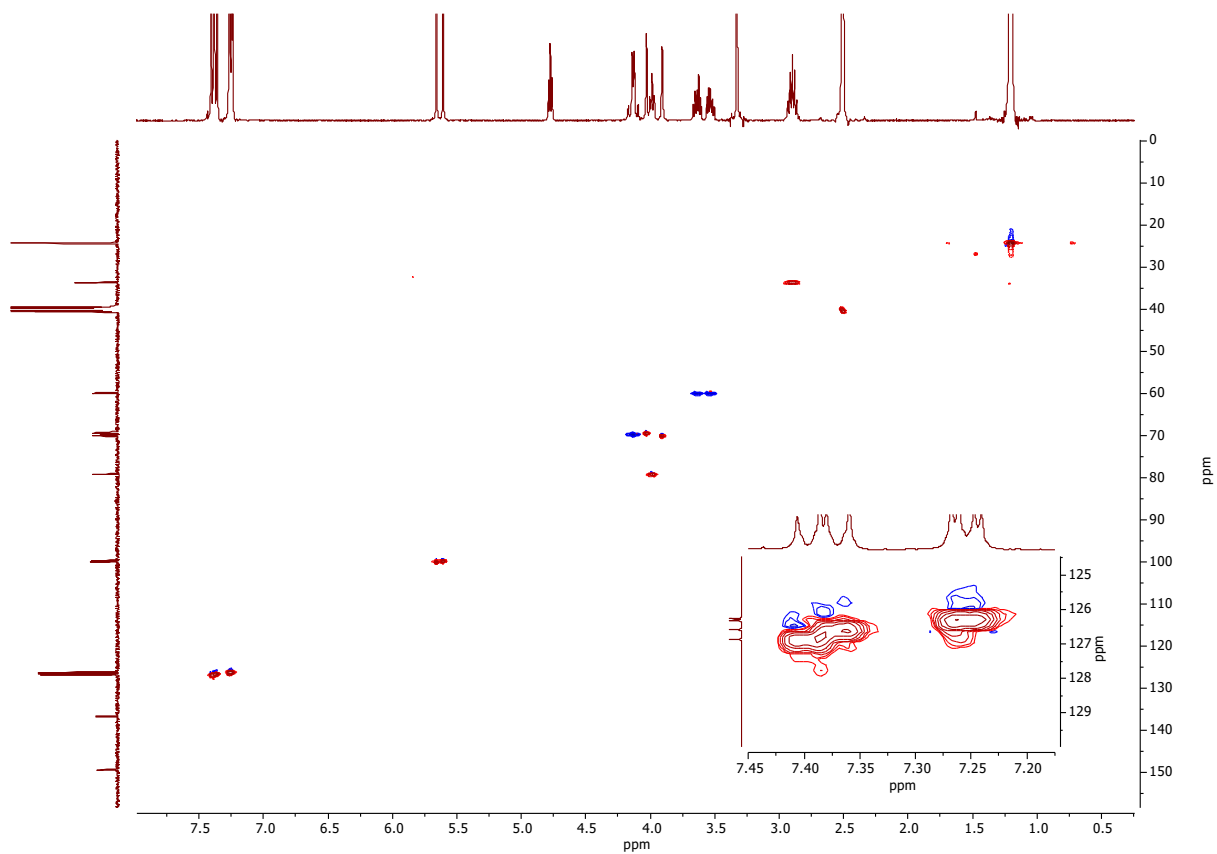
A 41 | HSQC of DBX-*i*Pr
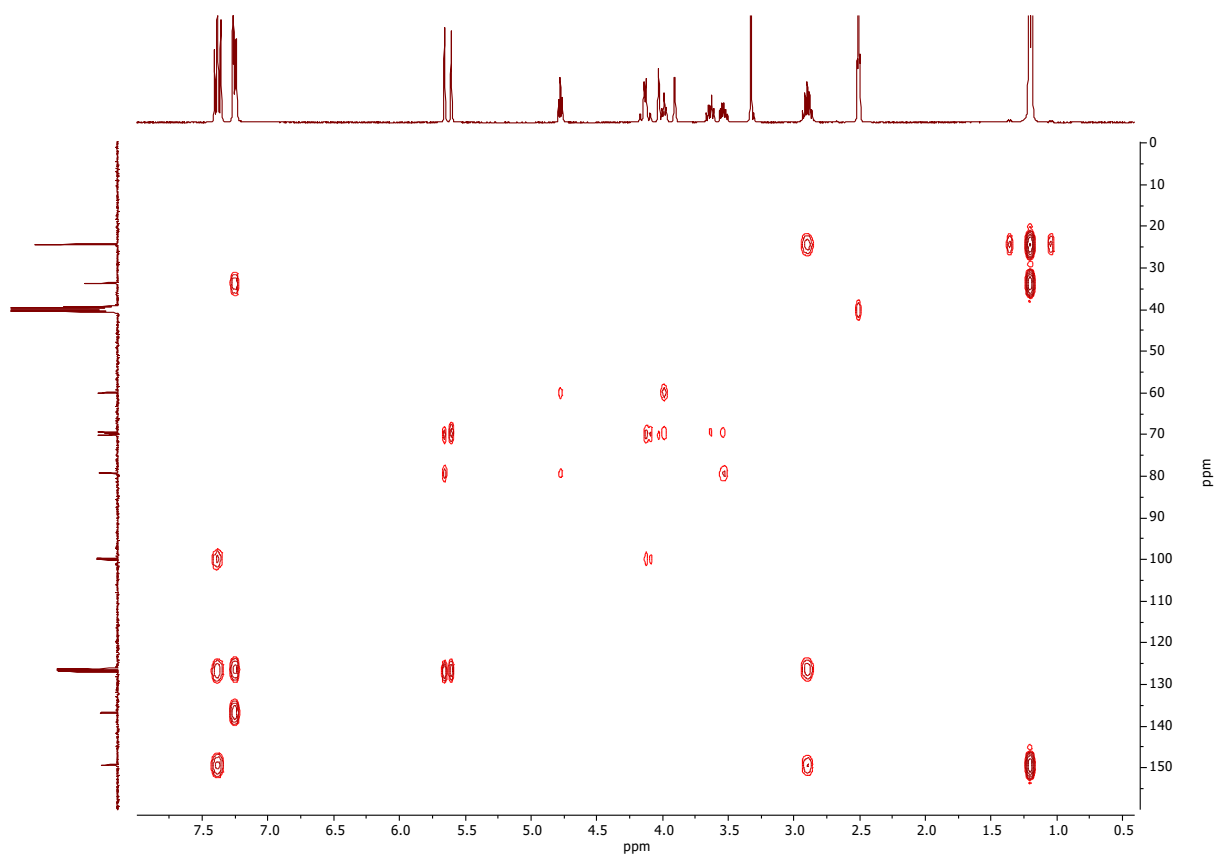
A 42 | HMBC of DBX-*i*Pr
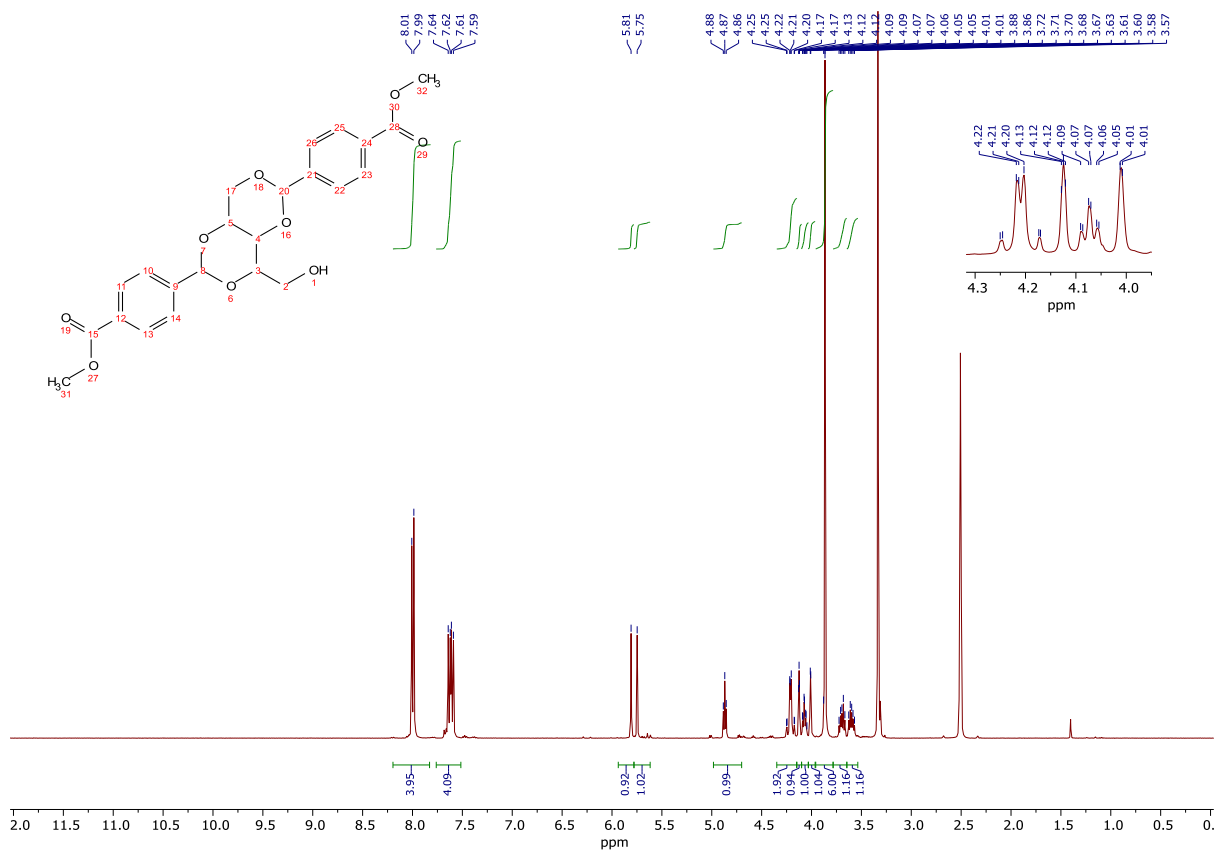
A 43 | ^{1}H NMR of DBX-CO$_2$Me
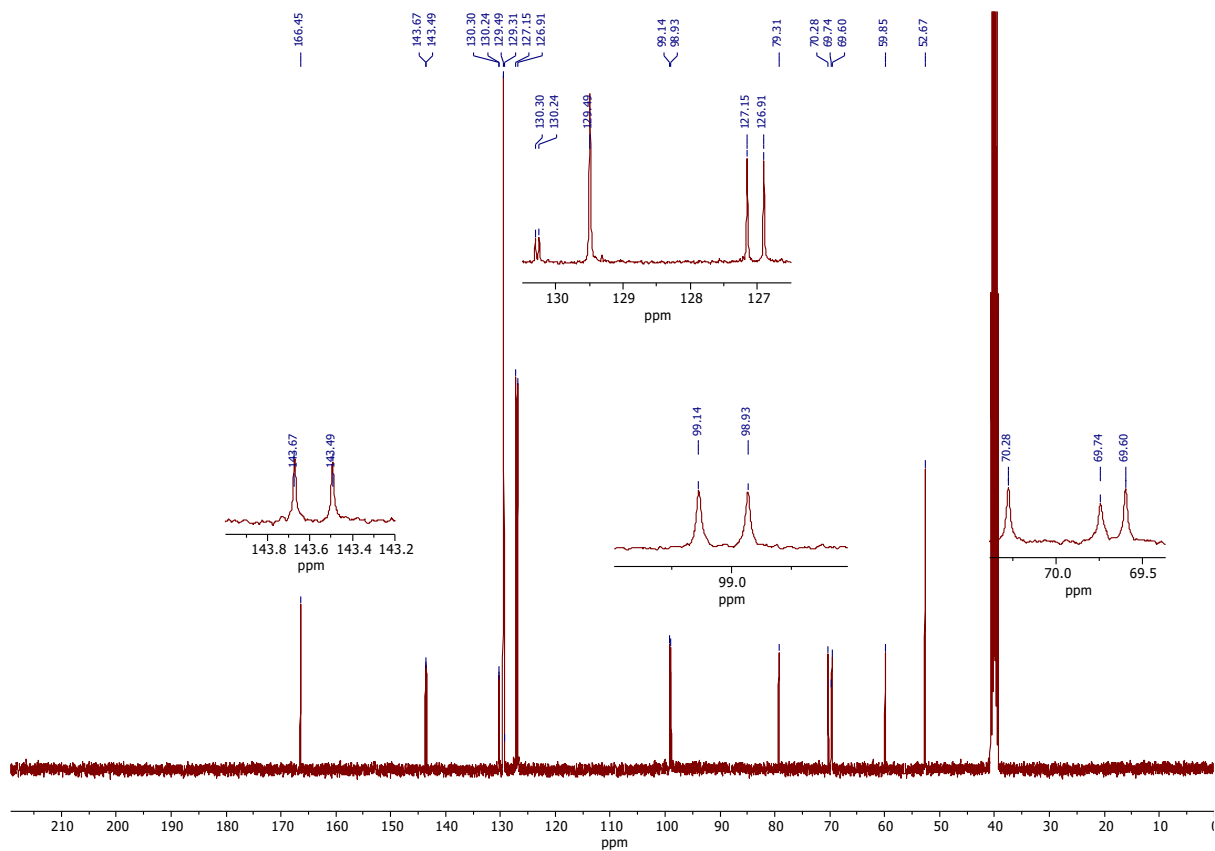
A 44 | ^{13}C NMR of DBX-CO$_2$Me
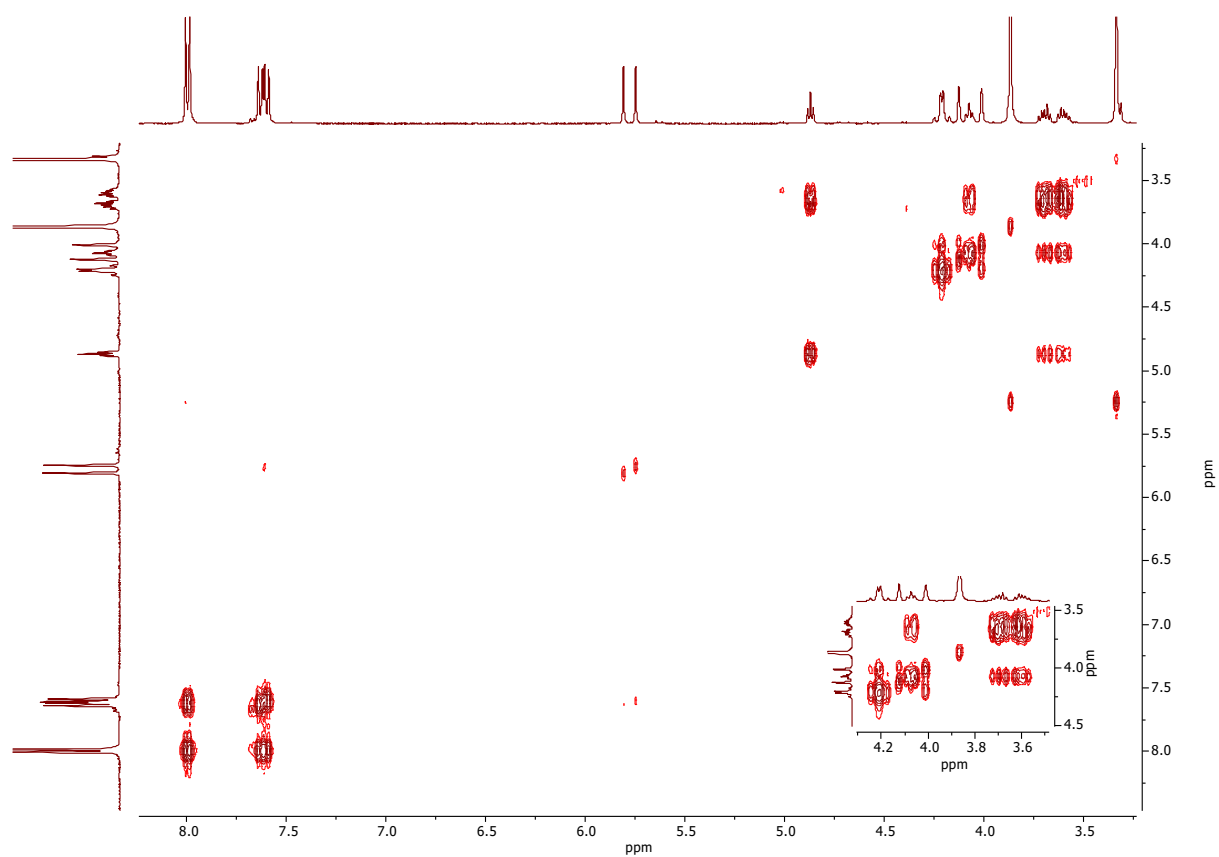
A 45 | COSY of DBX-CO$_2$Me
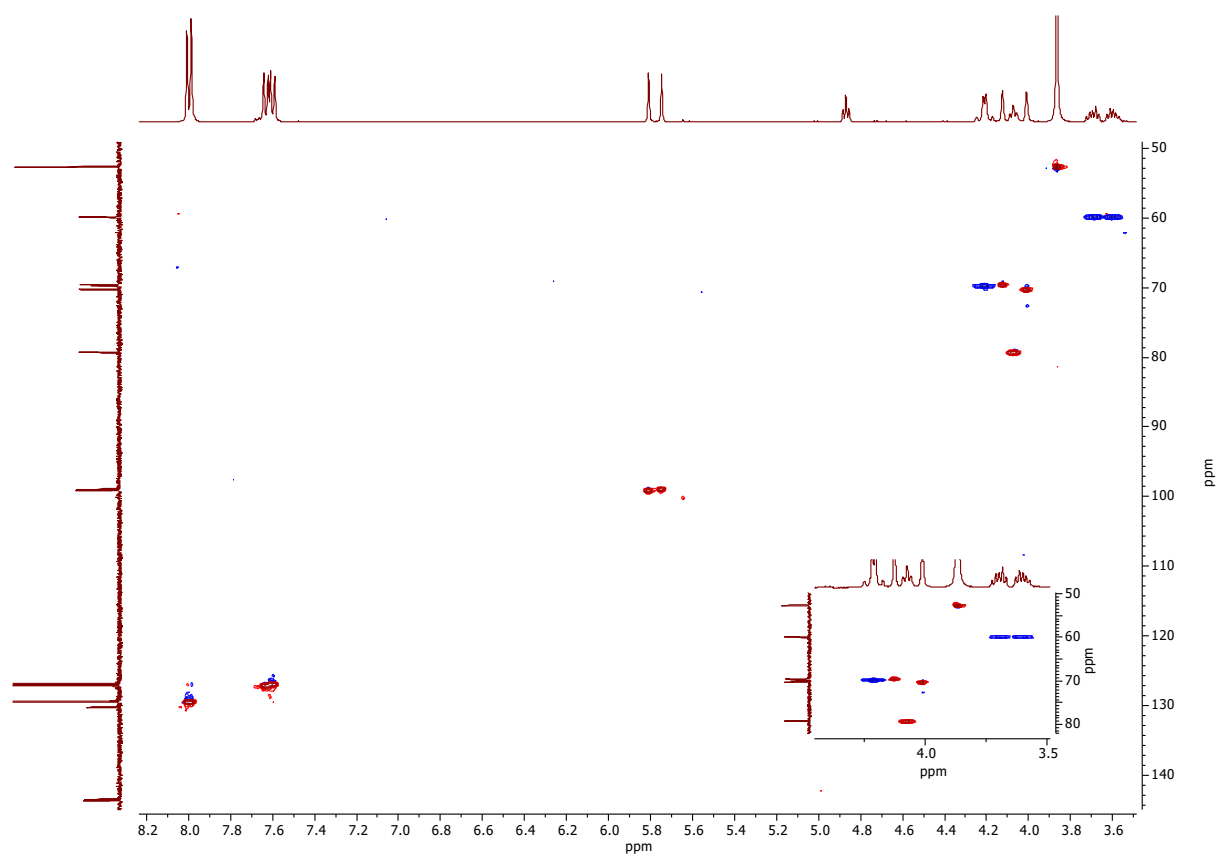
A 46 | HSQC of DBX-CO$_2$Me
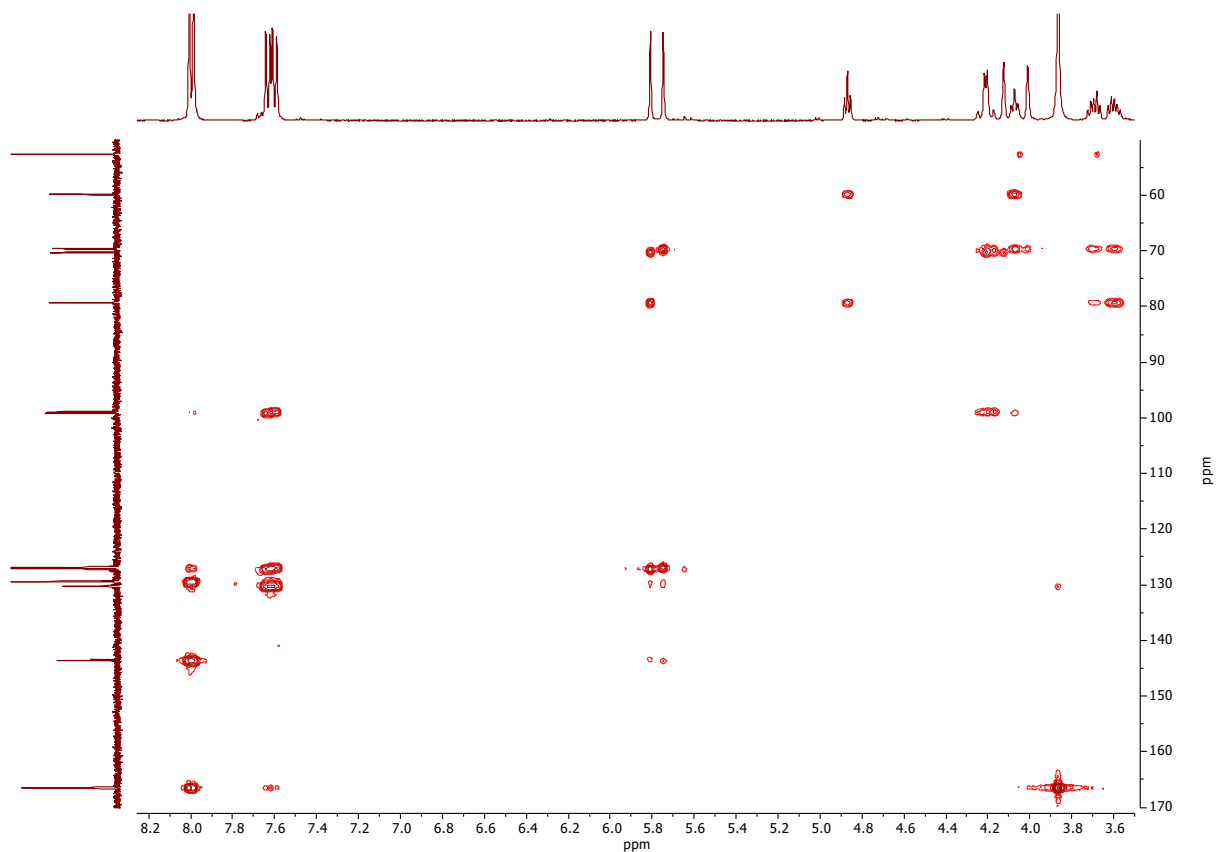
A 47 | HMBC of DBX-CO₂Me
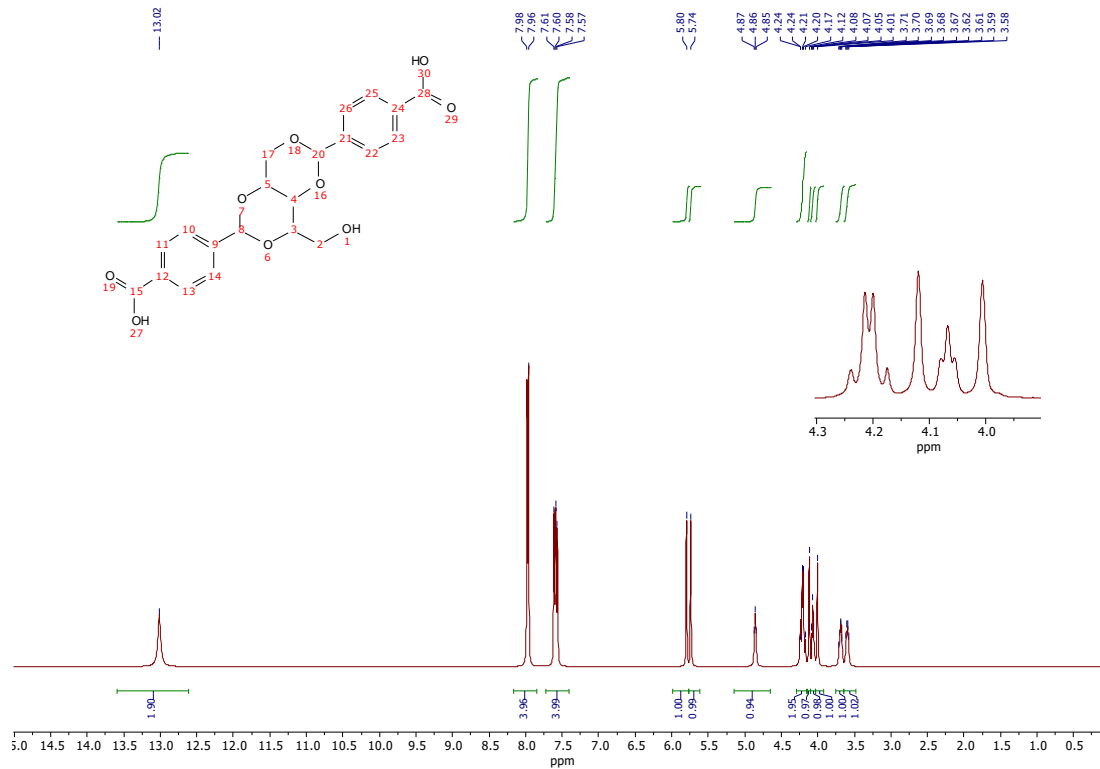
A 48 | ¹H NMR of DBX-CO₂H
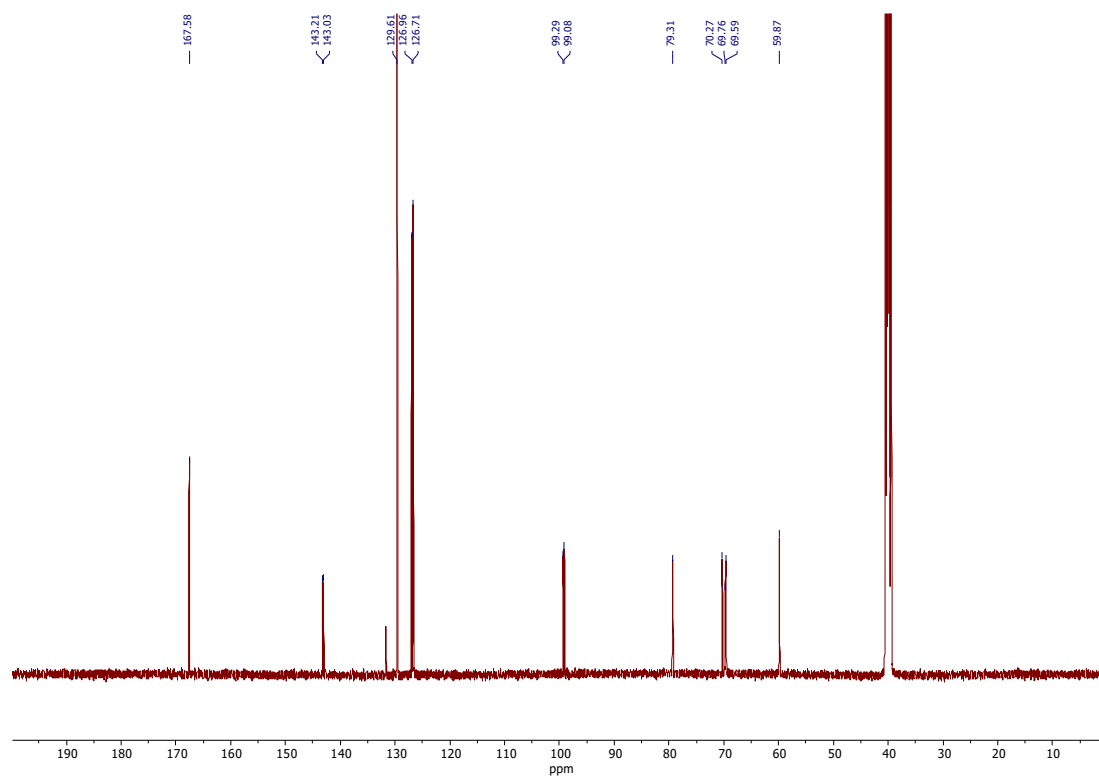
A 49 | ^{13}C NMR of DBX-CO$_2$H
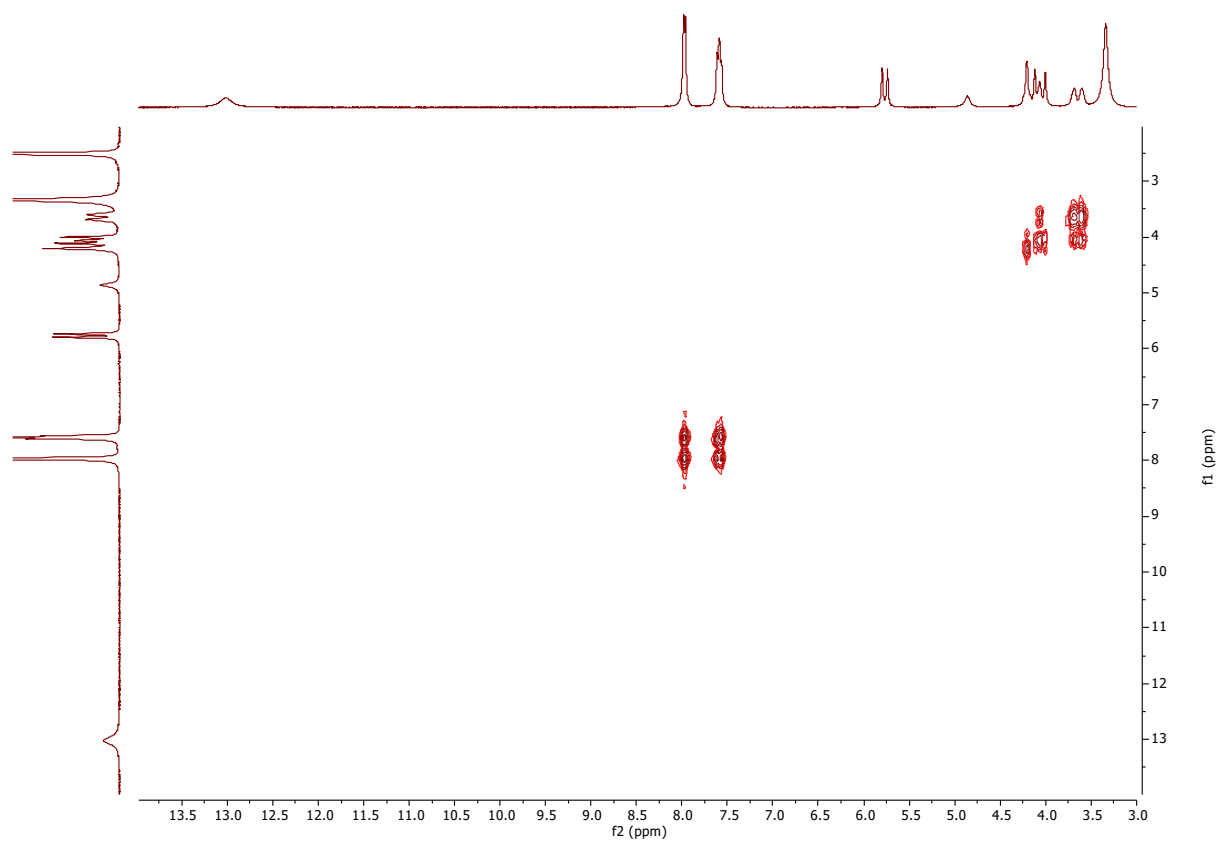
A 50 | COSY of DBX-CO$_2$H
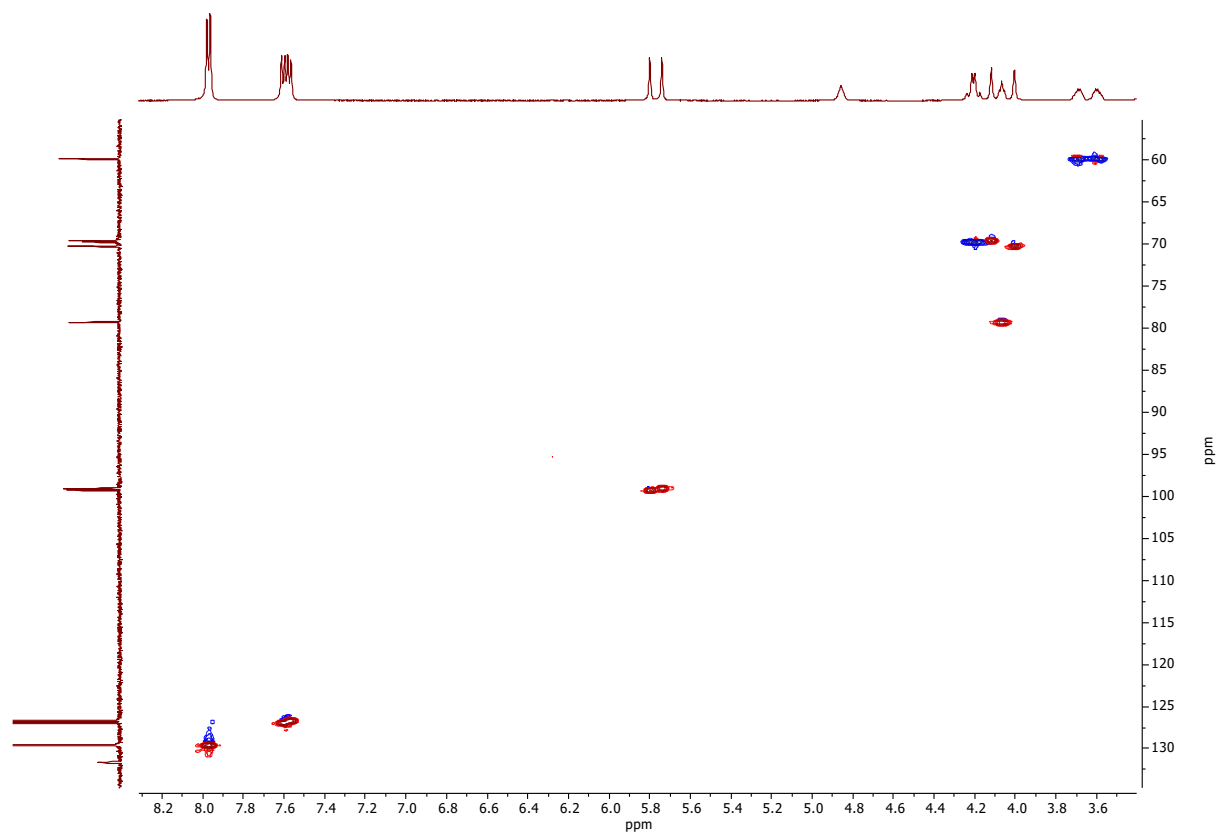
A 51 | HSQC of DBX-CO$_2$H
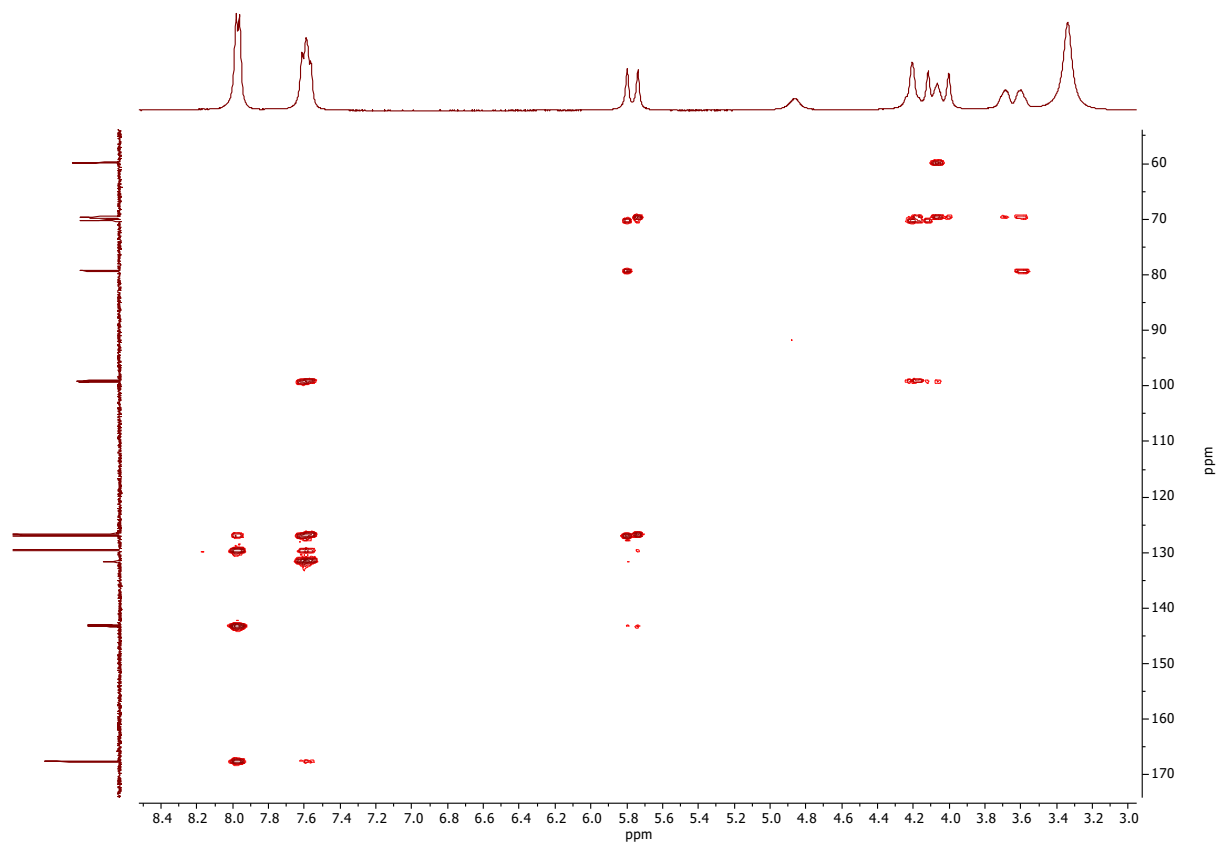
A 52 | HMBC of DBX-CO$_2$H
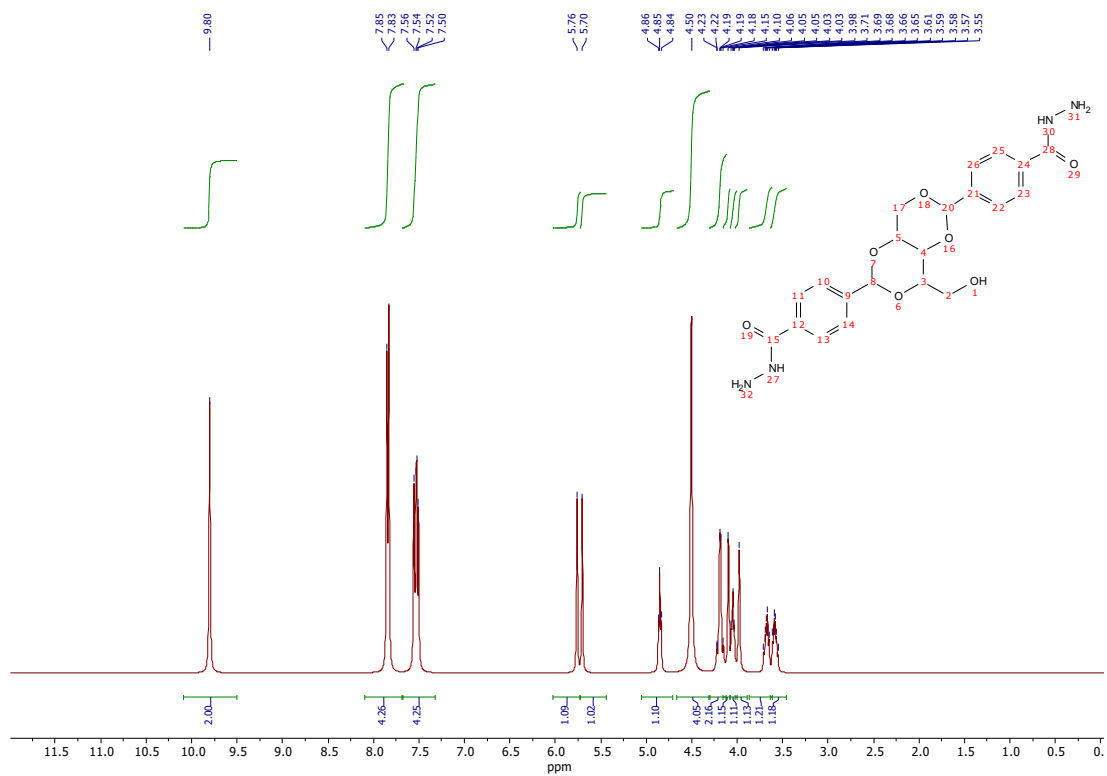
A 53 | ^{1}H NMR of DBX-CONHNH$_2$
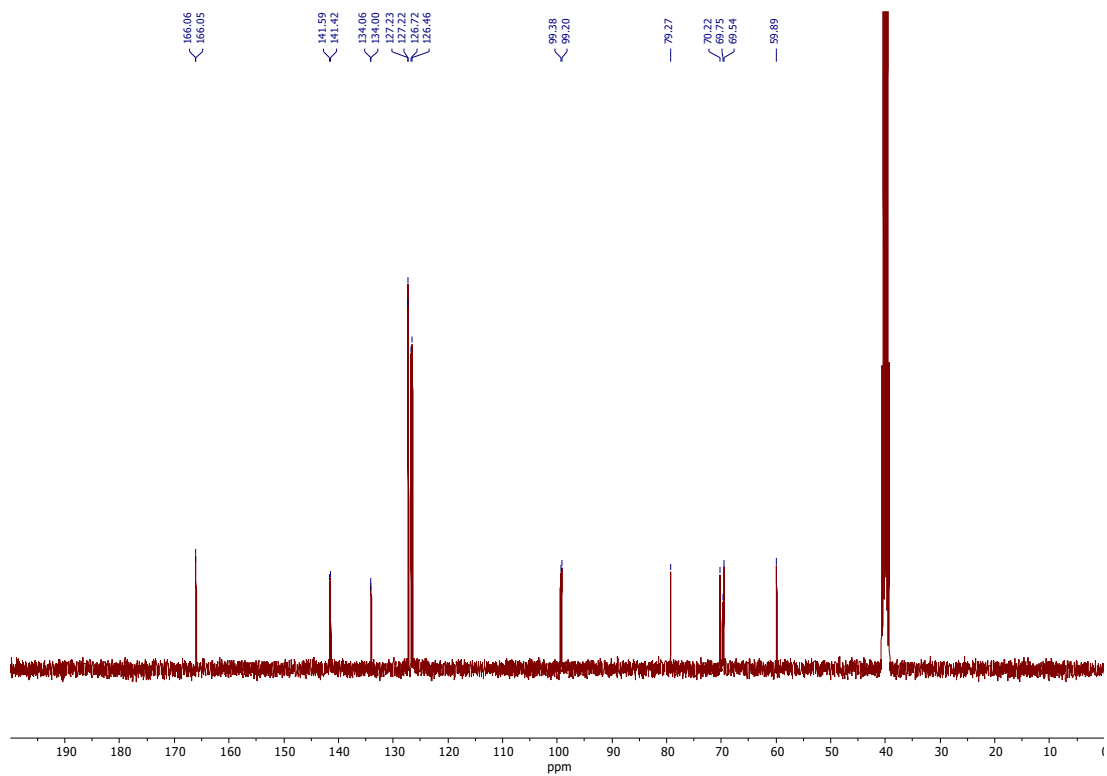
A 54 | ^{13}C NMR of DBX-CONHNH$_2$
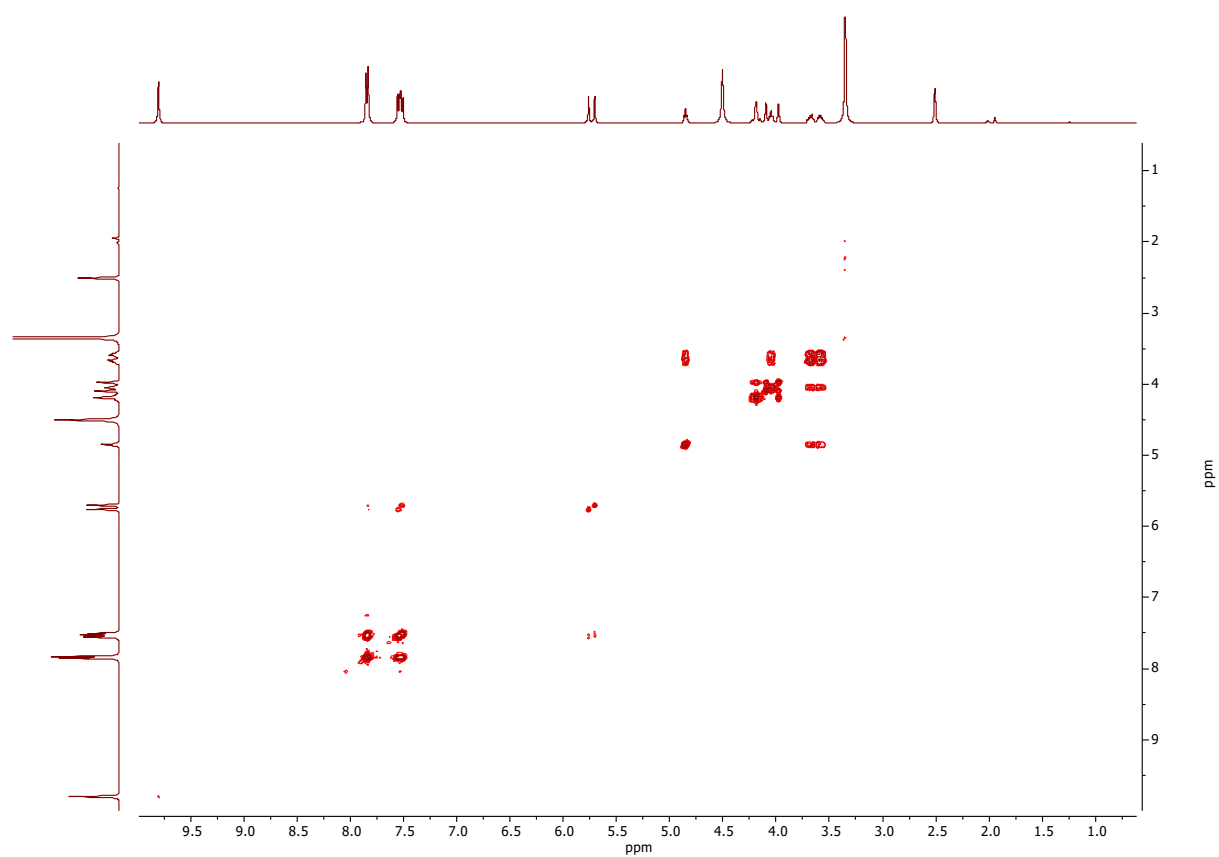
A 55 | COSY of DBX-CONHNH₂
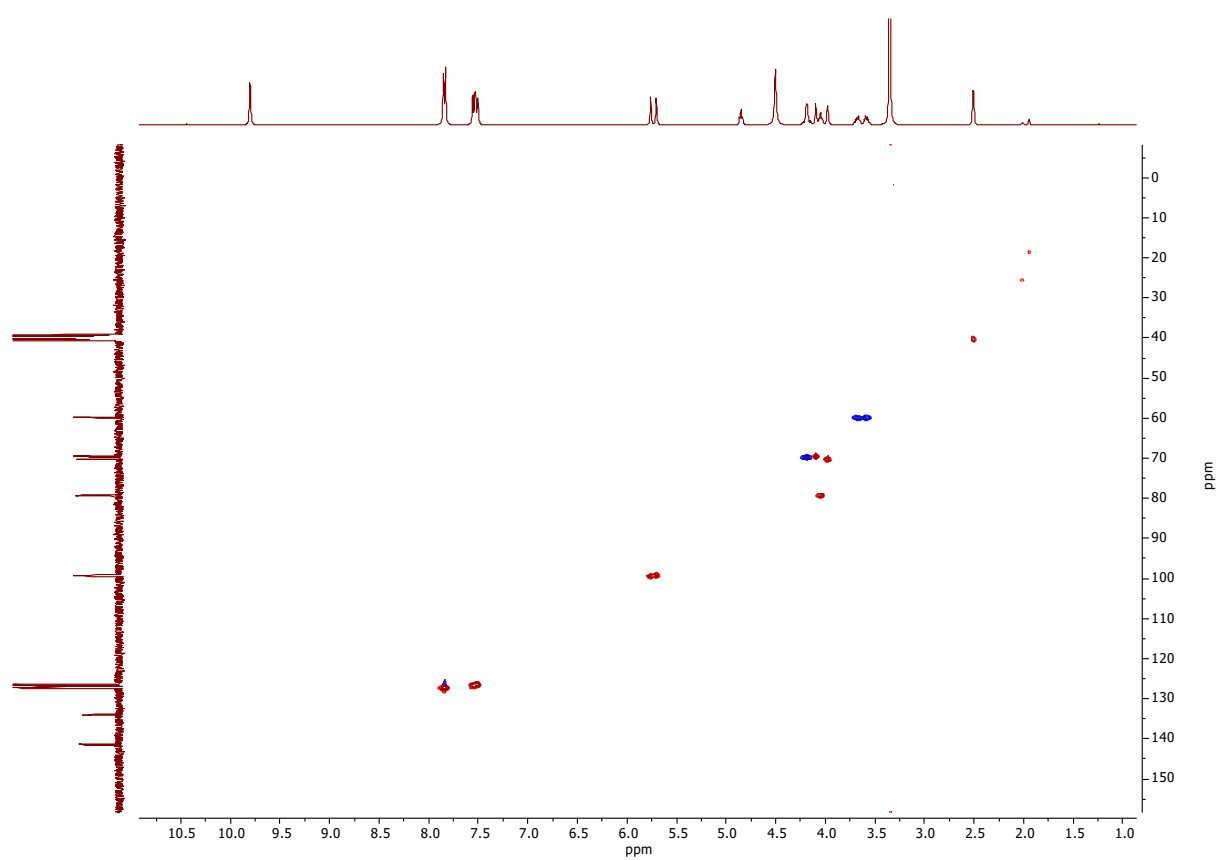
A 56 | HSQC of DBX-CONHNH₂
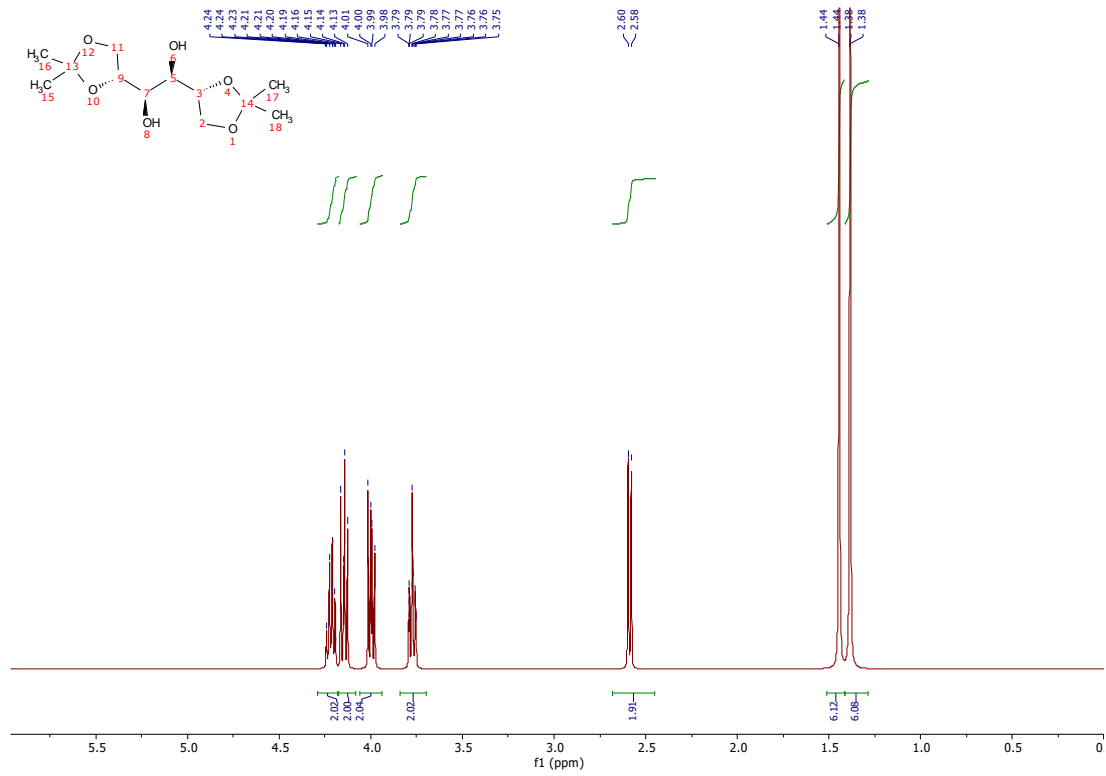
A 57 | ¹H NMR of MDA
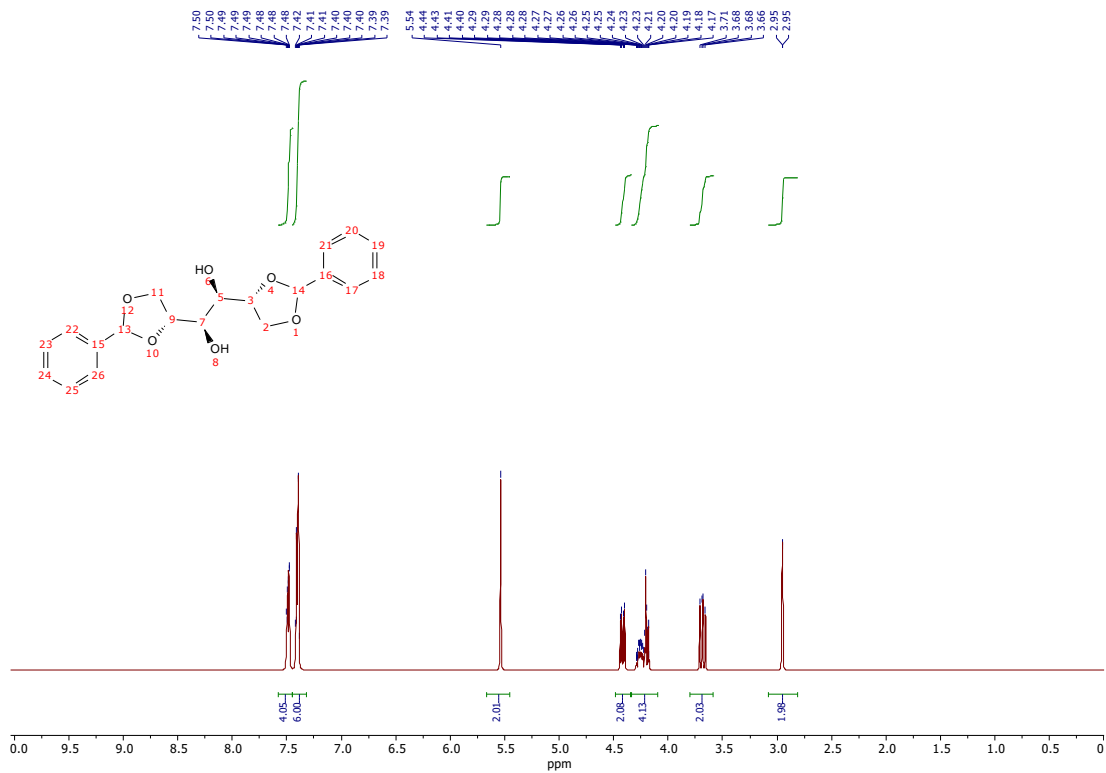
A 58 | ¹H NMR of MDP
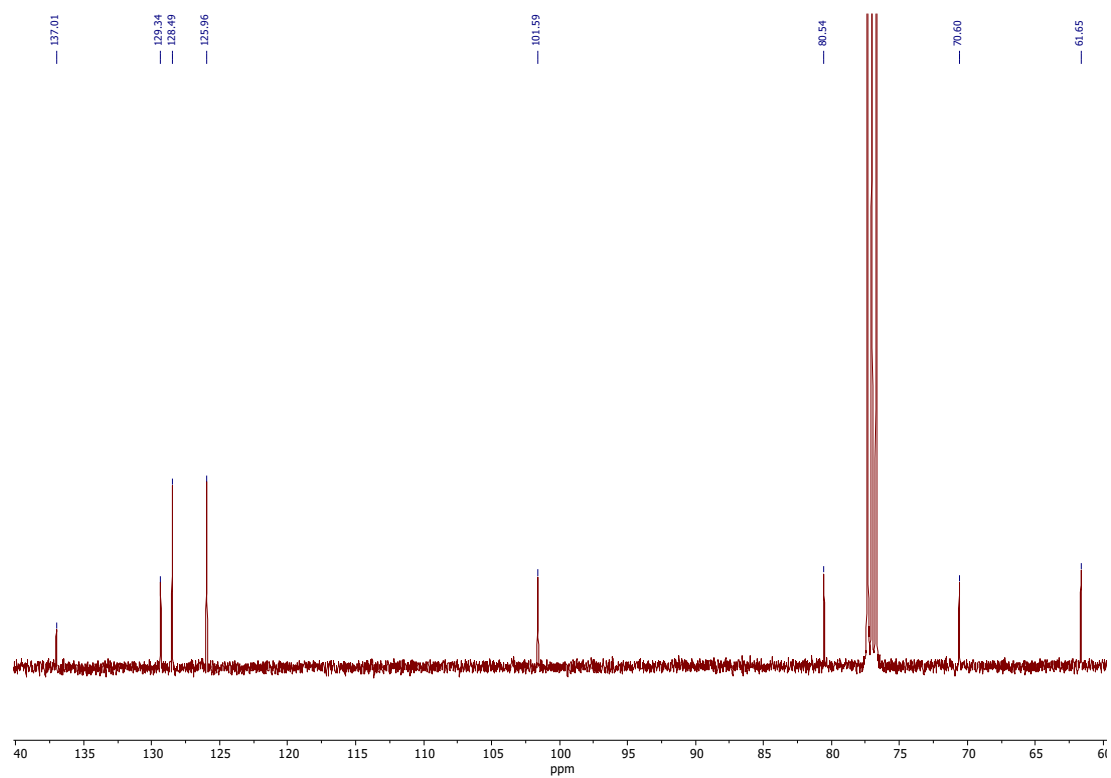
A 59 | ^{13}C NMR of MDP
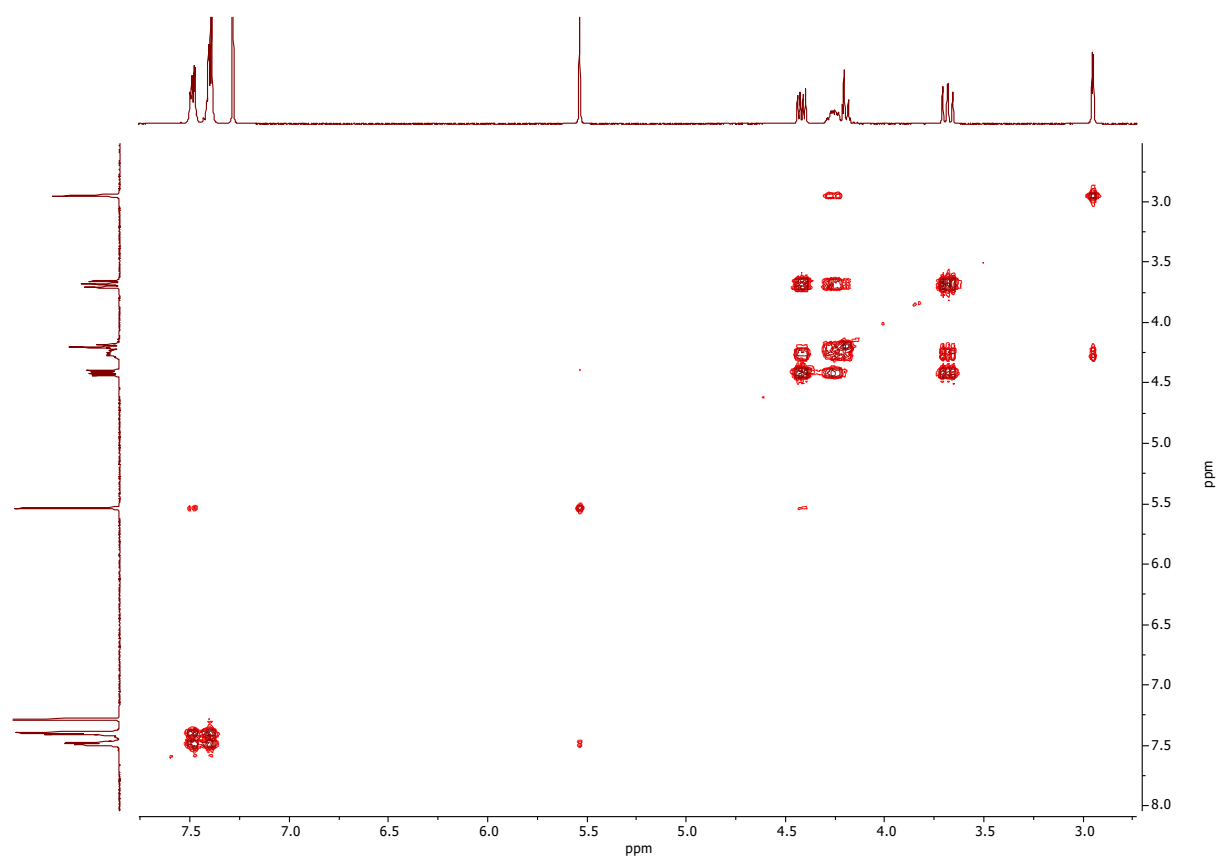
A 60 | COSY of MDP
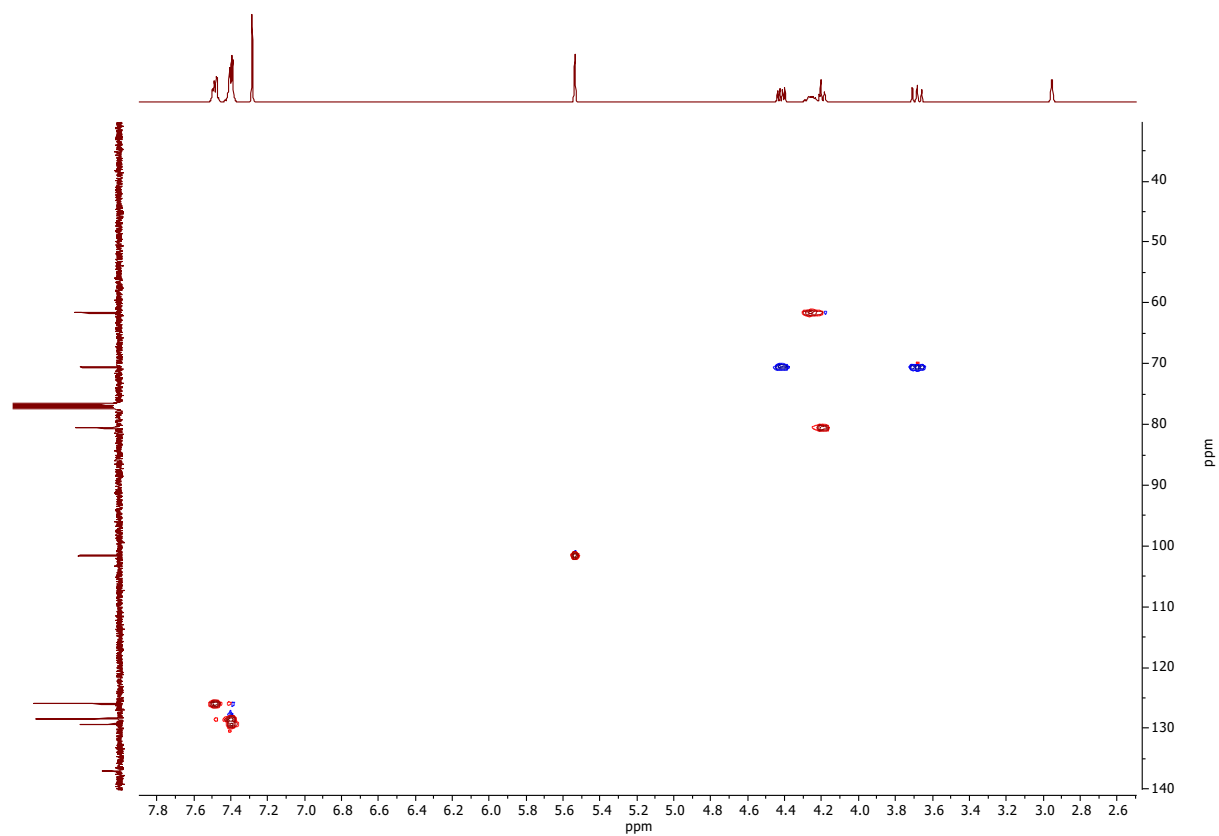
A 61 | HSQC of MDP
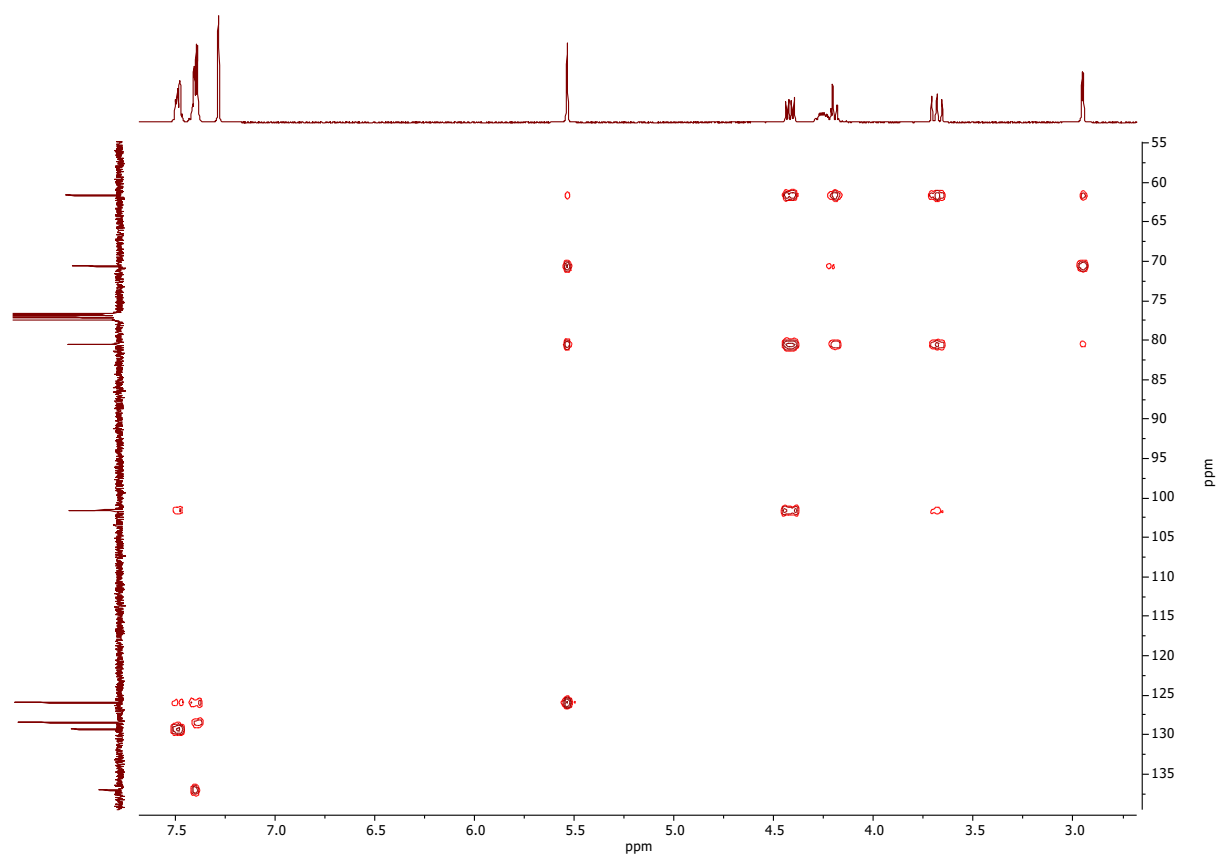
A 62 | HMBC of MDP
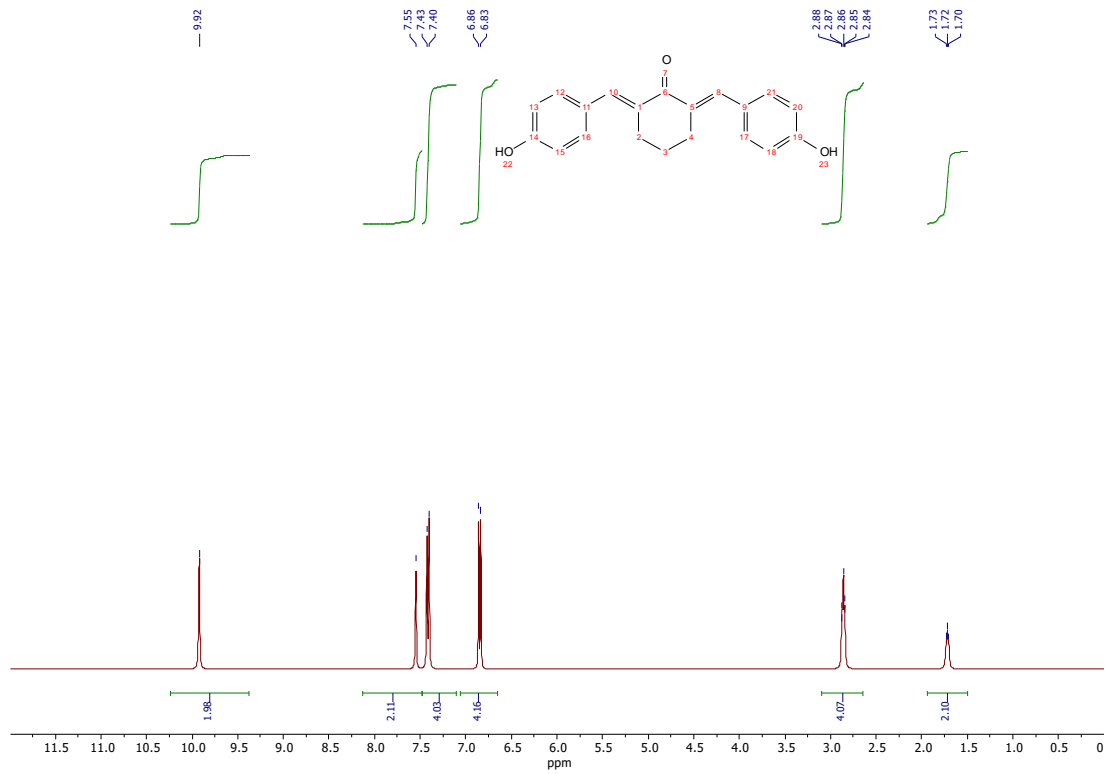
A 63 | ^{1}H NMR of BHC
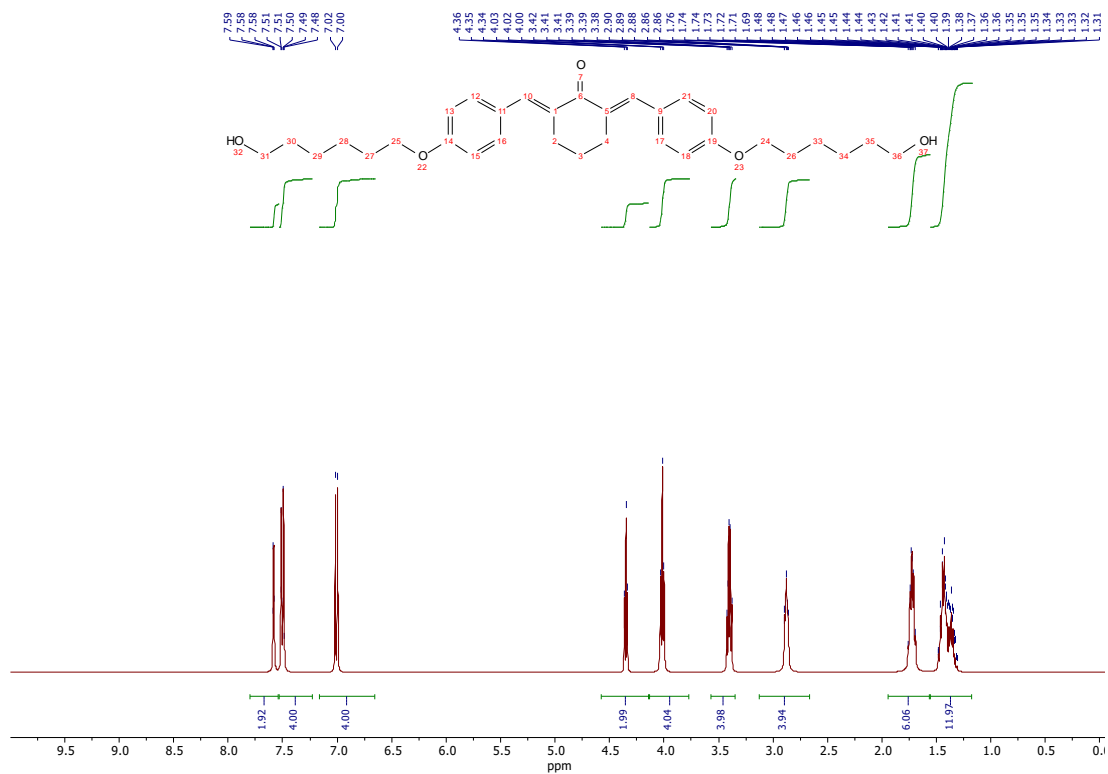
A 64 | ^{1}H NMR of BHC-6
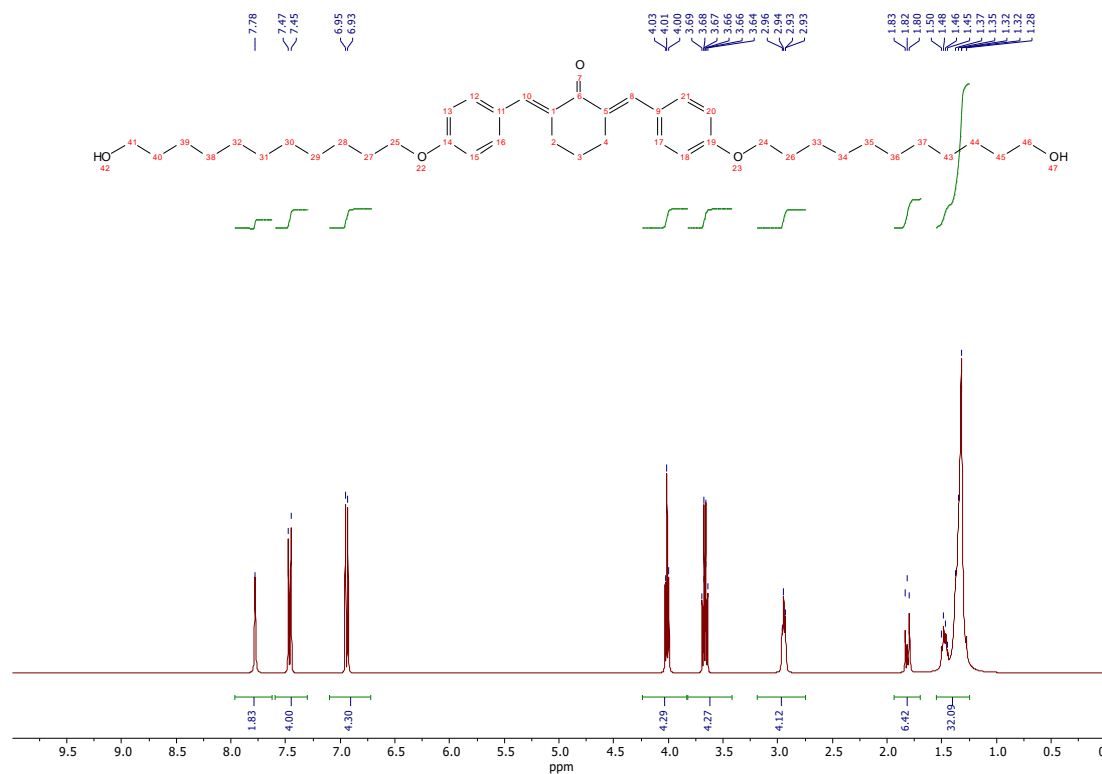
A 65 | ^{1}H NMR of BHC-11

A.Table 1 | Selected hydrogen bonding parameters

| D—H···A	D—H (Å)	H···A (Å)	D···A (Å)	D—H···A (°)
MBS-Cinn				
O2A—H2A···O4B^i	0.841	1.946	2.704 (11)	149.9
O8A—H8A···O8B	0.840	1.968	2.755 (10)	155.7
O8B—H8B···O4B^{ii}	0.840	1.937	2.653 (10)	142.5
MBS-Van				
O2—H2···O12^i	0.840	1.962	2.7898 (18)	168.3
O4—H4···O8^{iii}	0.825 (19)	1.84 (19)	2.6531 (17)	165.1 (3)
O8—H8···O4^{iv}	0.844 (19)	1.87 (2)	2.6649 (17)	155.9 (2)
O12—H12···O2^v	0.83 (2)	1.93 (2)	2.7580 (19)	174.9 (3)

Symmetry code(s): (i) x-1, y+1, z; (ii) x-1, y, z; (iii) -x, y+1/2, -z+1; (iv) x, y-1, z; (v) x+1, y, z.

A.Table 2 | Single crystal X-ray Experimental details

|	MBS-Cinn	MBS-Van
Chemical formula	$0.5(C_{15}H_{20}O_6) \cdot 0.5(C_{15}H_{18}O_6)$	$C_{14}H_{20}O_8$
M_r	296.31	316.30
Temperature (K)	120	120
Crystal system	Monoclinic	Monoclinic
Space group	$P2_1$	$P2_1$
a, b, c (Å)	4.7673 (11), 9.5601 (19), 31.386 (6)	8.92283 (14), 4.60123 (7), 17.4539 (3)
α, β, γ (°)	90, 92.31 (2), 90	90, 92.9088 (15), 90
V (Å^3)	1429.3 (5)	715.66 (2)
Z	4	2
Radiation type	Cu $K\alpha$	Cu $K\alpha$
μ (mm^{-1})	0.89	1.03
Crystal size (mm)	$0.27 \times 0.03 \times 0.02$	$0.20 \times 0.05 \times 0.03$
Reflections collected	8745	9752
Independent reflections	4045	2828
Reflections [$I > 2\sigma\mu\kappa, \lambda\varphi\varphi\lambda\kappa, \mu\varphi\varphi\varphi\varphi\eta\gamma\eta(I)$]	2892	2777
R_{int}	0.124	0.023
θ_{max} (°)	58.9	73.5
$(\sin \theta/\lambda)_{max}$ (Å^{-1})	0.556	0.622
$R[F^2 > 2\sigma (F^2)]$, $wR(F^2)$, S	0.088	0.025
wR(F^2) [all data]	0.224	0.067
Goodness-of-on on F^2	1.06	1.06
No. of reflections	4045	2828
No. of parameters	449	201
No. of restraints	697	7
Largest diff. Peak/hole (eÅ^{-3})	0.41, -0.28	0.21, -0.18
CCDC number	1945762	1945763
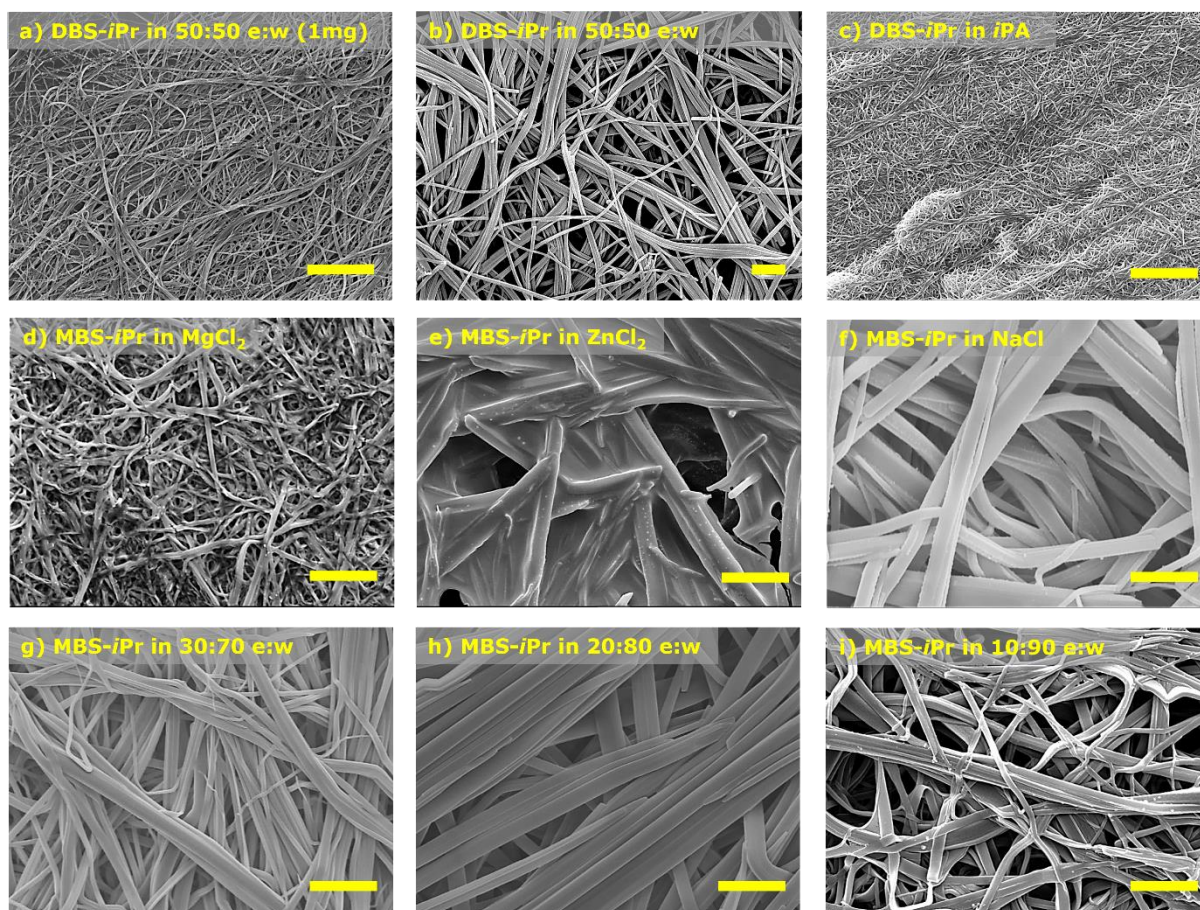
A 66 | SEM micrographs of DBS-*i*Pr and MBS-*i*Pr xerogels formed in different solvents. All in 1% w/v (except a – 0.1% w/v) upon heating and cooling. Conditions: xerogel prepared by drying the gel in ain and then coating with 5nm IR before imaging under vacuum at 5 kV. Scale bar in all images is 1 µm.
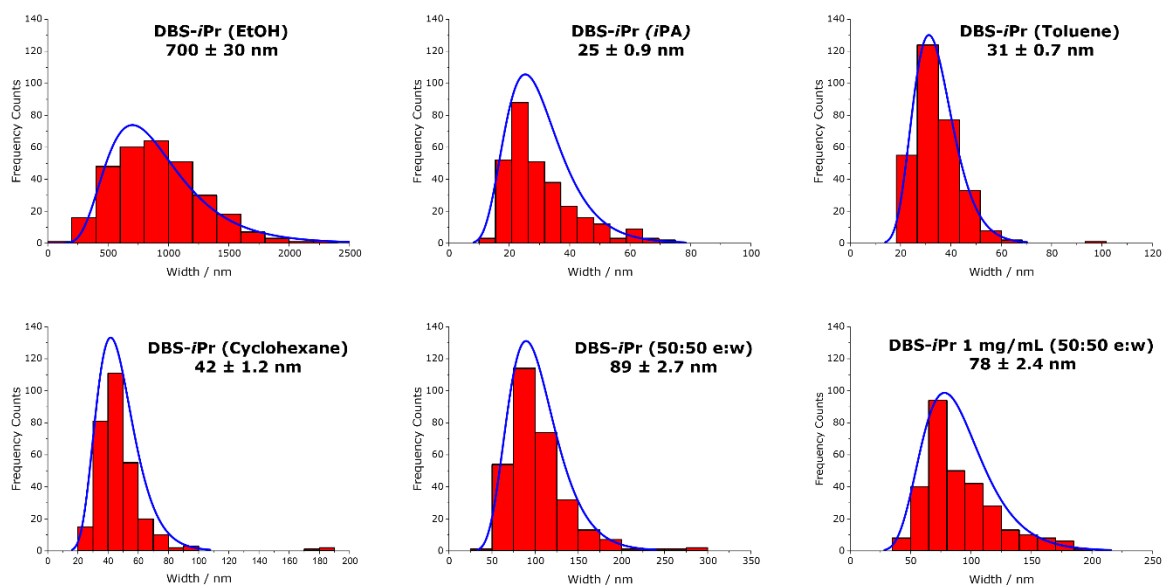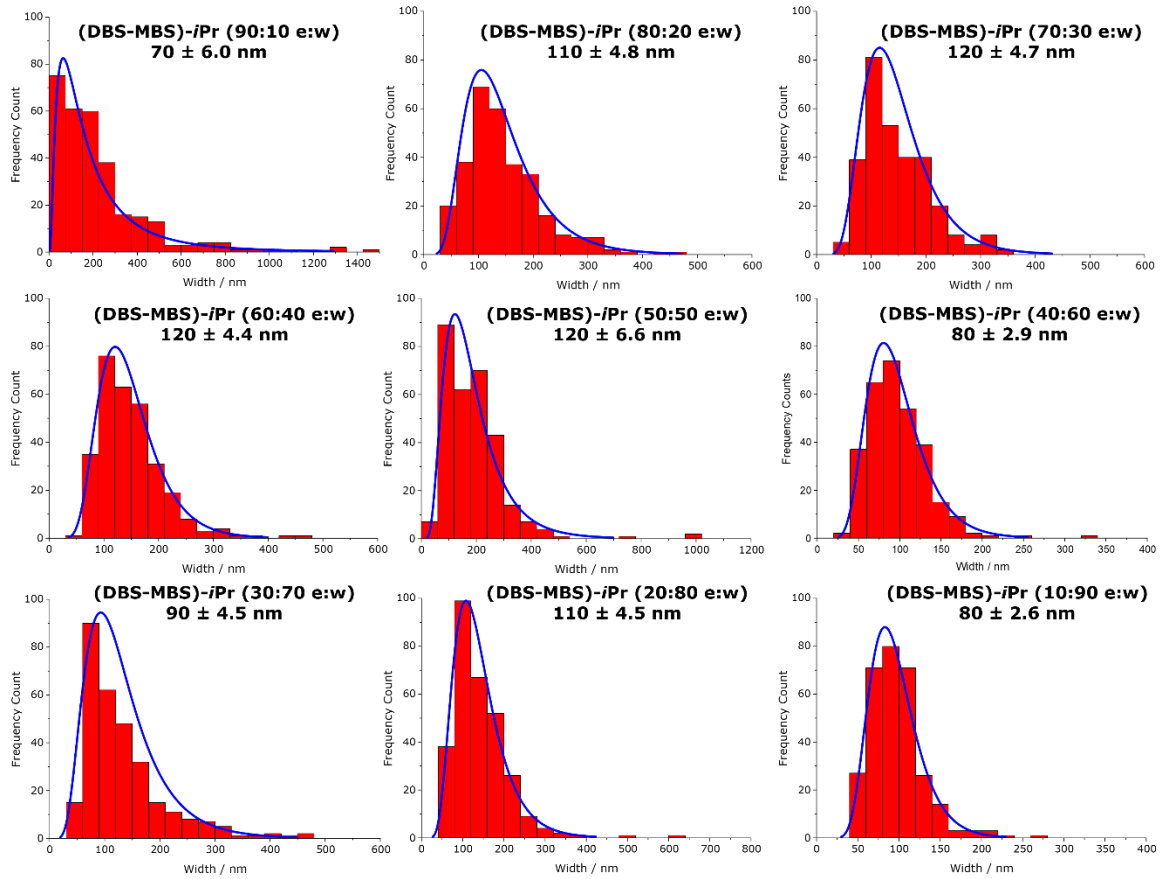
A 67 | Distribution histograms for DBS-*i*Pr xerogels width fibre dimensions from SEM images all at 10 mg mL^{-1} unless stated.
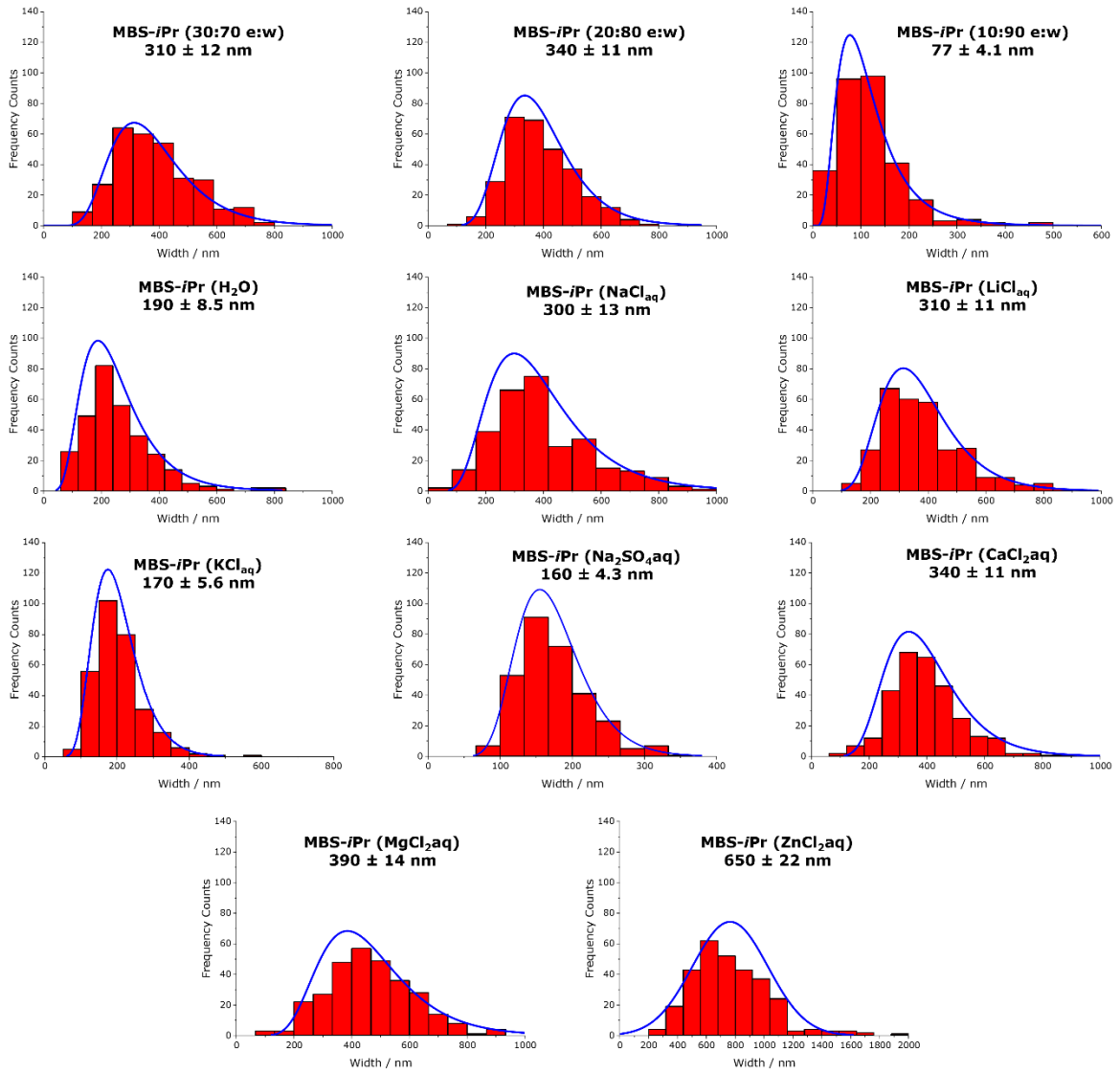
A 68 | Distribution histograms for MBS-*i*Pr xerogels width fibre dimensions from SEM images all at 10 mg mL^{-1}
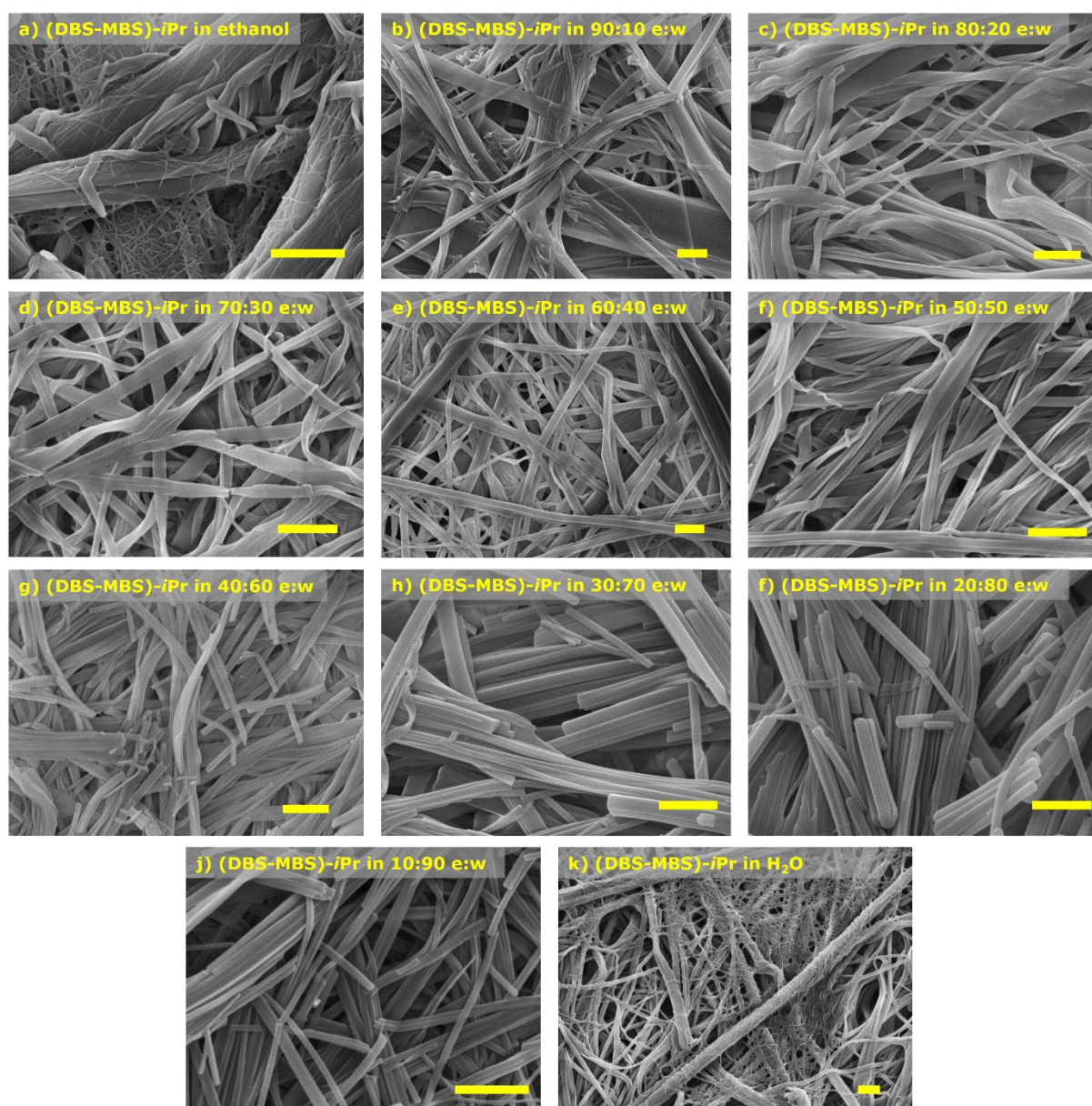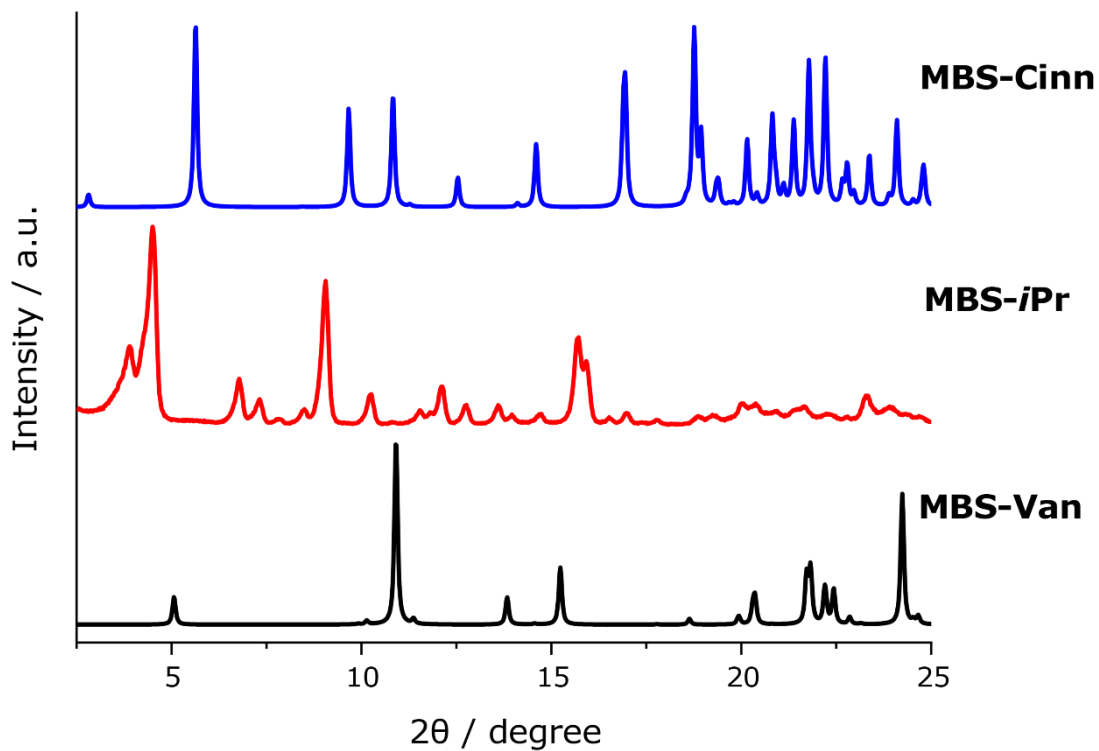
A 69 | SEM micrographs of equimolar xerogels formed in different solvents. All in 1% w/v upon heating and cooling. Conditions: xerogel prepared by drying the gel in ain and then coating with 5nm IR before imaging under vacuum at 5 kV. Scale bar in all images is 1 μm.
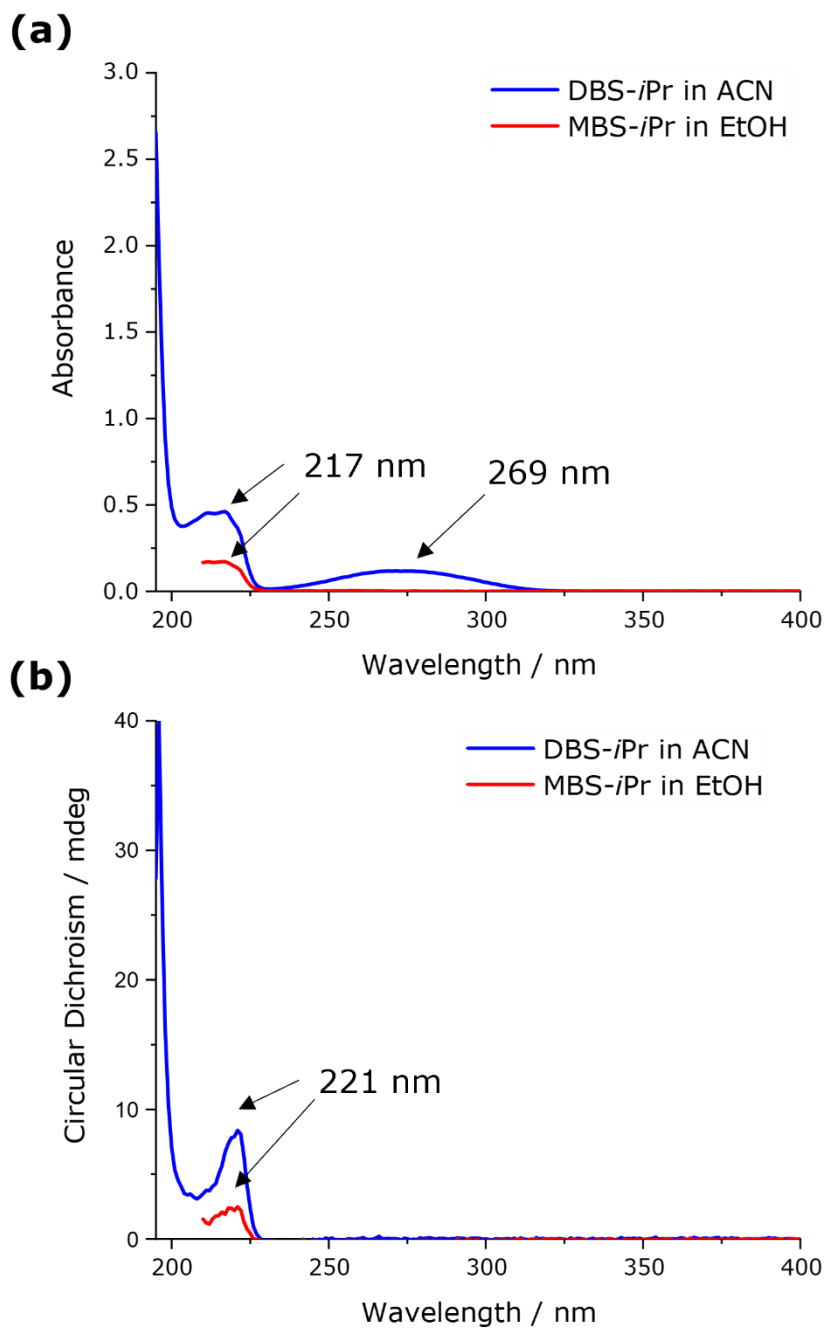
A 70 | Distribution histograms for (DBS-MBS)-*i*Pr xerogels width fibre dimensions from SEM images all at 10 mg mL^{-1}
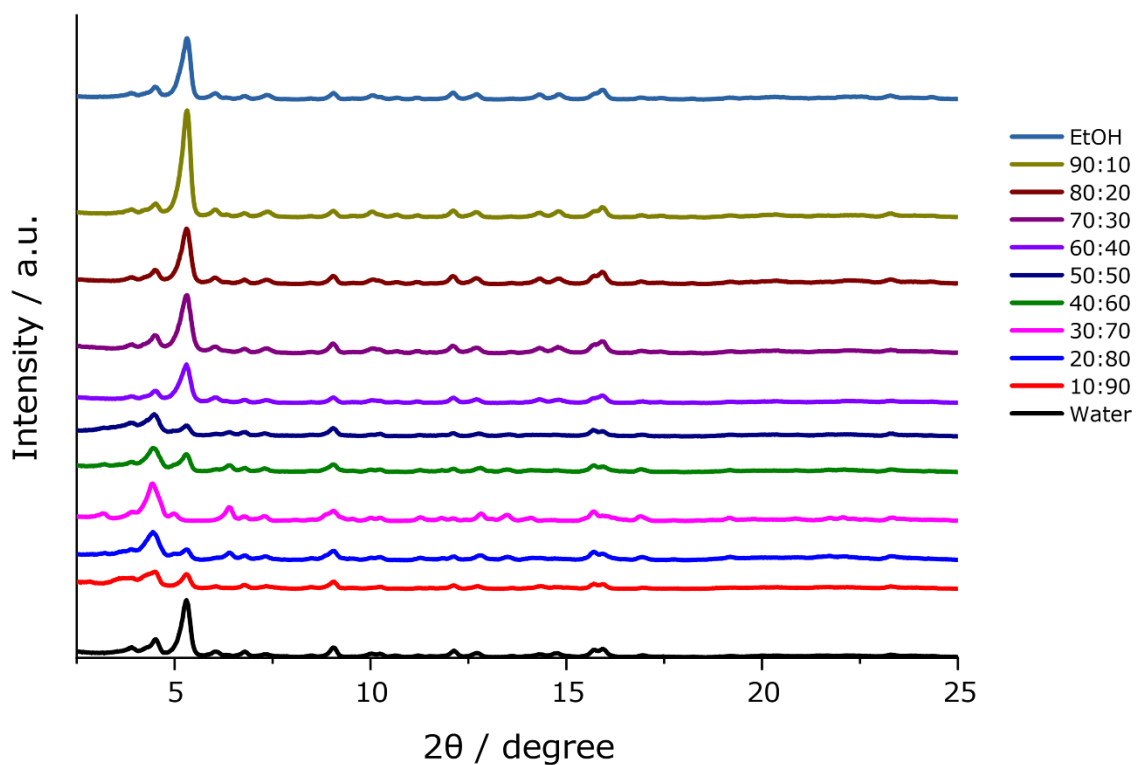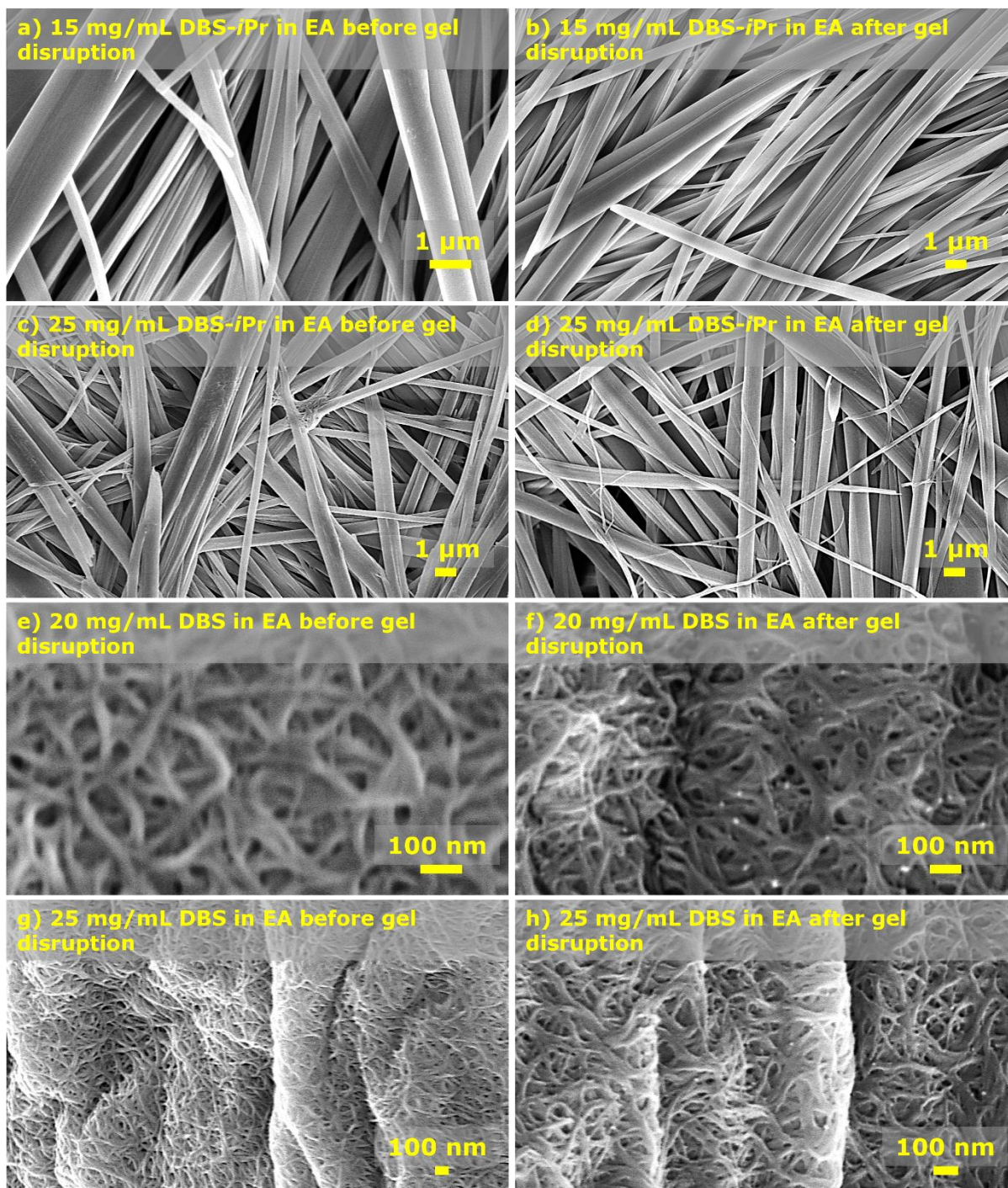
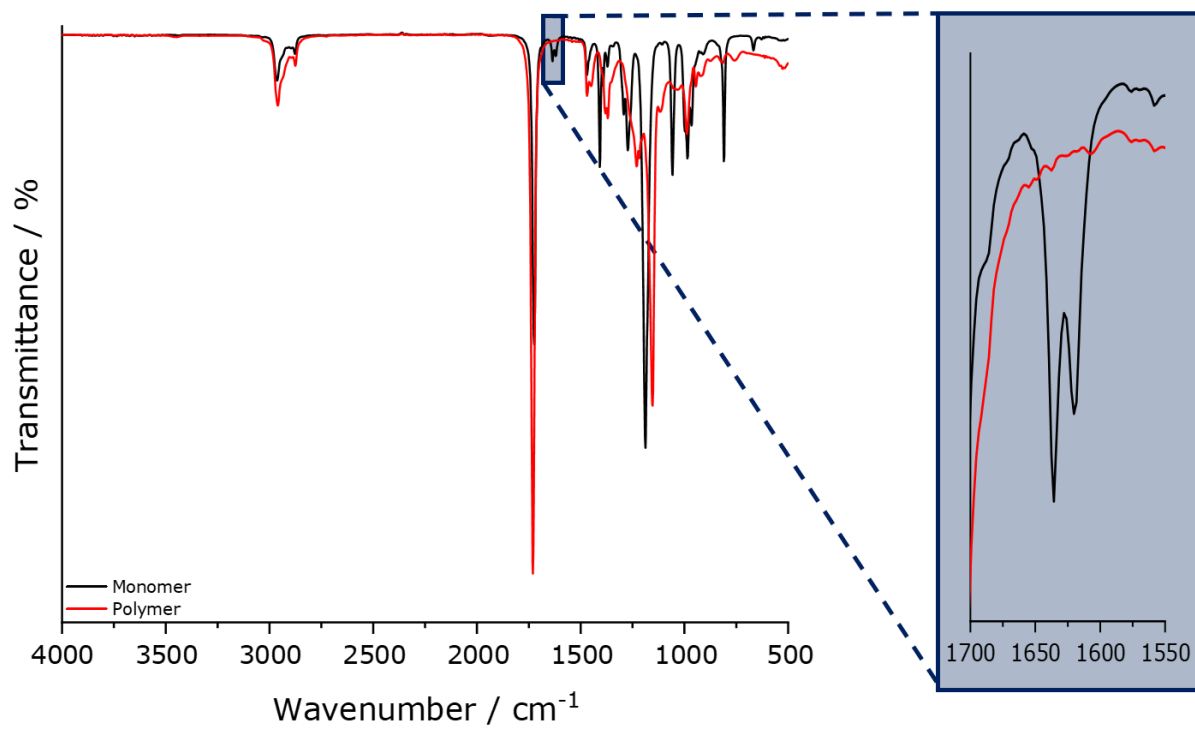A 71 | PXRD of equimolar xerogel made from all ethanolic/water solutions

A 72 | MBS-*i*Pr PXRD spectrum and the simulated PXRD of MBS-Cinn and MBS-Van from single crystal diffraction

(a)

(b)

A 73 | (a) Absorbance and (b) circular dichroism spectra for DBS-*i*Pr in acetonitrile (blue) and MBS-*i*Pr in ethanol (red).

A 74 | SEM micrographs of DBS-*i*Pr and DBS xerogels formed in ethyl acrylate. All in 1% w/v upon heating and cooling. Conditions: xerogel prepared by drying the gel in ain and then coating with 5 nm IR before imaging under vacuum at 5 kV. Scale bars in images are 1 μm for a – d, and 100 nm for e – h.

A 75 | FTIR of P*i*BA